Journal of Operational Oceanography

ISSN: (Print) (Online) Journal homepage: https://www.tandfonline.com/loi/tjoo20

Copernicus Marine Service Ocean State Report, Issue 5

Karina von Schuckmann ((Editor)), Pierre-Yves Le Traon ((Editor)), Neville Smith (Chair) ((Review Editor)), Ananda Pascual ((Review Editor)), Samuel Djavidnia ((Review Editor)), Jean-Pierre Gattuso ((Review Editor)), Marilaure Grégoire ((Review Editor)), Signe Aaboe, Victor Alari, Brittany E. Alexander, Andrés Alonso-Martirena, Ali Aydogdu, Joel Azzopardi, Marco Bajo, Francesco Barbariol, Mirna Batistić, Arno Behrens, Sana Ben Ismail, Alvise Benetazzo, Isabella Bitetto, Mireno Borghini, Laura Bray, Arthur Capet, Roberto Carlucci, Sourav Chatterjee, Jacopo Chiggiato, Stefania Ciliberti, Giulia Cipriano, Emanuela Clementi, Paul Cochrane, Gianpiero Cossarini, Lorenzo D'Andrea, Silvio Davison, Emily Down, Aldo Drago, Jean-Noël Druon, Georg Engelhard, Ivan Federico, Rade Garić, Adam Gauci, Riccardo Gerin, Gerhard Geyer, Rianne Giesen, Simon Good, Richard Graham, Marilaure Grégoire, Eric Greiner, Kjell Gundersen, Pierre Hélaouët, Stefan Hendricks, Johanna J. Heymans, Jason Holt, Marijana Hure, Mélanie Juza, Dimitris Kassis, Paula Kellett, Maaike Knol-Kauffman, Panagiotis Kountouris, Marilii Kõuts, Priidik Lagemaa, Thomas Lavergne, Jean-François Legeais, Pierre-Yves Le Traon, Simone Libralato, Vidar S. Lien, Leonardo Lima, Sigrid Lind, Ye Liu, Diego Macías, Ilja Maljutenko, Antoine Mangin, Aarne Männik, Veselka Marinova, Riccardo Martellucci, Francesco Masnadi, Elena Mauri, Michael Mayer, Milena Menna, Catherine Meulders, Jane S. Møgster, Maeva Monier, Kjell Arne Mork, Malte Müller, Jan Even Øie Nilsen, Giulio Notarstefano, José L. Oviedo, Cyril Palerme, Andreas Palialexis, Diego Panzeri, Silvia Pardo, Elisaveta Peneva, Paolo Pezzutto, Annunziata Pirro, Trevor Platt, Pierre-Marie Poulain, Laura Prieto, Stefano Querin, Lasse Rabenstein, Roshin P. Raj, Urmas Raudsepp, Marco Reale, Richard Renshaw, Antonio Ricchi, Robert Ricker, Sander Rikka, Javier Ruiz, Tommaso Russo, Jorge Sanchez, Rosalia Santoleri, Shubha Sathyendranath, Giuseppe Scarcella, Katrin Schroeder, Stefania Sparnocchia, Maria Teresa Spedicato, Emil Stanev, Joanna Staneva, Alexandra Stocker, Ad Stoffelen, Anna Teruzzi, Bryony Townhill, Rivo Uiboupin, Nadejda Valcheva, Luc Vandenbulcke, Håvard Vindenes, Karina von Schuckmann, Nedo Vrgoč, Sarah Wakelin & Walter Zupa

To cite this article: Karina von Schuckmann ((Editor)), Pierre-Yves Le Traon ((Editor)), Neville Smith (Chair) ((Review Editor)), Ananda Pascual ((Review Editor)), Samuel Djavidnia ((Review Editor)), Jean-Pierre Gattuso ((Review Editor)), Marilaure Grégoire ((Review Editor)), Signe Aaboe, Victor Alari, Brittany E. Alexander, Andrés Alonso-Martirena, Ali Aydogdu, Joel Azzopardi, Marco Bajo, Francesco Barbariol, Mirna Batistić, Arno Behrens, Sana Ben Ismail, Alvise Benetazzo, Isabella Bitetto, Mireno Borghini, Laura Bray, Arthur Capet, Roberto Carlucci, Sourav Chatterjee, Jacopo Chiggiato, Stefania Ciliberti, Giulia Cipriano, Emanuela Clementi, Paul Cochrane, Gianpiero Cossarini, Lorenzo D'Andrea, Silvio Davison, Emily Down, Aldo Drago, Jean-Noël Druon, Georg Engelhard, Ivan Federico, Rade Garić, Adam Gauci, Riccardo Gerin, Gerhard Geyer, Rianne

European Commission

COPERNICUS MARINE SERVICE

OCEAN STATE REPORT

Issue 5, 2021

Journal of Operational Oceanography
Volume 14, Supplement 1

Copernicus
Europe's eyes on Earth

Copernicus Marine Service

Implemented by
MERCATOR OCEAN INTERNATIONAL

Taylor & Francis
Taylor & Francis Group

MARINE

Journal of Operational Oceanography

Aims and scope
The *Journal of Operational Oceanography* will publish papers which examine the role of oceanography in contributing to the fields of:

- Numerical Weather Prediction
- Development of Climatologies
- Implications of Ocean Change
- Ocean and Climate Forecasting
- Ocean Observing Technologies
- Eutrophication
- Climate Assessment
- Shoreline Change
- Marine and Sea State Prediction
- Model Development and Validation
- Coastal Flooding
- Reducing Public Health Risks
- Short-Range Ocean Forecasting
- Forces on Structures
- Ocean Policy
- Protecting and Restoring Ecosystem health
- Controlling and Mitigating Natural Hazards
- Safe and Efficient Marine Operations

The *Journal of Operational Oceanography* will also publish papers which address the requirements of the:

- Global Ocean Observing System (GOOS)
- Global Climate Observing System (GCOS)
- Global Monitoring for Environment and Security (GMES)
- Global Earth Observing System of Systems (GEOSS)

The *Journal of Operational Oceanography* will also publish papers which address the needs of one or more of a wide range of end user communities including:

- Shipping
- Marine Energy
- Weather Services
- Fishing
- Port Management
- Wastewater Management
- Search and Rescue
- National Security
- Charting and Navigational Services
- Public Health
- Conservation
- Insurance and Re-insurance
- Recreation and tourism
- Marine Mineral Extraction
- Environmental Regulation
- Education
- Aquaculture
- Coastal Management

All submitted manuscripts are subject to initial appraisal by the Editor, and, if found suitable for further consideration, enter peer review by independent, anonymous expert referees. All peer review is single blind.

Authors are requested to submit manuscripts via the journal's online submission system following the Instructions for Authors.

Submitting to *Journal of Operational Oceanography*
For more information about the journal and guidance on how to submit, please see www.tandfonline.com/tjoo

Journal of Operational Oceanography

Print ISSN 1755-876X, Online ISSN 1755-8778

Subscription information
For information and subscription rates please see www.tandfonline.com/pricing/journal/tjoo

Informa UK Limited, trading as Taylor & Francis Group, has a flexible approach to subscriptions enabling us to match individual libraries' requirements. This journal is available via a traditional institutional subscription (either print with online access, or online only at a discount) or as part of our libraries, subject collections or archives. For more information on our sales packages please visit www.tandfonline.com/page/librarians

All current institutional subscriptions include online access for any number of concurrent users across a local area network to the currently available backfile and articles posted online ahead of publication. Subscriptions purchased at the personal rate are strictly for personal, non-commercial use only. The reselling of personal subscriptions is prohibited. Personal subscriptions must be purchased with a personal check or credit card. Proof of personal status may be requested.

Back issues: Taylor & Francis Group retains a two-year back issue stock of journals. Older volumes are held by our official stockists to whom all orders and enquiries should be addressed: Periodicals Service Company, 351 Fairview Ave., Suite 300, Hudson, New York 12534, USA. Tel: +1 518 537 4700; fax: +1 518 537 5899; email: psc@periodicals.com.

Ordering information: Please contact your local Customer Service Department to take out a subscription to the Journal: USA, Canada: Taylor & Francis, Inc., 530 Walnut Street, Suite 850, Philadelphia, PA 19106, USA. Tel: +1 800 354 1420; Fax: +1 215 207 0050. UK/Europe/Rest of World: T&F Customer Services, Informa UK Ltd, Sheepen Place, Colchester, Essex, CO3 3LP, United Kingdom. Tel: +44 (0) 20 7017 5544; Fax: +44 (0) 20 7017 5198; Email: subscriptions@tandf.co.uk.

Dollar rates apply to all subscribers outside Europe. Euro rates apply to all subscribers in Europe, except the UK where the pound sterling price applies. If you are unsure which rate applies to you please contact Customer Services in the UK. All subscriptions are payable in advance and all rates include postage. Journals are sent by air to the USA, Canada, Mexico, India, Japan and Australasia. Subscriptions are entered on an annual basis, i.e. January to December. Payment may be made by sterling check, dollar check, euro check, international money order, National Giro or credit cards (Amex, Visa and Mastercard).

Airfreight and mailing in the USA by agent named Air Business Ltd, c/o Worldnet Shipping Inc., 156-15, 146th Avenue, 2nd Floor, Jamaica, NY 11434, USA.

Periodicals postage paid at Jamaica NY 11431.

US Postmaster: Send address changes to *Journal of Operational Oceanography*, Air Business Ltd, c/o Worldnet Shipping Inc., 156-15, 146th Avenue, 2nd Floor, Jamaica, NY 11434, USA.

Subscription records are maintained at Taylor & Francis Group, 4 Park Square, Milton Park, Abingdon, OX14 4RN, United Kingdom.

All Taylor and Francis Group journals are printed on paper from renewable sources by accredited partners.

VOL. 14, NO. S1, SEPTEMBER 2021

COPERNICUS MARINE SERVICE OCEAN STATE REPORT, ISSUE 5

Editors

Karina von Schuckmann Pierre-Yves Le Traon

Review Editors

Neville Smith (Chair) Ananda Pascual Samuel Djavidnia

Jean-Pierre Gattuso Marilaure Grégoire

To cite the entire report

How to cite the entire report: von Schuckmann, K., P.-Y. Le Traon, N. Smith, A. Pascual, S. Djavidnia, J.-P. Gattuso, M. Grégoire (Eds.) (2021) Copernicus Marine Service Ocean State Report, Issue 5, Journal of Operational Oceanography, 14:sup1, s1–s185; DOI: 10.1080/1755876X.2021.1946240

To cite a specific section in the report (example)

S. Aaboe, S. Lind, S. Hendricks, E. Down, T. Lavergne and R. Ricker (2021). Sea-ice and ocean conditions surprisingly normal in the Svalbard-Barents Sea region after large sea-ice inflows in 2019. In: Copernicus Marine Service Ocean State Report, Issue 5, Journal of Operational Oceanography, 14:sup1, s140–s148; DOI: 10.1080/1755876X.2021.1946240

AUTHOR AFFILIATIONS (ALPHABETICAL BY NAME)

Signe Aaboe, MET Norway, Norway
Victor Alari, Tallinn University of Technology (TalTech), Estonia
Brittany E. Alexander, European Marine Board, Belgium
Andrés Alonso-Martirena, Qualitas Instruments S.A., Spain
Ali Aydogdu, Fondazione Centro Euro-Mediterraneo sui Cambiamenti Climatici, Italy
Joel Azzopardi, University of Malta, Malta
Marco Bajo, Institute of Marine Sciences (CNR-ISMAR), Italy
Francesco Barbariol, Consiglio Nazionale delle Ricerche, Istituto di Scienze Marine (CNR-ISMAR), Italy
Mirna Batistić, University of Dubrovnik, Institute for Marine and Coastal Research, Croatia
Arno Behrens, Helmholtz-Zentrum Geesthacht, Zentrum für Material- und Küstenforschung GmbH, Germany
Sana Ben Ismail, Institut National des Sciences et Technologies de la Mer (INSTM), Tunesia
Alvise Benetazzo, Consiglio Nazionale delle Ricerche, Istituto di Scienze Marine (CNR-ISMAR), Italy
Isabella Bitetto, COISPA Tecnologia & Ricerca, Italy
Mireno Borghini, Consiglio Nazionale delle Ricerche, Istituto di Scienze Marine (CNR-ISMAR), Italy
Laura Bray, Hellenic Centre of Marine Research, Greece
Arthur Capet, University of Liège, MAST, Department of Astrophysics, Geophysics and Oceanography, Belgium
Roberto Carlucci, Department of Biology, University of Bari; CoNISMa, Italy
Sourav Chatterjee, National Center for Polar Ocean Research (NCPOR), Ministry of Earth Sciences, India
Jacopo Chiggiato, Consiglio Nazionale delle Ricerche, Istituto di Scienze Marine (CNR-ISMAR), Italy
Stefania Ciliberti, Fondazione Centro Euro-Mediterraneo sui Cambiamenti Climatici, Italy
Giulia Cipriano, Department of Biology, University of Bari; CoNISMa, Italy
Emanuela Clementi, Euro-Mediterranean Center on Climate Change (CMCC), Italy
Paul Cochrane, Drift+Noise, Germany
Gianpiero Cossarini, National Institute of Oceanography and Applied Geophysics (OGS), Italy
Lorenzo D'Andrea, Laboratory of Experimental Ecology and Aquaculture, Dept. of Biology, University of Rome, Italy
Silvio Davison, Consiglio Nazionale delle Ricerche, Istituto di Scienze Marine (CNR-ISMAR), Italy
Emily Down, MET Norway, Norway
Aldo Drago, University of Malta, Malta
Jean-Noël Druon, Joint Research Centre, European Commission, Italy
Georg Engelhard, Centre for Environment, Fisheries and Aquaculture Science (Cefas), UK
Ivan Federico, Euro-Mediterranean Center on Climate Change (CMCC), Italy
Rade Garić, University of Dubrovnik, Institute for Marine and Coastal Research, Croatia
Adam Gauci, University of Malta, Malta
Riccardo Gerin, National Institute of Oceanography and Applied Geophysics (OGS), Italy
Gerhard Geyer, Helmholtz-Zentrum Geesthacht. Zentrum für Material- und Küstenforschung GmbH, Germany
Rianne Giesen, Royal Netherlands Meteorological Institute (KNMI), Netherlands
Simon Good, Met Office, UK
Richard Graham, Met Office, UK
Marilaure Grégoire, University of Liège, MAST, Department of Astrophysics, Geophysics and Oceanography, Belgium
Eric Greiner, Collect Localisation Satellites (CLS), France
Kjell Gundersen, Institute of Marine Research (IMR), Norway
Pierre Hélaouët, Marine Biological Association of the United Kingdom, UK
Stefan Hendricks, Alfred Wegener Institute Helmholtz Center for Polar and Marine Research, Germany
Johanna J. Heymans, European Marine Board, Belgium
Jason Holt, NOC, UK
Marijana Hure, University of Dubrovnik, Institute for Marine and Coastal Research, Croatia
Mélanie Juza, Balearic Islands Coastal Observing and forecasting System (SOCIB), Spain
Dimitris Kassis, Hellenic Centre of Marine Research, Greece
Paula Kellett, European Marine Board, Belgium
Maaike Knol-Kauffman, Norwegian College of Fishery Science, University of Tromsø - The Arctic University of Norway, Norway
Panagiotis Kountouris, Drift+Noise, Germany
Marilii Kõuts, Tallinn University of Technology (TalTech), Estonia
Priidik Lagemaa, Tallinn University of Technology (TalTech), Estonia
Thomas Lavergne, MET Norway, Norway
Jean-François Legeais, Collect Localisation Satellites (CLS), France
Pierre-Yves Le Traon, Mercator Ocean International, France
Simone Libralato, National Institute of Oceanography and Applied Geophysics (OGS), Italy
Vidar S. Lien, Institute of Marine Research (IMR), Norway
Leonardo Lima, Fondazione Centro Euro-Mediterraneo sui Cambiamenti Climatici, Italy
Sigrid Lind, Norwegian Polar Institute, Norway
Ye Liu, Swedish Meteorological and Hydrological institute (SMHI), Estonia

(Continued from previous page)

Diego Macías, European Commission, Joint Research Centre (JRC), Italy
Ilja Maljutenko, Tallinn University of Technology (TalTech), Estonia
Antoine Mangin, ACRI-ST, France
Aarne Männik,Tallinn University of Technology (TalTech), Estonia
Veselka Marinova, Institute of Oceanology, Bulgarian Academy of Science, Bulgaria
Riccardo Martellucci, National Institute of Oceanography and Applied Geophysics (OGS), Italy
Francesco Masnadi, Università di Bologna, Dipartimento di Scienze Biologiche, Geologiche e Ambientali (UNIBO-Bigea); Consiglio Nazionale delle Ricerche, Istituto per le Risorse Biologiche e le Biotecnologie Marine sede di Ancona (CNR-IRBIM), Italy
Elena Mauri, National Institute of Oceanography and Applied Geophysics (OGS), Italy
Michael Mayer, Department of Meteorology and Geophysics, University of Vienna, Austria and European Centre for Medium-Range Weather Forecasts, UK
Milena Menna, National Institute of Oceanography and Applied Geophysics (OGS), Italy
Catherine Meulders, University of Liège, MAST, Department of Astrophysics, Geophysics and Oceanography, Belgium
Jane S. Møgster, Institute of Marine Research (IMR), Norway
Maeva Monier, CLAD, Mercator Océan International, France
Kjell Arne Mork, Institute of Marine Research (IMR), Norway
Malte Müller, Development Centre for Weather Forecasting, Norwegian Meteorological Institute, Norway
Jan Even Øie Nilsen, Institute of Marine Research (IMR), Norway
Giulio Notarstefano, National Institute of Oceanography and Applied Geophysics (OGS), Italy
José L. Oviedo, Instituto de Ciencias Marinas de Andalucía, Consejo Superior de Investigaciones Científicas (ICMAN-CSIC), Spain
Cyril Palerme, Development Centre for Weather Forecasting, Norwegian Meteorological Institute, Norway
Andreas Palialexis, Joint Research Centre, European Commission, Italy
Diego Panzeri, National Institute of Oceanography and Applied Geophysics (OGS); Università degli Studi di Trieste, Italy
Silvia Pardo, Plymouth Marine Laboratory,UK
Elisaveta Peneva, Sofia University St. Kliment Ohrdiski, Bulgaria
Paolo Pezzutto, Consiglio Nazionale delle Ricerche, Istituto di Scienze Marine (CNR-ISMAR), Italy
Annunziata Pirro, National Institute of Oceanography and Applied Geophysics (OGS), Italy
Trevor Platt, Plymouth Marine Laboratory,UK
Pierre-Marie Poulain, National Institute of Oceanography and Applied Geophysics (OGS), Italy
Laura Prieto, Instituto de Ciencias Marinas de Andalucía, Consejo Superior de Investigaciones Científicas (ICMAN-CSIC), Spain
Stefano Querin, National Institute of Oceanography and Applied Geophysics (OGS), Italy
Lasse Rabenstein, Drift+Noise, Germany
Roshin P. Raj, Nansen Environmental and Remote Sensing Center (NERSC), Norway
Urmas Raudsepp, Tallinn University of Technology (TalTech), Estonia
Marco Reale, National Institute of Oceanography and Applied Geophysics (OGS); Abdus Salam, ICTP, Italy
Richard Renshaw, Met Office, UK
Antonio Ricchi, Department of Physical and Chemical Sciences/ CETEMPS, University of L'Aquila, Italy
Robert Ricker, Alfred Wegener Institute Helmholtz Center for Polar and Marine Research, Germany
Sander Rikka, Tallinn University of Technology (TalTech), Estonia
Javier Ruiz, Instituto Español de Oceanografía (IEO), Spain
Tommaso Russo, Laboratory of Experimental Ecology and Aquaculture, Dept. of Biology, University of Rome; CONISMA, Italy
Jorge Sanchez, Qualitas Instruments S.A., Spain
Rosalia Santoleri, Institute of Marine Sciences (CNR-ISMAR), Italy
Shubha Sathyendranath, Plymouth Marine Laboratory,UK
Giuseppe Scarcella, Consiglio Nazionale delle Ricerche, Istituto per le Risorse Biologiche e le Biotecnologie Marine sede di Ancona (CNR-IRBIM), Italy
Katrin Schroeder, Consiglio Nazionale delle Ricerche, Istituto di Scienze Marine (CNR-ISMAR), Italy
Stefania Sparnocchia, Consiglio Nazionale delle Ricerche, Istituto di Scienze Marine (CNR-ISMAR), Italy
Maria Teresa Spedicato, COISPA Tecnologia & Ricerca, Italy
Emil Stanev, Helmholtz-Zentrum Geesthacht, Zentrum für Material- und Küstenforschung GmbH, Germany
Joanna Staneva, Helmholtz-Zentrum Geesthacht. Zentrum für Material- und Küstenforschung GmbH, Germany
Alexandra Stocker, Department of Geography, Sweden
Ad Stoffelen, Royal Netherlands Meteorological Institute (KNMI), Netherlands
Anna Teruzzi, National Institute of Oceanography and Applied Geophysics (OGS), Italy
Bryony Townhill, Centre for Environment, Fisheries and Aquaculture Science (Cefas), UK
Rivo Uiboupin, Tallinn University of Technology (TalTech), Estonia
Nadejda Valcheva, Institute of Oceanology, Bulgarian Academy of Science, Bulgaria
Luc Vandenbulcke, University of Liège, MAST, Department of Astrophysics, Geophysics and Oceanography, Belgium
Håvard Vindenes, Institute of Marine Research (IMR), Norway
Karina von Schuckmann, Mercator Ocean International, France
Nedo Vrgoč, Institute of Oceanography and Fisheries, Croatia
Sarah Wakelin, NOC, UK
Walter Zupa, COISPA Tecnologia & Ricerca, Italy

Journal of Operational Oceanography

Volume 14 Supplement 1 September 2021

Special Issue: Copernicus Marine Service Ocean State Report, Issue 5 Supplement

CONTENTS

JOURNAL OF OPERATIONAL OCEANOGRAPHY
2021, VOL. 14, NO. S1, s1–s185
https://doi.org/10.1080/1755876X.2021.1946240

CMEMS OSR5 – Chapter 1

1.1. Introduction

Authors: Karina von Schuckmann, Pierre-Yves Le Traon

1.1.1. Copernicus Marine Service status and achievements

The first operational phase 2014–2021 of the Copernicus Marine Service has successfully implemented a unique European Union ocean monitoring and forecasting service (https://marine.copernicus.eu/). Thirty thousand expert downstream services and users are now connected to the service that responds to public and private user needs and policies related to all marine and maritime sectors: maritime safety, coastal environment monitoring, trade and marine navigation, fishery, aquaculture, marine renewable energy, marine conservation and biodiversity, ocean health, climate and climate adaptation, recreation, education, science and innovation. The Copernicus Marine Service organises the value chain that goes from observation to information (Le Traon et al. 2019) and is an essential tool for Ocean Governance (Section 1.4) and sustainable management of the ocean based on comprehensive ocean monitoring and forecasting capabilities.

The Copernicus Marine Service is unique by its coverage and comprehensiveness, its balance between state-of-the-art science and operational commitments, and the consistency of its portfolio where satellite observations, in situ observations, and model simulations are used coherently to describe the physical (blue), biogeochemical (green) ocean and sea-ice (white) state the European regional seas and the global ocean. The Copernicus Marine Service gathers a strong network of European ocean information producers. Thanks to a well-established and organised evolutions of the Copernicus Marine Service system of systems, the capabilities to operate a marine service responsive to user needs and scientific/technological advances have fully been demonstrated (CMEMS General Assembly 2020). The product and service portfolios have evolved from 2015 to 2021 with, in particular, the integration of new parameters (e.g. waves, carbon, turbidity, sea ice thickness and icebergs), the improvement of resolution and quality, longer time series, the full uptake of Sentinel missions (S1, S3 and recently S2) and the development of new means to access and visualise the data.

The Copernicus Marine Service provides invaluable observation and model products to assess and report on past and present marine environmental conditions and to analyse and interpret changes and trends in the marine environment as for example discussed in previous Ocean State Reports, https://marine.copernicus.eu/access-data/ocean-state-report, and as part of the Ocean Monitoring Indicator framework, https://marine.copernicus.eu/access-data/ocean-monitoring-indicators. The CMEMS Ocean State Reports and Ocean Monitoring Indicators provide, in particular, a unique ocean monitoring dashboard for policy and decision makers as well as for the general public to support actions and assess progresses in policy implementation. There have been excellent feedbacks on the annual Ocean State Reports and their high level summaries that are now part of the EU ocean state assessment landscape and provide a high visibility of the Copernicus Marine Service. They have also federated a unique pooling of EU scientific expertise to assess the state of the ocean based on the Copernicus Marine Service ocean monitoring products.

A remaining challege is to establish a comprehensive monitoring of the ocean, a challenge that demands international cooperation. In response, the Copernicus Marine Service has set up important partnerships with GOOS, OceanPredict, GEO and GEO Blue Planet. The UN Decade of Ocean Science for Sustainable Development (https://www.oceandecade.org/) will be a unique opportunity to develop further the required international cooperation to support delivery of the information, action and solutions needed to achieve the 2030 Agenda for Sustainable Development.

1.1.2. Plans for Copernicus 2

The Copernicus Marine Service has developed an ambitious plan for the next phase of the Copernicus programme (Copernicus 2). The objective is to further

establish CMEMS products as a worldwide reference, foster further the service uptake and respond to increasing and pressing user and policy needs (in particular the EU Green Deal – see Chapter 1 in the 4th issue of the CMEMS Ocean State Report, Peterlin et al. 2020) for improved ocean monitoring and prediction capabilities.

The plan identifies three levels of implementation for the evolution of the Copernicus Marine Service product and service portfolio over the period 2021–2027: baseline (continuity of service with incremental evolutions), enhanced continuity (major product improvements) and new services.

Baseline will be implemented from the start of Copernicus 2 to ensure the continuity of the present service and maintain a consistent blue, white and green offer. This includes incremental evolutions to improve product quality, integrate future Sentinel missions and new in-situ observations (e.g. Biogeochemical Argo, Claustre et al. 2020), to improve the estimation of product uncertainty and benefit from new capabilities of digital services through the WEkEO DIAS platform (https://wekeo.eu/). User interaction and user engagement will be strengthened by developing dedicated sectorial offers per applications and policies and enhancing the training and capacity building offer. The objective is also to re-enforce the Copernicus programmme consistency by producing marine data for the other Copernicus services and developing sectorial approaches (thematic hubs) with the other Copernicus Services (e.g. Coastal, Arctic).

The enhanced continuity and new services streams will build from present and future H2020 and Horizon Europe R&D projects and will be developed depending on budget and priorities. Improved digital services, ensemble forecasts, higher resolution, step change in Arctic monitoring, air/sea CO_2 fluxes, twentieth century reanalyses are proposed under the enhanced continuity scenario. Coastal, marine biology, climate projection (coastal, ecosystem) are proposed under the new services scenario. A strong priority is, in particular, to offer new services for the coastal ocean through a co-design and co-development approach between the Copernicus Marine Service and coastal marine services operated by EU Member States.

The Copernicus Marine Service Ocean State Reports and Ocean Monitoring Indicators will continue to be an essential component of the Copernicus Marine Service in Copernicus 2. The plan is to foster further the integration with other Copernicus Services and, in particular, with the Climate Change Service (https://climate.copernicus.eu/) to provide an integrated assessment of the state of ocean and climate. Links with international activities and organisations related to ocean and climate assessments (Intergovernmental Panel on Climate Change, Intergovernmental Oceanographic Commission; World Meteorological Organisation; UN World Ocean Assessment, Global Ocean Observing System, Global Climate Observing System, G7 Future of the Seas and Oceans Initiative, UN Decade of Ocean Science) will be strengthened. The Copernicus Marine Service could contribute, in particular, to the development of an international framework for ocean monitoring indicators. The delivery of meaningful Ocean Monitoring Indicators requires an adequate ocean observing system. This dependency will be documented. This is essential to advocate for the sustainability of the ocean observing system.

1.1.3. Major outcomes of the 5th issue of the Ocean State Report

The 5th issue of the CMEMS OSR incorporates a large range of topics for the blue, white and green ocean for all European regional seas, and the global scale over 1993–2019 with a special focus on 2019. As previous reports, this report is organised within four principal chapters:

- Chapter 1 provides the introduction and a synthesised overview, together with an informative section on ocean governance written in collaboration with the European Marine Board (https://www.marineboard.eu/).
- Chapter 2 includes various novel scientific analyses of the ocean state variability at subseasonal, seasonal and multi-annual scales.
- Chapter 3 connects science and policy by reporting science cases of (potential) socio-economic relavance.
- Chapter 4 highlights unusual events during the year 2019.

The reporting and indicators are focused on the seven Copernicus Marine Service regions, i.e. the global ocean, the Arctic, the North-West-Shelf, the Iberia-Biscay-Ireland, the Baltic Sea, the Mediterranean Sea and the Black Sea. The uncertainty assessment based on a 'multi-product-approach' is also used here (see von Schuckmann et al., 2018 for more details). The OSR is predominantly based on CMEMS products, and many analyses are complemented by additional datasets. CMEMS includes both satellite and in-situ high level products prepared by the Thematic Assembly Centres (TACs) – including reprocessed products – and modelling and data assimilation products prepared by Monitoring and Forecasting Centres (MFCs). Products are described in Product User Manuals (PUMs) and their

quality in the Quality Information Documents (QUID; CMEMS 2016). Within this report, all CMEMS products used are cited by their product name, and download links to corresponding QUID and PUM documents are provided. The use of other products has also been documented to provide further links to their product information, and data source.

The major outcomes of the fifth issue of the Copernicus Marine Service Ocean State Report are synthesised in Figure 1.1.1, and are summarised below.

Global / Large scale:

Investigations in OSR5 address three topics at large to global ocean scale: the development of an indicator to monitor the eutrophic and oligotrophic state in the ocean; a chlorophyll-a based indicator linked to a plankton-to-fish index as well as an improved indicator for an air–sea coupled mode of variability in the Indian Ocean.

Eutrophication is the process by which an excess of nutrients (mainly phosphorus and nitrogen) leads to increased growth of plant material in an aquatic body – an issue particularly of relevance in coastal regions and areas with restricted water flow. Eutrophication can be linked to anthropogenic activities, such as farming, agriculture, aquaculture, industry and sewage, and results in decreased water quality through enhanced plant growth (e.g. algal blooms) causing death by hypoxia of aquatic organisms. Oligotrophication is the opposite of eutrophication, where reduction in some limiting resource leads to a decrease in photosynthesis by aquatic plants, which might in turn reduce the capacity of the ecosystem to sustain the higher organisms in it. A new indicator of eutrophic and oligotrophic waters proposed in OSR5 derived from satellite chlorophyll-a data (Section 2.4) showed hardly any localities in the North Atlantic where the eutrophic flag was positive in 2019 (i.e. above the 1993–2017 P90 climatological reference). Oligotrophic flags were positive mostly along coastal waters, but also along scattered points within the 30–40°N latitudes. Waters flagged as eutrophic can be then classified as eutrophication or oligotrophication when the eutrophic state is sustained over several years, such as a significant trend over time. This indicator methodology has been distributed to EuroStat in the context of SDG14.1a eutrophication reporting over the period 1998–2019 for all European Seas.

The horizontal gradient of chlorophyll-a derived from remote sensing chl-a data and linked to a

Figure 1.1.1. Overview on major outcomes of this 5th issue of the CMEMS Ocean State Report.

plankton-to-fish index (Section 3.1) has been shown to be highly valuable to marine biologists and ecosystem modellers and, in turn, to regional fisheries management and authorities facing overexploitation and the effects of climate change. Marine policies will ultimately be efficiently supported by the use of chlorophyll-a gradient as a direct, observation-based, biological variable monitoring the marine ecosystem productivity across a wide range of spatial and temporal scales.

The Indian Ocean Dipole (IOD) is an air–sea coupled mode of variability in the Indian Ocean exacerbating moderate to extreme variations at the air–sea interface such as precipitation and ocean hydrography changes. OSR5 has analysed the classical IOD index – the Dipole Mode Index – based on Sea Surface Temperature (SST), and complemented the analysis with a sea level-based indicator demonstrating the increased performance of IOD monitoring based on a combined use of both indexes (Section 2.9). Results report on two particularly strong events in 1997 and 2019, inducing drought periods in the land areas bordering the eastern Indian Ocean, and extreme precipitation in the western part of the basin.

The North-Atlantic / Arctic gateway

Sea-ice conditions in the North-Atlantic / Artic gateway strongly impact ecosystem, weather, and economic activities, such as tourism, fisheries, and shipping. OSR5 has particularly emphasised blue, white and green oceanographic conditions at Svalbard, the Barent Sea and other areas of the Nordic Seas. The Fram Strait represents the major gateway for sea ice transport between the Arctic and North Atlantic Ocean, affecting the mass balance of the perennial ice cover in the Arctic. Contrary to previous results, OSR5 finds a significant, negative trend in the sea-ice area export through this strait over the last two and a half decades (1993–2019) as affected by a strong reduction of nearly 90% in average sea-ice thickness in the Barents Sea (Section 2.1).

In 2019 however, sea-ice conditions had been surprisingly normal around Svalbard and parts of the Barents Sea, albeit concurrent unusual low sea-ice extent in summer and autumn in the Arctic ocean. The OSR5 results (Section 4.1) have shown that sea-ice (old, and thick) redistribution from the Artic into this area have acted to recover the sea-ice cover and ocean stratification through adding sea ice and freshwater to the region. This supports that large sea-ice inflows act to maintain an Arctic-type ocean climate with a cold, stratified, and sea-ice covered water column and is a key player among others in the Arctic climate system. OSR5 also introduces a new tool (IcySea) providing near-real time monitoring (satellite images from the Sentinel 1 satellites) and sea-ice drift forecasts in the Svalbard area to inform operational planning and safety for the transport and navigation economic sector (Section 3.6).

OSR5 has also addressed Artic ocean warming over the past decades (1993–2019) – a critical missing piece of knowledge for global scale ocean warming linked to the current positive Earth energy imbalance: Currently, global ocean warming estimates are limited between 60° S and 60°N and less is known on the role of ocean warming in areas polewards 60°N latitude. In OSR5, the relative contribution of polar ocean warming north of 60°N to global ocean warming rates accounts for nearly 4% – a comparable value to its area fraction of the global ocean (Section 2.2). The ice-free ocean area warms substantially faster as compared to the ice-covered ocean, and this compensating effect leads to a warming trend of 0.6 (0.7) ± 0.2 Wm^{-2} for the upper 700 m (full-depth) ocean layer of the pan-Arctic region north of 60°N as consistently derived from the combined analysis of observations and reanalyses data over the period 1993–2019.

The molar nitrate:silicate ratio is an important indicator of nutrient availability related to the requirement of diatoms – a major group of microscopic algae, which underpin ocean biological productivity and transfer carbon from the surface to the deep layers of the ocean when they die. Globally, they are responsible for 40% of marine primary production and 40% of the particulate organic carbon exported to the deep ocean. Consequently, changes in diatom concentration can greatly influence global climate, atmospheric carbon dioxide concentration, and the function of marine ecosystems. OSR5 investigated for the first time a 30-year record (1990–2019) of water column silicate and nitrate in the Nordic Seas (Section 2.3), showing a steady increase of the nitrate:silicate ratio throughout the thirty-year period and linked to concurrent statistically significant decline in surface silicate. For this specific region, less access to silicate and other macronutrients in the Nordic Seas may shorten the spring diatom bloom period and hamper zooplankton growth, which in turn may have consequences for growth and development of commercially important fish stocks in these waters.

Baltic Sea:

A specific evaluation of eutrophication is also proposed for the Baltic Sea based on reanalysis results (Section 2.5) with particular focus on the nitrogen to phosphorus ratio, which has been reported to decrease in the water column across the entire Baltic Sea over the period 1993–2017, particularly in the Baltic Proper, the Gulf of Finland and the Gulf of Riga. An exception is the Gulf of Bothnia, which shows a relatively good

environmental state over this period. Decrease in the nitrogen to phosphorus ratio affects phytoplankton blooms, supports nitrogen-fixing cyanobacteria growth, which leads to increased production of organic matter – and its decomposition consequently decreases the oxygen content – and enables eutrophication to endure. In addition to changes in the nutrient ratio, cyanobacteria blooms are also facilitated by ocean warming from climate change. Based on the results obtained in OSR5, it is very likely that the Baltic Sea will continue to experience frequent cyanobacterial blooms in the future.

Even a single passage of an extreme storm associated with high waves forces high sea level at the coast and a rough sea outside the sheltered areas. In the Baltic Sea (Section 4.4), simultaneous high sea level and waves lead to significant coastal erosion and flooding of low-lying areas. Low sea levels may complicate operations of heavily loaded cargo ships at the ports. In Januray 2019 however, a very unusual situation was documented: high waves coincided with a low coastal sea level. In January 2019, the Bothanian Sea had been hit by a severe storm and record-breaking significant wave height of 8.1 m was recorded. Surprisingly, exceptionally low sea levels were concurrently recorded in many coastal stations (as low as −1.1 m), both on the Finnish and the Swedish side of the Gulf of Bothania. As discussed in Section 4.4, the interplay of the extreme event, local sea ice extent and ocean circulation changes have triggered these unusual conditions.

North Sea:
OSR5 also draws a linkage between extreme variability such as marine heat waves and cold spells and key fish and shellfish stocks in the North Sea (Section 3.2). Catches of sole and sea bass increased in years with cold-spells (1994, 1996, 1997, 2010, 2011, 2013 and 2018), while catches of red mullet and edible crabs decreased. For heatwaves (1998, 2002, 2003, 2006, 2007 and 2014–2019), the impact on fisheries catch data lagged the temperature events by five years: sole, European lobster and sea bass catches increased whilst red mullet catches reduced.

Mediterranean Sea:
OSR5 also focuses on the Mediterranean Sea which has been recognised to be a climatic hotspot. During the past decade, its water masses have experienced strong and fast increases in temperature and salinity, responding very rapidly to global warming and to changes in the regional freshwater budget – an outcome that is envisaged to be important for climate science, environmental agencies, concerned citizens as well as regional policy-makers (Section 2.6).

The monitoring of the spatial and temporal evolution of storms is crucial to provide an information service to responsible emergency entities like coastguards and civil protection units which might need to intervene even under harsh weather and sea conditions (Section 4.2). In such circumstances, accurate nowcasts and short-term predictions are essential to prepare interventions that are timely, effective and with minimal risk. This kind of service is also essential to provide information and guidance for safer navigation by avoiding the higher impacted sea areas or delaying transits. OSR5 also discussed a new approach for the Maltese shelf area to predict, monitor, and assess extreme meteo-marine conditions, to verify the evolution of the storms in real time, and to provide improved services to users such as for civil protection, marine safety, and risks to essential assets. The method (Section 4.2) is based on merging complement data from observation and modelling systems (CMEMS products, CALYPSO HF radar network), aided by the support of artificial intelligence techniques in-cooperating knowledge from past extreme events. The methods performance is demonstrated on two extreme events in January and December 2019.

The city of Venice in Italy experienced four exceptionally high tidal peaks in the week from 11 to 18 November 2019, flooding large parts of the city. Venice had not suffered from four successive extreme events within one single week before. The OSR5 results (Section 4.3) show that spring tides coincided with a very high mean November sea level during this week. Additionally, and concurrent with the tidal maximum, strong Sirocco winds pushed Adriatic Sea water towards Venice during three of the four exceptional water level events. For the most extreme event on 12 November, a storm passed over Venice just at the time of the maximum tide. The official forecast underestimated maximum water levels for this event as the model forcing did not resolve the local storm. Higher-resolution atmospheric model fields and the use of satellite wind observations for nowcasting may further improve water level forecasts under extreme conditions.

OSR5 also covers a study on the intensity and geographical distribution of maximum wave height in the Mediterranean and Black Seas over 27 years (1993–2019) using CMEMS wave model hindcasts and the wave model WAVEWATCH III® (Section 2.8). Results show that in 2019 maximum wave heights were smaller than usual in the Black Sea (up to −1.5 m), while in the South Mediterranean Sea higher-than-average wave heights (+2.5 m) are reported linked to atmospheric depressions that rapidly passed over this area.

OSR5 also demonstrated the strong linkage between changes in South Adriatic hydrography as triggered by

the ocean circulation – particularly for salinity – and the biodiversity in this area with potential effects on fish species of commercial interest (Section 3.5). These changes in the ecosystem can strongly impact economies and coastal communities that might need to adapt to the declining abundance of traditional target species and/or to the increasing abundance of other species, which previously were secondary to the local market.

The ecological and socio-economic consequences (e.g. on tourism, aquaculture, fisheries) of jellyfish outbreaks on the shorelines are relevant worldwide, and the development of prediction tools is critical to anticipate and mitigate the arrival of the jellyfish blooms (Section 3.4). While the Portuguese Man-of-War is not native to the Mediterranean Sea, their appearance had been reported several times during the past decade in the Gulf of Cadiz and in the Western Mediterranean. OSR5 presents a new forecasting system for the spread of this jellyfish which shows good skills during a strong event in 2018. The main potential benefits of this new forecasting system are to support coastal managers, and to minimise associated socio-economic losses.

Section 3.6 discusses the benefits of integrating the CMEMS variables in combination with trawl surveys into the modelling of fishery independent data for predicting fish species distribution in the Adriatic and Ionian basins. An integrated ecosystem approach is discussed, which incorporates anthropogenic and other environmental stressors into the advice for fisheries management. The results robustly demonstrate that the combined use of data improves the species distribution in the models.

The presence of invasive species in the Mediterranean Sea is much higher than in other European seas, and understanding the reasons behind the range expansion of this invasive species is important for minimising any possible impacts to the already highly pressurised Mediterranean marine ecosystem. OSR5 describes in Section 4.5 sightings of the invasive lionfish *Pterois miles* in the Ionian Sea, together with an analysis of ocean temperature in this region, and in 2019, warm water conditions have favoured the northward spread of this thermophilic species along the coast of the Mani Peninsula and the Greek mainland. These results are critical for ecological modellers and regional stakeholders involved aiming to monitor the spread of this generalist predator in their waters.

Black Sea:
In this 5th issue of the CMEMS OSR, topics tackled for the Black Sea include aspects of the basin-scale circulation, as well as discussing hypoxia monitoring in the northwestern part of the basin. The general circulation in the Black Sea features a cyclonic gyre encompassing the entire basin (Rim Current). OSR5 provides a new method for the Black Sea Rim Current ocean monitoring indicator (Section 2.7). Results over the period 1993–2019 show Rim current speed variations of 30% in close relation to the atmospheric circulation (e.g. wind) and an increase in Rim Current speed of ~0.1 m/s/decade.

During the 1970s to 1990s, large areas of the Black Sea, particularly along the Romanian and Ukrainian coasts, had been hit by severe hypoxia predominantly driven by eutrophication, and this dead zone reached up to 40,000 km^2 at its extreme in the 1990s. OSR5 (Section 3.8) analyses a Benthic Hypoxia index in this area over the period 1992–2019 depicting general recovery from the preceding eutrophication period (1980s), but also a re-increase in the severity of benthic hypoxia for the years 2016–2019 which is attributed to warming atmospheric conditions. Results demonstrate that a joint consideration of oceanographic and climate conditions and riverine and coastal nutrient discharge, incorperated into an operational indicator such as presented in this study could be a critical tool in support of coastal management and marine protection strategies.

1.2. Knowledge and data for international Ocean governance

Authors: Paula Kellett, Brittany E. Alexander, Johanna J. Heymans

1.2.1. What is international Ocean governance?

Covering 71% of the Earth's surface and holding 99% of the area that can be inhabited by life, the Ocean plays a pivotal role in sustaining life on Earth, including through the provision of climate regulation, food, energy, and many other resources. The Ocean, or 'blue', economy in Europe alone was estimated to have a turnover of €750 billion in 2018 (European Commission 2020) and there is significant interest in developing this further through increased jobs and by supporting innovation. However, over-exploitation of the Ocean as a result of human activities is a very real challenge, and coupled with increasing pressures from climate change impacts and pollution, its ability to continue supporting life on Earth is threatened. There is hence a balance to be achieved: in order to continue supporting life on Earth and to achieve the Sustainable Development Goals (SDGs), the Ocean must be productive, clean, healthy, and resilient. For this, we must ensure that human impacts on the Ocean and its

resources are managed sustainably. Given the interconnected nature of the Ocean, and that the majority of its volume lies outside of nation's Exclusive Economic Zones (EEZs), strong international cooperation is needed for the sustainable management of the Ocean as a global common through international Ocean governance. This includes rules, agreements, processes and institutions, which need to be organised in a way that ensures that the human use of the Ocean will be sustainable into the future.

At the core of the international Ocean governance system lies the United Nations Convention on the Law of the Sea (UNCLOS – United Nations 1982). This is an international agreement that defines both the rights and responsibilities that nations have when using and managing the Ocean and its resources. Building on this foundation, laws, frameworks, institutions and jurisdictional rights have been established at different regulatory levels (local, national, regional, international) and for different marine sectors (e.g. shipping, fishing, and research). However, this has made the Ocean governance system very fragmented, and there is often a lack of coordination between different organisations and governance systems. Coupled with this are the challenges of ratifying and enforcing laws and regulations, especially in areas beyond national jurisdiction (ABNJ), of gaining international agreements for governance in a timely manner, and of gaps in the legal framework, especially linked to emerging sectors (e.g. seabed mining).

More coordination is therefore needed across regulatory systems and marine sectors, and all stakeholders should be involved in the process of developing and implementing governance regulations for the sustainable management of the Ocean and its resources.

1.2.2. The role of Ocean observation and data in international Ocean governance

Knowledge underpins Ocean governance, and provides the means to understand the Ocean and its functioning, and develop appropriate measures for its sustainable management and use. Ocean observing allows the collection of data to monitor and report on the state of the Ocean, make predictions about its future, and to assess the impact of governance regulations and success towards achieving the intended sustainability goals. Observational data also help to ensure that the development of economic activities in the Ocean are indeed sustainable.

In order to plan for and assess the sustainable use of the Ocean, a wide range of different types of data, from different sources and different providers are required. Significant investment in Ocean observing systems and personnel, along with appropriate maintenance and support, is required in order to collect these data, and efficiency and coordination across Ocean observing systems are critical (EMB 2021). These are challenges that the Global Ocean Observing System[1] (GOOS) and the Group on Earth Observations[2] (GEO) are working to improve at the international level. Within this context the European Global Ocean Observing System[3] (EuroGOOS), the European Ocean Observing System[4] (EOOS), and the European Commission's Foreign Policy Instrument Action on international Ocean governance: EU component to global observations[5] (EU4OceanObs), are tackling these challenges at the European level. Data sharing and interoperability between marine data infrastructure are also key enablers for effective international Ocean governance.

1.2.3. The European state of play

In 2016, the European Commission published its Joint Communication on International Ocean Governance (IOG): An agenda for the future of our oceans (European Commission 2016), which aligned strongly with the UN 2030 Agenda for Sustainable Development (United Nations 2015) and specifically the targets of Sustainable Development Goal 14 (Life Below Water). The Communication outlined the European Commission's 50 planned actions for developing Ocean governance, not only in Europe but also internationally. The Communication was structured around three priority areas, one of which was 'strengthening international Ocean research and data': recognising the critical role that data and knowledge play in supporting the Ocean governance system.

The Joint Communication was followed by a report published in 2019, which examined the progress made towards implementing the 50 actions (European Commission 2019). The report highlighted the annual publication of the CMEMS Ocean State Report as one of the direct actions taken by the European Commission towards developing international Ocean governance. This report was initiated as a means to 'promote ocean research, data and science with the aim of developing comprehensive, reliable, comparable and accessible Ocean knowledge to improve policy-making, drive innovation and facilitate a sustainable "blue" economy'.

In addition, in 2019 the European Commission, together with the European External Action Service, established the IOG Forum.[6] The IOG Forum provided a platform for stakeholders within and beyond Europe to engage in interactive cross-sectoral and cross-boundary dialogue on Ocean challenges and governance

solutions in support of the follow-up of the EU's IOG Agenda. A diversity of stakeholders from across the globe have engaged with this initiative through a series of expert workshops, consultations and events, and the final recommendations[7] were launched during a high-Level event on 20 April 2021. As well as continuing to align with the UN 2030 Agenda for Sustainable Development, the future of the EU's IOG Agenda will also align closely with the European Green Deal,[8] the EU 2030 Biodiversity Strategy[9] and the aims of the UN Decade of Ocean Science for Sustainable Development.[10]

The activities of the IOG Forum have elicited a number of priority areas for action that are recommended to be addressed in the future EU IOG Agenda to ensure a clean, healthy, productive, resilient, and understood Ocean. The priority area on improving the Ocean knowledge system focuses on ensuring that future Ocean governance is knowledge-based and driven by inclusive and effective knowledge-policy interfaces.[11] This priority area emphasises the need to intensify transdisciplinary co-designed research to address key knowledge gaps, integrate knowledge from relevant stakeholders and knowledge sources, and ensure strong observations and data capacity. The EU has many strong initiatives that it can build on in order to take a leading role in addressing these recommendations including the European Data Strategy, 8th Environment Action Programme, Horizon Europe, and the Destination Earth/Digital Twin Ocean initiative.

1.2.4. The international state of play

In recent years there has been focus on the development of a new legal instrument under UNCLOS, which covers the conservation and sustainable use of marine biological diversity in areas beyond national jurisdiction (BBNJ).[12] This process formally began in 2015 and a revised draft text was published by the UN in early 2020.[13] Negotiations are ongoing, and data and observations will be key in supporting its implementation, as was highlighted in the Intergovernmental Oceanographic Commission of UNESCO (IOC) Report of the Executive Secretary[14] at its meeting on 3 February 2021, where the IOC proposed a State of the Ocean Report, to provide annual information about Ocean variables, and the status of Ocean observations (among other information). Strong data and observations will also be required to monitor progress towards commitments made as part of the Paris Agreement and the Convention on Biological Diversity. The upcoming UN Climate Change Conference (COP26) and the Convention on Biological Diversity's COP15, both to be held in 2021, offer critical opportunities to increase ambition and cooperation towards Ocean sustainability at the international level. Several nations, and the EU, have also committed to designating three new marine protected areas in the Antarctic, the successful management of which will rely on international cooperation for data sharing and observational infrastructure in these areas.

Ocean observations and data have also gained increased attention in other international fora. In the 2016 Tsukuba Communiqué, the Science and Technology ministers of the G7 group Member States (G7 Science and Technology Ministers 2016) recognised the importance of developing stronger scientific knowledge in order to develop 'appropriate policies to ensure the sustainable use of the seas and Ocean'. In order to achieve this, they stated their support for a number of actions linked to enhancing Ocean observations globally, promoting Ocean science and improving data sharing infrastructures, and strengthening collaboration to encourage regional developments in observing capabilities and knowledge networks. Subsequently, as presented in the G7 Future of the Seas and Oceans Working Group Statement to the OceanObs'19 Conference,[15] the G7 established a dedicated Coordination Centre for Ocean observation platforms, which will be interlinked with other G7 priority areas[16] and will interface with GOOS.

The OceanObs conferences, held every 10 years, are an opportunity for the Ocean observing community to discuss progress and define goals for the coming decade. At OceanObs'19 the importance of establishing effective collaborations with multiple stakeholders to advance effective Ocean governance was specifically recognised (Speich et al. 2019).

1.2.5. Where do we need to go from here?

Through all of the Ocean governance initiatives presented above, there is a clear message calling for improved co-ordination and increased stakeholder engagement in the co-design of Ocean research, observations and data. There is also a call for Ocean governance to be based on a sound foundation of knowledge that is effectively translated and available for use in policy-making so that sustainable and resilient management practices can be implemented. The Ocean observations and data communities have an integral part to play in both of these aims, including through actions such as the Ocean State Report. Knowledge cannot be developed without Ocean observations and data, and to support the co-ordination of Ocean governance at a global level, data need to be open, interoperable and guided by principles such as FAIR (Finadable,

Accessible, Interoperable, Resuable). The observations and data communities are key stakeholders in Ocean governance, and should be engaged in dialogues around Ocean governance.

Notes

1. https://www.goosocean.org/.
2. https://earthobservations.org/index.php.
3. https://eurogoos.eu/.
4. https://www.eoos-ocean.eu/.
5. https://www.eu4oceanobs.eu/.
6. https://webgate.ec.europa.eu/maritimeforum/en/frontpage/1469.
7. https://3rd-iog-forum.fresh-thoughts.eu/wp-content/uploads/sites/89/2021/04/IOG-recommendations-2021-WEB.pdf.
8. https://ec.europa.eu/info/strategy/priorities-2019-2024/european-green-deal_en.
9. https://ec.europa.eu/info/strategy/priorities-2019-2024/european-green-deal/actions-being-taken-eu/eu-biodiversity-strategy-2030_en.
10. https://oceandecade.org/.
11. https://webgate.ec.europa.eu/maritimeforum/sites/default/files/iog-discussion-paper-2020-v5.pdf.
12. https://www.un.org/bbnj/.
13. https://undocs.org/en/a/conf.232/2020/3.
14. https://oceanexpert.org/event/2805#documents.
15. http://www.oceanobs19.net/.
16. http://www.oceanobs19.net/wp-content/uploads/2019/09/G7-Joint-Statement-to-OceanObs19.pdf.

References

Section 1.1. Introduction

Claustre H, Johnson KS, Takeshita Y. 2020. Observing the global ocean with biogeochemical-argo. Ann Rev Mar Sci. 12 (1):23–48. doi:10.1146/annurev-marine-010419-010956.

CMEMS. 2016. Product quality strategy plan. Available from: https://marine.copernicus.eu/sites/default/files/CMEMS-PQ-StrategicPlan-v1.6-1_0.pdf.

CMEMS General Assembly. 2020. Available from: https://www.copernicus.eu/en/general-assembly-2020-general-session-presentations.

Le Traon PY, Reppucci A, Alvarez Fanjul E, Aouf L, Behrens A, Belmonte M, Bentamy A, Bertino L, Brando VE, Kreiner MB, et al. 2019. From observation to information and users: the Copernicus marine service perspective. In: Frontiers in marine science (Vol. 6, p. 234). Available from: https://www.frontiersin.org/article/10.3389/fmars.2019.00234.

Peterlin M, Isoard S, Royo Gelabert E. 2020. Copernicus marine service ocean state report, issue 4. J Oper Ocean. 13 (Supp. 1):S1–S172. doi:10.1080/1755876X.2020.1785097.

von Schuckmann K, Le Traon P-Y, Smith N, Pascual A, Brasseur P, Fennel K, Djavidnia S, Aaboe S, Fanjul EA, Autret E, et al. 2018. Copernicus marine service ocean state report. J Oper Oceanogr. 11(sup1):S1–S142. DOI:10.1080/1755876X.2018.1489208.

Section 1.2 Knowledge and data for international Ocean governance

European Commission. 2016. Joint communication to the European Parliament, The Council, The European Economic and Social Committee and the committee of the regions – international Ocean governance: an Agenda for the future of our Oceans. In: JOIN(2016) 49 final. Available from: https://ec.europa.eu/maritimeaffairs/sites/maritimeaffairs/files/join-2016-49_en.pdf.

European Commission. 2019. Improving international Ocean governance – two years of progress. In: JOIN(2019) 4. Available from: https://eur-lex.europa.eu/legal-content/EN/TXT/?uri=JOIN:2019:4:FIN.

European Commission. 2020. The EU blue economy report 2020. Publications Office of the European Union. Available from: website. https://ec.europa.eu/maritimeaffairs/sites/maritimeaffairs/files/2020_06_blueeconomy-2020-ld_final.pdf.

European Marine Board. 2021. Sustaining in situ ocean observations in the age of the digital ocean. EMB Policy Brief No. 9, June 2021. DOI:10.5281/zenodo.4836060.

G7 Science and Technology Ministers. 2016. Tsukuba communiqué. In: Meeting in Tsukuba, Ibaraki. Available from: https://www.japan.go.jp/g7/_userdata/common/data/20160517communique.pdf.

Speich S, Lee T, Muller-Karger FE, Lorenzoni L, Pascual A, Jin D, … Ackerman A. 2019. Editorial: Oceanobs'19: an Ocean of opportunity. Frontiers in marine science, 6. doi:10.3389/fmars.2019.00570.

United Nations. 1982. United Nations Convention on the Law of the Sea. Available from: https://www.un.org/depts/los/convention_agreements/texts/unclos/unclos_e.pdf.

United Nations. 2015. Transforming our world: the 2030 Agenda for sustainable development. In: A/RES/70/1. doi:10.1007/s13398-014-0173-7.2.

CMEMS OSR5 – Chapter 2

Table of content

Section 2.1 Modelled sea-ice volume and area transport from the Arctic Ocean to the Nordic and Barents Seas

Authors: Vidar S. Lien, Roshin P. Raj, Sourav Chatterjee

Statement of main outcome: The Fram Strait represents the major gateway for sea ice transport from the Arctic Ocean, affecting the mass balance of the perennial ice cover in the Arctic. Our model results show a distinct seasonal cycle in both sea ice area and volume transport with a maximum in winter, in agreement with observations and other model-based studies. Contrary to several previously published studies, we find a significant, negative trend in the sea-ice area export through Fram Strait over the last two and a half decades. Possible explanations for this discrepancy are discussed. The reduction in area transport translated into a reduction also in the volume transport. In the Barents Sea, a strong reduction of nearly 90% in average sea-ice thickness has diminished the sea-ice import from the Polar Basin.

Product used:

Ref. No.	Product name & type	Documentation
2.1.1	ARCTIC_REANALYIS_PHYS_002_003	PUM: https://marine.copernicus.eu/documents/PUM/CMEMS-ARC-PUM-002-ALL.pdf QUID: https://marine.copernicus.eu/documents/QUID/CMEMS-ARC-QUID-002-003.pdf

2.1.1. Introduction

The Arctic Ocean contains a large amount of freshwater, and the freshwater export from the Arctic to the North Atlantic influence the stratification, and, hence, the Atlantic meridional overturning circulation (e.g. Aagaard et al. 1985; Aagaard and Carmack 1989; Holland et al. 2001). The Fram Strait represents a major gateway for freshwater transport, both as liquid freshwater and as sea ice, from the Arctic Ocean to the North Atlantic through the East Greenland Current (e.g. Vinje et al. 1998; Fahrbach et al. 2001; Lique et al. 2009; Smedsrud et al. 2011; Rabe et al. 2013; Figure 2.1.1). Two main factors contributing to this are the vicinity to the area north of Greenland where the thickest multi-year pack ice in the Arctic resides, and the fact that the Fram Strait is the largest (and deepest) gateway between the Arctic Ocean and the World Ocean. The transport of sea ice through the Fram Strait is therefore important for the mass balance of the perennial sea-ice cover in the Arctic and represents an annual loss corresponding to about 10% of the total Arctic perennial sea-ice volume (e.g. Vinje et al. 1998; Rampal et al. 2011). Indeed, sea ice export through the Fram Strait has been found to explain 54% of the variations in Arctic winter multi-year sea ice volume changes (Ricker et al. 2018). However, while satellites provide high-quality data on the Arctic sea-ice extent, estimates of the sea-ice thickness, and, hence, total volume of the Arctic sea ice has up until recently been rather limited

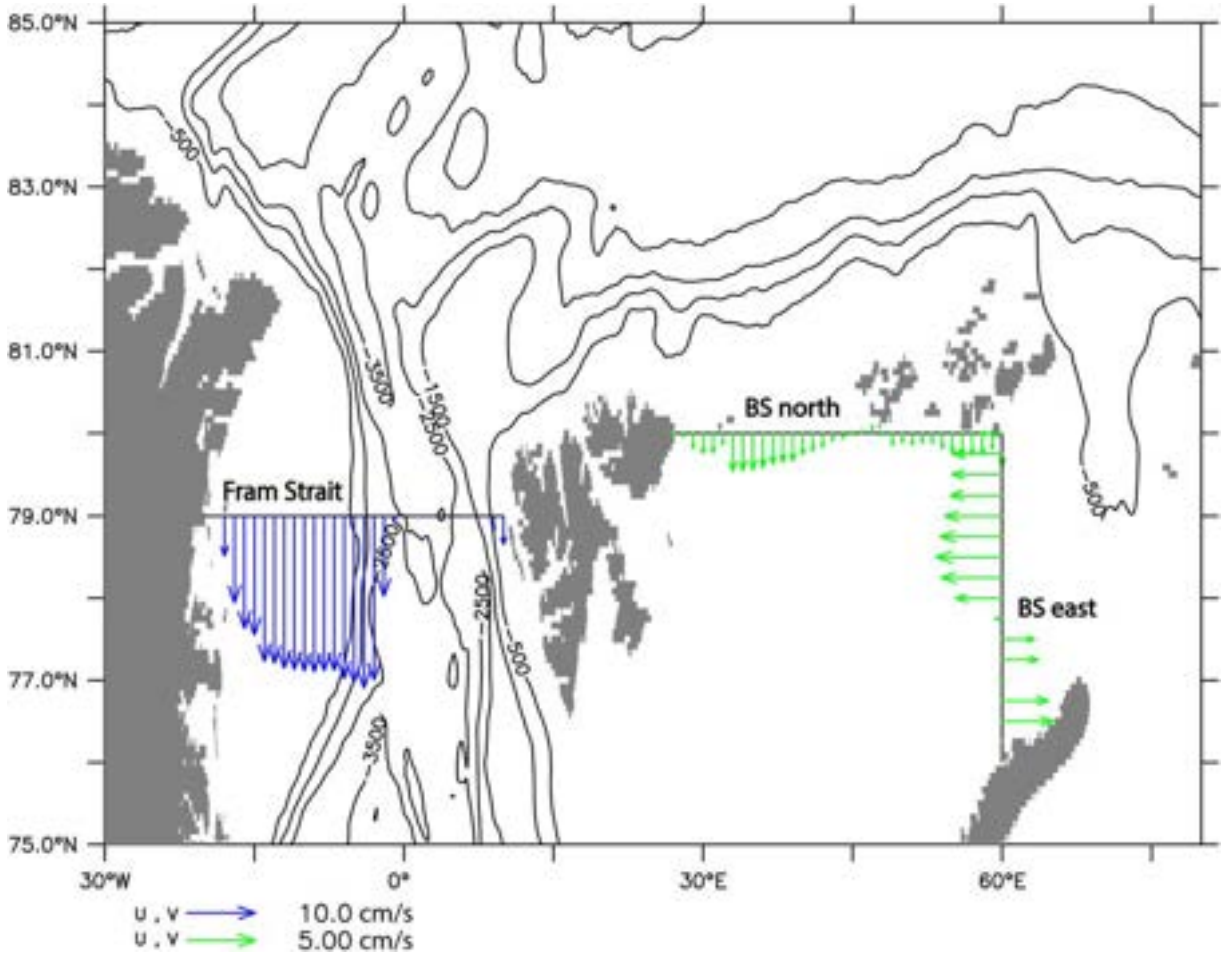

Figure 2.1.1. Map showing the location of the sections across the Fram Strait between Greenland and Spitsbergen, the Barents Sea north between Svalbard and Franz Josef Land, and the Barents Sea east between Franz Josef Land and Novaya Zemlya, used to estimate the area and volume of sea ice transport. Mean sea ice drift speed during the time period 1993–2019 is overlaid in arrows. Black isobaths are drawn at 500-meter intervals.

(e.g. Ricker et al. 2018), and consequently model re-analyses are often used for assessing sea-ice volume and transport (e.g. Zhang et al. 2017).

A large part of the interannual variability in the sea-ice export through the Fram Strait is explained by the large-scale synoptic forcing, while thermal wind forcing across the Fram Strait represents a persistent, although declining, atmospheric forcing (van Angelen et al. 2011). Moreover, the geostrophic winds across Fram Strait have been stronger in the 2000s compared with the period 1960s–1990s, which has caused an increase in the sea-ice transport, more than compensating for the decrease in the sea-ice concentration in the Fram Strait over the same period (Widell et al. 2003; Smedsrud et al. 2011). As an example, in 2007 anomalous wind conditions over the Arctic contributed to a strengthened transpolar drift and increased sea-ice export through the Fram Strait, reducing the amount of multi-year sea ice within the Arctic (Smedsrud et al. 2011; Zhang et al. 2008). However, Bi et al. (2018) found a decrease in the sea-ice volume export of 600 km^3/year in the period 2011–2014 compared to the periods 1990–1994 and 2003–2008. They attributed this decline first and foremost to changes in sea-ice drift, and to a lesser extent to changes in sea-ice thickness and even less to a decrease in the sea-ice concentration.

Another gateway of major exchange between the Arctic and the North Atlantic oceans is the Barents Sea (e.g. Smedsrud et al. 2013). Although there is a considerable net sea-ice transport from the Nansen Basin of the Arctic Ocean to the Barents Sea shelf both from the north and from the east (e.g. Sorteberg and Kvingedal 2006; Lind et al. 2018; Figure 2.1.1), this sea ice melts locally within the Barents Sea. However, the freshwater input from the melting sea ice in the central Barents Sea is reported to be an important factor in maintaining the pool of Arctic Water, and, thus, the Arctic conditions and strong stratification of the northern Barents Sea (Lind et al. 2018). Moreover, the presence of Arctic Water maintains the Polar Front towards the southern

Barents Sea dominated by warmer and more saline Atlantic Water (e.g. Loeng 1991). A borealization (e.g. Polyakov et al. 2020a) of the Barents Sea, where the influence of Atlantic Water increases at the expense of the influence from Arctic Water, has been found to be ongoing due to an increase in the temperature of the Atlantic Water in the southwest (e.g. Årthun et al. 2012; Fossheim et al. 2015; Onarheim et al. 2015), and further due to increasing temperature in the atmosphere, and, hence, weaker heat loss from the ocean (Skagseth et al. 2020). A declining sea-ice import from the Arctic Ocean and a subsequent weakening of the Arctic Water reservoir further adds to the borealization (Lind et al. 2018).

Here, we present net modelled sea-ice area and volume transport through the Fram Strait and into the Barents Sea and compare the results with observation-base estimates reported in literature. Furthermore, we provide a scientific rationale for including these transport time series as Ocean Monitoring Indicators for the Copernicus Marine Environmental Monitoring Service.

2.1.2. Material and methods

The Arctic Monitoring and Forecasting Center model (product 2.1.1) is the TOPAZ4 system based on a North Atlantic and Arctic configuration of the HYCOM ocean model coupled to a modified version of the CICE3 sea ice model at a horizontal resolution of 12 km, assimilating various observations once a week, including sea-ice concentrations from OSI SAF and thin-ice thickness (from SMOS, since 2014) with an Ensemble Kalman Filter (Xie et al. 2018). The best estimate output is the average of the 100-members ensemble. For further information about the model system and data assimilation, see Sakov et al. (2012). For composite analysis shown in Figure 4, time periods of high/low sea ice area export are determined as those above/below 1 STD of the mean for the full monthly time series during the time period 1993–2019.

We have chosen to calculate the sea-ice area and volume transport through the Fram Strait across the 79°N latitude. In some other studies the section is chosen differently. Generally, Spreen et al. (2009) found a convergence between a northern (80°N) and southern (76°N) section in summer (i.e. the transport at 80°N is larger than further south/downstream at 76°N), while in winter they found a divergence (i.e. the transport at 80°N was smaller than further south due to local ice production in the Greenland Sea). Thus, our results may not be directly comparable to results reported from the literature.

2.1.3. Results and discussion

The average monthly modelled sea ice export through the Fram Strait, both volume and area, follows the observations in terms of seasonal cycle, with a maximum in winter/spring (Oct–Apr) and a minimum in summer (Jul–Aug; Figure 2.1.2a,c). The maximum area export is found in March, with an average export of 133×10^3 km^2, and with a standard deviation of 36×10^3 km^2. However, because the maximum is governed both by the maximum sea-ice extent and favourable wind conditions, the actual month of the maximum area transport may vary between years. The minimum area export decreases to close to zero in July (9×10^3 km^2) but with a standard deviation of 20×10^3 km^2. For the full year, the average annual modelled sea-ice area export is 989×10^3 km^2. This is about 10% larger than the estimate of 880×10^3 km^2 reported by Smedsrud et al. (2017) for the period 1935–2014, based on observations of satellite radar images and surface pressure observations and estimated across 79°N. Moreover, they reported some tendency of a positive trend during recent decades. Similar results were reported by Zamani et al. (2019), although they used a different section located further upstream at 82°N that likely increases the transport estimate in summer and decreases the transport estimate in winter (Spreen et al. 2009). Zamani et al. (2019) estimated an annual sea-ice area transport of 860×10^3 km^2 for the period 1990–2010. Moreover, they found a positive trend of +10% per decade (i.e. an increase of around 90×10^3 km^2/year per decade). On the contrary, our model results indicate a negative, statistically significant ($p < 0.05$) trend of -1.0×10^3 km^2/month per year (i.e. on the order of -100×10^3 km^2/year per decade) for the period 1993–2019. However, we also find that the trend varies with the season, with the largest trend seen in winter while being close to zero in late spring and summer (Figure 2.1.2a). For the full period 1993–2019, this trend represents a 28% reduction in area transport. Other observation-based estimates based on ice motion and concentration fields are lower (Bi et al. 2016). They reported an average maximum sea-ice area transport of 78×10^3 km^2 in March, and an annual average area export totalling 644×10^3 km^2 (Tables 2.1.1 and 2.1.2).

Average modelled sea-ice volume export through the Fram Strait exhibits a seasonal cycle comparable to that of the sea-ice area export (Figure 2.1.2c), with a maximum of 167 km^3 in March, and a minimum of 13 km^3 in July and August. However, the variability is large, with a maximum standard deviation in February (88 km^3) and a minimum standard deviation in August

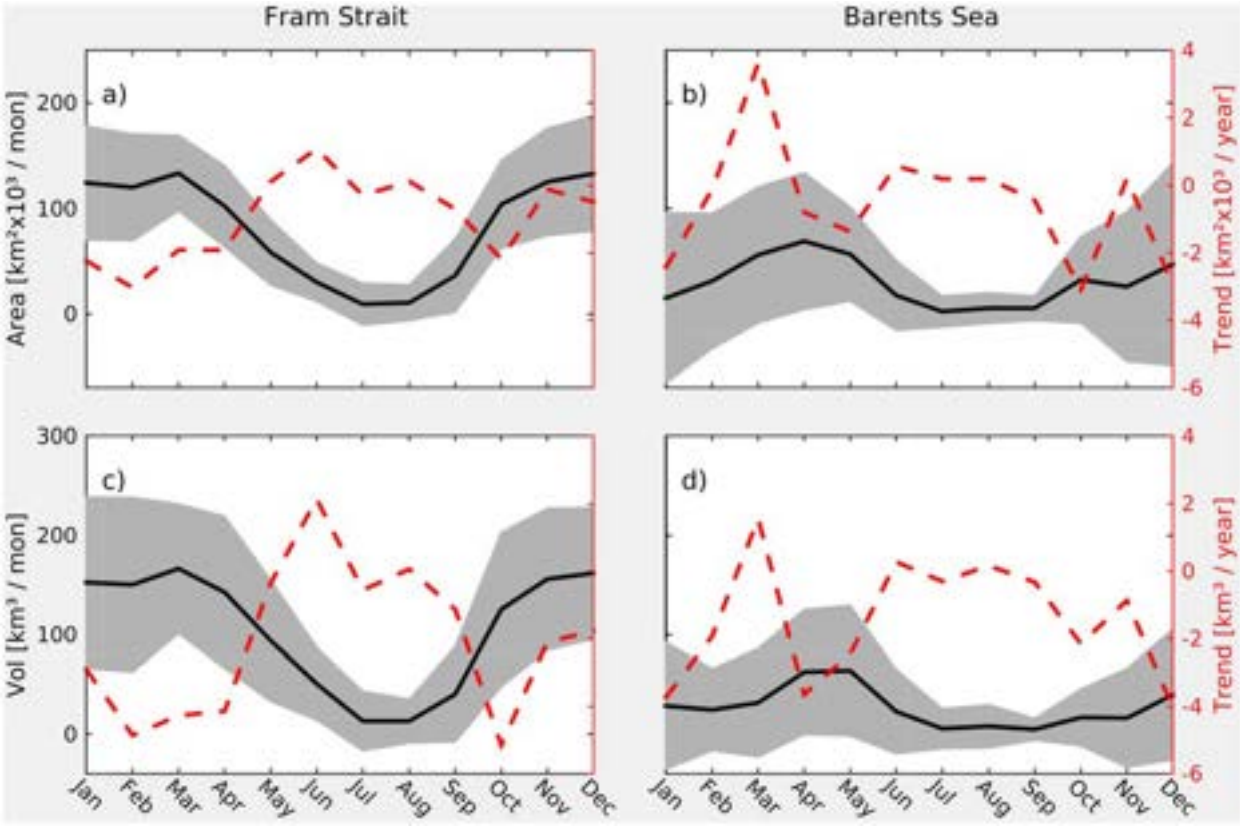

Figure 2.1.2. Seasonal cycle of modelled sea-ice area and volume transport and corresponding trend. (a) Black line shows monthly average sea-ice area transport through the Fram Strait for the period 1993–2019 (positive values southward). Grey shading shows the corresponding ±1 standard deviation. Red, broken line shows the linear trend per year for each month. (b) Similar to (a), but for sea-ice area transport into the Barents Sea (positive values into the Barents Sea). Note that the scale on the *y* axes are similar in (a) and (b). (c) Similar to (a), but showing sea-ice volume transport through the Fram Strait. (d) Similar to (c), but showing for the Barents Sea. Note that the scale on the *y* axes are similar in (c) and (d).

of 22 km^3 implying that there are also months where the net sea-ice transport is directed northwards. Indeed, the maximum modelled monthly sea-ice volume export is 353 km^3 (April 1995), while the minimum modelled monthly sea-ice volume export is −34 km^3 (July 2004; Figure 2.1.3c). Moreover, as for the sea-ice area transport, the actual month of the maximum area transport may vary between years. Our modelled estimates are comparable with observation-based estimates. Spreen et al. (2009) reported an average monthly sea-ice volume export estimate of 217 km^3 for the years 2003–2008, varying between 92 and 420 km^3, which is higher than our modelled estimates. Note, however, that Spreen et al. (2009) used a different section at 80° N which tended to overestimate the transport compared to further south in summer, and slightly underestimate in winter. Moreover, our results suggest that there was indeed an elevated export during the years 2003–2008 (Figure 2.1.3b,c). On the other hand, for the period 2010–2017, Ricker et al. (2018) using a section located at 82°N reported that monthly export estimates varied between 21 and 540 km^3. Annual export varied between 1250 km^3 for the year 2012–2013 and 1910 km^3 for the year 2011–2012 (Ricker et al. 2018), which is close to the average annual transport estimate of 1267 km^3 found in our model results. Based on both satellite and numerical model data Zhang et al. (2017) estimated an annual average sea-ice volume transport of 1132 km^3, ranging from 10 km^3/month in August to 145 km^3/month in March. On the higher end, Spreen et al. (2020) reported an average annual sea-ice volume transport of 2400 ± 640 km^3, which they considered to be a conservative estimate, based on satellite measurement of sea-ice drift and upward-looking sonar for measuring sea-ice

Table 2.1.1. Average sea-ice area transports through the Fram Strait.

	TOPAZ4	Smedsrud et al. (2017)	Bi et al. (2016)	Zamani et al. (2019)
Period	1993–2019	1935–2014	1988–2012	1990–2010
Model / Obs / Satellite	Model	Satellite + Obs	Satellite	Model
Area [10^3 km^2/ year]	989	880	644	860

Table 2.1.2. Average sea-ice volume transports through the Fram Strait. * Annual average calculated from 12 times monthly average.

	TOPAZ4	Spreen et al. (2020)	Zamani et al. (2019)	Spreen et al. (2009)	Ricker et al. (2018)	Ricker et al. (2018)	Zhang et al. (2017)
Period	1993–2019	1992–2014	1990–2010	2003–2008	2011–2012	2012–2013	1979–2012
Model / Obs / Satellite	Model	Satellite + ULS	Model	Satellite	Satellite	Satellite	Model + Satellite
Volume [km^3/year]	1267	2400	3300	2604*	1910	1250	1132

thickness. Based on linear regression, we find a statistically significant ($p < 0.05$) trend of −2.2 km^3/month per year during the period 1993–2019. This trend represents a decrease in the sea-ice volume transport of 43% over the period, which is larger than the relative reduction in sea-ice area transport, implying also a reduction in the average sea-ice thickness during the period. As for the sea-ice area transport, the trend in sea-ice volume transport through the Fram Strait varies with season. A strong, negative trend is found in winter and partly autumn (October), while a weak, positive trend is found in early summer (Figure 2.1.2c).

The model results do not show any statistically significant trend in the sea-ice thickness in the Fram Strait. However, there are some indications of decreasing thickness from the 1990s to the 2000s, a period during which Spreen et al. 2020, observed a negative trend in thickness of 15–21% per decade. This period was followed by an increase in the average modelled thickness from 2015 and onwards. Moreover, the first half of the period corresponds to the period when Hansen et al. (2013) reported a decline in the average sea-ice thickness in the Fram Strait from 3.0 m during the 1990s to 2.2 m during the period 2008–2011.

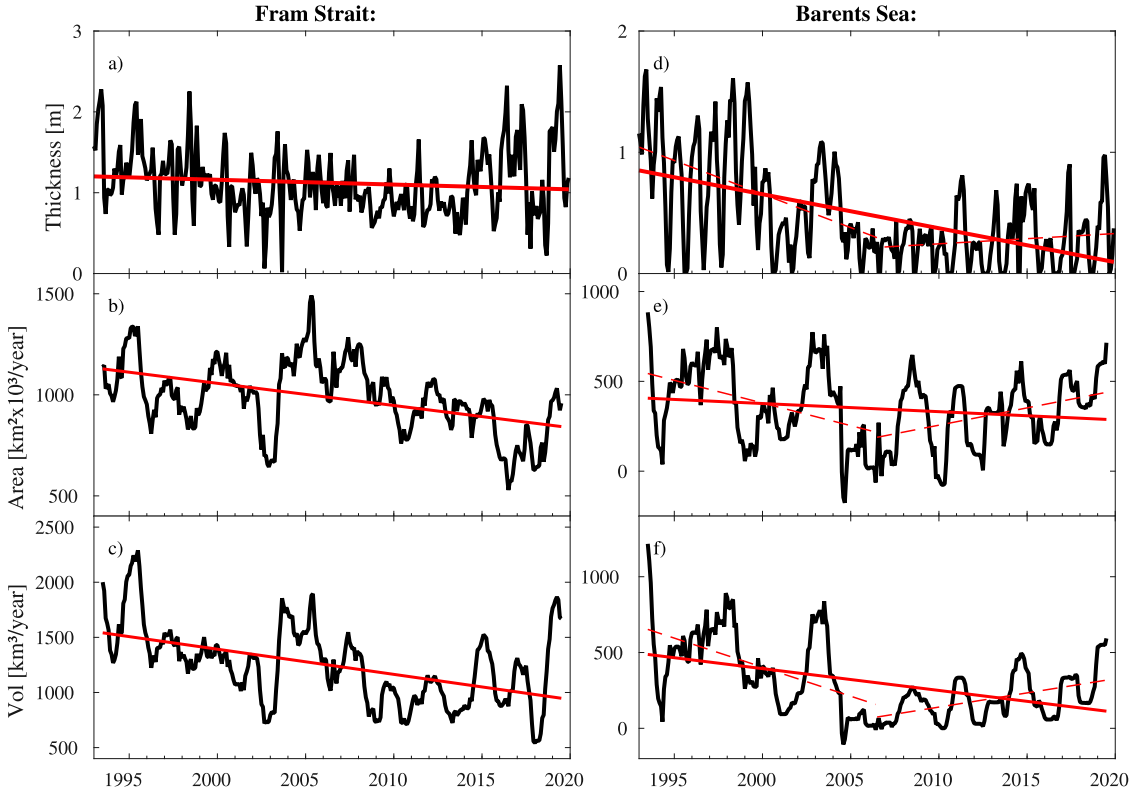

Figure 2.1.3. Time series showing modelled sea-ice thickness, area and volume transport. (a) Average monthly sea-ice thickness in the Fram Strait (black line). The red line shows the linear trend for the period 1993–2019. (b) Twelve-month cumulative sea-ice area transport through the Fram Strait (black line; positive southward). The red line shows the linear trend for the period 1993–2019. (c) Similar to (b), but showing sea-ice volume transport through the Fram Strait. (d) Similar to (a) but showing for the Barents Sea. The broken red lines show the linear trend for the periods 1993–2006 and 2007–2019, respectively. (e) Similar to (b), but showing sea-ice area transport into the Barents Sea. The broken red lines show the linear trend for the periods 1993–2006 and 2007–2019, respectively. (f) similar to (e), but showing sea-ice volume transport into the Barents Sea.

The Barents Sea ice area and volume transport seasonal cycle differ somewhat from that in the Fram Strait. A maximum is seen in late winter/early spring (April–May), along with a secondary maximum in December (Figure 2.1.2b,d). The modelled seasonal sea-ice area transport maximum is 69×10^3 km^2 in April, while the maximum sea-ice volume transport is 64 km^3 in May. A seasonal minimum in both area and volume transport is found in summer (Jul-Sep), with minimum values of 2×10^3 km^2 and 5 km^3, respectively. A secondary minimum is found in January (and also Feb-Mar for volume).

As for the Fram Strait, the time series of both sea-ice area and volume transport show large variability, although the sea-ice transport into the Barents Sea shows smaller seasonal variability than the sea-ice transport through the Fram Strait (Figures 2.1.2 and 2.1.3). Moreover, we find no significant trend in the modelled sea-ice area transport into the Barents Sea, while the volume transport exhibit a statistically significant ($p < 0.05$) linear trend of -1.5 km^3/year for the period 1993–2019, representing a total reduction of 84% over the period, using a linear regression analysis. However, there are some indications of a minimum during the 2000s, when the seasonal maximum seems to be more or less absent, while large seasonal maxima have ocurred in recent years leading to an increase in total volume transport (2014, 2017, and 2019; Figure 2.1.3f). While we did not find a significant trend in the sea-ice area transport overall, the linear regression indicated a reduction in the area transport of nearly 40% from 1993 to 2019. Moreover, there was an apparent minimum in the sea-ice area transport around 2007, followed by an apparent increase, especially after 2015 (Figure 2.1.3e). This contrasts with the findings of Lind et al. (2018), who reported a strong decline in the sea-ice area import to the Barents Sea from the 2000s until 2016. Our results show that the average thickness of the sea ice entering the Barents Sea decreased strongly between 1993 and 2005 (Figure 2.1.3d). From 2005 and onwards, however, there is no trend in the modelled thickness of the sea-ice entering the Barents Sea. Indeed, while we did not find a statistically significant change in the drift speed of the sea ice entering the Barents Sea (not shown), there is a statistically significant ($p < 0.05$), negative trend in the thickness of the sea ice that enters the Barents Sea, with a total reduction of 89% from 1993 to 2019 when using linear regression, but with the major part taking place prior to 2005. Similar to the Fram Strait, there was a strong increase in both the sea-ice area and volume transport in 2019 compared to the preceding years. This finding is in line with the reporting of the sea ice conditions around the Svalbard archipelago returning to 'normal' in 2019 through a combination of preconditioning from anomalous advection of thick multi-year sea ice from the Arctic Ocean and strong, northerly winds in the region (see Section 4.1 in this issue).

A major driver for the interannual variability of the Fram Strait sea-ice transport is the synoptic atmospheric circulation (e.g. van Angelen et al. 2011). Using ± 1 standard deviation to define high/low monthly transports, we find dipole patterns in the large-scale mean sea-level pressure and corresponding cross-sectional winds associated with anomalous sea-ice transport through all the three sections investigated (Figure 2.1.4). This result indicates that atmospheric forcing is a major driver also for the variability in the modelled sea-ice transport, and in agreement with findings based on observations (e.g. Tsukernik et al. 2010). However, our model results indicate a statistically significant, negative trend in the sea-ice area transport through the Fram Strait, opposite of the reported positive trend from increasing winds in recent decades in observations (e.g. Smedsrud et al. 2017) and model simulations (e.g. Zamani et al. 2019). Moreover, the main driver of the trend found in our model results is a negative trend in the sea-ice drift (not shown). On the other hand, the average modelled sea-ice concentration does not show any significant trend. Note, that although a negative trend in sea-ice volume transport was also found based on observations by Spreen et al. (2020), they concluded that a decrease in sea-ice thickness was the main driver of the negative trend. Possible explanations for this discrepancy include differences in the calculation of the area transport, uncertainties in the estimation of sea-ice drift (e.g. Sumata et al. 2015), and errors relating to the parameterisation of wind drag on sea ice in the model (e.g. Chikhar et al. 2019). Moreover, different studies refer to different areas for defining the Fram Strait. However, results presented by Spreen et al. (2020) indicate that the transport estimates are not sensitive to the exact flux gate location. A thorough investigation of these matters is beyond the scope of this study, but we will point out some aspects that could be further elaborated in future studies. Our model results show larger sea-ice drift on the Greenland shelf in the western Fram Strait (Figure 2.1.1) than observed (Smedsrud et al. 2017, see their Figure 2). This discrepancy points to differences in the treatment of fast ice and its impact on sea-ice drift in the model and the observation-based datasets. The current model configuration utilised in this study include a sea-ice model with an elastic-viscous-plastic rheology (Hunke and Dukowicz 1997), while an improved sea-ice

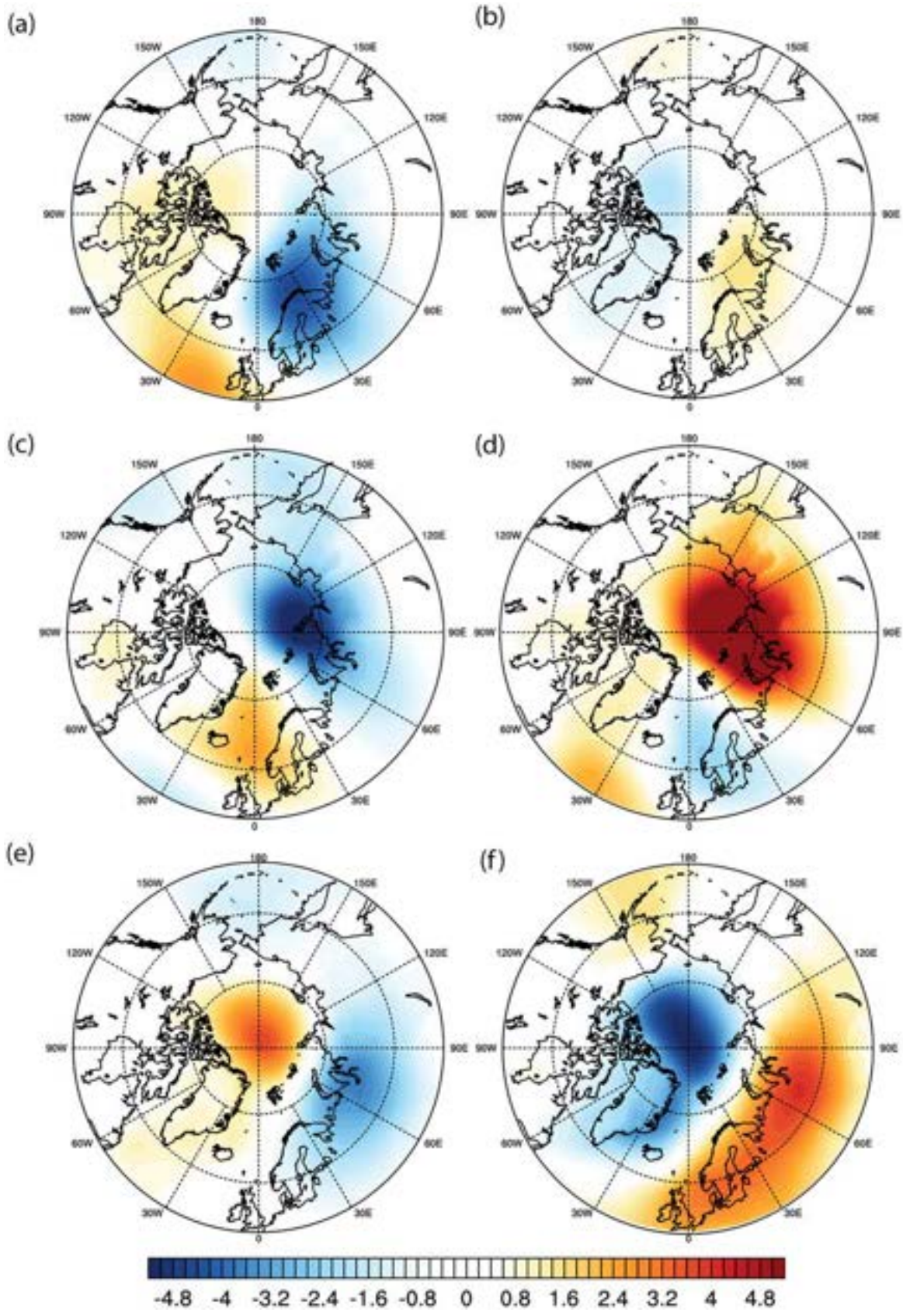

Figure 2.1.4. Composite sea-level pressure anomalies during periods of high sea-ice transport (left) and low sea-ice transport (right) through the Fram Strait (top; a,b), the Barents Sea north section (middle; c,d) and through the Barents Sea east section (bottom; e,f).

model using a Maxwell elastic-brittle rheology (Dansereau et al. 2016), which takes into account ice deformation, will be implemented in the near future.

Differences in the position of Fram Strait sea-ice export estimation may affect the transport estimates in several ways. Complex recirculation patterns within the Fram Strait area (e.g. Beszczynzka-Möller et al. 2012) cause uncertainties in the northward and southward sea-ice drift estimations dependent on the position of the transect used. Depending on the season, sea ice freezing or melting occurs along-stream from north to south in the Fram Strait (e.g. Spreen et al. 2009). Additionally, the West Spitsbergen Current flowing northward in the eastern parts of the Fram Strait is more or less ice free all year round at 79°N, while further north there is varying presence of sea ice, also depending on the northward flow of Atlantic Water (e.g. Ivanov et al. 2016; Polyakov et al. 2017).

The relation between the sea-ice thickness and drift to the total sea-ice volume import in the Barents Sea points toward a change in the properties of the sea ice upstream of the Barents Sea, that is, in the Nansen Basin of the Arctic Ocean (in agreement with the findings of a thinning sea ice cover by Polyakov et al. 2020b), rather than a change in atmospheric conditions affecting the general circulation, as the main driver of the changes in the sea-ice volume import to the Barents Sea during the period 1993–2019. However, our results indicate that the preconditioning through decreasing sea-ice thickness from less multi-year sea ice present in the Nansen Basin was a main driver of the decline in the sea-ice import to the Barents Sea in the 1990s and the first half of the 2000s, whereas after the mid-2000s, the area transport has increased (while the thickness has remained more or less constant), which indicates that changes to the general atmospheric circulation may have played an increasingly important role in the most recent decade.

Section 2.2. Ocean heat content in the High North

Authors: Michael Mayer, Vidar S. Lien, Kjell Arne Mork, Karina von Schuckmann, Maeva Monier, Eric Greiner

Statement of main outcome: This section presents an analysis of ocean heat content (OHC) north of 60°N. We use a range of data sources including in-situ data and ocean reanalyses, which are in remarkably good agreement despite the relatively sparse observational coverage. For the 1993–2019 period, we find a warming trend of 0.6 ± 0.2 Wm^{-2} for the upper 700 m and 0.7 ± 0.2 Wm^{-2} for the full-depth ocean north of 60°N. This suggests that neglecting the Arctic ocean in quasi-global OHC evaluations leads to an underestimate of ~4%, which is similar to its area fraction of the global ocean. The strongest warming below 700 m is found in the Norwegian and Greenland Seas. The ice-free ocean area warms substantially faster at a rate of 1.4 ± 0.5 (1.9 ± 0.7) Wm^{-2} in the upper 700 m (full-depth) ocean, compared to the ice-covered ocean which shows a non-significant warming rate of 0.2 ± 0.2 Wm^{-2}. The slow warming of the ice-covered Arctic Ocean thus masks the rapid and above-global-average warming of the ice-free ocean when considering the pan-Arctic region north of 60°N as a whole.

Product used:

Ref. No.	Product name & type	Documentation
2.2.1	INSITU_GLO_TS_REP_OBSERVATIONS_013_001_b	PUM: https://marine.copernicus.eu/documents/PUM/CMEMS-INS-PUM-013-001-b.pdf QUID: https://marine.copernicus.eu/documents/QUID/CMEMS-INS-QUID-013-001b.pdf
2.2.2	GLOBAL_REANALYSIS_PHY_001_031 (GREPv2)	PUM: https://marine.copernicus.eu/documents/PUM/CMEMS-GLO-PUM-001-031.pdf QUID: https://marine.copernicus.eu/documents/QUID/CMEMS-GLO-QUID-001-031.pdf
2.2.3	MULTIOBS_GLO_PHY_REP_015_002	PUM: https://marine.copernicus.eu/documents/PUM/CMEMS-MOB-PUM-015-002.pdf QUID: https://marine.copernicus.eu/documents/QUID/CMEMS-MOB-QUID-015-002.pdf

2.2.1. Introduction

Ocean heat content (OHC) is an important quantitative variable in the Earth's climate system, and provides a unique measure of the current status and prospects of global warming (von Schuckmann et al. 2016; Cheng et al. 2017). In the upper 700 m of the near-global (60°N-60°S) ocean, area averaged OHC has increased at a rate of 0.3 ± 0.1 Wm^{-2} during 1960–2018 and the rate increased to 0.9 ± 0.1 Wm^{-2} over the period 2005–2018 (von Schuckmann et al. 2020). The pan-Arctic (here defined as north of 60°N) – a region where near-surface warming has been reported to occur faster than the global average (e.g. Serreze and Barry 2011) – is usually not represented in the near-global global analysis of OHC, predominantly due to the fact of low subsurface temperature data coverage in this area. Recent studies have shown that the Arctic OHC is warming

at a rate close to the global warming rate (e.g. Mayer et al. 2016; von Schuckmann et al. 2018; Mayer et al. 2019). Under anthropogenic pressure, Arctic sea-ice cover is declining, thereby altering the ocean-atmosphere heat exchange through larger areas of open water. In addition, increased ocean heat transport to the Arctic is pushing oceanic conditions typical of sub-polar regions (e.g. a comparatively weak stratification) downstream into the northern polar basin, a process termed 'Atlantification' (e.g. Polyakov et al. 2017) affecting also ocean-ice fluxes (Polyakov et al. 2020). Thus, the OHC and its spatial distribution within the Arctic is a relevant metric at the interface of oceanic transports, surface fluxes, sea ice melt, and the global energy inventory.

The Nordic Seas (Norwegian, Greenland, and Iceland Seas) is a region of major water mass transformation in the northern loop of the global thermohaline circulation (e.g. Aagaard et al. 1985; Mauritzen 1996). Here, saline and relatively warm Atlantic Water flows through the Norwegian Sea to the east en-route to the Arctic Ocean, while colder and fresher water masses of Arctic origin flows southward through the Greenland Sea to the west. Especially the northern part of the Norwegian Sea, the Lofoten Basin, is a reservoir of Atlantic Water and represents a major heat sink, with strong and persistent heat loss to the atmosphere, and as will be shown in this contribution, above-average regional warming. The OHC as an integrated measure of the hydrographic conditions in the Norwegian Sea represent a robust indicator and precursor of the ocean heat transport to the Arctic Ocean (e.g. Furevik 2001). The variability in the OHC locally in the Nordic Seas is mainly a product of local air–sea fluxes and advection. Several studies have indicated that variation in ocean heat loss to the atmosphere can explain about half of the year-to-year OHC changes in the Norwegian Sea (e.g. Mork et al. 2019). Other studies have revealed that advection is the primary cause of interannual to decadal heat content variability in this area (e.g. Carton et al. 2011; Asbjørnsen et al. 2019). Thus, advection tends to play a dominating role in the OHC variability in the Norwegian Sea on time scales longer than one year (Mork et al. 2019).

Quantification of ocean warming in the high north is crucial for a better understanding of Arctic change. However, earlier assessments of Arctic OHC examined neither the spatial details of the trends nor the robustness of the results, which were obtained largely from reanalyses. Here we assess Arctic OHC in more detail than before and also examine the agreement of reanalysis products and in-situ observations for a better understanding of uncertainties.

2.2.2. Data & methods

OHC integrated over the upper 1000 m of the Norwegian Sea is calculated from Argo data (CORA-GLOBAL-5.1, Ref No 2.2.1), and is presented as anomalies (OHCA), relative to the World Ocean Atlas 2018 (WOA18; Locarnini et al. 2018) climatology using the latest averaging period, 2005–2017. For each Argo profile, the temperature climatology is interpolated horizontally and vertically to match the location and vertical resolution of the Argo profile (Mork et al. 2019). The advantage of using anomalies is that they are independent of the reference value. For each Argo profile, OHC anomalies are calculated above the reference depth h as

$$\mathrm{OHC} = c_p \rho_0 \int_{-h}^{0} (T - T_{\mathrm{clim}}) dz, \qquad (1)$$

where c_p is the heat capacity (4.0×10^3 Jkg^{-1} K^{-1}), ρ_0 is a reference density (1030 kgm^{-3}), and z is the vertical axis with $z = 0$ at the sea surface. Subscript 'clim' indicates climatological data from WOA18, and is a function of month, depth and location. The integrated depth, h, is set to 1000 m, as the upper 1000 m of the Norwegian Sea comprises the bulk of the Atlantic Water flow towards the Arctic. Monthly means with uncertainties (standard deviation) are calculated from all OHC anomalies for the Norwegian and Lofoten basins within each month.

To cover the full Arctic, we compute OHC from the Global Ocean Reanalysis Ensemble product (GREP; product ref. 2.2.2) at a ¼° spatial and monthly temporal resolution. We present results for the upper 300, 700 m, upper 1000 m and full-depth (average depth north of 60 N to 1240 m, maximum depth > 4600 m) OHC, covering 1993–2019. In addition to the GREP, we also present results from CMEMS ARMOR3D (Ref No 2.2.3; Guinehut et al. 2012). ARMOR3D is a weekly global product with a 1/4° spatial resolution and 33 vertical levels. It provides temperature, salinity, geostrophic currents and mixed layer gridded fields from 1993 to present. Satellite altimetry and sea surface temperature are combined with in situ data by optimal interpolation. In situ data include vertical profiles from moorings, scientific campaigns, autonomous profilers, gliders, ships of opportunity, sea mammals, as well as surface data from various buoys and ferry boxes. Satellite data cover most of the Arctic in summer (altimetry goes up to 82°N), and there is some data near Svalbard even in winter.

Anomalies of the GREP and ARMOR3D data are calculated with respect to their 1993–2014 climatology. For the comparison with Argo data, we use the same

climatology but additionally remove the long-term-means of the period for which Argo data is available (2002–2019 for the Norwegian Basin and 2005–2019 for the Lofoten Basin). Additionally, we provide regional averages for the ice-free ocean and ice-covered ocean. We use 30% annual mean sea ice concentration based on the GREP ensemble mean as a threshold for sea ice cover.

Trend estimates are based on the ordinary least squares method and are provided for the full 1993–2019 period. The uncertainty estimate used for significance testing takes into account random and structural errors as follows. Random errors are estimated from the standard errors of the linear regression coefficients of the GREP ensemble mean and the Argo OHC evolutions, respectively, taking temporal auto-correlation into account. Structural uncertainty for the GREP is estimated from the spread in the four OHC trends computed for the four reanalyses separately, divided by $\sqrt{n-1}$ ($\sqrt{3}$). For the Argo, 100 synthetic time series were constructed and the structural uncertainty was estimated by the standard deviation of the linear regression coefficients of these 100 time series. The synthetic time series were constructed by creating 100 random numbers for each month that were normally distributed around the monthly OHC estimate with a standard deviation equalling the uncertainty during the respective month. Random and structural errors are added in quadrature to obtain the uncertainty estimate used for significance testing.

2.2.3. Results

2.2.3.1. Reanalysis – observation comparison

Before examining the OHC in the pan-Arctic region from the gridded products (GREP and ARMORD3D), we perform a comparison between the estimated OHC from the reanalyses and observations based on Argo. The region is limited to the Lofoten and Norwegian basins of the Norwegian Sea, and the depth range is from the surface to 1000 m depth. The OHC is estimated according to equation (1). Due to limitations in the availability of Argo observations, the observation-based estimates are limited to the period June 2002 to July 2018 in the Norwegian basin and March 2005 to September 2018 in the Lofoten basin, respectively. In the comparison, the analysis of both the reanalysis-based and observation-based time series include the period covered by observations only. The time series based on the reanalyses and the observations are shown in Figure 2.2.1. Generally, OHCA estimates from both the GREP and ARMOR3D follow the observations in terms of both magnitude and variability. However, the observation-based estimates display larger month-to-month variability (Figure 2.2.1), which could be related to sampling noise in the observations that is smoothed by data assimilation. Based on monthly averages, the correlation, R, between the de-trended GREP and observation-based estimates is 0.59 ($p < 0.001$) in the Norwegian basin and 0.56 ($p < 0.001$) in the Lofoten basin. However, when we filter the time series using a 12-month moving

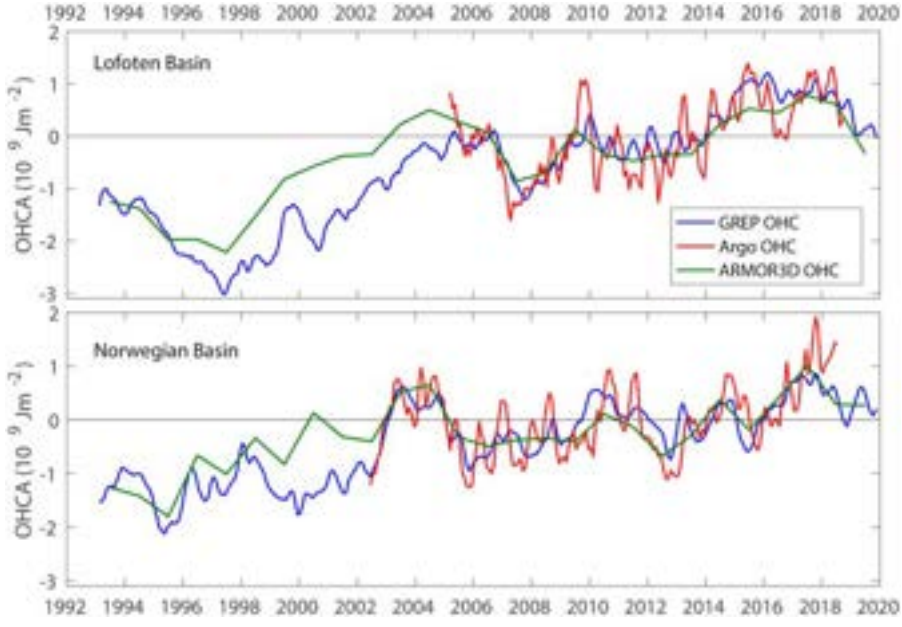

Figure 2.2.1. Time Series of 0–1000 m ocean heat content anomalies in the Lofoten (top) and Norwegian (bottom) basins estimated from Argo (Ref. No. 2.2.1) and the Global Ocean Reanalysis Ensemble product (Ref. No. 2.2.2). Note that GREP and Argo data represent three-monthly averaged OHCA, while ARMOR3D data represents annual OHCA.

boxcar window (i.e. annual averages), the correlation coefficients increase to $R = 0.85$ ($p < 0.001$) and $R = 0.90$ ($p < 0.001$) in the Norwegian and Lofoten basins, respectively. Another noteworthy feature of Figure 2.2.1 is that the agreement between the GREP and ARMOR3D is degraded prior to the availability of Argo data, which demonstrates the strong constraint that Argo provides on ocean state estimates.

The trends in the reanalysis-based OHC estimates are comparable to the observation-based estimates in both basins (1.22 ± 0.85 Wm^{-2} and 1.69 ± 0.92 Wm^{-2} in the Norwegian basin, 3.75 ± 0.96 Wm^{-2} and 3.16 ± 1.35 Wm^{-2} in the Lofoten basin, with 95% confidence intervals computed as described in the Data & Methods section). All trends are significant at the 95% level. Moreover, the individual trend estimates fall within the uncertainty range (1σ) of the associated estimate from the reanalyses/observations. Thus, there is a close agreement between the reanalysed and observed OHC estimates in both the Norwegian Sea basins, both in terms of trend during the 2000s and inter-annual variability. While there is a statistically significant correlation also on monthly timescales, this correlation is rather weak.

2.2.3.2. Ocean heat content in the high North from reanalyses

Figure 2.2.2a presents linear trends of upper 700 m OHC over 1993–2019. We focus on the spatial features that are statistically significant on the 95% level. Widespread and significant warming is present in the upper 700 m in basically all ice-free ocean north of 60N. Maximum warming is found in the Barents and Norwegian seas, with regional trends in the Norwegian Sea exceeding 6 Wm^{-2}, which is almost twice as high compared to the upper 300 m OHC trends (not shown). Strongest warming in the Barents Sea occurs in the southeastern part, which is in agreement with the findings of Skagseth et al. (2020). Weak but significant warming is present also in the shelf seas along the Siberian coast. Moderate but still significant warming is found also in the Beaufort Gyre, an area that is ice-covered most of the year. Weak and largely insignificant cooling is present around the Amundsen Basin. It is important to note that observational data in the sea-ice-covered areas is scarce, but at least the moderate warming in the Beaufort Gyre seems consistent with observation-based estimates. For example, Timmermans et al. (2018) found a halocline warming of ~0.3 Wm^{-2} during 1992–2015 in this region (based on the numbers in their Figure 1).

Figure 2.2.2b shows linear trends of OHC below 700 m. In the Norwegian and Greenland Seas, substantial warming is present at these depths, attaining values greater than 5 Wm^{-2}. Thus, full-depth OHC trends in the Nordic Seas exceed 10 Wm^{-2} regionally. In contrast, penetration of warming OHC trends below 700 m into the central Arctic is progressing relatively slowly according to the results from the GREP.

We now turn to regionally averaged OHC evolution during 1993–2019. Figure 2.2.3 presents a time series of upper 700 m OHC anomalies for the pan-Arctic,

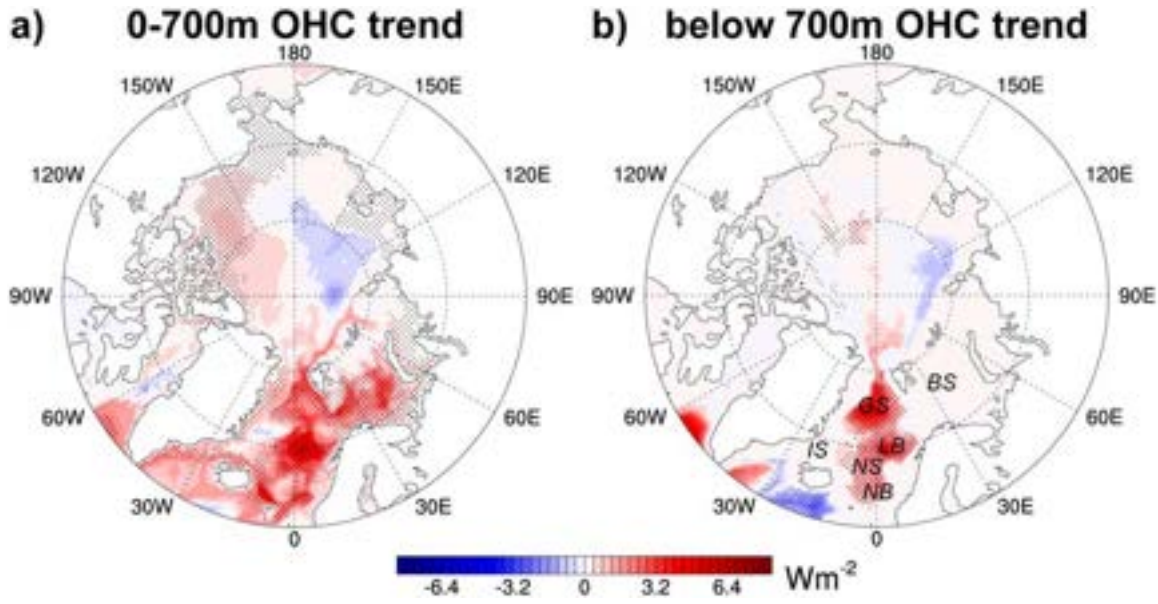

Figure 2.2.2. Linear OHC trends (converted to Wm^{-2}) (a) of the upper 700 m and (b) below 700 m for 1993–2019 from the GREP (Ref. No. 2.2.2). Stippling denotes regions where trends are significant at the 95% confidence level. Figure (b) additionally indicates the location of water bodies referred to in the text: Iceland Sea (IS), Norwegian Sea (NS) with two basins Lofoten Basin (LB) and Norwegian Basin (NB), Greenland Sea (GS), and Barents Sea (BS).

including results for the two sub-regions (ice-covered and ice-free). Pan-Arctic upper 700 m OHC has increased since 1993, with a much larger contribution from the ice-free Arctic Ocean. One should note that the ice-free ocean covers only ~37% of the total ocean area north of 60°N. This is consistent with Figs 2.2.2a and b showing particularly strong warming in the Greenland and Norwegian Seas. Remarkably rapid warming occurred in the ice-free Arctic ocean during 2002–2004, which can also be seen in the pan-Arctic OHC. More in-depth diagnostics reveal that this rapid warming signal persists when removing Argo data in an observing system experiment (not shown), suggesting that this is not an artefact from increased data coverage and is indeed a real climate signal. The long-term OHC increase and interannual signals, including the rapid warming in 2002–2004, are consistently shown also by ARMOR3D. Even in the data-sparse regions under sea ice, ARMOR3D yields similar results as the GREP.

Finally, we present area-averaged OHC trends for the pan-Arctic as well as the contributions from ice-free and ice-covered ocean in Figure 2.2.4. The 1993–2019 warming rate for the pan-Arctic was 0.4 ± 0.1 Wm^{-2} (0.44 ± 0.07 Wm^{-2} when allowing two decimals) in the 0–300 m layer and 0.6 ± 0.2 Wm^{-2} (0.57 ± 0.16 Wm^{-2}) in the 0–700 m layer. The trend is enhanced by a factor of ~1.3 when integrating down to 700 m, while the uncertainty increases by a factor of ~2.1. This indicates that the signal-to-noise ratio, defined as the ratio of the trend and its uncertainty, is smaller for the 0–700 m layer compared to the 0–300 m layer. For the full-depth ocean, warming is further enhanced to 0.7 ± 0.2 Wm^{-2} (0.74 ± 0.19 Wm^{-2}).

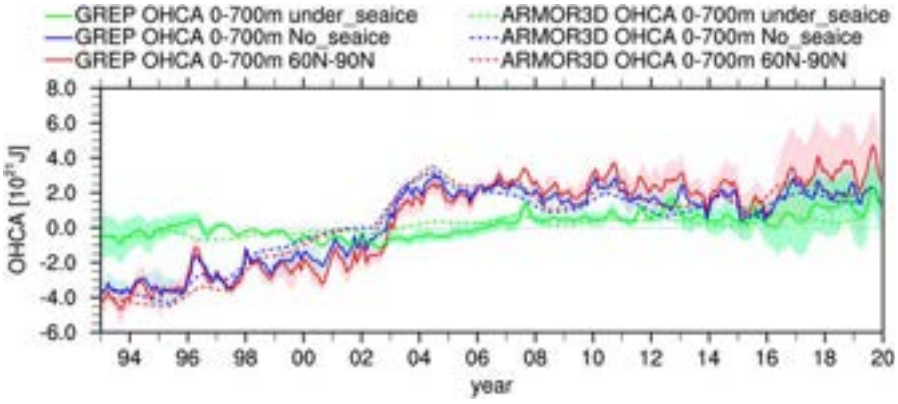

Figure 2.2.3. OHC anomaly (OHCA) of the upper 700 m in 10^{21} J relative to the 1993–2014 climatology for the Arctic Ocean north of 60 N and the partition into ice-covered regions (under_seaice) and ice-free regions (no_seaice). The partition is based on the annual mean sea ice concentration using a 30% threshold. Curves represent the GREP (Ref. No. 2.2.2) ensemble mean, and the shading represents the intra-ensemble spread. The dashed lines represent results from ARMOR3D (Ref. No. 2.2.3; based on annual mean values).

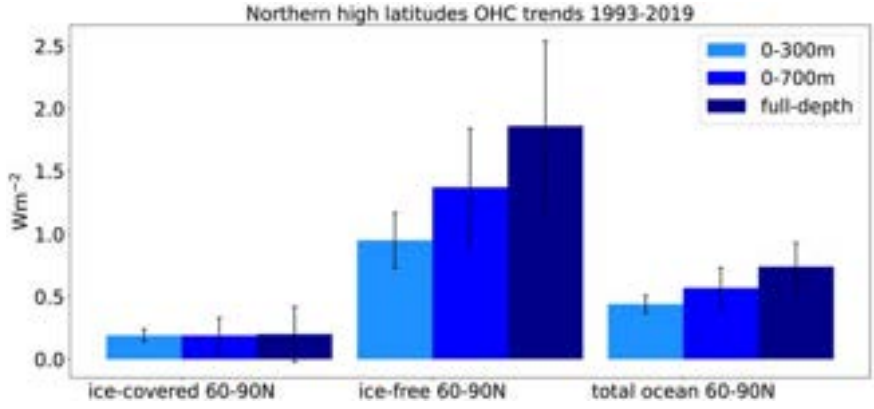

Figure 2.2.4. Linear OHC trends 1993–2019 for Arctic Ocean north of 60N and decomposition into ice-free and ice-covered ocean north of 60N (based on the 1993–2019 sea ice concentration climatology with a threshold of 30% concentration) estimated from the GREP (Ref. No. 2.2.2). Trends are converted to warming rates given in Wm^{-2}. The conversion factor from Wm^{-2} to ZJ/yr is 0.51 for the pan-Arctic Ocean, 0.17 for the ice-free ocean, and 0.34 for the ice-covered ocean. Uncertainties are the 1σ-uncertainties.

Warming is weak in the ice-covered ocean (both in area-specific and area-integrated units), probably because sea ice melt takes up a substantial amount of extra energy and the ocean below is protected from the atmosphere above (Mayer et al. 2019), which is elaborated on in the discussion. Upper 300 m trends are 0.2 ± 0.1 Wm^{-2}. Extending to the full-depth ocean does not alter the obtained trend, but uncertainty is much increased (0.2 ± 0.2 Wm^{-2}).

Strong warming is found in the ice-free ocean, with a warming trend of 1.0 ± 0.2 Wm^{-2} in the upper 300 m, 1.4 ± 0.5 Wm^{-2} in the upper 700 m layer, and 1.9 ± 0.7 Wm^{-2} in the full-depth ocean. We note the much higher signal-to-noise ratio of the trends in the ice-free ocean compared to the ice-covered ocean, which likely is a result of the much better observational coverage.

2.2.4. Discussion

We have shown that the GREP represents realistically the observed trend and temporal variability of OHC in the Norwegian Sea, which is a robust indicator of heat transport toward the Arctic Ocean. This finding indicates that the mechanisms that control the variability in Atlantic Water heat content en route to the Arctic Ocean are realistically represented in the GREP. We note that the GREP is not independent of the Argo data, as these observations are assimilated into ocean reanalyses. Moreover, the found agreement does not necessarily guarantee a correct balance of oceanic transports (e.g. Carton et al. 2011; Asbjørnsen et al. 2019), local air–sea heat fluxes (e.g. Segtnan et al. 2011; Mork et al. 2019), and shelf slope – basin exchange (e.g. Isachsen et al. 2012; Mork and Skagseth 2012) within the Norwegian Sea in the GREP, as a potentially strong contribution to regional OHC stems from data assimilation. However, we note that earlier studies found good agreement between oceanic transports obtained from oceanic reanalyses and mooring-derived data in the High North (e.g. Pietschnig et al. 2018; Uotila et al. 2019; Mayer et al. 2019), which provides additional confidence in our results. Nevertheless, more validation work beyond OHC is needed to further corroborate our findings.

A rapid increase in 0–700 m pan-Arctic OHC is reported during the period 2002–2004, with the open-water area accounting for most of the increase (Figure 2.2.3). However, while the increase in OHC persists for the pan-Arctic region as a whole, it represents a transient signal within the Norwegian Sea (Figure 2.2.1). This suggests an advective nature of the warming, where the signal propagates from the northern North Atlantic to the entrance of the Arctic Ocean in a few years (Furevik 2001; Årthun and Eldevik 2016). Thus, it may be a delayed effect of the rapid warming of the North Atlantic subpolar gyre in the mid-1990s as documented by Robson et al. (2012), in conjunction with observed changes to atmospheric circulation as discussed by Proshutinsky et al. (2015). Indeed, a temperature increase was observed in the Faroe-Shetland Channel in 2002, preceding the OHC increase observed in the Norwegian Sea in 2002–2003 (Figure 2.2.1) and subsequent temperature maxima in the Barents Sea Opening and the Fram Strait in 2006 (e.g. González-Pola et al. 2019).

The large difference in the rate of increase in OHC between open ocean and ice-covered areas is worthy of further discussion. The rapid warming of the ice-free ocean appears to be driven by a combination of increased ocean heat advection and decreased surface net heat loss. For example, Tsubouchi et al. (2020) found a general increase of ocean heat transport into the Nordic Seas after 2001, and Mork et al. (2019) found that both changes to oceanic transports and air–sea exchange play a role in the Norwegian Sea. Furthermore, Skagseth et al. (2020) showed that within the Barents Sea – a main area for oceanic heat loss in the Arctic region – a reduction in the turbulent heat loss from the Atlantic Water to the atmosphere due to increased air temperatures more than offset the increase in surface heat loss due to increased open water area and enhanced shortwave radiation absorption arising from the ice-albedo feedback. The contrastingly slow warming of the ice-covered Arctic Ocean indicates that a large fraction of the increased OHC in the upstream, ice-free areas is lost in the northward-moving seasonal and marginal ice zones either directly to the atmosphere, especially with trends towards larger areas of open waters (e.g. Ivanov et al. 2016; Skagseth et al. 2020), or through melting sea ice, as suggested by, e.g. Dmitrenko et al. (2014). However, a smaller residual fraction of the increase in OHC is advected into the ice-covered part of the Arctic, seen as a subsequent warming along the path of the Atlantic Water flow through the Fram Strait and also the St. Anna Trough and to the interior Polar Basin (Figure 2.2.2a; Lien and Trofimov 2013; Skagseth et al. 2020). In addition, the positive OHC trends in the Beaufort Gyre (Figure 2.2.2) can be linked with its acceleration in association with recent trends towards more anticyclonic atmospheric circulation in this region (Proshutinsky et al. 2015).

The distinction between OHC trends in ice-free and ice-covered regions helps to explain the surprising result of earlier studies (Mayer et al. 2016; von Schuckmann et al. 2018; Mayer et al. 2019) that pan-Arctic OHC increase is not stronger than its global average despite Arctic amplification in the near-surface climate. OHC

increase in the ice-free ocean north of 60N is indeed above global average values, but relatively weak trends under sea ice mask this when considering pan-Arctic trends. However, increased temperature in the Atlantic Water flowing into (formerly) ice-covered regions is also projected to continue in the future (Årthun et al. 2019). Thus, propagation of ocean heat downstream to the interior Polar Basin through advection may play an increasingly important role in Arctic Ocean warming in the coming decades. One important caveat of the results for the sea-ice-covered regions is the low number of observations in presence of sea ice. However, we do find good agreement between the GREP-based results and those from ARMOR3D, which use very different data assimilation approaches and use different observational data. Moreover, there is quantitative agreement with an observation-based study in the Beaufort Gyre (Timmermans et al. 2018), and the weak OHC increase under sea ice is physically plausible. Hence, we consider our results for sea-ice-covered regions reasonable, but our confidence intervals likely underestimate true uncertainty.

To put these results into a global context, it is useful to consider area-integrated quantities. The pan-Arctic linear full-depth OHC trend 1993–2019 converts to 0.38 ± 0.10 ZJ/yr. This can be compared to the 60S–60N 0–2000 m OHC trend of 9.20 ± 0.92 ZJ/yr (1993–2018) as estimated by von Schuckmann et al. (2020). Thus, neglect of the Arctic ocean in quasi-global OHC assessments leads to an underestimate of ~4%, which is similar to its area fraction of the global ocean.

Section 2.3. Declining silicate and nitrate concentrations in the northern North Atlantic

Authors: Kjell Gundersen, Vidar S. Lien, Jane S. Møgster, Jan Even Øie Nilsen, Håvard Vindenes (IMR)

Statement of main outcome: A comprehensive analysis of nutrient data in three regions of the Nordic Seas between 1990 and 2019, shows a statistically significant decline in surface silicate. This finding is in agreement with previous reports on silicate from the northern regions of the North Atlantic, but this is the first look at a 30-year record of water column silicate and nitrate in the Nordic Seas. Surface nutrient concentrations in the Nordic Seas appear to be regulated by the Subpolar Gyre situated south of Greenland and Iceland. The Subpolar Gyre Index has been in a decline for most of the period investigated, which means that the gyre has moved westward allowing more subtropical (and more nutrient depleted) water into the Nordic Seas. The largest decline in silicate occurred during the first ten years investigated and is still on a downward slope. We also found a statistically significant decline of silicate in Arctic Water in the Greenland Sea, but with a time-lag relative to the decline in Atlantic Water. Nitrate on the other hand, did not decline as uniformly and only had a significant drop midway through the time-series (2005–2009) and only in the Norwegian Sea, before it again increased to previous levels. The molar nitrate:silicate ratio however, showed a steady increase throughout the thirty year period investigated. Less access to silicate and other macronutrients in the Nordic Seas may shorten the spring diatom bloom period and hamper zooplankton growth, which in turn may have consequences for growth and development of commercially important fish stocks in these waters.

Product used:

Ref. No.	Product name & type	Documentation
2.3.1	INSITU_GLO_BGC_REP_OBSERVATIONS_013_046	PUM: https://marine.copernicus.eu/documents/PUM/CMEMS-INS-PUM-013-046.pdf QUID: https://marine.copernicus.eu/documents/QUID/CMEMS-INS-QUID-013-046.pdf
2.3.2	INSITU_GLO_NRT_OBSERVATIONS_013_03	PUM: https://marine.copernicus.eu/documents/PUM/CMEMS-INS-PUM-013.pdf QUID: https://marine.copernicus.eu/documents/QUID/CMEMS-INS-QUID-013-030-036.pdf

2.3.1. Introduction

Periodic changes in the eastward extent of the Subpolar Gyre (SPG), an important regulator of the North Atlantic thermohaline circulation, determines the inflow of high-saline water to the Nordic Seas (Hátún et al. 2005). Rey (2012) first noticed a bidecadal drop in dissolved silicic acid (silicate) concentrations in the Nordic Seas, along with an increase in salinities, and suggested that periods of relative weak North Atlantic Oscillation (NAO) caused warmer, high-saline Atlantic Water to enter the Norwegian Sea. The strength of the NAO determines the east–west positioning and frontal shifts of the SPG and hence, the magnitude of Atlantic Water influx to the Norwegian Sea (Sarafanov 2009). More recently, Hátún et al. (2017) were able to demonstrate that the shifting fronts of the SPG to a large extent determine surface hydrography, and silicate content, in several areas of the subpolar North Atlantic region (Norwegian Sea, Irminger Sea, Labrador Sea). Water entering the Greenland Sea does not only originate

from Atlantic Water, but has another pathway that may take years to decades through the Arctic and the Fram Strait (e.g. Schlosser et al. 1995). Given this time-lapse, diminishing silicate concentrations in the Norwegian and Barents Seas may not immediately appear in the Greenland Sea, as this region may be a mia mixture of Atlantic Water and Arctic waters.

Extended periods of reduced access to silicate, and possibly other nutrient elements, may have severe implications for the pelagic community composition in the Nordic Seas. The four nutrients most commonly measured in the Nordic Seas are nitrate, nitrite, phosphate and silicate. Of these, nitrite is a product of microbiological activity and appears in very low concentrations relative to nitrate, and phosphate is readily recyclable within the euphotic zone. Therefore, we expect to see more immediate effects from diminishing nutrient concentrations in the pool determining annual new production (nitrate) and in the single most important element for sustained diatom growth (silicate). North Atlantic spring blooms are often dominated by diatoms (Savidge et al. 1995) as these primary consumers of dissolved silicate rapidly respond to the high nutrient concentrations. Toward the end of the bloom however, silicate and other macronutrients are approaching depletion and the phytoplankton community becomes less buoyant. As the remnants of the spring bloom exit surface waters it becomes a major component of the export of particulate organic matter to the deep ocean (Honjo and Manganini 1993). The latter has led Pollock (1997) and others to suggest that available silicate in surface waters may determine atmospheric CO_2 drawdown via the 'biological pump' (Volk and Hoffert 1985). However, an overall decline in accessible silicate in surface waters, the end product of diminishing silicate concentrations in deeper waters, may reduce the length and magnitude of the annual phytoplankton spring bloom.

Diatoms are only competitive with other phytoplankton species at silicate concentrations higher than 2 µmol/L (Furnas 1990; Egge and Aksnes 1992). Therefore, reduced annual influx of silicate to the euphotic zone, relative to other macronutrients, may hasten the switch towards a flagellate dominated community and possibly regenerated production (Smayda et al. 1990). As of today, spring blooms in the Nordic Seas are mainly composed of diatoms (Rey 2004) and the magnitude and timing of each bloom is considered a deciding factor in both growth and recruitment of *Calanus finmarchicus* and *C. glacialis*, two of the most important calanoid copepods in the region (Melle et al. 2004). Calanoid copepods, such as the most abundant species, *C. finmarchicus*, appears to have a preference for diatoms (Meyer-Harms et al. 1999) and a number of studies have concluded that food quality affects copepod production and ultimately, growth at higher trophic levels (Barofsky et al. 2010, and references therein). Calanoid copepods in turn, are considered one of the main staples for several species of commercially important pelagic fish, both in the Norwegian Sea and the Barents Sea (Skjoldal et al. 2004; Gjøsæther 2009). Therefore, changes in the magnitude or composition of the spring bloom, and less significance of diatoms, may ultimately have direct implications for commercial fisheries in these regions.

Here we present an updated, 30 year time-series of silicate measurements from the Nordic Seas, as we also consider the fate of nitrate concentrations in these waters during the same period of time. The relative change between the two macronutrient concentrations (the nitrate:silicate-ratio) and its implications for phytoplankton growth and community composition, is also discussed.

2.3.2. Data and methods

The nutrient data used in this study, which include silicate and nitrate collected from the Nordic Seas between 1990 and 2019, are available from the *Copernicus Marine* database (product ref. 2.3.1; 2.3.2) and the majority of data (>99%) originate from the *Institute of Marine Research* (IMR). Therefore, we provide a detailed overview of the seawater sampling and rigorous data quality control at the IMR, that precedes the quality control procedures applied by the *Copernicus Marine Environment Monitoring Service* (CMEMS; Jaccard et al. 2020), where all data are further scrutinised by automated tests and all outliers are checked manually (product ref. 2.3.1; Jaccard et al. 2020). Only data flagged as 'good data' (flag = 1) were included in this study.

Seawater samples were collected from Niskin-type water bottles at predetermined depths triggered by a Conductivity Temperature Depth (CTD) instrument package mounted on a rosette. Up until the last millenium, the majority of nutrient samples were analysed in real time onboard the ships. As the research fleet expanded at IMR, the number of autoanalyzers could no longer match the number of ships operating simultaneously, and nutrient samples (20 mL) were poisoned with chloroform (200 µL) and stored in the fridge at +4°C for analysis at the home laboratory within 1–6 weeks after collection. The samples were allowed to acclimatise to room temperature as the chloroform was evacuated by vacuum, prior to analysis on an *Automated Analyzer* (AA) system. With one exception, all nutrients were run on homemade AA system assemblies (*Skalar*

and *Alpkem* hybrids) up until recently. The latest upgrade was the first complete AA system purchased from *Skalar Analytical B.V.* (Breda, The Netherlands). Although analytical instruments have changed over the years the nutrient chemistry has stayed the same. Colorimetric determinations of dissolved inorganic nutrients are based on the methods first described by Bendschneider and Robinson (1952) and Grasshoff (1965) with a number of minor adjustments suggested by the manufacturers (*Alpkem*, *Skalar Analytical*). The AA system measures nitrate (NO_3^-), nitrite (NO_2^-), phosphate (PO_4^-) and silicate (SiO_4^-) but only nitrate and silicate are reported in this study. Briefly, nitrate in seawater is reduced to nitrite coupled to a diazonium ion and, in the presence of aromatic amines, the resulting blue azo-dye is determined spectrophotometrically at 540 nm. The nitrate concentration is corrected for ambient nitrite (same analytical method as for nitrate, but without cadmium reduction) measured concurrently. Silicate (silicic acid) reacts to molybdate at low pH and the resulting silicomolybdate is reduced by ascorbic acid to a blue dye measured spectrophotometrically at 810 nm.

The *Plankton Chemistry Laboratory* at IMR maintains quality control of precision and accuracy by daily assessments of analytical standard curves and internal standards. Both nitrate and silicate concentrations are measured with a precision <0.2% and the accuracy deviate <1% from the internal standard. The laboratory is an active participant in the biannual intercomparisons initiated by the *QUASIMEME Laboratory Performance Studies* (https://www.quasimeme.org/), as well as other inter-laboratory comparisons, such as the *International Ocean Carbon Coordination Project* (IOCCP) intercalibration of nutrient analysis in 2017 (https://repository.oceanbestpractices.org/handle/11329/883).

In this study we focus on the deep water reservoir of nutrients in order to further document the decadal decline already reported in literature (Rey 2012; Hátún et al. 2017). Because the main source of nutrients in the Nordic Seas is the North Atlantic mode water, we used silicate and nitrate data from high-saline Atlantic Water collected in winter (January-March) in order to avoid effects of biological uptake by primary production. Therefore, we limit our study to silicate and nitrate data from two Atlantic Water regions (Figure 2.3.1) including Atlantic Water only (here defined by $S > 34.9$) in order to avoid continued supply of nutrients to surface waters through the year, as is the case with river runoff in coastal waters. In the Greenland Sea region we focus on water from the Arctic as a source of nutrients. Here Atlantic Water influence is mainly from the subsurface Return Atlantic Water from the Fram Strait in the north which can be traced by

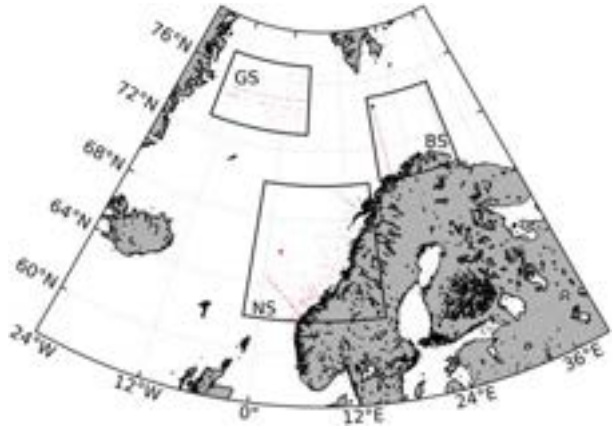

Figure 2.3.1. The Nordic Seas and all stations visited (blue dots) where nutrient data have been collected (product ref. 2.3.1; 2.3.2) and analysed in the period investigated (1990–2019). Black rectangles show the regions with data used in this study: NS (Norwegian Sea), BS (Barents Sea), GS (Greenland Sea).

temperature ($T > 0$°C). Therefore, we limit our study of the Greenland Sea to only include water with temperature below 0°C. We divided the data into two depth segments; the euphotic zone (0–50 m), and the core of Atlantic Water flow through the Nordic Seas below the euphotic zone (100–200 m). We included the euphotic zone (0–50 m) in this study in order to detect potential, temporal discrepancies between surface water nutrients and the large midwater reservoirs (100–200 m). Due to poor cruise coverage in winter in the Greenland Sea, we used deep water data only (100–200 m range) from the whole year in that region. Data from the whole year, and below 100 m depth in the Norwegian and Barents Seas, produced qualitatively similar results as when using winter data only (data not shown).

2.3.3. Results

Surface and deep water silicate concentrations from the three selected regions were binned in 5-year periods (Figure 2.3.2). To check the significance of any changes between two consecutive pentads (i.e. 5-year periods), we have used a two-tailed student's t-test with n-2 degrees of freedom, where n is the number of observations in the pentad with least observations among the two. We used higher than 95 % confidence ($p < 0.05$) to imply statistical significance (where p is the probability). No available data from the Barents Sea in the second period (1995–1999) met our selection criteria (region and salinity range) and is therefore not shown. There is a significant drop in silicate concentrations in both surface waters (0–50 m) and in the Atlantic Water (100–200 m), between the first two periods (1990–1999) and the subsequent periods in the Norwegian Sea, in both

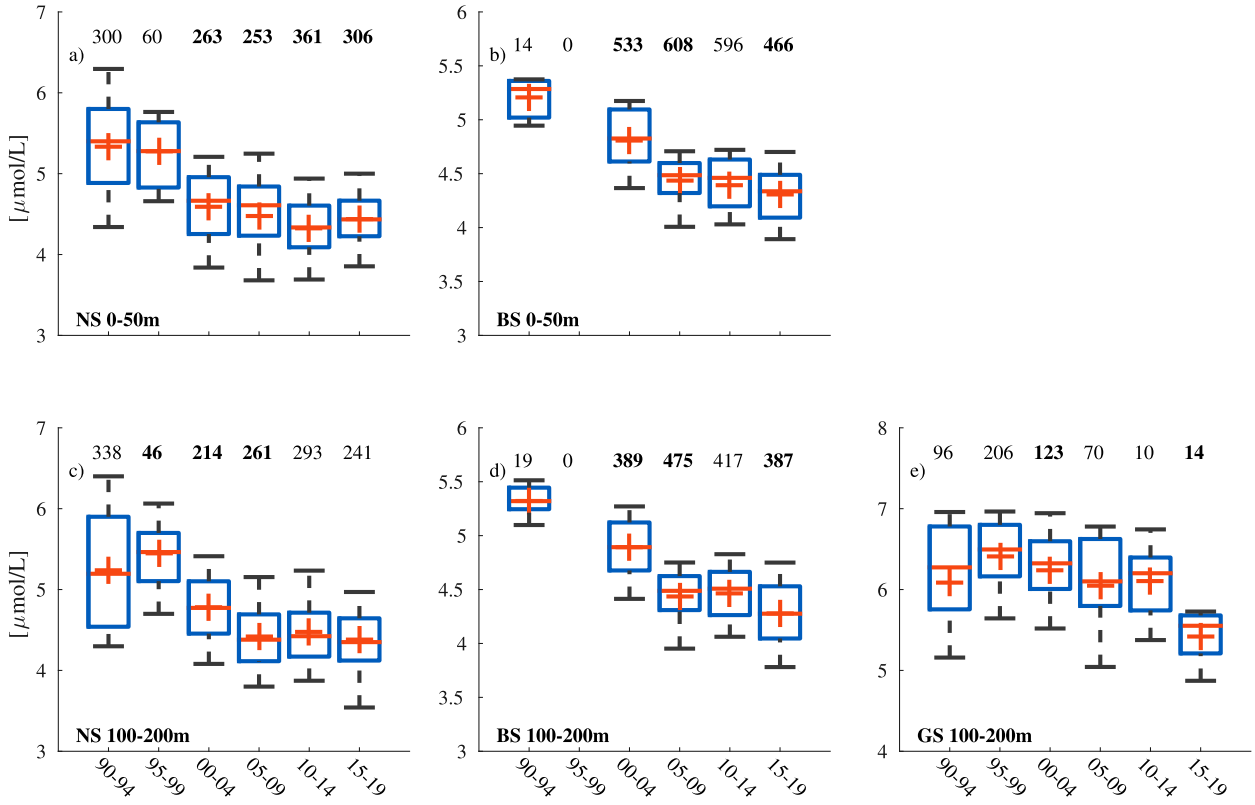

Figure 2.3.2. Box-whisker plots of silicate concentrations (in micromol per litre; obtained from product ref. 1.4.1) bin-averaged in 5-year periods. Blue box shows 25th–75th percentile, red bar shows median, red cross shows mean, and the whiskers show min/max values. (a) Norwegian Sea, 0–50 m. (b) Barents Sea, 0–50 m. (c) Norwegian Sea, 100–200 m. (d) Barents Sea, 100–200 m. (e) Greenland Sea, 100–200 m. Note the different scales on the *y*-axis. Sample size (*n*) is provided above each top whisker and shown in boldface where the change from the previous period is statistically significant (>95%).

depth layers, while in the Barents Sea the decline continues through the first half of the entire time-series in both layers (Figure 2.3.2). The largest decrease appeared in the deeper layer (100–200 m) in the Barents Sea, where silicate concentrations dropped by 19 % ($p < 0.05$) from 1990–1994 to 2015–2019. A statistically significant ($p < 0.05$) decrease of comparable magnitude (17 %) was also observed in the euphotic zone (0–50 m) between the same periods. The decline in the Norwegian Sea, during the same two periods of time, were 17% in surface waters and 16% in deeper waters. A larger part of the decrease occurred during the 1990–2004 period, followed by an apparent levelling off after 2005. The last period (2015–2019) showed a statistically significant decline compared to 2010–2014 in the Barents Sea (Figure 2.3.2).

Initially, silicate in the Greenland Sea showed no or only a little decline, except for a statistically significant decrease ($p < 0.05$) towards the end of the period investigated (Figure 2.3.2). It is possible that silicate concentrations in the Greenland Sea not only reflect the conditions in Arctic waters, as this region can also be directly influenced by Atlantic water masses from adjacent regions and that this influence may change over the study period. Therefore, we wanted to investigate the influence of Atlantic Water in the Greenland Sea. In order to do this, we used temperature instead of salinity as a proxy for Atlantic Water influence (due to the relatively larger differences in temperature than what we see in salinity, between Atlantic and Arctic water masses in the region) and compared silicate concentration and the associated in-situ temperature. We omitted all observations where $T > 0$°C, and our analysis revealed no correlation between silicate concentrations and in-situ temperature at each individual station ($R = -0.02$, $p = 0.69$; $n = 519$). We concluded that the observed changes in average silicate concentrations in the Greenland Sea were not caused by sampling in different water masses in different time-periods. Average temperature increased during the 5-year periods investigated (−0.86°C, −0.85°C, −0.60°C, −0.40°C, 0.41°C and −0.25°C, respectively). Average deeper layer silicate concentrations were overall, higher in the Greenland Sea for the entire period (6.0 µmol/L) compared to the Norwegian Sea (4.8 µmol/L) and the Barents Sea (4.5 µmol/L).

We observed a less dramatic decline in nitrate concentrations in all three regions (Figure 2.3.3). The decline in nitrate appeared more pronounced (significant at the $p < 0.05$ level) in the Norwegian and Barents Seas (Atlantic Water) during the first half of the periods investigated, while the decrease in the Greenland Sea (Arctic Water) appeared mostly in the latter half of the investigated period. In the Norwegian Sea, the average nitrate concentration decreased by 8 % in the euphotic zone and 9 % in the deeper waters, respectively, between 1990–1994 and 2005–2009. Subsequently, nitrate concentrations in the Norwegian Sea approached initial levels found in 1990–1994 (Figure 2.3.3). In the Barents Sea, maximum nitrate concentrations were observed in 2000–2004, followed by a decrease of 6 % in both surface and deeper waters until 2010–2014. The overall decline in nitrate concentrations in the Greenland Sea (9 %) was comparable to the other two regions in magnitude, but the drop was mostly confined to the latter half of the investigated period. Average concentrations of deep water nitrate were overall, higher in the Greenland Sea for the entire period (12.4 µmol/L) compared to the Norwegian Sea (11.3 µmol/L) and the Barents Sea (10.9 µmol/L).

As silicate showed an overall decline and nitrate appeared to recover during the latter half of the time-series (Figures 2.3.2 and 2.3.3), the relative proportion between the two macronutrients (the molar nitrate:silicate-ratio) showed an overall increase during the same period of time (Figure 2.3.4). There was an initial decline to 2.2 in the Norwegian Sea (1995–1999) prior to an increase and a subsequent levelling off around 2.5, both in the euphotic zone and in deeper waters. In the Barents Sea the ratio was 2.1 in both the euphotic zone and the deeper layer in the first period (1990–1994) before it increased to approximately 2.5. Note that we only have 19 and 14 data points (deep waters and surface layers, respectively) in the Barents Sea during the first 5-year period. Yet, the increase during this period (1990–1994) was significant at the 95% confidence level. The observed nitrate:silicate-ratios were >2.5 during the last 5-year period in both the Norwegian and Barents Seas. In the Greenland Sea, the nitrate:silicate-ratio remained stable around 2 during the entire period investigated (Figure 2.3.4).

2.3.4. Discussion

2.3.4.1. Decadal decline in silicate and nitrate, and the role of the SPG

Our compilation of surface and midwater nutrient concentrations over the last 30 years (1990–2019) show an abrupt and significant decline in silicate during the first

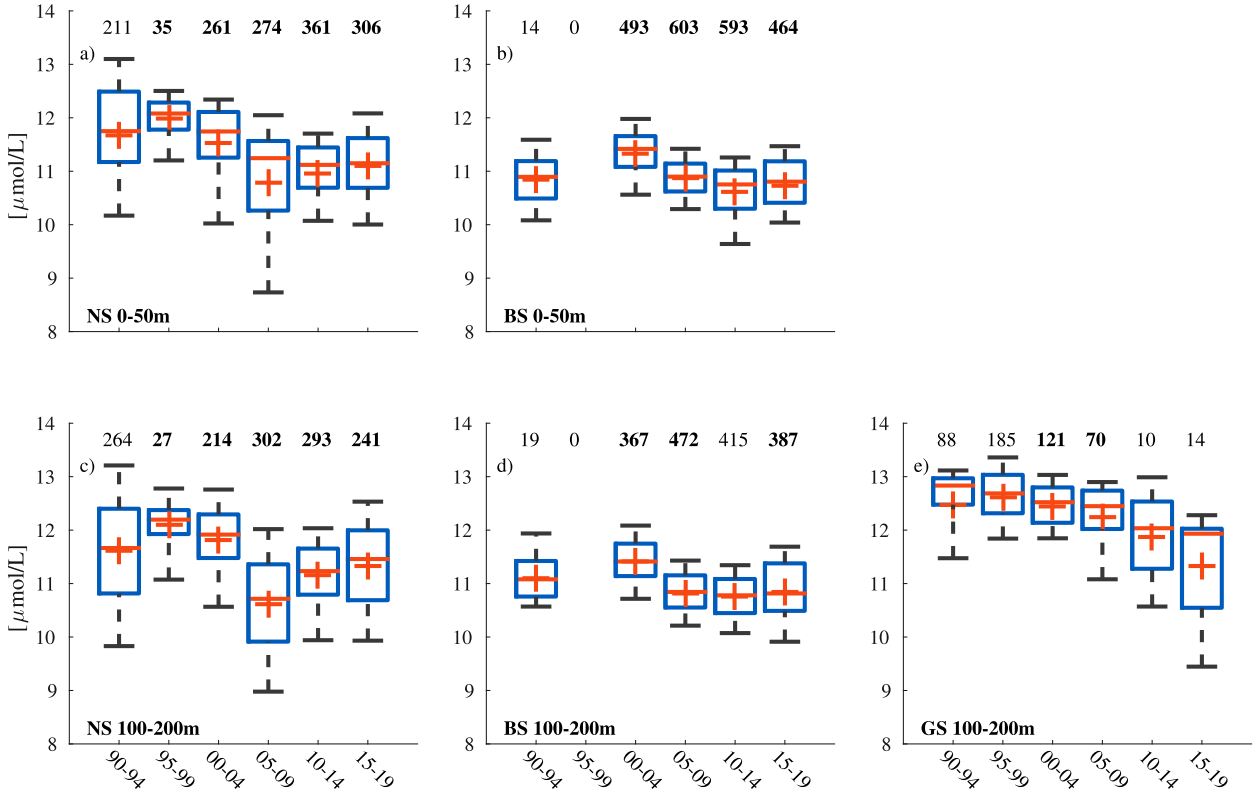

Figure 2.3.3. Same as Figure 1.4.2, but for nitrate (obtained from product ref. 1.4.1).

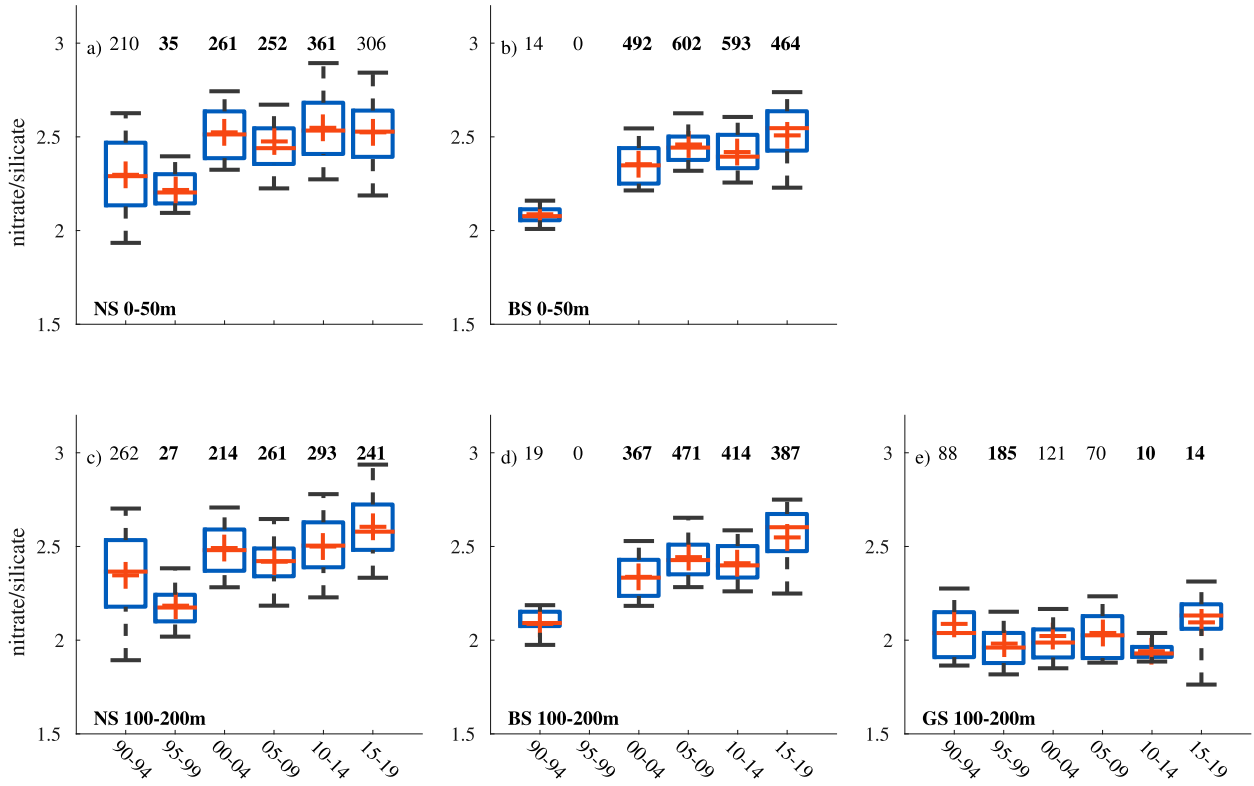

Figure 2.3.4. Same as Figure 2.3.2, but for the nitrate:silicate-ratio (obtained from product ref. 2.3.1).

decade (Figure 2.3.2). The decline is slower for nitrate and reaches a minimum after 15–20 years, followed by a subsequent increase (Figure 2.3.3). Rey (2012) noticed the same initial drop as in this study, as he used the same Nordic Seas data sets up until 2010. Hátún et al. (2017) focused much of their study on Arctic waters surrounding the southern tip of Greenland, but also observed the initial drop in the Nordic Seas as they used the same data sets as this study, but only up until 2015. Only one other study (Johnson et al. 2013) has reported a decline in nitrate from the Rockall Trough, a marginal region off Scotland in the Atlantic Water inflow entering the southern parts of the Nordic Seas.

Winter deep water mixing in open oceans will to a large extent determine nutrient concentrations in surface waters at the onset of the spring bloom each year, and our data also show that the reduction in silicate and nitrate is reflected in surface waters (0–50 m) in winter (Figures 2.3.2 and 2.3.3). The largest decline appears during the first half of the period investigated, coinciding with a major weakening of the Subpolar Gyre Index (Figure 2.3.5), as the index decreased strongly from 1994 to 1998. The SPG continued to decrease from 2000 and throughout the period, and this is also evident in the nutrient concentrations in the Norwegian and the Barents Seas (Figures 2.3.2 and 2.3.3). We observed concurrent increases in nitrate concentrations during periods of minor strengthening of the SPG (2005–2009 and 2012–2015), while there was no uniform and significant reversals in our 5-year bin-averaging of deep water and surface silicate concentrations during these periods.

We acknowledge that differences in the spatial sampling distribution between 5-year periods may affect our results by imposing artificial biases. However, most of the periods have similar spatial sampling distribution as depicted in Figure 2.3.1, with a few exceptions: In the Norwegian Sea, there are only data available from the *Ocean Weather Station Mike* (located at 66° N, 2° E) during the second period (1995–1999) and there are no observations from the Barents Sea during that period. Moreover, in the Greenland Sea there are only two stations (located in the southeastern corner) present in the fifth pentad (2010–2014). Thus, the higher silicate concentrations and lower nitrate:silicate-ratios seen in the Norwegian Sea in the second period is likely to be partly due to a spatial sampling bias compared with the other periods. Since we are using samples from Atlantic Water only (in the Norwegian and Barents seas), we argue that any spatial sampling bias is expected to be small as the samples nevertheless represent waters of similar origin. However, there could still be some effects of a time-lagged response to changes in the source waters when we are sampling the core of the

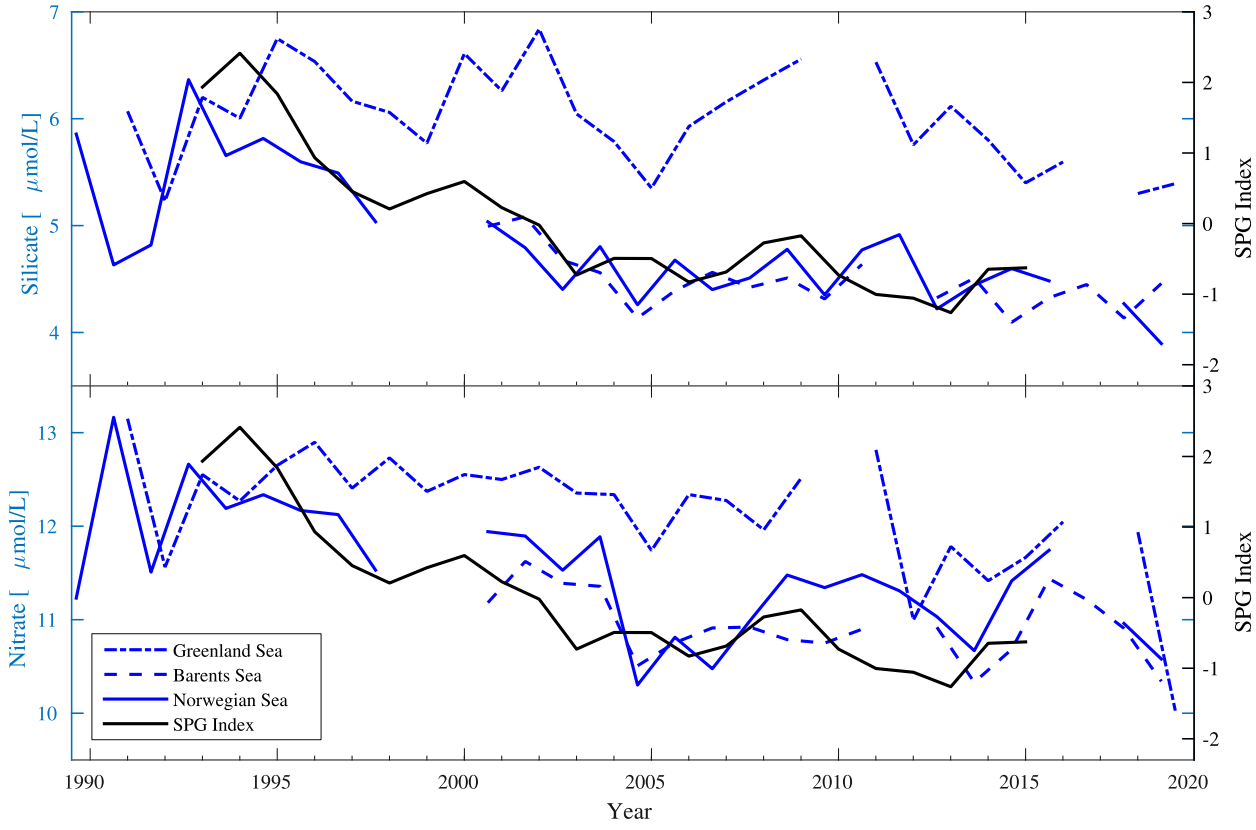

Figure 2.3.5. Time series of silicate concentrations (top panel, blue lines) and nitrate concentrations (bottom panel, blue lines) in the Norwegian Sea (solid line), the Barents Sea (dashed line) and the Greenland Sea (dash-dotted line) in the 100–200 m depth range. The data were obtained from product ref. 2.3.1; 2.3.2. Black lines show the annual Subpolar Gyre Index (data from Berx and Paye 2016). Values for the Norwegian and Barents seas represent January-March averages, and values from the Greenland Sea are annual deep water averages. Note that data from the Barents Sea only contain values from 1992 prior to the year 2000.

inflow along the shelf slope versus the ocean basins, due to shelf-basin exchange processes and residence times in the basins, but the use of 5-year bins is chosen in order to dampen such effects.

There is a statistically significant decline in Arctic deep water silicate in the Greenland Sea appearing approximately 15 years after the initial lowering of silicate and nitrate in Atlantic Water in the Norwegian and Barents Seas. Water entering the Greenland Sea can come from the North-Atlantic, the Arctic through the Fram Strait, or as a mixture of the two regions. The lack of correlation between silicate concentrations and sea temperature do suggest that the source water in the Greenland Sea gyre is of Arctic origin and entering the area through the Fram Strait. Also, since we observed a delay in decline of silicate in the Greenland Sea, relative to the adjacent Norwegian and Barent Seas (Figure 2.3.2), we may rule out the North-Atlantic as a source. Water travelling from the Norwegian and Barents Seas, through the Polar Basin and the East Greenland Current, to the Greenland Sea, has an approximate periodicity of several years to a few decades, depending on the depth (Schlosser et al. 1995). Therefore, the decadal-scale time lag of the decrease in nutrients in the Greenland Sea (Figure 2.3.2) suggests that nutrient concentrations in Arctic waters (indirectly spurred by changes in the Norwegian and Barents Seas) are also determining bioavailable silicate and nitrate in the Greenland Sea.

The decline in biologically available silicate throughout the northern North Atlantic in surface waters, has been attributed to changes in the SPG circulation (Hátún et al. 2017). This appears to concur with the decline in silicate, and nitrate, concentrations reported from the Norwegian and Barents Seas in this study, and is similar in scope to the observations made by Johnson et al. (2013) for nitrate and phosphate at the southern entrance to the Nordic Seas, in the Rockall Trough area. The drop in nutrient concentrations have already been attributed to a weakening and westward movement of the Subpolar Gyre Index (Rey 2012; Johnsen et al. 2013; Hatun et al. 2017) as less nutrient rich North Atlantic water has entered the Nordic Seas. Therefore, our reported decline in silicate is

similar to other findings in the same region and concur with an almost unidirectional weakening of the Subpolar Gyre Index in the period investigated (Figure 2.3.5). The rebound of nitrate during the latter half of the time-series, most prominent in the Norwegian Sea (Figure 2.3.4), coincides with a levelling off in the SPG in the 2005–2009 period. Since a weakening of the SPG appears to increase the inflow of southern, nutrient poor water, we assume that the adverse may diminish and perhaps alter the Nordic Seas inflow from the south. McCartney and Mauritzen (2001) concluded that the Nordic Seas inflow originate from upper ocean (0–800 m) subtropical waters, the subtropical mode water (STMW). Although silicate concentrations are similar in the gyre, measured nitrate concentrations in the eastern STMW are low (1–2 µmol/L) whereas they appear five times higher in the western part of the subtropical gyre (Garcia et al. 2006). Therefore, Nordic Seas inflow originating from the eastern STMW will carry a very different nutrient signature (i.e. the nitrate: silicate-ratio) to the Norwegian Sea, than water from the western side. If this difference in nitrate concentrations (and hence nitrate:silicate-ratios) is reflected in the Nordic Seas inflow, our results may suggest that a weakening of the SPG and increased inflow from the south to the Norwegian Sea, may carry proportionately more STMW of eastern origin. Adversely, we suggest that a levelling off or strengthening of the SPG will carry less STMW of eastern origin. The initial drop in Norwegian Sea nitrate levels took place in 2005–2009 (Figure 2.3.3) coinciding with a levelling off, but not strengthening, of the SPG index (Figure 2.3.3). Therefore, we suggest that this halt in the weakening of the SPG could have altered the subtropical mode water source and hence, caused a Nordic Seas inflow with a lower nitrate:silicate-ratio during that period of time. The drop in the SPG index is not as dramatic and unidirectional after 2009 as prior to 2005 (Figure 2.3.5), and this ubiquity may have retained existing inflow patterns leading to a continued rise in the nitrate:silicate-ratios in the Norwegian and Barents Seas during the remainder of the time investigated.

2.3.4.2. Phytoplankton community composition and zooplankton grazing

During an annual growth season, Officer and Ryther (1980) suggested two basic phytoplankton communities; the diatom-dominated ones and flagellated (non-diatom) primary producers. Due to their rapid growth at high nutrient concentrations (a typical scenario for early spring bloom conditions in these waters), the former community is outcompeting other phytoplankton at silicate concentrations >2 µmol/L, whereas flagellated cells only appear to flourish at silicate concentration <2 µmol/L (Furnas 1990; Egge and Aksnes 1992). However, more recent studies of the inflow waters to the Norwegian Sea (e.g. Daniels et al. 2015), may suggest that large diatom spring blooms at times are preceded by smaller phytoplankton with higher nutrient affinity (picoeukaryotes and nanoplankton, including nanosized diatoms) in the North Atlantic. Daniels et al. (2015) suggested that not only physico-chemical factors may determine regional spring blooms dynamics, as biological factors (e.g. microzooplankton grazing pressure, presence–absence of larger diatom seed populations) also may control bloom-formations in this region. Large diatom spring blooms in the Nordic Seas are often followed by flagellated, non-diatom phytoplankton, only interrupted by smaller episodes of minor diatom blooms towards the end of the growth season in the fall (McQuatters-Gollop et al. 2007). Therefore, as the spring bloom is depleting nutrients and silicate concentrations goes below 2 µmol/L, diatoms are not competitive with other phytoplankton until new nutrient intrusions (and silicate conc. >2 µmol/L) in surface waters at the end of the growth season in the fall. Zooplankton growth and development is closely tied in with feeding efficiency (Pond et al. 1996) and measured clearance and ingestion rates for *Calanus finmarchicus* are at a peak during diatom spring blooms in the Norwegian Sea (Meyer-Harms et al. 1999). Growth development and reproduction of zooplankton, such as *C. finmarchicus* in the Norwegian and Barents Seas, is highly dependent of the timing and magnitude of the spring diatom blooms in these oceans (Melle et al. 2004; Eiane and Tande 2009). Juvenile and to some extent adult fish, such as commercial stocks of herring, cod and capelin in the Norwegian and the Barents Seas, are in turn strongly dependent on successful zooplankton growth and reproduction each year (Skjoldal et al. 2004; Gjøsæther 2009). Therefore, lowered initial silicate concentrations may lead to less extensive spring diatom blooms and possibly, less successful growth and survival of zooplankton and, ultimately, fish larvae from commercial stocks in these oceans.

Chemosensory detection of phytoplankton means that zooplankton can discriminate between toxic and non-toxic cells, even within the same species expressing different levels of toxicity (e.g. Selander et al. 2006). The chemosensory capabilities in zooplankton are also used to assess food particle quality in order to optimise the intake of high quality foods (Mayzaud et al. 1996; Olsen et al. 2006). We still do not have a complete understanding of all the ques that determine 'high quality foods' but copepods are also known to be able to

discriminate different growth phases (and hence, a potentially different nutritional quality) in the same species of phytoplankton (Barofsky et al. 2010). This change in the 'phycosphere' (Moore et al. 1999) surrounding each phytoplankton cell will, amongst others, depend on nutrient availability and associated physical/chemical stress factors, that can create different reproductive outcomes and growth in zooplankton. Changes in the relative proportion of available nutrients (e.g. the nitrate:silicate-ratio) may also create stress in phytoplankton (diatoms) who are depending on silicate for cellular growth. Calculated nitrate:silicate-ratios in this study (Figure 2.3.3) were well above a molar ratio of 2 and hence, proportionately more nitrate than silicate was available at the onset of the spring bloom in all three regions investigated. This may indicate however, that if the decline in silicate are continuing, and on a larger scale than e.g. the decline in nitrate, the requisite for successful diatom spring blooms may also diminish. Successful reproductive outcomes for zooplankton (egg production and survival of nauplii) is highly dependent on access to an abundance of diatoms of optimal nutritional value (Jonasdottir 1994; Irigoien et al. 2000). Therefore, limited access to silicate for diatoms growth and development, may hamper zooplankton egg production and survival of zooplankton nauplii. If the negative Subpolar Gyre Index persist, the Nordic Seas may see longer periods of surface waters with silicate levels below 2 µmol/L (critical for successful diatom growth) and reduced growth and recruitment in zooplankton (e.g. *Calanus* sp.) may in turn have consequences for growth and development of fish larvae of commercially important stocks in these waters

Section 2.4. Eutrophic and oligotrophic indicators for the North Atlantic Ocean

Authors: Silvia Pardo, Shubha Sathyendranath, Trevor Platt

Products used:

Ref. No.	Product name & type	Documentation
2.4.1	ATL OC-CCI REP dataset OCEANCOLOUR_ATL_CHL_L3_REP_OBSERVATIONS_009_067	PUM: https://marine.copernicus.eu/documents/PUM/CMEMS-OC-PUM-009-ALL.pdf QUID: https://marine.copernicus.eu/documents/QUID/CMEMS-OC-QUID-009-066-067-068-069-088-091.pdf

Statement of main outcome: We have presented a satellite-based map of eutrophic/oligotrophic flags for the North Atlantic, for the year 2019. The flags were generated on the basis of comparison with the chlorophyll climatology for the area based on data from 20 previous years (1998–2017). The results showed hardly any localities where the eutrophic flag was positive, but some locations were positive for oligotrophic flag. Oligotrophic flags were positive mostly along coastal waters, but also along scattered points within the 30–40°N latitudes. They point to localities that should be on a watch to determine whether the trend is sustained into the future.

2.4.1. Introduction

Eutrophication is the process by which an excess of nutrients – mainly phosphorus and nitrogen – leads to increased growth of plant material in an aquatic body. Anthropogenic activities, such as farming, agriculture, aquaculture, industry and sewage, are the main source of nutrient input in problem areas (Jickells 1998; Schindler 2006; Galloway et al. 2008). Eutrophication is an issue particularly in coastal regions (Malone and Newton 2020) and areas with restricted water flow, such as lakes and rivers (Howarth and Marino 2006; Smith 2003). The impact of eutrophication on aquatic ecosystems is well known: nutrient availability boosts plant growth – particularly algal blooms – resulting in a decrease in water quality (Anderson et al. 2002; Howarth et al. 2000). This can, in turn, cause death by hypoxia of aquatic organisms (Breitburg et al. 2018), ultimately driving changes in community composition (Van Meerssche and Pinckney 2019). Eutrophication has also been linked to changes in the pH (Cai et al. 2011; Wallace et al. 2014) and depletion of inorganic carbon in the aquatic environment (Balmer and Downing 2011). Oligotrophication is the opposite of eutrophication, where reduction in some limiting resource leads to a decrease in photosynthesis by aquatic plants, which might in turn reduce the capacity of the ecosystem to sustain the higher organisms in it.

Eutrophication is one of the more long-lasting water quality problems in Europe (OSPAR ICG-EUT, 2017), and is on the forefront of most European Directives on water-protection. Efforts to reduce anthropogenically-induced pollution resulted in the implementation of the Water Framework Directive (WFD) in 2000 (Carvalho et al. 2019). In a similar way, the more recent Marine Strategy Framework Directive (MSFD) established in 2008 a requirement for EU member states to report on eutrophication and other water quality parameters for their regional seas for directive review purposes every 6 years. Various international conventions (e.g. OSPAR, Helsinki and Barcelona Conventions) and

commissions (e.g. HELCOM) promote ecological status monitoring in order to enforce said water directives.

As a proxy for phytoplankton biomass, chlorophyll concentration is frequently used in ecological status assessments as an indicator for eutrophication, either on its own (Ferreira et al. 2011; Van der Zande et al. 2019) or as part of multi-metric ensembles (Murray et al. 2019; Papathanasopoulou et al. 2019). While *in situ* sampling is a powerful tool for the acquisition of reference chlorophyll concentration baseline values, the resulting datasets frequently lack the temporal and spatial resolution needed for effective monitoring and subsequent management of the problem. This is particularly true for traditionally undersampled open-ocean regions, where the risk of eutrophication is considered very low.

The use of remotely-sensed ocean colour for eutrophication monitoring provides some advantages in temporal and spatial coverage, and can help to reduce the cost of implementation of water directives (NOWPAP 2007; Ferreira et al. 2011). Several studies have exploited satellite-derived chlorophyll concentration for the study of the eutrophication status of European regional seas, e.g. Cristina et al. (2015) for the Iberian Seas, Harvey et al. (2015) and Attila et al. (2018) for the Baltic Sea, Novoa et al. (2012) for the Bay of Biscay, Lefebvre et al. (2011) and Gohin et al. (2008, 2019) for the English Channel, and Coppini et al. (2012) for the global region, among many others.

Many of the studies cited above use percentile-derived thresholds to classify water bodies according to their ecological status. Recent efforts such as the Joint Monitoring Programme for the North Sea and the Celtic Sea (JMP NS/CS) and the Joint Monitoring Programme of the Eutrophication of the North Sea with Satellite data (JMP-EUNOSAT) have highlighted the need for a coherent and unified method to derive eutrophication indicators, as well as the importance of using a well-validated, high-quality satellite chlorophyll product (Baretta-Bekker et al. 2015; Blauw et al. 2019; Van der Zande et al. 2019) to compute them. In this work we follow these recommendations to develop an indicator suite based on chlorophyll P90 and P10 percentiles, as described in the following methods section. As an illustration, we use these indicators to report on the status of the CMEMS North Atlantic region during 2019.

2.4.2. Method

We have derived a suite of annual eutrophic and eutrophic indicator maps for the North Atlantic Ocean using satellite-derived chlorophyll concentration provided in the CMEMS North Atlantic OC-CCI REP product (product reference 2.4.1). The chlorophyll 90 percentile (P90) and chlorophyll 10 percentile (P10) were used to derive, respectively, the eutrophic and oligotrophic indicators. P90 and P10 are typically defined as dynamic thresholds such as 90% of the chlorophyll values are below the P90 value, and 10% of the chlorophyll values are below the P10 value. P90 is considered a good indicator of high chlorophyll episodes (Park et al. 2010), and is a standard metric in eutrophication status assessments in the region (Gohin et al. 2008). While P10 is not widely used in the context of eutrophication studies, it has been exploited in conjunction with P90 to provide the baselines of the annual chlorophyll cycle (Gohin et al. 2020).

Using the satellite-derived chlorophyll products distributed in the regional North Atlantic CMEMS REP Ocean Colour dataset (OC-CCI), we computed a set of daily P90 and P10 climatologies on a pixel-by pixel basis for the region of interest, as done in Gohin et al. (2008). The period selected for the climatology was 1998–2017. Most existing regional studies compute these percentile climatologies over a locally-defined productive season, i.e. March to October the Bay of Biscay and eastern English Channel in Gohin et al. (2008). In order to apply the method to a broader area such as the CMEMS North Atlantic region, in this paper we avoided the definition of a regional productive season and used the whole year in the calculation of the P90 and P10 climatologies instead.

The region covered by the CMEMS North Atlantic OC-CCI REP product (product reference 2.4.1) is characterised by strong seasonality in both concentration values and cloud cover, which might lead to irregular sampling (Sathyendranath et al. 2018). These effects have been shown to be the cause of relative errors of up to 30% in the estimation of P90 (Van der Zande et al. 2013). To minimise the effect of gaps in the data in the computation of these P90 and P10 climatological values, we imposed a threshold of 25% valid data for the daily climatology. For the 20-year 1998–2017 climatology this means that, for a given pixel and day of the year, at least 5 years must contain valid data for the resulting climatological value to be considered significant. Pixels where the P90 and P10 climatological values were non-significant were not considered in further calculations.

To assess the average regional status during 2019 when compared with these P90 and P10 percentile baselines, we computed time series of the 2019 daily area-averaged chlorophyll concentration, daily P90 climatology and daily P10 climatology. For consistency with the method employed to derive chlorophyll time series in previous Ocean State Reports (Sathyendranath

et al. 2018), pixel-area weighted averages were used to calculate the daily values.

Finally, to generate the eutrophic and oligotrophic indicator maps for 2019, we compared every valid daily observation over the year with the corresponding daily climatology on a pixel-by-pixel basis, to determine if values were above the P90 threshold, below the P10 threshold or within the [P10, P90] range. Values above the P90 threshold or below the P10 were flagged as anomalous. The number of anomalous and total valid observations were stored during this process. We then calculated the percentage of valid anomalous observations (above/below the P90/P10 thresholds) for each pixel, to create percentile anomaly maps in terms of % days per year. Lastly, we derived an annual eutrophic/oligotrophic flag map: if 25% of the valid observations for a given pixel and year were above the P90 threshold, the pixel was flagged as eutrophic. Similarly, if 25% of the observations for a given pixel were below the P10 threshold, the pixel was flagged as oligotrophic.

2.4.3. Results

Figure 2.4.1 shows the 2019 North Atlantic daily average time series for chlorophyll concentration (black), together with the P90 (red) and P10 (blue) time series of daily average climatologies, obtained using the CMEMS North Atlantic OC-CCI REP product (product reference 2.4.1). The daily average chlorophyll time series showcased primary (spring) and secondary (early winter) peaks consistent with previous assessments of the North Atlantic chlorophyll seasonal cycle (Sathyendranath et al. 2018; CMEMS OMI 2020). Changes in cloud cover and satellite coverage affect data availability and can cause considerable day-to-day variability in the time series, as shown in Figure 2.4.1. While the mean variability in daily coverage was less than 3% during 2019, it is worth mentioning that the average number of valid pixels during the winter months (November-January) was almost 10% lower than the average number of valid pixels during the rest of the year.

The percentile parameters also presented a distinct seasonality that matches the chlorophyll concentration; in particular P90 exhibited a strong spring bloom signal peaking in May. The average chlorophyll concentration in the area for 2019 was 0.24 mg m^{-3}, against values of 0.37 mg m^{-3} average P90 and 0.17 mg m^{-3} average P10. During 2019, the average daily chlorophyll concentration was well below the P90 climatological values during the first and second quarters of the year, and closer to the percentile climatologies during the second half of 2019. The analysis of the mean anomaly values revealed that chlorophyll was on average 31% lower than the P90 climatology and 48% higher than the P10 climatology during 2019.

While the time series comparison provides a comparison of 2019 with the average regional P90 and P10 climatologies, it offers very little information regarding the spatial location and significance of

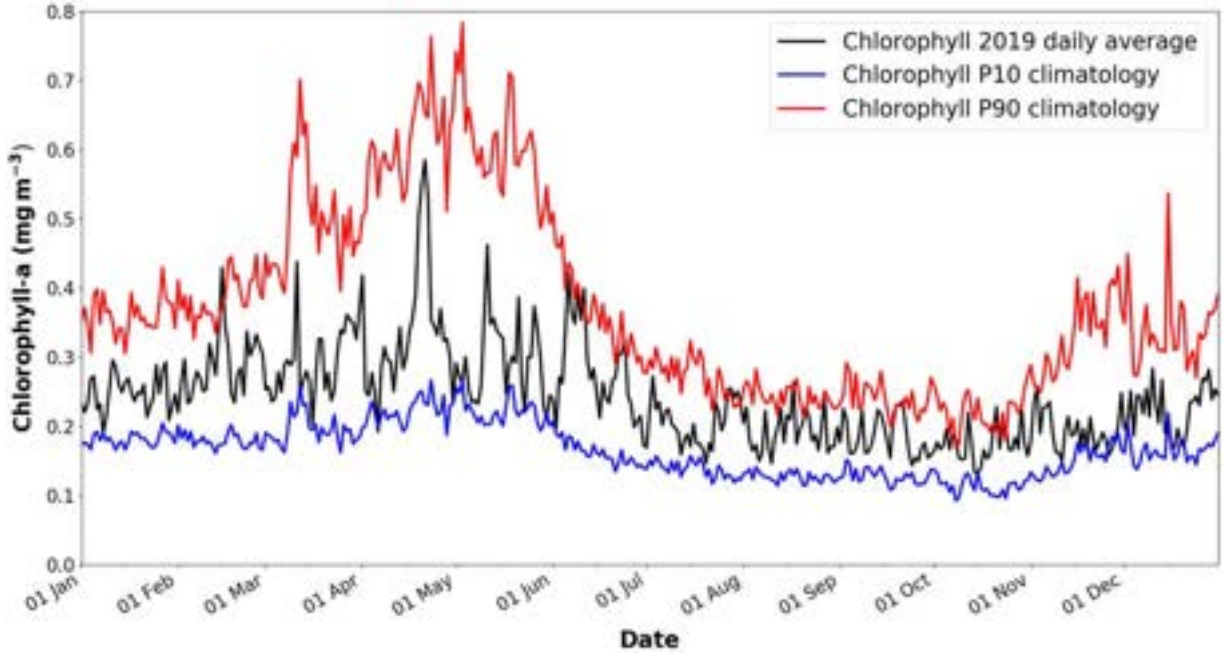

Figure 2.4.1. 2019 daily chlorophyll average for the North Atlantic Ocean (black), daily P90 (red) and P10 (blue) 1998–2017 climatological values, calculated using the CMEMS Ocean Colour ATL REP dataset (OC-CCI, product reference 2.4.1).

potential eutrophication and oligotrophication episodes. As we detailed in the methods section, to identify eutrophication and oligotrophication levels for the year we assessed the P90 and P10 anomalies on a daily pixels-by-pixel basis, and generated eutrophic and oligotrophic indicator maps based on the percentage of anomalous observations. The 2019 eutrophic indicator map for the North Atlantic is shown in Figure 2.4.2. On average, 6.4% of the valid observations acquired in the region were above the P90 climatological value (i.e. in a eutrophic state). For the North Sea, Bay of Biscay and coastal waters of Portugal and Spain, this value increased to 15–20% of the valid observations being above the P90 climatological value. Waters around the Canary Islands, west coast of Morocco, and some hotspots in the open ocean showcased values above the 25% threshold, reaching 50% of the valid observations in some cases (i.e. around 182 days for regions with continuous coverage). Note that a considerable portion of the region above 40 degrees North did not provide a measure of P90 anomaly. This was due to gaps in data lowering the significance of the P90 below the 5-year threshold we imposed in the climatology calculation. The eutrophic indicator distribution in this annual average map was consistent with the 2019 anomaly

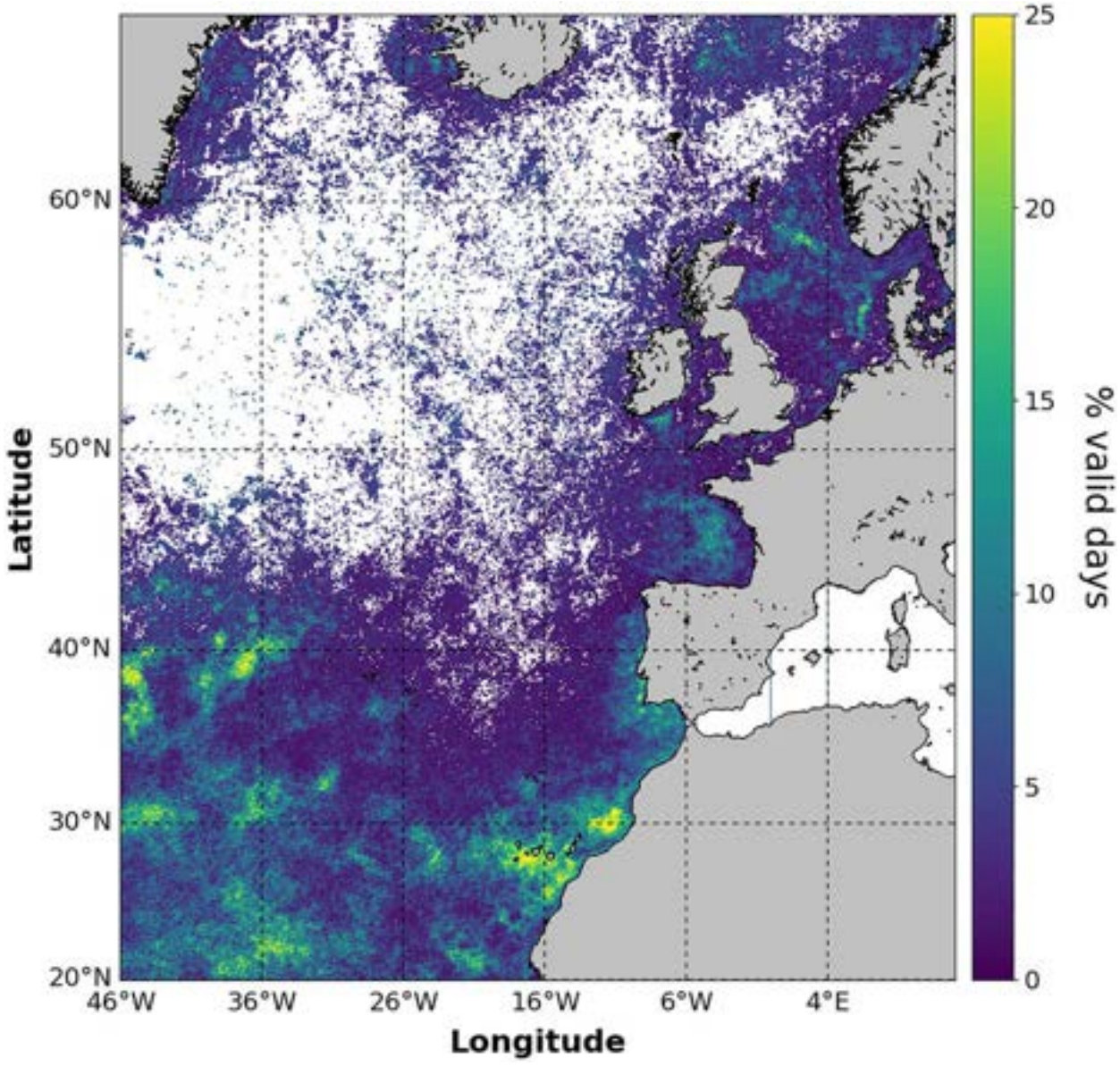

Figure 2.4.2. 2019 eutrophic indicator map for the North Atlantic Ocean, in terms of percentage of days with chlorophyll values above the 1998–2017 P90 climatological reference, calculated using the CMEMS Ocean Colour ATL REP dataset (OC-CCI, product reference 2.4.1).

(Sathyendranath et al. 2018; CMEMS OMI 2020), particularly with the positive anomalies reported for the Bay of Biscay and southern coast of Ireland.

The 2019 oligotrophic indicator map for the North Atlantic is shown in Figure 2.4.3. On average, 12.7% of the valid observations acquired in the region were below the P10 climatological value (i.e. in an oligotrophic state). Values for this indicator appeared to be polarised, with regions showing either no decrease in chlorophyll – less than 5% of the valid observations are below the P10 reference value – or values above the 25% threshold. Areas in the latter category included the coastal waters of Norway, Sweden and Denmark, the Iberian Shelf, the Celtic and Irish Seas, and the English Channel. Maximum values in hotspots for these areas were around 70% of the valid observations (i.e. around 255 days for regions with continuous coverage).

The oligotrophic indicator distribution in the annual average map was consistent with the negative anomalies found in the 2019 anomaly map for the same product and region (Sathyendranath et al. 2018; CMEMS OMI 2020), particularly with the strong decrease in chlorophyll concentration reported for the Iberian Shelf seas. The higher percentage values for this second indicator might be due to a non-proportional distribution of the observation between bloom and non-bloom periods, i.e. higher frequency of non-bloom observations.

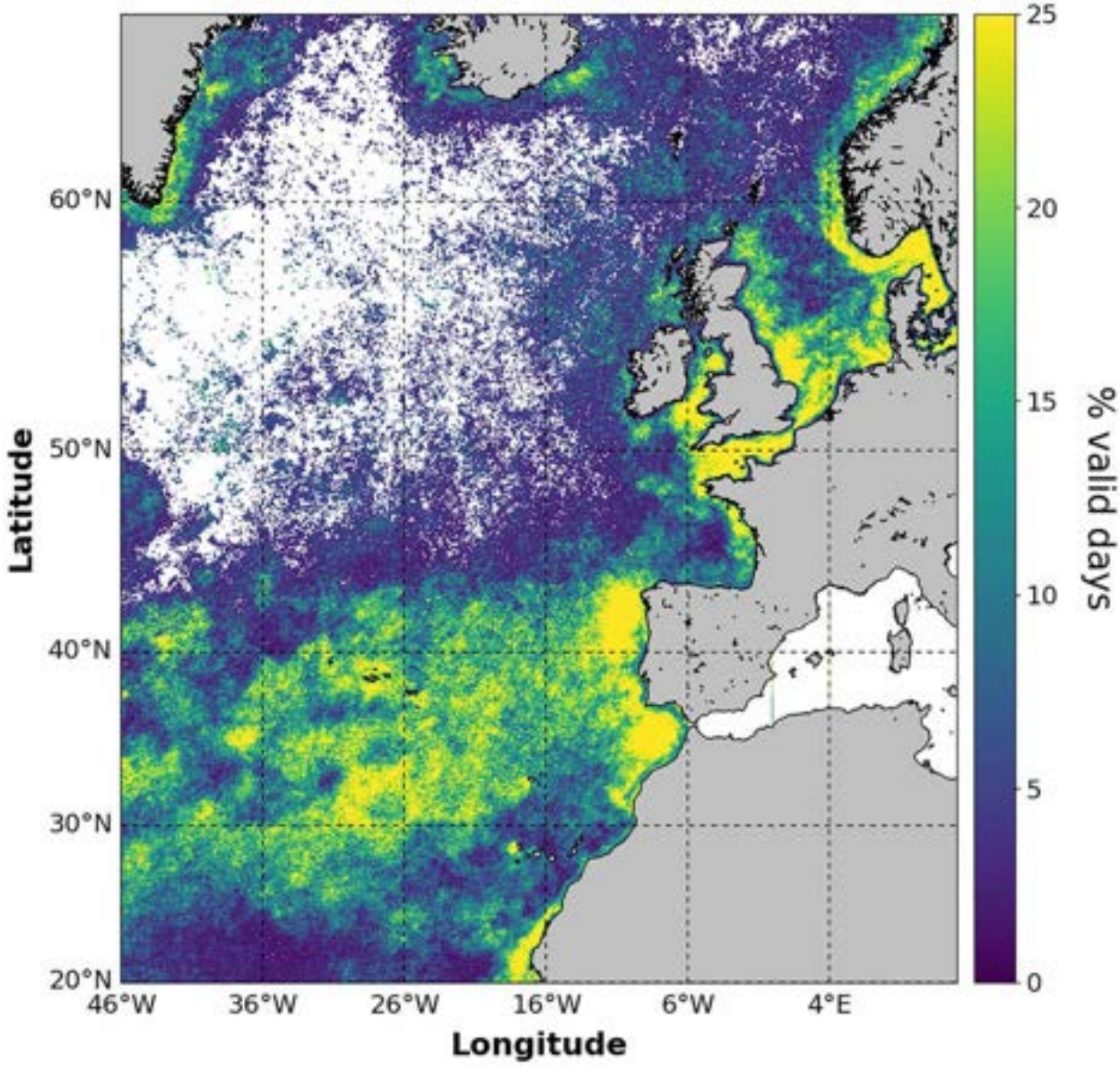

Figure 2.4.3. 2019 oligotrophic indicator map for the North Atlantic Ocean, in terms of percentage of days with chlorophyll values below the 1998–2017 P10 climatological reference, calculated using the CMEMS Ocean Colour ATL REP dataset (OC-CCI, product reference 2.4.1).

Using a 25% threshold, we derived the final 2019 annual eutrophic/oligotrophic flag indicator map for the North Atlantic, shown in Figure 2.4.4. Extensive coastal and shelf waters showed active oligotrophic flags for 2019, with areas including but not restricted to the Iberian Shelf waters, North Sea, Celtic Sea and Irish Sea. The results for the English Channel and the French Atlantic continental shelf are consistent with the decrease in eutrophication risk recently reported by Gohin et al. (2019) using both *in situ* and satellite chlorophyll data.

The flag indicator map showed very few areas with active eutrophic flags for 2019. The Third Integrated Report on the Eutrophication Status of the OSPAR Maritime Area (OSPAR ICG-EUT, 2017) reported an improvement from 2008 to 2017 in eutrophication

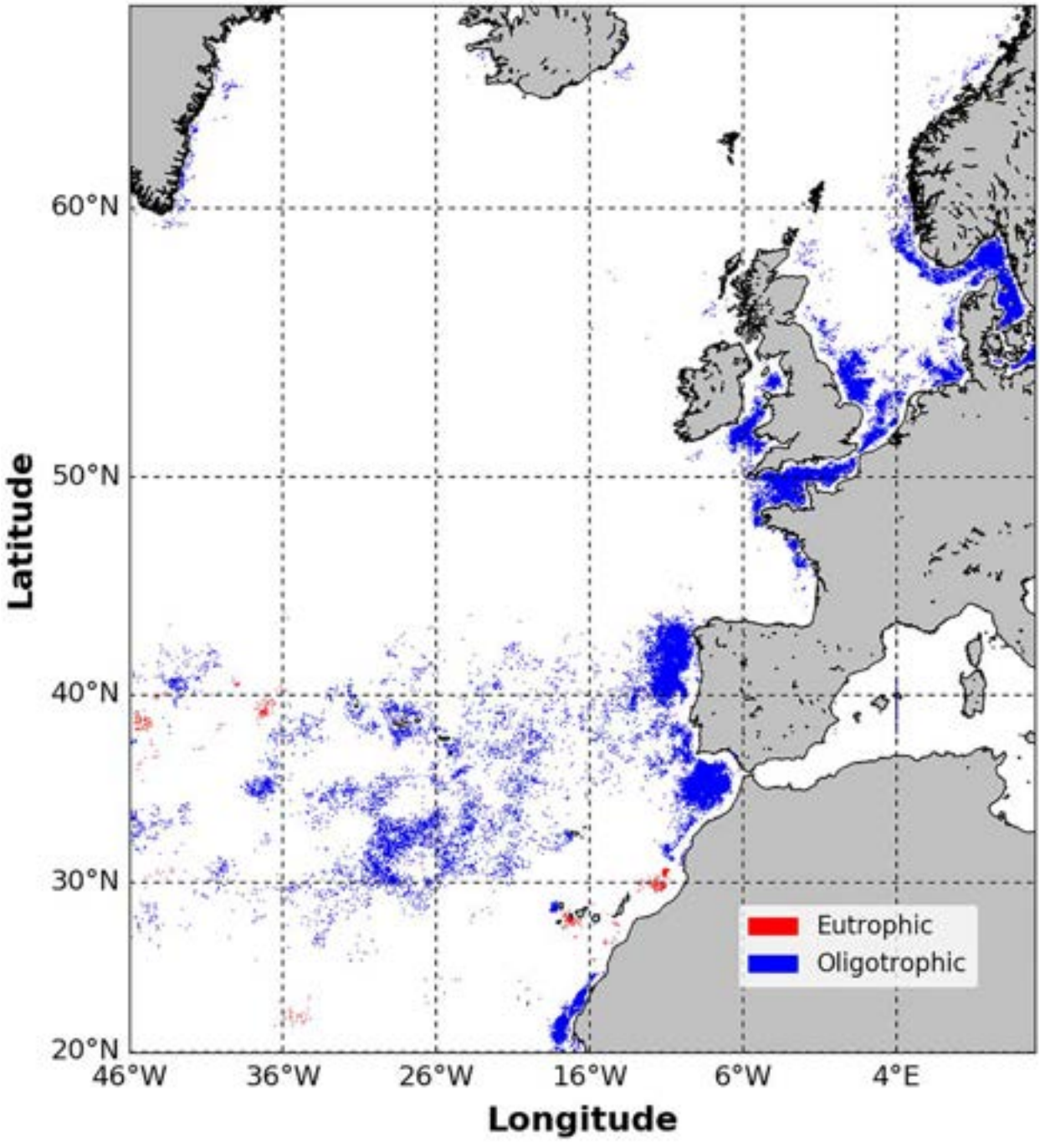

Figure 2.4.4. 2019 annual eutrophic (red) and oligotrophic(blue) flag indicator map calculated using the CMEMS Ocean Colour ATL REP dataset (OC-CCI, product reference 2.4.1). Active eutrophic flags indicate that more than 25% of the valid observations were above the 1998–2017 P90 climatological reference. Active oligotrophic flags indicate that more than 25% of the valid observations were below the 1998–2017 P10 climatological reference.

status across offshore and outer coastal waters of the Greater North Sea, with a decrease in the size of coastal problem areas in Denmark, France, Germany, Ireland, Norway and the United Kingdom. The absence of active eutrophic flags in the North Sea coastal regions might reflect these trends and a low occurrence of eutrophic episodes during 2019.

2.4.4. Conclusions

The indicators developed here provide a tool to monitor spatial and temporal variations in chlorophyll concentration. While various regions have been flagged as eutrophic/oligotrophic in the 2019 indicator map (Figure 2.4.4), we can only talk about eutrophication/oligotrophication when this state is sustained and showcases a significant trend across a longer period of time. Following studies will only benefit from progressive temporal extensions of the dataset (improving the significance of the climatologies) and from the incorporation of high-resolution satellite ocean colour datasets – such as Sentinel3 OLCI – into the CMEMS OC-CCI REP dataset.

From the results obtained in Figure 2.4.4, we can conclude that the occurrence of eutrophic episodes (chlorophyll concentration higher than the P90 climatological value for more than 25% valid observations) was very low during 2019. Nonetheless, the eutrophic indicator provided in Figure 2.4.2 included some significant P90 anomalies in the 15% to 25% range, and lowering the threshold from 25% to 15% would result in an increase in the areas flagged as eutrophic in Figure 2.4.4. This implies that the 2019 eutrophic episodes in those regions were shorter in duration than their typical phytoplankton growth season. While most regional studies identify the growth season as the standard period for heightened eutrophication risk, and employ it to compute P90 climatologies (Gohin et al. 2008), this paper employed whole-year datasets for the calculation of the P90 and P10 climatologies. This approach was motivated by the need to report on the broad CMEMS North Atlantic region, which includes both coastal and open waters characterised by different productive periods.

It is worth noting that the absence of flags in the top left quarter of Figure 2.4.4 was due to the low significance of the P90/P10 indicators. The impact of satellite data quality and availability in the accuracy of eutrophication indicators has been highlighted for various ocean colour datasets (Gohin et al. 2008; Ha et al. 2014), with Van der Zande et al. (2011) demonstrating that the mean relative error in the estimation of the P90 values can reach 25.4% for MERIS. While the use of the climate-grade CMEMS OC-CCI REP dataset ameliorates these issues by merging various bias-corrected ocean colour streams (increasing the coverage and sampling frequency), some well-known eutrophication problem areas seem to be below our threshold of detection using the percentile climatology method presented here. This is the case for the coastal waters of the Skagerrak and Kattegat straits, where the significance of the percentile climatologies was too small to confirm previous trends reported for these problem areas (Andersen et al. 2016).

Section 2.5. Nitrate, ammonium and phosphate pools in the Baltic Sea

Authors: Mariliis Kõuts, Ilja Maljutenko, Ye Liu, Urmas Raudsepp

Statement of outcome: Eutrophication is a challenge in the Baltic Sea, with estimates of annual total input of about 830 kT of nitrogen and 31 kT of phosphorus in 2014. Nutrient and oxygen pools were estimated using model reanalysis data. During the period of 1993–2017, the pelagic nitrate pool decreased from ~2400 to 1700 kT in the Baltic Sea. The reduction of the nitrate pool was uniform over the Baltic Sea, with the exception of the Gulf of Bothnia, where decrease in the intermediate layer was small or even turned into an increase in the deep layer. Pelagic ammonium pools increased in the deep layer of the Baltic Proper due to decreasing oxygen concentrations there. The pelagic phosphate pool increased from ~600 to 750 kT, with most of the increase taking place in the surface and intermediate layers. The pool in the deep layer remained on a more stable level, with only a slight increasing trend. The increase of the phosphate pool covers the Baltic Proper area. In the Gulf of Bothnia, a decrease of phosphate has occurred in the upper layers and a slight increase in the deep layer. Only slight changes in the oxygen pool can bring about significant changes in the nutrient pools. Decreasing dissolved inorganic nitrogen pools and increasing phosphorus pools in the water column across the entire Baltic Sea, with the exception of the Bothnian Bay, results in a decreasing nitrogen to phosphorus ratio.

Ref. No.	Product name & type	Documentation
2.5.1	BALTICSEA_REANALYSIS_BIO_003_012 Model reanalysis	PUM: https://marine.copernicus.eu/documents/PUM/CMEMS-BAL-PUM-003-012.pdf QUID: https://marine.copernicus.eu/documents/QUID/CMEMS-BAL-QUID-003-012.pdf

2.5.1. Introduction

Eutrophication is a major challenge in the Baltic Sea, with at least 97% of the region assessed as eutrophied in 2011–2016 according to the HELCOM thematic assessment of eutrophication (HELCOM 2018a). However, the validity of this statement is questionable, as the least eutrophied basin – the Gulf of Bothnia – constitutes as much as 25.16% of the Baltic Sea volume. The HELCOM Eutrophication Assessment (HELCOM 2018a) featured nutrient levels, specifically winter dissolved inorganic phosphate and nitrogen, in the upper 10 m of the water column. According to the assessment, dissolved inorganic nitrogen varied from 3–5 μmol l^{-1} in the Bothnian Bay to ~10 μmol l^{-1} in the Gulf of Riga. A similar pattern occurred with dissolved inorganic phosphorus levels, which varied from 0.04 μmol l^{-1} in the Bothnian Bay to ~1.3 μmol l^{-1} in the Gulf of Riga. The hypotheses about the Gulf of Bothnia showing a tendency to become eutrophied are currently emerging (Lundberg et al. 2009; Fleming-Lehtinen et al. 2015; Andersen et al. 2017).

Eutrophication is caused by the addition of nutrients from land that accumulate in the marine system. In 2014, the Baltic Sea received an annual total input of about 826,000 tons of nitrogen and 30,900 tons of phosphorus (HELCOM 2018a). Atmospheric inputs account for about 30% of total nitrogen inputs (HELCOM 2018a). The input has decreased since the 1980s to the level of the 1960s for nitrogen and to the level of the 1950s for phosphorus by 2014 (HELCOM 2018a). The importance of nutrients is illustrated by different trophic states the ecosystem can evolve into, depending on the scale of nutrient inputs (Meier et al. 2012; Saraiva et al. 2019; Murray et al. 2019). History has shown that a massive input of nutrients into any lake or sea, including the Baltic, results in a disrupted ecosystem that eventually brings about eutrophication (Gustafsson et al. 2012; Murray et al. 2019). The aforementioned reductions in nutrient inputs are expected to be reflected in the time series of the pools.

The aim of this study is to assess the nutrient status of the Baltic Sea using model reanalysis data for the period 1993–2017. Based on ur results, we can evaluate the possible problem areas as well as the success of mitigation measures so far. We can evaluate the state-of-the-art quality of the reanalysis in the Baltic Sea. We do not claim that our analyses are unique, but rather, we intend to provide another set of estimates of total nutrient pools to the family of already existing estimates. Having an 'ensemble' of estimates obtained with different tools narrows the interval of uncertainties around the 'true' value.

2.5.2. Materials and methods

The BALMFC CMEMS biochemistry reanalysis product (product reference 2.5.1) is calculated using the Nemo-Nordic physical model (Hordoir et al. 2019; Pemberton et al. 2017) coupled with the Swedish Coastal and Ocean Biogeochemical model (SCOBI) (Eilola et al. 2009; Almroth-Rosell et al. 2015). The model system uses the Localised Singular Evolutive Interpolated Kalman filter data assimilation method (LSEIK, Nerger et al. 2005).

The model domain consists of the North Sea and the Baltic Sea (Hordoir et al. 2019). The horizontal resolution of the Nemo-Nordic model is approximately 2 nautical miles, and there are 56 vertical levels. Vertical resolution varies from 3 m at the surface up to 10 m below the depth of 100 m. The numerical model simulation data for this research covers the period 1993–2017 (product reference 2.5.1). At the lateral boundaries in the western English Channel and along the Scotland-Norway boundary, the sea levels are prescribed using 24 nautical mile resolution storm-surge North Atlantic Model. Climatological monthly mean values of temperature, salinity and biogeochemical variables are used at the open boundary. Atmospheric deposition of biogeochemical substances is supplied as spatial maps of a monthly climatology.

The river runoff is specified as daily means for the whole reanalysis period, 1993–2017, from the output of the HYdrological Predictions for the Environment (HYPE) model (Donnelly et al. 2016). The nutrient loads are specified as monthly mean values. River runoff as well as nutrient load are spread over more than 250 rivers located in the Baltic Sea (Hordoir et al. 2019).

The meteorological forcing is from HIRLAM (High-Resolution Limited Area Model) with a 22 km resolution, from project Euro4M (Dahlgren et al. 2016; Landelius et al. 2016), and covers most of the reanalysis period, 1993–2011. From 2012 onwards, the meteorological forcing is from the UERRA reanalysis product (European Regional analysis) with an 11 km resolution.

The sea surface temperature from the Swedish Ice Service and in-situ measured temperature and salinity profiles from the ICES database (www.ices.dk) are assimilated into the physical model. In-situ profiles of nitrate, ammonium, phosphate and dissolved oxygen from the Swedish Ocean Archive database (SHARK; https://sharkweb.smhi.se) are assimilated into the biogeochemical model. In total, 3200 nitrate, 3500 ammonium, 4000 phosphate and 7500 dissolved oxygen profiles were assimilated into the model. Spatial data coverage was strongly inhomogeneous, with high density data at the Swedish coast and in the western Baltic

Sea, less so in the eastern Baltic sea, and in the Gulf of Riga and Gulf of Finland there were only a few profiles. The reanalysis has been produced using 72-hour cycling, which implies that every 72 h all available observations are assimilated into the model before a 72-hour forecast is made. When there was more than one observation per model layer, an average value of the observations in the same layer was used.

In addition to model reanalysis data validation provided in the QUID, we have compared model reanalysis data with the observation data at the central Gotland basin and in the Gulf of Riga for the period 1993–2017. The nutrients concentrations have been extracted at central Gotland basin (BMPJ1 / BY15) and from the Gulf of Riga (BMPG1/ G1) from the model simulation and compared with observational data extracted from two different databases. The observational data has been extracted from The Marine distributed databases in the NEST system (Wulff et al. 2013), which provides monthly mean aggregate data at reference depths, and from the EMODnet database (Buga et al. 2018), which provides data at measured time and depth levels.

Main statistics of the comparison at BY15 for surface and bottom nutrients are summarised in Table 2.5.1. We have used the data from the EMODnet database. The differences in the statistics for the NEST database and the model reanalysis were marginal compared to the EmodNet data. Cost function (CF) was formulated as $CF = |(M–D)/SD|$, where the bias (M–D) of the model mean (M) relative to the mean of observations (D) is normalised to the standard deviation (SD) of the observations (Eilola et al. 2009). Cost function values 0–1 indicate a good match between the model results and measurements, values 1–2 indicate a reasonable match and values above 2 indicate a poor match. Cost function shows that model reanalysis data are good (Table 2.5.1). In general, the model underestimates all nutrients except phosphates at the surface.

In order to assess the nutrient status of the Baltic Sea, we use the combination of time-series analyses of nitrogen and phosphorus pools in three different layers of the water column and spatial maps of vertically integrated mean concentrations for two periods: 1993–1999 and 2000–2017. The selection of these two periods is motivated by the temporal variations of the hypoxic area of the Baltic Sea. After the stagnation period, which was terminated by the Major Baltic Inflow in 1993 (e.g. Mohrholz 2018), hypoxia development has shown two regimes. The first period, from 1993 to 1999, represents an increase of hypoxic area from 20,000 km^2 to a level of about 60,000 km^2 (Savchuk 2018; Meier et al. 2019; Carstensen and Conley 2019; Carstensen et al. 2014). The second period, from 2000 to 2017, can be characterised as variations of hypoxic area around a mean level between 60,000 and 80,000 km^2 (Savchuk 2018).

The pools of nitrate, ammonium, phosphate and oxygen have been calculated from the biochemistry reanalysis product (product reference 2.5.1). We have separated the water column into 3 layers: upper layer 0–15 m, intermediate layer 15–80 m and deep layer 80 m and below. The time-series of winter (February) nitrate and phosphate in the 0–15 m layer of the upper water column integrated over the Baltic Sea is an estimate of nutrient availability for phytoplankton and the concurrent transformation into biomass during the productive seasons. The upper layer, down to 15 m, characterises the summer mixed layer depth where the nutrients are depleted by plankton production. The intermediate layer characterises nutrient pools down to the average wintertime mixed layer depth, i.e. the depth to which the water column is seasonally mixed. The deep layer characterises the nutrient pool which is within or below the permanent halocline and, therefore, not easily mixed into the euphotic layer and accessible to phytoplankton production. Time-series of nitrate and phosphate pools under the halocline indicate the intensity of removal processes and storage of nutrients in the deep parts of the Baltic Sea.

Time series of pelagic pools are calculated as spatial integrals of nitrate, ammonium, phosphate and oxygen concentrations from the daily mean fields of product reference 2.5.1 for the whole Baltic Sea and for the three different layers separately. The dissolved inorganic nitrogen pool is taken as the sum of nitrate and

Table 2.5.1. Mean and standard deviation (SD) of the model reanalysis data and measurements, model bias (model minus observations), root mean square difference (RMSD) and cost function (CF) at the central Gotland basin (station BY15). Units are $mmol/m^3$.

		MEAN obs	SD obs	MEAN mod	SD mod	BIAS	RMSD	CF
NH4	surf	**0.19**	**0.16**	**0.14**	**0.18**	−0.06	0.21	0.36
	bot	14.30	10.40	12.84	6.22	−1.46	7.69	0.14
NO3	surf	1.29	1.49	1.09	1.35	−0.20	0.69	0.13
	bot	2.07	4.17	1.24	2.57	−0.84	3.40	0.20
PO4	surf	0.29	0.23	0.44	0.19	0.15	0.22	0.68
	bot	4.64	1.45	3.90	0.76	−0.73	1.34	0.50

ammonia. The spatial distributions of nutrient pools (g/m2) are calculated as vertical integrals over different layers: 0–15 m, 15–80 m, 80 m to the bottom.

The sediment processes are included in the model (Almroth-Rosell et al. 2015), but the nutrient pools in the sediments are not included in the product reference 2.5.1 output list. Thus, the dynamics of benthic pools of nutrients is not analysed in this study.

2.5.3. Results

Over the period of 1993–2017, the nitrate pool decreased monotonically from about 2500 kT to 1400 kT in the Baltic Sea (Figure 2.5.1a). In the upper layer, peak values in winter fell from 800 kT to 400 kT. In the intermediate layer, which constitutes the largest part of the nitrate reserve in the water column, the drop was from ~1600 to 800 kT. The nitrate pool in the deep layer decreased from ~600 to ~400 kT.

The average ammonium pool was 350 kT (Figure 2.5.1b). The most notable changes have been taking place in the upper and intermediate layers since 2012. These have been followed by the decrease of the ammonium pool in the deep layer since 2014. We would like to note the seasonal variability of ammonium in the upper layer and partly in the intermediate layer. Our study shows the presence of ammonium in the upper layer in January. The phosphate pool has increased from 620 kT to 700 kT from 1993 to 2017 (Figure 2.5.1c). Changes in the phosphate pools in the upper layer were seasonal, but there was also a long-term increasing trend. Winter peak values increased from below 100 kT to slightly above, indicating increased availability of phosphate for the phytoplankton blooms in spring and summer. The biggest storage of phosphate pools lies in the intermediate layer, which increased from ~300 kT to a new more or less stable level of ~380 kT from 2005 onwards. Phosphate pools in the deep layer remained on a similar level throughout the study period (250–300 kT).

We complement the time series of nutrient pools with the total amount of oxygen in different layers (Figure 2.5.1d). In total, oxygen content decreased by 20 MT from 1993 to 2017. The most notable decrease of dissolved oxygen of about 13 MT occurred in the intermediate layer, while a 6 MT reduction took place in the deep layer. Over the time period of 1993–2017, oxygen pools decreased by 14 MT from 1993 to 1999 and by 6 MT from 2000 to 2017. The latter decrease took place in the intermediate layer.

Spatial distribution of vertically integrated and temporally averaged nitrate, ammonium, phosphate and bottom oxygen were calculated for two consecutive periods: 1993–1999 and 2000–2017. The spatial distribution of nutrient pools in February indicates a potential for spring bloom and the following cyanobacteria summer bloom (Laanemets et al. 2006). Nitrate pools are distributed homogeneously over the Baltic Sea sub-basins, with the exception of the Gulf of Riga during the period of 1993–1999 (and also during the following period) (Figure 2.5.2). In the Gulf of Riga, surface nitrate concentrations are overestimated about 10 times. From the data, mean nitrate concentration calculated over the period of 1993–2017 was 5.3 mmol N/m^3 but 54 mmol N/m^3 in the reanalysis. Bottom values at the depth of 44 m were 11 and 62 mmol N/m^3, respectively. The following reduction (up to 60%) has been relatively uniform over the Baltic Sea, with the exception of the Gulf of Bothnia where decrease in the intermediate layer has been small or even turned into an increase. Also, reduction of nitrate has been moderate in the Gulf of Riga. We would like to note that all nutrient pools are high in the Gulf of Riga (Figures 2.5.2–2.5.4). Model reanalysis has significantly overestimated ammonium and phosphate concentrations in the Gulf of Riga. Root mean square error between reanalysis and measurements in the surface of the Gulf of Riga are 2.7 mmol N/m^3 and 0.6 mmol P/m^3 for ammonium and phosphate, respectively. For the bottom, corresponding values are 4.0 mmol N/m^3 and 0.8 mmol P/m^3, respectively.

Ammonium contribution to dissolved inorganic nitrogen is in the range of 10–20%, as mentioned earlier in the time series analysis, with the exception of the bottom layer (Figure 2.5.3). In addition, while the ammonium pool has decreased in the upper and intermediate layers with a few exceptions, an increase in the deep layer has been significant, mostly in the Baltic Proper.

The phosphate pools are lower in the Gulf of Bothnia than elsewhere in the Baltic Sea (Figure 2.5.4). The distinction can be made between the Bothnian Sea with a moderate phosphate pool and the Bothnian Bay with low phosphate pool. Areas that stand out with high phosphate pools in the upper layer include the Gulf of Riga, the eastern part of the Gulf of Finland and river estuaries (Figure 2.5.4a). An overall increase of the phosphate pools (up to 60%) has occurred in the Baltic Proper, while a decrease has taken place in the Gulf of Bothnia, especially in the upper and intermediate layers (Figure 2.5.4).

Decrease of dissolved inorganic nitrogen pools and increase of phosphate pools in the upper layer of the Baltic Sea (except the Gulf of Bothnia) has resulted in the decrease of DIN:DIP ratio between two periods (Figure 2.5.5a,b). The DIN:DIP ratio decreased also in

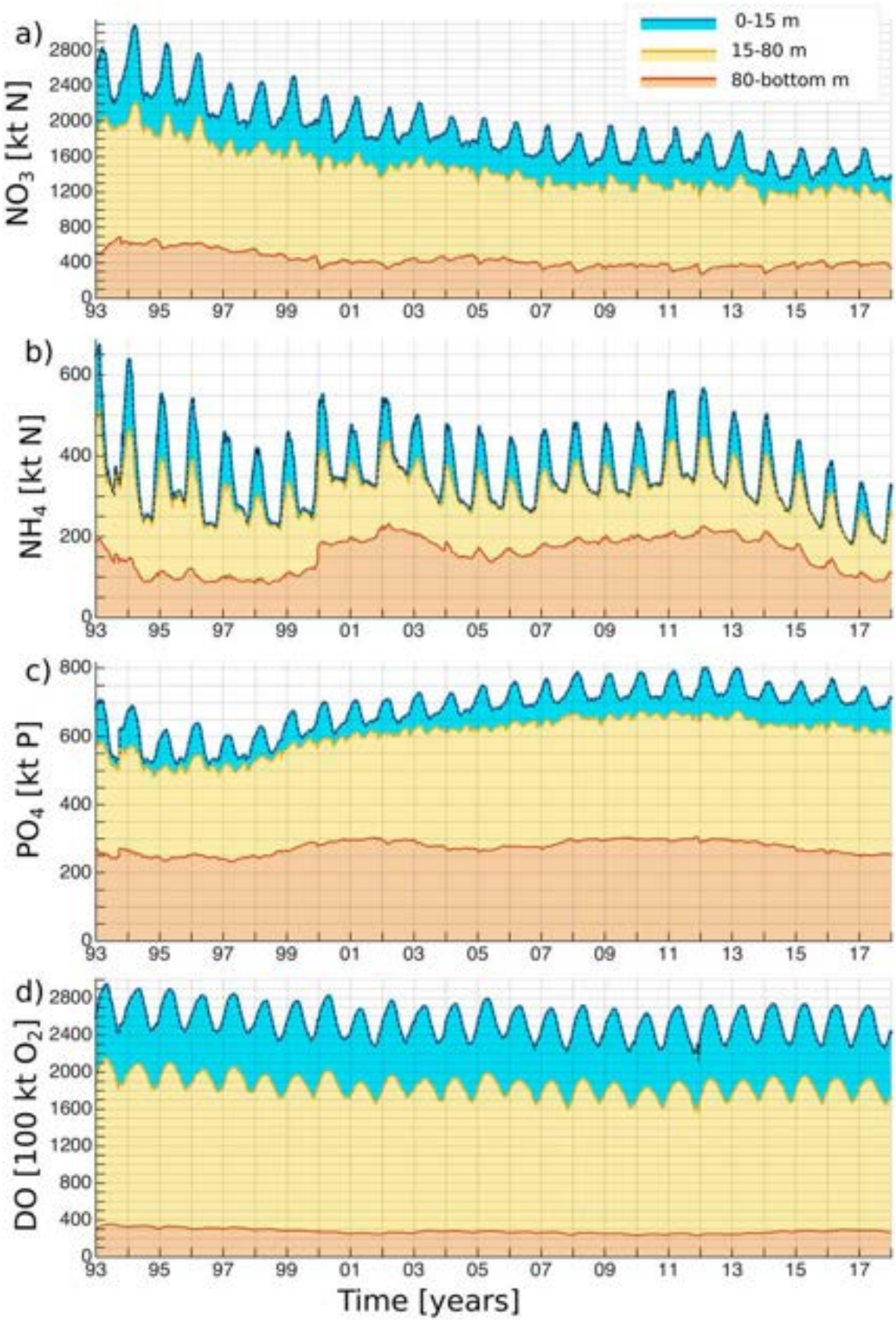

Figure 2.5.1. Stacked plot of time series of summarised dissolved nutrient pools: nitrate on (a), ammonium on (b), phosphate on (c) and dissolved oxygen on (d) in three different layers (Upper layer 0–15 m: blue; Intermediate layer 15–80 m: yellow; and Deep layer starting at 80 m and extending to the bottom: red) across the entire Baltic Sea. Time period is 1993–2017 (Product reference 2.5.1).

Table 2.5.2. Mean and standard deviation of different nutrient pools over the total period, first and last year.

Period	NH_4 MEAN	[kt] STD	NO_3 MEAN	[kt] STD	PO_4 MEAN	[kt] STD	O_2 MEAN	[100kt] STD
1993–2017	350	90	1850	360	680	70	2530	170
1993	440	120	2490	200	620	60	2690	170
2017	240	50	1430	120	700	20	2490	160

the Bothnian Sea but remained nearly unchanged in the Bothnian Bay, although both the inorganic nitrogen as well as phosphorus pools decreased in the surface layer there (Figures 2.5.2–2.5.4). On average, for the period of 1993–1999, the DIN:DIP ratio was less than 16 in the Baltic Proper and the Gulf of Finland but higher in the Gulf of Bothnia and the Gulf of Riga. Very high values of DIN:DIP ratio in the Bothnian Bay should be taken with caution. In the Bothnian Bay and partly in the Bothnian Sea, inorganic nitrogen and phosphorus concentrations are very small, which means that calculating the ratio of two small variables may result in an artificially high value. In the Gulf of Riga, inorganic nitrogen is unrealistically high but inorganic phosphorus moderately overestimated, which results in a high DIN:DIP ratio. We would like to note that the DIN:DIP ratio exceeds 16 in large river estuaries (Figure 2.5.5a,b), which indicates that there was no nitrogen limitation there, although a high phosphate content was present (Figure 2.5.4).

Spatial map of bottom dissolved oxygen concentration averaged over the period of 1993–1999 shows presence of hypoxia in the Baltic Proper (Figure 2.5.5c). That period was characterised by a significant decrease of oxygen content in the intermediate and deep layers of the Baltic Sea (Figure 2.5.5d). The latter is supported by the decrease of a dissolved oxygen pool from 2000 to 2017 in the intermediate layer (Table 2.5.3).

2.5.4. Discussion

The nutrient pools were estimated for the whole Baltic Sea from the model reanalysis. All things considered, getting estimations of total nutrient pools is a complicated task. In the case of modelling, it can be argued, and rightly so, that model-based estimates have large uncertainties due to deficiencies of the model in describing physical and biogeochemical processes, initial fields, external inputs and forcing. Furthermore, in the case of measurement based estimates, we again face the issue of large uncertainties, as measurements lack spatial and temporal resolution, are not made simultaneously and any kind of interpolation procedure introduces uncertainties in the estimates. Therefore, in this analysis we used reanalysis fields, which integrate both model simulation results and available measurements. Using the data assimilation technique is definitely an advantage, as it enables the improvement of the validity of the simulation product (e.g. Liu et al. 2014, 2017).

Long-term variations of the nutrient pools in the Baltic Sea (Gustafsson et al. 2017; Savchuk 2018) indicate that the time period for which the estimates of the pools are given should be explicitly stated when comparing the estimates from different sources. In this study, the analysis period was from 1993 to 2017. Over that period, the nitrate pool decreased monotonically from 2500 kT to 1400 kT (Figure 2.5.1a). The ammonium pool showed multi-year oscillatory variations superimposed to an overall decrease from 440 kT in 1993–240 kT in 2017 (Figure 2.5.1b, Figure 2.5.1c). Liu et al. (2014) have estimated a nitrate pool of 800 - 1100 kT and a phosphate pool of 500–600 kT for the period of 1970–1979. Their estimates varied almost two-fold depending on whether the model simulation was without data assimilation, with assimilation of physical data or with assimilation of physical and biogeochemical data. Savchuk (2018) has estimated that the dissolved inorganic nitrogen pool has decreased from ~ 1250 kT in 1990 to ~1100 kT in 2016. Dissolved inorganic phosphorus has increased from ~300 kT in 1993 to ~420 kT in 2000, and then almost monotonically to 500 kT in 2016. Gustafsson et al. (2017) estimates show a decrease of the dissolved inorganic nitrogen pool from 1500 kT in 1990 to 1150 kT in 2014 using the observations but variations around the mean level of 1200 kT without decreasing tendency over the same period using the simulation results. The dissolved inorganic phosphorus pool increased from about 400 kT in 1993 to about 600 kT in 2014 based on both the observations and simulation, but the temporal course within this time period was different (Gustafsson et al. 2017).

To summarise, temporal dynamics of dissolved inorganic nitrogen and phosphorus pools were similar to the other studies (Gustafsson et al. 2017; Savchuk 2018) but quantitatively overestimated. Here we suggest three explanations. Firstly, model reanalysis data validation for the Gulf of Riga showed that nitrate and ammonium concentrations have been significantly overestimated there. Only a few measured nutrient profiles were assimilated into the model. In general, the number of

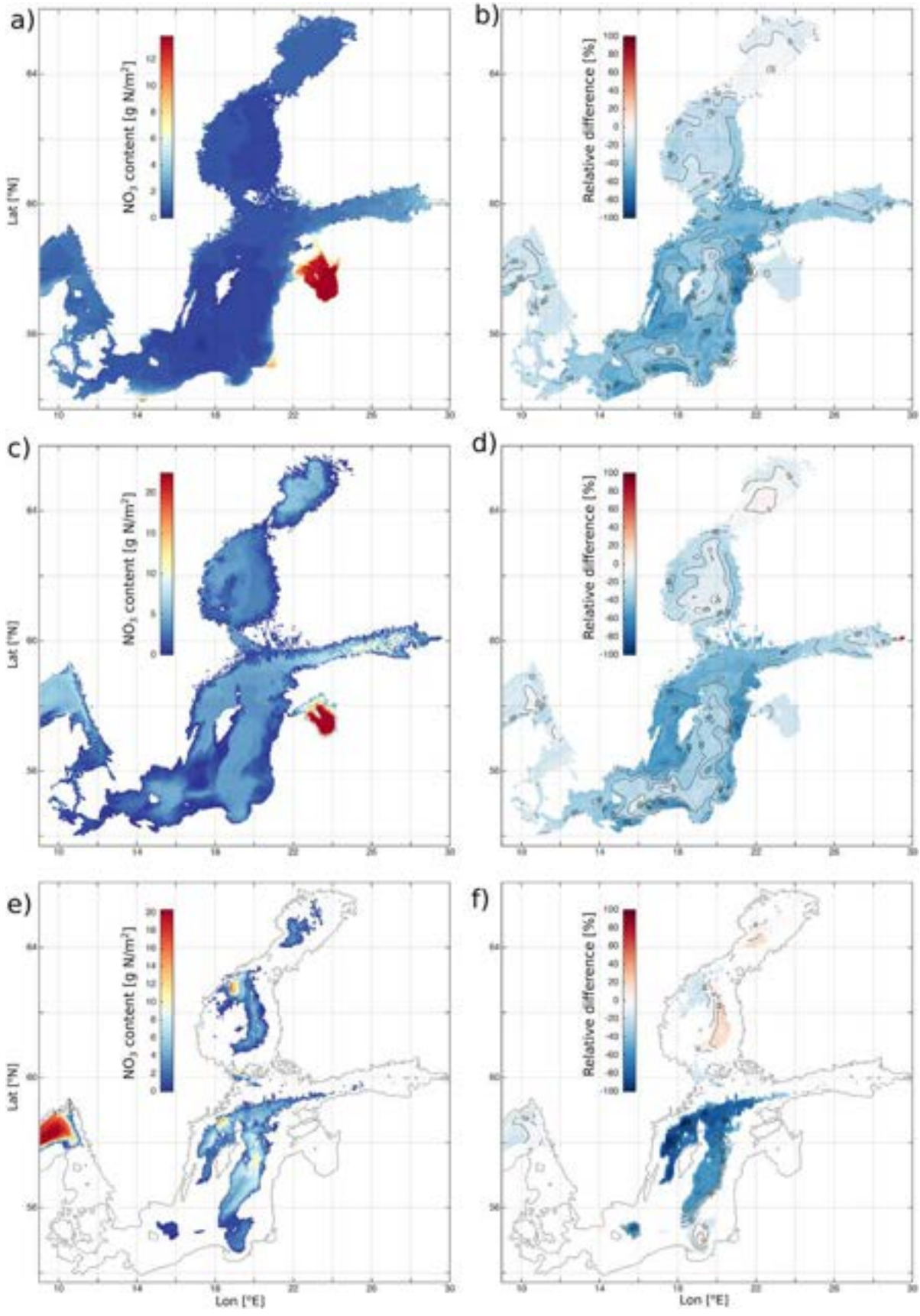

Figure 2.5.2. The mean nitrate pools in the different layers in February during the period of 1993–1999 in the left panels (a, c, e) and their relative changes ((*t* – ref)/ref)*100 for the period of 2000–2017 in the right panels (b, d, f) in the Baltic Sea. The left plots show nitrate pools as the amount of nitrogen per square meter. Different layers are depicted as 0–15 m on (a–b), 15–80 on (c–d) and 80-bottom on (e–f). The contour lines on (b), (d) and (f) show relative changes with a 10% step. The grey line on (c) and (d) shows the location of the coastline (Product reference 2.5.1).

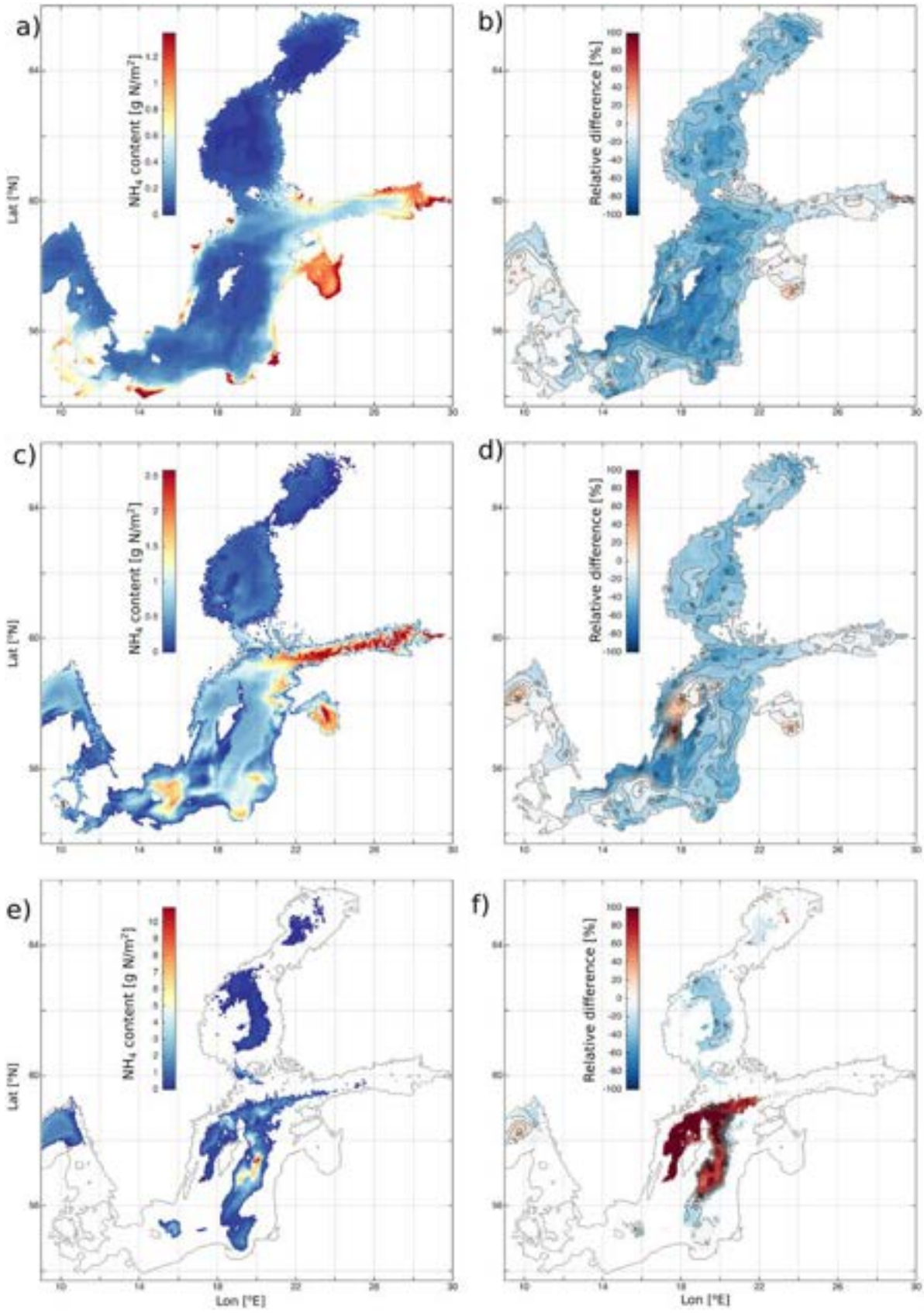

Figure 2.5.3. The mean ammonium pools in the different layers in February during the period of 1993–1999 in the left panels (a, c, e) and their relative changes ((*t* – ref)/ref)*100 for the period of 2000–2017 in the right panels (b, d, f) in the Baltic Sea. The left plots show ammonium pools as the amount of nitrogen per square meter. Different layers are depicted as 0–15 m on (a–b), 15–80 on (c–d) and 80-bottom on (e–f). The contour lines on (b), (d) and (f) show relative changes with a 10% step. The grey line on (c) and (d) shows the location of the coastline (Product reference 2.5.1).

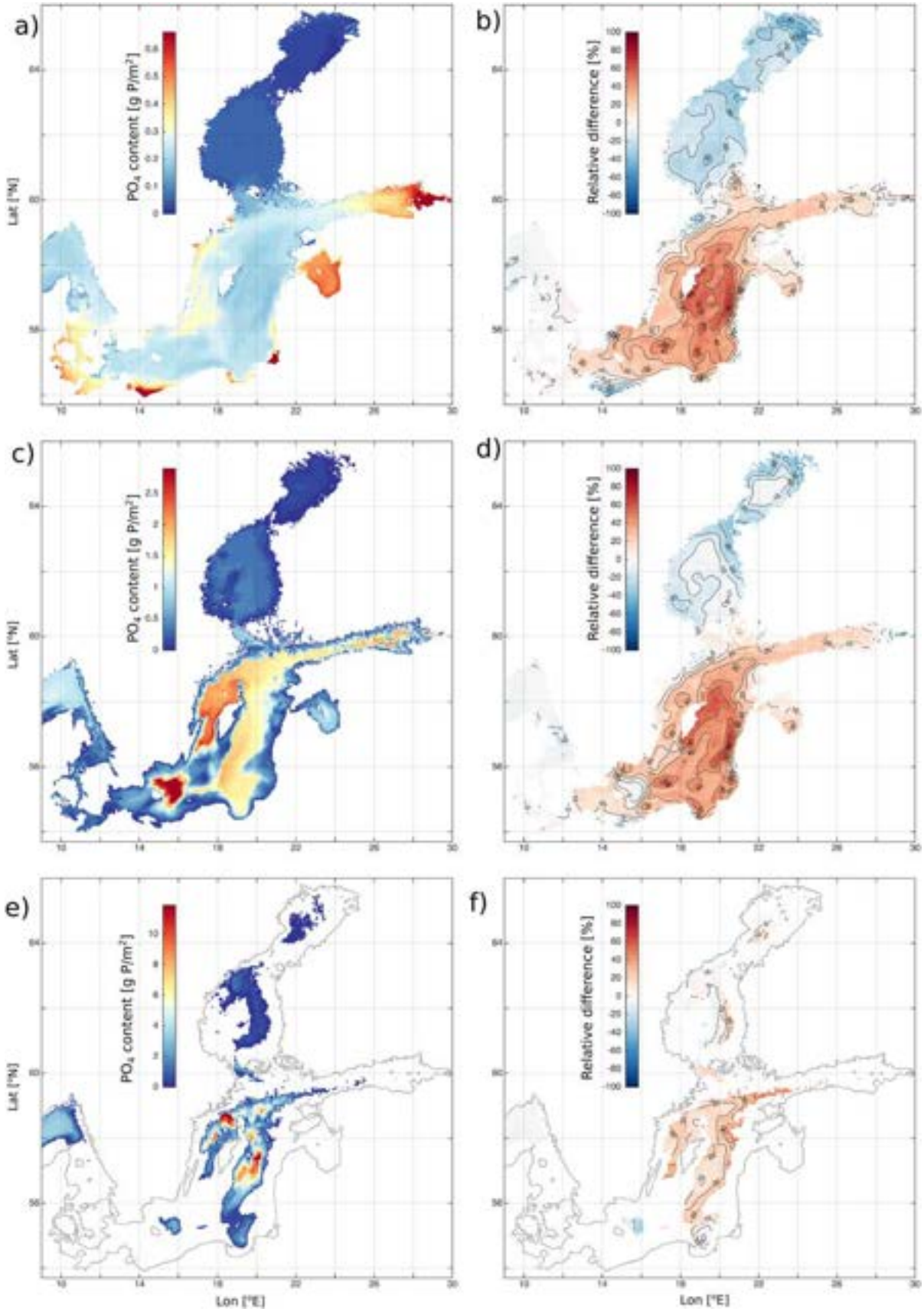

Figure 2.5.4. The mean phosphate pools in the different layers in February during the period of 1993–1999 in the left panels (a, c, e) and their relative changes ((*t* – ref)/ref)*100 for the period of 2000–2017 in the right panels (b, d, f) in the Baltic Sea. The left plots show phosphate pools as the amount of phosphorus per square meter. Different layers are depicted as 0–15 m on (a–b), 15–80 on (c–d) and 80-bottom on (e–f). The contour lines on (b), (d) and (f) show relative changes with a 10% step. The grey line on (c) and (d) shows the location of the coastline (Product reference 2.5.1).

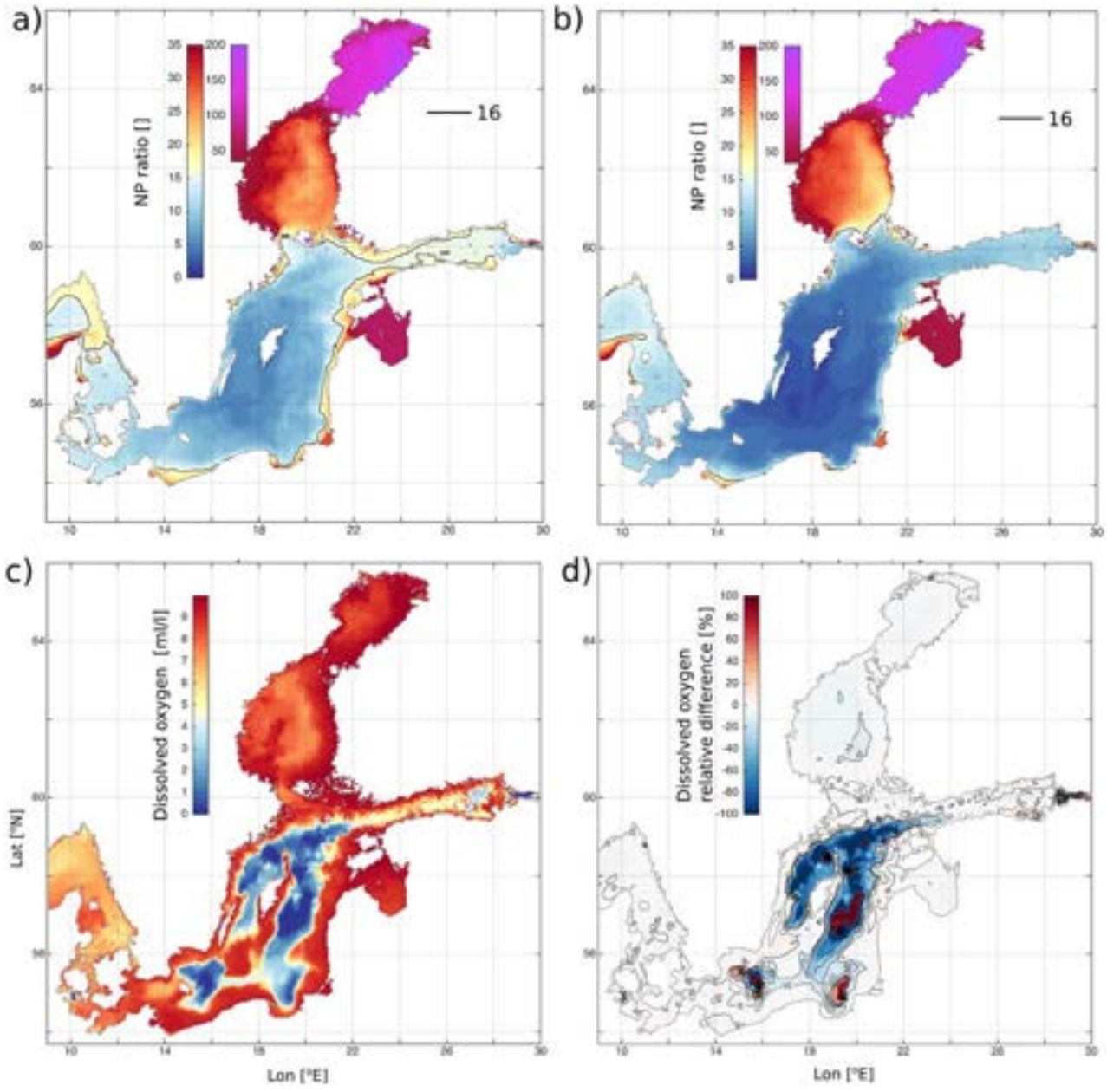

Figure 2.5.5. The mean DIN:DIP ratio (DIN/PO4) in the 0–15 m layer during the period of 1993–1999 (a) and during the period of 2000–2017 (b). The black contour corresponds to a DIN:DIP ratio of 16. The mean bottom dissolved oxygen concentration (ml/l) in February during the period of 1993–1999 (c) and the relative changes ((t – ref)/ref)*100 for the period of 2000–2017 (d). The contour lines on (d) show relative changes with a 30% step. The grey line on (d) shows the location of the coastline. Product reference 2.5.1.

Table 2.5.3. Mean and standard deviations (STD) of oxygen pools in different layers (TL – total layer, UL – upper layer, ML – middle layer, BL – bottom layer).

Period	TL O_2 MEAN	[100kt] STD	UL O_2 MEAN	[100kt] STD	ML O_2 MEAN	[100kt] STD	BL O_2 MEAN	[100kt] STD
1993–2017	2530	170	700	70	1560	100	270	27
1993	2690	170	710	70	1650	110	330	13
1999	2550	150	710	70	1580	80	270	4
2017	2490	160	700	70	1520	90	270	7

profiles assimilated into the model decreases significantly from the western part of the Baltic Sea towards east, which might influence the model values and provide an overestimation of nitrogen. Our comparison of the model data with measurements for the central Gotland basin showed good agreement. Secondly, during winter there was ammonium present in the upper layer and upper part of the intermediate layer (Figure 2.5.1b), which are well oxygenated and subject to intense nitrification. Geographically, the high content of ammonium was seen in the Gulf of Riga, the eastern part of the Gulf of Finland and in river estuaries (Figure 2.5.3a). There is almost no ammonium data assimilated in the model in the Gulf of Riga and eastern part of the Gulf of Finland. Comparison of model reanalysis data and independent measurements in the Gulf of Riga showed that at the surface ammonium concentrations were 0.4 and 2.0 mmol/m^3 in the measurements and model, respectively. Corresponding values at the depth of 44 m were 1.3 and 4.7 mmol/m^3, respectively. The coinciding of model and data was much better for the central Gotland basin (Figure 2.5.2), while the other study areas extend only to the Kattegat. We have kept the area within the limits of the biochemistry reanalysis product (product reference 2.5.1).

The general decrease of dissolved inorganic nitrogen is a reflection of several factors: decrease of dissolved inorganic nitrogen inputs, which have indeed been recorded (HELCOM 2018a, 2018b), and increased nitrogen removal from the system, which could be accelerated by the expanding hypoxic and anoxic areas, and the increasing amount of organic matter (Dalsgaard et al. 2013; Bonaglia et al. 2016). Nitrogen balance in the marine system is an interplay between several processes, including denitrification (in the hypoxic layer), anammox (newly anoxic conditions where sulphides have not yet formed) and dissimilatory nitrate reduction to ammonium (permanently anoxic conditions). Of these, denitrification plays the main role in the Baltic Sea, taking nitrogen out of the system (Gustafsson et al. 2012; Savchuk 2018). A correlation between hypoxic/anoxic area and denitrification has been recorded (Vahtera et al. 2007), indicating an intensification of this specific process as the area with favourable conditions expands (Savchuk 2018). However, nitrogen balance in marine areas and the relative contribution of different processes is still under debate (Dalsgaard et al. 2013; Savchuk 2018; Bonaglia et al. 2016, 2017).

Phosphorus pools have increased in the Baltic Sea. In the Baltic Proper, the increased water column phosphorus concentrations probably indicate that the sediments act as an ineffective phosphorus sink during anoxic periods (Meier et al. 2012). The positive winter dissolved phosphorus trend in the Bothnian Sea possibly reflects both the intrusion of and oxygen-deficient phosphorus-enriched water mass from the Baltic Proper (Rolff and Elfwing 2015) as well as the increasing input from the drainage basin (Kuosa et al. 2017). Phosphorus release from the sediments in the Bothnian Sea is unlikely, as oxygen conditions are relatively good at all times and the area is known for its phosphorus-binding ability (Asmala et al. 2017). The Gulf of Bothnia stands out as an area that performs differently from the rest of the Baltic Sea due to the differing biogeochemical conditions there – small to nonexistent stratification, sufficient oxygen conditions all year round, limited water exchange with the Baltic Proper, small external input of nutrients but high organic carbon load (Kuosa et al. 2017; Carstensen et al. 2020).

Decrease of DIN and increase of DIP results in the decrease of DIN:DIP ratio (Figure 2.5.5b). With some exceptions, inorganic nitrogen is the limiting nutrient for the spring bloom in the Baltic Sea (Granéli et al. 1990). Even in the formerly phosphorus limited Bothnian Sea the ecosystem has shifted towards nitrogen limitation (Rolff and Elfwing 2015; Kuosa et al. 2017). Our results still show a DIN:DIP ratio higher than 16 in the Bothnian Sea but are consistent with the results by Liu et al. (2017).

Changes in nutrient ratio play an important role in the eutrophication of a sea (or a lake) (Granéli et al. 1990). In the Baltic Sea, the relatively low nitrogen to phosphorus ratio means that excess phosphorus remains in the euphotic zone after the spring bloom has finished (Figure 2.5.1; Savchuk 2018). This limitation strengthens in the Baltic Sea as nitrogen is removed from the system even more rapidly, while phosphorus starts to be released from the sediments when the water turns anoxic (Conley et al. 2009; Viktorsson et al. 2013).

Decrease in the nitrogen to phosphorus ratio results in a change of the timing and distribution of phytoplankton blooms, as the spring bloom can weaken due to less nitrogen available in the euphotic zone (Raudsepp et al. 2019; Groetsch et al. 2016). However, the fate of the summer bloom is less clear (Raudsepp et al. 2018, 2019). Nitrogen limitation is known to be among the factors that enhance nitrogen-fixing cyanobacteria growth, which in turn leads to increased decomposition of organic matter and the consequent oxygen deficiency in the system (Vahtera et al. 2007; Savchuk 2018). In addition to the changes in dissolved inorganic nitrogen, increased dissolved inorganic phosphorus pools in the Baltic Sea, driven by perennial and seasonal anoxia, enable eutrophication to endure, as phosphorus is not removed from the system as effectively and continues

to cycle through the trophic levels as long as there are consumers available (Viktorsson et al. 2013). In addition to changes in the nutrient ratio, cyanobacteria blooms are also facilitated by elevated water temperature (Kahru and Elmgren 2014), which is granted by climate change (Meier et al. 2012; Meier 2015). Based on this information, it is very likely that we will continue to experience frequent cyanobacterial blooms in the future. Nevertheless, the extent and trend of these blooms is difficult to predict based solely on (winter) nutrient levels, as there are several other factors in play, which obscure the trend and cause regular interannual oscillations of cyanobacterial blooms(Kahru et al. 2018), the mechanism of which is yet to be explained (Kahru and Elmgren 2014; Kahru et al. 2018). Still, we would like to note that the areas of the Baltic Proper where dissolved inorganic nitrogen decreases and phosphorus increases overlap with an intense cyanobacteria bloom area (Kahru and Elmgren 2014). Also, the area in the eastern Bothnian Sea where both nitrogen and phosphorus pools slightly increase in the deep layer coincides with the area with occasional cyanobacteria blooms (Kahru and Elmgren 2014).

It is well known that hypoxic and anoxic areas have increased over the past two decades in the Baltic Sea (Carstensen et al. 2014; Reusch et al. 2018; Hansson et al. 2020). Therefore, it is somewhat surprising that oxygen content in the deep layer has decreased only marginally (Figure 2.5.1d). This counterintuitive looking result is readily explained by the hypsographic curve of the Baltic Sea and its sub-basins (Jakobsson et al. 2019). The area of the Baltic Sea bottom has been the main subject for the investigations of increasing hypoxia and anoxia (Carstensen et al. 2014; Reusch et al. 2018; Meier et al. 2019). The volume prone to low oxygen concentration (≤2 ml/l) envelopes ~2500 km^3 of water (Kõuts et al. 2021). The Gulf of Bothnia, which has well-oxygenated water due to weak vertical stratification, consists of a large water volume of 2865 km^3 below the depth of 80 m. Therefore, taking into consideration the total volume of the Baltic Sea, the decrease of the oxygen pool is seemingly moderate. The relatively good environmental state of the Gulf of Bothnia assuages the overall 'poor state of the Baltic Sea'.

In the context of different sub basins of the Baltic Sea with their specific physico-biogeochemical conditions, eutrophication is a severe problem in the Baltic Proper, the Gulf of Finland and the Gulf of Riga. Recently, the Major Baltic Inflows, which are known to disrupt the formation of dissolved inorganic nitrogen and phosphorus pools, do not oxygenate the bottoms for long (Neumann et al. 2017). The study by Meier et al. (2019) suggests an increase in the amount of organic matter that is transported to the deep layers of the Baltic Sea, where intense decomposition accelerates deoxygenation at the bottom and water column alike, rapidly restoring hypoxic/anoxic conditions present pre-Major Baltic Inflow. Reducing oxygen conditions, in turn, facilitates the release of ammonium (Conley et al. 2009) and phosphate from the sediments, which act as fertilisers for the oncoming blooms, creating a positive-feedback loop that maintains hypoxia (Vahtera et al. 2007; Savchuk 2018). The correlation between nutrient pools and oxygen conditions in the Baltic Sea has been shown earlier (Eilola et al. 2009; Savchuk 2018) and in our results and can be explained by the accelerating of the so-called 'vicious circle' (Vahtera et al. 2007).

Section 2.6. Long term changes monitored in two Mediterranean Channels

Authors: Sana Ben Ismail, Katrin Schroeder, Jacopo Chiggiato, Stefania Sparnocchia, Mireno Borghini

Statement of main outcomes: The Mediterranean Sea is a mid-latitude marginal sea which has been recognised to be a climatic hotspot. During the past decade, its water masses have experienced strong and fast increases in temperature and salinity, evidencing the tendency of this area to respond very rapidly to global warming and to changes in the regional freshwater budget. Based on in situ data here it is shown where and how fast these changes occur, with a particular focus on the Western Mediterranean Deep Water and the Intermediate Water. Such trends are at least one order of magnitude higher than the global mid-latitude average trends. Indicator-type curves, routinely updated, for subsurface temperature and salinity evolution represent an outcome that is envisaged to be important for climate science, environmental agencies, concerned citizens as well as regional policy-makers.

CMEMS Products used:

Ref. No.	Product name & type	Documentation
2.6.1	INSITU_MED_NRT_OBSERVATIONS_01_035/ MO_TS_MO_SardiniaChannel ftp://nrt.cmems-du.eu/Core/INSITU_MED_NRT_OBSERVATIONS_013_035/med_multiparameter_nrt/history/MO/MO_TS_MO_SardiniaChannel.nc (daily mooring data from 2003 to 2019)	QUID: https://cmems-resources.cls.fr/documents/QUID/CMEMS-INS-QUID-013-030-036.pdf PUM: https://cmems-resources.cls.fr/documents/PUM/CMEMS-INS-PUM-013.pdf

(*Continued*)

Continued.

Ref. No.	Product name & type	Documentation
2.6.2	INSITU_MED_NRT_OBSERVATIONS_013_035/ MO_PR_CT_SicilyChannel ftp://nrt.cmems-du.eu/Core/INSITU_MED_NRT_OBSERVATIONS_013_035/med_multiparameter_nrt/history/MO/MO_TS_MO_6101022.nc (daily mooring data from 1993 to 2019)	QUID: https://cmems-resources.cls.fr/documents/QUID/CMEMS-INS-QUID-013-030-036.pdf PUM: https://cmems-resources.cls.fr/documents/PUM/CMEMS-INS-PUM-013.pdf

2.6.1. Introduction

Climate change is one of the key topics of our century (Collins et al. 2019). The study of processes related to climate change in the atmosphere, the open ocean, the deep sea or even in shallow coastal waters require sustained long-term observations (Ryabinin et al. 2019; Sloyan et al. 2019). With more than 90% of anthropogenic accumulated heat absorbed by the oceans, monitoring long-term changes of its heat content, and over its full depth, is essential to quantify the planetary heat budget (Meyssignac et al. 2019). Subsurface temperature and subsurface salinity are two of the Essential Climate Variables (ECVs), as defined by the Global Climate Observing System (GCOS) as they play a key role in regulating Earth's climate, its variability and change. The monitoring of deep temperature and salinity from seasonal to longer timescales (i.e. interannual, decadal, and multidecadal), addresses both natural climate variability and human-driven climate change.

The Mediterranean Sea is a mid-latitude marginal sea, particularly responsive to climate change as reported by recent studies (Schroeder et al. 2017). Sea straits and channels are peculiar areas of the World Ocean as they represent a connection of relatively small spatial extension between different oceanic basins. This often implies that some gross oceanographic features of the surrounding zones can exert a deep influence on the channel dynamics, and vice versa. The continuous monitoring of these choke points allows us to intercept different water masses, and thus to document how they changed over time (Schroeder et al. 2019). This monitoring in the Mediterranean, in many cases, is done under the umbrella of the CIESM HYDROCHANGES (HC) program (https://www.ciesm.org/marine/programs/hydrochanges.htm). Here we report the long-term time series of physical data collected in two of these choke points: the Sardinia Channel (1900 m) and the Sicily Channel (400 m). The temporal evolution of the characteristics of the water masses crossing the Sicily Channel have been discussed in detail in the CMEMS Ocean State Report #3 (Schroeder et al. 2019). Over the past 20 years, there had been a considerable amount of results achieved on the circulation in the Western Mediterranean Sea. However, the Sardinia Channel remains one of the regions where the dynamical processes and water exchanges are not yet clearly identified. This contribution is therefore focused mainly on the estimate of temporal trends of deep water mass properties in the Sardinia Channel as a key deep region exchange within Mediterranean Basin (its discussion in the OSR#3 was limited to an overall picture of the range of variability of the deep water mass properties). Here we also include an updated discussion of the intermediate water properties that can be observed in the Sicily Channel, to continue the comparison of the two channels.

The long-term records of two HC moorings in two Mediterranean channels reveal how fast the response to climate change can be in a marginal sea compared to the global ocean (Schroeder et al. 2017), and demonstrates the essential role of long time series in the ocean. We investigate the causes of the observed trends and in particular discuss the role of a changing climate over the Mediterranean.

2.6.2. Study site description and monitored water masses

The Sardinia Channel, in the Western Mediterranean (WMED) is a wide opening between Tunisia and Sardinia, which has a sill at about 1900 m in a narrow deep trench that allows exchanges of the upper part of the deep waters to occur between the Algerian (depths > 2500 m) and the Tyrrhenian (depths > 3000 m) subbasins (Astraldi et al. 1999), as shown in Figure 2.6.1B and C. The upper part of the Western Mediterranean Deep Water (WMDW), which is trapped in the Algerian subbasin, is thus overflowing the sill when uplifted by even denser WMDW formed during dense water formation events in the Gulf of Lion during winter. This upper WMDW, circulating anticlockwise and alongslope may enter the Sardinia Channel directly following the Algerian slope. The Tyrrhenian Sea is filled up with warm and salty Tyrrhenian Deep Water (TDW), a mixing product between Levantine/Cretan Intermediate Waters (LIW/CIW), hereafter simply called Intermediate Water (IW), originated in the Eastern Mediterranean (EMED), and the WMDW that entered the Tyrrhenian Sea from the west. The TDW can only exit

the basin through the Sardinia Channel (being the Corsica Channel, at the north, too shallow to allow for deep water mass exchanges). These two deep water masses (WMDW and TDW) are generally located at different places within the channel, with the HC mooring being located mainly within the denser WMDW vein. As described by Schroeder et al. (2016), the WMDW has experienced a significant increase of heat and salt content over the past decades, due both to a gradual process and to an abrupt event, called Western Mediterranean Transition (WMT).

The Sicily Channel separates the Mediterranean Sea into its two basins, the EMED and the WMED, and it is the most important Mediterranean passage after Gibraltar. As at Gibraltar, there is a two-layer system that is maintained by the excess of evaporation over the EMED. Its monitoring is fundamental for the quantification of the highly variable exchanges between the two basins, particularly with regard to heat and salt fluxes. Between Cape Bon (Tunisia) and Mazara del Vallo (Italy), a ridge divides the channel longitudinally into two trenches each with very different cross-sectional areas (Figure 2.6.1D and E). The axis of the Sicilian trench and adjacent to the wide Sicilian plateau is directed northwards, is very narrow, and has a maximum depth of 450 m (mooring C01). The Tunisian trench is wider, deeper, and with a sill depth at about 530 m located some 20 nm to the south-west of the other (mooring C02). The monitoring of the bottom layer in both trenches (where the intermediate waters and the upper part of the deep waters of eastern origin pass) started in 1993. As described in Figure 2.6.1E the AW flows in a cyclonic path around the EMED. At intermediate depths in the EMED, two water masses are formed during winter convection events, the LIW in the Levantine Basin and the CIW in the Cretan Sea. At deeper levels, the Eastern Mediterranean Deep Water (EMDW) is found. These water masses are spread and mixed in the Ionian Basin before partly overflowing into the

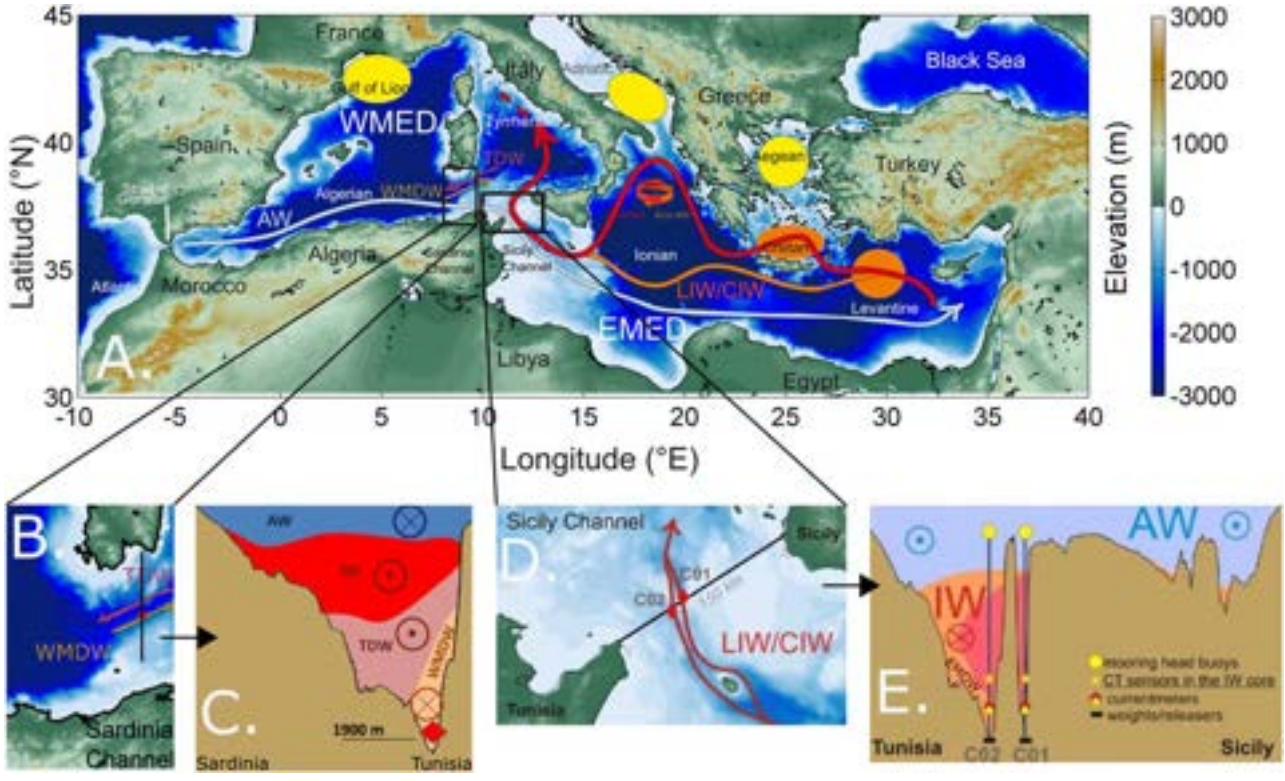

Figure 2.6.1. (A) The Mediterranean Sea where deep (yellowish ellipses) and intermediate (reddish ellipses) water formation sites are highlighted as well as the circulation schemes for the Atlantic Water (AW, light blue arrow) and the LIW/CIW (red arrow), the black rectangles indicate the monitored areas; (B) zoom on the Sardinia Channel where the position of the deep mooring is shown (red diamond), that allows to intercept the eastward flowing WMDW (light brown arrow); (C) vertical schematic section of the transect between Sardinia and Tunisia, showing the four-layers system of water masses flowing in opposite directions (AW in blue flowing eastward, IW in red flowing westward, TDW in dark pink flowing westward, WMDW in light brown flowing eastward); (D) zoom on the Sicily Channel where the positions of the two moorings are shown (red diamonds), that allows to intercept the westward flowing IW (red arrows); (E) the vertical schematic section of the transect between Tunisia and Sicily, showing the two-layer system of water masses flowing in opposite directions (AW in light blue flowing eastward; IW in orange flowing westward, where the darker orange indicates higher salinity, the salinity maximum identifying the core of the IW) and the positions of instruments along the C01 and C02 lines located in two parallel deep trenches.

Tyrrhenian Sea through the Sicily Channel (Ben Ismail et al. 2012, 2014).

2.6.3. Datasets and methods

For the Sardinia Channel (38.3341°N, 9.33265°E), data were collected by a SB37 probe at 1960 dbar. The original time-series was resampled to hourly sampling first (after November 2017 the sampling was every 15 min) and filtered with median filtering with one month time-window, in order to remove high frequency events (order of days), thus removing the effect of the occasional TDW westward flow from the baseline eastward WMDW flow. Trends in WMDW thermohaline properties are then estimated as the slope of the linear regression model, provided along with the standard error of the coefficient.

In the Sicily Channel, the two HC moorings have been operational since 1993 in positions 37.380° N, 11.591° E (C01) and 37.285° N, 11.5° E (C02). From 1993 to November 2002 temperature and conductivity have been recorded by means of Aanderaa RCM7 current meters, with an accuracy of 0.05°C and 0.05 for T and S, respectively. Since November 2002, SBE37 probes have been used, which further improved the quality of the measurements, yielding 0.002°C and 0.001 for T and S, respectively. The nominal depth of the instruments is 400 m, which is however subject to slight variations between servicing of the mooring, of the order of a few tens of meters. As temperature and salinity time series at both sites are very similar only the C02 time series are shown in Figure 2.6.3.

2.6.4. Results

The time series of θ, S and density collected at the sill (1900 m) of the Sardinia Channel since July 2003 are shown in Figure 2.6.2. A continuous warming trend (Figure 2.6.2A) at a rate of $0.0067 \pm 3.47{*}10^{-6}$°C year^{-1}, is well evident, accounting for a total deep temperature increase of about 0.114°C from 2003 to 2019. The salinity trend (Figure 2.9.2B) also shows a salinification at a rate of $0.0032 \pm 2.02{*}10^{-6}$ year^{-1}, with a total deep salinity increase of about 0.054 from 2003 to 2019. The density trend (Figure 2.9.2C) component shows a continuous densification at a rate of $0.0011 \pm 9.60{*}10^{-7}$ kg m^{-3} year^{-1}, with a total deep density increase of about 0.0187 kg m^{-3} from 2003 to 2019.

The time series shows an alternation of WMDW presence (lower θ and S, between 12.81 and 12.86, and ~38.45; thus, an eastward moving water mass) and TDW presence ('pulses' of higher θ and S, >12.86 often exceeding 12.9°C, and S >38.46 sometimes >38.48; thus a westward flowing water mass). These short bursts of warmer and more saline water (the temporary outflow of TDW) are a feature that is not further investigated here.

To complete the picture, here we show also an update of the temperature and salinity time series collected at 400 m depth at the Sicily Channel, in Figure 2.6.3, which has been already presented in OSR#3 up to 2017 (see Schroeder et al. 2019, OSR#3). Here the thermohaline properties of the IW and the upper portion of the EMDW are monitored since 1993, showing increasing temperature and salinity trends at least one order of magnitude stronger than those observed at intermediate depths in different parts of the global ocean (Schroeder et al. 2017).

The representation of the time series as a TS-diagram (Figure 2.6.4) gives a hint on how large the range of variability is in the intermediate water mass layer (with respect to the one found in the deep water in the Sardinia Channel), and the well evident upward-right shift of the diagram with time, with a strong acceleration after 2011 (as reported in OSR#3 and in Schroeder et al. (2017), where the different trends during the different periods are described).

2.6.5. Discussion and conclusion

Long-term θ and S increases have been documented for the WMDW and for the IW in previous studies, by various authors and for different periods (Table 2.6.1). In

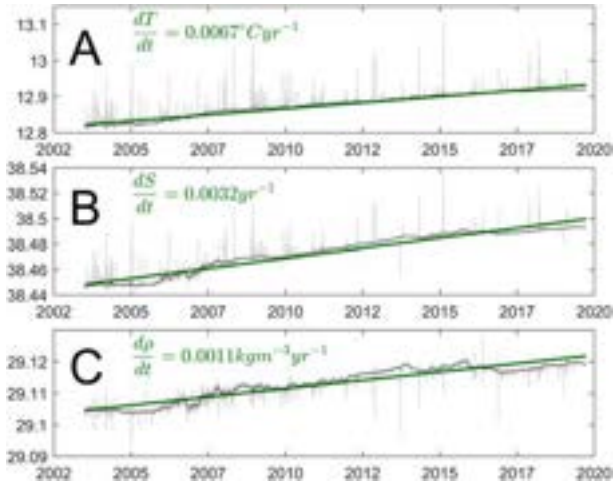

Figure 2.6.2. (new data set) Time series of (A) potential temperature (B) practical salinity and (C) density at 1900 m depth in the Sardinia Channel (mooring). The monthly mean time-series is shown in black. The green line represents the long-term trend line (data product used: 2.6.1).

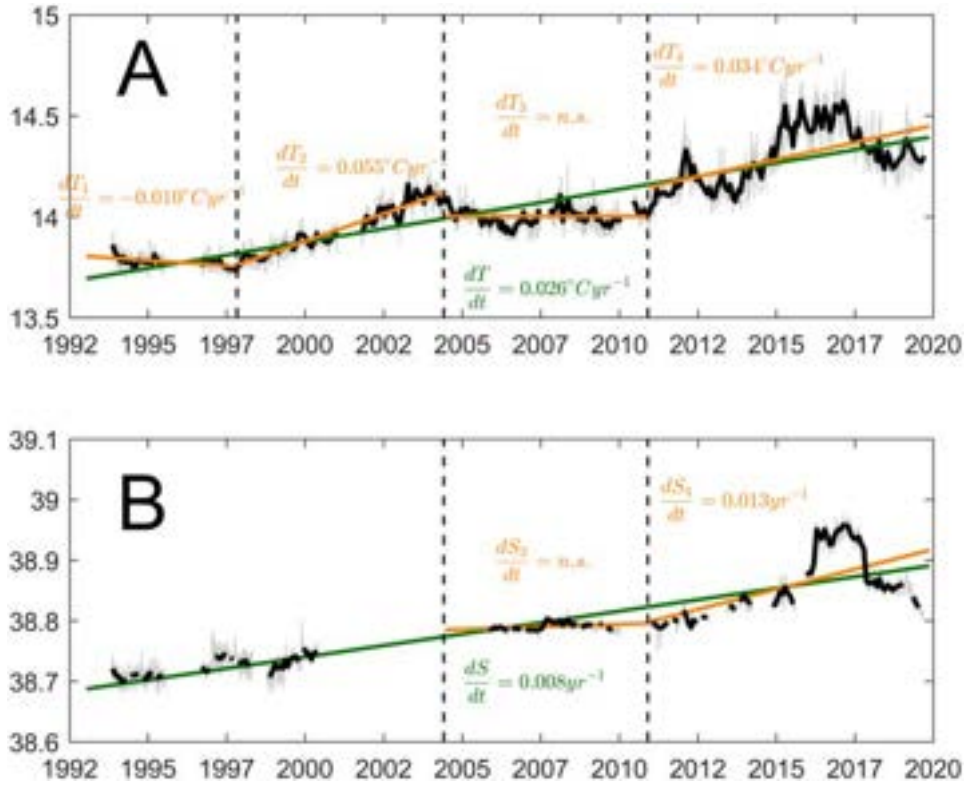

Figure 2.6.3. Daily (grey) and monthly (black) time series (1993–2017) of (A) temperature and (B) salinity at 400 m in the Sicily Channel (mooring, product ref. 2.3.1), updated from Schroeder et al. (2017)

addition to its gradual changes, since 2005 the WMDW have experienced significant thermohaline changes, which are comparable to the Eastern Mediterranean Transient (EMT, see Roether et al. 1996), both in terms of intensity and observed effects (Schroeder et al. 2008): the Western Mediterranean Transition (WMT, Schroeder et al. 2016) The production of high volumes of anomalously warm and salty new deep water during the winters 2004/2005 and 2005/2006 uplifted the old WMDW by several hundreds of meters in almost the whole western basin, inducing an abrupt increase in the deep heat and salt contents, thus resulting in a change in the deep stratification.

The monitoring at the Sardinia Channel shows very clearly that these interannual trends are significantly stronger than the global average trends. The global ocean full-depth average warming derived from a combination of repeat hydrography and Argo data collected in the period 2000–2016 is 0.0022 ± 0.0003°C year^{-1}, while the deep layer (2000–4000 m) warmed globally at 0.003°C year^{-1} and the abyssal layer (4000–6000 m) at 0.004°C year^{-1} (Desbruyères et al. 2017). Globally integrated, salinity change is estimated at about 0.0002 per 60 years (i.e. $3.33*10^{-6}$ year$^{-1;}$ Skliris et al. 2014), but of course there are significant regional differences, with fresh regions tending to become fresher, and salty regions tending to become saltier (in the Atlantic, salinity gain is found almost everywhere between 30S and 50N, of the order of 0.001 year^{-1}, whereas the Pacific sees almost basin-wide freshening, according to Skliris et al. 2014).

According to Schroeder et al. (2016), while until 2005 only the 'classical' old deep water was found at the sill, the new denser ones started to cross it since then, being uplifted by even denser new deep waters that were produced in the following winters. The study by Schroeder et al. (2016), making use of an extensive dataset (repeated CTD stations and the HC mooring data), showed that by 2014 the whole layer below 500 m, i.e. the halocline/thermocline and the deep water, has densified to values of 29.11–29.12 kg m^{-3}, becoming denser than the 'classical' resident water found at <3000 m in the Tyrrhenian Sea.

The long term strong warming and salinification of intermediate water: since the mid '90s its temperature and salinity have increased by 0.28°C/decade and 0.08 /decade in the Sicily Channel are shown in Figure 2.6.3, and also reported in Schroeder et al. (2019) where the intermediate water flowing from east to west may be intercepted. According to the authors, warmer and drier regional climatic conditions over the eastern basin are favouring the formation of increasingly

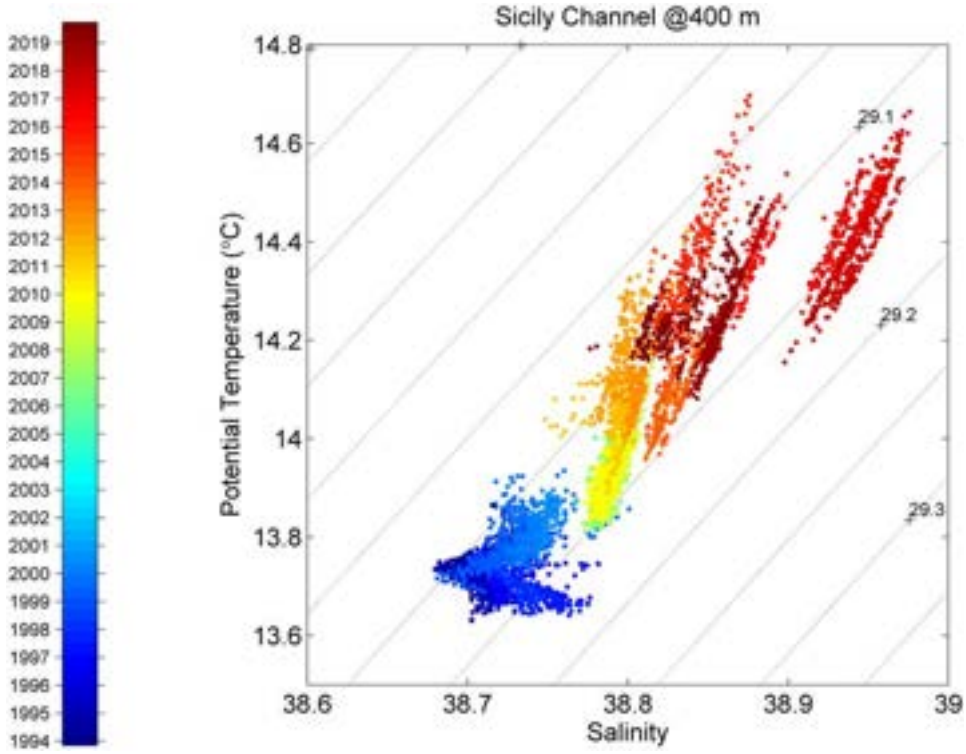

Figure 2.6.4. Temporal evolution of the TS diagram (potential temperature vs salinity) in the Sicily Channel at 400 m depth, the colour code indicates the years from 1993 to 2019 (data product used: 2.6.2).

warmer and saltier intermediate water: indeed, the Levantine region in particular is undergoing a dramatic drought since the late '90s (Cook et al. 2016), the driest period in the past 500 years.

These data confirm previous findings that classified the Mediterranean Sea as a climatic hotspot, with its water masses having experienced strong and fast increasing temperature and salinity. Based on in situ data here it is shown where and how fast these changes occur, with a particular focus on the Western Mediterranean Deep Water and the Intermediate Water. Such trends are at least one order of magnitude higher than the global mid-latitude average trends. Indicator-type curves, routinely updated, for subsurface temperature and salinity evolution represent an outcome that is envisaged to be important for climate science, environmental agencies, concerned citizens as well as regional policy-makers.

Section 2.7. Interannual variations of the Black Sea Rim Current

Authors: Elisaveta Peneva, Emil Stanev, Stefania Ciliberti, Leonardo Lima, Ali Aydogdu, Veselka Marinova, Nadejda Valcheva

Products used:

Ref. No	Product Name and Type	Documentation
2.7.1		

(*Continued*)

Table 2.6.1. Long-term θ and S increases (trends) computed in different locations and different periods in Mediterranean Sea.

Location (Water Mass)	θ Trend	S Trend	Years	Reference
Western Mediterranean (WMDW)	0.0016°C year^{-1}	0.0008 year^{-1}	1960–1995	Krahmann and Schott (1998)
Western Mediterranean (WMDW)	0.0027°C year^{-1}	0.0019 year^{-1}	1969–1987	Leaman and Schott (1991)
Western Mediterranean (WMDW)	0.0034°C year^{-1}	0.0011 year^{-1}	1959–2000	Béthoux et al. (1998)
Western Mediterranean (WMDW)	0.00047°C year^{-1}	0.0006 year^{-1}	1900–2008	Vargas-Yáñez et al. (2010)
Western Mediterranean (WMDW)	0.004°C year^{-1}	0.001 year^{-1}	1943–2015	Vargas-Yáñez et al. (2017)
Tyrrhenian Sea (TDW)	0.016°C year^{-1}	0.008 year^{-1}	1990s	Fuda et al. (2002)
Ligurian Sea (IW)	0.0068°C year^{-1}	0.0018 year^{-1}	1960–1992	Béthoux and Gentili (1996)
Western Mediterranean (WMDW)	0.0083°C year^{-1}	0.0069 year^{-1}	1909–1989	Rohling and Bryden (1992)
Gibraltar (Mediterranean outflow water)	0.3°C year^{-1}	0.06 year^{-1}	1980–2000	Millot et al. (2006)
Sicily Channel (IW)	0.05°C year^{-1}	0.02 year^{-1}	1995–2009	Ben Ismail et al. (2014)
Sicily Channel (IW)	0.024°C year^{-1}	0.006 year^{-1}	1993–2016	Schroeder et al. (2017)
Sardinia Channel (WMDW)	0.0067°C year^{-1}	0.0032 year^{-1}	2003–2019	This study

Continued.

Ref. No	Product Name and Type	Documentation
	Black Sea Physics Reanalysis (BLKSEA_REANALYSIS_PHYS_007_004) (new release of Dec 2020, for the period 1993–2019)	PUM https://marine.copernicus.eu/documents/PUM/CMEMS-BS-PUM-007-004.pdf QUID https://marine.copernicus.eu/documents/QUID/CMEMS-BS-QUID-007-004.pdf (new release of Dec 2020)
2.7.2	Black Sea Gridded L4 Sea Level Anomalies and derived variables reprocessed (1993-ongoing) SEALEVEL_BS_PHY_L4_REP_OBSERVATIONS_008_042	PUM https://marine.copernicus.eu/documents/PUM/CMEMS-SL-PUM-008-032-062.pdf QUID https://marine.copernicus.eu/documents/QUID/CMEMS-SL-QUID-008-032-062.pdf
2.7.3	ERA5 reanalysis hourly data on single levels	https://cds.climate.copernicus.eu/cdsapp#!/dataset/reanalysis-era5-single-levels?tab=overview

Statement of the main outcome: The general circulation in the Black Sea features a cyclonic gyre encompassing the entire basin (Rim Current), which flows approximately over the continental slope, separating the coastal environment from the open sea. The speed of Rim Current varies from year to year giving an overall measure of the intensity of the circulation. The latter is important for many physical and biogeochemical processes such as the formation of the vertical stratification, replenishment of the Cold Intermediate Layer (CIL), dynamics of mesoscale eddies propagating along the gyre, biogeochemistry dynamics, heat redistribution within the basin, anchovy and other fish distribution, pollution dispersion. The data from satellite altimeters and physical modelling is used to identify the most representative areas where one can get stable estimates of the annual mean speed of the Rim Current for the period 1993–2019. An Ocean Monitoring Index, reflecting the annual state of the cyclonic circulation, referred as Black Sea Rim Current Index (BSRCI), is determined and its interannual variations are studied. The time-series of the BSRCI suggest that the Black Sea Rim current speed varies within ~30% in the period 1993–2019 with positive trend of ~0.1 m/s/decade. It is found that the Rim current is in close relation to the regional atmospheric circulation and the mean velocity variation is linked to the wind curl above the basin. This proves that the Sverdrup relation applies to the Black Sea Rim current.

2.7.1. Introduction

The Black Sea is a deep semi-enclosed sea with dimensions of 1000 by 500 km in zonal and meridional direction and maximal depth of ~2 km. The basin circulation is driven by the regional winds and large freshwater river inflow in the north-western part (including the main European rivers Danube, Dnepr and Dnestr). The major cyclonic gyre, which encompasses the sea is referred to as Rim current. The position and mean speed of the Rim current have been studied using observational data (Oguz et al. 1992, 1993; Korotaev et al. 2003; Zatsepin et al. 2003; Kubryakov and Stanichny 2015) and numerical simulations (Staneva et al. 2001; Stanev et al. 2003; Capet et al. 2012; Miladinova, Stips et al. 2020). According to Ivanov and Belokopytov (2013), there are three characteristic zones with different regimes of currents: coastal zone of very variable flow; main Black Sea Rim Current zone (following approximately the 1000 m isobaths); and open sea area. The Rim current is quasi-geostrophic and the Sverdrup balance approximately applies to it (Stanev et al. 2000). It varies seasonally, intensifying in winter due to the dominating severe northeastern winds in the region (Stanev et al. 2000). The Rim current occasionally breaks into two main gyres – the western and eastern gyres (Oguz et al. 1992). Another specific element of the Black Sea circulation is the generation of mesoscale eddies near the coast, mostly anticyclones, travelling with the main current (Blatov et al. 1984; Stanev 1990; Simonov and Altman 1991; Oguz et al. 1992, 1993; Ozsoy and Unluata 1998; Staneva et al. 2001; Korotaev et al. 2003; Zatsepin et al. 2003).

The Rim current shows a significant interannual variability (Stanev and Peneva 2002), following the controlling factors variations – winds and fresh water fluxes. Consequently, this impacts the vertical stratification, the cold intermediate water formation, the patterns of the biological activity and the coastal mesoscale eddies' propagation along the current and their evolution. The higher circumpolar speed leads to enhanced dispersion of pollutants, less degree of exchange between open sea and coastal areas, enhanced baroclinicity, intensification of the heat redistribution which is important for the winter freezing in the northern zones (Simonov and Altman 1991). Fach (2015) finds that the anchovy larval dispersal in the Black Sea is strongly controlled at the basin scale by the Rim Current and locally – by mesoscale eddies.

Several recent studies of the Black Sea pollution claim that the understanding of the Rim Current behaviour and how the mesoscale eddies evolve would help to predict the transport of various pollution such as oil spills (Korotenko 2018) and floating marine litter (Stanev

and Ricker 2019) including microplastic debris (Miladinova, Macias et al. 2020) raising a serious environmental concern today.

To summarise, the intensity of the Black Sea Rim Current could give a valuable integral measure for a great deal of physical and biogeochemical processes manifestation. Thus our objective is to develop a comprehensive index reflecting the annual mean state of the Black Sea general circulation to be used by policy makers and various end users.

2.7.2. Interannual variability of the Rim current speed

The Rim current shape, position and speed vary largely from season to season and from year to year. A recent study by Miladinova et al. (2020) finds that the Rim current speed has been increasing for the past six decades. Trajectories of surface drifters (Zhurbas et al. 2004; Stanev 2005) and profiling floats over the last ~fifteen years (Stanev et al. 2019) demonstrated that the 1000 m isobath is the approximate leading line for the Rim current core, but this is not always the case, seen by the modelling, altimeter and in-situ data. Thus, the first step in our analysis is to determine the region where the Rim current normally passes and could be well identified.

The main source of data for the Black Sea surface current velocity in our analysis is the CMEMS Black Sea reanalysis (BS REA) (product ref. 2.7.1). The modelling system, assimilation scheme and results from validation against observations is described in details in the relevant Quality Information Document (QUID, see the link in the table above). The BS REA is extensively validated against temperature and salinity data from satellite and Argo autonomous profilers' data. Concerning the current velocity, the QUID gives only a qualitative comparison with published articles and information on the climatology of the surface surface velocity fields, due to unavailability of reliable long-term measurements of the current speed in the basin. However, Rim current is quasi-geostrophic and thus it could be approximated with the geostrophic velocity calculated by the sea surface height (SSH) slope. Thus, the error in representing the SSH gives a measure for the quality of the model current velocity. According to the QUID the time-averaged RMSD of SSH anomaly against the satellite altimeter sea level anomaly is ~2–3 cm which is a very good estimate and is within the range of the altimeter measurement error. This good agreement between observations and numerical simulations is explained by the fact that the operational model assimilates along-track altimeter data.

Additionally to support the analysis, we will take advantage of another CMEMS product – the Black Sea Gridded L4 Sea Level Anomalies and derived variables (product ref. 2.7.2).

Figure 2.7.1 shows the mean surface current velocity (a) from the CMEMS Black Sea reanalysis together with the mean for the period 1993–2018 geostrophic current anomaly (b) derived from the reprocessed altimeter data. The regions with large current velocity are following approximately the continental slope (Figure 2.7.1a) as described in many literature studies (cited in the Introduction section). Similar patterns of the annual mean currents could be found also in Grayek et al. (2015).

The geostrophic current anomaly is calculated from the slope of the sea level anomaly (Figure 2.7.1b) and thus is generally revealing the area with large surface height variation, e.g. current velocity variation. However, if the current is permanent and quasi-stationary, it might not show large variations. Two areas with prominent anomalies are seen – in the easternmost part and in the central western part. These are the quasi-permanent anticyclonic Batumi and Sevastopol eddies (Staneva et al. 2001; Poulain et al. 2005; Kubryakov et al. 2018). In these areas the circulation is very unstable and not a good candidate to represent the basin-wide geostrophic circulation. For this reason these two areas are not considered in the further analysis.

The averaged Rim current position is better identified in the model simulations in Figure 2.7.1a, where the mean sea surface velocity for the considered 27 years period is shown. Three areas of intense currents are well identified: western – near the Romanian and Bulgarian coast; northern – from the Caucasus coast to the Crimea Peninsula (33E–39E); and southern – from the Sakarya region to the Sinop Peninsula (31.5E–35E).

Our objective is to define a measure of the Rim current intensity using firm fixed geographical parameters, in such a way that it could be calculated from different data sources. Thus, we consider the area confined between the 200 and 1800 m isobaths in the northern section 33E–39E, and in the southern section 31.5E–35E (Figure 2.7.1c) as a representative of the Rim current. Note, that thus we avoid the areas of the quasi-permanent Sevastopol and Batumi eddies.

As far as the intensification of the current along the western coast is concerned, it could result from rapid changes in river runoff or response of shallow shelf to the atmospheric forcing. Because we are here interested in the variability of baroclinic ocean, we will not address the western current as a representative measure of the Rim current.

Figure 2.7.2 is a multi-year plot of the annual mean sea surface velocity which clearly shows the interannual

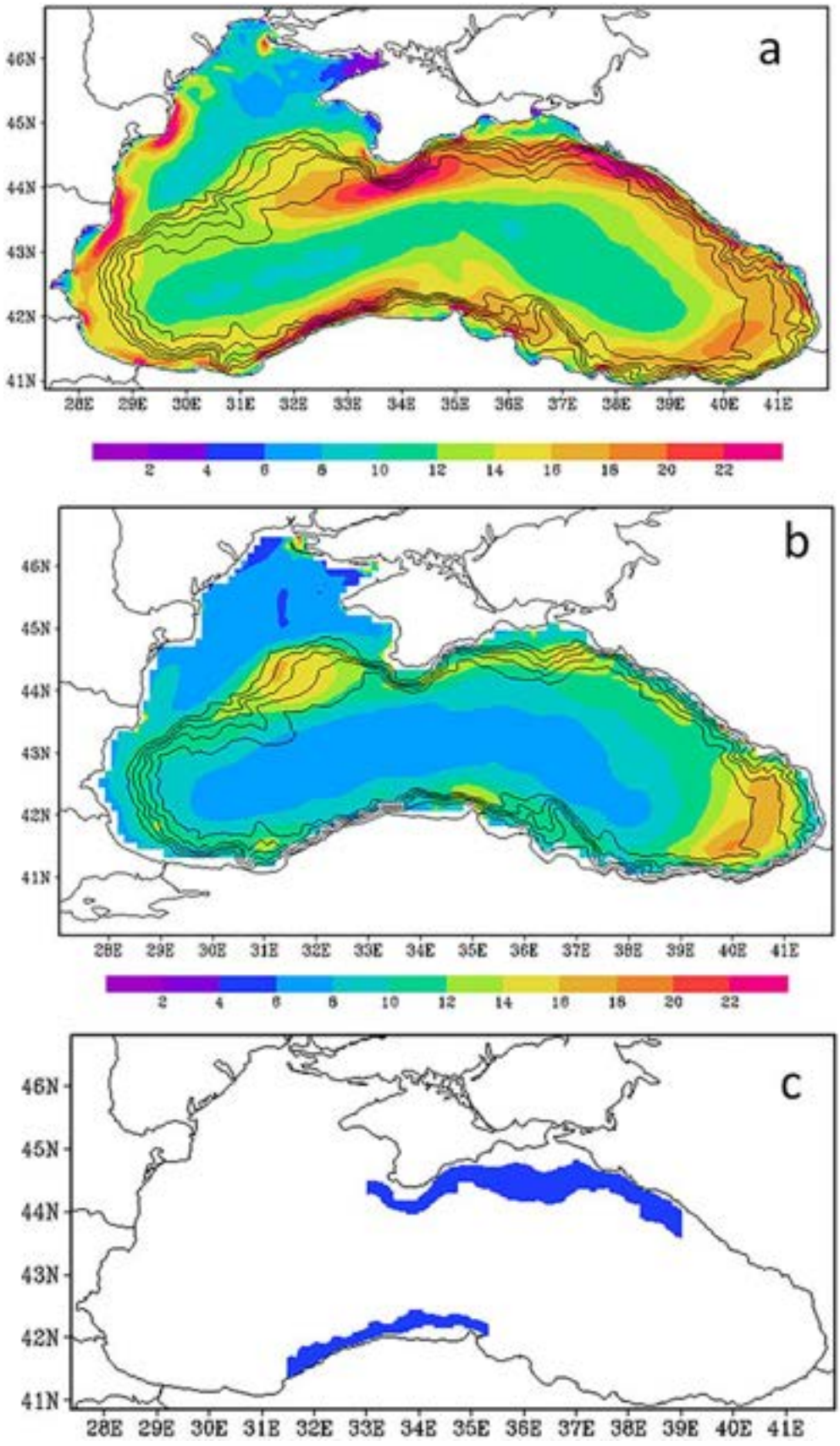

Figure 2.7.1. (a) Mean sea surface velocity for the period 1993–2019 [cm/s]; (b) Mean geostrophic current anomaly for the period 1993–2019 [cm/s]; the black contours on both plots show the 200, 600, 1000, 1400 and 1800 m isobaths taken from GEBCO bathymetry (www.gebco.net); (c) the region between isobaths 200 and 1800 m used for the calculations further.

variation in the shape and speed of the Rim current. Nevertheless, it is seen that the Rim current is well distinguished in the selected areas in Figure 2.7.1c every year. Notable, although the overall similarity in the velocity patterns, each year shows specific patterns. The eastern branch of the Rim gyre is more evident in the period 2002–2010, in the following years it weakens. The western branch of the Rim current is well observed in 1993, then in 2008, 2015 and 2017. The Sevastopol eddy is especially pronounced in 2005. Batumi eddy is very well seen in 2006, 2011, 2015.

2.7.3. Black Sea Rim current index (BSRCI)

In order to construct an index reflecting the intensity of the Rim current, we use the long-term mean values of the sea surface current speed averaged in the areas, shown in Figure 2.7.1c and respectively the annual mean value.

$$\mathrm{BSRCI} = \frac{\bar{V}_{ann} - \bar{V}_{cl}}{\bar{V}_{cl}} \quad (1)$$

where $\bar{V}$ denotes the representative area average, the '*ann*' denotes the annual mean for each individual year in the analysis, and '*cl*' indicates the long-term mean over the whole period 1992–2019. In general, the BSRCI is defined as the relative annual anomaly from the long-term mean speed. It is near zero if the annual mean state is close to the 'normal' one. Positive BSRCI indicates more intense Rim current than the average one, negative – less intense. The number +1

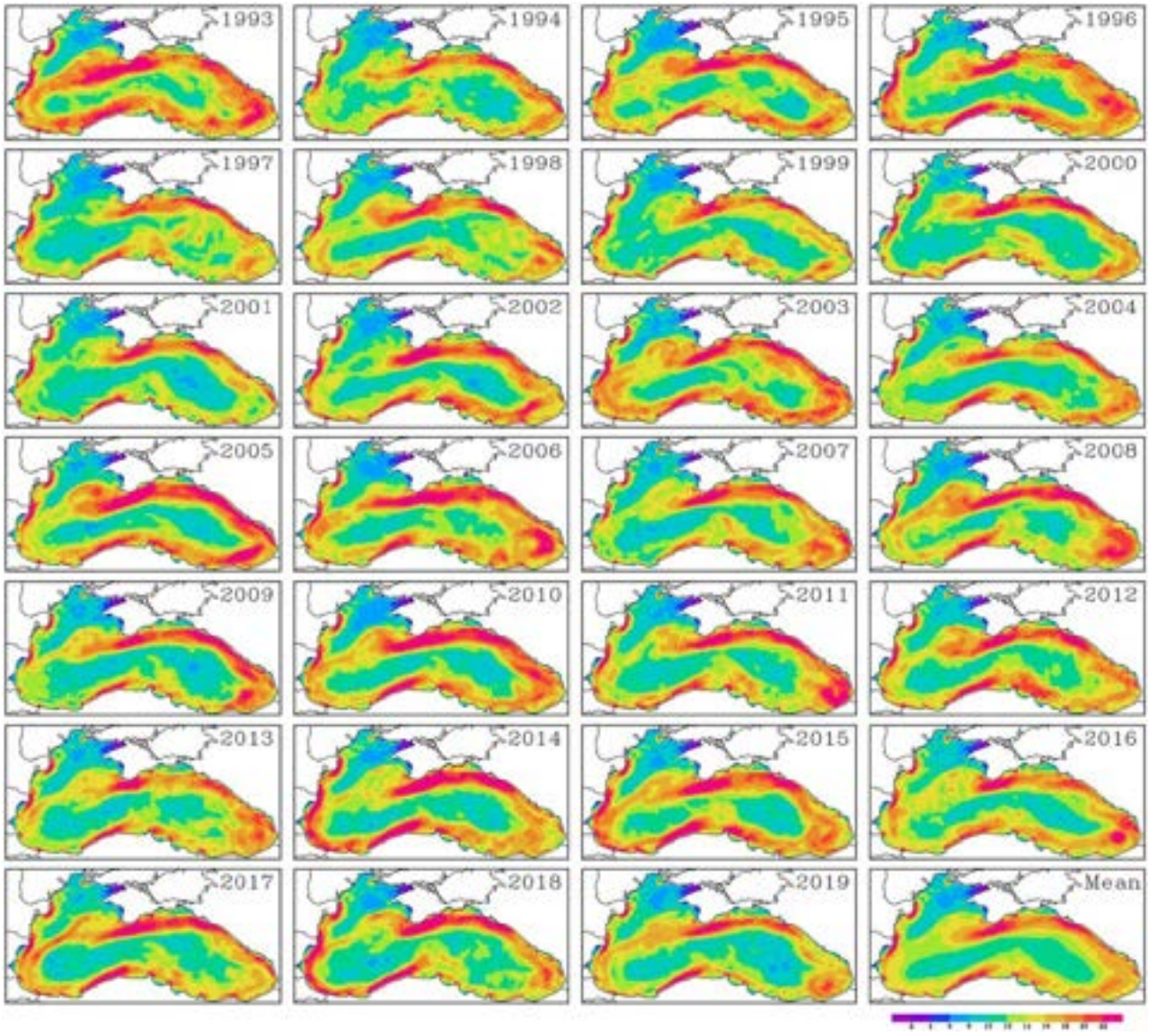

Figure 2.7.2. Annual mean sea surface velocity [cm/s] for the period 1992–2019 from the CMEMS Black Sea reanalysis data.

would mean double Rim current speed than usual, and −0.5 – half of the norm.

In other words, positive BSRCI would mean higher circumpolar speed, enhanced baroclinicity, enhanced dispersion of pollutants, less degree of exchange between open sea and coastal areas, intensification of the heat redistribution, etc.

The results from the calculation of the Black Sea Rim Current Index are summarised in Figure 2.7.3. Additionally, we calculate the index for the north and south part only, denoted $BSRCI_n$ and $BSRCI_s$.

The time-series of the BSRCI shown in Figure 2.7.3 suggest that the Black Sea Rim current speed varies within ∼30% in the period 1993–2018 with a positive tendency of ∼0.1 m/s/decade. In the years 2005 and 2014 there is evidently higher mean velocity, and on the opposite end are the years –2004, 2013 and 2016. There is a general agreement in the curves corresponding to the northern and southern sections of the gyre (blue and red in Figure 2.7.3): the increased speed of the gyre in the north is in phase with the increased speed in the south. However, in some periods discrepancy could be found: in 1996–1999 the southern component was less intense than the northern; the opposite is observed in 2000.

The main factor which triggers the inter-annual variability of the Rim current seems to be the atmospheric forcing (as suggested by Stanev et al. 2000). In order to check this we have used the ERA5 hourly reanalysis data for the surface wind (product ref. 2.7.3). The wind curl is calculated for every hour in the period 1993–2019 and then it is averaged for the Black Sea surface area and each individual year. The result is shown with grey curve in Figure 2.7.3. It is clear that the wind relative vorticity is predominantly positive (cyclonic) during the period. The variation of BSRCI and the wind curl are in phase (grey vs. green line in Figure 2.7.3) and in a good linear correlation (the Pearson correlation coefficient is 0.67). Furthermore, the linear trend of the two curves is similarly positive. This proves that the Black Sea Rim Current could be regarded as Sverdrup balanced flow and thus linked tightly to the regional atmosphere circulation.

2.7.4. Conclusions

The Copernicus Marine Service Black Sea Physics Reanalysis is used to study the interannual variation of the most prominent dynamic feature in the Black Sea circulation, the cyclonic Rim current, in the period 1993–2019. The speed and the position of the Rim Current varies from year to year giving an overall measure of the intensity of the circumpolar motion. The annual mean surface current velocity map shows that the area with most intense current is approximately confined between the isobaths 200–1800 m. The intensity of the western and eastern branch is different for each individual year in the period 1993–2019 as well as the presence of the quasi-permanent Batumi and Sevastopol eddies.

Two geographic areas, confined between the isobaths 200 and 1800 m, are chosen as representative for the Rim current estimates: northern section– from the Caucasus coast to the Crimea Peninsula (33E–39E); and southern section – from Sakarya region to the Sinop Peninsula (31.5E–35E). In these areas, the Rim current provides an overall representation of the geostrophic circulation. Defining these areas of interest as such avoids the influence of the unstable western coastal flow, as well the quasi-permanent Batumi and Sevastopol eddies.

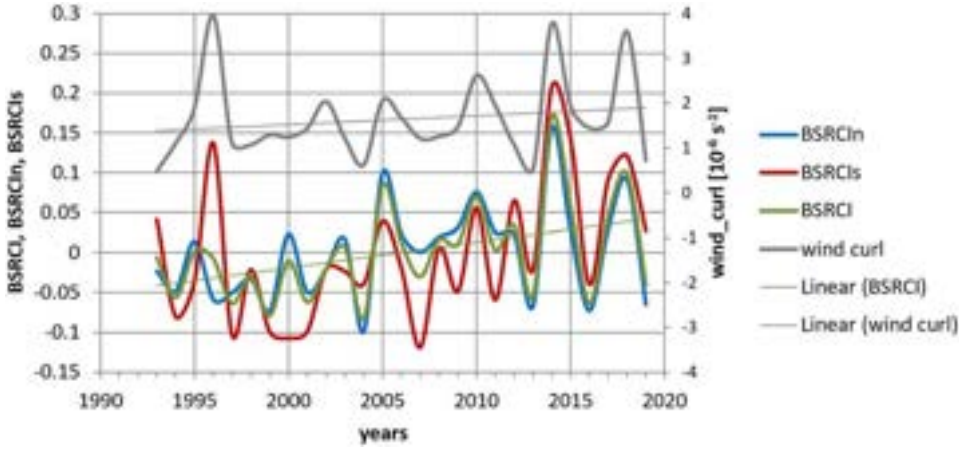

Figure 2.7.3. BSRCI (green), $BSRCI_n$ (blue) and $BSRCI_s$ (red) for the period 1993–2019, calculated from Equation (1) for the regions in Figure 2.7.1c. The grey curve represents the annual mean wind curl averaged for the Black Sea area based on the hourly ERA5 reanalysis.

The annual mean current speed averaged in those areas is used to calculate the Black Sea Rim Current Index as the relative annual anomaly of the long-term mean speed. The BSRCI value characterises the annual circulation state: a value close to zero would mean close to the average conditions, positive value indicates enhanced circulation, and negative value – weaker circulation than usual. The time-series of the BSRCI suggest that the Black Sea Rim current speed varies within ∼30% in the period 1993–2019 with a positive trend of ∼0.1 m/s/decade. In the years 2005 and 2014 there is evidently higher mean velocity, and on the opposite end are the years –2004, 2013 and 2016.

The constructed BSRCI is compared with the annual mean wind vorticity above the Black Sea, the surface wind data are taken from the ERA5 reanalysis. The wind curl is predominantly positive throughout the period with similar positive tendency as the BSRCI. It is found that the Rim current is in phase with the wind curl with Pearson coefficient of 0.67, proving that the Sverdrup balance is generally valid for the Rim current.

The calculated Black Sea Rim Current index reflects the annual state of the Black Sea circulation compared to the long-term mean. It could be used to characterise the baroclinicity of the Black Sea, the exchange between the open sea and coastal areas, the heat redistribution in the basin, the fish species distribution, etc. The relation between the Rim current and the atmospheric circulation gives a possibility to use the BSRCI when studying the climate feedback mechanisms in the region.

Table 2.7.1. The calculated values of the annual BSRCI for the period 1993–2019.

Year	BSRCI
1993	−0.01
1994	−0.06
1995	0.0
1996	−0.01
1997	−0.06
1998	−0.03
1999	−0.08
2000	−0.01
2001	−0.06
2002	−0.02
2003	0.01
2004	−0.08
2005	0.084
2006	0.01
2007	−0.03
2008	0.02
2009	0.01
2010	0.07
2011	0.00
2012	0.03
2013	−0.06
2014	0.17
2015	0.06
2016	−0.06
2017	0.04
2018	0.10
2019	−0.04

Section 2.8. Climatology and 2019 anomaly of maximum waves in the Mediterranean and Black Seas

Authors: Alvise Benetazzo, Francesco Barbariol, Joanna Staneva, Silvio Davison, Antonio Ricchi, Arno Behrens, Gerhard Gayer, Paolo Pezzutto

Statement of main outcome: There is general consensus that high-quality predictions of extreme events during marine storms can substantially contribute to avoiding or minimising human and material damage, especially in busy waterways such as the Mediterranean and Black Seas. Reliable wave forecasts and hindcasts, together with long-term statistical analysis of extreme conditions, are then of utmost importance for monitoring marine areas. So far, however, the wave climate characterisation (average and anomaly relative to the average) has focused on the bulk characterisation of the significant wave height H_s, and it has lacked a description of the individual waves, such as the maximum ones that may occur at a given location in the sea. To fill this gap, in this section, we provide the intensity and geographical distribution of the maximum waves in the Mediterranean and Black Seas over 27 years (1993–2019), by representing the average annual (1993–2018) and anomaly for 2019 relative to the average of the 99th percentile of the expected maximum wave height H_m and crest height C_m. The analysis combines wave model hindcasts available through CMEMS model setup and the wave model WAVEWATCH III®, both forced with ECMWF ERA5 reanalysis winds. Results show that in 2019 maximum waves were smaller than usual in the Black Sea (anomalies of H_m up to −1.5 m), while in the Mediterranean Sea a markedly positive anomaly (+2.5 m for H_m) was found in the southern part of the basin. The peculiar 2019 configuration seems to be caused by a widespread atmospheric stability over the Black Sea and by depressions that rapidly passed over the Mediterranean Sea.

Product used:

Ref. No.	Product name and type	Documentation
2.8.1	BLKSEA_REANALYSIS_WAV_007_006 Model reanalysis	PUM: https://marine.copernicus.eu/documents/PUM/CMEMS-BS-PUM-007-006.pdf QUID: https://marine.

(*Continued*)

Continued.

Ref. No.	Product name and type	Documentation
		copernicus.eu/documents/QUID/CMEMS-BS-QUID-007-006.pdf
2.8.2	BLKSEA_ANALYSIS_FORECAST_WAV_007_00 Model analysis	PUM: https://marine.copernicus.eu/documents/PUM/CMEMS-BS-PUM-007-003.pdf QUID: https://marine.copernicus.eu/documents/QUID/CMEMS-BS-QUID-007-003.pdf
2.8.3	ERA5 10 m (U, V) wind components. Years 1993–2019 Model reanalysis	https://www.ecmwf.int/en/forecasts/datasets/reanalysis-datasets/era5
2.8.4	WW3 wave spectrum parameters. Years 1993–2019 Model hindcast	https://polar.ncep.noaa.gov/waves/wavewatch/
2.8.5	NCEP/NCAR CDAS sea level pressure and geopotential height (500 hPa) Model reanalysis	The NCEP/NCAR 40-Year Reanalysis Project (Kalnay et al. 1996)

2.8.1. Context and methodology

Spectral models have made significant improvements over the last decades in predicting bulk wave parameters, such as the significant wave height, wave periods and directions, and they continue to provide an essential part of marine weather analysis (Cavaleri et al. 2020; Fanjul et al. 2019). As a result, significant wave height in the global seas (ECMWF 2017a) and in the Mediterranean and Black Seas (see e.g. Sartini et al. 2017; Arkhipkin et al. 2014) has been assessed thoroughly. On the contrary, little is known about the skill of models with focus on parameters of extreme individual waves, such as the maximum crest and wave heights (Ochi 1998). However, recent developments and applications of state-of-the-art spectral models used higher-order moments of the directional wave spectrum in statistical theories of linear and nonlinear extremes to infer the shape and likelihood of the largest waves during marine storms (Barbariol et al. 2017; ECMWF 2017b) and over long-term sequence of events up to the climatic scales (Barbariol et al. 2019). In this context, during the CMEMS Service Evolution project LATEMAR (*LArgesT wavEs in MARine environment: new products for wave model forecast*) the Monitoring and Forecasting Centres (MFC) wave models (WAVEWATCH III®, hereinafter WW3, and WAM) have been endowed with common routines designed to evaluate the maximum wave statistics for a given sea state.

In this context, we focus on the Mediterranean and Black Seas, which have complex wind and wave patterns. Indeed, the Mediterranean Sea is heavily influenced by the high pressure of the Azores, by the Atlantic low pressure that moves over it, and by their interaction with the local orography (Trigo et al. 2002). The most intense and long-lasting atmospheric events occur between November and March, bringing dominant northwesterly winds blowing over most of the western Mediterranean Sea. The central-eastern Mediterranean sub-basin (Adriatic, Ionian, Aegean seas) is also influenced by the displacement of cyclones moving east or southeast (Campins et al. 2011). These can trigger an outbreak of continental cold air, especially in the period between December and February (Vagenas et al. 2017), when the concomitance between Mediterranean cyclogenesis and the presence of continental high pressure on Eastern Europe is more likely. This dipole configuration pushes masses of very cold and dry air onto the "mild" Mediterranean Sea, increasing the cyclone intensity which will tend to move over the Aegean, thus pushing into further cold air from the north. The structure of the Russian high-pressure system and the position of the northern European low-pressure system regulate instead the dynamics of the Black Sea (Arkhipkin et al. 2014). As highlighted in Arkhipkin et al. (2014) and Sizov and Chekhlan (2010), prolonged conditions of negative North Atlantic Oscillation (i.e. NAO < −1) may lead to positive anomalies in frequency, duration and intensity of storms over the Black Sea (during winter). Vice versa, strongly positive NAO conditions (NAO > +1), between February and March, may correspond to negative anomalies of stormy events.

In this section, we use model results to estimate the statistics of the space–time extreme waves, which represent the maximum waves that may occur at the focusing condition of large 3D wave trains (Benetazzo et al. 2017, 2015; Boccotti 2000; Fedele 2012; Magnusson et al. 1999). The space–time extreme value analysis provides the short-term/range probability functions of maximum waves crossing a finite, 2D sea surface region with orthogonal sides X and Y over a temporal duration D. From the theoretical distributions, for the characterisation of extremes, the expected values $\langle H_m \rangle$ and $\langle C_m \rangle$ are computed for each model spectrum ($\langle\cdot\rangle$ is the expectation operator). The choice of the three values of X, Y, and D influences the estimations, and it is constrained by the inherent requirements of statistical homogeneity and stationarity of the sea state. Typical, reliable values for the 3D space–time region are $X = 100$ m, $Y = 100$ m, and $D = 1200$ s (see Benetazzo et al. 2020) which represent the characteristic horizontal footprint of an offshore platform ($XY = 100 \times 100$ m^2) and the typical wave buoy record length (20 min). In the following, we shall concentrate on the more severe conditions for the

maximum wave heights, by representing the average annual extreme climate with reference to years from 1993 to 2018, and the anomaly for 2019 that resulted to be a peculiar year for winds and waves in the Mediterranean and Black Seas.

Since the design of coastal and offshore structures requires a reliable estimation of maximum wave height (DNV GL 2017), the expected impact of our study is directed towards the improvement of the definition of the environmental loads over the lifetime of a ship or structure (e.g. wind energy turbines or oil and gas platforms). Indeed, a reduction of the uncertainties of the metocean conditions will have a direct impact on structure and mooring loads, both for ultimate limit state and fatigue design, and warning criteria for ships. These results can be obtained through hindcast and forecast studies that include maximum wave parameters, which are aimed also at expanding the wave CMEMS products catalogue by providing novel wave diagnostics.

2.8.2. Wave maxima pattern and variability in the Mediterranean Sea

Pattern and variability of wave maxima in the Mediterranean Sea have been investigated with a hindcast analysis by running the wave model WW3 (version 6.07; https://polar.ncep.noaa.gov/waves/) for the 27-year long period from 1993 to 2019 over a regular grid with horizontal resolution of 0.05° (~5 km). To represent wave growth and decay, we used the ST4 source-term parameterisation of Ardhuin et al. (2010), relying on the default values (Tolman and the WAVEWATCH III Development Group 2014), but with adjusted coefficients $\beta_{max} = 1.55$ and $z_{0,max} = 0.002$ that are supposed to perform well for younger seas, accordingly to the results of TEST405 of the Ardhuin et al.'s study. Propagation was computed using a third-order accurate scheme, together with the discrete interactions approximations for nonlinear wave-wave interactions, and subgrid-scale obstructions (e.g. small islands) were included. In shallow water, bottom friction was modelled using the JONSWAP parameterisation with default values (Hasselmann et al. 1973), as well as the depth-induced wave breaking was parametrised following Battjes and Janssen (1978). The ETOPO1 relief model was used to define the bottom topography and coastlines.

WW3 was forced by horizontal wind fields at 10-m height ($\boldsymbol{U}_{10}$) provided at 0.25° and 1-hour resolution by the ERA5 reanalysis (https://www.ecmwf.int/en/forecasts/datasets/reanalysis-datasets/era5) produced by the European Centre for Medium-Range Weather Forecasts (ECMWF). Although ERA5 may lack the resolution to adequately account for the effect of the surrounding orography on developing fetch-limited winds in semi-enclosed seas (Cavaleri et al. 2018; Cavaleri and Bertotti 2004), the worthiness of ERA5 at Mediterranean basin scale is assured nonetheless via direct comparison of model wind speeds and significant wave heights with satellite altimeter measurements derived from the Integrated Marine Observing System database (IMOS, https://catalogue-imos.aodn.org.au; Ribal and Young 2019), which is expected to provide robust results within the range of wind speeds and wave heights one can encounter in the Mediterranean and Black Sea (Young et al. 2017). Error metrics for ERA5 speeds U_{10} compared to IMOS altimeter (ENVISAT) data (05/2002–12/2010; 464294 entries) show an overall bias of −0.26 m/s, a mean absolute error of 1.08 m/s, and a best-fit linear slope of 0.94. At the 99th percentile, the U_{10} model minus observation residual is −1.5 m/s. An analogous comparison using the Ribal and Young's data of H_s over the entire Mediterranean Basin between model results and ENVISAT altimeter measurements (05/2002–12/2010; 497333 entries) yields an overall model minus observation bias of −0.12 m, a mean absolute error of 0.26 m and a best-fit linear slope of 0.87. At the 99th percentile, the H_s residual is −0.5 m, which we assume it may be the order of uncertainty (i.e. underestimation) in the displayed maximum wave statistics due to the wave model setup and forcing.

Figure 2.8.1 shows that individual maximum waves (years 1993–2018) are triggered in offshore regions, where high winds and long fetch are simultaneously present (Cavaleri and Sclavo 2006; Sartini et al. 2017; Soukissian et al. 2018; von Schuckmann et al. 2019). Such conditions are met in the northwestern Mediterranean basin, south of the Gulf of Lion, through the Balearic Sea to western Sardinia. They result from northerly winds dominant in the western Mediterranean Sea (Mistral or Tramontana) that are funnelled and accelerated by local orography and act over a large area (Menendez et al. 2014). This region is where many ship accidents happened in the Mediterranean Sea, due to the hit with very high, single waves, for instance the *Grand Voyager* cruise ship accident in 2005, the *Louis Majesty* cruise accident in 2010 (Cavaleri et al. 2012) or the *Jean Nicoli* ferry accident in 2017.

South of the Gulf of Lion, extreme expected values (1993–2018 average of annual 99th percentile) derived from the probability distribution of H_m and C_m are at most 11 and 7 m, respectively, and do not exceed 6 and 4 m in the more enclosed sub-basins (Figure 2.8.1). A large area with mid-to-high maximum waves ($<H_m>$ and $<C_m>$ up to 9 and 5.5 m, respectively) is located in the southern Mediterranean, between Italy and Libya. We do observe large regional

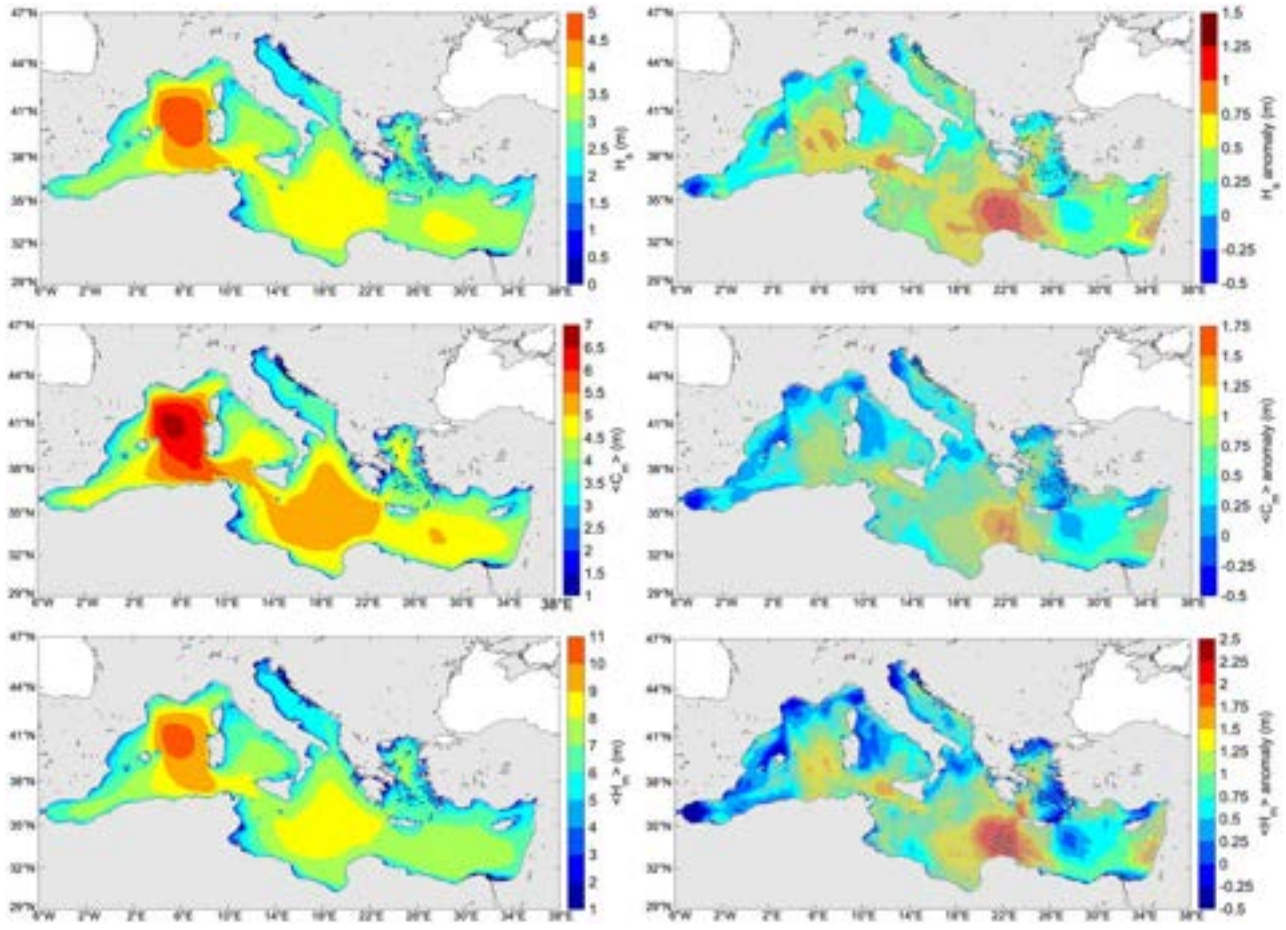

Figure 2.8.1. Mediterranean Sea significant (H_s) and maximum ($<H_m>$ and $<C_m>$) wave height climate (reference period 1993–2018) and anomaly for 2019. Intensity and spatial variability of the 1993–2018 average annual 99th percentile (left) and 2019 anomaly of the 99th percentile (right) of H_s (top), maximum crest height $<C_m>$ (middle) and maximum wave height $<H_m>$ (bottom). Grey crosses (circles) in right panels depict locations where the 2019 anomaly of the 99th percentile heights exceeds the inter-annual (1993–2018) 90th percentile. Product ref. 2.8.4 (This dataset generated and analysed during the current study is available from the corresponding author on reasonable request).

differences with maximum values that reflect meteorological features. The anomaly for 2019 shows a weak meridional difference: the southern basin experienced higher extreme waves than usual (positive anomaly) relative to long-term average stormy conditions (at most +2.5 m and +1.75 m for maximum wave and crest height, respectively), while small positive anomalies are visible in the northern sub-basins. Figure 2.8.1 also provides evidence (grey crosses) that large portions of the Mediterranean Sea experienced unusual conditions during the year 2019, since the 99th percentile heights exceeded the inter-annual (1993–2018) 90th percentile.

2.8.3. Wave maxima pattern and variability in the Black Sea

In the Black Sea, a 28-year wave reanalysis (1992–2019) was produced using the wave model WAM cycle 6.0 (Product ref. 2.8.1 and 2.8.2.). The solution of the energy balance equation is provided with 3-km resolution, and for 24 uniformly spaced directions and 30 frequencies f logarithmically spaced from 0.042 to 0.66 Hz at intervals of $\Delta f / f = 0.1$. The wave model accounts for depth refraction and depth-induced wave breaking and it is driven by the hourly ERA5 U_{10} wind fields. The setup includes a continuous data assimilation into the wave model fields using satellite data (wind speed and significant wave height) recorded by the JASON radar altimeters.

In the Black Sea, the strongest dominant winds are the northeasterly Bora and the southwesterly Lodos, prevalent during winter months, which cause correspondingly high waves (Arkhipkin et al. 2014). Indeed, the average annual 99th percentile significant wave height distribution for the 1993–2018 period shows (Figure 2.8.2) that the highest waves (H_s values as high as 4 m) are located in the southwestern most part

of the Black Sea, in line with previous studies covering years 2000–2016 (Fanjul et al. 2019). Similarly to the pattern of H_s, the average space–time extreme wave heights in the Black Sea are largest in the southwestern part of the Basin (near the Bosporus), with values of $<H_m>$ ($<C_m>$) up to 8 m (5 m), whereas in the more eastern part maximum wave heights are lower and below 5 m (3.5 m).

During the year 2019, anomalies of the annual 99th percentile significant wave height are negative over the whole Black Sea (up to −0.8 m in the central region), possibly indicating a weaker atmospheric activity compared to the reference period. This condition is different from the strong longitudinal dependency present in 2017 (Fanjul et al. 2019), when negative extreme significant wave height anomalies were present in the western part and positive anomalies in the central-eastern sector. The same widespread negative anomaly for 2019 is found also when looking at the extreme wave heights (Figure 2.8.2, middle and bottom panels), with values of $<H_m>$ ($<C_m>$) reaching about −1.5 m (−1.2 m) in the central Black Sea, and progressively lower towards the coasts.

2.8.4. Atmospheric interpretation of the anomaly for 2019

The peculiarity (i.e. with opposite sign) of the anomaly for 2019 of extreme waves in the Mediterranean and Black Sea is discussed using as reference the corresponding anomalies of the mean sea level pressure and geopotential height. In addition, the NAO index is here used as an indicator of the European atmospheric dynamics on a synoptic scale. Indeed, from a meteorological point of view, the Azores high pressure (also known as 'Azores High'), the high Russian-Siberian pressure system, and the baroclinic waves which move eastward from the Atlantic Ocean influence the atmospheric dynamics of the Mediterranean and Black Sea basin (Trigo et al. 2002). The relevance of these

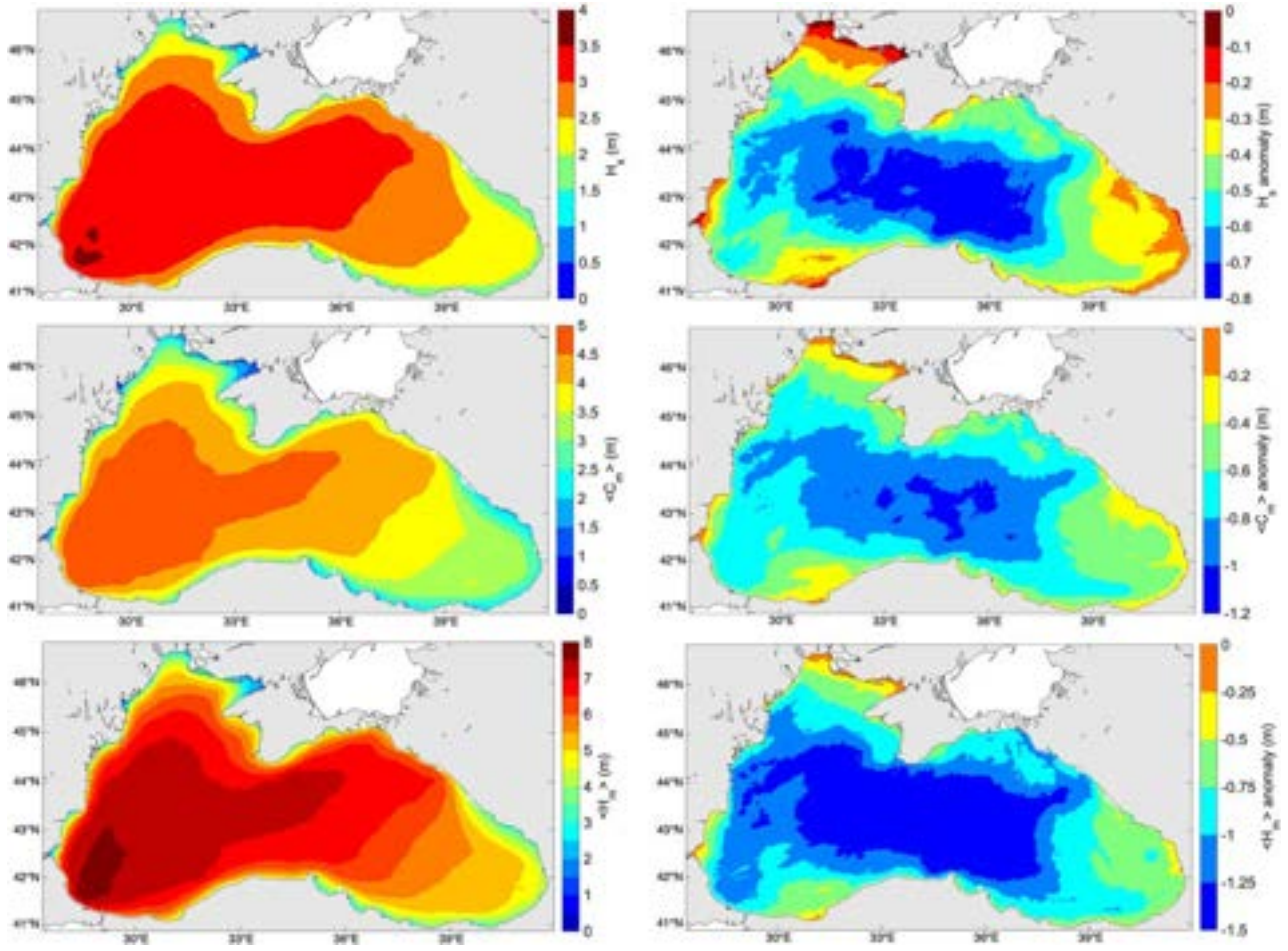

Figure 2.8.2. Black Sea significant (H_s) and maximum ($<H_m>$ and $<C_m>$) wave height climate (reference period 1993–2018) and anomaly for 2019. Intensity and spatial variability of the 1993–2018 average annual 99th percentile (left) and 2019 anomaly of the 99th percentile (right) of H_s (top), maximum crest height $<C_m>$ (middle) and maximum wave height $<H_m>$ (bottom). Product ref. 2.8.1 and 2.8.2.

atmospheric factors varies according to the seasons and to the sub-basin of interest.

As it is shown in Figure 2.8.3, on the western Mediterranean, in the January–February–March (J–F–M) quarter there was a positive sea level pressure anomaly (about 10 hPa) and a positive geopotential anomaly at 500 hPa (higher than 60 dam). This configuration suggests a relatively stable winter and spring period, with the Azores high pressure imposing northern trajectories on Atlantic low pressure (in accordance with the positive NAO; bottom panel of Figure 2.8.3). On the Aegean Sea, we observe a negative pressure anomaly of about −6 hPa and an intense geopotential anomaly at 500 hPa of about −70 dam. This configuration is frequent in periods when the Azores High of the permanently envelops the western Mediterranean. This configuration conveys cold air from northern Europe to the Ionian Sea and the Aegean Sea, activating cyclogenesis and advections of continental cold air with northerly winds. In the same period, the pressure anomaly over the Black Sea is positive but relatively limited, with a strong anomaly over Russia, which suggests the absence of the Russian-Siberian anticyclone. Accordingly, the anomaly of the geopotential is zero. This configuration causes long, stable, or little perturbed, periods over this basin.

The April–May–June (A–M–J) period shows a marked negative anomaly of sea level pressure and geopotential on the Tyrrhenian Sea and a strong positive anomaly on Eastern Europe and Russia. This configuration is typical to cause strong atmospheric variability on the Western Mediterranean, with cyclogenesis moving towards northeast, hence not significantly affecting the Aegean Sea or the Black Sea. The 2019 summer period in the Mediterranean area (typically spanning July–August–September, J–A–S) was characterised by

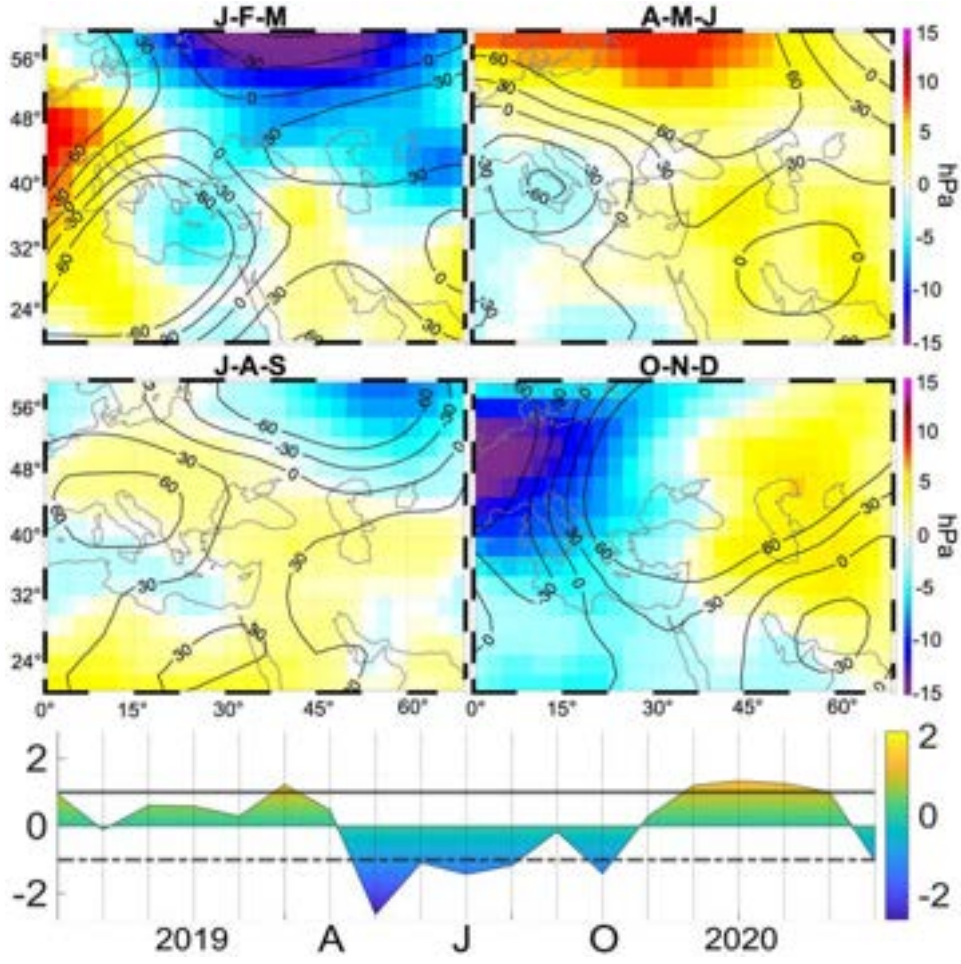

Figure 2.8.3. Anomaly for 2019 of the sea-level pressure (shaded area, in hPa) and of the geopotential height at the reference altitude of 500 hPa (black contour, in dam), for the quarters J-F-M (top-left), A-M-J (top-right), J-A-S (middle-left) and O-N-D (middle-right). The season separation is chosen to fit the seasonal dynamics of the cyclogenesis in the Mediterranean Sea (Trigo et al. 2002). On the bottom panel, the evolution of the NAO index (Visbeck et al. 2001) in the period 2018/10-2020/04 is depicted; the three months of April (A), July (J), and October (O) 2019 are indicated. The solid and dotted grey lines show the NAO values of +1 and −1, respectively. Data from NCEP/NCAR CDAS 40-year Reanalysis. Product ref. 2.8.5.

strongly negative NAO, positive anomalies of sea level pressure and geopotential at 500 hPa on the whole Mediterranean Sea, suggesting a very mild and stable summer. From October to December (October–November–December, O–N–D), there was a very intense dipole between the western Mediterranean and Russia. With the former affected by a negative pressure anomaly of about −18 hPa and −40 dam of geopotential, while the continental sector was affected by positive anomalies of pressure of about 5 hPa and geopotential anomalies larger than 70 dam.

This atmosphere configuration for 2019 and the timing of the positive NAO index in the winter months suggest atmospheric stability on the Black Sea and depressions rapidly passing over the Mediterranean Sea from the Gulf of Lion to the Aegean Sea. This overall dynamics, combined with the feature of the first quarter, may explain the positive anomaly of wave heights observed on the Aegean basin, and the strong spatial variability that is observed in the western Mediterranean. Further studies will need to be carried out, however, in particular to estimate the extreme values and direction of the minimum pressures, and to characterise the pattern of the specific storms that led to the generation of extreme waves.

2.8.5. Conclusions

In the last decade worldwide seas were hit by severe storms (see e.g. ECMWF 2019), which caused serious damage in offshore and coastal zones and focused public attention on the importance of having reliable and comprehensive wave forecasts, especially during extreme events. Additionally, human activities such as offshore wind power industry, oil industry and coastal recreation also regularly necessitate operational information on the maximum wave height with high resolution in space and time. There is thus a broad consensus that high-quality predictions and a deep understanding of extreme waves caused by storms could substantially contribute to the improvement of the marine warning system, thereby avoiding or minimising human and material damage and losses.

This result can be achieved by including the description/statistics of the maximum wave parameters in both operational forecast and hindcast studies. In this context, we have assessed the 1993–2018 climatology (99th percentile) of the maximum wave heights in the Mediterranean and Black Seas and characterised the anomaly for 2019 in the light of the previous quarter of a century. We found that the most extreme conditions occur in the northwestern Mediterranean basin, south of the Gulf of Lion through the Balearic Sea to western Sardinia, and in the southwestern part of the Black Sea. In 2019, most of the Mediterranean Sea experienced more severe conditions than usual, while the Black Sea was characterised by calmer conditions, as a consequence of the atmospheric configuration over the central and eastern Europe, which caused an atmospheric stability over the Black Sea and frequent storms over the Mediterranean region. We stress that future regular monitoring of maximum wave heights is expected to improve our understanding of the conditions that are more favourable to the generation of very large waves in the world oceans.

Acknowledgements

The work was supported by the Copernicus Marine Environment Monitoring Service (CMEMS) LATEMAR project. CMEMS is implemented by Mercator Ocean in the framework of a delegation agreement with the European Union. This work has also been conducted as part of the bilateral project EOLO-1 ("Extreme Oceanic waves during tropical, tropical-like, and bomb cyclones") between CNR-ISMAR and the University of Tokyo (Japan; Prof. Takuji Waseda). Antonio Ricchi funding have been provided via the PON "AIM" - Attraction and international mobility program AIM1858058. Joanna Staneva acknowledges H2020 IMMERSE Project, Arno Behrens was supported by CMEMS Waveflow project and G. Gayer by ESA Black Sea and Danube Regional Initiative (EO4BS).

Section 2.9. Strong positive Indian Ocean Dipole events over the period 1993–2019

Authors: Simon Good, Jean-François Legeais, Richard Graham

Statement of main outcome: The Indian Ocean Dipole (IOD) is a mode of variability traditionally characterised by sea surface temperature (SST) anomalies on the eastern and western sides of the Indian Ocean. The IOD is associated with extremes of weather on either side of the Indian Ocean basin. In this study, an index of IOD phase – the Dipole Mode Index (DMI) – has been calculated for the period 1993 to March 2020. DMI is defined using SST anomalies, but in this study a similar indicator has also been evaluated using Sea Level Anomaly (SLA) data. These DMI time series show that there have been three particularly strong DMI events during the studied period, in 1994 (according to the SST DMI only), 1997 and 2019. In each case, the IOD was in its positive phase and there were positive western anomalies and negative eastern anomalies with low precipitation occurring over the eastern Indian Ocean. Widespread increased precipitation over the western Indian Ocean also occurred in 1997 and 2019, when

the SLA-based DMI was very high. Analysis of the DMI time series confirms that SLA-based DMI correlates better with precipitation in the west than the SST-based DMI, with the opposite true for the east. Therefore, use of the SST- and SLA-based DMI together provides a more informative way to characterise the IOD state than the SST DMI alone.

Products used:

Ref. No.	Product name & type	Documentation
2.9.1	SST-GLO-SST-L4-REP-OBSERVATIONS-010-011 – satellite and in situ sea surface temperature observational product	PUM: https://marine.copernicus.eu/documents/PUM/CMEMS-SST-PUM-010-011.pdf QUID: https://marine.copernicus.eu/documents/QUID/CMEMS-SST-QUID-010-011.pdf
2.9.2	SST-GLO-SST-L4-NRT-OBSERVATIONS-010-001 – satellite and in situ sea surface temperature observational product	PUM: https://marine.copernicus.eu/documents/PUM/CMEMS-SST-PUM-010-001.pdf QUID: https://marine.copernicus.eu/documents/QUID/CMEMS-SST-QUID-010-001.pdf
2.9.3	SEALEVEL_GLO_PHY_L4_REP_OBSERVATIONS_008_047 – satellite sea level anomalies observational product	PUM: https://marine.copernicus.eu/documents/PUM/CMEMS-SL-PUM-008-032-051.pdf QUID: https://marine.copernicus.eu/documents/QUID/CMEMS-SL-QUID-008-032-051.pdf
2.9.4	SEALEVEL_GLO_PHY_L4_NRT_OBSERVATIONS_008_046 – satellite sea level anomalies observational product	PUM: https://marine.copernicus.eu/documents/PUM/CMEMS-SL-PUM-008-032-051.pdf QUID: https://marine.copernicus.eu/documents/QUID/CMEMS-SL-QUID-008-032-051.pdf
2.9.5	GPCP monthly precipitation dataset	GPCP Precipitation data provided by the NOAA/OAR/ESRL PSL, Boulder, Colorado, USA, from their Web site at https://psl.noaa.gov/ Adler et al. (2003)

2.9.1. Introduction

The Indian Ocean Dipole (IOD) is an air–sea coupled mode of variability in the Indian Ocean characterised by sustained fluctuations in sea surface temperature (SST) which tend to be of opposite sense in the eastern and western sides of the basin (Saji et al. 1999). There is uncertainty about the dynamics of IOD events (Lu et al. 2018). Yang et al. (2015) attributed one-third of the total IOD variance to forcing by El Niño-Southern Oscillation (ENSO) and the remainder to internal variability that occurs in the absence of ENSO forcing. By convention, positive (negative) IOD phases are associated with positive (negative) SST anomalies in the western basin and negative (positive) anomalies in the eastern basin. Saji et al. (1999) used these regional differences to define an indicator of IOD phase: The Dipole Mode Index (DMI). Sea level anomalies (SLAs) in the Indian Ocean also correlate with both IOD and ENSO indices, with positive correlations in the west and negative in the east (Duan et al. 2020).

Circulation changes related to an active IOD modify the atmospheric circulation of the Walker cell over the Indian Ocean. Positive IOD is associated with easterly trade wind anomalies at low-levels which act to maintain or enhance the SST anomalies (e.g. through upwelling at the eastern boundary) – a feedback that sustains the pre-existing IOD phase. Rainfall anomalies associated with positive IOD include decreased convection and below normal rainfall over the Maritime Continent as well as parts of Australia (Ashok et al. 2003); while over eastern Africa, increased rainfall is found during the 'Short-Rains' season (September-December) that includes the time of the IOD peak. In general, a negative IOD is associated with opposite signed anomalies in wind and rainfall. The IOD is also associated with air temperature anomalies: for example, a positive IOD is linked to warm air temperature anomalies in parts of Australia. Positive IOD events have also been connected to the occurrence of bushfires in southeast Australia (Cai et al. 2009). In addition to the above-mentioned impacted regions, Ashok et al. (2001) have argued for an impact on Indian summer monsoon rainfall through modulation of the rainfall teleconnection to the ENSO.

Positive IOD occurrences can be separated into moderate and extreme events. The latter is associated with cool SST anomalies which spread further westward than in the former case and enhanced precipitation occurs in the west (Cai et al. 2014, which includes a detailed description of the dynamics of these occurrences). Extreme positive IOD events are projected to become more frequent through climate change (Cai et al. 2014, 2018). An extreme positive IOD event occurred in 2019 and recent studies have examined its causes. Du et al. (2020) found that the event was triggered by warm water in the south-west tropical Indian Ocean originating from the weak El Niño event of 2018 and propagated by Rossby waves. Wang et al. (2000) performed a heat budget analysis and found that the 2019 extreme event was uniquely characterised by negative air–sea heat fluxes which reinforced the cool

SST anomalies. Lu and Ren (2020) link the event to a high interhemispheric atmospheric pressure gradient causing northward flow and resulting in wind-evaporation-SST and thermocline feedback.

Although the DMI is commonly used to define the IOD state, it has been shown to not fully characterise extreme events (Cai et al. 2014; Yang et al. 2020). In this paper, the signature of the IOD since 1993 is examined in satellite data records of SST and SLA to determine the extent to which the latter dataset provides additional information on the IOD state compared to SST alone. In particular, the DMI indicator of the IOD state, which, as far as the authors are aware, was only previously calculated from SST anomalies, is also evaluated here using SLA data. Although the regions used in the calculation of DMI were defined for SST, Duan et al. (2020) show a west–east contrast in the correlations between SST DMI and SLA that suggests they may be also valid for SLA. Deepa et al. (2018) analysed SLA in the Indian Ocean using empirical orthogonal function (EOF) analysis. Their first EOF also contains a contrast between west and east, albeit with an indication that the southern edge of the box used to calculate DMI may be too far north. The SST and SLA data and corresponding DMI time series are compared to a precipitation dataset. A particular focus is placed on strong positive IOD events that have occurred since 1993. The human and economic impacts of the 2019 event are also discussed.

2.9.2. Methods

Calculation of DMI was performed using averaged SST anomalies and SLA over the two regions defined by Saji et al. (1999) – specifically, regions in the western tropical Indian Ocean (50°E – 70°E; 10°S – 10°N) and south east tropical Indian Ocean (90°E – 110°E; 10°S – 0°S). The indices are defined as the anomalies in the Western region minus anomalies in the Eastern region.

The SST DMI has been calculated using daily, global, spatially complete SST data covering January 1993 to March 2020 generated by the Operational Sea Surface Temperature and Ice Analysis (OSTIA) system (Good et al. 2020). Prior to 2019, a reprocessed (REP) version of the OSTIA data is used (dataset 2.9.1). This is extended using a near real time (NRT) data stream (dataset 2.9.2). The principal difference between the REP and NRT products is the input data sources. The REP production utilises reprocessed versions of the data (in particular, climate datasets produced by the European Space Agency Climate Change Initiative (ESA CCI) and the Copernicus Climate Change Service (C3S) (Merchant et al. 2019)), while the NRT product uses data that are available rapidly to allow fast generation of the OSTIA products for applications such as numerical weather prediction. As the difference in data sources might cause a discontinuity between the REP and NRT products, NRT data from 2018 onwards were used in order to provide a year of overlap with the REP product to check consistency. See data use table for full details of the datasets used.

The daily REP and NRT data files were averaged to create monthly means. A monthly climatology for the period 1993–2014 was calculated by averaging the monthly means. Monthly anomalies were then generated by differencing the monthly means and the climatology. Area averages were calculated for each month for the Western and Eastern regions described above, and from these the DMI was generated.

The SST-based monthly area average in the Niño3.4 region – defined as 170°W to 120°W, 5°S to 5°N (Trenberth et al. 2020) – was also calculated.

The SLA DMI derived from altimeter sea level measurements has also been computed based on daily delayed-time reprocessed (REP, version DUACS DT-2018; dataset 2.9.3) and near real time maps of sea level anomalies produced by CMEMS (dataset 2.9.4; see data use table for full details of the datasets used). The sea level anomalies are referenced to the 20-year period covering 1993–2012. The time series of these daily maps has been detrended (from the global mean sea level trend) and the seasonal cycle has been estimated (from a sinusoid adjustment) and removed. Monthly means were then computed. The transition between delayed-time and near real time sea level data is in October 2019 and the relatively low bias observed at this particular time between both types of data makes possible the analysis of the SLA-based DMI time series. Area-averaged mean sea level was then computed for each month for the Western and Eastern Indian Ocean regions and, from these, the DMI was generated.

The Global Precipitation Climatology Project (GPCP) monthly precipitation dataset (Adler et al. 2003) was provided by the NOAA/OAR/ESRL PSL, Boulder, Colorado, USA, from their website at https://psl.noaa.gov (dataset 2.9.5). Precipitation anomalies were calculated by removing the monthly average over the period 1993–2014.

2.9.3. Results

Figure 2.9.1 shows the monthly time series of DMI and the area averages of the Western and Eastern Indian Ocean regions from which the DMI is calculated. The differences between the SST REP (black lines)

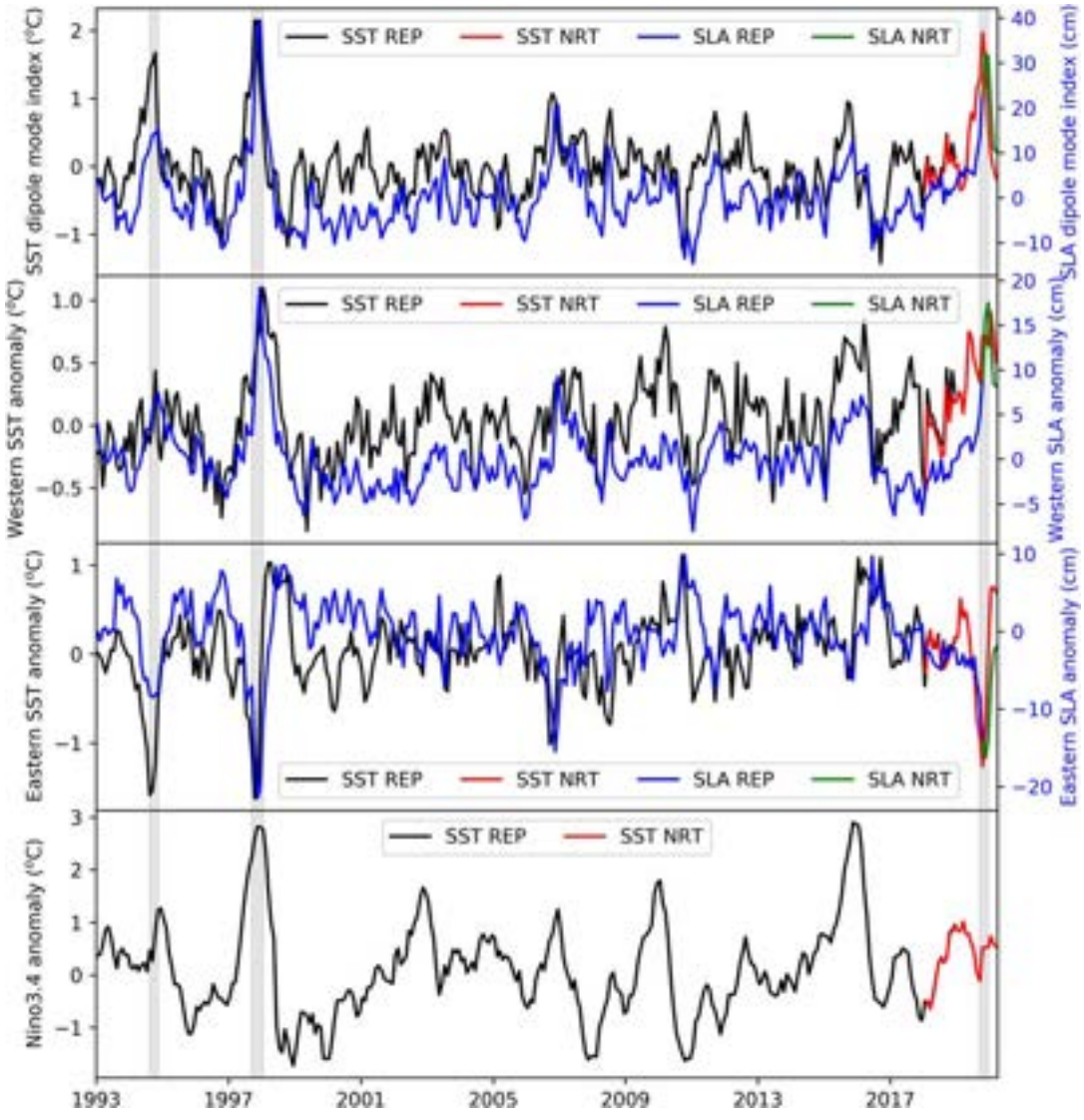

Figure 2.9.1. Time series of DMI based on SST and SLA, and the western and eastern regions of the Indian Ocean which are used in the calculation of DMI. The SST anomalies in the Niño3.4 region of the Pacific Ocean are also shown. The time series from the SST REP product are shown in black, SST NRT in red, SLA REP in blue and SLA NRT in green. Periods when the SST DMI is at least 1.2 are shown in grey.

and NRT (red) products are small compared to the signal in the time series. Therefore, it is reasonable to use the NRT data to extend the time series from the REP product. The time series based on SLA are shown in the same way using blue and green. The SST and SLA time series show clear similarities for the Western and Eastern regions as well as the DMI, for which their correlation coefficient is 0.65 (Table 2.9.1). Notably, the large-amplitude peaks and troughs in both DMI series occur simultaneously, although the lower-amplitude variability is often less well matched.

Two exceptionally large positive DMI events can be seen in the time series from both SST and SLA. These occurred in 1997 and 2019 and both peaked in October. In the SLA DMI time series, the 2019 event is weaker than 1997, but they have approximately the same magnitude in the SST time series. In the SST time series, a further strong event occurred in 1994, also peaking in October. The same feature is present but is relatively weak in the SLA time series. This 1994 event was associated with anomalously low temperature and – less prominently – SLA in the Eastern Tropical Indian Ocean region, while the 1997 event was associated with strong positive SST and SLA anomalies in the Western region simultaneous with strong negative anomalies in the Eastern region. In contrast, the 2019 event was characterised by rapid development of negative SST and SLA anomalies in the east coupled with already positive anomalies in the western region, resulting in a strong positive DMI.

Table 2.9.1. Correlation between time series of DMI from SST and SLA and SST anomalies in the Niño34 region.

Correlation coefficient	SLA DMI	Niño3.4
SST DMI	0.65	0.35
SLA DMI	–	0.57

The large positive DMI occurrences in 1994 and 1997 correspond to peaks in the eastern Pacific Ocean SST anomalies (Figure 2.9.1, Niño3.4 anomalies), which are characteristic of El Niño events. The 1994 and 1997 SST DMI events have similar magnitude but the anomaly in the Niño3.4 region is much stronger in 1997 than 1994, similar to the relative strength seen in the SLA DMI series. In contrast, at the time of the strong SST and SLA DMI event in 2019 the eastern Pacific Ocean SST anomalies were unremarkable. Correlation coefficients between the two DMI series and the Niño3.4 anomalies (Table 2.9.1) shows that the SLA DMI time series is more consistent with the Niño3.4 anomalies than the SST DMI. The time series also contains some indications of temporal offsets. If applying lags to the monthly Niño3.4 time series, the peak correlation coefficient between it and the SST DMI time series occurs if the Niño3.4 series lags by two months. This might be expected since the DMI peaks in October while ENSO events are known to peak in northern hemisphere winter (e.g. Tziperman et al. 1998). In contrast, the peak correlation between SLA DMI and Niño3.4 occurs with no lag, further demonstrating a stronger relationship between SLA DMI and ENSO than between SST DMI and ENSO. This relationship is to be expected since ENSO affects the Indian Ocean through Walker circulation changes, creating wind anomalies (Xie and Zhou 2017) that drive SLA changes (e.g. Deepa et al. 2018).

Figure 2.9.2, upper row, shows correlations between the two DMI time series and global SST anomalies estimated over the period January 1993 to March 2020. As might be expected, the SST DMI (left column) is highly correlated with the SST anomalies in the regions from which it is calculated. The SLA DMI (right column) is most highly correlated with SST anomaly in the western Indian Ocean and the tropical eastern Pacific, with only weak negative correlations with the eastern Indian Ocean. The lower row, left panel, in Figure 2.9.2 shows correlations between the SST DMI series and precipitation anomalies. The highest correlations are focussed in the regions that define the DMI. In contrast, the correlations between SLA DMI and precipitation (Figure 2.9.2, bottom right panel) have broader spread, and correlations over eastern Africa and the tropical Pacific Ocean are higher than those derived from SST DMI.

The SST, sea level and precipitation anomalies in October of the year of each of the strong IOD events are shown in Figure 2.9.3. In 1994, the SST DMI indicated a strong event, but the SLAs are weaker leading to lower SLA DMI values (upper panel of Figure 2.9.1). The precipitation anomalies are below average over the Maritime Continent but relatively neutral over eastern Africa. SLAs and – in particular – SST anomalies in the Indian Ocean during the 1997 and 2019 events have a similar distinctive pattern to each other. Negative anomalies around the maritime

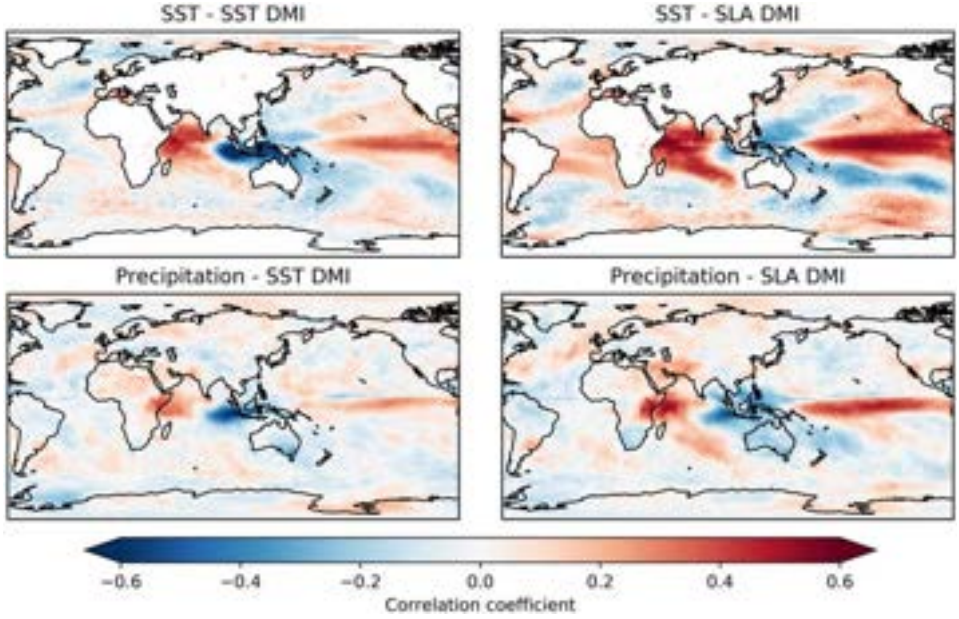

Figure 2.9.2. Correlation coefficient between the SST and SLA DMI time series and SST and precipitation anomalies.

continent are surrounded by positive anomalies to the north and a line of positive anomalies extending from the north-west to the south. Low precipitation occurred in the eastern Indian Ocean in both cases. However, the pattern of higher than normal precipitation in the western Indian Ocean differs between the years: in 1997 it is focused on eastern Africa, while in 2019 positive precipitation anomalies in the eastern basin are weaker than in 1997 over eastern Africa, and extend more widely over the Arabian Sea to coastal parts of India. Therefore, the three strong IOD events have different signatures in SST, sea level and precipitation anomalies, with a further indication based on 1994 that the SST anomalies are a better predictor of precipitation over the Maritime Continent than SLA, and the opposite for eastern Africa.

2.9.4. Discussion

As presented above, significant interaction and correlation can be found on a basin scale during strong IOD events between the ocean and the atmosphere. In particular, extreme weather conditions are observed during such events in the eastern African countries and countries

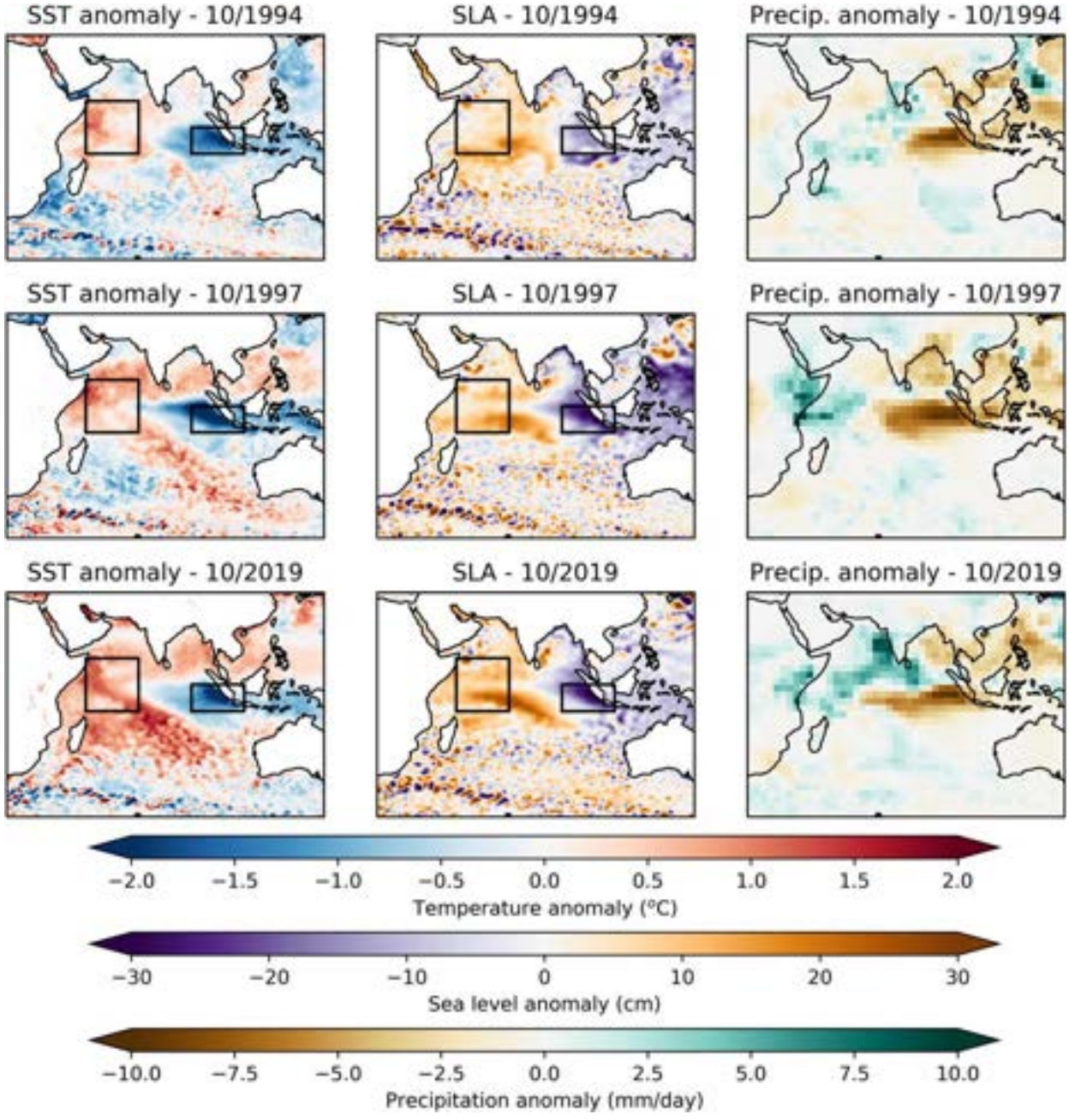

Figure 2.9.3. SST, sea level and precipitation anomalies at the peak of strong IOD events.

bounding the eastern Indian Ocean. For example, during the last quarter of 2019, warm and dry conditions have been experienced in Australia, contributing to some of the most significant wildfires ever seen in the country (CSIRO 2020). In contrast, 2019 saw heavy rainfall over Eastern Africa affecting almost 3.4 million people (OCHA 2020). In addition to the damage related to floods, locust outbreaks have occurred in Eastern Africa, the Middle East and South Asia, which can lead to famine and food insecurity for the local population and huge economic consequences (FAO 2020).

Extreme IOD events therefore have huge consequences and, for example as noted in CSIRO (2020), climate change can act to exacerbate this over time by increasing the length and intensity of the conditions needed for wildfires to occur. Given this, it is important to continue to improve monitoring of IOD events in order to better understand them and to enhance their prediction.

In this study, an SLA variant of the DMI has been introduced and empirically shown to provide complementary information on rainfall compared to the SST DMI. It is noted that rainfall anomalies associated with the IOD often linger beyond the time when the SST DMI index has returned to neutral. This was evident in the 2019 case with notable persistence of rainfall in East Africa into 2020, well after the usual end of the Short Rains season in December. Continuing dry anomalies were also noted in Indonesia and were referred to as a 'residual effect' of the 2019 IOD event in the March 2020 issue of the WMO El Niño/La Niña Update.[17] We speculate that anomalies in the Indian Ocean Walker circulation may persist after the SST DMI returns to neutral, and that the SLA DMI, through coupling with surface pressure, may be a more robust indicator of the Walker circulation anomalies, and thus – at least in some cases – better correlated with rainfall.

2.9.5. Conclusion

The IOD is a coupled ocean-atmosphere mode of variability in the Indian Ocean that impacts temperature and precipitation in the region. For example, in 2019 the IOD was associated with flooding in Eastern Africa and wild fires in Australia. It is therefore important to understand and monitor the IOD.

The IOD state has previously been quantified in SST using the DMI, which is the difference in temperature anomaly between the eastern and western tropical Indian Ocean. In this study, a similar indicator has, as far as the authors are aware, been produced for the first time using altimeter SLAs. These SST and SLA-based records both show that there have been two strong DMI events since 1993, which peaked in October 1997 and 2019. A further strong event occurs in the SST record in October 1994, but is weaker in the SLA DMI time series.

Two of the three strong positive DMI events occurred at the same time as warm anomalies in the Eastern Pacific Ocean, which characterise El Niño events. Analysis of the time series revealed that the SLA-based DMI time series is more closely in phase with and correlated with ENSO than is the SST-based DMI. DMI also correlates with precipitation anomalies in the Indian Ocean region, with the SLA DMI correlating best with precipitation in the west and SST DMI in the east. Examination of the strong IOD events of 1994, 1997 and 2019 showed that the precipitation anomalies broadly followed this relationship in those years.

These results suggest that the SST and SLA DMI can be used together to provide a more informative characterisation of IOD events than using SST DMI alone.

Note

17. https://public.wmo.int/en/media/press-release/wmo-expects-above-average-temperatures-no-el-ni%C3%B1o.

References

Section 2.1. Modelled sea-ice volume and area transport from the Arctic Ocean to the Nordic and Barents Seas

Aagaard K, Carmack EC. 1989. The role of sea ice and other fresh water in the Arctic circulation. J Geophys Res. 94 (C10):14485–14498.

Aagaard K, Swift JH, Carmack EC. 1985. Thermohaline circulation in the Arctic Mediterranean seas. J Geophys Res. 90 (C7):4833–4846.

Årthun M, Eldevik T, Smedsrud LH, Skagseth Ø, Ingvaldsen RB. 2012. Quantifying the influence of Atlantic heat on Barents Sea Ice variability and retreat. J Clim. 25:4736–4743.

Beszczynzka-Möller A, Fahrbach E, Schauer U, Hansen E. 2012. Variability in Atlantic water temperature and transport at the entrance to the Arctic Ocean, 1997–2010. ICES J Mar Sci. 69(5):852–863.

Bi H, Sun K, Zhou X, Huang H, Xu X. 2016. Arctic Sea Ice area export through the Fram Strait estimated from satellite-based data: 1988–2012. IEEE J Select Top Appl Ear Observat Remot Sens. 9(7):3144–3157.

Bi HB, Wang YH, Zhang WF, Zhang ZH, Liang Y, Zhang Y, Hu WM, Fu M, Huang HJ. 2018. Recent satellite-derived sea ice volume flux through the Fram Strait: 2011–2015. Acta Oceanologica Sinica. 37(9):107–115.

Chikhar K, Lemieux JF, Dupont F, Roy F, Smith GC, Brady M, Howell SEL, Beaini R. 2019. Sensitivity of ice drift to form drag and ice strength parameterization in a coupled ice-ocean model. Atmos Ocean. 57(5):329–349.

Dansereau V, Weiss J, Saramito P, Lattes P. 2016. A Maxwell elasto-brittle rheology of sea ice modelling. Cryosphere. 10 (3):1339–1359.

Fahrbach E, Meincke J, Østerhus S, Rohardt G, Schauer U, Tverberg V, Verduin J. 2001. Direct measurements of volume transports through Fram Strait. Polar Res. 20 (2):217–224.

Fossheim M, Primicerio R, Johannesen E, Ingvaldsen RB, Aschan MM, Dolgov AV. 2015. Recent warming leads to a rapid borealization of fish communities in the Arctic. Nat Clim Change. doi:10.1038/nclimate2647.

Hansen E, Gerland S, Granskog MA, Pavlova O, Renner AHH, Haapala J, Løyning TB, Tschudi M. 2013. Thinning of Arctic sea ice observed in Fram Strait: 1990–2011. J Geophys Res-Ocean. 118(10):5202–5221.

Holland MM, Bitz CM, Eby M, Weaver AJ. 2001. The role of ice-ocean interactions in the variability of the North Atlantic thermohaline circulation. J Clim. 14(5):656–675.

Hunke EC, Dukowicz JK. 1997. An elastic-viscous-plastic mode for sea ice dynamics. J Phys Oceanogr. 27:1849–1867.

Ivanov V, Alexeev N, Koldunov N, Repina I, Sandø A, Smedsrud L, Smirnov A. 2016. Arctic Ocean heat impact on regional ice decay – a suggested positive feedback. J Phys Oceanogr. 46:1437–1456.

Lind S, Ingvaldsen RB, Furevik T. 2018. Arctic warming hotspot in the northern Barents Sea linked to declining sea ice import. Nat Clim Change. doi:10.1038/s41558-018-0205-y.

Lique C, Treguier AM, Scheinert M, Penduff T. 2009. A model-based study of ice and freshwater transport variability along both sides of Greenland. Clim Dyn. 33:685–705.

Loeng H. 1991. Features of the physical oceanographic conditions of the Barents Sea. Polar Res. 10(1):5–18.

Onarheim IH, Eldevik T, Årthun M, Ingvaldsen RB, Smedsrud LH. 2015. Skillful prediction of Barents Sea ice cover. Geophys Res Lett. 42(13):5364–5371.

Polyakov IV, Alkire MB, Bluhm BA, Brown KA, Carmack EC, Chierici M, Danielson SL, Ellingsen I, Ershova EA, Gårdfeldt K, et al. 2020a. Borealization of the Arctic Ocean in response to anomalous advection from sub-Arctic Seas. Front Mar Sci. 7:491. doi:10.3389/fmars.2020.00491.

Polyakov IV, Pnyushkov AV, Alkire MB, Ashik IM, Baumann TM, Carmack EC, Goszczko I, Guthrie J, Ivanov VV, Kanzow T, et al. 2017. Greater role for Atlantic inflows on sea-ice loss in the Eurasian Basin of the Arctic ocean. Science. doi:10.1126/science.aai8204.

Polyakov IV, Rippeth TP, Fer I, Alkire MB, Baumann TM, Carmack EC, Ingvaldsen R, Ivanov VV, Janout M, Lind S, et al. 2020b. Weakening of cold halocline layer exposes Sea Ice to oceanic heat in the Eastern Arctic Ocean. J Clim. 33:8107–8123. doi:10.1175/JCLI-D-19-0976.1.

Rabe B, Dodd PA, Hansen E, Falck E, Schauer U, Mackensen A, Beszczynska-Möller A, Kattner G, Rohling EJ, Cox K. 2013. Liquid export of Arctic freshwater components through the Fram Strait 1998–2011. Ocean Sci. 9(1):91–109.

Rampal P, Weiss J, Dubois C, Campin J-M. 2011. IPCC climate models do not capture Arctic sea ice drift acceleration: consequences in terms of projected sea ice thinning and decline. J Geophys Res. 116:C00D07. doi:10.1029/2011JC007110.

Ricker R, Girard-Ardhuin F, Krumpen T, Lique C. 2018. Satellite-derived sea ice export and its impact on Arctic ice mass balance. The Cryosphere. 12:3017–3032.

Sakov P, Counillon F, Bertino L, Lisæter KA, Oke PR, Korablev A. 2012. TOPAZ4: an ocean-sea ice data assimilation system for the North Atlantic and Arctic. Ocean Sci. 8 (4):633–656.

Skagseth Ø, Eldevik T, Årthun M, Asbjørnsen H, Lien VS, Smedsrud LH. 2020. Reduced efficiency of the Barents Sea cooling machine. Nat Clim Change. doi:10.1038/s41558-020-0772-6.

Smedsrud LH, Esau I, Ingvaldsen RB, Eldevik T, Haugan PM, Li C, Lien VS, Olsen A, Omar AM, Otterå OH, et al. 2013. The role of the Barents Sea in the climate system. Rev Geophys. 51:415–449.

Smedsrud LH, Halvorsen MH, Stroeve JC, Zhang R, Kloster K. 2017. Fram Strait sea ice export variability and September Arctic sea ice extent over the last 80 years. Cryosphere. 11(1):65–79.

Smedsrud LH, Sirevaag A, Kloster K, Sorteberg, Sandven S. 2011. Recent wind driven high sea ice area export in the Fram Strait contributes to Arctic sea ice decline. Cryosphere. 5(4):821–829.

Sorteberg A, Kvingedal B. 2006. Atmospheric forcing on the barents sea winter ice extent. J Clim. 19(19):4772–4784. y. [accessed 2021 Jul 12]. https://journals.ametsoc.org/view/journals/clim/19/19/jcli3885.1.xml

Spreen G, de Steur L, Divine D, Gerland S, Hansen E, Kwok R. 2020. Arctic sea ice volume export through Fram Strait from 1992 to 2014. J Geophys Res – Ocean. 125(6): e2019JC016039.

Spreen G, Kern S, Stammer D, Hansen E. 2009. Fram Strait sea ice volume export estimated between 2003 and 2008 from satellite data. Geophys Res Lett. 36:L19502.

Sumata H, Kwok R, Gerdes R, Kauker F, Karcher M. 2015. Uncertainty of Arctic summer ice drift assessed by high-resolution SAR data. J Geophys Res – Ocean. 120 (8):5285–5301.

Tsukernik M, Deser C, Alexander M, Tomas R. 2010. Atmospheric forcing of Fram Strait sea ice export: a closer look. Clim Dyn. 35:1349–1360.

van Angelen JH, van den Broeke MR, Kwok R. 2011. The Greenland Sea Jet: a mechanism for wind-driven sea ice export through Fram Strait. Geophys Res Lett. 38: L12805.

Vinje T, Nordlund N, Kvambekk Å. 1998. Monitoring ice thickness in Fram Strait. J Geophys Res. 103(C5):10437–10449.

Widell K, Østerhus S, Gammelsrød T. 2003. Sea ice velocity in the Fram Strait monitored by moored instruments. Geophys Res Lett. 30(19):1982. doi:10.1029/2003GL018119.

Xie J, Counillon F, Bertino L. 2018. Impact of assimilating a merged sea-ice thickness from CryoSat-2 and SMOS in the Arctic reanalysis. The Cryosphere. 12(11):3671–3691. DOI:10.5194/tc-12-3671-2018.

Zamani B, Krumpen T, Smedsrud LH, Gerdes R. 2019. Fram Strait sea ice export affected by thinning: comparing high-resolution simulations and observations. Clim Dyn. 53:3257–3270.

Zhang JL, Lindsay R, Steele M, Schweiger A. 2008. What drove the dramatic retreat of Arctic sea ice during summer 2007? Geophys Res Lett. 35(11):L11505.

Zhang ZH, Bi HB, Sun K, Huang HJ, Liu YX, Yan LW. 2017. Arctic sea ice volume export through the Fram Strait from combined satellite and model data: 1979–2012. Acta Oceanologica Sinica. 36:44–55.

Section 2.2. Ocean heat content in the High North

Aagaard K, Swift JH, Carmack C. 1985. Thermohaline circulation in the Arctic Mediterranean Seas. J Geophys Res. 90 (C3):4833–4846.

Årthun M, Eldevik T. 2016. On anomalous ocean heat transport toward the Arctic and associated climate predictability. J Clim. 29:689–704.

Årthun M, Eldevik T, Smedsrud LH. 2019. The role of Atlantic heat transport in future Arctic winter sea ice loss. J Clim. 32:3327–3341.

Asbjørnsen H, Årthun M, Skagseth Ø, Eldevik T. 2019. Mechanisms of ocean heat anomalies in the Norwegian sea. J Geophys Res Oceans. 124(4):2908–2923. DOI:10.1029/2018JC014649.

Carton JA, Chepurin GA, Reagan* J, Hakkinen S. 2011. Interannual to decadal variability of Atlantic Water in the Nordic and adjacent seas. J Geophys Res. 116:C11035. DOI:10.1029/2011JC007102.

Cheng L, Trenberth KE, Fasullo J, Abraham J, Boyer TP, von Schuckmann K, Zhu J. 2017. Taking the pulse of the planet. Eos. 98. doi:10.1029/2017EO081839. Published on 13 September 2017.

Dmitrenko IA, Kirillov SA, Serra N, Koldunov NV, Ivanov VV, Schauer U, Polyakov IV, Barber D, Janout M, Lien VS, et al. 2014. Heat loss from the Atlantic water layer in the St. Anna Trough (northern Kara Sea): causes and consequences. Ocean Sci. 10:719–730.

Furevik T. 2001. Annual and interannual variability of Atlantic Water temperatures in the Norwegian and Barents Seas: 1980–1996. Deep-Sea Res I. 48:383–404.

González-Pola C, Larsen KMH, Fratantoni P, Beszczynska-Möller A, eds. 2019. ICES report on Ocean climate 2018. ICES cooperative research report no. 349. 122 pp. doi:10.17895/ices.pub.5461.

Guinehut S, Dhomps A, Larnicol G, Le Traon P-Y. 2012. High resolution 3-d temperature and salinity fields derived from in situ and satellite observations. Ocean Sci. 8(5):845–857.

Isachsen PE, Koszalka I, LaCasce JH. 2012. Observed and modeled surface eddy heat fluxes in the eastern Nordic seas. J Geophys Res. 117:C08020.

Ivanov V, Alexeev V, Koldunov NV, Repina I, Sandø AB, Smedsrud LH, Smirnov A. 2016. Arctic Ocean heat impact on regional ice decay: a suggested positive feedback. J Phys Oceanogr. 46:1437–1456.

Lien VS, Trofimov AG. 2013. Formation of Barents Sea branch water in the north-eastern Barents Sea. Polar Res. 32:18905.

Locarnini RA, Mishonov AV, Baranova OK, Boyer TP, Zweng MM, Garcia HE, Reagan JR, Seidov D, Weathers K, Paver CR, Smolyar I. 2018. World Ocean Atlas 2018, volume 1: temperature. A. mishonov technical Ed.; NOAA Atlas NESDIS 81, 52 p.

Mauritzen C. 1996. Production of dense overflow waters feeding the North Atlantic across the Greenland-Scotland Ridge. Part 1: evidence for a revised circulation scheme. Deep Sea Res Part I. 43:769–806.

Mayer M, Haimberger L, Pietschnig M, Storto A. 2016. Facets of Arctic energy accumulation based on observations and reanalyses 2000–2015. Geophys Res Lett. 43:10420–10429. doi:10.1002/2016GL070557.

Mayer M, Tietsche S, Haimberger L, Tsubouchi T, Mayer J, Zuo H. 2019. An improved estimate of the coupled Arctic energy budget. J Clim. 32(22):7915–7934.

Mork KM, Skagseth Ø. 2012. Heat content in the Norwegian Sea, 1995–2010. ICES J Mar Sci. 69:826–832.

Mork KM, Skagseth Ø, Søiland H. 2019. Recent warming and freshening of the Norwegian Sea observed by Argo data. J Climate. 32:3695–3705.

Pietschnig M, Mayer M, Tsubouchi T, Storto A, Stichelberger S, Haimberger L. 2018. Volume transports and temperature distributions in the main arctic gateways: a comparative study between an ocean reanalysis and mooring-derived data. doi:10.31223/osf.io/5hg3z.

Polyakov IV, Pnyushkov AV, Alkire MB, Ashik IM, Baumann TM, Carmack EC, Goszczko I, Guthrie J, Ivanov VV, Kanzow T, et al. 2017. Greater role for Atlantic inflows on sea-ice loss in the Eurasian Basin of the Arctic Ocean. Science. 356(6335):285–291.

Polyakov IV, Rippeth TP, Fer I, Alkire MB, Baumann TM, Carmack EC, Ingvaldsen R, Ivanov VV, Janout M, Lind S, Padman L, et al. 2020. Weakening of cold halocline layer exposes sea ice to oceanic heat in the Eastern Arctic Ocean. J Clim. 33(18):8107–8123.

Proshutinsky A, Dukhovskoy D, Timmermans M-L, Krishfield R, Bamber JL. 2015. Arctic circulation regimes. Phil Trans R Soc A 373:20140160. doi:10.1098/rsta.2014.0160

Robson J, Sutton R, Lohmann K, Smith D, Palmer MD. 2012. Causes of the rapid warming of the North Atlantic Ocean in the mid-1990s. J Clim. 25:4116–4134.

Segtnan OH, Furevik T, Jenkins AD. 2011. Heat and freshwater budgets of the Nordic seas computed from atmospheric reanalysis and ocean observations. J Geophys Res. 116:C11003.

Serreze MC, Barry RG. 2011. Processes and impacts of Arctic amplification: a research synthesis. Global Planet Change. 77:85–96. doi:10.1016/j.gloplacha.2011.03.004.

Skagseth Ø, Eldevik T, Årthun M, Asbjørnsen H, Lien VS, Smedsrud LH. 2020. Reduced efficiency of the Barents Sea cooling machine. Nat Clim Change. doi:10.1038/s41558-020-0772-6.

Timmermans ML, Toole J, Krishfield R. 2018. Warming of the interior Arctic Ocean linked to sea ice losses at the basin margins. Sci Adv. 4(8):eaat6773.

Tsubouchi, et al. 2020. Increased ocean heat transport into the Nordic Seas and Arctic Ocean over the period 1993–2016. Nat Clim Chang. 11:21–26. doi:10.1038/s41558-020-00941-3.

Uotila P, Goosse H, Haines K, Chevallier M, Barthélemy A, Bricaud C, Carton J, Fučkar N, Garric G, Iovino D, et al. 2019. An assessment of ten ocean reanalyses in the polar regions. Clim Dyn. 52(3–4):1613–1650.

von Schuckmann, K, et al. 2018. Copernicus Marine service Ocean state report. J Oper Oceanogr 11:S1–S142. https://marine.copernicus.eu/science-learning/ocean-state-report/oceanstate-report-2nd-issue/.

von Schuckmann K, Cheng L, Palmer MD, Tassone C, Aich V, Adusumilli S, Beltrami H, Boyer T, Cuesta-Valero FJ, Desbruyères D, et al. 2020. Heat stored in the earth system: where does the energy go? The GCOS Earth heat inventory team. Earth Syst Sci Data Discuss. doi:10.5194/essd-2019-255. in review.

Von Schuckmann K, Palmer MD, Trenberth KE, Cazenave A, Chambers D, Champollion N, Hansen J, Josey S, Loeb N, Mathieu P-P, et al. 2016. An imperative to monitor earth's energy imbalance. Nat Clim Change. 6(2):138–144.

Section 2.3. Declining silicate and nitrate concentrations in the northern North Atlantic

Barofsky A, et al. 2010. Growth phase of the diatom skeletonema marinori influences the metabolic profile of the cells and the selective feeding of the copepod Calanus spp. J Plankt Res. 32:263–272.

Bendschneider K, Robinson RI. 1952. A new spectrophotometric method for the determination of nitrite in seawater. J Mar Res. 2:87–96.

Berx B, Payne M. 2016. Sub-polar gyre index. doi:10.7489/1806-1.

Daniels CJ, et al. 2015. Phytoplankton dynamics in contrasting early stage North Atlantic spring blooms: composition, succession, and potential drivers. Biogeosciences. 12:2395–2409.

Egge J, Aksnes D. 1992. Silicate as regulating nutrient in phytoplankton competition. Mar Ecol Prog Ser. 83:281–289.

Eiane K, Tande KS. 2009. Meso and microzooplankton, pp. 209–234. In: Sakshaug E., G. Johnsen, K. Kovac, editor. Ecosystem Barents Sea. Norway: Tapir Academic Press; 587 pp.

Furnas MJ. 1990. In situ growth rates of marine phytoplankton: approaches to measurement, community and species growth rate. J Plankton Res. 12:1117–1151.

Garcia HE, et al. 2006. World Ocean Atlas 2005, vol. 4, nutrients (phosphate, nitrate, silicate), 396 pp. In: Levitus S, editor. NOAA Atlas NESDIS, vol. 64. Silver Spring, MD: NOAA.

Gjøsæther H. 2009. Commercial fisheries (fish, seafood and marine mammals), pp. 373–414. In: Sakshaug E., G. Johnsen, K. Kovac, editor. Ecosystem Barents Sea, 587 pp.

Grasshoff K. 1965. On the Automatic Determination of Phosphate, Silicate and Fluoride in Seawater. ICES Hydrographic Committee Report No. 129. ICESHydrographic Committee Report No. 129. ICES. https://www.ices.dk/.

Hátún H, et al. 2005. Influence of the Atlantic Subpolar gyre on the thermohaline circulation. Science. 309:1841–1844.

Hátún H, et al. 2017. The subpolar gyre regulates silicate concentrations in the North Atlantic. Sci Rep. 7:14576.

Honjo S, Manganini SJ. 1993. Annual biogenic particle fluxes to the interior of the North Atlantic Ocean studied at 34-degrees N 21-degrees W and 48 degrees N 21 degrees W. Deep-Sea Res II. 40:587–607.

Irigoien X, et al. 2000. Feeding selectivity and egg production of Calanus helgolandicus in the English Channel. Limnol Oceanogr. 45:44–54.

Jaccard, P. et al. 2020. Quality information document for global ocean reprocessed in-situ observations of biogeochemical products. Issue 2.0, 77 pp. doi:10.13155/54846

Johnson C, et al. 2013. Declining nutrient concentrations in the northeast Atlantic, as a result of a weakening Subpolar Gyre. Deep-Sea Res. 82:95–107.

Jonasdottir SH. 1994. Effects of food quality on reproductive success in Acartia tonsa and Acartia hudsonica - laboratory observations. Mar Biol. 121:67–81.

Mayzaud P, et al. 1996. The influence of food quality on the nutritional acclimation of the copepod Acartia clausi. In: 6th international conference on Copepoda, Elsevier, Germany, pp. 483–493.

McCartney MS, Mauritzen C. 2001. On the origin of warm inflow to the Nordic Seas. Prog Oceanogr. 51:125–214.

McQuatters-Gollop A, et al. 2007. A long-term chlorophyll data set reveals regime shift in North Sea phytoplankton biomass unconnected to nutrient trends. Limnol Oceanogr. 52:635–648.

Melle W, et al. 2004. Zooplankton: the link to higher trophic levels. In: Skjoldal H.R, editor. The Norwegian Sea Ecosystem. Norway: Tapir Academic Press; p. 209–234.

Meyer-Harms B, et al. 1999. Selective feeding on natural phytoplankton by Calanus finmarchicus before, during, and after the 1997 spring bloom in the Norwegian Sea. Limnol Oceanogr. 44:154–165.

Moore PE, et al. 1999. Physical constraints of chemoreception in foraging copepods. Limnol Oceanogr. 44:166–177.

Officer CB, Ryther JH. 1980. The possible importance of silicon in marine eutrophication. Mar Ecol Prog Ser. 3:83–91.

Olsen MB, et al. 2006. Copepod feeding selectivity on microplankton, including the toxigenic diatoms, Pseudo-nitzchia spp. in the coastal Pacific Northwest. Mar Ecol Prog Ser. 326:207–220.

Pollock DE. 1997. The role of diatoms, dissolved silicate and Antarctic glaciation in glacial/interglacial climate change; a hypothesis. Global Planet Change. 14:113–125.

Pond D, et al. 1996. Environmental and nutritional factors determining seasonal variability in the fecundity and egg viability of Calanus helgolandicus in coastal waters off Plymouth, UK. Mar Ecol Prog Ser. 143:45–63.

Rey F. 2004. Phytoplankton: the grass of the ocean. In: Skjoldal H.R, editor. The Norwegian Sea Ecosystem. Norway: Tapir Academic Press; p. 97–136.

Rey F. 2012. Declining silicate concentrations in the Barents Sea. ICES J Mar Sci. 69:208–212.

Sarafanov A. 2009. On the effect of the North Atlantic Oscillation on temperature and salinity of the subpolar North Atlantic intermediate and deep waters. ICES J Mar Sci. 66:1448–1454.

Savidge G, et al. 1995. A study of the spring bloom in the N–E Atlantic Ocean in 1990. Deep Sea Res. 42:599–617.

Schlosser P, et al. 1995. The role of the large-scale Arctic Ocean circulation in the transport of contaminants. Deep-Sea Research II. 42:1341–1367.

Selander E, et al. 2006. Copepods induce paralytic shellfish toxin production in marine dinoflagellates. Proc R Soc Lond Ser B. 273:1673–1680.

Skjoldal HR, et al. 2004. Food webs and trophic interactions. In: Skjoldal H.R, editor. The Norwegian Sea Ecosystem. Norway: Tapir Academic Press; p. 447–506.

Smayda TJ, et al. 1990. Novel and nuisance phytoplankton blooms in the sea: evidence for global epidemic. In: Graneli E, editor. Toxic marine phytoplankton. New York, NY: Elsevier; p. 29–40.

Volk T, Hoffert MI. 1985. Ocean Carbon pumps: analysis of relative strengths and efficiencies in Ocean-driven atmospheric CO_2 changes. In: Sundquist E.T., W.S. Broecker, editor. The Carbon cycle and atmospheric CO_2: natural variations archean to present, geophysical monograph series, vol. 32. doi:10.1029/GM032p0099

Section 2.4. Eutrophic and oligotrophic indicators for the North Atlantic Ocean

Andersen JH, Kallenbach E, Murray C, Ledang AB. 2016. Eutrophication in the Danish parts of the North Sea, Skagerrak and Kattegat 2006–2014. A literature-based status assessment. NIVA Denmark Report. https://brage.bibsys.no/xmlui/handle/11250/2406499.

Anderson DM, Glibert PM, Burkholder JM. 2002. Harmful algal blooms and eutrophication: nutrient sources, composition, and consequences. Estuaries. 25:704–726. doi:10.1007/BF02804901.

Attila J, Kauppila P, Kallio KY, Alasalmi H, Keto V, Bruun E, Koponen S. 2018. Applicability of earth observation chlorophyll-a data in assessment of water status via MERIS – with implications for the use of OLCI sensors. Remote Sens Environ. 212:273–287. doi:10.1016/j.rse.2018.02.043.

Balmer MB, Downing JA. 2011. Carbon dioxide concentrations in eutrophic lakes: undersaturation implies atmospheric uptake. Inland Waters. 1(2):125–132. doi:10.5268/IW-1.2.366.

Baretta-Bekker H, Sell A, Marco-Rius F, Wischnewski J, Walsham P, Malin Mohlin L, Wesslander K, Ruiter H, Gohin F, Enserink L. 2015. The chlorophyll case study in the JMP NS/CS project. Document produced as part of the EU project: 'Towards joint Monitoring for the North Sea and Celtic Sea' (Ref: ENV/PP 2012/SEA).

Blauw A, Eleveld M, Prins T, Zijl F, Julien Groenenboom J, Gundula Winter G, Kramer L, Troost T, Bartosova A, Johansson J, et al. 2019. Coherence in assessment framework of chlorophyll-a and nutrients as part of the EU project 'Joint monitoring programme of the eutrophication of the North Sea with satellite data' (Ref: DG ENV/MSFD Second Cycle/2016). Activity 1 Report.

Breitburg D, Levin LA, Oschlies A, Grégoire M, Chavez FP, Conley DJ, Garçon V, Gilbert D, Gutiérrez D, Isensee K, Jacinto GS. 2018. Declining oxygen in the global ocean and coastal waters. Science. 359(6371):eaam7240.

Cai W, Hu X, Huang W. 2011. Acidification of subsurface coastal waters enhanced by eutrophication. Nature Geosci. 4:766–770. 10.1038/ngeo1297.

Carvalho L, Mackay EB, Cardoso AC, Baattrup-Pedersen A, Birk S, Blackstock KL, Borics G, Borja A, Feld CK, Ferreira MT, et al. 2019. Protecting and restoring Europe's waters: an analysis of the future development needs of the water framework directive. Sci Total Environ. 658:1228–1238. doi:10.1016/j.scitotenv.2018.12.255.

CMEMS OMI catalogue. 2020. ATLANTIC_OMI_HEALTH_OceanColour_anomalies. Available from: https://resources.marine.copernicus.eu/?option=com_csw&view=details&product_id=ATLANTIC_OMI_HEALTH_OceanColour_anomalies.

Coppini G, Lyubartsev V, Pinardi N, Colella S, Santoleri R, Christiansen T. 2012. Chl-a trends in European seas estimated using ocean-colour products. Ocean Sci Discus. 9:1481–1518. doi:10.5194/osd-9-1481-2012.

Cristina S, Icely J, Goela PC, DelValls TA, Newton A. 2015. Using remote sensing as a support to the implementation of the European Marine Strategy Framework Directive in SW Portugal. Cont Shelf Res. 108:169–177.

Ferreira JG, Andersen JH, Borja A, Bricker SB, Camp J, Cardoso da Silva M, Garcés E, Heiskanen A-S, Humborg C, Ignatiades L, et al. 2011. Overview of eutrophication indicators to assess environmental status within the European Marine strategy framework directive. Estuarine Coastal Shelf Sci. 93(2):117–131. doi:10.1016/j.ecss.2011.03.014.

Galloway JN, Townsend AR, Erisman JW, Bekunda M, Cai Z, Freney JR, Martinelli LA, Seitzinger SP, Sutton MA. 2008. Transformation of the nitrogen cycle: recent trends, questions, and potential solutions. Science. 320(5878):889–892. doi:10.1126/science.1136674.

Gohin F, Bryère P, Lefebvre A, Sauriau P-G, Savoye N, Vantrepotte V, Bozec Y, Cariou T, Conan P, Coudray S, et al. 2020. Satellite and in situ monitoring of Chl-a, turbidity, and total suspended matter in coastal waters: experience of the year 2017 along the French coasts. J Mar Sci Eng. 8(9):665. doi:10.3390/jmse8090665.

Gohin F, Saulquin B, Oger-Jeanneret H, Lozac'h L, Lampert L, Lefebvre A, Riou P, Bruchon F. 2008. Towards a better assessment of the ecological status of coastal waters using satellite-derived chlorophyll-a concentrations. Remote Sens Environ. 112:3329e3340.

Gohin F, Van der Zande D, Tilstone G, Eleveld MA, Lefebvre A, Andrieux-Loyer F, Blauw AN, Bryère P, Devreker D, Garnesson P, et al. 2019. Twenty years of satellite and in situ observations of surface chlorophyll-a from the northern Bay of Biscay to the eastern English Channel. Is the water quality improving? Remote Sens Environ. 233:111343. doi:10.1016/j.rse.2019.111343.

Ha NTT, Koike K, Nhuan MT. 2014. Improved accuracy of chlorophyll-a concentration estimates from MODIS imagery using a two-band ratio algorithm and geostatistics: as applied to the monitoring of eutrophication processes over tien Yen Bay (Northern Vietnam). Remote Sens (Basel). 6:421–442.

Harvey ET, Kratzer S, Philipson P. 2015. Satellite-based water quality monitoring for improved spatial and temporal retrieval of chlorophyll-a in coastal waters. Remote Sens Environ. 158:417–430. doi:10.1016/j.rse.2014.11.017.

Howarth RW, Anderson DB, Cloer JE, Elfring C, Hopkinson CS, Lapointe B, Malone T, Marcus N, McGlathery K, Sharpley AN, et al. 2000. Nutrient pollution of coastal rivers, bays, and seas. Issues Ecol. 7:1–16.

Howarth, RW, Marino R. 2006. Nitrogen as the limiting nutrient for eutrophication in coastal marine ecosystems: Evolving views over three decades. Limnol Oceanogr. 51 (1, part 2). doi:10.4319/lo.2006.51.1_part_2.0364.

Jickells TD. 1998. Nutrient biogeochemistry of the coastal zone. Science. 281:217–222. doi:10.1126/science.281.5374.217.

Lefebvre A, Guiselin N, Barbet F, Artigas LF. 2011. Long-term hydrological and phytoplankton monitoring (1992–2007) of three potentially eutrophicated systems in the eastern English Channel and the southern bight of the North Sea ICES. J Mar Sci. 68(10):2029–2043. 10.1093/icesjms/fsr149.

Malone TC, Newton A. 2020. The globalization of cultural eutrophication in the coastal ocean: causes and consequences. Front Mar Sci. 7:670. doi:10.3389/fmars.2020.00670.

Murray CJ, Müller-Karulis B, Carstensen J, Conley DJ, Gustafsson BG, Andersen JH. 2019. Past, present and future eutrophication status of the Baltic Sea. Front Mar Sci. 6(2). doi:10.3389/fmars.2019.00002.

Novoa S, Chust G, Sagarminaga Y, Revilla M, Borja A, Franco J. 2012. Water quality assessment using satellite-derived chlorophyll – a within the European directives, in the southeastern Bay of biscay. Mar Pollut Bull. 65:739–750. doi:10.1016/j.marpolbul.2012.01.020.

NOWPAP CEARAC – Northwest Pacific Action Plan Special Monitoring and Coastal Environmental Assessment Regional Activity Centre. 2007. Eutrophication monitoring guidelines by Remote Sensing for the NOWPAP region. Toyama City, Japan. Availble from: https://www.cearac-project.org/wg4/publications/Eutrophication_GL_RS.pdf.

OSPAR ICG-EUT. Axe, P., Clausen, U., Leujak, W., Malcolm, S., Ruiter, H., Prins, T., Harvey, E.T. (2017). Eutrophication Status of the OSPAR Maritime Area. Third Integrated Report on the Eutrophication Status of the OSPAR Maritime Area.

Papathanasopoulou E, Simis S, Alikas K, Ansper A, Anttila S, Attila J, Barillé AL, Barillé L, Brando V, Bresciani M, et al. 2019. Satellite-assisted monitoring of water quality to support the implementation of the water framework directive. EOMORES White Paper. 28. doi:10.5281/zenodo.3463051.

Park Y, Ruddick K, Lacroix G. 2010. Detection of algal blooms in European waters based on satellite chlorophyll data from MERIS and MODIS. Int J Remote Sens. 31:6567–6583.

Sathyendranath S, Pardo S, Benincasa M, Brando VE, Brewin RJW, Mélin F, Santoleri R. 2018. 1.5. Essential variables: Ocean colour in Copernicus Marine service Ocean state report – issue 2. J Operat Oceanogr. 11(Suppl. 1)):1–142. doi:10.1080/1755876X.2018.1489208.

Schindler DW. 2006. Recent advances in the understanding and management of eutrophication. Limnol Oceanogr. 51:356–363.

Smith VH. 2003. Eutrophication of freshwater and coastal marine ecosystems a global problem. Environ Sci Poll Res. 10:126–139. 10.1065/espr2002.12.142.

Van der Zande D, Lacroix G, Desmit X, Ruddick K. 2011. Impact of irregular sampling by MERIS on eutrophication monitoring products for WFD and MSFD applications. Proceedings of the 6th 683 EuroGOOS Conference, Sopot, Poland; p. 348–357.

Van der Zande D, Lavigne H, Blauw A, Prins T, Desmit X, Eleveld M, Gohin F, Pardo S, Tilstone G, Cardoso Dos Santos J. 2019. Enhance coherence in eutrophication assessments based on chlorophyll, using satellite data as part of the EU project 'Joint monitoring programme of the eutrophication of the North Sea with satellite data' (Ref: DG ENV/MSFD Second Cycle/2016). Activity 2 Report.

Van der Zande D, Ruescas A, Storm T, Embacher S, Stelzer K, Ruddick K. 2013. Monitoring eutrophication in the North Sea: an operational CHL-P90 tool. Proceedings of IOCS2013 conference held in Darmstadt, Germany, 6–8 May 2013.

Van Meerssche E, Pinckney JL. 2019. Nutrient loading impacts on Estuarine phytoplankton size and community composition: community-based indicators of eutrophication. Estuaries Coasts. 42:504–512. doi:10.1007/s12237-018-0470-z.

Wallace RB, Baumann H, Grear JS, Aller RB, Gobler CJ. 2014. Coastal ocean acidification: The other eutrophication problem. Estuarine Coastal Shelf Sci. 148:1–13. doi:10.1016/j.ecss.2014.05.027.

Section 2.5. Nitrate, ammonium and phosphate pools in the Baltic Sea

Almroth-Rosell E, Eilola K, Kuznetsov I, Hall PO, Meier HM. 2015. A new approach to model oxygen dependent benthic phosphate fluxes in the Baltic Sea. J Mar Sys. 144:127–141. doi:10.1016/j.jmarsys.2014.11.007.

Andersen JH, Carstensen J, Conley DJ, Dromph K, Fleming-Lehtinen V, Gustafsson BG, Josefson AB, Norkko A, Villnäs A, Murray C. 2017. Long-term temporal and spatial trends in eutrophication status of the Baltic Sea. Biol Rev. 92(1):135–149. doi:10.1111/brv.12221.

Asmala E, Carstensen J, Conley DJ, Slomp CP, Stadmark J, Voss M. 2017. Efficiency of the coastal filter: nitrogen and phosphorus removal in the Baltic Sea. Limnol Oceanogr. 62:S222–S238. doi:.10.1002/lno.10644.

Bonaglia S, Hylén A, Rattray JE, Kononets MY, Ekeroth N, Roos P, Thamdrup B, Brüchert V, Hall PO. 2017. The fate of fixed nitrogen in marine sediments with low organic loading: an in situ study. Biogeosciences. 14(2):285–300. doi:10.5194/bg-14-285-2017.

Bonaglia S, Klawonn I, De Brabandere L, Deutsch B, Thamdrup B, Brüchert V. 2016. Denitrification and DNRA at the Baltic Sea oxic–anoxic interface: substrate spectrum and kinetics. Limnol Oceanogr. 61(5):1900–1915. doi:10.1002/lno.10343.

Buga L, Sarbu G, Fryberg L, Magnus W, Wesslander K, Gatti J, Leroy D, Iona S, Larsen M, Koefoed Rømer J, et al. 2018. EMODnet Thematic Lot n° 4/SI2.749773 EMODnet Chemistry Eutrophication and Acidity aggregated datasets v2018, doi: 10.6092/EC8207EF-ED81-4EE5-BF48-E26FF16BF02E.

Carstensen J, Andersen JH, Gustafsson BG, Conley DJ. 2014. Deoxygenation of the Baltic Sea during the last century. Proc Natl Acad Sci USA. 111(15):5628–5633. doi:10.1073/pnas.1323156111.

Carstensen J, Conley DJ. 2019. Baltic Sea hypoxia takes many shapes and sizes. Limnol Ocean Bull. 28(4):125–129. doi:10.1002/lob.10350.

Carstensen J, Conley DJ, Almroth-Rosell E, Asmala E, Bonsdorff E, Fleming-Lehtinen V, Gustafsson BG, Gustafsson C, Heiskanen AS, Janas U, Norkko A. 2020. Factors regulating the coastal nutrient filter in the Baltic Sea. Ambio. 49(6):1194–1210. doi:10.1007/s13280-019-01282-y.

Conley DJ, Björck S, Bonsdorff E, Carstensen J, Destouni G, Gustafsson BG, Hietanen S, Kortekaas M, Kuosa H, Markus Meier HE, Müller-Karulis B. 2009. Hypoxia-related processes in the Baltic Sea. Environ Sci Technol. 43 (10):3412–3420. doi:10.1021/es802762a.

Dahlgren P, Landelius T, Kallberg P, Gollvik S. 2016. A high resolution regional reanalysis for Europe Part 1: 3-dimensional reanalysis with the regional high resolution limited area model (HIRLAM). Q J Roy Meteor Soc. 698:2119–2131. doi:10.1002/qj.2807.

Dalsgaard T, De Brabandere L, Hall PO. 2013. Denitrification in the water column of the central Baltic Sea. Geochim Cosmochim Acta. 106:247–260. doi:10.1016/j.gca.2012.12.038.

Donnelly C, Andersson JC, Arheimer B. 2016. Using flow signatures and catchment similarities to evaluate the E-HYPE multibasin model across Europe. Hydrolog. Sci J. 61:255–273. doi:10.1080/02626667.2015.1027710.

Eilola K, Meier HM, Almroth E. 2009. On the dynamics of oxygen, phosphorus and cyanobacteria in the Baltic Sea; a model study. J Mar Sys. 75(1–2):163–184. doi:10.1016/j.jmarsys.2008.08.009.

Fleming-Lehtinen V, Andersen JH, Carstensen J, Łysiak-Pastuszak E, Murray C, Pyhälä M, Laamanen M. 2015. Recent developments in assessment methodology reveal that the Baltic Sea eutrophication problem is expanding. Ecol Indic. 48:380–388. doi:10.1016/j.ecolind.2014.08.022.

Granéli E, Wallström K, Larsson U, Granéli W, Elmgren R. 1990. Nutrient limitation of primary production in the Baltic Sea area. Ambio. 19(3):142–151.

Groetsch PM, Simis SG, Eleveld MA, Peters SW. 2016. Spring blooms in the Baltic Sea have weakened but lengthened from 2000 to 2014. Biogeosciences. 13(17):4959–4973. doi:10.5194/bg-13-4959-2016.

Gustafsson BG, Schenk F, Blenckner T, Eilola K, Meier HM, Müller-Karulis B, Neumann T, Ruoho-Airola T, Savchuk OP, Zorita E. 2012. Reconstructing the development of Baltic Sea eutrophication 1850–2006. Ambio. 41(6):534–548. doi:10.1007/s13280-012-0318-x.

Gustafsson E, Savchuk OP, Gustafsson BG, Müller-Karulis B. 2017. Key processes in the coupled carbon, nitrogen, and phosphorus cycling of the Baltic Sea. Biogeochemistry. 134:301–317. doi:10.1007/s10533-017-0361-6.

Hansson M, Viktorsson L, Andersson L. 2020. Oxygen Survey in the Baltic Sea 2019-Extent of Anoxia and Hypoxia, 1960–2019. SMHI, Report Oceanography No. 67.

HELCOM. 2018a. HELCOM Thematic assessment of eutrophication 2011–2016. Baltic Sea Environment Proceedings No. 156.

HELCOM. 2018b. Sources and pathways of nutrients to the Baltic Sea. Baltic Sea Environment Proceedings No. 153.

Hordoir R, Axell L, Höglund A, Dieterich C, Fransner F, Gröger M, Liu Y, Pemberton P, Schimanke S, Andersson H, et al. 2019. Nemo-Nordic 1.0: a NEMO-based ocean model for the Baltic and North seas – research and operational applications. Geosci Model Dev. 12:363–386. doi:10.5194/gmd-12-363-2019.

Jakobsson M, Stranne C, O'Regan M, Greenwood SL, Gustafsson B, Humborg C, Weidner E. 2019. Bathymetric properties of the Baltic Sea. Ocean Science. 15(4):905–924. doi:10.5194/os-15-905-2019.

Kahru M, Elmgren R. 2014. Multidecadal time series of satellite-detected accumulations of cyanobacteria in the Baltic Sea. Biogeosciences. 11(13):3619–3633. doi:10.5194/bg-11-3619-2014.

Kahru M, Elmgren R, Di Lorenzo E, Savchuk O. 2018. Unexplained interannual oscillations of cyanobacterial blooms in the Baltic Sea. Sci Rep. 8(1):Article number 6365. doi:10.1038/s41598-018-24829-7.

Kõuts M, Maljutenko I, Elken J, Liu Y, Hansson M, Viktorsson L, Raudsepp U. 2021. Recent regime of persistent hypoxia in the Baltic Sea. Environ Res Comm. DOI:10.1088/2515-7620/ac0cc4.

Kuosa H, Fleming-Lehtinen V, Lehtinen S, Lehtiniemi M, Nygård H, Raateoja M, Raitaniemi J, Tuimala J, Uusitalo L, Suikkanen S. 2017. A retrospective view of the development of the Gulf of Bothnia ecosystem. J Mar Sys. 167:78–92. doi:10.1016/j.jmarsys.2016.11.020.

Laanemets J, Lilover MJ, Raudsepp U, Autio R, Vahtera E, Lips I, Lips U. 2006. A fuzzy logic model to describe the cyanobacteria Nodularia spumigena blooms in the Gulf of Finland, Baltic Sea. Hydrobiologia. 554(1):31–45. doi:10.1007/s10750-005-1004-x.

Landelius T, Dahlgren P, Gollvik S, Jansson A, Olsson E. 2016. A high resolution regional reanalysis for Europe Part 2: 2D analysis of surface temperature, precipitation and wind. Q J Roy Meteor Soc. 142:2132–2142. doi:10.1002/qj.2813.

Liu Y, Meier HEM, Eilola K. 2014. Improving the multiannual, high-resolution modelling of biogeochemical cycles in the Baltic Sea by using data assimilation. Tellus A: Dyn Meteorol Oceanogr. 66(1):24908. doi:10.3402/tellusa.v66.24908.

Liu Y, Meier HEM, Eilola K. 2017. Nutrient transports in the Baltic Sea – results from a 30-year physical–biogeochemical reanalysis. Biogeosciences. 14:2113–2131. doi:10.5194/bg-14-2113-2017.

Lundberg C, Jakobsson BM, Bonsdorff E. 2009. The spreading of eutrophication in the eastern coast of the Gulf of Bothnia, northern Baltic Sea–An analysis in time and space. Estuarine Coastal Shelf Sci. 82(1):152–160. doi:10.1016/j.ecss.2009.01.005.

Meier HEM. 2015. Projected change – marine physics. In: Second assessment of climate change for the Baltic Sea basin. BACC II author team, 2015. Cham: Springer International Publishing; p. 243–252.

Meier HEM, Andersson HC, Arheimer B, Blenckner T, Chubarenko B, Donnelly C, Eilola K, Gustafsson BG, Hansson A, Havenhand J, et al. 2012. Comparing reconstructed past variations and future projections of the Baltic Sea ecosystem – first results from multi-model ensemble simulations. Environ Res Lett. 7(3):034005. doi:10.1088/1748-9326/7/3/034005.

Meier HEM, Eilola K, Almroth-Rosell E, Schimanke S, Kniebusch M, Höglund A, Pemberton P, Liu Y, Väli G, Saraiva S. 2019. Disentangling the impact of nutrient load and climate changes on Baltic Sea hypoxia and eutrophication since 1850. Clim Dyn. 53(1–2):1145–1166. doi:10.1007/s00382-018-4296-y.

Mohrholz V. 2018. Major baltic inflow statistics–revised. Front Mar Sci. 5:384. doi:10.3389/fmars.2018.00384.

Murray CJ, Muller-Karulis B, Carstensen J, Conley DJ, Gustafsson B, Andersen JH. 2019. Past, present and future eutrophication status of the Baltic Sea. Front Mar Sci. 6:2. doi:10.3389/fmars.2019.00002.

Nerger L, Hiller W, Schröter J. 2005. A comparison of error subspace Kalman filters. Tellus A: Dyn Meteorol Oceanogr. 57(5):715–735. doi:10.1111/j.1600-0870.2005.00141.x.

Neumann T, Radtke H, Seifert T. 2017. On the importance of Major Baltic Inflows for oxygenation of the central Baltic Sea. J Geophys Res Ocean. 122(2):1090–1101. doi:10.1002/2016JC012525.

Pemberton P, Löptien U, Hordoir R, Höglund A, Schimanke S, Axell L, Haapala J. 2017. Sea-ice evaluation of NEMONordic 1.0: a NEMO–LIM3.6-based ocean–sea-ice model setup for the North Sea and Baltic Sea. Geosci Model Dev. 10:3105–3123. doi:10.5194/gmd-10-3105-2017.

Raudsepp U, She J, Brando VE, Kõuts M, Lagemaa P, Sammartino M, Santoleri R. 2018. Eutrophication and hypoxia in the Baltic Sea. In: Copernicus Marine Service Ocean State Report, Issue 2. J Operat Oceanogr. 11(Supp. 1):s13–s16. doi:10.1080/1755876X.2018.1489208.

Raudsepp U, She J, Brando VE, Santoleri R, Sammartino M, Kõuts M, Uiboupin R, Maljutenko I. 2019. Phytoplankton blooms in the Baltic Sea. In: Copernicus Marine Service Ocean State Report, Issue 3. J Operat Oceanogr. 12 (Supp. 1):s26. doi:10.1080/1755876X.2019.163307530.

Reusch TB, Dierking J, Andersson HC, Bonsdorff E, Carstensen J, Casini M, Czajkowski M, Hasler B, Hinsby K, Hyytiäinen K, et al. 2018. The Baltic Sea as a time machine for the future coastal ocean. Sci Adv. 4(5): eaar8195. doi:10.1126/sciadv.aar8195.

Rolff C, Elfwing T. 2015. Increasing nitrogen limitation in the Bothnian Sea, potentially caused by inflow of phosphate-rich water from the Baltic proper. Ambio. 44(7):601–611. doi:10.1007/s13280-015-0675-3.

Saraiva S, Meier HEM, Andersson H, Höglund A, Dieterich C, Gröger M, Hordoir R, Eilola K. 2019. Baltic Sea ecosystem response to various nutrient load scenarios in present and future climates. Clim Dyn. 52(5-6):3369–3387. doi:10.1007/s00382-018-4330-0.

Savchuk OP. 2018. Large-scale nutrient dynamics in the Baltic Sea, 1970–2016. Front Mar Sci. 5:95. doi:10.3389/fmars.2018.00095.

Vahtera E, Conley DJ, Gustafsson BG, Kuosa H, Pitkänen H, Savchuk OP, Tamminen T, Viitasalo M, Voss M, Wasmund N, Wulff F. 2007. Internal ecosystem feedbacks enhance nitrogen-fixing cyanobacteria blooms and complicate management in the Baltic Sea. Ambio. 186–194. doi:10.1579/0044-7447(2007)36[186:IEFENC]2.0.CO;2.

Viktorsson L, Ekeroth N, Nilsson M, Kononets M, Hall POJ. 2013. Phosphorus recycling in sediments of the central Baltic Sea. Biogeosciences. 10(6):3901. doi:10.5194/bg-10-3901-2013.

Wulff F, Sokolov A, Savchuk O. 2013. Nest–a decision support system for management of the Baltic Sea. A User manual. Stockholm: Baltic Nest Institute, Stockholm University, Sweden.

Section 2.6. Long term changes monitored in two Mediterranean Channels

Astraldi M, Balopoulos S, Candela J, Font J, Gačíc M, Gasparini GP, Manca B, Theocharis A, Tintoré J. 1999. The role of straits and channels in understanding the characteristics of Mediterranean circulation. Prog Oceanogr. 44:65–108.

Ben Ismail S, Sammari C, Gasparini GP, Béranger K, Mouldi B, Aleya L. 2012. Water masses exchanged through the Channel of sicily: evidence for the presence of new water masses on the Tunisian side of the channel. Deep Sea Res I. 63(2012):65–81.

Ben Ismail S, Schroeder K, Sammari C, Gasparini GP, Borghini M, et al. 2014. Interannual variability of water mass properties in the Tunisia-Sicily channel. J Mar Syst. 135:14–28.

Béthoux JP, Gentili B. 1996. The Mediterranean Sea, coastal and deep-sea signatures of climatic and environmental changes. J Marine Syst. 7:383–394.

Béthoux JP, Gentili B, Tailliez D. 1998. Warming and freshwater budget change in the Mediterranean since the 1940s, their possible relation to the greenhouse effect. Geophys Res Lett. 25:1023–1026.

Collins M, Sutherland M, Bouwer L, Cheong S-M, Frölicher T, Jacot Des Combes H, Koll Roxy M, Losada I, McInnes K, Ratter B, et al. 2019. Extremes, abrupt changes and managing risk. In: H.-O. Pörtner, D.C. Roberts, V. Masson-Delmotte, P. Zhai, M. Tignor, E. Poloczanska, K. Mintenbeck, A. Alegría, M. Nicolai, A. Okem, J. Petzold, B. Rama, N.M. Weyer, editor. IPCC special report on the Ocean and Cryosphere in a changing climate. In press.

Cook BI, Anchukaitis KJ, Touchan R, Meko DM, Cook ER. 2016. Spatiotemporal drought variability in the Mediterranean over the last 900 years. J Geophys Res Atmos. 121:2060–2074. DOI:10.1002/2015JD023929.

Desbruyères D, McDonagh EL, King BA. 2017. Global and full-depth Ocean temperature trends during the early twenty-first century from Argo and repeat hydrography. J Clim. 30:1985–1997. doi:10.1175/JCLI-D-16-0396.1.

Fuda J-L, Etiope G, Millot C, Faveli C, Calcara M, Smriglio G, Boschi E. 2002. Warming, salting and origin of the Tyrrhenian deep water. Geophys Res Lett. 29(18):1886. doi:10.1029/2001gl014072.

Krahmann G, Schott F. 1998. Long term increases in Western Mediterranean salinities and temperatures: anthropogenic and climatic sources. Geophys Res Lett. 25(22):4209–4212.

Leaman KD, Schott F. 1991. Hydrographic structure of the convection regime in the Gulf of lions: winter 1987. J Phys Oceanogr. 21:575–598.

Meyssignac B, Boyer T, Zhao Z, Hakuba MZ, Landerer FW, Stammer D, Köhl A, Kato S, L'Ecuyer T, Ablain M, et al. 2019. Measuring global Ocean heat content to estimate the earth energy imbalance. Front Mar Sci. 6:432. doi:10.3389/fmars.2019.00432.

Millot C, Candela J, Fuda J-L, Tber Y. 2006. Large warming and salinification of the Mediterranean outflow due to changes in its composition. Deep-Sea Res. 53:656–666. doi:10.1016/j.dsr.2005.12.017,.

Roether W, Manca BB, Klein B, Bregant D, Gerogopolous D, Beitzel V, Kovacevic V, Luchetta A. 1996. Recent changes in Eastern Mediterranean deep waters. science. New Series. 271(5247):333–335.

Rohling EJ, Bryden H. 1992. Man-induced salinity and temperature increase in the western Mediterranean deep water. J Geophys Res. 97:11191–11198.

Ryabinin V, Barbière J, Haugan P, Kullenberg G, Smith N, McLean C, Troisi A, Fischer A, Aricò S, Aarup T, et al. 2019. The UN decade of Ocean science for sustainable development. Front Mar Sci. 6:470. doi:10.3389/fmars.2019.00470.

Schroeder K, et al. 2016. Abrupt climate shift in the Western Mediterranean Sea. Sci Rep. 6:23009. doi:10.1038/srep23009.

Schroeder K, Chiggiato J, Ben Ismail S, Borghini M, Patti B, Sparnocchia S. 2019. Mediterranean deep and intermediate water mass properties. In: Copernicus Marine service Ocean state report, issue 3. J Operat Oceanogr. 12 (Supp. 1):s18–s21. doi:10.1080/1755876X.2019.1633075.

Schroeder K, Chiggiato J, Josey SA, Borghini M, Aracri S, Sparnocchia S. 2017. Rapid response to climate change in a marginal sea. Sci Rep. 7:4065. doi:10.1038/s41598-017-04455-5.

Schroeder K, Ribotti A, Borghini M, Sorgente R, Perilli A, Gasparini GP. 2008. An extensive western Mediterranean deep water renewal between 2004 and 2006. Geophys Res Lett. 35:L18605. doi:10.1029/2008GL035146.

Skliris N, Marsh R, Josey SA, Good SA, Liu C, Allan RP. 2014. Salinity changes in the World Ocean since 1950 in relation to changing surface freshwater fluxes. Clim Dyn. 43:709–736. doi:10.1007/s00382-014-2131-7.

Sloyan BM, Wilkin J, Hill KL, Chidichimo MP, Cronin MF, Johannessen JA, Karstensen J, Krug M, Lee T, Oka E, et al. 2019. Evolving the physical global Ocean observing system for research and application services through international coordination. Front Mar Sci. 6:449. doi:10.3389/fmars.2019.00449.

Vargas-Yáñez M, García-Martínez MC, Moya F, Balbín R, López-Jurado JL, Serra M, Zunino P, Pascual J, Salat J. 2017. Updating temperature and salinity mean values and trends in the Western Mediterranean: the RADMED project. Prog Oceanogr. 157:27–46. doi:10.1016/j.pocean.2017.09.004.

Vargas-Yáñez M, Moya F, García-Martínez MC, Tel E, Zunino P, Plaza F, Salat J, Pascual J, López-Jurado JL, Serra M. 2010. Climate change in the Western Mediterranean Sea 1900–2008. J Mar Sys. 82:171–176. doi:10.1016/j.jmarsys.2010.04.013.

Section 2.7. Interannual variations of the Black Sea Rim Current intensity

Blatov AS, Bulgakov NP, Ivanov VA, Kosarev AN, Tujilkin VS. 1984. Variability of hydrophysical fields in the Black Sea (in Russian), 240 pp. St. Petersburg, Russia: Gidrometeoizdat.

Capet A, Barth A, Beckers J-M, Grégoire M. 2012. Interannual variability of Black Sea's hydrodynamics and connection to atmospheric patterns. Deep-Sea Res Pt II. 77–80:128–142. doi:10.1016/j.dsr2.2012.04.010.

Fach B. 2015. Modeling the influence of hydrodynamic processes on anchovy distribution and connectivity in the Black Sea. Turkish J Fisher Aquatic Sci. 14:1–2. doi:10.4194/1303-2712-v14_2_06.

Grayek S, Stanev EV, Schulz-Stellenfleth J. 2015. Assessment of the Black Sea observing system. A focus on 2005–2012 Argo campaigns. Ocean Dyn. 65:1665–1684. doi:10.1007/s10236-015-0889-8.

Ivanov VA, Belokopytov VN. 2013. Oceanography of the Black Sea. Editorial publishing board of Marine Hydrophysical Institute, 210 p., Printed by ECOSY-Gidrofizika, Sevastopol.

Korotaev G, Oguz T, Nikiforov A, Koblinsky C. 2003. Seasonal, interannual, and mesoscale variability of the Black Sea upper layer circulation derived from altimeter data. J Geophys Res (Ocean). 108:C4. doi:10. 1029/2002JC001508, 2003.

Korotenko KA. 2018. Effects of mesoscale eddies on behavior of an oil spill resulting from an accidental deepwater blowout in the Black Sea: an assessment of the environmental impacts. PeerJ. 6:e5448. doi:10.7717/peerj.5448. PMID: 30186680; PMCID: PMC6119461.

Kubryakov AA, Bagaev AV, Stanichny SV, Belokopytov VN. 2018. Thermohaline structure, transport and evolution of the Black Sea eddies from hydrological and satellite data. Prog Oceanogr. 167:44–63. doi:10.1016/j.pocean.2018.07.007.

Kubryakov AA, Stanichny SV. 2015. Seasonal and interannual variability of the Black Sea eddies and its dependence on characteristics of the large-scale circulation. Deep-Sea Res Pt I. 97:80–91. doi:10.1016/j.dsr.2014.12.002.

Miladinova S, Macias D, Stips A, Garcia-Gorriz E. 2020. Identifying distribution and accumulation patterns of floating marine debris in the Black Sea. Mar Pollut Bull. doi:10.1016/j.marpolbul.2020.110964.

Miladinova S, Stips A, Macias Moy D, Garcia-Gorriz E. 2020. Pathways and mixing of the north western river waters in the Black Sea estuarine. Coastal Shelf Sci. 236. doi:10.1016/j.ecss.2020.106630

Oguz T, Latun VS, Latif MA, Vladimirov VV, Sur HI, Markov AA, Özsoy E, Kotovshchikov BB, Eremeev VV, Ünlüata Ü. 1993. Circulation in the surface and intermediate layers of the Black Sea. Deep Sea Res Part I. 40(8). doi:10.1016/0967-0637(93)90018-X

Oguz T, La Violette PE, Ünlüata Ü. 1992. The upper layer circulation of the Black Sea: its variability as inferred from hydrographie and satellite observations. J Geophys Res. 97(CS):12569–12584.

Ozsoy E, Unluata U. 1998. The Sea, vol. 11, The Black Sea, edited by A. Robinson and K. Brink. New York: John Wiley.

Poulain PM, Barbanti R, Motyzhev S, Zatsepin A. 2005. Statistical description of the Black Sea near-surface circulation using drifters in 1999–2003. Deep Sea Res Part I. 52(12):2250–2274.

Simonov AI, Altman EN, eds. 1991. Hydrometeorology and hydrochemistry of the USSR seas, vol. IV, The Black Sea, 430 pp. St. Petersburg, Russia: Gidrometeoizdat.

Stanev EV. 1990. On the mechanisms of the Black Sea circulation. Earth Sci Rev. 28:285–319.

Stanev EV. 2005. Understanding Black Sea dynamics: overview of recent numerical modelling. Oceanography. 18(2):52–71.

Stanev EV, Bowman MJ, Peneva EL, Staneva JV. 2003. Control of Black Sea intermediate water mass formation by dynamics and topography: comparison of numerical simulations, surveys and satellite data. J Mar Res. 61:59–99.

Stanev EV, Le Traon P-Y, Peneva EL. 2000. Sea level variations and their dependency on meteorological and hydrological forcing: analysis of altimeter and surface data for the Black Sea. J Geophys Res. 105(C7):17203–17216. doi:10.1029/1999JC900318.

Stanev EV, Peneva E, Chtirkova B. 2019. Climate change and regional ocean water mass disappearance: case of the Black Sea. J Geophys Res: Ocean. 124:4803–4819. doi:10.1029/2019JC015076.

Stanev EV, Peneva EL. 2002. Regional sea level response to global climatic change: Black Sea examples. Glob Planet Change. 32:33–47.

Stanev EV, Ricker M. 2019. The fate of marine litter in semi-enclosed seas: a case study of the Black Sea. Front Mar Sci. doi:10.3389/fmars.2019.00660.

Staneva J, Dietrich DE, Stanev EV, Bowman MJ. 2001. Rim current and coastal eddy mechanisms in an eddy-resolving Black Sea general circulation model. J Mar Syst. 31(1):137–157. doi:10.1016/S0924-7963(01)00050-1.

Zatsepin AG, Ginzburg AI, Kostianoy AG, Kremenetskiy VV, Krivosheya VG, Stanichny SV, Poulain P-M. 2003. Observations of Black Sea mesoscale eddies and associated

horizontal mixing. J Geophys Res. 108:3246. doi:10.1029/2002JC001390.

Zhurbas VM, Zatsepin AG, Grigor'eva YV, Eremeev VN, Kremenetsky VV, Motyzhev SV, Poyarkov SG, Poulain P-M, Stanichny SV, Soloviev DM. 2004. Water circulation and characteristics of currents of different scales in the upper layer of the Black Sea from drifter. Oceanology. 44(1):30–43.

Section 2.8. Climatology and 2019 anomaly of maximum waves in the Mediterranean and Black Seas

Ardhuin F, Rogers E, Babanin A, Filipot J-F, Magne R, Roland A, Van Der Westhuysen A, Queffeulou P, Lefevre J-M, Aouf L, Collard F. 2010. Semi-empirical dissipation source functions for ocean waves: part I, definition, calibration and validation. J Phys Oceanogr. 40:1917–1941. doi:10.1175/2010JPO4324.1.

Arkhipkin VS, Gippius FN, Koltermann KP, Surkova GV. 2014. Wind waves in the Black Sea: results of a hindcast study. Nat Hazards Earth Syst Sci. 14:2883–2897. doi:10.5194/nhess-14-2883-2014.

Barbariol F, Alves J-HGM, Benetazzo A, Bergamasco F, Bertotti L, Carniel S, Cavaleri L, Chao Y, Chawla A, Ricchi A, et al. 2017. Numerical modeling of space-time wave extremes using WAVEWATCH III. Ocean Dyn. 67:535–549. doi:10.1007/s10236-016-1025-0.

Barbariol F, Bidlot J-R, Cavaleri L, Sclavo M, Thomson J, Benetazzo A. 2019. Maximum wave heights from global model reanalysis. Prog Oceanogr. 175:139–160. doi:10.1016/j.pocean.2019.03.009.

Battjes JA, Janssen JPFM. 1978. Energy loss and set-up due to breaking of random waves. In: Proc. 16th Int. Conf. Coastal Engineering, ASCE., pp. 569–587.

Benetazzo A, Barbariol F, Bergamasco F, Sandro C, Sclavo M, Yoo J, Cavaleri L, Kim SS, Bertotti L, Barbariol F, Shim JS. 2017. Space-time extreme wind waves: analysis and prediction of shape and height. Ocean Model. 113:201–216. doi:10.1016/j.ocemod.2017.03.010.

Benetazzo A, Barbariol F, Bergamasco F, Torsello A, Carniel S, Sclavo M. 2015. Observation of extreme sea waves in a space-time ensemble. J Phys Oceanogr. 45:2261–2275. doi:10.1175/JPO-D-15-0017.1.

Benetazzo A, Barbariol F, Davison S. 2020. Short-term/range extreme-value probability distributions of upper bounded space-time maximum Ocean waves. J Mar Sci Eng. 8:679. doi:10.3390/jmse8090679.

Boccotti P. 2000. Wave mechanics for Ocean engineering. New York: Elsevier Science B.V. 496 pp.

Campins J, Genovés A, Picornell MA, Jansà A. 2011. Climatology of Mediterranean cyclones using the ERA-40 dataset. Int J Climatol. 31:1596–1614. doi:10.1002/joc.2183.

Cavaleri L, Abdalla S, Benetazzo A, Bertotti L, Bidlot J-R, Breivik Ø, Carniel S, Jensen RE, Portilla-Yandun J, Rogers WE, et al. 2018. Wave modelling in coastal and inner seas. Prog Oceanogr. 167:164–233. doi:10.1016/j.pocean.2018.03.010.

Cavaleri L, Barbariol F, Benetazzo A. 2020. Wind–wave modeling: where we are. Where to go. J Mar Sci Eng. 8:260. doi:10.3390/jmse8040260.

Cavaleri L, Bertotti L. 2004. Accuracy of the modelled wind and wave fields in enclosed seas. Tellus A. 56:167–175.

Cavaleri L, Bertotti L, Torrisi L, Bitner-Gregersen E, Serio M, Onorato M. 2012. Rogue waves in crossing seas: The Louis Majesty accident. J Geophys Res Ocean. 117:1–8. doi:10.1029/2012JC007923.

Cavaleri L, Sclavo M. 2006. The calibration of wind and wave model data in the Mediterranean Sea. Coast Eng. doi:10.1016/j.coastaleng.2005.12.006.

DNV GL. 2017. DNVGL-RP-C205: environmental conditions and environmental loads. DNV GL Recommended Practice. August:1–259.

ECMWF. 2017a. Twenty-one years of wave forecast verification. ECMWF Newsletter, Number 150. https://www.ecmwf.int/en/newsletter/150/meteorology/twenty-one-years-wave-forecast-verification.

ECMWF. 2017b. Part VII: ECMWF wave model IFS documentation – part VII: ECMWF wave model. IFS Documentation CY43R3. p. 1–99.

ECMWF. 2019. ECMWF severe event catalogue for evaluation of multi-scale prediction of extreme weather. Technical Memo. 851:1–32.

Fanjul EÁ, de Pascual Collar Á, Gómez BP, De Alfonso M, Sotillo MG, Staneva J, Clementi E, Grandi A, Zacharioudaki A, Korres G, et al. 2019. Sea level, sea surface temperature and SWH extreme percentiles: combined analysis from model results and in situ observations. In: Copernicus Marine Service Ocean State Report, Issue 3. J Operat Oceanogr. 12(Supp. 1):s31–s39. doi:10.1080/1755876X.2019.1633075.

Fedele F. 2012. Space–time extremes in short-crested storm seas. J Phys Oceanogr. 42:1601–1615. doi:10.1175/JPO-D-11-0179.1.

Hasselmann K, Barnett TP, Bouws E, Carlson H, Cartwright DE, Enke K, Ewing JA, Gienapp H, Hasselmann DE, Kruseman P, et al. 1973. Measurements of wind-wave growth and swell decay during the Joint North Sea wave project (JONSWAP). Deutches Hydrogr Inst A. 8:1–95.

Kalnay E, Kanamitsu M, Kistler R, Collins W, Deaven D, Gandin L, Iredell M, Saha S, White G, Woollen J, et al. 1996. The NCEP/NCAR 40-year reanalysis project. Bull Am Meteorol Soc. 77:437–471.

Magnusson A, Donelan M, Drennan W. 1999. On estimating extremes in an evolving wave field. Coast Eng. 36:147–163. doi:10.1016/S0378-3839(99)00004-6.

Menendez M, García-Díez M, Fita L, Fernández J, Méndez FJ, Gutiérrez JM. 2014. High-resolution sea wind hindcasts over the Mediterranean area. Clim Dyn. 42:1857–1872. doi:10.1007/s00382-013-1912-8.

Ochi, M.K., 1998. Ocean waves, Ocean waves: the stochastic approach. Cambridge: Cambridge University Press, 319 pp. doi:10.1017/CBO9780511529559.

Ribal A, Young IR. 2019. 33 years of globally calibrated wave height and wind speed data based on altimeter observations. Sci Data. 6:77. doi:10.1038/s41597-019-0083-9.

Sartini L, Besio G, Cassola F. 2017. Spatio-temporal modelling of extreme wave heights in the Mediterranean Sea. Ocean Model. 117:52–69. doi:10.1016/j.ocemod.2017.07.001.

Sizov AA, Chekhlan AE. 2010. Hydrometeorological characteristics of the Black-Sea region in the years with extreme values of the Sargasso–Black-Sea index. Phys Oceanogr. 20:99–108. doi:10.1007/s11110-010-9070-6.

Soukissian T, Karathanasi F, Axaopoulos P, Voukouvalas E, Kotroni V. 2018. Offshore wind climate analysis and variability in the Mediterranean Sea. Int J Climatol. 38:384–402. doi:10.1002/joc.5182.

Tolman, H.L. and the WAVEWATCH III® Development Group. 2014. User manual and system documentation of WAVEWATCH III version 4.18. Technical note 316, NOAA/NWS/ NCEP/MMAB, 282 pp. +Appendices.

Trigo IF, Bigg GR, Davies TD. 2002. Climatology of cyclogenesis mechanisms in the Mediterranean. Mon Wea Rev. 130:549–569.

Vagenas C, Anagnostopoulou C, Tolika K. 2017. Climatic study of the marine surface wind field over the Greek Seas with the use of a high resolution RCM focusing on extreme winds. Climate. 5:29. doi:10.3390/cli5020029.

Visbeck MH, Hurrell JW, Polvani L, Cullen HM. 2001. The North Atlantic Oscillation: past, present, and future. Proc Natl Acad Sci USA. 98:12876–12877.

von Schuckmann K, Le Traon P-Y, Smith N, Pascual A, Brasseur P, Fennel K, Djavidnia S, Aaboe S, Fanjul EA, Autret E, et al. 2018. Copernicus marine service ocean state report. J Oper Oceanogr. 11(sup1):S1–S142. DOI:10.1080/1755876X.2018.1489208.

Young IR, Sanina E, Babanin AV. 2017. Calibration and cross validation of a global wind and wave database of altimeter, radiometer, and scatterometer measurements. J Atmos Oceanic Technol. 34(6):1285–1306.

Section 2.9. Strong positive Indian Ocean Dipole events over the period 1993 to 2019

Adler RF, Huffman GJ, Chang A, Ferraro R, Xie P, Janowiak J, Rudolf B, Schneider U, Curtis S, Bolvin D, et al. 2003.: The version 2 global precipitation climatology project (GPCP) monthly precipitation analysis (1979-present). J Hydrometeor. 4:1147–1167. doi:10.1175/1525-7541(2003)004<1147:TVGPCP>2.0.CO;2.

Ashok K, Guan Z, Yamagata T. 2001. Impact of the Indian Ocean Dipole on the relationship between the Indian Monsoon Rainfall and ENSO. GRL. 28(23):4499–4502. doi:10.1029/2001GL013294.

Ashok K, Guan Z, Yamagata T. 2003. Influence of the Indian Ocean Dipole on the Australian winter rainfall. GRL. 30 (15):1821. doi:10.1029/2003GL017926.

Cai W, Cowan T, Raupach M. 2009. Positive Indian Ocean Dipole events precondition southeast Australia bushfires. Geophys Res Lett. 36:L19710. doi:10.1029/2009GL039902.

Cai W, Santoso A, Wang G, Weller E, Wu L, Ashok K, Masumoto Y, Yamagata T. 2014. Increased frequency of extreme Indian Ocean Dipole events due to greenhouse warming. Nature. 510:254–258. doi:10.1038/nature13327.

Cai W, Wang G, Gan B, Wu L, Santoso A, Lin X, Chen Z, Jia F, Yamagata T. 2018. Stabilised frequency of extreme positive Indian Ocean Dipole under 1.5°C warming. Nat Commun. 9:1419. doi:10.1038/s41467-018-03789-6.

CSIRO. 2020. The 2019–20 bushfires: a CSIRO explainer. Available from: https://www.csiro.au/~/media/Environment/BushfireFactsheet060220.pdf.

Deepa JS, Gnanaseelan C, Kakatkar R, Parekh A, Chowdary JS. 2018. The interannual sea level variability in the Indian Ocean as simulated by an ocean general circulation model. Int J Climatol. 38:1132–1144. doi:10.1002/joc.5228.

Du Y, Zhang Y, Zhang L-Y, Tozuka T, Ng B, Cai W. 2020. Thermocline warming induced extreme Indian Ocean dipole in 2019. Geophys Res Lett. 47:e2020GL090079. doi:10.1029/2020GL090079.

Duan J, Li Y, Zhang L, Wang F. 2020. Impacts of the Indian Ocean Dipole on Sea level and Gyre circulation of the Western tropical Pacific Ocean. J Climate. 33:4207–4228. doi:10.1175/JCLI-D-19-0782.1.

FAO, United Nations, Desert Locusts. 2020. https://www.fao.org/locusts/en/. Last access: 26 May 2020.

Good S, Fiedler E, Mao C, Martin MJ, Maycock A, Reid R, Roberts-Jones J, Searle T, Waters J, While J, Worsfold M. 2020. The current configuration of the OSTIA system for operational production of foundation sea surface temperature and ice concentration analyses. Remote Sens. 12:720. doi:10.3390/rs12040720.

Lu B, Ren H, Scaife AA, Wu J, Dunstone N, Smith D, Wan J, Eade R, MacLaclan C, Gordon M. 2018. An extreme negative Indian Ocean Dipole event in 2016: dynamics and predictability. Clim Dyn. 51:89–100. doi:10.1007/s00382-017-3908-2.

Lu B, Ren H-L. 2020. What caused the extreme Indian Ocean Dipole event in 2019? Geophys Res Lett. 47: e2020GL087768. doi:10.1029/2020GL087768.

Merchant CJ, Embury O, Bulgin CE, Block T, Corlett GK, Fiedler E, Good SA, Mittaz J, Rayner NA, Berry D, et al. 2019. Satellite-based time-series of sea-surface temperature since 1981 for climate applications. Sci Data. 6:223. doi:10.1038/s41597-019-0236-x.

OCHA, Eastern Africa Region: regional floods and Locust Outbreak Snapshot. 2020. [cited 2020 May 26] Available from: https://reliefweb.int/sites/reliefweb.int/files/resources/ROSEA_20200117_EasternAfrica_Flood_Snapshot_Jan2020_def.pdf

Saji NH, Goswami BN, Vinayachandran PN, Yamagata T. 1999. A dipole mode in the tropical Indian Ocean. Nature. 401:360–363. doi:10.1038/43854.

Trenberth, Kevin, National Center for Atmospheric Research Staff, eds. Last modified 21 Jan 2020. "The Climate Data Guide: Nino SST Indices (Nino 1 + 2, 3, 3.4, 4; ONI and TNI)." Available from: https://climatedataguide.ucar.edu/climate-data/nino-sst-indices-nino-12-3-34-4-oni-and-tni

Tziperman E, Cane MA, Zebiak SE, Xue Y, Blumenthal B. 1998. Locking of El Niño's peak time to the end of the calendar year in the delayed oscillator picture of ENSO. J Climate. 11:2191–2199. doi:10.1175/1520-0442(1998)011<2191:LOENOS>2.0.CO;2.

Wang G, Cai W, Yang K, Santoso A, Yamagata T. 2020. A unique feature of the 2019 extreme positive Indian Ocean Dipole event. Geophys Res Lett. 47:e2020GL088615. doi:10.1029/2020GL088615.

Xie S, Zhou Z. 2017. Seasonal modulations of El Niño–related atmospheric variability: Indo–Western Pacific Ocean feedback. J Climate. 30:3461–3472. doi:10.1175/JCLI-D-16-0713.1.

Yang K, Cai W, Huang G, Wang G, Ng B, Li S. 2020. Oceanic processes in ocean temperature products key to a realistic presentation of positive Indian Ocean Dipole nonlinearity. Geophys Res Lett. 46:e2020GL089396. doi:10.1029/2020GL089396.

Yang Y, Xie S, Wu L, Kosaka Y, Lau N, Vecchi GA. 2015. Seasonality and predictability of the Indian Ocean Dipole mode: ENSO forcing and internal variability. J Climate. 28:8021–8036. doi:10.1175/JCLI-D-15-0078.1.

CMEMS OSR5 – Chapter 3

Table of content

Section 3.1. The chlorophyll-a gradient as primary Earth observation index of marine ecosystem feeding capacity

Authors: Jean-Noël Druon, Antoine Mangin, Pierre Hélaouët, Andreas Palialexis

Statement of main outcome: An efficient ocean management for fisheries requires accurate data over large spatial scales. The horizontal gradient of chlorophyll-a (and the derived mesozooplankton habitat) exemplifies a plankton-to-fish index in support of a sustainable ocean management that targets fisheries and ecosystem productivity. The gradient of chlorophyll-a, which expresses the productivity of fronts, showed to sustain the development of mesozooplankton and to attract predators (primarily fish) when the activity period is longer than three to four weeks (Druon et al. 2019). Only productivity features active from weeks to months, such as within eddies or semi-permanent currents, can contribute to the 10–20% of the total phytoplankton productivity that is transferred along marine food chains in the global ocean. Our results highlight that the level of chlorophyll-a gradient occurrence at global scale (area-averaged), which is associated to the mesozooplankton feeding habitat and fish productivity, is maintained over the period 2003–2019 despite the warming of the surface ocean. This suggests that the surface ocean mixing – likely of atmospheric origin – globally tends to compensate for the stabilising effect of thermal stratification. Regional variabilities, however, are highly contrasted with positive and negative trends.

Daily values of chlorophyll-a gradient can be computed at global scale for the last two decades up to near real-time. This is critical to improve our understanding of the plankton-to-fish dynamics, especially under the current effects of climate change, and to build observation-based operational products that will inform the future spatial and dynamic ocean management. The computation of such gradient requires a specific expertise in ocean colour, making them difficult to obtain for non-specialists. Their operational availability could therefore offer a critical benefit to marine biologists and ecosystem modellers and, in turn, to regional fisheries management and Authorities facing overexploitation and the effects of climate change. International marine policies will ultimately be efficiently supported by the use of chlorophyll-a gradient as a direct, observation-based, biological variable monitoring the marine ecosystem productivity across a wide range of spatial and temporal scales.

Products used:

Ref. No.	Product name and type	Documentation
3.1.1	OCEANCOLOUR_MED_CHL_L3_NRT_OBSERVATIONS_009_040 Single sensor MED CHL L3 1 km Sentinel 3 - OLCI	PUM: http://marine.copernicus.eu/documents/PUM/CMEMS-OC-PUM-009-ALL.pdf QUID: http://marine.copernicus.eu/documents/QUID/CMEMS-OC-QUID-009-038to045-071-073-078-079-095-096.pdf
3.1.2	OCEANCOLOUR_BS_CHL_L4_NRT_OBSERVATIONS_009_045 Single sensor BLACK SEA CHL L3 1 km Sentinel 3 - OLCI	PUM: http://marine.copernicus.eu/documents/PUM/CMEMS-OC-PUM-009-ALL.pdf

(*Continued*)

Supplemental data for this article can be accessed https://doi.org/10.1080/1755876X.2021.1946240

Continued.

Ref. No.	Product name and type	Documentation
		QUID: http://marine.copernicus.eu/documents/QUID/CMEMS-OC-QUID-009-038to045-071-073-078-079-095-096.pdf
3.1.3	OCEANCOLOUR GLOBAL CHL L3 4 km NASA MODIS-Aqua and 9 km SeaWiFS	https://oceancolor.gsfc.nasa.gov/l3/
3.1.4	Favourable feeding habitat of Mesozooplankton in the North Atlantic Ocean – monthly 2003–2018 (frequency of occurence, %)	https://data.jrc.ec.europa.eu/dataset/ac456798-24d1-4d76-aeca-fcb3eb0c7e73

3.1.1. Introduction

Sea surface chlorophyll-a is the only marine biological variable that is quantified from space. Ocean colour sensors allow for frequent observations of this variable and thus offer a unique proxy of phytoplankton dynamics (Dutkiewicz et al. 2019). While satellite-derived chlorophyll-a renders possible to monitor the surface ocean primary productivity (chapter 3.2. in OSR4; von Schuckmann et al. 2020), it remains a comparatively weak proxy of the productivity transferred along marine foodwebs, which starts with zooplankton, since about 80% (upwelling) to 90% (oceanic waters) of the primary production is remineralised (Raymont 1980; Libralato et al. 2008).

High levels of horizontal gradient of chlorophyll-a, or productivity fronts, result from the resurgence of subsurface nutrient-rich waters such as in upwellings, at the edge or in the core part of eddies or along a semi-permanent current (e.g. Brandini et al. 2000; Kouketsu et al. 2016). Productivity fronts were shown to attract fish and top predators (Polovina et al. 2001; Valavanis et al. 2004; Druon et al. 2012, 2015, 2016, 2017; Briscoe et al. 2017; Panigada et al. 2017) as being active long enough (from weeks to months) to allow the development of mesozooplankton populations (Druon et al. 2019). These productivity fronts, mostly efficient at mesoscale for zooplankton production, represent a spatial proxy of food availability for fish populations and feeding hotspot for the pelagic ecosystem when associated to the active aggregation of highly mobile predators (e.g. for bluefin tuna in Druon et al. 2016; of fin whale in Panigada et al. 2017). Productivity frontal features exist at smaller scales when their resilience allows phytoplankton development (few days), but are generally inefficient to transfer the energy to medium-size zooplankton (mesozooplankton, 0.2–20 mm) that requires several weeks of continuous primary production to develop (Figure 3.1.1).

Ocean colour remote sensing is central to the detection of productivity fronts because not all frontal features detected by satellite-derived temperature do correspond to chlorophyll-a fronts, and vice versa, due to a variable cross-front contrast for sea surface temperature and chlorophyll-a (Kahru et al. 2012). Furthermore, thermal fronts are often masked during the summer due to increased vertical stratification near the surface, whereas chlorophyll-a fronts are less affected (Pegau et al. 2002; Takahashi and Kawamura 2005).

The habitat analyses suggest that the horizontal gradient of chlorophyll-a is a better proxy than chlorophyll-a when seeking the spatial distribution of mesozooplankton and marine predators. We emphasise in this paper that, while this variable requires an advanced knowledge in ocean colour limitations, its availability would greatly help the marine biologist community to produce robust, observation-based, plankton-to-fish indicators from local to global scale in nowcast and hindcast modelling, such as input data to develop more robust full ecosystem models (Hernvann et al. 2020).

3.1.2. Methods

The meso-scale frontal features of productivity identified in the mesozooplankton habitat study (product 3.1.4 for the North Atlantic in the product table) were detected daily by computing the horizontal gradient of chlorophyll-a from ocean colour sensors at 1/24 degree resolution from MODIS-Aqua and 1/12 degree from SeaWiFS sensors (CI-Hu algorithm reprocessed in January 2018, product 3.1.3 in the product table). This algorithm employs the standard *OC4v6* algorithm merged with the colour index (*CI*) of Hu et al. (2012) for the relatively clear water. The empirical relationship of Pitarch et al. (2016) was used in the Baltic Sea to correct from the chlorophyll-a overestimation generated by the high content of dissolved organic matter. Daily chlorophyll-a data are pre-processed (i) to limit the loss of coverage after the horizontal gradient computation due to scattered cloud coverage and associated missing data and (ii) to filter out eventual stripes from the optical sensor. Iterations of a median filter are used to recover missing data on the edge of the valid data, while a Gaussian-smoothing procedure allows for removing potential sensor stripes (Druon et al. 2012). Chlorophyll-a gradient (*gradCHL*) was derived from the daily chlorophyll-a data using a bi-directional gradient norm over a three by three grid-cell window as follows:

$$gradCHL = \sqrt{Dx^2 + Dy^2}$$

with *Dx* and *Dy*, the longitudinal and latitudinal chlorophyll-a horizontal gradient, respectively, corrected by the pixel size in km. Small and large chlorophyll-a fronts refer to variable levels of chlorophyll-a gradient values. Compared to the central front location, the gradient computation allows for quantifying how the front can potentially support high trophic levels since chlorophyll-a gradient values were linked to the mesozooplankton biomass (the higher gradient, the higher biomass; biomass estimated from the Continuous Plankton Recorder based on 131 taxa, Druon et al. 2019).

The chlorophyll-a gradient computation can only be performed using single sensor chlorophyll-a data as merged data from different sensors inevitably lead to gradients generated at the interface between data of different sensors. In the perspective of increasing coverage area, the merging of gradients from various sensors likely presents less difference than the gradient obtained from the merging of chlorophyll-a products as satellite imagery is, by nature, efficient in detecting horizontal contrasts (relative levels) compared to absolute levels. Note, however, that chlorophyll-a gradients are sensitive to the spatial resolution (the lower resolution, the lower chlorophyll-a gradient value) so that the unit is to be expressed in mg chlorophyll-a.m^{-3}.km^{-1}. A resolution of 1/24 degrees showed to capture the main productivity features of importance for the pelagic ecosystem (see habitat studies herein).

The mesozooplankton habitat is a daily value between 0 and 1, directly derived from the log-transformed value of the chlorophyll-a gradients after a close relationship was found with the mesozooplankton biomass (Druon et al. 2019). The habitat formulation is computed on a daily basis in each grid cell using (i) the horizontal gradient of chlorophyll-a (rescaled values from 0 to 1) and (ii) a suitable range of chlorophyll-a content (value of 0 or 1). The range of suitable chlorophyll-a and minimum value of gradient (*gradCHLmin*) suitable for mesozoopankton are derived using the same cluster analysis as in Druon et al. (2019) but applied to the 2018 reprocessed chlorophyll-a data by NASA. The maximum slope of the cumulated distribution of chlorophyll-a gradient at the location of mesozooplankton presence is used to define the gradient where the daily habitat function reaches the maximum value of 1 (intermediate gradient value, *gradCHLint*). The mesozooplankton habitat is therefore bounded, at its lower limit, by the minimum size of influential productivity fronts and, at its upper limit, by a maximum chlorophyll-a content representing a potential limit by eutrophication. Continuous daily values of habitat between 0 and 1 are applied for increasing chlorophyll-a gradient levels (linear increase in log-scale) from *gradCHLmin* to *gradCHLint*.

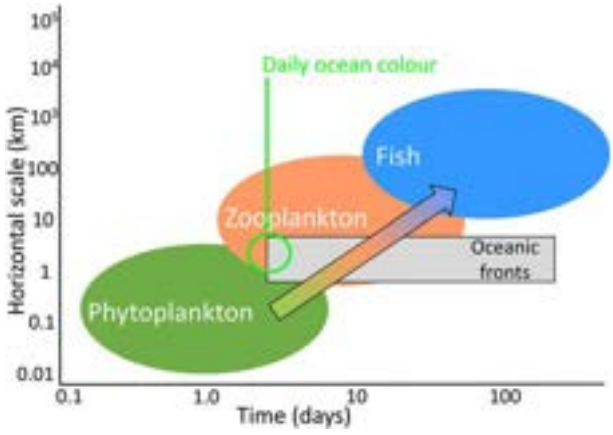

Figure 3.1.1. Schematic representation of time and space scales involved in the development of phytoplankton, zooplankton and fish. Productive fronts, which are areas of continuous primary production for weeks to months, are efficient vectors of energy from phytoplankton to medium-size zooplankton and appropriately tracked by daily ocean colour. This defines a high ecotrophic efficiency, i.e. a high proportion of the net annual production consumed by higher trophic levels.

Even if we only present here the results of chlorophyll-a gradients and mesozooplankton habitat from MODIS-Aqua (4 km, since July 2002), other sensor data are available for various periods and resolutions with an increasing optical quality with time. The available sensors currently are CZCS (9 or 4 km, October 1978–June 1986 – not continuous), OCTS (9 or 4 km, November 1996–June 1997), SeaWiFS (4 or 9 km, 1997–2010), MERIS (4 or 1 km, 2002–2012), VIIRS (since 2012) and Sentinel 3a and 3b since February 2016 and April 2018 respectively (1 km, 300 m). The herein multiannual global product of chlorophyll-a gradient is at 4 km resolution and result from daily estimates (daily to monthly to annual). As mentioned above, and due to the imagery nature of this satellite observation, the merging of chlorophyll-a gradients from different sensors at the same spatial resolution would increase daily spatial coverage. Gradient products derived from high-resolution chlorophyll-a data, starting with 300 m, may interact with human-induced activities such as the track of large ships, the latter being able to mix the upper productive ocean layer over a sufficient spatial scale.

3.1.3. Results and discussion

Figure 3.1.2 describes an example of the two steps of daily chlorophyll-a gradient computation from the original chlorophyll-a data (panel a) with (1) a median filter

followed by a Gaussian smoothing (panel b) and (2) a bi-directional gradient norm over a 3 by 3 grid-cell window (panel c) for 18 July 2019 in the western Mediterranean Sea. The median filter and Gaussian smoothing allows for a reasonable interpolation at the edge of existing data with a chlorophyll-a recovery mean relative error below 5% (S.I. of Druon et al. 2012). This process allows for a substantial recovery of the original data (about +11% in the example of Figure 3.1.2) depending on data and the associated cloud distribution. The relative gain in coverage is much higher after the gradient calculation (+22% in the presented example). The use of the median filter and Gaussian smoothing procedure is therefore particularly relevant in habitat coverage in cases of dappled cloud occlusions. This procedure also removes the sensor stripes that may occur in specific optical configurations (zoomed area in panel a, Figure 3.1.2) and are substantially amplified by the gradient computation (panels d and e, Figure 3.1.2). While filtering out extremely low levels of chlorophyll-a gradient, this smoothing procedure however maintains the smallest productivity features of influence to mesozooplankton as attested by the relationship with the mesozooplankton biomass (Figure 3.1.3, pink line on panel a) towards low levels.

Environments where productivity may mostly occur in the subsurface layer, and consequently not seen by satellite optical sensors, are generally considered to be substantially less productive than when occurring near the surface because of the exponential decrease of light with increasing depth. Areas where a deep chlorophyll-a maximum occurs may thus characterise a quantitatively low source for mesozooplankton feeding, albeit locally important.

Another potential limitation of the approach is the presence of suspended inorganic matter and coloured dissolved organic matter (Gohin et al. 2002) which may bias the chlorophyll-a estimation in river-influenced coastal waters. This bias mostly occurs near river plumes and in the Baltic Sea where dissolved organic matter content is high. In these areas, this bias can be overcome by using a mixed chlorophyll-a algorithm (OC5 and CI-Hu) as adopted by the CMEMS GlobColour product (Garnesson et al. 2019). The empirical chlorophyll-a correction presently used in the Baltic Sea (Pitarch et al. 2016) is a first-order correction leading to a symmetric and zero-centred error distribution. High levels of the chlorophyll-a (above 10.0 $mg.m^{-3}$, see Table 3.1.1) resulting of an overestimation from above-mentioned particulate or dissolved matter or corresponding to potentially eutrophicated areas are set to a zero value for the mesozooplankton habitat.

Table 3.1.1. Habitat parameterisation used to define the environmental envelope of mesozooplankton in the North Atlantic Ocean, where CHL and gradCHL are the sea surface chlorophyll-a content and horizontal gradient from the MODIS-Aqua sensor, respectively (CHL data reprocessed by NASA in 2018).

Parameter values for mesozooplankton suitable habitat	Minimum value	Intermediate value	Maximum value
CHL ($mg.m^{-3}$)	0.089*	N/A	10.0*
gradCHL ($mg\ m^{-3}.km^{-1}$)	0.0002*	0.00876**	N/A

*Values identified using the same type of cluster analysis as in Druon et al. (2019).
**See also Figure 3.1.3.

The habitat products using the 2018 reprocessed chlorophyll-a data shows a direct link with the relative biomass of mesozooplankton for relatively low levels of chlorophyll-a gradient (between *gradCHLmin* and *gradCHLint*, Figure 3.1.3, panel a) similarly to Druon et al. (2019). This link suggests that relatively small productivity fronts are less resilient than larger productive features as a minimum of three to four weeks of continuous primary production is needed to reach high mesozooplankton biomass levels (Druon et al. 2019). These small fronts may correspond to productivity features in development that host a growing mesozooplankton population or to dying features with decreasing plankton populations. The relatively lower than expected biomass values of mesozooplankton at high levels of chlorophyll-a gradient (high habitat values near and above *gradCHLint*, Figure 3.1.3, panel a) correspond to large and resilient productivity fronts hosting a well-developed mesozooplankton population although likely impacted by predation from higher trophic level organisms. The highest *gradCHL* levels matching the maximum mesozooplankton biomass may relate to the less frequent highly productive fronts that are uncontrolled by predation. The panel b of Figure 3.1.3 highlights an example of a daily distribution of mesozooplankton habitat (continuity of Figure 3.1.2(c)) resulting of small (habitat value about between 0.15 and 0.75) and large (habitat value above 0.75) productivity fronts. These areas respectively correspond to mostly open waters and either river-influenced coastal areas or the Alboran Sea that is influenced by the Atlantic surface waters.

The panel a of Figure 3.1.4 describes the latitudinal dynamics of mesozooplankton in the North Atlantic, with peaks of biomass from May to June-July (south to north) and seasonal duration of relatively high biomass levels from three (30–40°N) to seven months (40–50°N), and five to four months in the northern areas

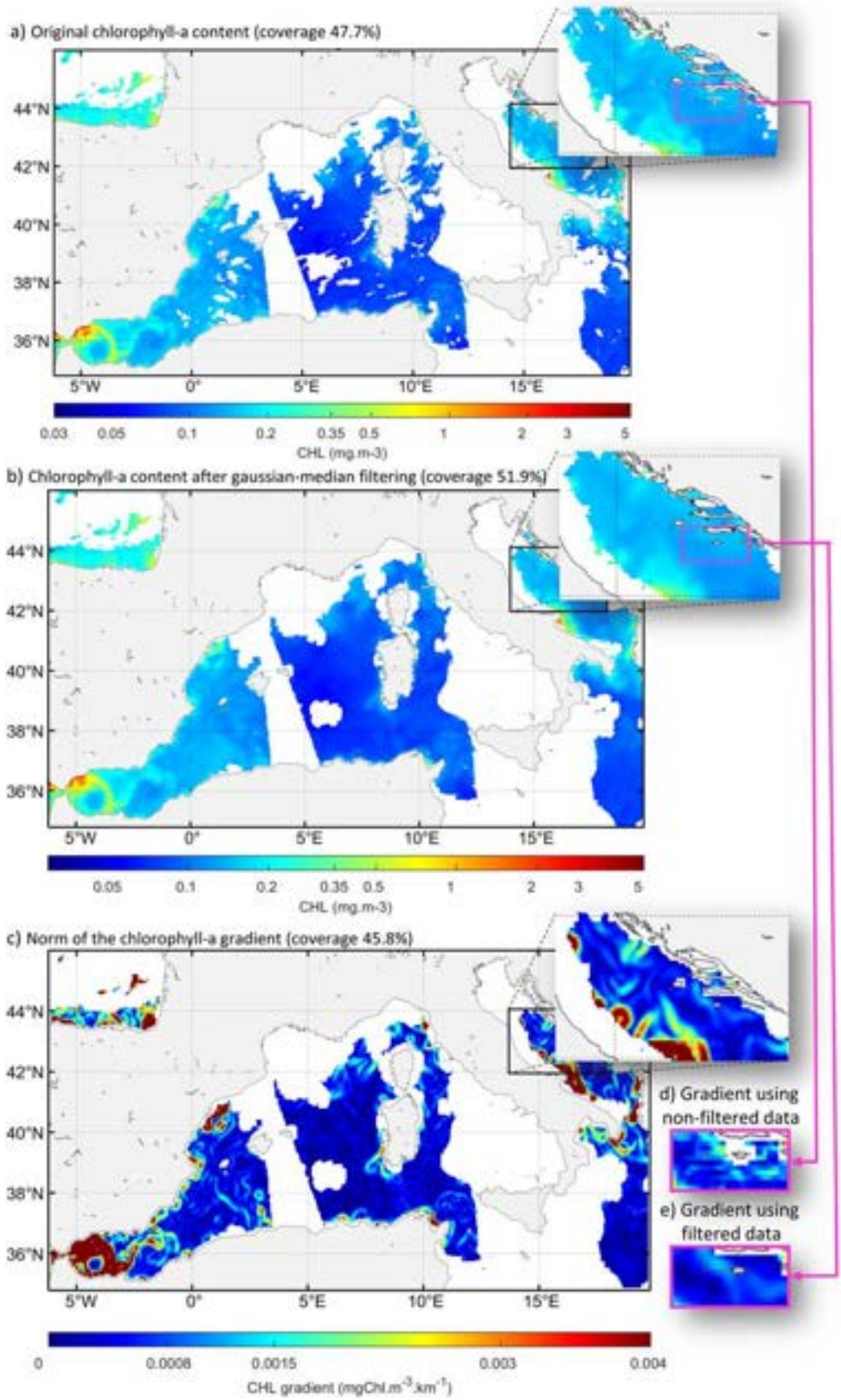

Figure 3.1.2. Example of daily chlorophyll-a processing from MODIS-Aqua sensor (product 3.1.3 in the product table) on 18 July 2019 in the western Mediterranean Sea: (a) original data, (b) data after median filter and Gaussian smoothing, (c) norm of horizontal gradient of chlorophyll-a, (d) zoomed area of the gradient norm using non-filtered data and (e) zoomed area of the gradient norm using filtered data. Note the reduced loss of coverage after the gradient computation (c, 45.8%) compared to the original data (a, 47.7%) due to the median interpolation at the edge (b, 51.9%). Slight sensor stripes on the original data (zoomed area in a) are removed after the Gaussian smoothing (zoomed area in b and e) and would be kept otherwise (d).

(50–60°N and 60–70°N respectively). Peak levels of biomass in the northern latitudes are however about three-fold higher (0.17 vs 0.06 in relative units). This simple, algorithm-type, habitat model generally predicts accurately the suitable conditions for the development of mesozooplankton as shown by the distribution of habitat at the location and time of observed biomass (Figure 3.1.4). The lower habitat level in August and September in the latitude range of 40–50°N may result of the presence of a relatively shallow subsurface chlorophyll-a maximum, which is not sensed by ocean colour sensors. Higher habitat levels, such as in August and September in the latitude range of 60–70°N and in winter in the latitude range of 30–40°N, are likely caused by both the important reduction of day length (see habitat weighted by day length in relative values, dashed line) and predation, which are not accounted for in the habitat estimate. The habitat weighted by day length refers to a notion of daily productivity (daily identification of a chlorophyll-a front multiplied by the relative time of daily activity). While the habitat weighted by day length slightly better correlates with the mesozooplankton biomass (Spearman's r of 0.935, $p \approx 0$, and 0.89, $p \approx 0$, respectively), we decided to keep the notion of daily habitat for mesozooplankton and to develop in parallel a more generic index of Ocean Productivity available to Fish (OPFish, first description in Druon 2017). The OPFish index, based on chlorophyll-a gradient preferences for different trophic levels and on day length, is being successfully compared to spatial fisheries data in the European Seas (Druon et al., 2021). Both the mesozooplankton habitat and OPFish index are different notions (habitat and production, respectively) which can be useful metrics depending on the application.

The global distribution of mesozooplankton habitat from 2003 to 2019 is an extrapolation from the North Atlantic analysis, which covered mesozooplankton taxa from tropical to subpolar latitudes (Druon et al. 2019). This global distribution shows large spatial variability, especially between maximum levels in upwelling areas and minimum levels in the centre of tropical gyres (Figure 3.1.5, panel a). The map of absolute trend informs on contrasting regional variations under the current effects of climate change (e.g. negative trend globally in the tropical Pacific and positive trend in the North Atlantic, Figure 3.1.5, panel b). The maximum levels of mean regional trend over the period 2003–2019 can reach up to about ±1%/year in mesozooplankton habitat frequency unit (% of time occurrence). Therefore, these maximum trend levels represents about ±17% difference in absolute unit over this 17-year period in the global mean map (Figure 3.1.5, panel a). The short time-series of global annual means (Figure 3.1.5, panel c) displays relatively limited oscillations (between 40 and 42.7% in absolute units), which appears to be periodic (6–8 years).

However, the most striking result is the absence of global mean trend observed from the regional trend map (and slightly positive trend from the global annual means, Figure 3.1.5(c)) of chlorophyll-a gradient occurrence despite the surface ocean warming (OSR3; von Schuckmann et al. 2019). This reveals that the turbulent-driven hydrodynamics – likely of atmospheric origin – tends to compensate for the effect of thermal stratification (see discussion in Druon et al. 2019). In turn, this means that the current global marine productivity useful for the upper trophic levels is likely to be maintained. This does not preclude from a negative trend in the future as the warming continues (Allen et al. 2019) considering the complex feedbacks at the ocean-atmosphere interface. Regionally, however, spatial contrasts of changes in mesozooplankton habitat and fish potential feeding do occur and, if decreasing, it will constrain the available resource and force local populations to adapt.

3.1.4. Conclusions

The daily horizontal gradient of chlorophyll-a, and the associated mesozooplankton habitat, is a prevailing proxy of primary productivity available to zooplankton and upper trophic levels because productivity fronts are active long enough to sustain zooplankton development (at least three to four weeks). The chlorophyll-a gradient and associated mesozooplankton feeding habitat provides appropriate information on the useful fraction (10–20%) of the primary productivity transferred along marine food chains and primarily in the pelagic ecosystems. The distribution of the mesozooplankton habitat over the period 2003–2019 highlights (1) a stable global productivity available to high trophic levels despite the surface ocean warming and (2) substantial positive and negative regional trends. This is critical information for regional fisheries management and food security of coastal communities as regards to their adaptation to climate change. Similarly, this information is essential for adapting the effort of industrial fisheries to local fish production and evolving towards sustainable fishing.

The community of marine sciences can highly benefit from the availability of chlorophyll-a gradient to derive advanced analysis in ecosystem functioning and fisheries, including hindcast in the past two decades and nowcast for dynamic ocean management of utmost

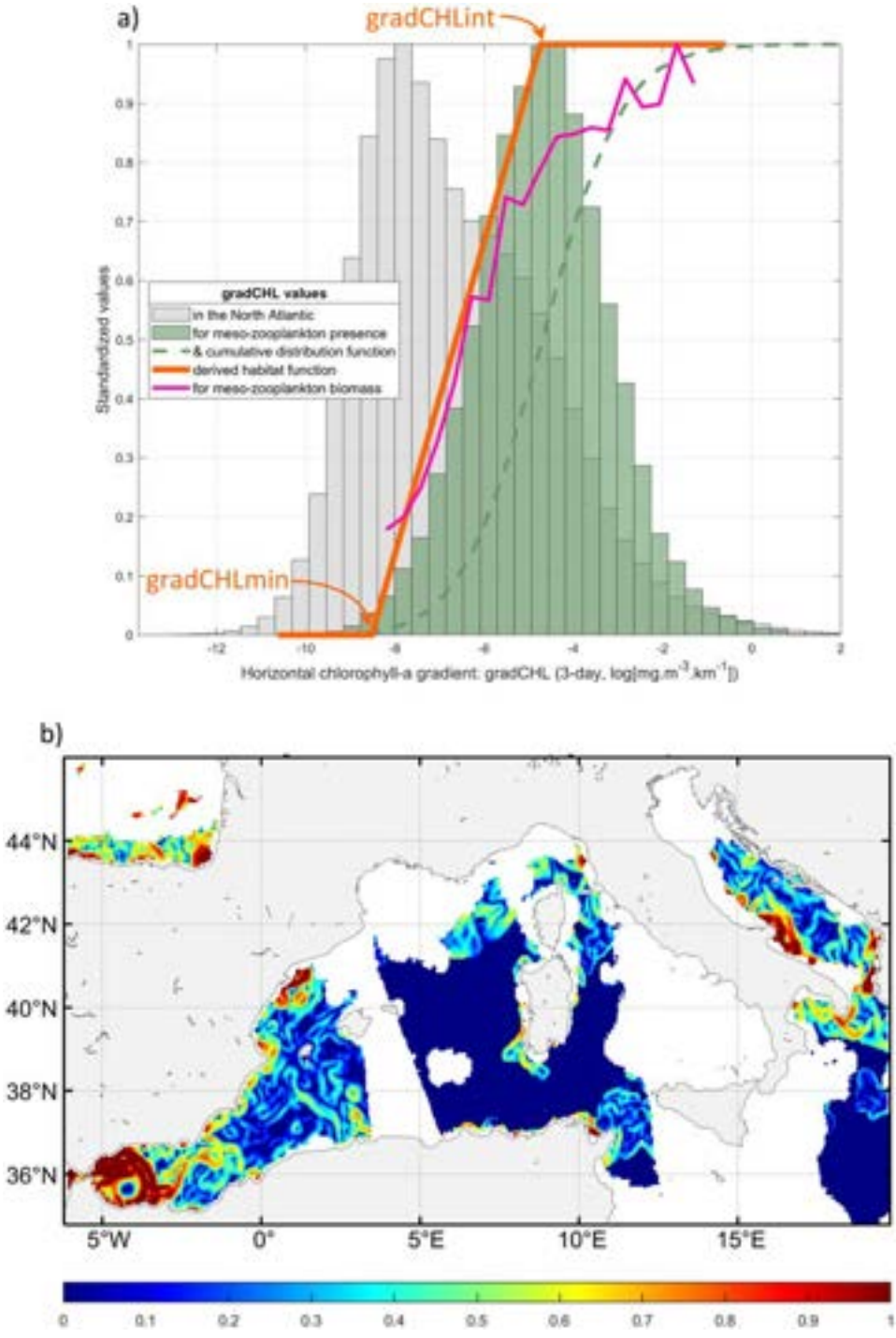

Figure 3.1.3. (a) Standardised frequencies of relative units of chlorophyll-a horizontal gradient (gradCHL; log-transformed) for the whole North Atlantic (background grey histogram) and only for locations where mesozooplankton are present (green histogram, 3-day mean values around the observation day were chosen to increase the number of matching points). The maximum slope of the cumulative distribution of mesozooplankton presence (green dashed line) was used to define the daily habitat linear function (orange line). The mean mesozooplankton biomass (pink line, relative unit) is superimposed. Compared to Druon et al. (2019), this plot represents the latest calibration using the chlorophyll-a data reprocessed by NASA in 2018 (gradCHLmin = 0.0002 mg m^{-3} km^{-1}, gradCHLint = 0.00876 mg m^{-3} km^{-1}). (b) Example of daily mesozooplankton habitat for 18 July 2019 in the western Mediterranean Sea derived from the chlorophyll-a gradient (continuity of Figure 3.1.2c) (also including 0.089 < CHL < 10.0 mg.m^{-3}). See also Table 3.1.1.

importance in times of climate change. The products resulting of the use of the chlorophyll-a gradient and mesozooplankton habitat will provide great support to policies such as the EU Common Fisheries Policy (European Commission 2013) (e.g. spatial fishing capacities), the Marine Strategy Framework Directive

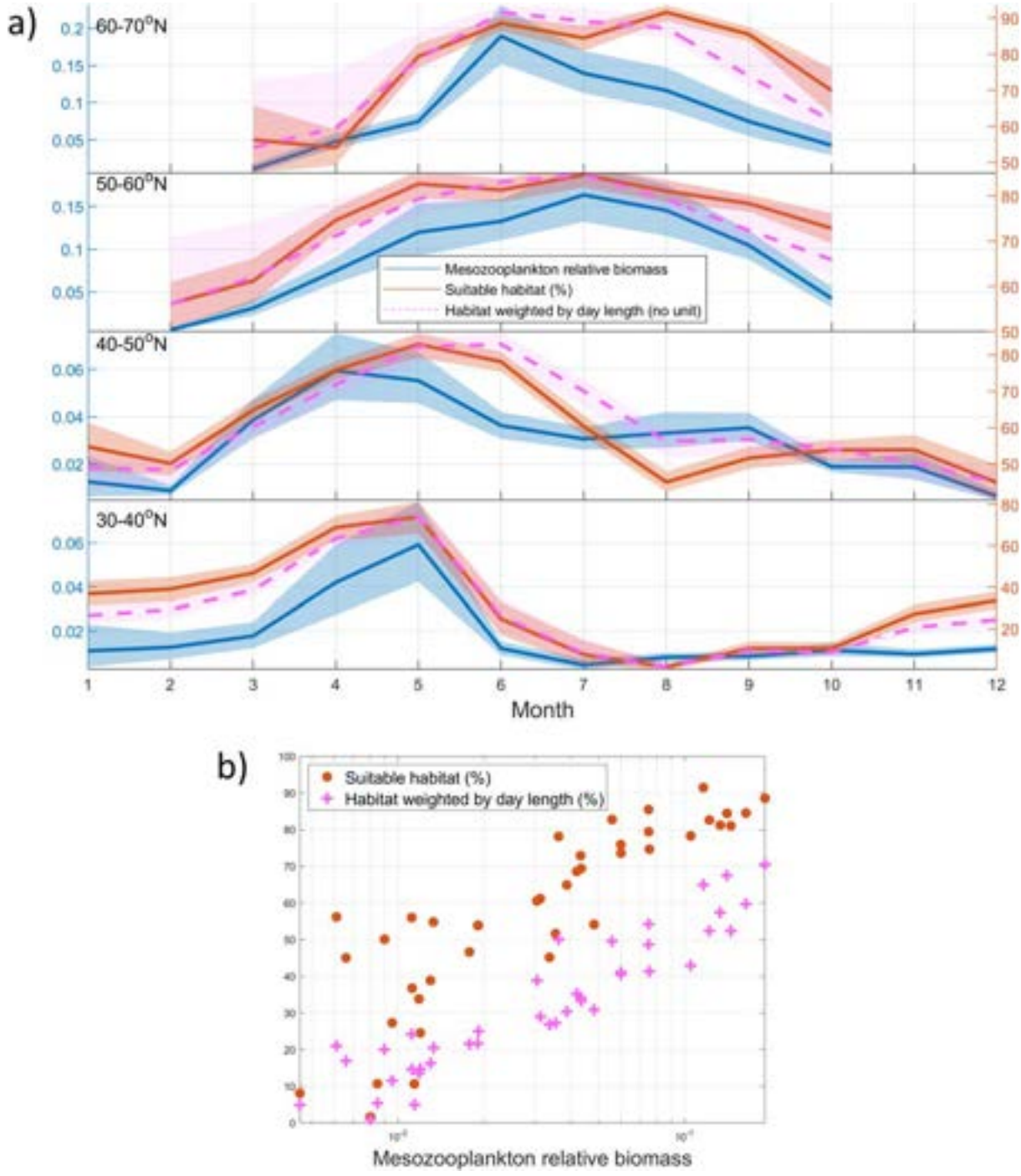

Figure 3.1.4. (a) Monthly mean mesozooplankton relative biomass (blue line), corresponding mean suitable habitat (red line) and mean habitat weighted by day length (dashed pink line) from 2003 to 2016 by 10° latitude range from 30°N to 70°N and for longitudes from 50°W to 10°W in the North Atlantic (see box in Figure 3.1.5(a) and Druon et al. 2019 for details on the data). The 5th and 95th percentile are also represented in respective light colours (the number of matching points by latitude range from south to north are 452, 1929, 1203, 672). (b) Same data presented as mesozooplankton relative biomass versus habitat (red dots) and habitat weighted by day length in relative value (pink plus signs). The Spearman's rank coefficient correlation between the 4256 pairs of mesozooplankton biomass and habitat is 0.89 ($p \approx 0$), and 0.935 ($p \approx 0$) for the habitat weighted by day length.

(European Commission 2008, 2017) (descriptor D1 pelagic habitats, D3 commercially exploited fish, D4 food webs), the EU Biodiversity strategy for 2030 and the United Nations Sustainable Development Goal 14 ('to conserve and sustainably use the oceans, seas and marine resources for sustainable development').

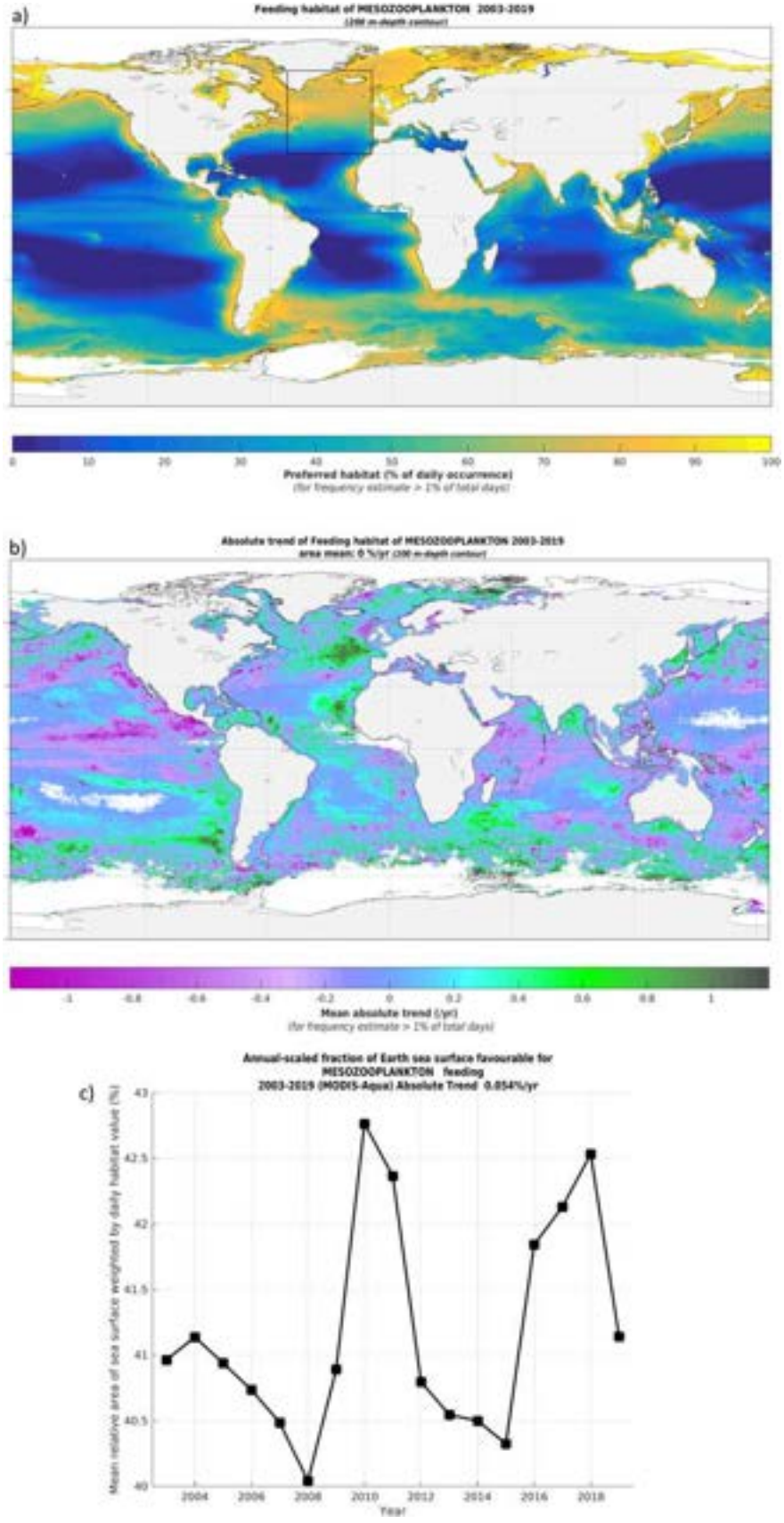

Figure 3.1.5. (a) Suitable feeding habitat for mesozooplankton in the global ocean as a mean value for 2003–2019 (the box refers to area used in Figure 3.1.4, 200 m-depth contour is shown), (b) regional trends in absolute value (computed from the local annual means) and (c) global annual variability (expressed in absolute habitat value of the global surface ocean). The mesozooplankton feeding habitat is defined by the presence of large productivity fronts and is expressed as the frequency of occurrence weighted by the front gradient value. Positive regional trends represent an increase in frequency of occurrence of productivity fronts. Blank areas correspond to cloud or sea ice cover, or to habitat suitability with chlorophyll-a detection below 5% of the total number of days in the considered period.

Section 3.2. Marine heatwaves and cold-spells, and their impact on fisheries in the North Sea

Authors: Sarah Wakelin, Bryony Townhill, Georg Engelhard, Jason Holt, Richard Renshaw

Statement of main outcome: Extremes in temperature can have harmful impacts on marine life, affecting reproduction and growth, and also causing mortality when organism tolerance limits are exceeded. To our knowledge, this is the first study to identify a link between extreme temperature events and key fish and shellfish stocks in the North Sea. For the southern North Sea, widespread anomalous heatwaves and cold-spells occurred throughout the period 1993–2019 but with no significant trends in the extent or magnitude of events. Winter cold-spells occurred in 1994, 1996, 1997, 2010, 2011, 2013 and 2018. There were widespread heatwaves in 1998, 2002, 2003, 2006, 2007 and 2014–2019. Catches of sole and sea bass increased in years with cold-spells, while catches of red mullet and edible crabs decreased. For heatwaves, the impact on fisheries catch data lagged the temperature events by five years: sole, European lobster and sea bass catches increased whilst red mullet catches reduced.

Product used:

Ref. No.	Product name and type	Documentation
3.2.1	NORTHWESTSHELF_REANALYSIS_PHYS_004_009 Model reanalysis	PUM: http://marine.copernicus.eu/documents/PUM/CMEMS-NWS-PUM-004-009.pdf QuID: http://marine.copernicus.eu/documents/QUID/CMEMS-NWS-QUID-004-009.pdf
3.2.2	NORTHWESTSHELF_ANALYSIS_FORECAST_PHYS_004_001_B Model analysis/forecast	PUM: http://marine.copernicus.eu/documents/PUM/CMEMS-NWS-PUM-004-001.pdf QuID http://marine.copernicus.eu/documents/QUID/CMEMS-NWS-QUID-004-001-b.pdf
3.2.3	Cefas/Defra Fisheries Activity Database	https://www.gov.uk/guidance/fishing-activity-and-landings-data-collection-and-processing

3.2.1. Introduction

The marine environment is subject to temperature variability both in the short and long term, with potential consequences for marine life. Extreme heatwaves and cold-spells arise from anomalous surface heating, transport or mixing effects (IPCC 2019; Benthuysen et al. 2020). The impact of temperature anomalies on the marine ecosystem depends on their duration and amplitude compared with timescales of the ecological response and the susceptibility of the various components of the ecosystem to the change. There is increasing attention to short timescale warming events, termed marine heatwaves (e.g. Hobday et al. 2016 and references therein). These have particularly been investigated in tropical regions, for example with respect to coral bleaching events (e.g. Donner et al. 2005) and impacts on seaweeds and fish communities (Wernberg et al. 2013). Regions which have a high proportion of species at the warm edge of their range are particularly vulnerable to marine heatwaves (Smale et al. 2019), such as in Southern California and South East Australia where mass die-offs of kelps, and associated fauna, have been seen (Wernberg et al. 2016; Oliver et al. 2018; Arafeh-Dalmau et al. 2020). The marine heatwave in the North East Pacific in 2014 (known as the Blob) caused huge impacts on marine life, including die-off of seabirds and range shifts of fish (Bond et al. 2015 and references therein). Marine cold-spells have received less coverage, but can also impact on marine ecosystems causing large-scale fish and invertebrate mortalities (Szekeres et al. 2016; Schlegel et al. 2017).

Globally, marine heatwaves have 'very likely' increased in frequency, duration, intensity and extent over the period 1982–2016 (Collins et al. 2019; IPCC 2019). Primarily due to an increase in mean ocean temperature, it is expected that marine heatwaves will intensify further in the current century (Collins et al. 2019), with widespread ecosystem impacts (e.g. Oliver et al. 2019). The North Sea is predicted to be an area of high impact from marine heatwaves (Smale et al. 2019), and it is considered as a global marine hotspot, where waters are warming fastest (Hobday and Pecl 2014). It has also experienced impacts on fish and invertebrates from historical and more recent cold-spells (Woodhead 1964; Guardian 2018). Climate change fisheries research in the North Sea tends to focus on average temperatures (e.g. Simpson et al. 2011; Engelhard et al. 2014; Akimova et al. 2016). Here we present preliminary analyses of heatwaves and cold-spells in the North Sea, where the impacts of short duration temperature events have received much less attention. We focus on sustained (longer than 5 days) temperature events that are extreme relative to the phase of the seasonal cycle. We use fish catch data to explore possible effects on fisheries.

3.2.2. Methods

3.2.2.1. Temperature analysis

We use daily temperature data from the northwest European Shelf reanalysis (from 1993 to 2018; product reference 3.2.1) and analysis/forecast (for 2019; product reference 3.2.2) models and analyse near-bottom temperatures averaged over International Council for the Exploration of the Sea (ICES) rectangles (ICES 1977) in

the North Sea. Using code downloaded from https://github.com/ecjoliver/marineHeatWaves (Hobday et al. 2016), the daily temperatures are used to calculate a climatological (mean) annual cycle and the 10th and 90th percentiles for 1993–2019, which are then smoothed using a 31-day moving mean. Following Hobday et al. (2016), we identify marine heatwaves as periods of at least 5 consecutive days when the temperature exceeds the threshold of the 90th percentile. By analogy, we define marine cold-spells to be periods of 5 or more days when the temperature is lower than the 10th percentile. For each event, the start and end dates, duration and mean temperature anomaly are identified. To quantify the duration and spatial coverage of temperature events, we define the event spread to be the percentage of ICES rectangles and days experiencing extreme temperatures per time period. For example, an event with extreme temperatures every day in all ICES rectangles used in the fisheries analysis (see below) would have an event spread of 100%.

3.2.2.2. Fisheries analysis

To assess the impacts of heatwaves and cold-spells on fisheries, commercial fish and shellfish species known from previous studies (e.g. Perry et al. 2006; Simpson et al. 2011) to be particularly affected by temperature were chosen for analysis. These were cod (*Gadus morhua*), haddock (*Melanogrammus aeglefinus*), sole (*Solea solea*), sea bass (*Dicentrarchus labrax*), mackerel (*Scomber scombrus*), John Dory (*Zeus faber*), red mullet (*Mullus surmuletus*), edible crab (*Cancer pagurus*), European lobster (*Homarus gammarus*) and Norway lobster (*Nephrops norvegicus*). Cod, haddock, mackerel and Norway lobster are considered to have a more northerly affinity around the UK, and so are associated with colder temperature, whereas the other species are considered to be more warm-affinity species. For these species, monthly landings data for 1993–2016 for England and Wales was obtained from the Cefas Fisheries Activity Database (product reference 3.2.3), for each North Sea ICES rectangle.

Initial exploratory analysis was carried out by identifying years with known heatwaves or cold-spells in the literature that coincided with those years identified in the extreme event analysis, such as the cold winter of 1996 (Loewe 1996), and the European heatwave of 2006 (Chiriaco et al. 2014). There were more cold-spells and heatwaves in the southern part of the North Sea, south of 57°N, where moreover the coverage of English and Welsh fisheries data was most exhaustive, hence this area was chosen for the analysis here. Statistical analyses were performed to determine if there were correlations between the occurrence of cold-spells or heatwaves and the catches in a year or quarter. For each species, the total catches in each year, and for each quarter of each year, both for the entire study area and within each ICES rectangle were calculated. Cold-spells in quarter 1 are particularly important for fisheries because these are generally the lowest temperatures that animals experience. For some species there is a clear trend in catches over the time series, and so the catch data were detrended by modelling the long-term trend in the data using a general linear model, and then retaining the residuals to represent detrended catches. Correlations were then performed using these detrended catches for each year, and for each quarter, and the total number of ICES rectangles in which a cold-spell or heatwave started in each quarter or year. No significant correlations were found in the same year or quarter for heatwaves, and so one, two and five year time lags between catches and heatwave occurrence were tested. Lags at one and two years were examined to assess direct effects on survival, and lags at five years were assessed based on the time it takes for offspring to grow from egg or larvae stage to a large enough size to be caught by the fishery.

3.2.3. Results

3.2.3.1. Temperature events

During the period 1993–2019, marine heatwaves occurred in all years except for 1996 and 2013 and marine cold-spells occurred in every year except for 2016 (Figure 3.2.1). 1996 and 2013 were particularly cold years with widespread marine cold-spells identified in all seasons. Using the extreme temperature events identified in the fisheries analysis above, event spread thresholds were defined in order to determine all years with widespread quarter 1 (January to March) cold-spells and all years with widespread heatwaves. Extensive quarter 1 cold-spells (event spread > 15%) are apparent in 1994, 1996, 1997, 2010, 2011, 2013 and 2018. Years identified as having extensive heatwaves (event spread > 7%) are 1998, 2002, 2003, 2006, 2007 and 2014–2019. The largest seasonal signal is from anomalously warm temperatures during the period from quarter 4 in 2006 to quarter 2 in 2007. The spread of marine heatwaves/cold-spells is correlated with the magnitude of the event anomalies (for heatwaves: $r = 0.24$, P-value = 0.029; for cold-spells: $r = -0.38$, P-value = 0.001), that is, more widespread temperature events tend to be of higher magnitude. There are no trends in event spreads or mean anomalies with time (tested using the Mann-Kendall non-parametric test for trend analysis, Kendall 1975; Mann 1945).

3.2.3.2. Impact of temperature extremes on fisheries catches

3.2.3.2.1. Heatwaves: Species showing increased or decreased catches. There were no significant correlations between heatwaves and fisheries catches in the same year,

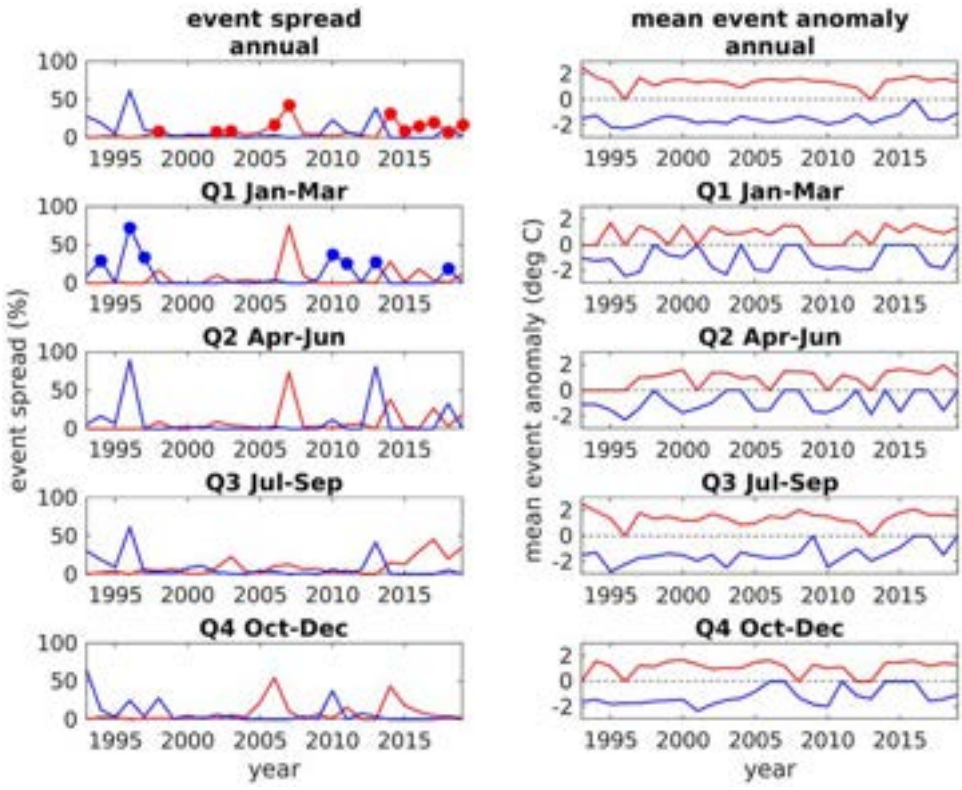

Figure 3.2.1. Left column: Event spread for each year and divided into quarters for marine heatwaves (red) and marine cold-spells (blue); red dots identify years with more widespread heatwaves and blue dots are years with cold Q1s. Right column: Annual and quarterly mean temperature event anomalies for marine heatwaves (red) and marine cold-spells (blue). Event data are for the North Sea south of 57°N using ocean reanalysis (product reference 3.2.1) and analysis/forecast (product reference 3.2.2) data.

or one or two years later. There were significant correlations between the occurrence of heatwaves and the catches for four species five years later (Table 3.2.1). Sole, European lobster and sea bass all had increased catches five years after years with more heatwaves. Red mullet had reduced catches five years after years with more heatwaves. European lobster catches generally increased over the study period, but this was especially pronounced in years five years after heatwave years (Figure 3.2.2). No correlations were found with heatwaves for edible crab, Norway lobster, cod, haddock, mackerel or John Dory.

3.2.3.2.2. Cold-spells: Species showing increased or decreased catches. Catches of several species showed correlations with the occurrence of cold-spells (Table 3.2.2). Sole and sea bass catches were positively correlated to cold-spell occurrence, with higher catches in years with more cold-spells; the reverse was found for red mullet. For edible crabs, there were lower catches in quarter 1, in years with more cold-spells in quarter 1 (Figure 3.2.3). No correlations were found with cold-spells for European lobster, Norway lobster, cod, haddock, mackerel or John Dory.

3.2.4. Discussion

While it is well established that the North Sea has warmed substantially in recent decades (e.g. Huthnance et al. 2016), with many documented impacts on fish species and the fisheries dependent on these (e.g. Simpson et al. 2011; Heath et al. 2012; Pinnegar et al. 2016), to our knowledge, this is the first study to have systematically identified extreme temperature events and how these may have impacts on key fish and shellfish stocks. It was observed that widespread cold-spells were especially clustered around the start of the time series examined (notably 1993, 1994 and 1996), but have also occurred more recently (e.g. winters of 2010–2011, 2018). Likewise, widespread heatwaves have occurred both earlier and later in the time series (notably in 2006, 2007, 2014 and 2018). These occurrences of widespread cold-spells as well as heatwaves at various points throughout the time series indicate it is important to look at their potential impacts on fisheries, on top of the general, long-term trend in mean sea temperatures in the North Sea.

For heatwaves in the North Sea, no in-year effects were found on fisheries catches. This may be because the temperatures are not high enough to cause mortality

to less mobile species, or because mobile species are able to move away. Lagged effects were observed where five years after a heatwave the catches of some species changed, indicating that there could be spawning or growth effects from the heatwaves. There was a five year lag between heatwaves and increased European lobster and sea bass catches. This would coincide with the time it takes from being spawned to reaching landing size, which is around 5–7 years in European lobster (at 87 mm; Sheehy et al. 1996), and around 4–7 years in sea bass (at 42 cm; Ares 2016). In sole, growth rate and the growing period increase with higher North Sea summer and winter temperatures respectively (Teal et al. 2008), which might explain the increased catches of sole five years after heatwaves. It is less clear what might cause the increased catches of sole in cold-spell years, but there is evidence that during very cold years, particularly in the past, sole tend to enter deeper water, where it is less cold, when cold winters were more frequent (Woodhead 1964; Engelhard et al. 2011). There are records of mass mortalities of sole in cold winters and physiological damage which changes sole behaviour and makes them more vulnerable to being caught (Horwood and Millner 1998). Therefore, sole catches may increase after heatwaves due to the physiological benefits of warmer waters, but also during or after cold-spells when sole may be easier to catch. Red mullet (landing size 16 cm and age 1 year; ICES 2019) showed decreased catches in cold-spell years, and also after heatwaves. Red mullet are a typical warm-water species, with distribution south to the Mediterranean. In the North Sea, research indicates that during winter, the fish may migrate northwards, to escape the colder, shallow southern North Sea (Beare et al. 2005). While this supports the results here of reduced catches in the southern part of the North Sea in cold-spell years, it remains less clear why catches of red mullet might be lower five years after heatwave years. Likewise, it is unexpected that seabass catches are higher during years of cold-spells. There may be other factors causing these results, such as fishing or changes to migration behaviour or spatial shifts (Jacox et al. 2020), trophic or foodweb effects, and further investigation is needed in these cases.

The results show particularly negative crab catches in quarter 1 during cold-spells. This has been shown

Table 3.2.1. Significant correlations (*P*-value < 0.05) between heatwave occurrence and detrended annual catches (product reference 3.2.3).

	Heatwaves (5 year lag)	
	Pearson correlation coefficient r	*P*-value
Sole	0.604	0.006
European lobster	0.493	0.032
Sea bass	0.483	0.036
Red mullet	−0.470	0.043

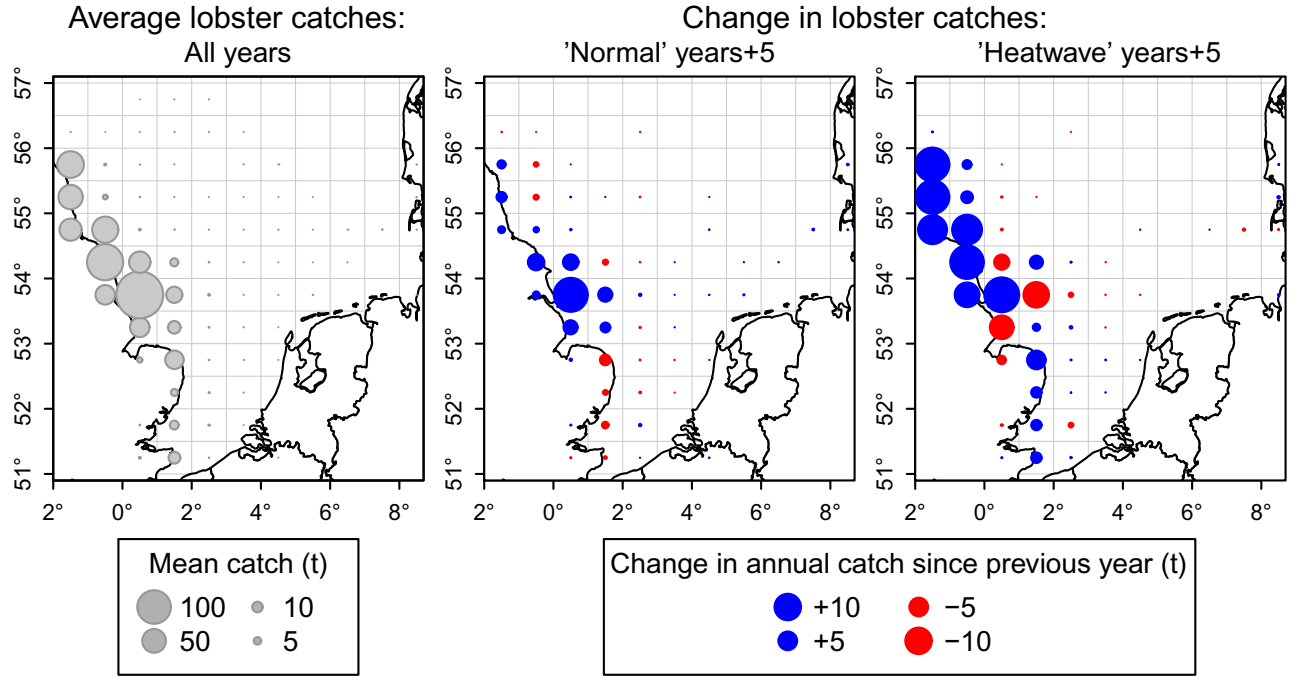

Figure 3.2.2. Left panel: average annual catches of European lobster (indicated by sizes of grey symbols). Middle and right panels: Change in annual catch of European lobster since the previous year (blue: increase; red: decrease), 5 years later than 'typical' years (middle) and 5 years later than the 'heatwave' years of 1998, 2002, 2003, 2006 and 2007. Sizes of blue and red symbols proportional to the change in catch per rectangle since the previous year (product reference 3.2.3).

Table 3.2.2. Significant correlations (P-value < 0.05) between cold-spell occurrence and detrended annual catches (product reference 3.2.3) for sole, sea bass and red mullet, and Q1 catches for edible crab.

	Annual cold-spells		Q1 cold-spells		Q2 cold-spells	
	Pearson correlation coefficient r	*P*-value	Pearson correlation coefficient r	*P*-value	Pearson correlation coefficient r	*P*-value
Sole	0.475	0.019	0.464	0.022	0.470	0.020
Sea bass	0.420	0.042	0.472	0.020	0.519	0.009
Red mullet	−0.418	0.042	−0.415	0.044	−0.433	0.035
Crab Q1			−0.451	0.027		

anecdotally in the past, but is shown here in the fisheries data. News articles have recorded negative effects of cold-spells to crustaceans, when swimming crabs were killed in huge numbers in Kent in 2010 (BBC 2010) and lobsters and crabs were washed ashore in large numbers in the winter of 2018 (Guardian 2018). This might be due to cold-induced physiological challenges experienced by these crustaceans (Stephens 1985).

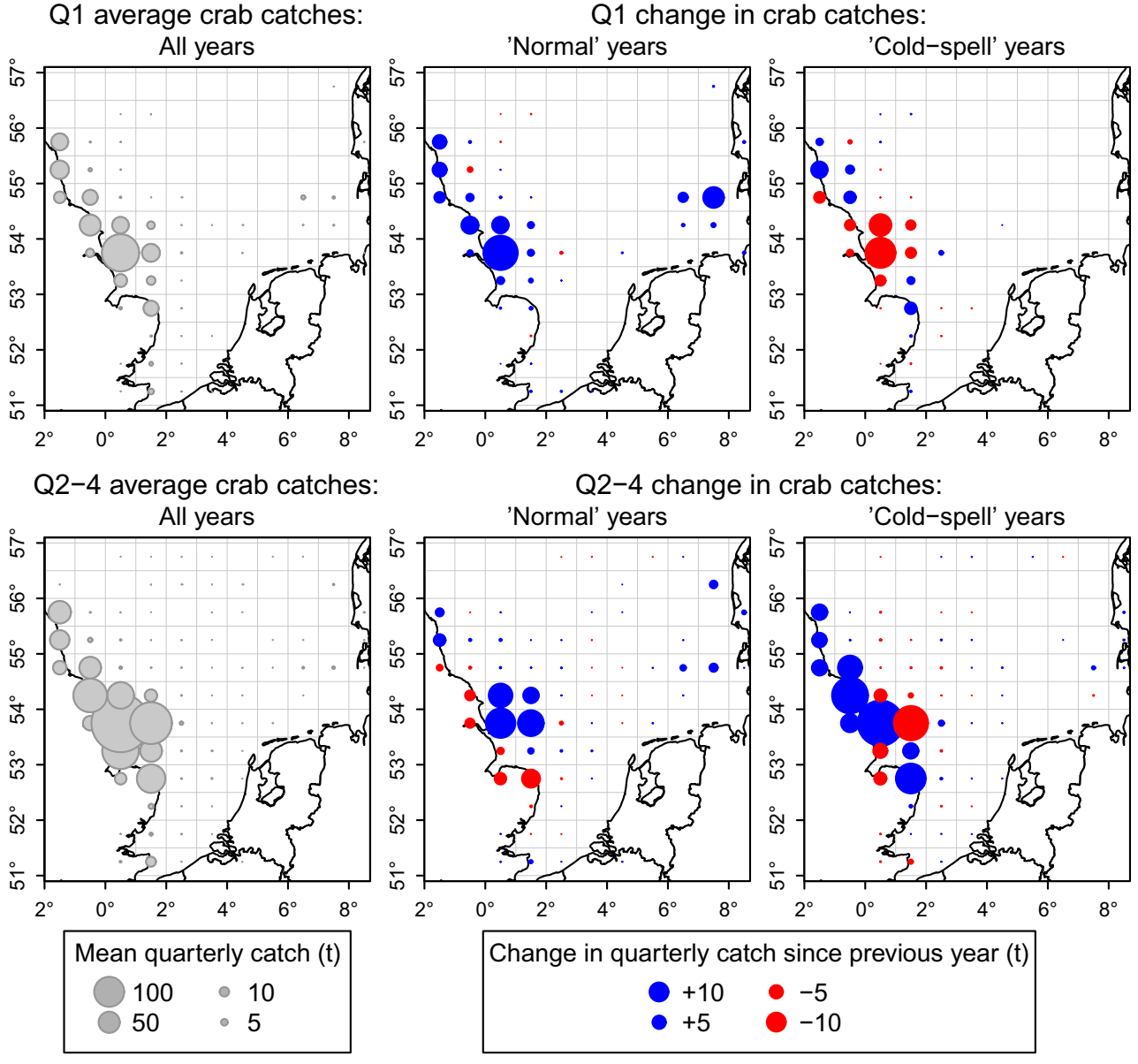

Figure 3.2.3. Left panels: average quarterly catches of edible crab (indicated by sizes of grey symbols), in quarter 1 (top) and in quarters 2–4 (bottom). Middle and right panels: increases (blue) or decreases (red) in edible crab catches since the previous year, compared between 'typical' years (middle) and years with extremely cold weather conditions during quarter 1 (right). Top panels: change in quarter 1 catches since the previous year; bottom panels: changes in quarter 2–4 catches (averaged per quarter) since the previous year. Sizes of symbols proportional to change in catches. Timespan: 1994–2016. 'Cold-spell' years are: 1994, 1996, 1997, 2010, 2011, and 2013.

For some species' catches no correlations were found with temperature extremes, despite anecdotal evidence of temperature effects. For example, Norway lobster catches have suffered during cold-spells in the past, thought to be because the animals go into deeper, warmer, water (BBC 2013). The study here focused on the southern North Sea, whereas this effect was seen in Scotland, and so would not have been seen in the data. Similarly mackerel is mainly an Atlantic/northern North Sea species, and so any effects may not have been found when looking only at the southern part of the North Sea. Previous studies on temperature and fisheries in the North Sea have tended to use average temperatures in their analysis, or studied the long term changes caused by gradual temperatures (e.g. Simpson et al. 2011; Engelhard et al. 2014; Akimova et al. 2016). As such, these studies may not have picked up on the shorter term impacts found by looking only at fisheries catches and cold-spells or heatwaves, and vice versa. Also, many studies look at the UK or North Sea as a whole, and the findings here only reflect the southern North Sea. For cod, haddock and John Dory, while these species' distributions are known to be affected by long term changes in temperature, it may be that briefer events do not affect their distribution or physiology or at least are not observable in the fisheries catches. They are also all mobile species, and so they may move away for the duration of the temperature extremes, returning once temperatures recover.

3.2.5. Conclusions

This study has highlighted that the North Sea warming trend over the past three decades has been punctuated by both heatwaves and cold-spells, which have occurred irregularly but at various time points throughout this period. There was evidence that these temperature extremes can be linked with changes in fisheries catches – either negative such as reduced edible crab catches during cold-spell events, or positive such as the lagged associations between heatwaves and increased lobster and sole catches, five years on. Lagged effects are suggestive of effects on the recruitment and survival of juveniles, only witnessed in the fisheries catches once individuals are sufficiently large to be caught.

So far, this study has only begun to explore the likely multitude of effects that cold or warm temperature extremes may have on marine life, initially focussing on species important to fisheries. Further analysis could explore any link between large scale climate, such as the North Atlantic Oscillation (NAO), and the occurrence or duration of heatwaves and cold-spells, and consideration of future temperature extremes. It is recommended that further research looks at a broader range of data sources, including from fisheries-independent surveys and ecosystem surveys, using various statistical modelling techniques. It is further recommended that a much broader range of species be looked at – including not only the commercially important species, but also those of conservation concern, and species from different levels across the trophic chain. Given the known, dramatic impacts that marine heatwaves (e.g. Bond et al. 2015; Hobday et al. 2016) as well as cold-spells (e.g. Szekeres et al. 2016) can have on marine life, it is imperative that due consideration is given to the effects that extreme sea temperatures can have on marine life in European waters and other temperate areas in the world, and the implications for society of these extreme events.

Section 3.3. Massive occurrence of the jellyfish Portuguese Man-of-War in the Mediterranean Sea: Implication for coastal management

Authors: Laura Prieto, Diego Macías, José L. Oviedo, Mélanie Juza, Javier Ruiz

Statement of main outcome: An intense swarm of the Atlantic jellyfish species, the Portuguese Man-of-War (*Physalia physalis*), was observed in 2018 in the Mediterranean Sea. This jellyfish has not yet colonised the Mediterranean Sea but is the jellyfish species in this basin with the highest impact on the tourism sector since it is responsible for the only casualty registered by a jellyfish sting. This study develops a forecasting system of the spread of this jellyfish in the Western Mediterranean that combines the occurrence of *P. physalis* sightings on the Atlantic side of the Strait of Gibraltar with a coupled hydrodynamic-Lagrangian model. The model takes into account the drifting of colonies with currents and winds. The model validation was performed using observational data from previous years and with different wind drags. The comparison of the model outputs with observational data provides a solid prognosis of the event in 2018 for the Western Mediterranean. The main benefits of this new forecasting system are to potentially help coastal managers, and to minimise associated socio-economic losses.

Products table:

Ref. No.	Product name and type	Documentation
3.3.1	MMF (Marine Modelling Framework)	System description: https://mcc.jrc.ec.europa.eu/main/document.py?Num=0&mot=towards%20an%20integrated&classement=&code=201603214045

(*Continued*)

Continued.

Ref. No.	Product name and type	Documentation
		Data source: https://mcc.jrc.ec.europa.eu/main/index.py Scientific references: Macias et al. (2019)
3.3.2	WIND_GLO_WIND_L4_REP_OBSERVATIONS_012_003	PUM: http://marine.copernicus.eu/documents/PUM/CMEMS-OSI-PUM-012-003.pdf QUID: http://resources.marine.copernicus.eu/documents/QUID/CMEMS-WIND-QUID-012-002-003-005.pdf
3.3.3	Data of Portuguese Man-of-War sightings from 2005–2018	Data source: https://laboratorioredIam.cica.es/VisorRediam/?conf=https://laboratorioredIam.cica.es/visorRediam/visorLitoral/visor_litoral_3.json Scientific reference: Prieto et al. (2015)

3.3.1. Introduction

The term 'jellyfish' covers many different organisms from the gelatinous plankton that belong to various Phyla and groups. In the present study, as jellyfish we are referring to either cnidaria from these two classes: scyphozoan or hydrozoan. Jellyfish blooms are naturally and/or anthropogenically induced outbursts of their populations in a specific time and location. The place where they occur depends strongly on the jellyfish species and the spatio-temporal scales of variability of their ecosystem. Some jellyfishes live in the open ocean (e.g. *Pelagia noctiluca*, *Physalia physalis*), others occupy the surface layer (e.g. *Cotylorhiza tuberculata*, *Physalia physalis*, *Velella velella*) and others dwell in coastal waters, usually in confined bays where their benthic life stages are attached (e.g. *Rhizostoma pulmo*, *Cotylorhiza tuberculata*).

The ecological and socio-economic consequences of jellyfish outbreaks on the shorelines are relevant worldwide and benefit from improved understanding of mechanisms driving the jellyfish swarms. This is important for the north-western Mediterranean Sea area due to the impact on the tourism sector (Prieto et al. 2015). Additional major consequences of these organism's blooms have been reported, such as the interference with aquaculture (Bosch-Belmar et al. 2017) and fisheries activities (Purcell et al. 2007), or the clogging of power plant cooling systems (Angel et al. 2016). Therefore, the development of tools for the prediction of future scenarios aiming to anticipate the arrival of the blooms at the shorelines is key to mitigating their impact (Ferrer et al. 2015; Ferrer and Pastor 2017). The identification of the target species and their location combined with modelling and knowledge of their population dynamics provides an initial step toward providing outlooks and warnings (Prieto 2018).

Currently, there is a concern that jellyfishes are becoming more prevalent in various regions around the Mediterranean Sea (Kogovsek et al. 2010; Brotz et al. 2012). The Mediterranean region is very sensitive to the impact of jellyfish swarms due to its semi-enclosed characteristic. The most abundant and frequent jellyfish within the basin that affects fisheries and aquaculture is the *Pelagia noctiluca*. Nevertheless, there is another jellyfish that imperceptibly impacts those sectors while for the tourism sector, a single sighting can imply the closure of a beach. This is the Portuguese Man-of-War (*Physalia physalis*), responsible for the only reported casualty in the Mediterranean by jellyfish sting in 2010 in Sardinian waters (Prieto et al. 2015). The importance of the tourism industry in the Mediterranean is well-known (Ciscar et al. 2001) and, for example, only during 2015, the European Union destinations in southern and Mediterranean Europe account for 49% of the international tourism within the European Union (World Tourism Organization 2018). In terms of tourism's contribution to GDP, countries in Mediterranean Europe stand out compared to the rest of the European countries. Spain shows the highest contribution on the continent (10.9%), followed by Portugal (9.2%), France (7.0%), and Italy (6.0%). Greece, with a contribution of 5.3%, is only surpassed by Hungary and Austria as non-Mediterranean countries (data corresponding to 2014; World Tourism Organization 2018). There are also relevant figures for the percentage of employment directly and indirectly depending on the tourism sector, with Spain leading with 13%, and other Mediterranean countries, such as Croatia and Italy, with 12% and 10%, respectively (World Tourism Organization 2018, table 9.2). In 2016, 25% of the tourism in Mediterranean Europe had the seaside as their main destination (Eurostat 2020), a destination type potentially threatened by jellyfish blooms.

Each Portuguese Man-of-War is a colony of hydrozoans and its development, morphology, and colony organisation are unique (Munro et al. 2019). Colonies are composed of functionally specialised bodies (termed zooids). The Portuguese Man-of-War lives at the air–sea interface and uses part of a gas-filled enlarged float (pneumatophore) as a sail to travel with the wind and surface currents, dragging behind it long tentacles (with dactylozooids, tentacles for catching prey and self-defence; gonoids, for reproduction; and gastrozooids, for digestion). The individual zooids cannot

survive separately and behave as a single animal (Mapstone 2014). When humans get in contact with *P. physalis,* several envenomation syndromes develop (Badré 2014), inducing acute pain and a local cutaneous reaction involving erythema and inflammation (Cazorla-Perfetti et al. 2012; Labadie et al. 2012). Systemic symptoms are also observed, including respiratory distress, neurological, musculoskeletal, digestive signs (Haddad et al. 2013; Badré 2014), and sometimes death (Burnett and Gable 1989).

The Portuguese Man-of-War is not native to the Mediterranean Sea. This species is usually found in the tropical and subtropical areas of the Pacific, Atlantic, and Indian Oceans (Kirkpatrick and Pugh 1984), at latitudes ranging from 55°N to 40°S. Therefore, European tourism could be under a potential threat by this foreign species. In fact, several stakeholders are involved when Portuguese Man-of-War are spotted in the Mediterranean Sea: local, regional, and national governmental services (such as fisheries, environmental and emergency administrations), the European Commission, the private tourism sector, fishermen, offshore aquaculture operators, dive clubs, marine protected area supervisors, lifeguards, sailors or enthusiast naturalists.

The causes of previous episodes of 'Portuguese Man-of-War years' that bring these open Atlantic populations to the vicinity of the Strait of Gibraltar and, subsequently, to the Mediterranean Sea have already been scientifically described (Prieto et al. 2015). They are related to the large-scale interannual atmospheric fluctuation (negative North Atlantic Oscillation index, Hurrel and National Center for Atmospheric Research Staff 2020) and local atmospheric conditions (strong and persistent westerlies winds) in the north-eastern Atlantic. In 2018, the Mediterranean basin experienced swarms of *P. physalis*, and in this study we aim to bring the study of this jellyfish another step forward. While Prieto et al. (2015) focused on the Atlantic side of the Strait of Gibraltar, the present study proposes a comprehensive analysis of the meteorological and oceanographic conditions in the Western Mediterranean since the appearance of *P. physalis* in the Strait of Gibraltar and afterwards as they spread inside the basin during a typical 'Physalia-year'. The goal of this study is to provide a new prognosis tool to predict the spreading of this jellyfish in the Western Mediterranean.

3.3.2. Methods

3.3.2.1. Observational data

Sightings of Portuguese Man-of-War in the Gulf of Cadiz and in the Western Mediterranean were compiled over the period 2005–2018 from different sources: published scientific articles, media, national and regional agencies, and personal communication. The unique events of large swarms on both sides of the Strait of Gibraltar occurring in 2010, 2013, and 2018 were carefully reported by the *Consejería de Medio Ambiente* (Ministry of Environment) of the Andalusian regional government (Spain), who monitored the entire Spanish coast and counted and measured all stranded colonies. The *Consejería de Medio Ambiente* (Ministry of Environment) of the Balearic Islands (Spain) regional government had carried out the same monitoring during the 2018 event. Additionally, *P. physalis* sightings were analysed from the database of the Jellywatch Program (htttp://jellywatch.org) and the PERSEUS Jellyfish Spotting (http://www.perseus-net.eu/en/jellyfish_map/index.html). The data from the 2005–2017 period were used to create the model that is described in the following subsection, while the data for the year 2018 were used to assess the model.

3.3.2.2. Hydrodynamic model

The model used to spread the colonies covers the whole Mediterranean basin and has been developed by the Joint Research Centre (Macias et al. 2014). It consists of a 3D hydrodynamic-biogeochemical coupled simulation. It has been previously applied to the horizontal currents of the Mediterranean and the impact on the dispersion of floating particles (Macias et al. 2019). Every six hours, 3D fields of simulated ocean currents, temperature, and salinity were stored and coupled off-line with the Lagrangian module described below.

3.3.2.3. Lagrangian model

Considering their morphology, the Portuguese Man-of-War drift with the surface currents and winds as Lagrangian tracers. Lagrangian simulations were performed using the free modelling tool Ichthyop v.3.3 (http://www.ichthyop.org, Lett et al. 2008) coupled off-line with the ocean model described above. This Lagrangian model was also used in Prieto et al. (2015).

Each virtual *P. physalis* colony was simulated as a passive drifter floating at the sea surface and advected by the surface currents (computed by the hydrodynamic model described previously) and dragged by a percentage of the wind speed at 10 m (obtained from satellite and distributed by CMEMS, Product ref. 3.3.2). The percentage of this wind drag that is added to the movement of the virtual colonies is a key forcing parameter and different values have been used in previous studies (e.g. Ferrer et al. 2015; Prieto et al. 2015; Headlam et al. 2020). Therefore, we performed a validation exercise using the two previous 'Physalia-years' that occurred in 2010 and 2013 in the Mediterranean. For each year,

we performed specific simulations, as detailed below, considering a range of wind drags: 10%, 5%, 1%, 0.5% and 0% of the wind velocity at 10 m. For each specific wind drag, the surface current velocity provided by the hydrodynamic model was modified in each model grid according to the wind field over that specific region and for each time-step.

The model results were then compared to the observed arrival time of *P. physalis* colonies in the Western Mediterranean. A 'match' was defined if on the day an observation is made the model simulates the presence of at least one virtual *P. physalis* colony in that particular area. The results from this set of simulations showed that the highest percentage of 'matches' (83%) occurred with 0.5% of wind drag applied.

Due to the fact that it is impossible to know how many colonies of *P. physalis* enter the Mediterranean through the Strait of Gibraltar on a given day without a robust protocol monitoring system, a systematic consistent approach was followed. The forecasting system relies on the assumption that the number of *P. physalis* that pass through the Strait of Gibraltar every day is 10x the number of colonies beached in the Gulf of Cadiz. In this way, the simulation has a discontinuous entrance of colonies in the model both in time (the days of the sightings) and in number. The position of each virtual colony within the Mediterranean Sea was tracked and stored until the end of each simulation year.

3.3.3. Results

Before evaluating the performance of the new model, we analysed if the conditions previously considered as conducive to the arrival of *P. physalis* colonies near the Gulf of Cadiz occurred in 2018. In particular, during the week from 26 February until 5 March, strong westerly storms occurred in the Gulf of Cadiz and the daily North Atlantic Oscillation index during these days was negative (mean −1.145 provided by the United States National Oceanic and Atmospheric Administration). Concurrently, and lasting for several weeks, thousands of Portuguese Man-of-War colonies were washed up on the shore in the Gulf of Cadiz. A significant correlation between the NAO index and *P. physalis* sightings exists ($r = -0.67$, $p < 0.05$), considering the 14 year data set from 2005 to 2018. Therefore, the climate and atmospheric conditions of the north-eastern Atlantic that were previously identified (Prieto et al. 2015) as key environmental descriptors for forecasting water mass dynamics in the area of study, are still considered fundamental factors in the simulation of *P. physalis* swarm events. The spatial and temporal scales at which the NAO index effects occur are large, but the atmospheric importance in the case of this jellyfish is that winter storms affect southern Europe more strongly. When this occurs together with persistent strong westerly winds in the Gulf of Cadiz, the probability that the colonies are within the continental shelf is higher.

In Figure 3.3.1, the mean surface wind (at 10 m) from satellite reprocessed products (Product Ref. No. 3.3.2) during March 2018 is represented for the whole Mediterranean Sea, showing an important prevalence of strong south-westerly winds in the Western Mediterranean. The spread of the jellyfish in the Western Mediterranean is clearly observed (Figure 3.3.2) where the accumulated sightings of *P. physalis* during April 2018 are presented (Product Ref. No. 3.3.3). From the Strait of Gibraltar, the colonies followed the main surface currents (Product Ref. No. 3.3.1), together with the surface wind trajectory (CMEMS product Ref. No. 3.3.2.) that prevailed the month before in that part of the basin.

Using the forecasting system, a probabilistic daily simulation can be obtained for the position of *P. physalis* inside the Mediterranean Sea. In Figure 3.3.3, all the beached and free floating colonies for a particular month (April 2018, in order to compare to Figure 3.3.2) are shown.

In order to evaluate the accuracy and reliability of the forecasting system, when the first sightings of *P. physalis* were observed on the Atlantic side of the Strait of Gibraltar (from 26 February until 5 March 2018), the model was run. This way, we could test if the arrival time of the colonies in the Western Mediterranean was successfully represented by the model run. To do that, we looked at the position of all virtual colonies for each day and counted how many were within the studied area. Subsequently, we compared these time series of virtual *P. physalis* abundance with the observations to identify the 'matches'. The percentages of matches were evaluated in two regions: the Alboran Sea and the Balearic Islands region, where the results were 94% and 100%, respectively.

However, this comparison does not provide an assessment of the model's ability to correctly predict the temporal presence of *P. physalis* in the Western Mediterranean. Therefore, we compared the initial day of the temporal windows for the Alboran and Balearic Seas for the different years in both the observations and the model. The correlation analysis between the data and the model was significant ($p < 0.01$), showing that the model approach was able to correctly predict the first day that the colonies appeared in the Alboran

and Balearic Seas when the time of entrance in the Mediterranean is known.

An example showing that the simulation output provided support in a management perspective is that we could alert the Regional Government of the Balearic Islands on 8 March 2018, allowing them to prepare to act around mid-April for the arrival of the colonies. The management of *P. physalia* on these islands represented a paradigm of successful scientific knowledge transfer to society as it was mirrored in a press interview with the Coordinator of the Environment of the Regional Government (https://www.diariodemallorca.es/mallorca/2018/05/22/carabela-portuguesa-sobrevivira-mediterraneo-agua/1315576.html) on 22 May 2018 and a new protocol for the Spanish Emergency Agency was developed based on both observational and modelling data.

3.3.4. Discussion

This study provides coastal managers and stakeholders a prognosis tool that can be used to anticipate the arrival of *P. physalis* at the Western Mediterranean Sea. To build this data set of virtual colonies drift, a careful design, calibration, and validation of the Lagrangian model was conducted. A key aspect of *P. physalis* spread is that the colony feels the combined effects of the ocean current and the surface wind. Previous studies, with different spatial scales, used 10% (Prieto et al. 2015), 2–4.5% (Ferrer and Pastor 2017), 1.8% (Ferrer et al. 2015), and 4.5% (Headlam et al. 2020) of the wind speed. Moreover, the precise value of the wind drag to be added to the current velocity might be dependent on the hydrodynamic model used, with its particular features (e.g. incorporation of waves, Stokes drift, tidal effects, etc.). This is why a calibration exercise was performed with previous 'Physalia-years' in order to find the best fit for the Western Mediterranean and the hydrodynamic model used.

As a limitation to the comparison of the observed data (Figure 3.3.2) with the simulated data (Figure 3.3.3), we are aware that observations from the southern Mediterranean shoreline are missing, as they are very difficult to obtain and mainly only available years later through published scientific literature. Therefore, data limitations prevent a more robust and complete model validation. Nevertheless, the strength of the proposed forecasting tool is that with only the data obtained on the Atlantic side of the Strait of Gibraltar, and comparing the simulated data with the observed data available in the Mediterranean basin, the prognosis of *P. physalis* is possible and provides support in terms of a management perspective. This tool could be extended to the whole basin, adding other forcings to the model. For example, in order to obtain better simulation results in the eastern part of the basin, the model should incorporate the effect of temperature on the mortality of the colonies, a forcing that is missing in the present forecasting model.

The impact on tourism is probably the main socio-economic concern resulting from potential *P. Physalis* swarms in the Mediterranean, but there are only few quantifications of these threats. This impact can be analysed by estimating the change in tourist visits in a particular year, and the associated economic losses. This can derive both from a negative tourist experience associated with the occurrence of an actual bloom and from the negative expectations of the potential tourists about an area that has suffered blooms in the past or that is receiving a lot of attention in the media because of increasing jellyfish sightings. As an example, Ghermandi et al. (2015) used a

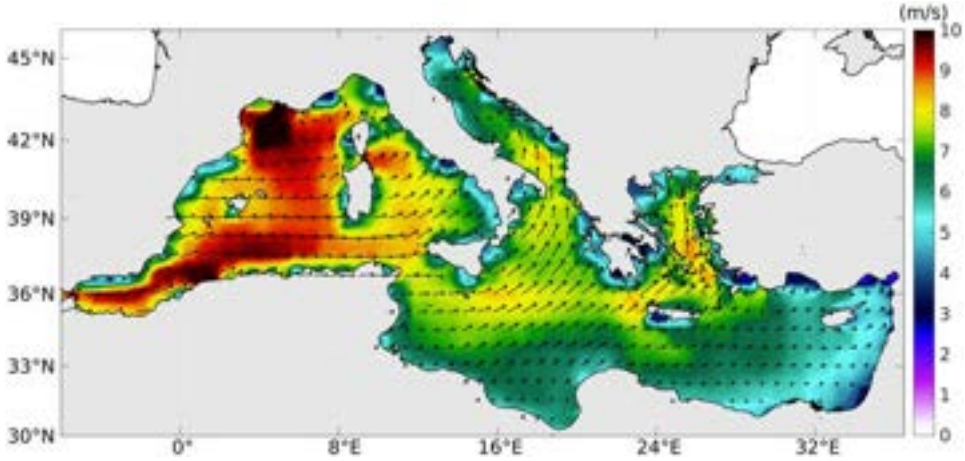

Figure 3.3.1. Monthly wind speed (m/s) and direction (at 10 m) in the Mediterranean Sea during March 2018 (CMEMS Product Ref. No. 3.3.2.).

Figure 3.3.2. Locations of all the sightings of *Physalia physalis* colonies in the Western Mediterranean Sea during April 2018 (Product Ref. No. 3.3.3).

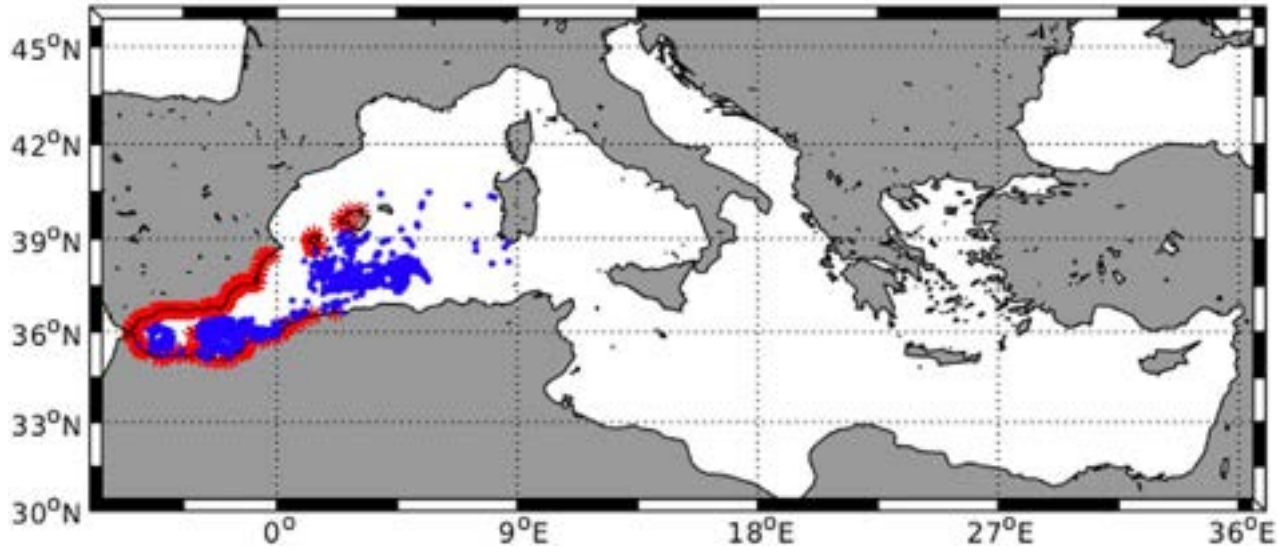

Figure 3.3.3. Output of the forecast model to predict the spread of *Physalia physalis* colonies in the Mediterranean basin. In order to compare with (Figure 3.3.2), the red dots are the summary of all the beached *Physalia physalis* colonies during April 2018. The blue dots are the free colonies still floating in the water on 30 April 2018, that will continue to spread along the basin.

socio-economic survey to estimate the expected change in beach recreational visits and the associated economic losses resulting from a *Rophilema Nomadica* outbreak in the city of Tel-Aviv (Israel). Their results show that a bloom could reduce the number of seaside visits by 3.5–10%, with a welfare loss between 1.8 and

6.2 million Euros. The authors also analysed the potential benefits associated to the real-time public information system for early detection of blooms. They found that respondents in their sample were willing to pay an average of 20 Euros to contribute towards investing in such a system. Ghermandi et al. (2015) illustrated how the potential threat to the tourist industry and the benefits of an early detection system can be quantified.

An indirect indicator of the social awareness of jellyfish blooms, and their potential impact on tourism, can be assessed through the number of media items (internet, newspapers, radio) including 'Portuguese Man-of War' in a year for an area in which these blooms occurred as compared to years when they did not. An analysis shows that in 2018, a year with a particular frequency of *P. physalis* sightings in the Mediterranean, there were 100 reports while in 2017 and 2019, this number dropped to six and 21, respectively. It would be interesting to assess whether the year following a jellyfish bloom (with the concomitant increase in the number of social reports), the number of tourists in the area decreases. The establishment of an early detection system that minimises the impact of the arrival of *P. physalis* at a shoreline, by removing the colony before it reaches the beach, can mitigate the concomitant negative social perception, with its consequent benefits (or avoided losses) for the tourist sector.

The Strait of Gibraltar is the only entry point for the Portuguese Man-of-War from the Atlantic Ocean to the Mediterranean Sea. Consequently, establishing monitoring capabilities at the Strait of Gibraltar is optimal for the control of the spreading of these organisms to the Mediterranean Sea.

3.3.5. Conclusions

By combining the Portuguese Man-of-War sightings on the Atlantic side of the Strait of Gibraltar with the hydrodynamic conditions of ocean currents and surface winds over the Western Mediterranean, an early warning system has been developed using a modelling approach. Once the Portuguese Man-of-War enter the Alboran Sea, they spread into the Mediterranean following the meteorological and oceanographic conditions, enabling a warning system of *P. physalis* presence in the Western Mediterranean for following few months. Taking into account that this is a transversal issue across several disciplines and that it affects diverse interfaces as science/policy, science/societal, science/private sector and economy (Kontogianni and Emmanouilides 2014; Ghermandi et al. 2015), the main conclusion of this study is that using the observational data of Portuguese Man-of-War in the Strait of Gibraltar and incorporating them in the model presented here for the Western Mediterranean, the forecasting system developed can potentially help the affected coastal managers, minimising both economic losses and threats to human health.

Acknowledgements

This study has been funded by by CSIC (Project 2019AEP203) and by the Project Agreement 'Sistema de Observación y Predicción de Medusas en el Mar Balear' among Govern des Illes Balears, SOCIB and CSIC (Disposición 15052, BOE núm. 310, 2020). The authors would like to thank the Editorial Board, two anonymous reviewers from OSR4 and two new anonymous reviewers from OSR5, whose comments have really improved the content and analysis of this work.

Section 3.4. Recent changes of the salinity distribution and zooplankton community in the South Adriatic Pit

Authors: Elena Mauri, Milena Menna, Rade Garić, Mirna Batistić, Simone Libralato, Giulio Notarstefano, Riccardo Martellucci, Riccardo Gerin, Annunziata Pirro, Marijana Hure, Pierre-Marie Poulain

Statement of main outcome The South Adriatic Pit (SAP) is one of the most important sources of dense water for the Eastern Mediterranean. Relevant interannual changes of haline properties in the area are detected in the recent years. These variations, besides being interesting from an oceanographic and climatic point of view, have also ecological and economic impacts. The observed changes of salinity distribution clearly influence the zooplankton community and their effects cascade up to higher trophic level species depending on their trophic preferences, competitions and grazing. In this context, different salinity distributions lead to a different plankton abundance with potential effects on fish species of commercial interest. These changes in the ecosystem can strongly impact on the sea-related economies and coastal communities that might need to adapt to the declining abundance of traditional target species and/or to the increasing abundance of other species, which previously were secondary to the local market. In this work, mesozooplankton biomass were observed in three years quite different according to the salinity distribution in the upper 50 m: 2016, characterised by relatively

low salinity, 2017 characterised by high salinity and 2018 with extremely low salinity. These years are used to estimate the net productivity. The outcomes highlight greater potential for fish production in the post convective period (April-June) of 2018 under an influence of a low salinity water mass compared to the other years, representing a first rough quantification of oceanographic impacts on fisheries sector.

Data use:

Ref. No.	Product name and type	Documentation
3.4.1	INSITU_MED_NRT_ OBSERVATIONS_013_035	PUM: http://marine.copernicus.eu/documents/PUM/CMEMS-INS-PUM-013.pdf QUID: http://marine.copernicus.eu/documents/QUID/CMEMS-INS-QUID-013-030-036.pdf
3.4.2	INSITU_MED_TS_REP_ OBSERVATIONS_013_041	PUM: http://marine.copernicus.eu/documents/PUM/CMEMS-INS-PUM-013.pdf QUID: http://marine.copernicus.eu/documents/QUID/CMEMS-INS-QUID-013-041.pdf
3.4.3	Zooplankton samples collected in the framework of numerous oceanographic cruises conducted by the Institute for Marine and Coastal Research of the University of Dubrovnik founded by the Croatian Ministry of Science, Education and Sports, Croatian Science Foundation, Croatian Science Foundation (grant number: IP-2014-09-2945) and ESAW. Request data to mirna.batistic@unidu.hr	

3.4.1. Introduction

The open-ocean deep convection is a winter process that allows the relocation of heat and salt content from the surface water masses to the deeper layer. The South Adriatic Pit (SAP) – together with the Gulf of Lion and the Aegean Sea – is one of the three major sites of deep convection in the Mediterranean Sea (Cardin et al. 2011; Houpert et al. 2016). For this reason, the SAP has been extensively monitored during the last forty years by traditional shipboard techniques (Klein et al. 2000; Manca et al. 2002). Starting in 2012, traditional methods have been complemented by float measurements and glider surveys providing a more detailed spatio-temporal dataset (Kokkini et al. 2019). The area of the SAP is extremely dynamic during the winter period and it is characterised by strong vertical mixing affecting the top or most of the water column, depending on the severity of the weather conditions. The hydrological characteristics of the basin are also strongly influenced by the general circulation and the river runoff (Russo and Artegiani 1996). The Adriatic general circulation (Figure 3.4.1(a)) consists of the inflowing northward coastal current located along the eastern coast (Eastern Adriatic Current – EAC), recirculating eventually in sub-basin cyclonic gyres (Poulain and Cushman-Roisin 2001; Cushman-Roisin et al. 2001; Lipizer et al., 2014). The Adriatic surface waters exist along the western coast (Western Adriatic Current – WAC; Figure 3.4.1(a)), characterised by a reduced salinity due to the rivers contribution from the northern part of the basin. The cold North Adriatic Bottom Water (NABW), which is formed during the winter in the northern part of the Adriatic (Poulain and Cushman-Roisin 2001; Janeković et al. 2014; Kokkini et al. 2018), moves southward spreading over the whole basin (Vilibić and Supić 2005; Carniel et al. 2012) cascading into the SAP at depths greater than 700 m (Mauri et al. 2016). In the southern basin, a counterclockwise rotation characterises the mid and surface water column (Poulain and Cushman-Roisin 2001; Poulain and Cushman-Roisin 2001; Zonn and Kostianoy 2016). Waters from the North Ionian Sea enter into the SAP via the eastern portion of the Otranto Channel and join the EAC (Figure 3.4.1(a)).

The above scenario suggests the complexity of the hydrography of the South Adriatic due to the integration of the surface and/or intermediate waters of north Adriatic and/or Ionian origin, and the more or less intense winter convection mixing. The variations of these processes affect the thermohaline properties of the Adriatic Deep Water (AdDW), which represents the main source of dense water for the eastern Mediterranean. The AdDW thermohaline characteristics impact the 'Mediterranean Overturning Circulation', that in turn, is an important component in the Mediterranean climate modulation.

The influence of the decadal and seasonal variations on the thermohaline properties, and the zooplankton community composition of the SAP, is well described in literature (Batistić et al. 2014). The advection of the water masses with different physical and biogeochemical properties from the Ionian Sea (Civitarese et al. 2010; Batistić et al. 2014; Batistić et al. 2019) are strongly correlated to the biodiversity. Before the 2000s, the knowledge of the phytoplankton communities and the biological oceanography of the SAP was limited since only sporadic samplings were performed. These samplings have shown in specific years phytoplankton

blooms extending into April (Viličić et al. 1989, 1995; Viličić 1991, 1994, 1998; Socal et al. 1999; Turchetto et al. 2000; Boldrin et al. 2002). The temporal extension was ascribed to the local extended winter climatic conditions (Gačić et al. 2002; Cerino et al. 2012; Gacic and Civitarese 2012), which induces the vertical convention that brings nutrients from the deep to the surface. Such variability of physical forcing modulates the duration and timing of phytoplankton blooms and the related production in the SAP (Gačić et al. 2002).

Marine trophic webs are triggered by the phytoplankton growth therefore, zooplankton blooms follow phytoplankton blooms; the short life (within days) cycle groups such as Appendicularia respond first after which, Copepods with longer life cycle (within weeks) reacts. Rarely, spring salp blooms occur in the SAP (Boero et al. 2013), causing a cessation of phytoplankton blooms (Batistić et al. 2018). Salps filter large amounts of seawater influencing the pelagic ecosystem dynamic. They consume the entire daily primary production (Pakhomov et al. 2002), filtering other zooplankton such as crustacea, fish larvae and juveniles pathway, and affecting the fish recruitment (Boero et al. 2008).

Recent investigations in the SAP focused on the vertical distribution of zooplankton or diel vertical migration (Batistić et al. 2012; Ursella et al. 2018; Njire et al. 2019) under the influence of the winter vertical convection. Studies in the Adriatic coastal regions showed that seasonal changes of water temperature and spatial salinity variation has a strong influence (or, play a key role) on the zooplankton abundance (Vidjak et al. 2012). Conversely, the influence of long-term haline changes on total zooplankton abundances in the area was never investigated, together with the salinity changes and their effects on zooplankton communities cascade up to higher trophic level species according to trophic preferences, competitions, grazing effects.

Besides direct influence of salinity and oceanographic variables on fish egg development (Morello and Arneri 2009), water circulation in SAP has been connected with long term fluctuations of relevant commercial species such as anchovy and sardines (Grbec et al. 2002). Other than physiological preferences, the analysis suggests the possible influence of plankton composition and production on fish community productivity (Dragičević et al. 2017). A fluctuation of the fish productivity strongly affects the sea-related economies that might adapt to the abundance fluctuation of their traditional target species (e.g. anchovy *Engraulis encrasicolus* and sardine, *Sardina pilchardus*) and/or of species which were previously less important to the local market (e.g. the bluefish, *Pomatomus saltatrix*). The present work focuses on recent interannual salinity variations observed in the upper layer (0–100 m) as described by Argo floats. The aim is to define possible correlations between these changes and the zooplankton abundance. We present for the first-time data on zooplankton abundance and composition in the open South Adriatic in hydro climatically different years. Possible cascading effects of changes in the plankton community on species of commercial interest and fisheries landing potential are estimated and described.

3.4.2. Method

The Argo profiling floats deployed in the SAP were equipped with Sea-Bird CTD sensors. The physical data were processed and quality-controlled in delayed-mode for P, T, and S data following the Argo Quality Control Manual for CTD and Owens and Wong (2009), Notarstefano and Poulain (2010, 2013), Wong et al. (2020) to exclude potential sensor drift. The two floats used in this work (WMO 6901822 and WMO 3901978) are programmed with a cycle length of 5 days, a parking depth of 350 m and a maximal profiling depth that reaches the bottom of the SAP (about 1200 m). The parking depth at 350 m allows Argo floats to be confined to the pit for a long time, as its edge is shallower. The profiles on the periphery of the SAP reach the bottom at shallower depths as shown in Figure 3.4.1(b).

In the period 2016–2018 monthly or biweekly (Jan and Jun 2016; Feb, May and Jul 2017) zooplankton samples were collected at the station P-1200 (42.22°N, 17.71°E, 1200 m deep). The layers 0–50 m and 50–100 m were sampled using 250-µm meshed Nansen closing net (1 m^2 mouth surface area and 255 cm length) and preserved in 2.5% CaCO3 buffered formaldehyde. The collected samples were observed with an Olympus SZX16 stereomicroscope to count the aggregated abundances of the three main zooplankton groups (Calanoida, Oithonida and Appendicularia) that accounted for 84–97% (91% on average) of specimens in each sample. Each sample was divided in subsamples, in order to count at least 500 individuals out of the total. Copepoda (Calanoida and Oithonida) and Appendicularia were counted, which make most of the mesozooplankton. The abundance of all groups is presented as the number of specimens per cubic metre (ind. m^{-3}). Chl-a was measured at the time of zooplankton sampling using WETLabs ECO fluorometer connected to a Seabird SBE 19plus CTD instrument. The sensor was factory calibrated with *Thalassiosira weissflogii* monoculture.

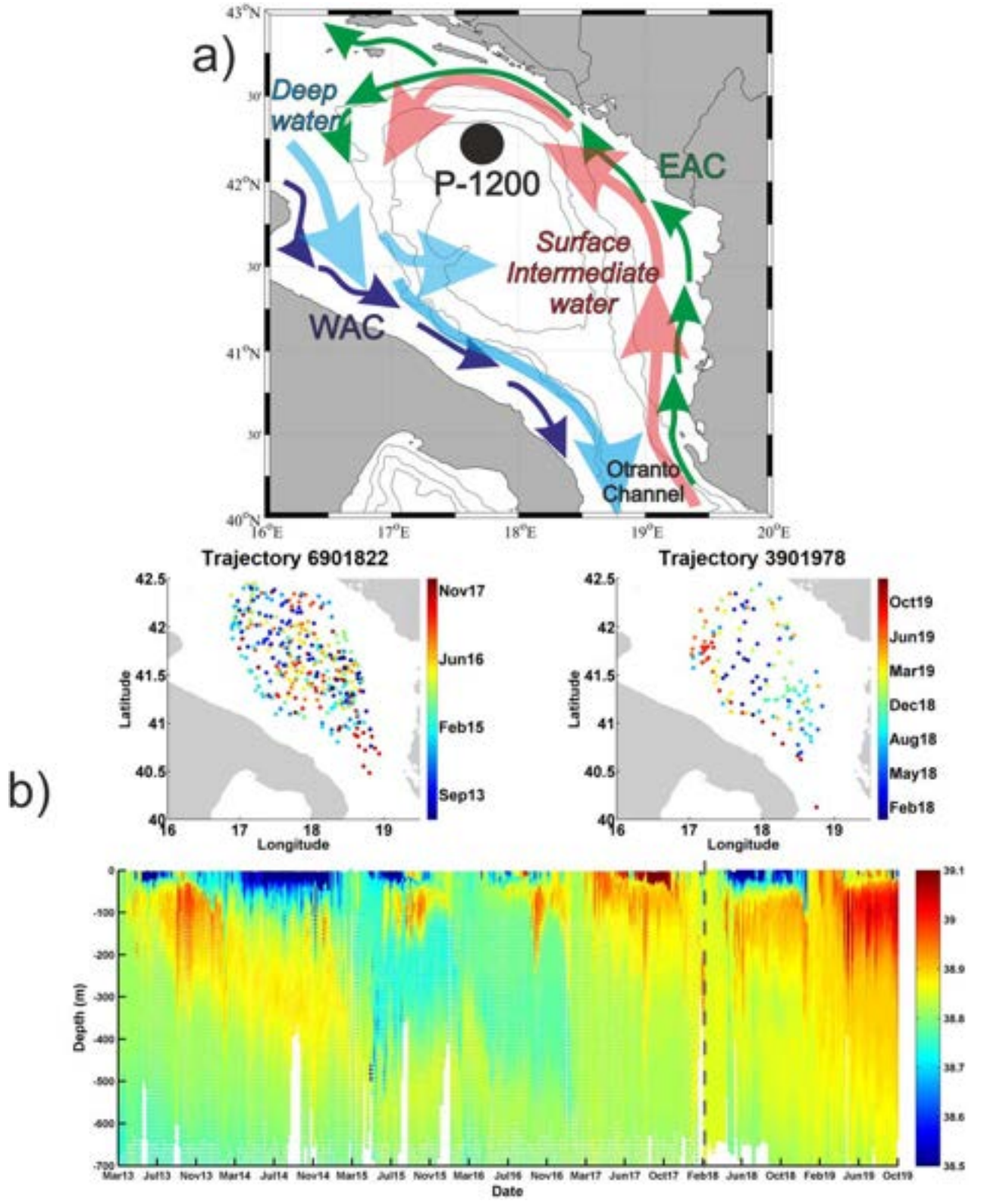

Figure 3.4.1. (a) Schematic representation of the main surface currents (solid arrows) and water masses (transparent arrows) in the SAP. Blue and green solid arrows describe the circulation of the WAC and EAC, respectively. Light blue and light red transparent arrows describe the outflow of deep waters (NABW and AdDW) and the inflow of surface and intermediate waters, respectively. Black circle shows the geographical location of the P-1200 station used for zooplankton measurements. Acronyms are defined in the text. (b) Float tracks (WMO 6901822 and WMO 3901978 – Product ref. 3.4.2) colour-coded by time and relative Hovmöller diagram of salinity (in PSU) in the SAP from 2013 to 2019. The vertical dotted line separates the profiles of the float WMO 6901822 from those of the float WMO 3901978.

The dry mass was estimated from mesozooplankton settled volumes and by applying the conversion formula obtained from ICES Zooplankton methodology manual (Harris et al. 2000). Dry mass was then converted to carbon following the method described in Hernández-León et al. (2019). Zooplankton biomass was used to estimate the potential sustainable fish biomass at higher trophic levels based on simplified energy approaches (Benović 2000; Fogarty et al. 2016). Such approach assumes that a fraction of the phytoplankton production and of zooplankton secondary production, extrapolated from biomass measures, is available to upper trophic levels such as planktivorous fish and this available food is transformed into fish biomass considering a fixed efficiency. A rough estimate of plankton production is obtained by considering an average productivity of the phytoplankton (1.185 and 1.165 d^{-1} in deep and superficial), zooplankton community (0.58 d^{-1}) emerging from other works (D'Alelio et al. 2016). Furthermore, although the predated fraction is changing across time, according to predator and plankton densities and encounter rate, at the beginning we assumed that the fraction of phytoplankton and zooplankton available to predators is specific but proportional to their biomass monthly production. In particular, the fraction of production available to upper trophic levels (5%, 17% and 95% for superficial phytoplankton, deeper phytoplankton and zooplankton, respectively) were extracted from detailed plankton food web analyses conducted in D'Alelio et al. (2016). Successively, the simplified approach assumes that the consumed prey energy is transformed into higher trophic levels production at an average transfer efficiency (14.25% ± 6.03%, average and standard deviation) considered from the results of a meta-analysis from several food web models (Libralato et al. 2008). Conversion factor from C to wet weight for fish was set to 1/9 gC gww-1 as widely used (Pauly and Christensen 1995). The energetic approach allows estimating the monthly average of potential planktivorous biomass production at higher trophic levels in t ww km^{-2} $month^{-1}$. Uncertainty on the potential production was calculated varying the transfer efficiency within the standard deviation range, since this parameter has the highest sensitivity on estimates.

3.4.3. Results and discussion

More than 1400 salinity profiles extracted in the SAP before 2015 from the SeaDataNet dataset, evidence the salinity maximum between 100 and 400 m of depth (the typical layer of the Levantine Intermediate Water). This vertical structure is also confirmed by the floats entrapped in the SAP in 2013 and 2014 (Figure 3.4.1(b)). From 2015 the float (Figure 3.4.1(b); see also Kokkini et al. 2018) and glider (Kokkini et al. 2019) data show important changes in the salinity distribution. In 2015 and 2016 the Levantine Intermediate Water high salinity signature is deeper than 400 m and a shallower subsurface salinity maximum located between 50 and 200 m of depth is evident. The lowest salinity concentrations are found in the top 50 m layer. Peculiar salinity profiles marked by a double salinity maximum are observed in 2015, 2016 and 2018; whereas in 2017 unusually high salinity values (over 39 PSU) occurred in the upper 0–100 m layer as result of both local and remote drivers (Paklar et al., 2020). The double salinity maximum is induced by a combination of events: the winter deep water convection and the intrusion of water masses of low salinity at intermediate depth.

In 2016 and 2017, the abundance of mesozooplankton in the upper 100 m is similar and the maximum is registered in March (Figure 3.4.2). In 2018 maximal abundance is shifted in April and an exceptional maximum for the oligotrophic open South Adriatic is recorded in the top 50 m layer, of 1423 ind m^{-3} (98% Copepods) out of which Calanoid Copepod abundance is 922 ind. m^{-3}. The timing of Copepod maximum observed in April 2018 is not uncommon; similar conditions are reported in the past by Hure et al. (1980), Hure and Kršinić (1998) and Batistić et al. (2003). This peak is comparable to the results of April 1993 (Batistić et al. 2003), when an abundance of Calanoid Copepods of around 700 ind. m^{-3} is associated with the East Mediterranean transient (EMT) and the consequent inflow of Atlantic Water into the SAP. During EMT period an increase of nutrients and consequently an increase in phytoplankton abundance and biomass was registered (Grbec et al. 2009; Vilibić et al. 2012; Mattia et al. 2013; Batistić et al. 2019). Latest investigations have also pointed out that in spring salp blooms in the open South Adriatic can play an important role in modulating phytoplankton and zooplankton blooms (Batistić et al. 2019).

The data in Figure 3.4.2 are not simply comparable with the literature, which frequently provides abundance per unit area (m^2) or seasonal and/or annual averages of zooplankton concentrations in terms of total Copepods or only Calanoid Copepods (Hure et al. 1980; Hure and Kršinić 1998). The few comparable studies in the SAP estimate a monthly number of around 450 ind. m^{-3} of Copepods (Miloslavić et al. 2012), with a maximum of 700 ind m^{-3} in the earlier 1990s (Batistić et al. 2003). The zooplankton data in the open Sea shown in the present work are featured for the first time giving an important contribution to the paucity of those kinds

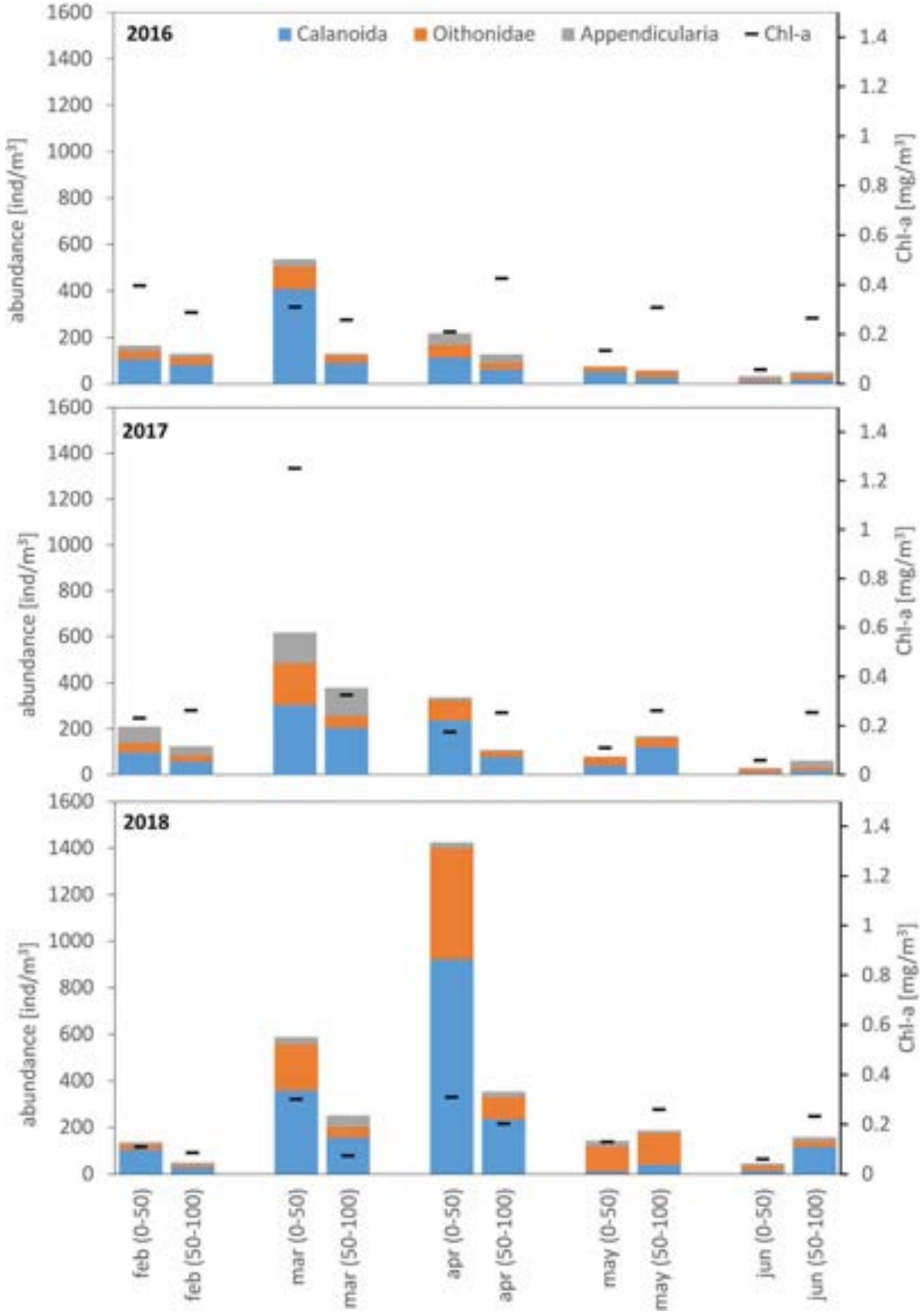

Figure 3.4.2. Histograms of zooplankton abundance distribution (Calanoida, Oithonida and Appendicularia; *y*-axis on the left) and Chl-a concentration integrated on the respective layer (horizontal black lines; *y*-axis on the right) at P-1200 station in the layers 0–50 m and 50–100 m for the period 2016–2018. The biweekly samples are averaged to obtain a monthly value and only the three years common months are displayed (data source: University of Dubrovnik – mirna.batistic@unidu.hr).

of data. In the literature the highest Copepod abundances in the SAP are commonly recorded in the period between April and June (e.g. Hure et al. 1980; Hure and Kršinić 1998; Batistić et al. 2003) which is considered to be associated with the typical seasonal phytoplankton maximum (Viličić et al. 1989; Viličić et al. 1989).

The period January–March is generally influenced by strong vertical mixing events and the salinity values become homogeneous in the whole layer affected by the mixing. In these months the mesozooplankton communities are similar in abundance and composition over the years analysed (Figure 3.4.2). Also the Chlorophyll concentration does not show a striking variability, except in March 2017 when a peak of 1.3 mg m^{-3} occurs. From April, the stratification in the upper layer and the ingression of water with different salinities can drive changes in the mesozooplankton communities. In particular, April 2018 looks very different from the previous two years: after the winter convection and in concomitance to the ingression of less salty water (Figure 3.4.1(b)), a peak in the mesozooplankton abundance is visible in the first 100 m (Figure 3.4.2). High numbers of Calanoida and Oithonidae are present in April 2018 in the upper layer and constitute a high percentage of the total mesozooplankton presence in the following months.

The salinity changes and their effects on zooplankton communities cascade up to higher trophic level species according to trophic preferences, competitions, grazing effects that are difficult to measure and to assess. Mesozooplankton biomass observed in relative and marked low (2016 and 2018) and high (2017) surface salinity scenarios are used to estimate net productivity. The 2016 is characterised by shallow vertical mixing (up to 400 m) and double salinity maximum while, in 2017 and 2018 there is a deeper winter vertical mixing (up to 700 m) which triggered stronger plankton production. Average transfer efficiency and predation mortality are considered for zooplankton groups to estimate the potentially supported biomasses of commercial fish as potential yield. The energetic approach provides a first rough approximation of monthly potential production of planktivorous species (Figure 3.4.3). Two peaks in productivity are highlighted in March 2017 and in April 2018. The first is related to the high chlorophyll concentration right after the convection process while the second, to the high zooplankton abundance that follows the ingression of low salinity water mass in the upper 50 m. Distribution and abundance of the mesozooplankton (Figure 3.4.2), as well as estimates of potential for sustaining planktivorous fish biomass (Figure 3.4.3), show comparable values in the period January-March, when also the recorded salinity values are closer to each other over the three years. On the other hand, the variability of abundance and distribution of mesozooplankton are higher in the post convection period (April-June), when also the salinity variations are larger.

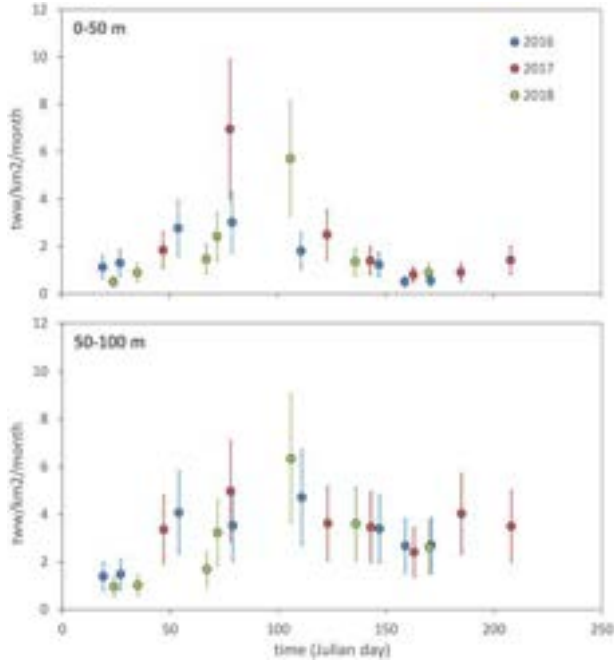

Figure 3.4.3. Estimates of potential for sustaining planktivorous fish biomass and relative error bars in the layers 0–50 m and 50–100 m for the period 2016–2018, which are estimated from zooplankton and phytoplankton community biomass using the energetic approach.

The peak in potential productivity estimated in March 2017 in the upper layer (6.95 t km^{-2} $month^{-1}$; Figure 3.4.3) is mainly due to the measured high phytoplankton concentration (see Figure 3.4.2). Analogous peak in tertiary productivity in April 2018 in the upper layer (5.70 t km^{-2} $month^{-1}$; Figure 3.4.3) is instead mostly due to the measured high mesozooplankton abundances (see Figure 3.4.2).

Notably, the average of potential productivity in April-June is lower in the 0–50 m layer (1.02 ± 0.43 t km^{-2} $month^{-1}$ in 2016; 1.56 ± 0.66 t km^{-2} $month^{-1}$ in 2017; 2.64 ± 1.12 t km^{-2} $month^{-1}$ in 2018) while it is higher in the 50–100 m layer (3.37 ± 1.43 t km^{-2} $month^{-1}$ in 2016; 3.16 ± 1.34 t km^{-2} $month^{-1}$ in 2017; 4.19 ± 1.77 t km^{-2} $month^{-1}$ in 2018) assuming that planktivorous fish and invertebrates can exploit both layers. The largest potential productivity values detected in 2018 are resulting in large part from mesozooplankton, which is the preferred prey of important commercial planktivorous such as anchovy and sardine (e.g. Borme et al. 2009, 2013). This contrasts with productivity estimates of 2017, which are mainly due to phytoplankton and might represent the source of food for ecologically important noncommercial species such as pelagic Polychaeta (Guglielmo et al. 2019). Although other oceanographic factors (e.g. temperature) can influence migration and thus the co-occurrence of fish and zooplankton, the energetic approach

provides a first order approximation of the potential bottom-up effects of stratification and zooplankton abundance on the fish populations and a first estimate of oceanographic impacts on fisheries sector.

Modifications induced by salinity changes on plankton communities might result in tangible impacts on fishermen's livelihoods. Indeed, changes in zooplankton diversity, abundance and secondary production can influence fish populations in complex ways by influencing their spawning, growing and survival potential according to feeding preferences of different fish life stages. Yet, long term fluctuation of landings of small pelagic species has been linked to changes in oceanographic features (Grbec et al. 2002): this work concurs in showing the potential decrease in the productivity of fish communities, with inevitable effects on fishing activities. More detailed analyses on spatial changes in salinity and zooplankton community patterns might also reveal further effects, such as fish population displacements to follow trophic opportunities: this additional effect implies the need for fishermen to modify their fishing grounds. Therefore, the impacts on the economy of the fisheries sector resulting from large oceanographic changes might range from short term decreased productions to inefficiencies for identifying new fishing grounds to the long-term modification of costs due to increased fuel consumption if exploited areas are patchy and distant from actual fishing ports. This work showed that oceanographic conditions can influence the fish production potential and therefore, represents a conservative first rough estimate of impacts of oceanographic features on fisheries. The present work wants to be a preliminary attempt and a pilot study to evaluate the potential relationship between salinity and zooplankton community. Additional plankton data will be collected during future field campaigns and deeper statistical analysis will be planned in order to further investigate these aspects.

Acknowledgements

This study has been funded by the Italian Ministry of University and Research as part of the Argo-Italy program and by the Croatian Science Foundation, under projects AdMedPlan (IP-2014-09-2945) and DiVMaD (IP-2019-04-9043).

3.5. Delivering high quality sea-ice information around the Svalbard archipelago to marine end-users

Authors: Cyril Palerme, Panagiotis Kountouris, Alexandra Stocker, Maaike Knol-Kauffman, Paul Cochrane, Malte Müller, Lasse Rabenstein

Ref. No.	Product name and type	Documentation
3.5.1	Sentinel-1 Synthetic Aperture Radar (SAR) images	
3.5.2	SEAICE_GLO_SEAICE_L4_NRT_OBSERVATIONS_011_006 (version 1.1) Remote Sensing	PUM: http://resources.marine.copernicus.eu/documents/PUM/CMEMS-SI-PUM-011-006.pdf QUID: http://resources.marine.copernicus.eu/documents/QUID/CMEMS-SI-QUID-011-001to007-009to013.pdf
3.5.3	ARCTIC_ANALYSIS_FORECAST_PHYS_002_001_a Model	PUM: http://resources.marine.copernicus.eu/documents/PUM/CMEMS-ARC-PUM-002-ALL.pdf QUID: http://resources.marine.copernicus.eu/documents/QUID/CMEMS-ARC-QUID-002-001a.pdf
3.5.4	Automatic Identification System (AIS) data from the Norwegian Coastal administration (Kystverket)	https://ais-public.kystverket.no/faq/
3.5.5	Version 2 of the global sea ice concentration climate data record (OSI-430-b product) of the Ocean and Sea Ice Satellite Application Facility (OSI-SAF) Remote sensing	Lavergne et al. (2019) http://osisaf.met.no/p/ice/ice_conc_cdr_v2.html
3.5.6	European Centre for Medium-Range Weather Forecasts (ECMWF) operational wind forecasts Model	https://www.ecmwf.int/en/forecasts/documentation-and-support

Statement of main outcome There is a growing demand for reliable sea-ice information around the Svalbard archipelago due to the stretching of operational seasons of maritime activities. However, many ships operating in the Arctic lack reliable internet connections (for instance, only Iridium Next satellite communication is available), and data visualisation is still cumbersome since scientific knowledge is needed to visualise the data properly. There is therefore a need for sea-ice products which can be easily downloaded and interpreted by end-users even when using low-bandwidth connections. In this section, we discuss the recent evolution of the maritime traffic around the Svalbard archipelago and the development of an application for delivering sea-ice information tailored to user needs. This application will provide information for near-real time monitoring (satellite images from the Sentinel-1 satellites) and sea-ice drift forecasts in the Svalbard area and its surroundings. The sea-ice drift forecasts are produced using machine learning techniques combining sea-ice forecasts from the TOPAZ4 system with wind forecasts and sea-ice observations. These calibrated forecasts outperform the sea-ice drift forecasts

from TOPAZ4, and provide more accurate information to end-users.

3.5.1. Introduction

Climate change affects marine systems most drastically in polar regions. During the last decades, the Svalbard archipelago has experienced a particularly strong temperature increase associated with sea-ice decline (Isaksen et al. 2016; Hanssen-Bauer et al. 2019). Due to declining sea-ice, new and remote areas are becoming accessible and seasonal maritime activity is increasing in many Arctic regions, whereas the operational season is extending in Svalbard. Consequently, new shipping routes are projected (Lasserre 2015; Melia et al. 2017) and early patterns of increased fishing activity in the high North are already becoming visible,[18] following migrating fish stocks (Fossheim et al. 2015; Frainer et al. 2017). The popularity of 'last chance tourism' has increased the number of cruise vessels operating in remote areas (Lemelin et al. 2010; Palma et al. 2019).

Svalbard has a unique climate that makes it attractive for maritime activities to take place at such high latitudes. The West Spitsbergen Current transports warm Atlantic water leaving the west coast free of sea-ice year-round, while the east coast is ice covered most of the year. Increasing water temperature prevents sea-ice from forming and is thinning the present ice cover, resulting in a decline of sea-ice concentration over the winter months (Onarheim et al. 2014; Renner et al. 2018). Furthermore, the sea-ice cover around Svalbard is changing from multi-year ice to predominantly first-year ice (Renner et al. 2013; Rosel et al. 2018). Thus, both the thickness and extent of the ice cover are declining around the archipelago (Kwok et al. 2009; Rosel et al. 2018).

Although the number of vessels operating around Svalbard has remained fairly stable between 2012 and 2019 (Figure 3.5.1), these numbers are expected to grow in the future. For example, the past decade has seen the total number of cruise passengers growing by 73% from 38,737 in 2008 to 66900 in 2018 (Stautland 2019). Recent studies show an increase in operational seasons and an expansion of operational areas around Svalbard (Stocker et al. 2020), showing that growing numbers of vessels sail into areas higher than 80 degrees north (Aase and Jabour 2015; Bystrowska 2019). In recent years, there has been a large rise in the number of smaller vessels in the Arctic (IPCC 2019).

Although it is expected that maritime activity around Svalbard will continue to increase, there are uncertainties related to how these sectors will develop. In its most recent Svalbard strategy, the Norwegian government emphasises the need to assess preparedness and safety challenges arising from increased activity in the remote waters around Svalbard.

Vessel operators in Arctic environments have highly specific needs with regard to information services, due to the challenging, remote, and dynamic environments in which they operate, where Internet connectivity is highly limited (Lamers et al. 2018; Wagner et al. 2020). The changing activity patterns in the Arctic, in combination with progress in information and communication technology and the desire to improve customised data conveyance from provider to user, has stimulated the establishment of collaborative platforms for the development of tailor-made services (Knol et al. 2018). The remainder of this chapter will describe one such initiative in depth.

3.5.1.1. The IcySea application

The IcySea application has been developed in order to provide reliable sea-ice services to end-users in a user-friendly interface which can work even with a limited internet connection. The application consists of two main parts, the backend structure and the user client frontend. The backend runs at a dedicated computing facility on land, and processes sea ice concentration observations, Sentinel-1 Synthetic Aperture Radar images, and ice drift forecast data. It uses the optimised ice drift forecasts to derive 10-day point trajectories with a daily step, revealing the ice movement. Figure 3.5.2 reveals the area covered by the ice service as this is formed by the set of the grid points, which we use to calculate the trajectories. The trajectories are calculated using a Lagrangian approach. For each point, we derive via a linear interpolation its horizontal and vertical velocity components, and we calculate the displacement at each axis. Then, we calculate its new location and repeat the procedure for all time steps. Due to the temporal resolution of the sea-ice drift observations used for training the random forest algorithms (24 h), we were limited to use daily temporal resolution for calculating sea-ice trajectories.

Further, the backend processes Sentinel-1 SAR images (product reference 3.5.1) and makes them available to the frontend in near-real-time (NRT) which, for this data source, is 2–3 h after satellite acquisition. The images are radiometrically calibrated, denoised and terrain corrected. They are then segmented into subregion tiles, a necessary step which ensures a moderate image size and thus allows the data to be transferred under low bandwidth connections (such as Iridium Next). A key feature of the application design is to keep data transfer costs to a minimum, and fully controlled by the user. There are no hidden downloading processes on the

background and further, the imagery data are optimised in size and resolution.

The users will have the possibility to select whether or not to download the relevant files. Before any download happens, the user will be informed about the data date and their size, and can select between two spatial resolutions: 300 and 30 m. The metadata exchange (file size, date etc.) is just a few bytes, while each tile is expected to be approximately 50 kb and 2 Mb for the 300 and 30 m resolution image respectively. The whole process, including data collection and processing is fully automated.

The frontend is platform independent and uses web application technologies. Most importantly, it works offline by design, and it is portable across both desktop and mobile platforms. Special attention was given to ensure a high quality user experience while at the same time keeping it easy to use and user friendly. The frontend also includes a high resolution landmask, a graticule to aid navigation, and toggleable data layers that the user will have full control to switch on and off. To keep distortions at a minimum around the Pole, data are visualised using a polar stereographic projection.

IcySea design and development follows feedback and experience gained over the last 5 years from users and clients of the Drift Noise GmbH. Nautical crews of expedition cruise ships, research ice breakers, cargo ships and ice pilots operating in Arctic and Antarctic, provided us with valuable feedback on their needs and the features that such an Application should include. Furthermore, during IcySea's development we have engaged test users like AECO (Association of Arctic Expedition Cruise Operators), Fiskebåt (Norwegian fishing vessels owners association) the Maritimt Forum Nord, and FUGRO a hydrographic survey company. The application will be tested by these users, and their feedback will further drive the development.

3.5.1.2. Calibration of sea-ice drift forecasts

Information about sea-ice drift is of crucial importance for marine end-users operating in the Arctic (Jeuring and Knol-Kauffman 2019). It can help to assess how fast sea-ice conditions are changing and can therefore influence decision making. Short-term sea-ice drift forecasts are produced by numerical prediction models, but are nevertheless affected by biases (Hebert et al. 2015; Schweiger and Zhang 2015; Rabatel et al. 2018). However, statistical methods can be used to reduce the errors and improve forecast accuracy.

For the IcySea application, random forest algorithms have been developed in order to produce 10-day sea-ice drift forecasts with daily time steps. Different algorithms have been developed for predicting the direction and the speed of sea-ice drift, as well as for different lead times. The random forest algorithms (Breiman 2001) combine many decision trees in order to assess relationships between a set of predictor variables and a target variable (100 trees have been used for developing the models of the IcySea application). Furthermore, the calibrated sea-ice drift forecasts are produced only where the sea-ice concentration predicted by the TOPAZ4 system (Sakov et al. 2012, product reference 3.5.3) is larger than 10%.

The target variables (sea-ice drift direction and speed) used for developing and evaluating the calibrated forecasts are computed from the Sentinel-1 observations (MOSAIC product, reference 3.5.2). Short-term wind forecasts (direction and speed) from the European Centre for

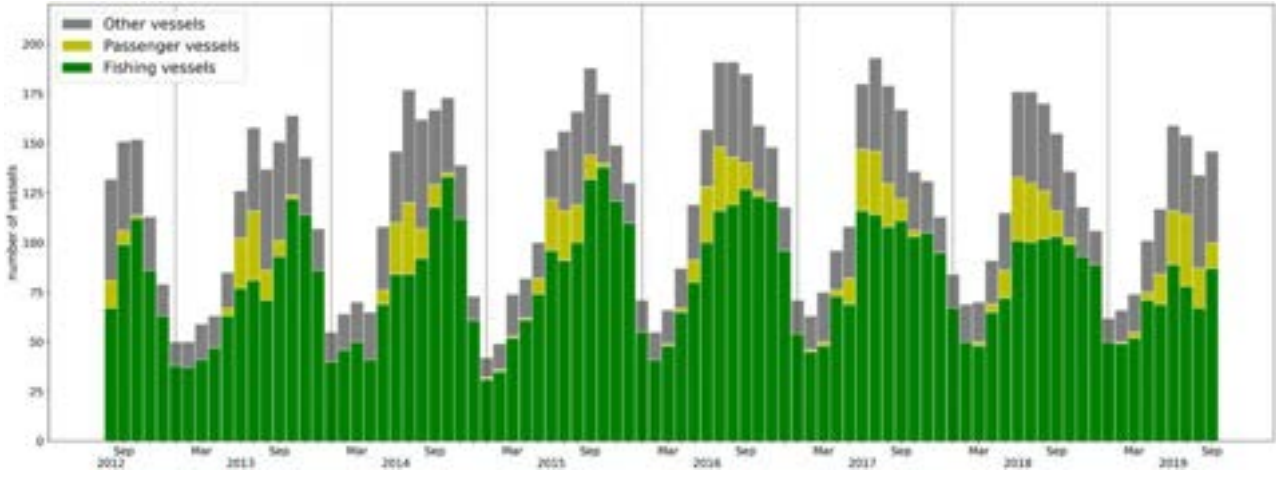

Figure 3.5.1. Figure from Stocker et al. (2020). Automatic Identification System (AIS) data (product reference 3.5.4) from the Norwegian Coastal administration (Kystverket) was used to illustrate the number of unique vessels per month in the Svalbard Fisheries Protection Zone between January 2012 and September 2019. Green: fishing vessels, yellow: passenger vessels (oversea and expedition cruise ships) and grey: other categories (bulk carriers, container ships, research vessels, etc.).

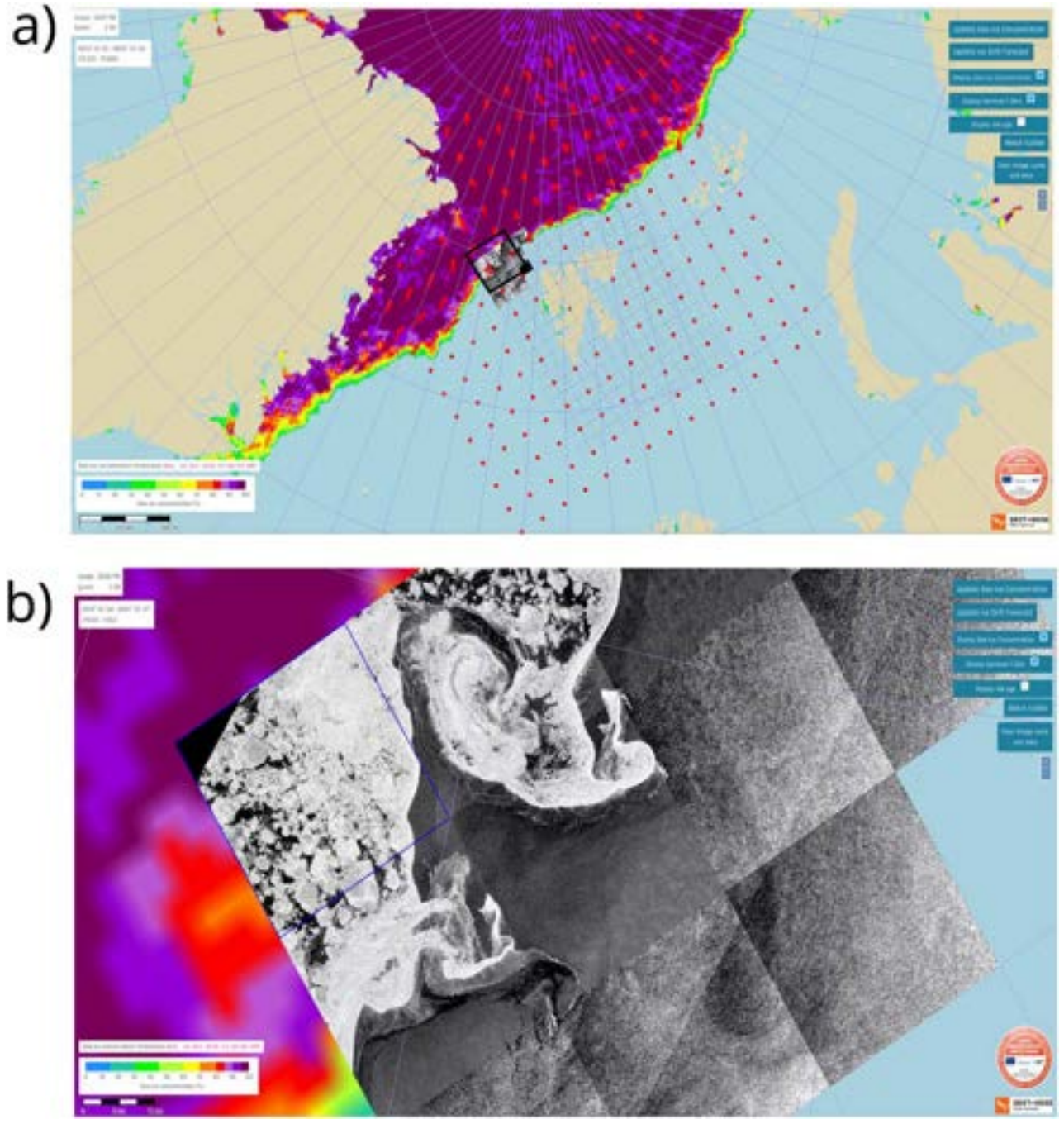

Figure 3.5.2. (a) Illustration of the IcySea service. The area in which calibrated ice drift forecasts are available is revealed by the red grid points. Ice movement is denoted by a set of points such that they form a trajectory; opaque red colour denotes the starting forecast days (initial point position) and transparent colours the end of the forecast (final point position). Tiled Sentinel-1 SAR images (product reference 3.5.1) are plotted in grey. (b) Zoomed example from the black subdomain in subfigure (a), of a Synthetic Aperture Radar image (product reference 3.5.1) from Sentinel-1 at 30 m spatial resolution showing the advantage of this data stream, to reveal the spatial sea-ice structure. Open sea and ice floes can be easily identified. Data layers can be easily turned off/on with a simple click of a button.

Medium-Range Weather Forecasts (ECMWF, product reference 3.5.6), and sea-ice forecasts (drift direction, drift speed, concentration and thickness) from the TOPAZ4 system (product reference 3.5.3) are used as predictor variables. In addition, sea-ice concentration observations from the Ocean and Sea Ice Satellite Application Facility (Lavergne et al. 2019, product reference 3.5.5) during the day preceding the forecast start date, as well as the geographical coordinates of the grid points (x and y coordinates) from the TOPAZ4 system and the distance to the nearest coastline are also used as predictor variables. It is worth noting that all the predictor and target variables

have been interpolated on the grid used in the TOPAZ4 system (polar stereographic grid at 12.5 km spatial resolution) before developing the statistical models. The relationships between sea-ice drift, near surface wind and sea-ice conditions (sea-ice concentration and thickness) are complex and not linear (Yu et al. 2020). Nevertheless, random forest algorithms are suitable for assessing nonlinear relationships between a set of predictor variables and a target variable. Furthermore, the data from all the grid points within the TOPAZ4 domain in the Arctic have been concatenated in order to create a large database for training the random forest models.

A period of three years and eight months (from 11 August 2016 to 30 April 2020) has been used for training the random forest algorithms. There is one training dataset per week (forecasts starting on Thursdays) for each grid point covered by the Sentinel-1 observations (MOSAIC product, reference 3.5.2) during the target date. While all the datasets from this period have been taken into account for developing the models used for

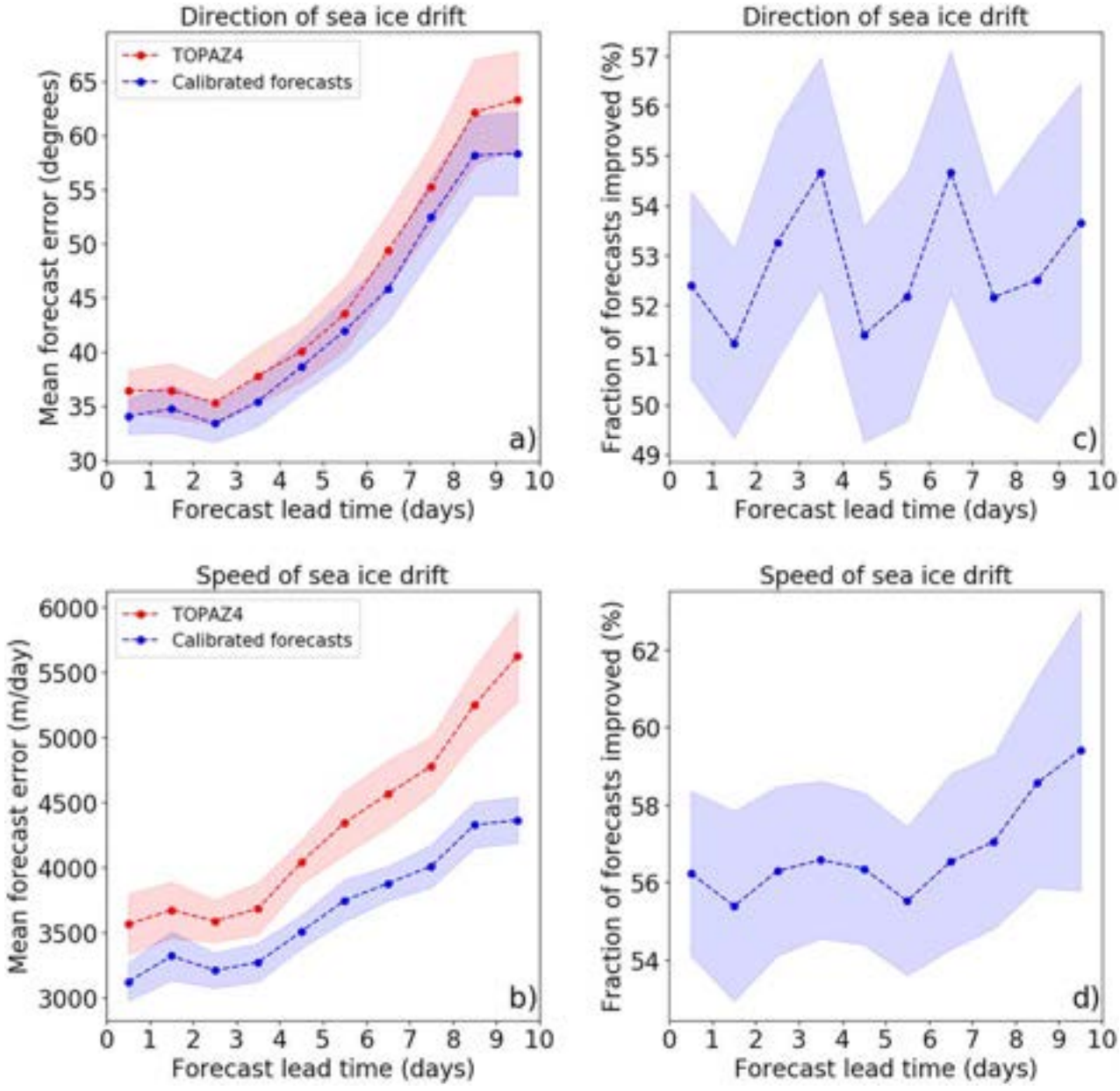

Figure 3.5.3. Performances of the calibrated forecasts and the TOPAZ4 forecasts (product reference 3.5.3) for the area shown in Figure 3.5.2(a). The sea-ice drift observations from the product 3.5.2 (SAR observations) have been used as the reference in this evaluation. (a, b) Mean absolute error for the drift direction (a) and the drift speed (b). (c,d) Fraction of forecasts improved by the calibration for the drift direction (c) and the drift speed (d). The shaded areas represent the standard deviations of the results over 50 different selections of the datasets used for training and for testing the algorithms.

the forecasts delivered on the IcySea application (between 3.5 and 3.8 millions of individual datasets depending on the lead time), only 80% of these datasets have been taken into account for training the models used for evaluating the performances of the algorithms. The remaining 20% of the datasets were used to evaluate the performances of the statistical models. The selection of the datasets used for training and testing the models is a random process (according to the forecast start date), and has been repeated 50 times in order to test the influence of this selection on the performances of the calibrated forecasts.

The performances of the calibrated forecasts for the area shown in Figure 3.5.2(a) are presented in Figure 3.5.3. Overall, there is a larger improvement for the speed than for the direction of sea-ice drift. Nevertheless, the calibrated forecasts outperform the TOPAZ4 forecasts for all the lead times for the direction and the speed of sea-ice drift (lower mean absolute errors). Furthermore, most of the calibrated forecasts have lower errors than the TOPAZ4 forecasts (Figure 3.5.3(c,d)). On average, about 53% of the forecasts are improved by the calibration for the drift direction and 57% for the drift speed. The calibrated forecasts delivered on the IcySea application are therefore more accurate than the forecasts produced by the TOPAZ4 system.

3.5.2. Conclusion

Maritime traffic around the Svalbard archipelago has shown changing patterns during the last decade, with expanding seasons and operational areas (Stocker et al. 2020). In this challenging operational environment, sea-ice remains one of the major sources of uncertainty for navigating in this area, and there is a need for sea-ice information that can be easily downloaded and visualised by end-users. The IcySea application addresses this need by delivering satellite images and sea-ice drift forecasts in a user-friendly interface. The calibration method developed for the IcySea application improves the accuracy of sea-ice drift forecasts compared to the forecasts from TOPAZ4. Furthermore, it is designed to work offline and the data can be downloaded under low-bandwidth connections, which is a common limitation in the Arctic. This application should therefore contribute to improving operational planning and safety in the Svalbard area.

Section 3.6. Developing spatial distribution models for demersal species by the integration of trawl surveys data and relevant ocean variables

Authors: Panzeri D., Bitetto I., Carlucci R., Cipriano G., Cossarini G., D'Andrea L., Masnadi F., Querin S., Reale M., Russo T., Scarcella G., Spedicato M.T., Teruzzi A., Vrgoč N., Zupa W., Libralato S.*

Statement of main outcome: Demersal species play a fundamental role in fisheries, thus understanding their distribution and abundance through bottom trawl surveys is crucial for stock and fisheries management. Oceanographic (e.g. biogeochemical, physical) and fishing covariates might be considered, in addition to spatio-temporal variables (latitute, longitude, depth, year and month), to better explain trawl survey data. Here, we analyse biomass indices (kg/km^2) for European hake, common sole, mantis shrimp, red mullet and common cuttlefish from scientific trawl surveys carried out in the Adriatic Sea and the Western Ionian Sea. We used three different Generalised Additive Model (GAM) approaches (Gaussian, Tweedie and Delta) to fit and predict species biomass distribution. In order to evaluate trade-offs in using different covariates, we compared the results obtained from GAM approaches based only on spatiotemporal variables and GAMs including also oceanographic and fishing effort covariates.

The Delta-GAM approach performed better for European hake, mantis shrimp and common cuttlefish, while GAMs based on Gaussian and Tweedie were performing better for the red mullet and common sole, respectively. The results highlighted that adding specific oceanographic and effort covariates to spatiotemporal variables improved the performances of spatial distribution models especially for European hake, mantis shrimp and red mullet. Significant additional explanatory variables were bottom temperature, bottom dissolved oxygen, salinity, particulate organic carbon, and fishing effort for European hake; the same variables and pH for mantis shrimp; chlorophyll-a, pH, sea surface temperature, bottom dissolved oxygen, nitrate and effort for the red mullet; phosphate and salinity for common sole; bottom temperature, bottom dissolved oxygen, and phosphate for the common cuttlefish.

The findings highlight that more accurate estimates of spatial distribution of demersal species biomass from trawl survey data can generally be obtained by integrating oceanographic variables and effort in GAMs approaches with potential impacts on stock assessment and essential fish habitats identification.

Products used

Ref. No.	Product name and type	Documentation
3.6.1	MEDSEA_REANALYSIS_PHYS_006_004	PUM: http://marine.copernicus.eu/documents/PUM/CMEMS-MED-PUM-

(*Continued*)

Continued.

Ref. No.	Product name and type	Documentation
		006-004.pdf QUID: http://marine.copernicus.eu/documents/QUID/CMEMS-MED-QUID-006-004.pdf
3.6.2	MEDSEA_REANALYSIS_BIO_006_008	PUM: http://marine.copernicus.eu/documents/PUM/CMEMS-MED-PUM-006-008.pdf QUID: http://marine.copernicus.eu/documents/QUID/CMEMS-MED-QUID-006-008.pdf
3.6.3	MEDITS: Mediterranean International Trawl Survey; bottom trawl survey up to 800 m depth. From 1994 to 2018 on average 326 sampling sites (hauls) per year were conducted in the Adriatic and Northern Ionian Sea.	Bertrand et al. (2002), Spedicato, Massutí, et al. (2019), MEDITS-Handbook (2017)
3.6.4	SOLEMON: Sole Monitoring, modified beam trawl surveys conducted in the Northern Adriatic Sea up to a depth of 100 m; on average 70 sampling (hauls) per year from 2005 to 2018.	Scarcella et al. (2011), SoleMon Handbook 2019 (http://dcf-italia.cnr.it/assets/lineeguida/lin1/2019/SOLEMON-Handbook_2019_Ver_4.pdf)

3.6.1. Introduction

Marine fish and invertebrates that live and feed close to the marine seabed, i.e. the demersal species, play a fundamental role in fisheries. In the Mediterranean and Black Sea, these species constitute approximately 20% of the total landed weight (more than 230,000 tons/year) and 50% of the total landed value (FAO 2018). In order to ensure the sustainability of exploitation, a set of fisheries management measures and restrictions are adopted also considering scientific information on the status of resources. Clearly, management actions are particularly relevant and impacting in large areas of the Mediterranean Sea where demersal resources play a central role in local fishing communities and economies, such as the Adriatic and Ionian seas. Therefore, it is of paramount importance to increase accuracy of scientific information used to inform management.

Scientific bottom trawl surveys provide quantification of abundance and biomass (hereafter termed indices) by species, i.e. fishery-independent data, that are used for manifold purposes related to management: stock assessment (e.g. Cotter et al. 2009), evaluation of spatio-temporal distribution of demersal resources (e.g. Carlucci et al. 2009), estimates of population and community densities (e.g. Spedicato, Zupa, et al. 2019), and the development of ecosystem models (e.g. Grüss et al. 2018; Moullec et al. 2019). Sampling protocols of multiannual surveys are usually standardised for sampling design, gear geometry, sampling season, sampling locations to allow comparability of the trawl survey data across space and time. However, unavoidable small deviances (e.g. sampling period) or changes (e.g. vessel) during sampling may affect the abundance and biomass indices obtained from trawl surveys.

In order to test the potential benefits on using oceanographic and effort variables in addition to spatio-temporal covariates (latitute, longitude, depth, year and month) to improve species distribution models based on trawl survey data, Generalised Additive Models (GAMs) were chosen for their wide application and suitability with trawl survey data (Grüss et al. 2014; Lauria et al. 2017; Tserpes et al. 2019). GAMs allow to predict species abundance and biomass over the domain (Maunder and Punt 2004; Rubec et al. 2016; Potts and Rose 2018) and provide estimates useful for tuning stock assessment models (Cao et al. 2017; Orio et al. 2017). Furthermore, GAMs are deemed appropriate for mapping species distribution that is useful in ecosystem models (Fulton et al. 2011; Grüss et al. 2014), or for identifying Essential Fish Habitats (e.g. Colloca et al. 2015; Druon et al. 2015).

In addition to monitoring deviances, environmental changes and anthropogenic stressors may cause life-history responses, and their impacts on survey estimates are difficult to disentangle. Satellite data are successfully used to provide environmental variables (e.g. sea surface temperature; sea surface chlorophyll concentration) to be included in models to describe the spatial distribution of some pelagic species (Giannoulaki et al. 2008; Schismenou et al. 2017). However, these variables might be insufficient to model the distribution of demersal species, which may require additional oceanographic variables close to seabed such as those provided by the Copernicus Marine Environment Monitoring Service (CMEMS). The relative high number and the quality of the CMEMS products, as well as their high temporal coverage and spatial resolution, provide biogeochemical and physical oceanographic variables that can be useful to improve the analysis of abundance and biomass indices derived from trawl surveys (e.g. Sion et al. 2019; Tserpes et al. 2019).

In addition, the displacement of fishing fleets derived from satellite-based tracking devices, such as Vessel Monitoring System (VMS) and/or Automatic Identification System (AIS), is a valuable source of information on the distribution and spatial aggregation of marine resources (Bastardie et al. 2014; Russo et al. 2018). The yearly distribution of fisheries, in

fact, represents a good track of the distribution of the targeted resource rather than a measure of the direct impact on it (which is a much longer term effect). Thus increasing accuracy of distribution of the species might be gained embedding fishing effort among the explanatory variables.

In this work, therefore, we propose an integrated approach useful to fisheries management by combining trawl survey data, oceanographic variables and fishing effort estimates. Biomass indices of demersal fish from scientific trawl surveys carried out in the Adriatic Sea and in the Western Ionian Sea (Adriatic-Ionian macro-region, EUSAIR 2014) are analysed with a set of GAM approaches using as explanatory variables the relevant biogeochemical and physical variables from CMEMS products and the distribution of fishing effort from VMS/AIS data. The objective of the study is to contrast models with spatiotemporal variables only and with different sets of additional explanatory variables in order to explore the improvement on estimates of demersal species distribution when environmental variables and effort are included into species distribution models.

3.6.2. Material and methods

We used data from the bottom trawl surveys conducted in the Adriatic Sea and North Western Ionian Sea, i.e. in the geographical sub-areas (GSAs) 17, 18 and 19 as defined by the FAO-GFCM (General Fisheries Commission for the Mediterranean Sea). We used MEDITS (Mediterranean International Trawl Survey; Spedicato, Massutí, et al. 2019) data from 1994 to 2018 that consists on average 326 sampling sites (bathymetrical range 10–800 m) per year in the three GSAs (Product Ref. 3.6.3) and SOLEMON (Sole Monitoring; Scarcella et al. 2011; Grati et al. 2013) from 2005 to 2018, that consists on average 70 sampling sites per year in GSA 17 (bathymetrical range 10–100 m) (Product Ref. 3.6.4). Indices of demersal species biomass (kg/km^2) were retrieved from the MEDITS dataset for European hake (*Merluccius merluccius*) and red mullet (*Mullus barbatus*) and from the SOLEMON dataset for common sole (*Solea solea*), mantis shrimp (*Squilla mantis*) and common cuttlefish (*Sepia officinalis*).

For each species, GAMs were applied to fit biomass indices by sampling site, set as a response variable, while spatiotemporal variables, oceanographic variables and fishing effort were tested as covariates. Among the spatiotemporal variables we used geographic coordinates (latitude, longitude expressed in UTM coordinates), depth (m), month and year of the observations. Among all the variables available from the 3D monthly CMEMS Mediterranean reanalysis fields (Product Ref. 3.6.1 and 3.6.2) relevant oceanographic variables were considered on the basis of known ecological importance for chosen demersal species (Carlucci et al. 2018; Bitetto et al. 2019) as well as proxies for productivity and favourable environments. The relevant oceanographic variables considered were the water temperature (°C) and dissolved oxygen (mmol/m^3) at the sea bottom, water column averages of nitrate and phosphate concentration (mmol/m^3), chlorophyll-a (mg/m^3), particulate organic carbon (mg/m^3), pH and salinity. These variables were derived from the CMEMS dataset that covers the period 1999–2018, has a spatial horizontal resolution of 1/16° and 72 unevenly vertical levels (Simoncelli et al. 2019; Teruzzi et al. 2019). Furthermore, commercial trawling effort expressed as trawling time (in hours) per year at spatial resolution of 1/16° was estimated from VMS/AIS data for the period 2008–2018 (Russo et al. 2014) and was tested as explanatory variable on the basis of the evidence that fishing effort is a good track of species density. Although different time frames were initially adopted (depeding on the available explanatory variables), here we report the analysis performed on the time frame 2008–2018 that allowed the complete overlap between trawl survey, CMEMS and effort datasets. The explanatory variables were preliminarily selected using the VIF approach (Variance Inflation Factor; Sheather 2009) with a threshold of VIF<5 to avoid collinearity (see also Orio et al. 2017; Sion et al. 2019).

The results of the VIF analysis identified for all the species the spatiotemporal variables, i.e. year, month, depth, latitude, longitude, to be included as explanatory variables. Furthermore, the VIF analysis by species allowed to include additional explanatory variables without collinearity extracted from CMEMS reanalysis and fishing effort: the VIF results showed to be species-specific. Thus the complete model for European hake included the spatiotemporal variables and the bottom temperature, bottom dissolved oxygen, nitrate concentration, salinity, bottom particulate organic carbon, and fishing effort. For the red mullet the following explanatory variables were retained after VIF analysis in the most complete model: month, latitude, longitude, year, depth, pH, chlorophyll-a, sea surface temperature, bottom dissolved oxygen, nitrate, salinity and effort. For the common cuttlefish, the complete set of variables after VIF included month, latitude, longitude, year, depth, bottom temperature, bottom dissolved oxygen, nitrate, phosphate and effort. For common sole the complete set of variables included month, latitude, year, depth, average phosphate, bottom temperature, bottom dissolved oxygen, salinity, average phosphate, pH and effort. For mantis shrimp the set of variables

are month, latitude, year, depth, bottom temperature, bottom dissolved oxygen, salinity, particulate organic carbon, pH and fishing effort (more details in Supplemetary Material).

Different GAM distribution families were applied in order to demonstrate the potential benefits of using additional variables disregarding the model structure. GAMs were developed using Gaussian probability distributions with identity link on trawl survey biomass data log-transformed for all species, except common cuttlefish, for which better results were obtained by using square root transformation. GAMs were also applied using Tweedie probability distributions with lognormal link on untransformed biomass indices. Furthermore, the Delta-GAM approach was implemented in two steps: (i) a binomial occurrence model was used to fit presence/absence data (binomial family error distribution logit link function), (ii) a Gaussian distribution model with identity link function on transformed biomass for presence-only data (Grüss et al. 2014; Lauria et al. 2017). A grid of regular points with the same resolution of the selected CMEMS product (1/16°) and covering the study area was created to predict species biomass distribution by the selected models (Tserpes et al. 2019; Spedicato, Zupa, et al. 2019). For Delta-GAM the final spatial distribution of species biomass as kg/km^2 is obtained by multiplication of Gaussian and Binomial models' predictions to the grid of the model's domain (Grüss et al. 2014; Lauria et al. 2017).

For each species and all GAMs distribution families (Delta, Gaussian and Tweedie), a back-stepwise approach was used. This started from the most complete integrated approach, given by the spatiotemporal variables (geographical coordinates, depth, year, month) combined with all the most meaningful additional biogeochemical, physical and fishing effort variables identified by VIF analysis (model 0). Then the back-stepwise approach consisted in decreasing the number of explanatory variables by successively removing those with lower F statistics till to obtain the model with spatiotemporal variables only. Thus, the back-stepwise approach resulted in a set of models having different explanatory variables to obtain the response variable ($R = \log$ kg/km^2 or presence/absence) (see Supplementary Material). Each model was subjected to a calibration-validation process, thus it was fitted on a training dataset made by randomly choosing 70% of the data (calibration) and testing it on the remaining 30% of records (validation). The training and testing were repeated using 50 runs on datasets randomly selected and without replacement. The best model was selected on the basis of measures of model's performance evaluated through explained deviance (%ED) and prediction errors (AIC, Akaike Information Criterion) on the training datasets as well as correlation coefficient (R^2) of the model predictions on the testing dataset.

For each model with decreasing number of explanatory variables (model 0, model 1, model 2, etc.), the mean of each measure of model's performance (%ED, AIC, R2) was calculated from the 50 runs and compared using the Tukey's test (Tukey 1949). This comparison allows to assess the improvement of performances when different sets of additional variables were used in the models. The best model was chosen based on AIC, but other measures of performance were reported for showing their general consistency.

The chosen model for each species is used to obtain maps of the biomass distribution (kg/km^2) on the most relevant month (July and November, for MEDITS and SOLEMON species, respectively). The maps allowed identifying areas of high biomass density (hot-spots) in the GSAs 17, 18 and 19. Furthermore, a set of spatial indicators (Woillez et al. 2009) permitted to compare models' performances in describing the spatial distribution of demersal species when including or not additional explanatory variables. The set of indicators are the Spreading area (SA), i.e. a measure of the area occupied by the population weighted by the biomass; the latitude of the centroid or centre of gravity of data (CGY), which represents the mean geographic location of the population; the longitude of the centroid (CGX); the distance (D) between the centroid estimated on observations and the centroid estimated on predictions (Woillez et al. 2009; Rufino et al. 2018). Distribution statistics (first and third quartile, median) and performance indicators (mean absolute error MAE and R^2) were also estimated. Comparing such indicators calculated on raw trawl survey data, on models based only on spatiotemporal variables and on the chosen best models using the complete set of significant variables, allow to quantify the improvement of adopting the integrated approach, i.e. embedding biogeochemical, physical and fishing effort, in species distribution models.

3.6.3. Results and discussion

For European hake, mantis shrimp and common cuttlefish the Delta-GAM models were performing better while for the red mullet and common sole the best results were obtained using the Gaussian model and Tweedie, respectively (details are reported in Supplementary material). Figure 3.6.1 shows measures of performance (%ED, AIC, R2) resulting from the back-stepwise approach applied to the most

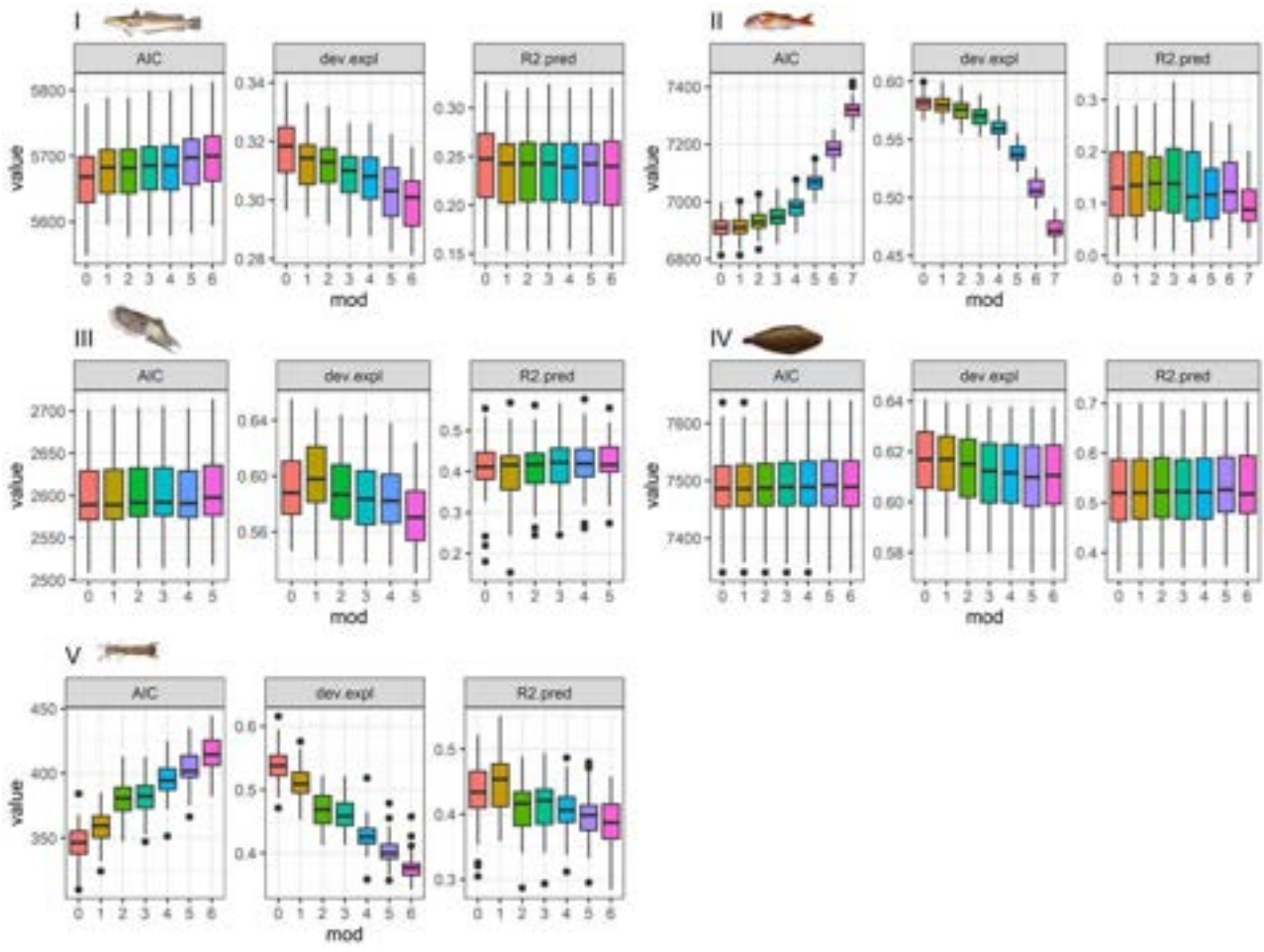

Figure 3.6.1. Performances of the best GAMs in describing the distribution of demersal species for models using a decreasing number of explanatory variables. The best model was Delta-GAM for European hake, common cuttlefish and mantis shrimp (shown the Delta-Gaussian in panels I, III and V, respectively), Gaussian for red mullet (panel II) and Tweedie for common sole (panel IV). For all species the starting model represents the one (model 0) including all the covariates resulting from VIF analysis and including spatiotemporal variables, environmental CMEMS variables and fishing effort (Product Ref. 3.6.1 and 3.6.2, respectively). Successively one variable at each step is removed to reach the minimal model (model 6 for European hake, common sole and mantis shrimp; model 7 for red mullet; model 5 for common cuttlefish) with spatiotemporal variables only. Box-plots synthesise results of the 50 runs of the training/testing procedure in terms of Akaike Information Criterion (AIC), explained deviance (dev-expl) on the 70% training dataset and correlation coefficient (R^2) for the remaining testing dataset.

appropriate family of GAM models for each species (only Delta-Gaussian is reported in the figure for European hake, mantis shrimp and common cuttlefish; the full Delta-GAM results for these species are reported in Supplementary material). Results for the 50 trials of training/testing demonstrate the model improvements when using CMEMS and effort variables in GAMs (Tukey's tests are reported in Supplementary material).

For European hake, the average AIC for Delta-Gaussian increased from 5600 for the model including the complete set of variables (model 0, panel I) to 5700 for the minimal model with spatiotemporal variables only (model 6, panel I). Coherently, the average % ED decreased from 0.32–0.29, and R^2 decreased from 0.24–0.23 from model with complete set of variables to model with spatiotemporal variables (Figure 3.6.1, panel I). For red mullet AIC increased from 6950 to 7340, %ED decreased from 0.57–0.47 and R2 decreased from 0.12–0.09 from the complete to the minimal model (Figure 3.6.1, panel II). For mantis shrimp AIC increased from 350 to 420, %ED decreased from 0.55–0.37, and R2 decreased from 0.44–0.38 from the complete to the minimal model (Figure 3.6.1, panel V). For common cuttlefish and common sole (panels III and IV) the differences in AIC and R2 are less marked when moving from the complete model (0) to the model with spatiotemporal variables (model 5 and 6) but yet the improvement is appreciable in terms of %ED. For all species analysed,

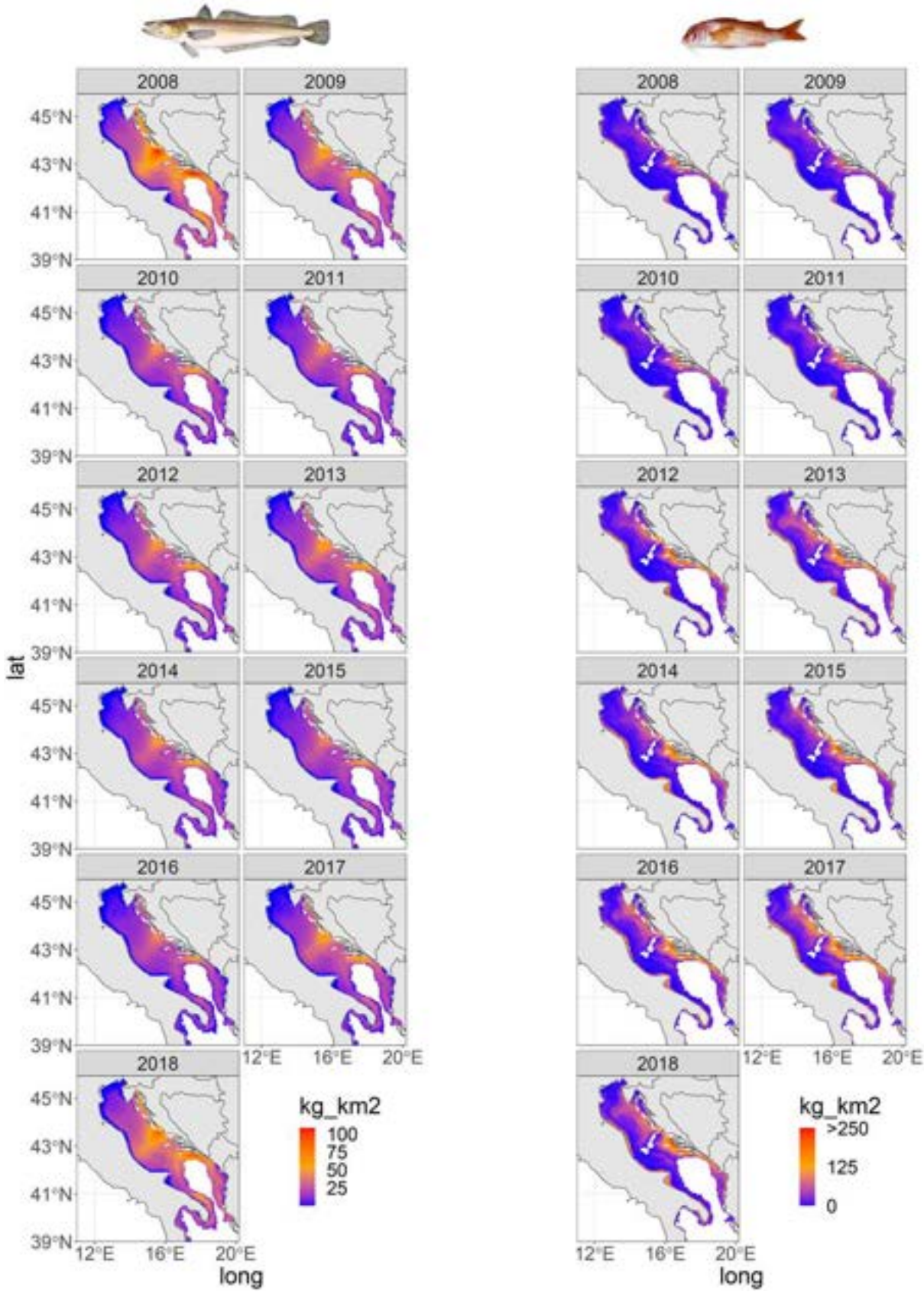

Figure 3.6.2. Yearly maps of estimated biomass (kg/km^2) of European hake (left) and red mullet (right) in the Adriatic and Western Ionian Sea (GSA 17-18-19) obtained with the best GAM model applied on MEDITS trawl survey data for years 2008–2018 (Product Ref. 3.6.3) and with all the additional environmental and effort variables (model 0).

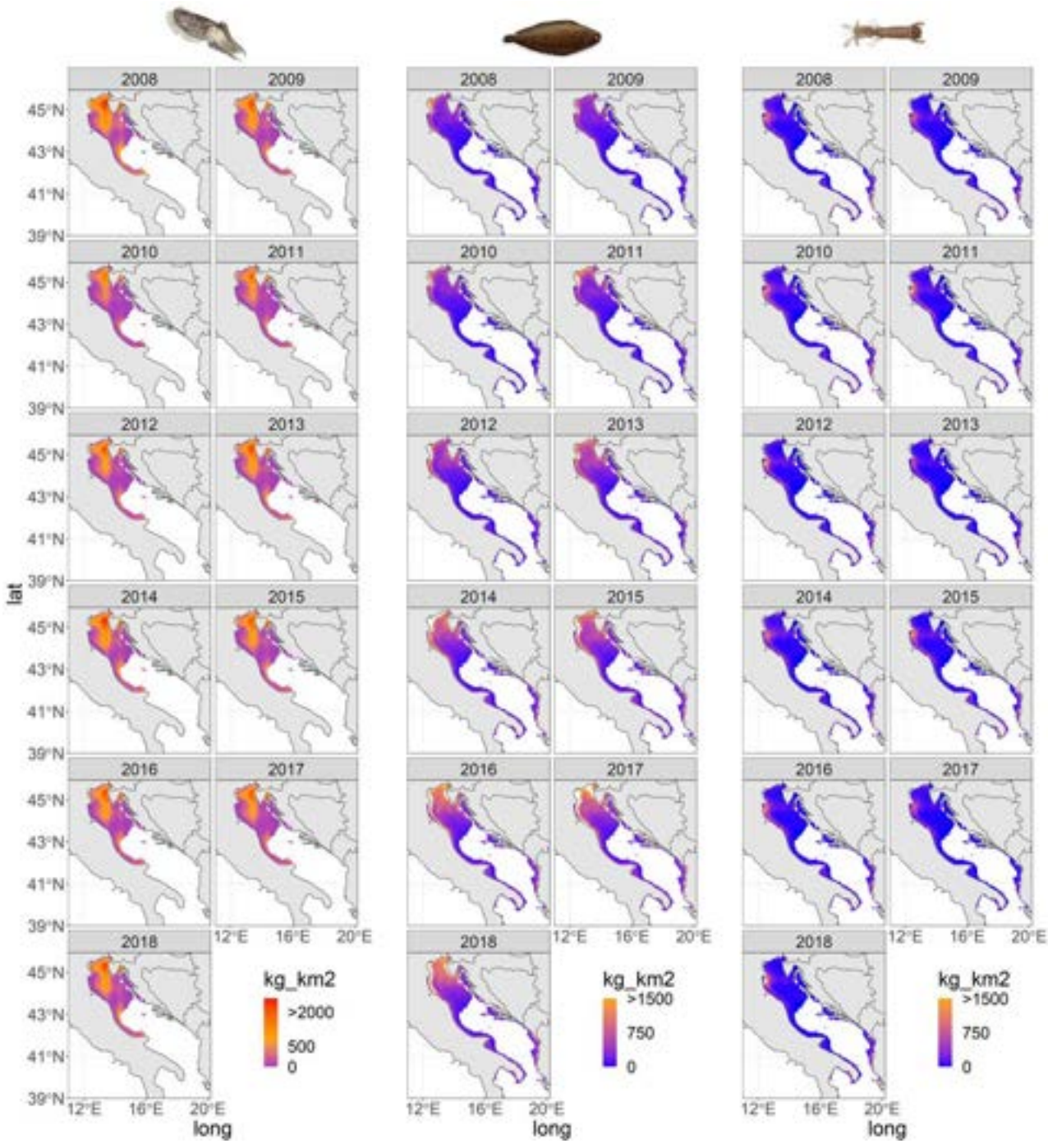

Figure 3.6.3. Yearly maps of estimated biomass (kg/km^2) of common cuttlefish (left), common sole (centre) and mantis shrimp (right) in the Adriatic Sea (GSA 17-18) obtained with the best GAM model applied on SOLEMON trawl survey data for years 2008–2018 (Product Ref. 3.6.4) and with all the additional environmental and effort variables (model 0).

the training/testing approach highlighted that best performances in terms of capabilities to represent trawl survey biomass data (ED% and R2) and performance indicators such as AIC were obtained when the integrated approach was used, i.e. when the spatial model for species distribution included biogeochemical, physical (Product ref. 3.6.1) and fishing effort (Product ref. 3.6.2) as additional explanatory variables (model 0).

For each demersal species the best model has specific significant covariates in addition to spatiotemporal variables. Bottom temperature, bottom dissolved oxygen, salinity, particulate organic carbon, and fishing effort resulted significant variables for European hake. The

same variables and pH resulted sigificant for mantis shrimp. Chlorophyll-a, pH, sea surface temperature, bottom dissolved oxygen, nitrate and effort were significant for the red mullet. Bottom temperature, bottom dissolved oxygen, and phosphate for the common cuttlefish. Average phosphate and salinity were significant for common sole (more details in the Supplementary materials).

Figure 3.6.2 shows distribution maps for the years 2008–2018 as obtained by the best complete model for European hake and red mullet based on MEDITS trawl survey data. For European hake (Figure 3.6.2, left panel) the maps highlight higher biomass in 2008 and 2018, hot spots of biomass (as high as 100 kg/km^2) in the central-eastern part of the Adriatic Sea in recent years (particularly in 2018), low biomass of this species, especially in the northern part of the basin, and a prevalence of a north–south gradient. For the red mullet (Figure 3.6.2, right panel) results show that high biomass (up to 200 kg/km^2, particularly in years 2017/2018) is associated to coastal strip in the western part of the basin, while in the eastern part biomass is more widely distributed with a prevalence of south–north gradients. The application of the best complete GAM model for common cuttlefish, common sole and mantis shrimp based on SOLEMON trawl surveys result in distribution maps reported in Figure 3.6.3. The hot spot for common cuttlefish is consistently identified in the North-East Adriatic, in front of Istra peninsula, with highest biomass (peaks of 2000 kg/km$^{2)}$ especially in 2008 and 2014 (Figure 3.6.3, left panels). Common sole is showing higher densities along the North-western coast of the Adriatic, but high biomass are obtained also in the central part of the Northern Adriatic in recent years (2016–2018; central panels). The mantis shrimp resulted to be mainly distributed along the North-western coast in the area interested by the Po

Table 3.6.1. Comparison among indicators calculated on observations, i.e. the original trawl survey data (Product Ref. 3.6.3, 3.6.4), on the results of the GAM model with spatiotemporal variables and on results of the best GAM model including additional oceanographic variables (Product Ref. 3.6.1, 3.6.2) and effort (model 0). Distribution indicators (first and third quartile, median), performance indicators (MAE, R^2) and spatial indicators such as Spreading area (SA), latitudinal centroid (CGY) longitudinal centroid (CGX) and distance (D) of the centroid of model to that of data are reported for the five demersal species analysed. The column 'improvement' reports the improvement on the indicator value when using model with environmental variables with respect to indicator calculated on results of the model without additional variables (observations-model0/observations-model 6 or 7).

	Red mullet (*Mullus barbatus*), GSA 17, 18, 19, 2008–2018				Common cuttlefish (*Sepia officinalis*), GSA 17, 2008–2018			
	Observations	Model 7	Model 0	Improvement	Observations	Model 6	Model 0	Improvement
1st.Qu	0	3.11	**2.38**	23%	0	9.2	**6.13**	33%
Median	1.95	8.48	**7.91**	18%	133.48	116.22	**125.45**	53%
3rd.Qu	23.55	20.36	**23.88**	19%	558.44	**474.37**	465.51	−10%
R2	–	0.08	**0.15**		–	0.56	**0.61**	
MAE	–	39.97	**36.89**		–	240.96	**227.83**	5.44%
SA	701.6	1142.5	**1094**	11%	235.8	273.21	**272.51**	1.87%
CGX	15.52	15.98	**15.73**	55%	13.3	**13.29**	12.28	
CGY	42.59	**42.52**	42.8	–	44.66	**44.74**	44.75	−12.50%
D	0	38.68	**29.53**	24%		**9.43**	10.2	−8.16%
	European hake (*Merluccius merluccius*), GSA 17, 18, 19, 2008–2018				Mantis shrimp (*Squilla mantis*), GSA 17, 2008–2018			
	Observations	Model 6	Model 0	improvement	Observations	Model 6	Model 0	improvement
1st.Qu	2.99	3.75	**3.67**	11%	0	2.65	**1.22**	54%
Median	15.75	13.68	**14.82**	55%	36.91	**25.23**	24.5	−6%
3rd.Qu	34.68	25.96	**26.33**	4%	326.95	90.19	**115.48**	10%
R2	–	0.32	0.32		–	0.3	**0.46**	
MAE	–	16.13	**15.94**		–	202.69	**169.76**	
SA	1552.02	2272.55	**2263.34**	1.30%	192.95	352.34	**267.37**	53%
CGX	16.18	16.18	16.16	–	13.01	13.15	**13.01**	100%
CGY	42.09	**42.18**	42.19	−11%	44.26	44.15	**44.23**	72%
D	0	**10.89**	11.83	−8.63%		16.99	**2.93**	82%
	Common sole (*Solea solea*), GSA 17, 2008–2018							
	Observations	Model 6	Model 0	improvement				
1st.Qu	127.07	**103.43**	92.21	−47%				
Median	439.64	296.35	**302.75**	4.46%				
3rd.Qu	1155.34	717.12	**728.82**	2.66%				
R2	–	0.35	**0.44**					
MAE	–	538.92	**491.55**					
SA	311.66	447.79	**403.05**	32%				
CGX	12.98	13.01	**12.97**	133%				
CGY	44.57	44.6	**44.6**	0				
D		16.99	**2.83**	83%				

river plume with biomasses as high as 1500 kg/km^2 especially in the years 2011, 2012, 2018 (Figure 3.6.3, right panels).

The spatial and temporal distributions shown are coherent with previous results (Sartor et al. 2017). For example, results from Sion et al. (2019) on European hake show for 2011 and 2013 higher biomass values in the eastern-central Adriatic sea, while in 2015 a general lower biomass of this species was estimated, with similar outcomes to the ones we found in this paper (Figure 3.6.2). Tserpes et al. (2019) also highlights a biomass increasing trend for red mullet after 2008, which is in line with the recent stock assessment outcomes (GFCM 2019; STECF 2019). Similarly, Figure 3.6.2 highlights that this biomass increase corresponds to a spreading of the population in the study area.

The set of indicators for evaluating performances of the complete (model 0) or spatiotemporal (model 6 or 7) models contrasted with observations show that the integrated approach embedding biogeochemical, physical and fishing effort variables has improved performances (Table 3.6.1). In particular, indicators in Table 3.6.1 suggest that models' distribution statistics (quartiles and median) are closer to observed data when the integrated approach is used (i.e. the model 0). Exceptions are the first quartile for common sole, the third quartile for common cuttlefish, and the median for mantis shrimp. It is worth to note the relevant improvement of median values for hake and cuttlefish (+55% and +53%, respectively) when the spatial model of species distribution includes additional biogeochemical, physical and fishing effort data (Table 3.6.1). MAE and R^2 showed that consistency of model to the data improves for all species (except R^2 for European hake) when additional variables are included (Table 3.6.1). The spatial indicators used to evaluate the modelling results in terms of variations of the area occupied by the populations and their mean geolocation (e.g. Woillez et al. 2009) show improvements for red mullet, common sole, and mantis shrimp when the models include additional biogeochemical, physical and effort variables. For all these species the centroids of spatial distribution and the spreading area of the best model (model 0) are closer to those estimated on the observed data than to models with no additional explanatory variables (model 6 or 7; Table 3.6.1). For European hake and common cuttlefish, the spreading area improved when additional explanatory variables are included, but not the centroid position. This result and some low improvements of model 0 with respect to the model with spatiotemporal variables only is possibly related to complex influences of other environmental factors such as seabed type and habitats on the spatial distribution of species (in particular for European hake and common cuttlefish). Overall, the approach quantified the relevance of biogeochemical and physical variables derived from CMEMS and fishing effort from VMS/AIS in improving the spatial distribution of demersal species based on trawl survey data. Results highlight species-specific improvements that should be considered also in relation to the use of spatial distribution model (Brodie et al. 2020).

Key objectives of the Common Fisheries Policy (EU 2013) are the achievement of MSY in the short term and the implementation of an ecosystem approach to fisheries management which is often based on fishery indepedent data. Thus we consider that the integrated approach proposed here represents an important step for incorporating anthropogenic (fishing effort) and other environmental stressors (biogeochemical and physical variables) into the advice for fisheries management.

The improved models including enviromental and effort variables, in fact, can be used for a year by year evaluations of species distribution, for explaining and understanding species displacement. This is of paramount importance for a spatially based management of the resources that relies upon the identification of best fishing grounds, spawning or nursery areas, and generally aiming at defining fisheries managed areas (Lauria et al. 2017). The improved accuracy of species distributions based on enviromental and effort variables as obtained inthis study can potentially support co-management initiatives involving fisheries organisations and other stakeholders (e.g. those carried out by the Mediterranean Advisory Council, MEDAC). In particular, sharing such outcomes with the bottom trawl industry could lead to an increase in the awareness of the sector and consequently to the reduction of the alarming footprint of the fisheries in the Adriatic and Western Ionian Seas (Amoroso et al. 2018).

Furthermore, it is largely acknowledged that most of the presently used stock assessment models are too simplistic since they often consider species populations without integrating the role of key environmental drivers, which is a challenging but crucial frontier in the time of global changes. Taking into consideration environmental factors is also pivotal for the MSY objective, as climate change impacts on the fish community would require moving below fishing mortality at FMSY to ensure sustainable exploitation of marine stocks (Travers-Trolet et al., 2020). An optimised approach for the analysis of trawl survey data is relevant for the stock assessments and advices carried out by Scientific Advisory Committee of the General Fisheries

Commission for the Mediterranean Sea (SAC-GFCM) and the Scientific, Technical and Economic Committee for Fisheries (STECF) of the European Commission, as fisheries-independent data are essential for fishery management. The prediction of biomass indices on the whole domain over time with the integrated models proposed here takes into account the influence of relevant oceanographic variables and could be appropriately used for tuning stock assessment models such as, for example, surplus production models that need the catch time series and the survey abundance aggregated indices.

Since most analytical stock assessment models use survey indices by age or length as tuning indices, a further step for future insights is represented by the modelling in similar way also demographic indices, as length and/or age. Moreover, modelling of demographic indices can be useful also for progressing on the geolocation of sensitive life stages of the species, thus addressing further key questions of spatial fishery management.

These spatial distribution models for demersal species were developed for the best extension of trawl survey data to the whole study area from 2008 to 2018. The approach developed here highlights the relevance of integrating oceanographic variables in the analysis of trawl survey data before their use as inputs in stock assessment (Cao et al. 2017) and ecosystem modelling (see for example, Melaku Canu et al. 2010; Grüss et al. 2014; Grüss et al. 2018). This approach sets the basis for providing projections of the potential effects on species distribution and biomass of future environmental changes.

Applying the identified best GAMs models for making future predictions of species distribution is facilitated by the availability of oceanographic variables under future scenarios of climatic changes and appears strongly conditioned to assumptions on the future distribution of fishing effort that are also dependent from policies and regulations. Therefore, using the models developed here for making future scenarios might be considered with caution, needing further specific investigations of model validity to changed conditions. Yet the models can still provide a first order approximation of potential large scale effects, such as displacements of biomass centre of gravity and spreading area due, for example, to climate change. Although the relative distribution pattern might be well predicted by the model, many factors, such as recruitment success and species interactions for example are not included, thus efforts should be addressed in the future for testing additional modelling approaches and for improving the accuracy of these species distribution models.

In conclusion, the present study aims at investigating the influence of environmental variables on the biomass distribution of the most important commercial fishery species in the Adriatic and Western Ionian basin by modelling the data obtained from trawl surveys using different GAM approaches. GAMs are commonly used because they have the advantage of accounting for spatial and temporal autocorrelation of the data. The approach used here robustly demonstrates in which cases oceanographic variables extracted from CMEMS products and effort from VMS/AIS, result in improving species distribution models. Although there is still room for improvements, the work presented here is a remarkable starting point for better understanding species-environment relationships and for understanding the benefits of integrating the CMEMS variables into the modelling of fishery independent data for predicting the species distribution in the Adriatic and Ionian basins.

Acknowledgements

The MEDITS surveys have been carried out with the financial support of the European Commission until 2001 and subsequently within the Data Collection Framework. The SoleMon surveys have been carried out with the financial support of Italian Ministry of Agriculture (MIPAAF) and National Research Council (CNR) until 2016 and subsequently within the Data Collection Framework. The European Commission, the Member States of Italy and Croatia and the FAO AdriaMed Project are thankfully acknowledged. This work results from activities of the project FAIRSEA (Fisheries in the Adriatic Region – a Shared Ecosystem Approach) funded by the 2014–2020 Interreg V-A Italy – Croatia CBC Programme [Standard project ID 10046951].

Section 3.7. A benthic hypoxia index (BH-index) for assessing the Good Environmental Status of the Black Sea's north-western shelf waters

Authors: Arthur Capet, Luc Vandenbulcke, Catherine Meulders, Marilaure Grégoire

Product Table:

Ref. No.	Product name & type	Documentation
3.7.1	BLKSEA_REANALYSIS_BIO_007_005 Black Sea biogeochemistry hindcast	PUM: http://marine.copernicus.eu/documents/PUM/CMEMS-BS-PUM-007-005.pdf QUID: http://marine.copernicus.eu/documents/QUID/

(*Continued*)

Continued.

Ref. No.	Product name & type	Documentation
		CMEMS-BS-QUID-007-005.pdf
3.7.2	NOAA World Ocean Database 2018	Home page:https://www.nodc.noaa.gov/OC5/SELECT/dbsearch/dbsearch.html
3.7.3	EMODnet Chemistry : Black Sea – Eutrophication and Acidity aggregated datasets 1935/2016 v2018	Product page: https://www.emodnet-chemistry.eu/products/catalogue#/metadata/19839515-f32d-4a6c-8f3f-dcc7e75671ae

Statement of main outcome: We present the Benthic Hypoxia (BH) index, a model-based metric built to survey areas prone to the development of seasonal benthic hypoxia, and its application to the case of the Black Sea northwestern shelf. This BH-index is a useful synthetic tool to report on the state of benthic hypoxia and its evolution in sensitive areas. Its trends for the Black Sea northwestern shelf (1992–2019) depicts a general recovery from the preceding eutrophication period (80's), but also a re-increase in the severity of benthic hypoxia for the years 2016–2019 which is attributed to warming atmospheric conditions. This suggests that management and protection measures aimed at preventing ecological and economical damage induced by benthic hypoxia could be optimised by adoption of a regulation strategy for riverine and coastal nutrient discharge that takes air temperature scenarios foreseen by climate models into account.

3.7.1. Introduction

In his seminal paper on the revival of Dead Zones, Mee (2006) raises awareness of the seasonal occurrence of hypoxia along the Romanian and Ukrainian coasts of the Black Sea in the 70s and 80s. The occurrence of these dead zones is thought to have killed an estimated 60 million tons of bottom living species. Mee estimates that the area of this dead zone reached up to 40,000 km^2 at its extreme in the 90s, which represents more than half of the shelf, and is almost twice the area of the dead zone off the Mississippi River delta in the Gulf of Mexico. Eutrophication has been identified as the main driver of the Black Sea hypoxic events that occurred from the end of the 70s until early 90s (Zaitsev and Mamaev 1997). Indeed, increases in nitrogen and phosphorus inputs from the Danube, Dniester and Dnieper rivers to the northwestern shelf intensified phytoplankton blooms, of which a significant fraction reaches the bottom to be degraded by bacteria (Kemp et al. 2009). From the end of spring until late summer, the shelf circulation is anti-cyclonic and hence the Danube's discharges are first transported to the northern shelf where they lead to large blooms (Yunev et al. 2007). During this period, the water column is strongly stratified by the formation of a seasonal thermocline and also by the presence of a halocline associated with the river discharges (Capet et al. 2013). This strong stratification prevents the ventilation of bottom waters and leads to the occurrence of an oxygen minimum zone at the bottom. In the 90's, nutrient runoff sharply decreased due to agricultural and industrial activity that slowed down due to the economic collapse in eastern Europe; it has often been argued that the Black sea shelf recovered from bottom hypoxia after the decrease of eutrophication (Langmead et al. 2009), as can be demonstrated for the macrobenthic community composition, although not before the mid 2000s (Stevens et al. 2019). Indeed, Capet et al. (2013) show that bottom hypoxia still occurred in summer over the northern part of the shelf, as is corroborated by in situ evidence (Mikhailov et al. 2002; Friedrich et al. 2014; Friedrich et al. 2017, 2019). A likely explanation for this delayed reduction of hypoxia lies at the seafloor: accumulated organic matter in the sediments during the years of eutrophication continues to consume oxygen at a high rate. This benthic oxygen consumption adds to pelagic respiration below the pycnocline, and supports the depletion of oxygen in bottom waters. This ecosystem inertia has already been pointed out as a factor that delays the recovery from hypoxia and complicates predictions of the time scale necessary to restore the system (Conley et al. 2009; Capet et al. 2013; Fennel and Testa 2019). The time scale of the inertia induced by the accumulation of organic matter in Black Sea shelf sediments in the years of eutrophication has been estimated at 9 years (Capet et al. 2013), and can be documented from benthic oxygen consumption records (Grégoire and Friedrich 2004). It is noteworthy that this inertial mechanism is further sustained by the fact that hypoxic events contribute to the preservation of benthic organic matter (Lichtschlag et al. 2015; Jessen et al. 2017). Over the last decade, climate warming with reduced spring ventilation (lower oxygen solubility) and the extension of the summer stratification period are the main drivers of seasonal hypoxia (Capet et al. 2013).

The ways in which benthic hypoxia affects coastal ecosystems are numerous and complex. Indeed, while

mass lethal events are obvious, coastal deoxygenation at sub-lethal thresholds can damage ecosystems at multiple levels (Breitburg et al. 2018; Capet et al. 2020). For example, it can reduce survival and growth or alter behaviour and reproduction of individual organisms. The ecological niches can be modified as well as the distributions and interactions between predators and their prey. Hence, to properly qualify the severity of hypoxia as a threat to coastal ecosystems and downstream economies, we ought to both quantify the harm done to the different components of this ecosystem, and determine whether its resilience is affected.

This can be achieved by characterising the occurrence of hypoxic events in terms of metabolic thresholds, and temporal and spatial extension. Given the limited extent of hypoxic events in terms of time, horizontal and vertical dimensions, specific monitoring systems should be based on a priori knowledge of these events. Numerical models are key to optimising such monitoring systems. In addition, models may provide synoptic indices, summarising for non-scientific use the variations in the severity of seasonal hypoxia, while preventing the biased conclusions that may arise from the sole consideration of inadequate monitoring surveys.

Here, we have used the BS-MFC-BIO-MYP simulations (cf. Product 3.7.1) in order to investigate benthic hypoxia over the Black Sea north-western shelf, and we propose a new indicator of hypoxia, that is computed over the period 1992–2019.

3.7.2. Methods

3.7.2.1. The model

The BAMHBI biogeochemical model that is used to produce the BS-MFC-BIO-RAN simulations accounts for oxygen, carbon, nitrogen, phosphorus and silica transfers across 35 state variables covering dissolved nutrients (5), phyto- (6) and zooplankton (4), bacteria (2), pelagic (6) and benthic (5) detritus (Grégoire et al. 2008; Capet et al. 2016). Formerly coupled with the GHER hydrodynamical engine (Vandenbulcke et al. 2010), the BAMHBI model is now coupled with the NEMO 3.6 model. River forcings were compiled from (Ludwig et al. 2009). Climatological river forcings reconstructed from this dataset are used from 2010 onwards, due to lack of more appropriate datasets including both discharge and nutrient loads, which obviously limits the capacity of the model to resolve oxygen dynamics over the last decade. Atmospheric conditions are provided from the ECMWF ERA5 dataset at a 0.25° grid resolution. The following analysis exploits the daily average, 3km-resolution reanalysis product V202007 (see Product Ref. 3.7.1 for more details).

3.7.2.2. Specific validation

Extensive datasets are needed to validate the model's ability to resolve seasonal benthic hypoxia. Observations are required over the affected area, close to the seafloor, and should have been obtained during months for which hypoxia prevails. Merging data from the NOAA World Ocean Database (Product Ref. 3.7.2) and the EMODnet database (Product Ref. 3.7.3), such requirements are only met simultaneously for a few years.[19] Since bottom oxygen dynamics are decoupled from the surface during the stratified period, two distinct datasets were selected for (1) surface: observations from the surface to the first 20% of the water column depth and, (2) bottom waters: observations deeper than 80% of the water column depth. Only data located in areas with a water depth larger than 15 m were considered. Data scarcity prevents any sensible interannual considerations in the validation exercise, and strongly limits the appraisal of changes in the spatial extent of hypoxic events. However, the comparison allows one to appreciate the model behaviour with respect to the seasonal variations of oxygen in surface and bottom waters.

3.7.2.3. The BH-index

The BH-index (Capet et al. 2013) characterises the intensity of the hypoxic stress for the entire shelf on an annual basis. It accounts for both the temporal and spatial extent of hypoxic conditions as defined by a fixed threshold of oxygen concentration at the seafloor. The BH-index can be derived for different thresholds, to better target specific populations or metabolic/ecosystem processes (Vaquer-Sunyer and Duarte 2011). In the present case, we consider the threshold of $[O_2]$<60 μM (BH-60) and 120 μM (BH-120), suggested to represent lethal (Vaquer-Sunyer and Duarte 2008) and non-lethal impacts (Hrycik et al. 2017; Low and Micheli 2018), respectively. The BH-index is defined as the integral, over the year and over the shelf, of the area affected by oxygen concentration below the chosen threshold. It is normalised by the average duration of the hypoxic period, and

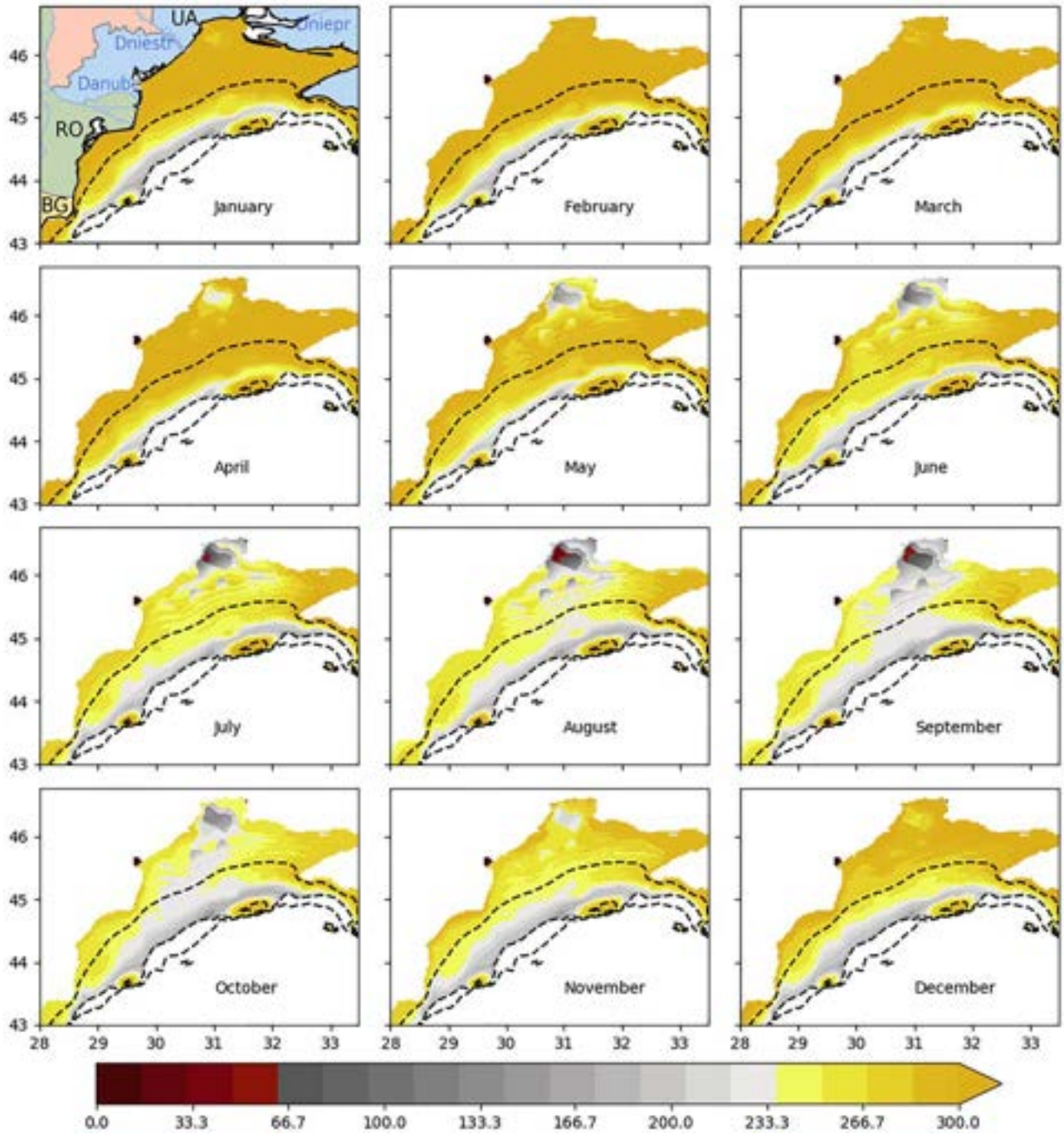

Figure 3.7.1. Monthly climatology of oxygen concentration in bottom waters (μM) as depicted by the BS-MFC-BIO-RAN (Product ref. 3.7.1) reanalysis over the period [1992–2009]. Dotted lines locate the 40, 80 and 120 m iso-bathymetric contours. Boundaries of Bulgaria (BG), Romania (RO) and Ukraine (UA) are indicated on the first panel, as well as the three major rivers that discharge into the area.

Table 3.7.1. Summary of model skill metrics (e.g. Stow et al. 2009) in comparison with in-situ observations.

	N	Bias – [μM]	RMS – [μM]	Nash-Sutcliffe	Correlation
All data	21,850	26.9	69.1	0.10	0.51
Surface data	2578	−4.5	52.3	0.21	0.49
Bottom data	5232	40.5	84.6	−0.03	0.50

thus expressed in terms of km²:

$$BH = \frac{1}{\underline{D}} \int_{year} A(t)dt,$$

where $A(t)$ is the area affected by $[O_2] < 60$ (resp. 120) μM, at time t (which corresponds to a daily index in our case). D is the timescale of the hypoxic event

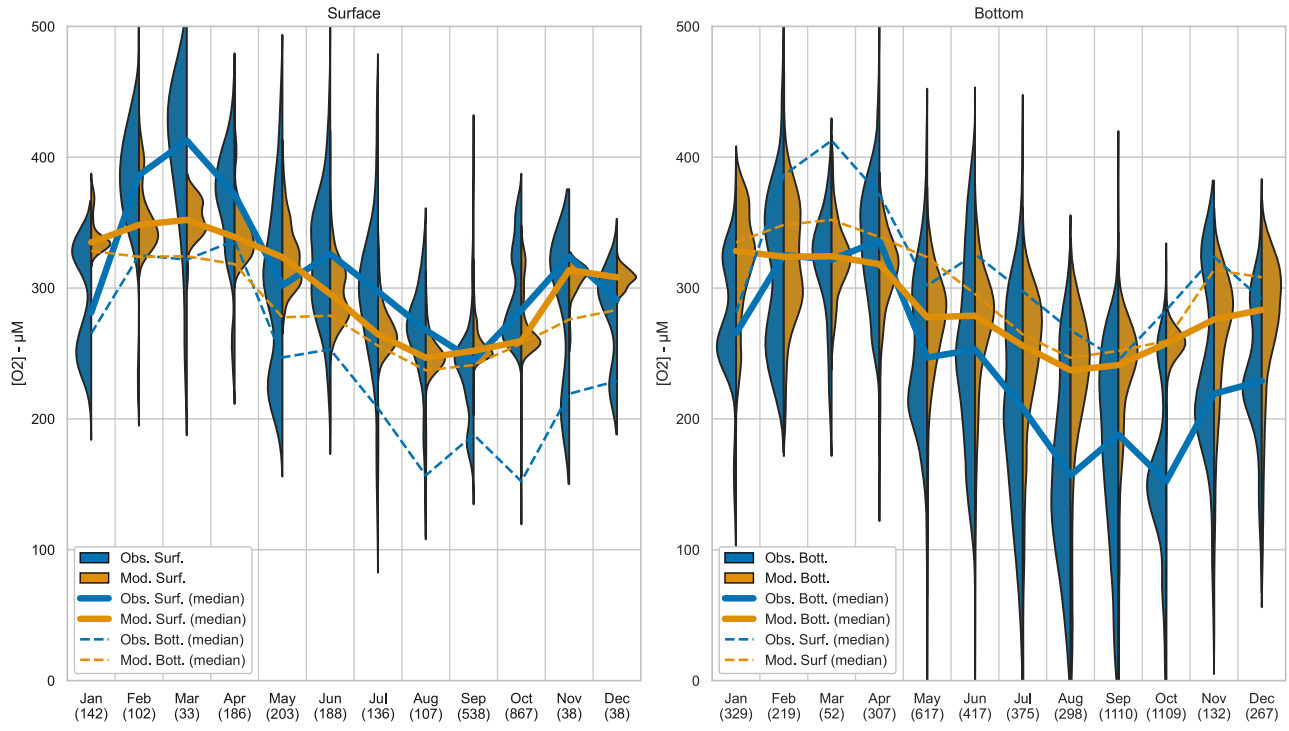

Figure 3.7.2. Seasonal variations (1992–2019) in oxygen concentration observed (blue) and simulated at observation locations (orange) over the northwestern shelf of the Black Sea. Left (resp. right) panel shows monthly distributions for surface (resp. bottom) values. Bold lines indicate the medians of these monthly distributions. Dotted lines repeat the monthly medians obtained for bottom (resp. surface) on the left (resp. right) panel in order to highlight the vertical gradient in oxygen profiles. Numbers on the X-axis indicate the number of available observations.

given by

$$D = \frac{1}{max(A(t))} \int_{year} A(t)dt.$$

$\underline{D}$ is its average, equal to 95 days for the [1992–2019] period. Elements of the BH-index computation are illustrated on Figure 3.7.3.

3.7.3. Results

3.7.3.1. General morphology of the seasonal hypoxia

The seasonal dynamics of bottom hypoxia simulated by the NEMO-BAMHBI model are similar in many ways to that obtained with the former GHER-BAMBHI setup (Capet et al. 2013), but differs in terms of simulated intensity. On a technical level, the two studies differ in terms of: the hydrodynamic model and, in particular, its vertical coordinate system and mixing scheme; reprocessed riverine inputs; grid resolution and simulation period.

The oxygen concentration ($[O_2]$) of the surface waters is regulated by air–sea oxygen fluxes and maintained close to saturation. As stratification isolates bottom water from the surface, oxygen concentration at the seafloor starts decreasing in April in the northernmost part of the Ukrainian shelf (Figure 3.7.1). This less-oxygenated zone extends southward during summer until reaching the shelf break in September. The ventilation of bottom waters takes place in October/November and induces an increase in bottom $[O_2]$ that is much more rapid than its decrease in spring (Figure 3.7.3). Aside from this seasonal cycle over the shallow part of the shelf, the permanent low oxygen concentrations of bottom waters along the shelf edge reflects the nearby presence of the characteristic permanent oxycline in the centre of the Black Sea.

3.7.3.2. Validation

Model skill statistics are evaluated with a point-to-point comparison of 21,850 oxygen measurements selected for areas with water depth deeper than 15 m and shallower than 80 m. These statistics return overall satisfying results, although improvements should be pursued to further refine the resolution of benthic hypoxia in the northwestern Black Sea shelf. Isolating the surface and bottom subsets reveals a difference in terms of bias, with slight underestimation prevailing in

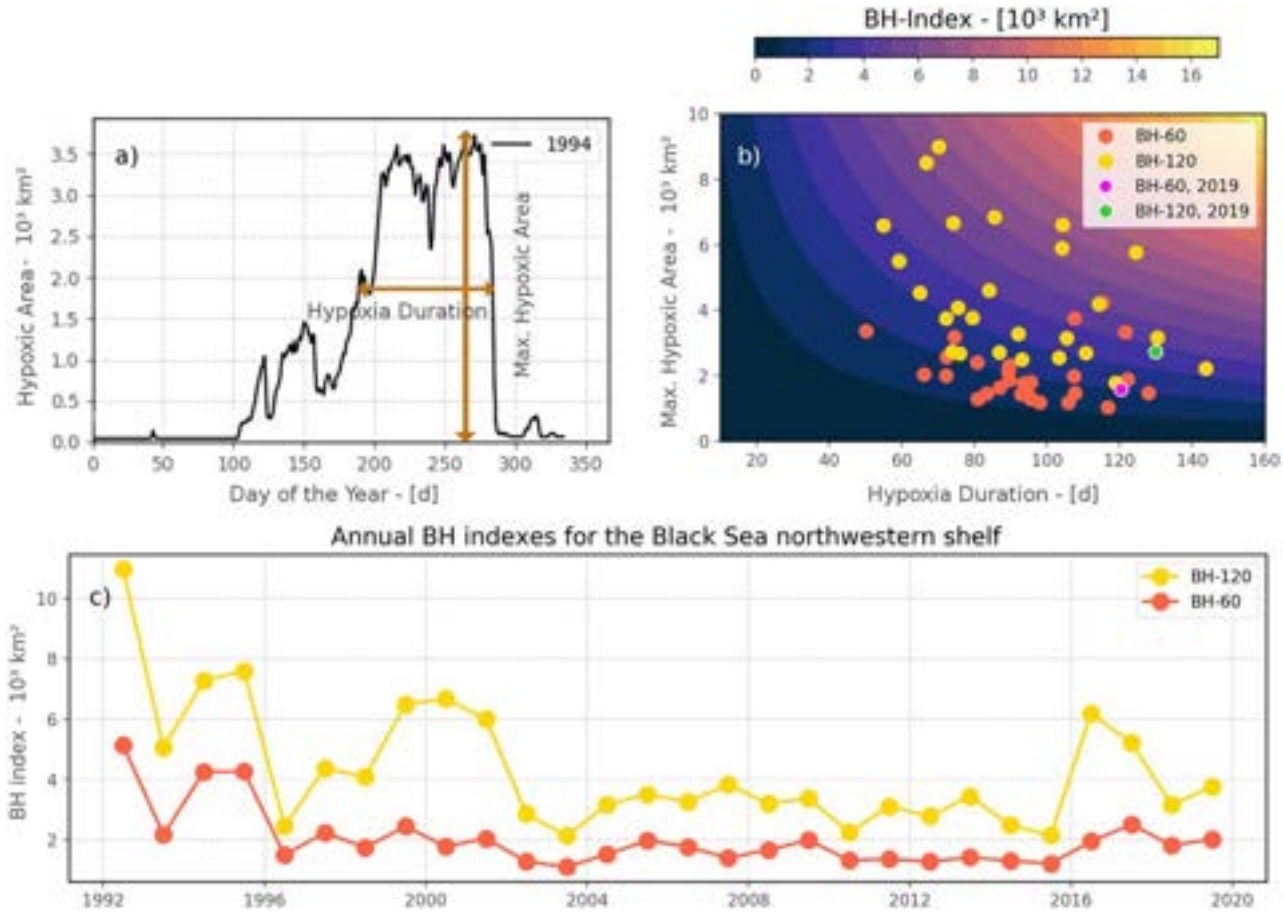

Figure 3.7.3. (a, b) Illustration of the elements considered in the computation of the BH-index. (c) The BH-60 and BH-120 values obtained annually from the BS-MFC-BIO-RAN (product Table 3.7.1). (a) Example of the hypoxic area dynamics for the year 1994, using an hypoxic threshold of 60 μM. (b) In the hypothetical case where A(t), the hypoxic area as a function of year day, follows a Gaussian form, there is a direct relationship between maximum hypoxic area, duration of the hypoxia, and BH-index values indicated with coloured contours. Annual components of the BH-60 and BH-120 indexes are depicted for each year, highlighting 2019. (c) Inter-annual trends in BH-60 and BH-120 over the period 1992–2019.

surface waters, and overestimation in bottom waters (Table 3.7.1).

These subsetted data allow us to detail the seasonal dynamics of these biases (Figure 3.7.2). Oxygen concentration in surface water, i.e. from the surface to the first 20% of the water column depth, appears to be underestimated from February to April, which is likely associated with an efficient oxygenation of cold surface waters that is not accurately resolved by the current model implementation. The most important aspect to highlight here is the overestimation of bottom oxygen concentration by the model in summer. Simulated values at the bottom rarely reach concentrations as low as the observational records. In addition, the summer range between surface and bottom values is always smaller in the simulations than in the observations. These comparisons suggest a lack of vertical resolution in the model grid and/or imperfect vertical mixing scheme. Nevertheless, this exercise shows that the model still predict a decrease in bottom oxygen concentration that is in good correlation with that being observed, although the simulated severity of hypoxia is likely to be underestimated in the current setup.

3.7.3.3. BH-index over the (1992–2019) period

It is important to stress that the simulation period (1992–2019) starts right after a strong reduction of nutrient discharge in this area, after a decade of high nutrient loads, which enriched the seafloor in organic content and sustained benthic oxygen consumption for several years. Here, this enrichment is thus embedded in the simulation through the initial conditions, although a detailed study of the ecosystem response to these changes in nutrient inputs (i.e. the recovery trajectory; Steckbauer et al. 2011) should rather be based on a simulation encompassing both the eutrophication and nutrient reduction phases (ie. 1970–2020).

In general, both the BH-60 and BH-120 indexes indicate a gradual recovery from this eutrophication

period, with some noticeable interannual variations (Figure 3.7.3(c)). As mentioned above, climatological river forcing data were used to force the simulations from 2010 onwards, which had the visible effect of reducing year-to-year variability. This stresses the importance of the increase in BH-60 and BH-120 values over the last several years. As analysed by Capet et al. (2013), variations in air temperature affect the regional dynamics of benthic hypoxia in several ways. Warm springs (March) lower the oxygen solubility of the mixed waters, hence reducing the initial amount of oxygen stored in bottom waters when the thermocline settles down. Warm late summers (August–October) maintain stratified conditions and prevent the ventilation of bottom waters, hence extending periods of hypoxia. Since variability in riverine discharge could not be considered to simulate the last decade, only variability in atmospheric conditions can explain the resurgence of benthic hypoxia. Indeed, during the period 2016–2019, air temperature in the area was above the full period average (1992–2019) by 1.1°C and 0.6°C for March and August–October, respectively (data from ERA5). The critical role of regional air–sea interactions in the dynamics of benthic hypoxia calls for (i) assessing more closely the ability of ERA5 forcing products to realistically reproduce local trends in atmospheric conditions, and (ii) considering the use of dynamic downscaling methods to enhance the resolution of air–sea interaction processes.

Finally, it is remarkable that increases in sub-lethal events (see the BH-120 in Figure 3.7.3(c)) do not systematically correspond to increases in more severe events (i.e. BH-60), as seen for the years 1999–2001. This illustrates the need to combine the assessment of BH-indexes for different thresholds targeting locally relevant species or functional groups.

3.7.4. Conclusion

We present the BH-index, a metric built from a biogeochemical model reanalysis with the aim to monitor areas prone to the development of seasonal benthic hypoxia, such as the Black Sea northwestern shelf. The BH-index is designed to characterise with a single number the annual severity of benthic hypoxia. It can be adapted for specific oxygen concentration thresholds, for instance in order to characterise the pressure on a given species or ecosystem function.

Detailed assessment of the Black Sea simulation highlights the importance of targeted in-situ data collection to characterise the morphology of hypoxic events. While simulated concentrations show overall satisfactory comparison with observations and follow observed seasonal variations in the surface and bottom layers, the comparison points towards an underestimation of the seasonal hypoxia phenomenon by the current model set-up.

The increase of the BH-index over the northwestern Black Sea shelf during the last 5 years implies the need for close attention to near-future trends. Since annually resolved nutrient loads were not considered for the last decade (i.e. 2010–2019), increasing air temperature appears to be sufficient to sustain an increase in the severity of benthic hypoxia.

This suggests that management and protection measures aimed at preventing ecological and economical damage induced by benthic hypoxia could be optimised by adopting a regulation strategy for riverine and coastal nutrient discharge that takes into account the rise in air temperature foreseen by climate models.

To support the implementation of environmental policies (e.g. MSFD) and safeguard environmental recovery over the northwestern Black Sea shelf, we strongly advise (1) to prioritise the delivery of reliable riverine load estimates; (2) to provide and adopt monitoring protocols focused on the areas and period of the year whose sensitivity to hypoxia is stressed by mechanistic model studies; (3) to encourage the use of a synthetic model-based synoptic index for long term trend assessment, such as the BH-index presented here. Given similarities in driving processes, the above recommendations likely apply to other areas prone to seasonal hypoxia.

Acknowledgments

Part of the in-situ oxygen data and metadata used in this study are provided by EMODnet Chemistry under the support of DG MARE Call for Tenders MARE/2008/03-lot3, MARE/2012/10-lot4,EASME/EMFF/2016/006-lot4, EASME/2019/OP/0003-lot4

Notes

18. https://earthobservatory.nasa.gov/images/91981/shipping-responds-to-arctic-ice-decline.
19. Only [1992–1996, 1998–1999, 2002 and 2007] have more than 100 near-bottom observations for [May–November].

References

Section 3.1. The chlorophyll-a gradient as primary Earth observation index of marine ecosystem feeding capacity

https://fishreg.jrc.ec.europa.eu/web/fish-habitat/publications-and-press-release.

Allen M, Antwi-Agyei P, Aragon-Durand F, Babiker M, Bertoldi P, Bind M, Brown S, Buckeridge M, et al. 2019. Technical summary: global warming of 1.5°C. An IPCC special report on the impacts of global warming of 1.5°C above pre-industrial levels and related global greenhouse gas emission pathways, in the context of strengthening the global response to the threat of climate change, sustainable development, and efforts to eradicate poverty. Intergovernmental Panel on Climate Change.

Brandini FP, Boltovskoy D, Piola AR, Kocmur S, Rottgers R, Abreu PC, Mendes Lopes R. 2000. Multiannual trends in fronts and distribution of nutrients and chlorophyll in the southwestern Atlantic (30–62°S). Deep Sea Res I. 47:1015–1033.

Briscoe DK, Hobday AJ, Carlisle A, Scales K, Eveson JP, Arrizabalaga H, Druon JN, Fromentin JM. 2017. Ecological bridges and barriers in pelagic ecosystems. Deep Sea Res Part II Top Stud Oceanogr. 140:182–192.

Druon J-N, Fiorentino F, Murenu M, Knittweis L, Colloca F, Osio C, Mérigot B, Garofalo G, Mannini A, Jadaud A, et al. 2015. Modelling of European hake nurseries in the Mediterranean Sea: an ecological niche approach. Prog Oceanogr. 130:188–204.

Druon JN. 2017. Ocean productivity index for fish in the Arctic: first assessment from satellite derived plankton-to-fish favourable habitats, EUR 29006 EN. Publications Office of the European Union. ISBN 978-92-79-77299-3, JRC109947. https://doi.org/10.2760/28033.

Druon JN, Chassot E, Murua H, Lopez J. 2017. Skipjack tuna availability for purse seine fisheries is driven by suitable feeding habitat dynamics in the Atlantic and Indian Oceans. Front Mar Sci. 4:315. DOI:10.3389/fmars.2017.00315.

Druon JN, Fromentin JM, Hanke A, Arrizabalaga H, Damalas D, Tičina V, Quílez-Badia G, Ramirez K, Arregui I, Tserpes G, et al. 2016. Habitat suitability of the Atlantic bluefin tuna by size class: an ecological niche approach. Prog Oceanogr. 142:30–46. doi:10.1016/j.pocean.2016.01.002.

Druon JN, Gascuel D, Gibin M, Zanzi A, Fromentin JM, Colloca F, Hélaouët P, Coll M, Mannini A, Bluemel J, et al. 2021. Mesoscale productivity fronts and local fishing opportunities in the European Seas. Fish Fish. DOI:10.1111/faf.12585.

Druon JN, Hélaouët P, Beaugrand G, Fromentin JM, Palialexis A, Hoepffner N. 2019. Satellite-based indicator of zooplankton distribution for global monitoring. Nat Sci Rep. 9:4732. DOI:10.1038/s41598-019-41212-2.

Druon JN, Panigada S, David L, Gannier A, Mayol P, Arcangeli A, Cañadas A, Laran S, Di Méglio N, Gauffier P. 2012. Potential feeding habitat of fin whales in the western Mediterranean Sea: an environmental niche model. Mar Ecol Prog Ser. 464:289–306. DOI:10.3354/meps09810.

Dutkiewicz S, Hickman AE, Jahn O, Henson S, Beaulieu C, Monier E. 2019. Ocean colour signature of climate change. Nat Commun. 10:578. DOI:10.1038/s41467-019-08457-x.

European Commission. 2008. Directive 2008/56/EC of the European Parliament and of the Council of 17 June 2008 establishing a framework for community action in the field of marine environmental policy (Marine Strategy Framework Directive) (text with EEA relevance).

European Commission. 2013. REGULATION (EU) No 1380/2013 OF THE EUROPEAN PARLIAMENT AND OF THE COUNCIL of 11 December 2013 on the Common Fisheries Policy, amending Council Regulations (EC) No 1954/2003 and (EC) No 1224/2009 and repealing Council Regulations (EC) No 2371/2002 and (EC) No 639/2004 and Council Decision 2004/585/EC.

European Commission. 2017. Commission Decision (EU) 2017/848 of 17 May 2017 laying down criteria and methodological standards on good environmental status of marine waters and specifications and standardised methods for monitoring and assessment, and repealing decision 2010/477/EU (Text with EEA relevance).

Garnesson P, Mangin A, Fanton d'Andon O, Demaria J, Bretagnon M. 2019. The CMEMS GlobColour chlorophyll-a product based on satellite observation: multi-sensor merging and flagging strategies. Ocean Sci. 15(3):819–830. DOI:10.5194/os-15-819-2019.

Gohin F, Druon JN, Lampert L. 2002. A five channel chlorophyll concentration algorithm applied to SeaWiFS data processed by SeaDAS in coastal waters. Int J Remote Sens. 23:1639–1661 (not open access).

Hernvann PY, Gascuel D, Grüss A, Druon JN, Kopp D, Perez I, Piroddi C, Robert M. 2020. The Celtic Sea through time and space: ecosystem modeling to unravel fishing and climate change impacts on food-web structure and dynamics. Front Mar Sci. 7:1018. DOI:10.3389/fmars.2020.578717.

Hu C, Lee Z, Franz B. 2012. Chlorophyll aalgorithms for oligotrophic oceans: a novel approach based on three-band reflectance difference. J Geophys Res. 117:C01011. DOI:10.1029/2011JC007395.

Kahru M, Di Lorenzo E, Manzano-Sarabia M, Mitchell BG. 2012. Spatial and temporal statistics of sea surface temperature and chlorophyll fronts in the California current. J Plankton Res. 34(9):749–760. DOI:10.1093/plankt/fbs010.

Kouketsu S, Kaneko H, Okunishi T, Sasaoka K, Itoh S, Inoue R, Ueno H. 2016. Mesoscale eddy effects on temporal variability of surface chlorophyll a in the Kuroshio extension. J Oceanogr. 72:439–451. DOI:10.1007/s10872-015-0286-4.

Libralato S, Coll M, Tudela S, Palomera I, Pranovi F. 2008. Novel index for quantification of ecosystem effects of fishing as removal of secondary production. Mar Ecol Prog Ser. 355:107–129.

Panigada S, Donovan G, Druon JN, Lauriano G, Pierantonio N, Pirotta E, Zanardelli M, Zerbini A, Notarbartolo di Sciara G. 2017. Satellite tagging of Mediterranean fin whales: working towards the identification of critical habitats and the focussing of mitigation measures. Nat Sci Rep. 7:3365. DOI:10.1038/s41598-017-03560-9.

Pegau WS, Boss E, Martinez A. 2002. Ocean color observations of eddies during the summer in the Gulf of California. Geophys Res Lett 29:1295. DOI:10.1029/2001GL014076.

Pitarch J, Volpe G, Colella S, Krasemann H, Santoleri R. 2016. Remote sensing of chlorophyll in the Baltic Sea at basin scale from 1997 to 2012 using merged multi-sensor data. Ocean Sci. 12(2):379–389.

Polovina JJ, Howell E, Kobayashi DR, Seki MP. 2001. The transition zone chlorophyll front, a dynamic global feature

defining migration and forage habitat for marine resources. Prog Oceanogr. 49:469–483.
Raymont JEG. 1980. Plankton & productivity in the oceans: volume 1: phytoplankton, 1- marine plankton. 2nd ed. Oxford: Pergamon Press Ltd.
Takahashi W, Kawamura H. 2005. Detection method of the Kuroshio front using the satellite-derived chlorophyll-a images. Remote Sens Environ. 97:83–91.
Valavanis DV, Kapantagakis A, Katara I, Palialexis A. 2004. Critical regions: A GIS-based model of marine productivity hotspots. Aquat Sci. 66:139–148. DOI:10.1007/s00027-003-0669-2.
von Schuckmann K, Le Traon P-Y, Smith N, Pascual A, Djavidnia S, Gattuso J-P, Grégoire M, Nolan G. 2019. Copernicus marine service ocean state report, issue 3. J Oper Oceanogr. 12:S1–S123.
von Schuckmann K, Le Traon P-Y, Smith N, Pascual A, Djavidnia S, Gattuso J-P, Grégoire M, Nolan G. 2020. Copernicus marine service ocean state report, issue 4. J Oper Oceanogr. 13:sup1, S1–S172. DOI:10.1080/1755876X.2020.1785097.

Section 3.2. Marine heatwaves and cold-spells, and their impact on fisheries in the North Sea

Akimova A, Núñez-Riboni I, Kempf A, Taylor MH. 2016. Spatially-resolved influence of temperature and salinity on stock and recruitment variability of commercially important fishes in the North Sea. PLoS One. 11: e0161917. DOI:10.1371/journal.pone.0161917.
Arafeh-Dalmau N, Schoeman DS, Montano-Mactezuma G, Micheli F, Rogers-Bennett L, Olguin-Jacobson C, Possingham HP. 2020. Marine heat waves threaten kelp forests. Science. 367:635. DOI:10.1126/science.aba5244.
Ares E. 2016. UK and European sea bass conservation measures. House of Commons Library. Briefing Paper 00745. http://researchbriefings.files.parliament.uk/documents/SN00745/SN00745.pdf.
BBC. 2010. Thousands of dead crabs wash up on Kent's beaches. BBC News. http://news.bbc.co.uk/1/hi/england/kent/8456514.stm.
BBC. 2013. Cold weather hits lobster supplies. BBC News. https://www.bbc.co.uk/news/uk-scotland-scotland-business-22297644.
Beare D, Burns F, Jones E, Peach K, Reid D. 2005. Red mullet migration into the northern North Sea during late winter. J Sea Res. 53:205–212.
Benthuysen JA, Oliver ECJ, Chen K, Wernberg T. 2020. Advances in understanding marine heatwaves and their impacts. Front Mar Sci. DOI:10.3389/fmars.2020.00147.
Bond NA, Cronin MF, Freeland M, Mantua N. 2015. Causes and impacts of the 2014 warm anomaly in the NE Pacific. Geophys Res Lett. 42:3414–3420. DOI:10.1002/2015GL063306.
Chiriaco M, Bastin S, Yiou P, Haeffelin M, Dupont J-C, Stéfanon M. 2014. European heatwave in July 2006: observations and modeling showing how local processes amplify conducive large-scale conditions. Geophys Res Lett. 41:5644–5652. DOI:10.1002/2014GL060205.
Collins M, Sutherland M, Bouwer L, Cheong S-M, Frölicher T, Jacot Des Combes H, Koll Roxy M, Losada I, McInnes K, Ratter B, et al. 2019. Extremes, abrupt changes and managing risk. In: Pörtner H-O, Roberts DC, Masson-Delmotte V, Zhai P, Tignor M, Poloczanska E, Mintenbeck K, Alegría A, Nicolai M, Okem A, Petzold J, Rama B, Weyer NM, editors, IPCC special report on the ocean and cryosphere in a changing climate. In press.
Donner SD, Skirving WJ, Little CM, Oppenheimer M, Hoegh-Guldberg OVE. 2005. Global assessment of coral bleaching and required rates of adaptation under climate change. Glb Chg Bio. 11:2251–2265.
Engelhard GH, Pinnegar JK, Kell LT, Rijnsdorp AD. 2011. Nine decades of North Sea sole and plaice distribution. ICES J Mar Sci. 68:1090–1104. doi:10.1093/icesjms/fsr031.
Engelhard GH, Righton DA, Pinnegar JK. 2014. Climate change and fishing: a century of shifting distribution in the North Sea. Glb Chg Bio. 20:2473–2483. doi:10.1111/gcb.12513.
Guardian. 2018. Mass die-off of sea creatures follows freezing UK weather. https://www.theguardian.com/environment/2018/mar/05/mass-die-off-of-sea-creatures-follows-freezing-uk-weather.
Heath MR, Neat FC, Pinnegar JK, Reid DG, Sims DW, Wright PJ. 2012. Review of climate change impacts on marine fish and shellfish around the UK and Ireland. Aquatic Conserv Mar Freshw Ecosyst. 22:337–367.
Hobday AJ, Alexander LV, Perkins SE, Smale DA, Straub SC, Oliver ECJ, Benthuysen JA, Burrows MT, Donat MG, Feng M, et al. 2016. A hierarchical approach to defining marine heatwaves. Prog Oceanogr. 141:227–238. DOI:10.1016/j.pocean.2015.12.014.
Hobday AJ, Pecl GT. 2014. Identification of global marine hotspots: sentinels for change and vanguards for adaptation action. Rev Fish Biol Fish. 24:415–425. DOI:10.1007/s11160-013-9326-6.
Horwood JW, Millner RS. 1998. Cold induced abnormal catches of sole. J Mar Biol Assoc UK. 78:345–347.
Huthnance J, Weisse R, Wahl T, Thomas H, Pietrzak J, Souza AJ, van Heteren S, Schmelzer N, van Beusekom J, Colijn F, et al. 2016. Recent change – North Sea. In: Quante M, Colijn F, editors. North Sea region climate change assessment. Cham: Springer International Publishing; p. 85–136. DOI:10.1007/978-3-319-39745-0_3.
ICES. 1977. ICES statistical rectangle coding system. CM 1977/Gen:3. http://ices.dk/sites/pub/CM%20Doccuments/1977/Gen/ICES%20Statistical%20Rectangle%20System%20Gen0377.pdf.
ICES. 2019. Working Group on the assessment of demersal stocks in the North Sea and Skagerrak (WGNSSK). ICES Scientific Reports. 1:7. 1271 pp. http://doi.org/10.17895/ices.pub.5402.
IPCC. 2019. IPCC special report on the ocean and cryosphere in a changing climate, Pörtner H-O, Roberts DC, Masson-Delmotte V, Zhai P, Tignor M, Poloczanska E, Mintenbeck K, Alegría A, Nicolai M, Okem A, Petzold J, Rama B, Weyer NM, editors. In press.
Jacox MG, Alexander MA, Bograd SJ, Scott JD. 2020. Thermal displacement by marine heatwaves. Nature. 584:82–86.
Kendall M. 1975. Rank correlation methods. 4th ed. London: Charles Griffith.
Loewe P. 1996. Surface temperatures of the North Sea in 1996. Deutsche Hydrographische Zeitschrift. 48:175–184. DOI:10.1007/BF02799386.

Mann HB. 1945. Nonparametric tests against trend. Econometrica. 13(3):245–259. DOI:10.2307/1907187.
Oliver ECJ, Burrows MT, Donat MG, Gupta AS, Alexander LV, Perkins-Kirkpatrick SE, Benthuysen JA, Hobday AJ, Holbrooj NJ, Moore PJ, et al. 2019. Projected marine heatwaves in the 21st century and the potential for ecological impacts. Front Mar Sci. DOI:10.3389/fmars.2019.00734.
Oliver ECJ, Lago V, Hobday AJ, Holbrook NJ, Ling SD, Mundy CN. 2018. Marine heatwaves off eastern Tasmania: trends, interannual variability, and predictability. Prog Oceanogr. 161:116–130. DOI:10.1016/j.pocean.2018.02.007.
Perry AL, Low PJ, Ellis JR, Reynolds JD. 2006. Climate change and distribution shifts in marine fishes. Science. 308:1912–1915. DOI:10.1126/science.1111322.
Pinnegar JK, Engelhard GH, Jones MC, Cheung WWL, Peck MA, Rijnsdorp AD, Brander KM. 2016. Chapter 12: socio-economic impacts – fisheries. In: Quante M, Colijn C, editors. North Sea region climate change assessment (NOSCCA), regional climate studies. Berlin: Springer; p. 375–395.
Schlegel RW, Oliver ECJ, Wernberg T, Smit AJ. 2017. Nearshore and offshore co-occurrence of marine heatwaves and cold-spells. Prog Oceanogr. 151:189–205. DOI:10.1016/j.pocean.2017.01.004.
Sheehy MRJ, Shelton PMJ, Wickins JF, Belchier M, Gaten E. 1996. Ageing the European lobster *Homarus gammarus* by the lipofuscin in its eyestalk ganglia. Mar Ecol Prog Ser. 143:99–111.
Simpson SD, Jennings S, Johnson MP, Blanchard JL, Schön P-J, Sims DW, Genner ML. 2011. Continental shelf-wide response of a fish assemblage to rapid warming of the sea. Curr Biol. 21:1565–1570. DOI:10.1016/j.cub.2011.08.016.
Smale DA, Wernberg T, Oliver ECJ, Thomsen M, Harvey BP, Straub SC, Burrows MT, Alexander LV, Benthuysen JA, Donat MG, et al. 2019. Marine heatwaves threaten global biodiversity and the provision of ecosystem services. Nat Clim Change. DOI:10.1038/s41558-019-0412-1.
Stephens PJ. 1985. The effects of temperature and acclimation on crustacean nerve-muscle physiology. Biol Bull. 169:92–105.
Szekeres P, Eliason EJ, Lapointe D, Donaldson MR, Brownscombe JW, Cooke SJ. 2016. On the neglected cold side of climate change and what it means to fish. Clim Res. 69:239–245. DOI:10.3354/cr01404.
Teal LR, de Leeuw JJ, van der Veer HW, Rijnsdorp AD. 2008. Effects of climate change on growth of 0-group sole and plaice. Mar Ecol Prog Ser. 358:219–230.
Wernberg T, Bennett S, Babcock RC, de Bettignies T, Cure K, Depczynski M, Dufols F, Fromont J, Fulton CJ, Hovey RK, et al. 2016. Climate-driven regime shift of a temperate marine ecosystem. Science. 353:169–172. DOI:10.1126/science.aad8745.
Wernberg T, Smale DA, Tuya F, Thomsen MS, Langlois TJ, de Bettignies T, Bennett S, Rousseaux CS. 2013. An extreme climatic event alters marine ecosystem structure in a global biodiversity hotspot. Nat Clim Change. 3:78–82.
Woodhead PMJ. 1964. The death of North Sea fish during the winter of 1962/63, particularly with reference to the sole, *Solea vulgaris*. Helgol Mar Res. 10:283–300. DOI:10.1007/BF01626114.

Section 3.3. Massive occurrence of the jellyfish Portuguese Man-of-War in the Mediterranean Sea: implication for coastal management

Angel DL, Edelist D, Freeman S. 2016. Local perspectives on regional challenges: jellyfish proliferation and fish stock management along the Israeli Mediterranean coast. Reg Environ Change. 16(2):315–323.
Badré S. 2014. Bioactive toxins from stinging jellyfish. Toxicon. 91:114–125.
Bosch-Belmar M, Azzurro E, Pulis K, Milisenda G, Fuentes V, Yahia OK, Micallef A, Deidun A, Piraino S. 2017. Jellyfish blooms perception in Mediterranean finfish aquaculture. Mar Policy. 76:1–7.
Brotz L, Cheung WWL, Kleisner K, Pakhomov E, Pauly D. 2012. Increasing jellyfish populations: trends in large marine ecosystems. Hydrobiologia. 690:3–20.
Burnett JW, Gable WD. 1989. A fatal jellyfish envenomation by the Portuguese Man-ó-War. Toxicon. 27:823–824.
Cazorla-Perfetti DJ, Loyo J, Lugo L, Acosta ME, Morales P, Hadda V, Jr, Rodriguez-Morales AJ. 2012. Epidemiology of the Cnidarian *Physalia physalis* stings attended at a health care center in beaches of Adicora, Venezuela. Travel Med Infect Dis. 10:263–266.
Ciscar JC, Iglesias A, Feyen L, Szabó L, Van Regemorter D, Amelung B, Nicholls R, Watkiss P, Christensen OB, Dankers R, Garrote L. 2001. Physical and economic consequences of climate change in Europe. Proc Natl Acad Sci USA. 108:2678–2683.
Eurostat. 2020. Tourism database. Available at the Eurostat website [accessed 2020 Dec 1]. https://ec.europa.eu/eurostat/web/tourism/data/database.
Ferrer L, Pastor A. 2017. The Portuguese Man-of-War: gone with the wind. Reg Stud Marine Sci. 14:53–62.
Ferrer L, Zaldua-Mendizabal N, Del Campo A, Franco J, Mader J, Cotano U, Uriarte A, Aranada JA. 2015. Operational protocol for the sighting and tracking of Portuguese Man-of-War in the southeastern Bay of Biscay: observations and modeling. Cont Shelf Res. 95:39–53.
Ghermandi A, Galil B, Gowdy J, Nunes PALD. 2015. Jellyfish outbreak impacts on recreation in the Mediterranean Sea: welfare estimates from a socioeconomic pilot survey in Israel. Ecosyst Serv. 11:140–147.
Haddad V, Jr, Virga R, Bechara A, Lang da Silveira F, Morandini AC. 2013. An outbreak of Portuguese Man-of-War (*Physalia physalis* – Linnaeus, 1758) envenoming in Southeastern Brazil. Rev Soc Bras Med Trop. 46(5):641–644.
Headlam J, Lyons K, Kenny J, Lenihan ES, Quigley DTG, Helps W, Dugon MM, Doyle TK. 2020. Insights on the origin and drift trajectories of Portuguese man of war (*Physalia physalis*) over the Celtic Sea shelf area. Estuarine Coastal Shelf Sci. 246:107033.
Kirkpatrick PA, Pugh PR. 1984. Siphonophores and velellids. Synop Br Fauna New Ser. 29:1–154.
Kogovsek T, Bogunovic B, Malej A. 2010. Recurrence 1571 of bloom-forming scyphomedusae: wavelet analysis of a 200-year time series. Hydrobiologia. 645:81–96.
Kontogianni AD, Emmanouilides CJ. 2014. The cost of a gelatinous future and loss of critical habitats in the Mediterranean. ICES J Mar Sci. DOI:10.1093/icesjms/fst194.

Labadie M, Aldabe B, Ong N, Joncquiert-Latarjet A, Groult V, Poulard A, Coudreuse M, Cordier L, Rolland P, Chanseau P, de Haro L. 2012. Portuguese Man-of-War (*Physalia physalis*) envenomation on the aquitaine coast of France: an emerging health risk. Clin Toxicol. 50:567–570.
Lett C, Verley P, Mullon C, Parada P, Brochier T, Penven P, Blanke B. 2008. A Lagrangian tool for modelling ichthyoplankton dynamics. Environ Model Softw. 23(9):1210–1214.
Macias D, Cózar A, Garcia-Gorriz E, González-Fernández D, Stips A. 2019. Surface water circulation develops seasonally changing patterns of floating litter accumulation in the Mediterranean Sea. A modelling approach. Mar Pollut Bull. 149:110619.
Macias D, Garcia-Gorriz E, Piroddi C, Stips A. 2014. Biogeochemical control of marine productivity in the Mediterranean Sea during the last 50 years. Global Biogeochem Cycles. 28(8):897–907.
Mapstone GM. 2014. Global diversity and review of Siphonophorae (Cnidaria: Hidrozoa). PLoS One. 9(2): e87737. doi:10.1371/journal.pone.0087737.
Munro C, Vue Z, Behringer RR, Dunn CW. 2019. Morphology and development of the Portuguese man of war, *Physalia physalis*. Sci Rep. 9:15522. doi:10.1038/s41598-019-51842-1.
Hurrell J, National Center for Atmospheric Research Staff, editors. 2020. The climate data guide: Hurrell North Atlantic Oscillation (NAO) Index (station-based). [accessed 2020 Apr 24]. https://climatedataguide.ucar.edu/climate-data/hurrell-north-atlantic-oscillation-nao-index-station-based.
Prieto L. 2018. Diagnosis, prognosis, and management of jellyfish swarms. In: Chassignet EP, Pascual A, Tintoré J, Verron J, editors. New Frontiers in operational oceanography. p. 737–758. DOI:10.17125/gov2018.ch28.737.
Prieto L, Macías D, Peliz A, Ruiz J. 2015. Portuguese Man-of-War (*Physalia physalis*) in the Mediterranean: a permanent invasion or a casual appearance? Sci Rep. 5:11545.
Purcell JE, Uye S-I, Lo W-T. 2007. Anthropogenic causes of jellyfish blooms and direct consequences for humans: a review. Mar Ecol Prog Ser. 350:153–174.
World Tourism Organization. 2018. European Union tourism trends. Madrid: UNWTO. DOI:10.18111/9789284419470.

Section 3.4. Recent changes of the salinity distribution and zooplankton community in the South Adriatic Pit

Batistić M, Garić R, Jasprica N, Ljubimir S, Mikuš J. 2018. Bloom of the heterotrophic dinoflagellate Noctiluca scintillans (Macartney) Kofoid & Swezy, 1921 and tunicates *Salpa fusiformis* Cuvier, 1804 and *Salpa maxima* Forskål, 1775 in the open southern Adriatic in 2009. J Mar Biol Assoc UK. 99:1049–1058. DOI:10.1017/S0025315418001029.
Batistić M, Garić R, Molinero JC. 2014. Interannual variations in Adriatic Sea zooplankton mirror shifts in circulation regimes in the Ionian Sea. Clim Res. 61:231–240.
Batistić M, Jasprica N, Carić M, Čalić M, Kovačević V, Garić R, Njire J, Mikuš J, Bobanović-Ćolić S. 2012. Biological evidence of a winter convection event in the South Adriatic: a phytoplankton maximum in the aphotic zone. Cont Shelf Res. 44:57–71. DOI:10.1016/j.csr.2011.01.004.
Batistić M, Mikuš J, Njire J. 2003. Chaetognaths in the South Adriatic: vertical distribution and feeding. J Mar Biol Ass UK. 83(6):1301–1306.
Batistić M, Viličić D, Kovačević V, Jasprica N, Garić R, Lavigne H, Carić M. 2019. Occurrence of winter phytoplankton bloom in the open southern Adriatic: relationship with hydroclimatic events in the Eastern Mediterranean. Cont Shelf Res. 174:12–25.
Benović A. 2000. Zooplankton biomass and fish production in the Adriatic Sea. CIESM Workshop Series. 12:23–24.
Boero F, Belmonte G, Bracale R, Fraschetti S, Piraino S, Zampardi S. 2013. A salp bloom (Tunicata, Thaliacea) along the Apulian coast and in the Otranto channel between March-May 2013. F1000Res. 2:181.
Boero F, Bouillon J, Gravili C, Miglietta MP, Parsons T, Piraino S. 2008. Gelatinous plankton: irregularities rule the world (sometimes). Mar Ecol Prog Ser. 356:299–310.
Boldrin A, Miserocchi S, Rabitti S, Turchetto MM, Balboni V, Socal G. 2002. Particulate matter in the southern Adriatic and Ionian Sea: characterization and downward fluxes. J Mar Sys. 33–34:389–410.
Borme D, Tirelli V, Brandt SB, Umani SF, Arneri E. 2009. Diet of *Engraulis encrasicolus* in the northern Adriatic Sea (Mediterranean): ontogenetic changes and feeding selectivity. Mar Ecol Prog Ser. 392:193–209. DOI:10.3354/meps08214.
Borme D, Tirelli V, Palomera I. 2013. Feeding habits of European pilchard late larvae in a nursery area in the Adriatic Sea. J Sea Res. 78:8–17. DOI:10.1016/j.seares.2012.12.010.
Cardin V, Bensi M, Pacciaroni M. 2011. Variability of water mass properties in the last two decades in the South Adriatic Sea with emphasis on the period 2006–2009. Cont Shelf Res. 31:951–965. DOI:10.1016/j.csr.2011.03.002.
Carniel S, Bergamasco A, Book JB, Hobbs RW, Sclavo M, Wood WT. 2012. Tracking bottom waters in the southern Adriatic Sea applying seismic oceanography techniques. Cont Shelf Res. 44:30–38. DOI:10.1016/j.csr.2011.09.004.
Cerino F, Bernardi Aubry F, Coppola J, La Ferla R, Maimone G, Socal GG, Totti C. 2012. Spatial and temporal variability of pico-, nano- and micro phytoplankton in the offshore waters of the southern Adriatic Sea (Mediterranean Sea). Cont Shelf Res. 44:94–105.
Civitarese G, Gačić M, Eusebi Borzelli GL, Lipizer M. 2010. On the impact of the Bimodal Oscillating System (BiOS) on the biogeochemistry and biology of the Adriatic and Ionian Seas (eastern Mediterranean). Biogeosciences. 7:3987–3997. doi:10.5194/bg-7-3987-2010.
Cushman-Roisin B, Gacic M, Poulain P-M, Artegiani A. 2001. Chapter 8: toward the future. In: Cushman-Roisin B, Gacic M, Poulain P-M, Artegiani A, editors. Physical oceanography of the Adriatic Sea – past, present and future. Dordrecht: Kluwer Academic Publishers; p. 241–245.
D'Alelio D, Libralato S, Wyatt T, Ribera D'Alcala M. 2016. Ecological-network models link diversity, structure and function in the plankton food-web. Sci Rep. 6:21806.
Dragičević B, Matić-Skoko S, Dulčić J. 2017. Fish and fisheries of the eastern Adriatic Sea in the light of climate change, trends in fisheries and aquatic animal health, berillis,

panagiotis (ur.). Sharjah: Bentham e-books. str. 1–22. DOI:10.2174/97816810858071170101.

Fogarty MJ, Rosenberg AA, Cooper AB, Dickey-Collas M, Fulton EA, Gutiérrez NL, Hyde KJ, Kleisner KM, Kristiansen T, Longo C, Minte-Vera CV. 2016. Fishery production potential of large marine ecosystems: a prototype analysis. Environ Develop. 17:211–219.

Gacic M, Civitarese G. 2012. Introductory notes on the South Adriatic oceanography. Cont Shelf Res. 44:2–4.

Gačić M, Civitarese G, Miserocchi S, Cardin V, Crise A, Mauri E. 2002. The open-ocean convection in the Southern Adriatic: a controlling mechanism of the spring phytoplankton bloom. Cont Shelf Res. 22:1897–1908.

Grbec B, Dulčić J, Morović M. 2002. Long-term changes in landings of small pelagic fish in the eastern Adriatic – possible influence of climate oscillations over the northern hemisphere. Clim Res. 20:241–252. doi:10.3354/cr020241.

Grbec B, Morović M, Paklar GB, Kušpilić G, Matijević S, Matić F, Ninčević Gladan Ž. 2009. The relationship between the atmospheric variability and productivity in the Adriatic Sea area. J Mar Biol Assoc UK. 89:1549–1558.

Guglielmo R, Bergamasco A, Minutoli R, Patti FP, Belmonte G, Spanò N, Zagami G, Bonanzinga V, Guglielmo L, Granata A. 2019. The Otranto channel (South Adriatic Sea), a hot-spot area of plankton biodiversity: pelagic polychaetes. Sci Rep. 9:19490.

Harris R, Wiebe P, Lenz J, Skjodal HR, Huntley M., editors. 2000. ICES zooplankton methodology manual. London: Academic Press. p. 684.

Hernández-León S, Pilar Olivar M, Fernández de Puelles ML, Bode A, Castellón A, López-Pérez C, Tuset VM, González-Gordillo JI. 2019. Zooplankton and micronekton active flux across the tropical and subtropical Atlantic Ocean. Front Mar Sci. 6:535. DOI:10.3389/fmars.2019.00535.

Houpert L, Durrieu de Madron X, Testor P, Bosse A, d'Ortenzio F, Bouin MN, Dausse D, Le Goff H, Kunesch S, Labaste M, Coppola L. 2016. Observations of open-ocean deep convection in the northwestern Mediterranean Sea: seasonal and interannual variability of mixing and deep water masses for the 2007–2013 period. J Geophys Res Oceans. 121:8139–8171. DOI:10.1002/2016JC011857.

Hure J, Ianora A, Scotto di Carlo B. 1980. Spatial and temporal distribution of copepod communities in the Adriatic Sea. J Plankton Res. 2:295–316.

Hure J, Kršinić F. 1998. Planktonic copepods of the Adriatic Sea. Spatial and temporal distribution. Nat Croat. 7:1–135.

Janeković I, Mihanović H, Vilibić I, Tudor M. 2014. Extreme cooling and dense water formation estimates in open and coastal regions of the Adriatic Sea during the winter of 2012. J Geophys Res Oceans. 119:3200–3218. DOI:10.1002/2014JC009865.

Klein B, Roether W, Civitarese G, Gacic M, Manca BB, d'Alcala MR. 2000. Is the Adriatic returning to dominate the production of Eastern Mediterranean deep water? Geophys Res Lett. 27(20):3377–3380. DOI:10.1029/2000GL011620.

Kokkini Z, Mauri E, Gerin R, Poulain P-M, Simoncelli S, Notarstefano G. 2019. On the salinity structure in the South Adriatic as derived from float and glider observations in 2013–2016. Deep-Sea Research Part II. 171:104625. p. 11.

Kokkini Z, Notarstefano G, Poulain P-M, Mauri E, Gerin R, Simoncelli S. 2018. In Von Schuckmann et al., 2018. Unusual salinity pattern in the South Adriatic Sea. Copernicus marine service ocean state report 2018-09-08. J Oper Oceanogr. 11(sup1):S1–S142.

Libralato S, Coll M, Tudela S, Palomera I, Pranovi F. 2008. Novel index for quantification of ecosystem effects of fishing as removal of secondary production. Mar Ecol Prog Ser. 355:107–129. doi:10.3354/meps07224.

Lipizer M, Partescano E, Rabitti A, Giorgetti A, Crise A. 2014. Qualified temperature, salinity and dissolved oxygen climatologies in a changing Adriatic Sea. Ocean Sci.10:771--797. DOI:10.5194/os-10-771-2014.

Manca BB, Kovacevic V, Gacic M, Viezzoli D. 2002. Dense water formation in the southern Adriatic Sea and spreading into the Ionian Sea in the period 1997–1999. J Mar Sys. 33:133–154. DOI:10.1016/S0924-7963(02)00056-8.

Mattia G, Zavatarelli M, Vichi M, Oddo P. 2013. The eastern Mediterranean Sea biogeochemical dynamics in the 1990s: a numerical study. J Geophys Res Oceans. 118:2231–2248.

Mauri E, Gerin R, Poulain P-M. 2016. Measurements of water-mass properties with a glider in the south-western Adriatic Sea. J Oper Oceanogr. 9(sup1):s3–s9. DOI:10.1080/1755876X.2015.1117766.

Miloslavić M, Lučić D, Njire J, Gangai B, Onofri I, Garić R, Žarić M, Miri Osmani F, Pestorić B, Nikleka E, Shumka S. 2012. Zooplankton composition and distribution across coastal and offshore waters off Albania (southern Adriatic) in late spring. Acta Adriat. 53(2):163–178.

Morello EB, Arneri E. 2009. Anchovy and sardine in the Adriatic Sea – an ecological review. In: Gibson RN, Atkinson RJA, Gordon JDM, editors. Oceanography and marine biology: an annual review, volume 47. CRC Press; p. 209–255.

Njire J, Batistić M, Kovačević V, Garić R, Bensi M. 2019. Tintinnid ciliate communities in pre- and post-winter conditions in the southern Adriatic Sea (NE Mediterranean). Water. 11:2329. DOI:10.3390/w11112329.

Notarstefano G, Poulain P-M. 2010. Delayed mode quality control of Argo salinity data in the Mediterranean and Black Sea. 2010-01-01 – Tech. Rep. 2010/32 OGA 6 SIRE.

Notarstefano G, Poulain P-M. 2013. Delayed mode quality control of Argo salinity data in the Mediterranean Sea: a regional approach 2013/103 Sez. OCE 40 MAOS 19pp.

Owens WB, Wong APS. 2009. An improved calibration method for the drift of the conductivity sensor on autonomous CTD profiling floats by θ–S climatology. Deep Sea Res Part I. 56(3):450–457.

Paklar GB, Vilibic I, Grbec B, Matc F, Mihanovich H, Dzoic T, Santic D, Sestanovic S, Solic M, Ivatek-Sahdan S, et al. 2020. Record-breaking salinities in the middle Adriatic during summer 2017 and concurrent changes in the microbial food web. Prog Oceanog. 185:102345. DOI:10.1016/j.pocean.2020.102345.

Pakhomov EA, Froneman PW, Perissinotto R. 2002. Salp/krill interactions in the Southern Ocean: spatial segregation and implications for the carbon flux. Deep Sea Res Part II. 49(9–10):1881–1907.

Pauly D, Christensen V. 1995. Primary production required to sustain global fisheries. Nature. 374(6519):255–257.

Poulain P-M, Cushman-Roisin B. 2001. Chapter 3: circulation. In: Cushman-Roisin B, Gacic M, Poulain P-M,

Artegiani A, editors. Physical oceanography of the Adriatic Sea – past, present and future. Dordrecht: Kluwer Academic Publishers; p. 67–109.
Russo A, Artegiani A. 1996. Adriatic Sea hydrography. Sci Mar. 60(2):33–43.
Socal G, Boldrin A, Bianchi F, Civitarese G, De Lazzari A, Rabitti S, Totti C, Turchetto MM. 1999. Nutrient, particulate matter and phytoplankton variability in the photic layer of the Otranto strait. J Mar Sys. 20:381–398.
Turchetto MM, Bianchi F, Boldrin A, Malaguti A, Rabitti S, Socal G, Strada L. 2000. Nutrients, phytoplankton and primary production processes in oligotrophic areas (southern Adriatic and northern Ionian seas). Atti Assoc Ital Oceanol Limnol. 13(2):269–278.
Ursella L, Cardin V, Batistić M, Garić R, Gačić M. 2018. Evidence of zooplankton vertical migration from continuous southern Adriatic buoy current-meter records. Prog Oceanogr. 167:78–96.
Vidjak O, Bojanić N, Bojanić N, Matijević S, Kušplić G, Ninčević G, Skejić S, Grbec B. 2012. Environmental drivers of zooplankton variability in the coastal eastern Adriatic (Mediterranean Sea). Acta Adriat. 52(2):243–262.
Vilibić I, Matijević S, Šepić J, Kušpilić G. 2012. Changes in the Adriatic oceanographic properties induced by the Eastern Mediterranean transient. Biogeosciences. 9:2085–2097.
Vilibić I, Supić N. 2005. Dense water generation on a shelf: the case of Adriatic Sea. Ocean Dyn. 55:403–415. DOI 10.1007/s10236-005-0030-5.
Viličić D. 1991. A study of phytoplankton in the Adriatic Sea after the July 1984 bloom. Internationale Revue der Gesamten Hydrobiologie. 76(2):197–211.
Viličić D. 1994. Distribution of phytoplankton biomass in relation to oceanographic conditions in the Adriatic Sea. Period Biol. 96:444–446.
Viličić D. 1998. Phytoplankton taxonomy and distribution in the offshore southern Adriatic. Nat Croat. 7(2):127–141.
Viličić D, Leder N, Gržetić Z, Jasprica N. 1995. Microphytoplankton in the Strait of Otranto (eastern Mediterranean). Mar Biol. 123:619–630.
Viličić D, Vučak Z, Škrivanić A, Grzetić Z. 1989. Phytoplankton blooms in the oligotrophic open South Adriatic waters. Mar Chem. 28(1–3):89–107.
Wong A, Keeley R, Carval T, Argo Data Management Team. 2020. Argo quality control manual for CTD and trajectory data. DOI:10.13155/33951.
Zonn IS, Kostianoy AG. 2016. The Adriatic Sea. In: Joksimović A, Djurović M, Semenov A, Zonn I, Kostianoy A, editor. The Boka Kotorska Bay environment. The handbook of environmental chemistry, Vol. 54. Cham: Springer; p. 19–42.

Section 3.5. Delivering high quality sea-ice information around the Svalbard archipelago to marine end-users

Aase JG, Jabour J. 2015. Can monitoring maritime activities in the European high Arctic by satellite-based automatic identification system enhance polar search and rescue? Polar J. 5(2):386–402.
Breiman L. 2001. Random forests. Mach Learn. 45:5–32. DOI:10.1023/A:1010933404324.
Bystrowska M. 2019. The impact of sea ice on cruise tourism on Svalbard. Arctic. 72(2):151–165.
Fossheim M, Primicerio R, Johannesen E, Ingvaldsen RB, Aschan MM, Dolgov AV. 2015. Recent warming leads to a rapid borealization of fish communities in the Arctic. Nat Clim Change. 5(7):673.
Frainer A, Primicerio R, Kortsch S, Aune M, Dolgov AV, Fossheim M, Aschan MM. 2017. Climate-driven changes in functional biogeography of Arctic marine fish communities. Proc Natl Acad Sci USA. 114(46):12202–12207.
Hanssen-Bauer I, Førland EJ, Hisdal H, Mayer S, Sandø AB, Sorteberg A. 2019. Climate in Svalbard 2100 – a knowledge base for climate adaptation. http://www.miljodirektoratet.no/Documents/publikasjoner/M1242/M1242.pdf.
Hebert DA, Allard RA, Metzger EJ, Posey PG, Preller RH, Wallcraft AJ, Phelps MW, Smedstad OM. 2015. Short-term sea ice forecasting: an assessment of ice concentration and ice drift forecasts using the U.S. Navy's Arctic cap nowcast/forecast system. J Geophys Res Oceans. 120:8327–8345. DOI:10.1002/2015JC011283.
IPCC. 2019. Summary for policymakers. In: Pörtner H-O, Roberts DC, Masson-Delmotte V, Zhai P, Tignor M, Poloczanska E, Mintenbeck K, Alegría A, Nicolai M, Okem A, Petzold J, Rama B, Weyer NM, editors, IPCC special report on the ocean and cryosphere in a changing climate. In press.
Isaksen K, Nordli Ø, Førland EJ, Łupikasza E, Eastwood S, Niedźwiedź T. 2016. Recent warming on Spitsbergen – influence of atmospheric circulation and sea ice cover. J Geophys Res Atmos. 121:11,913–11,931. DOI:10.1002/2016JD025606.
Jeuring J, Knol-Kauffman M. 2019. Mapping weather, water, ice and climate knowledge & information needs for maritime activities in the Arctic. SALIENSEAS participatory mapping survey report.
Knol M, Arbo P, Duske P, Gerland S, Lamers M, Pavlova O, Doksæter Sivle A, Tronstad S. 2018. Making the Arctic predictable: the changing information infrastructure of Arctic weather and sea ice services. Polar Geogr. 41(4):279–293.
Kwok R, Cunningham GF, Wensnahan M, Rigor I, Zwally HJ, Yi D. 2009. Thinning and volume loss of the Arctic Ocean sea ice cover: 2003–2008. J Geophys Res. 114:C07005. DOI:10.1029/2009JC005312.
Lamers M, Duske P, van Bets L. 2018. Understanding user needs: a practice-based approach to exploring the role of weather and sea ice services in European Arctic expedition cruising. Polar Geogr. 1–17. DOI:10.1080/1088937X.2018.1513959.
Lasserre F. 2015. Simulations of shipping along Arctic routes: comparison, analysis and economic perspectives. Polar Rec. 51(3):239–259.
Lavergne T, Sørensen AM, Kern S, Tonboe R, Notz D, Aaboe S, Bell L, Dybkjær G, Eastwood S, Gabarro C, et al. 2019. Version 2 of the EUMETSAT OSI SAF and ESA CCI sea-ice concentration climate data records. Cryosphere. 13(1):49–78. doi:10.5194/tc-13-49-2019.
Lemelin H, Dawson J, Stewart EJ, Maher P, Lueck M. 2010. Last-chance tourism: The boom, doom, and gloom of visiting vanishing destinations. Curr. Issues Tour.. 13(5):477–493.

Melia N, Haines K, Hawkins E, Day J. 2017. Towards seasonal Arctic shipping route predictions. Environ Res Lett. 12 (8):084005.

Onarheim IH, Smedsrud LH, Ingvaldsen RB, Nilsen F. 2014. Loss of sea ice during winter north of Svalbard. Tellus A Dyn Meteorol Oceanogr. 66(1):23933. DOI:10.3402/tellusa.v66.23933.

Palma D, Varnajot A, Dalen K, Basaran IK, Brunette C, Bystrowska M, Korablina AD, Nowicki RC, Ronge TA. 2019. Cruising the marginal ice zone: climate change and Arctic tourism. Polar Geogr. 42(4):215–235.

Rabatel M, Rampal P, Carrassi A, Bertino L, Jones CKRT. 2018. Impact of rheology on probabilistic forecasts of sea ice trajectories: application for search and rescue operations in the Arctic. Cryosphere. 12:935–953. DOI:10.5194/tc-12-935-2018.

Renner AHH, Hendricks S, Gerland S, Beckers J, Haas C, Krumpen T. 2013. Large-scale ice thickness distribution of first-year sea ice in spring and summer north of Svalbard. Ann Glaciol. 54(62):13–18. DOI:10.3189/2013AoG62A146.

Renner AHH, Sundfjord A, Janout MA, Ingvaldsen RB, Beszczynska-Möller A, Pickart RS, Pérez-Hernández MD. 2018. Variability and redistribution of heat in the Atlantic water boundary current North of Svalbard. J Geophys Res Oceans. 123(9):6373–6391. DOI:10.1029/2018JC013814.

Rosel A, Itkin P, King J, Divine D, Wang C, Granskog MA, Krumpen T, Gerland S. 2018. Thin sea ice, thick snow, and widespread negative freeboard observed during N-ICE2015 North of Svalbard: sea ice and snow during N-ICE2015. J Geophys Res Oceans. 123(2):1156–1176. DOI:10.1002/2017JC012865.

Sakov P, Counillon F, Bertino L, Lisæter KA, Oke PR, Korablev A. 2012. TOPAZ4: an ocean-sea ice data assimilation system for the North Atlantic and Arctic. Ocean Sci. 8:633–656. doi:10.5194/os-8-633-2012.

Schweiger AJ, Zhang J. 2015. Accuracy of short-term sea ice drift forecasts using a coupled ice-ocean model. J Geophys Res Oceans. 120:7827–7841. DOI:10.1002/2015JC011273.

Stautland K. 2019. New rules for passenger ships in Svalbard. Norwegian Maritime Authority https://www.sdir.no/en/news/news-from-the-nma/new-rules-for-passenger-ships-in-svalbard/.

Stocker A, Renner AHH, Knol-Kauffman M. 2020. Sea ice variability and maritime activity around Svalbard in the period 2012–2019. Sci Rep. 10. DOI:10.1038/s41598-020-74064-2.

Wagner PM, Hughes N, Bourbonnais P, Stroeve J, Rabenstein L, Bhatt U, Little J, Wiggins H, Fleming A. 2020. Sea-ice information and forecast needs for industry maritime stakeholders. Polar Geogr. 43(2–3):160–187.

Yu X, Rinke A, Dorn W, Spreen G, Lüpkes C, Sumata H, Gryanik VM. 2020. Evaluation of Arctic sea ice drift and its dependency on near-surface wind and sea ice conditions in the coupled regional climate model HIRHAM–NAOSIM. Cryosphere. 14:1727–1746. DOI:10.5194/tc-14-1727-2020.

Section 3.6. Developing spatial distribution models for demersal species by the integration of trawl surveys data and relevant ocean variables

Amoroso RO, Pitcher CR, Rijnsdorp AD, Mcconnaughey RA, Parma AM, Suuronen P, Silva C. 2018. Bottom trawl fishing footprints on the world's continental shelves. Proc Natl Acad Sci U S A. 115(43):E10275–E10282.

Bastardie F, Rasmus Nielsen J, Miethe T. 2014. DISPLACE: a dynamic, individual-based model for spatial fishing planning and effort displacement – integrating underlying fish population models. Can J Fish Aquat Sci. 71:366–386. DOI:10.1139/cjfas-2013-0126.

Bertrand JA, De Sola LG, Papaconstantinou C, Relini G, Souplet A. 2002. The general specifications of the MEDITS surveys. Sci Mar. 66(Suppl. 2):9–17.

Bitetto I, Romagnoni G, Adamidou A, Certain G, Di Lorenzo M, Donnaloia M, Lembo G, Maiorano P, Milisenda G, Musumeci C, et al. 2019. Modelling spatio-temporal patterns of fish community size structure across the northern Mediterranean Sea: an analysis combining MEDITS survey data with environmental and anthropogenic drivers. Sci Mar. 83(S1):141–151. DOI:10.3989/scimar.05015.06A.

Brodie SJ, Thorson JT, Carroll G, Hazen EL, Bograd S, Haltuch MA, Holsma KK, Kotwicki S, Samhouri JF, Willis-Norton E, Selden RL. 2020. Trade-offs in covariate selection for species distribution models: a methodological comparison. Ecography. 43(1):11–24.

Cao J, Thorson JT, Richards RA, Chen Y. 2017. Spatiotemporal index standardization improves the stock assessment of northern shrimp in the Gulf of Maine. Can J Fish Aquat Sci. 74(11):1781–1793.

Carlucci R, Bandelj V, Ricci P, Capezzuto F, Sion L, Maiorano P, Libralato S. 2018. Exploring spatio-temporal changes in the demersal and benthopelagic assemblages of the northwestern Ionian Sea (central Mediterranean Sea). Mar Ecol Prog Ser. 598:1–19.

Carlucci R, Lembo G, Maiorano P, Capezzuto F, Marano CA, Sion L, Spedicato MT, Ungaro N, Tursi A, D'Onghia G. 2009. Nursery areas of red mullet (*Mullus barbatus*), hake (*Merluccius merluccius*), and deepwater rose shrimp (*Parapenaeus longirostris*) in the eastern-central Mediterranean Sea. Estuar Coast Shelf Sci. 83:529–538.

Colloca F, Garofalo G, Bitetto I, Facchini MT, Grati F, Martiradonna A, Mastrantonio G, Nikolioudakis N, Ordinas F, Scarcella G, et al. 2015. The seascape of demersal fish nursery areas in the North Mediterranean Sea, a first step towards the implementation of spatial planning for trawl fisheries. PLoS One. 10(3):e0119590. DOI:10.1371/journal.pone.0119590.

Cotter J, Petitgas P, Abella A, Apostolaki P, Mesnil B, Politou C-Y, Rivoirard J, Rochet M-J, Spedicato MT, Trenkel VM, Woillez M. 2009. Towards an ecosystem approach to fisheries management (EAFM) when trawl surveys provide the main source of information. Aquat Living Resour. 22:243–254. DOI:10.1051/alr/2009025.

Druon JN, Fiorentino F, Murenu M, Knittweis L, Colloca F, Osio C, Sbrana M. 2015. Modelling of European hake nurseries in the Mediterranean Sea: an ecological niche approach. Prog Oceanogr. 130:188–204.

EU. 2013. Council regulation (EU) 1385/2013 of 17 December 2013, amending Council Regulations (EC) No 850/98 and (EC) 1224/2009, and Regulations (EC) 1069/2009, (EU) No 1379/2013 and (EU) 1380/2013 of the European Parliament and of the Council, following the amendment of the status of Mayotte with regard to the

European Union. Official Journal of the European Communities L 354/86.
EUSAIR. 2014. Communication from the Commission to the European Parliament, the Council, the European Economic and Social Committee of the Regions concerning the European Union Strategy for the Adriatic and Ionian Region. COM (2014) 357 final.
FAO. 2018. The state of Mediterranean and Black Sea fisheries. Rome: General Fisheries Commission for the Mediterranean. 172 pp.
Fulton EA, Link JS, Kaplan IC, Savina-Rolland M, Johnson P, Ainsworth C, Smith DC. 2011. Lessons in modelling and management of marine ecosystems: the Atlantis experience. Fish Fisheries. 12(2):171–188.
GFCM. 2019. Report of Working Group on Stock Assessment of Demersal Species (WGSAD). http://www.fao.org/gfcm/technical-meetings/detail/en/c/1274921/.
Giannoulaki M, Valavanis VD, Palialexis A, Tsagarakis K, Machias A, Somarakis S, Papaconstantinou C. 2008. Modelling the presence of anchovy Engraulis encrasicolus in the Aegean Sea during early summer, based on satellite environmental data. Hydrobiologia. 612:225–240.
Grati F, Scarcella G, Polidori P, Domenichetti F, Bolognini L, Gramolini R, Vasapollo C, Giovanardi O, Raicevich S, Celić I, et al. 2013. Multi-annual investigation of the spatial distributions of juvenile and adult sole (Solea solea, L.) in the Adriatic Sea (northern Mediterranean). J Sea Res. 84:122–132.
Grüss A, Chagaris DD, Babcock EA, Tarnecki JH. 2018. Assisting ecosystem-based fisheries management efforts using a comprehensive survey database, a large environmental database, and generalized additive models. Mar Coast Fish. 10(1):40–70.
Grüss A, Drexler M, Ainsworth CH. 2014. Using delta generalized additive models to produce distribution maps for spatially explicit ecosystem models. Fish Res. 159:11–24.
Lauria V, Garofalo G, Fiorentino F, Massi D, Milisenda G, Piraino S, Russo T, Gristina M. 2017. Species distribution models of two critically endangered deep-sea octocorals reveal fishing impacts on vulnerable marine ecosystems in central Mediterranean Sea. Sci Rep. 7(1):1–14.
Maunder MN, Punt AE. 2004. Standardizing catch and effort data: a review of recent approaches. Fish Res. 70(2–3):141–159.
MEDITS-Handbook. 2017. Version n. 9, MEDITS Working Group: 106 pp.
Melaku Canu D, Solidoro C, Cossarini G, Giorgi F. 2010. Effect of global change on bivalve rearing activity and the need for adaptive management. Clim Res. 42:13–26. doi:10.3354/cr00859.
Moullec F, Veleza L, Verley P, Barrier N, Ulses C, Carbonara P, Esteban A, Follesa C, Gristina M, Jadaud A, et al. 2019. Capturing the big picture of Mediterranean marine biodiversity with an end to end model of climate and fishing impacts. Prog Oceanogr. 178:102179.
Orio A, Florin A-B, Bergström U, Šics I, Baranova T, Casini M. 2017. Modelling indices of abundance and size-based indicators of cod and flounder stocks in the Baltic Sea using newly standardized trawl survey data. ICES J Mar Sci. 74(5):1322–1333. doi:10.1093/icesjms/fsx005.
Potts SE, Rose KA. 2018. Evaluation of GLM and GAM for estimating population indices from fishery independent surveys. Fish Res. 208:167–178.
Rubec PJ, Kiltie R, Leone E, Flamm RO, McEachron L, Santi C. 2016. Using delta-generalized additive models to predict spatial distributions and population abundance of juvenile pink shrimp in Tampa Bay, Florida. Mar Coast Fish. 8 (1):232–243.
Rufino MM, Bez N, Brind'Amour A. 2018. Integrating spatial indicators in the surveillance of exploited marine ecosystems. PLoS One. 13(11):e0207538.
Russo T, D'Andrea L, Parisi A, Cataudella S. 2014. VMSbase: an R-package for VMS and logbook data management and analysis in fisheries ecology. PLoS One. 9:e100195. DOI:10.1371/journal.pone.0100195.
Russo T, Morello EB, Parisi A, Scarcella G, Angelini S, Labanchi L, et al. 2018. A model combining landings and VMS data to estimate landings by fishing ground and harbor. Fish Res. 199:218–230. doi:10.1016/j.fishres.2017.11.002.
Sartor P, Mannini A, Carlucci R, Massaro E, Queirolo S, Sabatini A, Scarcella G, Simoni R, editors. 2017. Sintesi delle conoscenze di biologia, ecologia e pesca delle specie ittiche dei mari italiani [Synthesis of the knowledge on biology, ecology and fishery of the halieutic resources of the Italian seas]. Biol Mar Mediterr. 24(Suppl. 1):608.
Scarcella G, Fabi G, Grati F, Polidori P, Domenichetti F, Bolognini L, Celic I. 2011. SoleMon survey for the study of flatfish stocks in the central and northern Adriatic Sea. International Flatfish Symposium 2011, IJmuiden.
Schismenou E, Tsoukali S, Giannoulaki M, Somarakis S. 2017. Modelling small pelagic fish potential spawning habitats: eggs vs spawners and in situ vs satellite data. Hydrobiologia. 788(1):17–32.
Sheather S. 2009. A modern approach to regression with R. New York (NY): Springer.
Simoncelli S, Fratianni C, Pinardi N, Grandi A, Drudi M, Oddo P, Dobricic S. 2019. Mediterranean Sea physical reanalysis (CMEMS MED-Physics) [Data set]. Copernicus Monitoring Environment Marine Service (CMEMS). https://doi.org/10.25423/MEDSEA_REANALYSIS_PHYS_006_004.
Sion L, Zupa W, Calculli C, Garofalo G, Hidalgo M, Jadaud A, Lefkaditou E, Ligas A, Peristeraki P, Bitetto I, et al. 2019. Spatial distribution pattern of European hake, Merluccius merluccius (Pisces: Merlucciidae), in the Mediterranean Sea. Sci Mar. 83(S1):21–32.
Spedicato MT, Massutí E, Mérigot B, Tserpes G, Jadaud A, Relini G. 2019. The MEDITS trawl survey specifications in an ecosystem approach to fishery management. Sci Mar. 83(S1):9–20. DOI:10.3989/scimar.04915.11X.
Spedicato MT, Zupa W, Carbonara P, Fiorentino F, Follesa MC, Galgani F, García-Ruiz C, Jadaud A, Ioakeimidis C, Lazarakis G, et al. 2019. Spatial distribution of marine macro-litter on the seafloor in the northern Mediterranean Sea: the MEDITS initiative. Sci Mar. 83 (S1):257–270. DOI:10.3989/scimar.04987.14A.
STECF (Scientific, Technical and Economic Committee for Fisheries). 2019. Stock assessments part 2: European fisheries for demersal species in the Adriatic Sea (STECF-

19-16). Publications Office of the European Union. ISBN 978-92-76-14558-5, JRC119057. DOI:10.2760/95875.
Travers-Trolet M, Bourdaud P, Genu M, Velez L, Vermard Y. 2020. The risky decrease of fishing reference points under climate change. Front Mar Sci. 7:850. DOI:0.3389/fmars.2020.568232.
Teruzzi A, Bolzon G, Cossarini G, Lazzari P, Salon S, Crise A, Solidoro C. 2019. Mediterranean Sea biogeochemical reanalysis (CMEMS MED-biogeochemistry) [Data set]. Copernicus Monitoring Environment Marine Service (CMEMS). https://doi.org/10.25423/MEDSEA_REANALYSIS_BIO_006_008.
Tserpes G, Massuti E, Fiorentino F, Facchini MT, Viva C, Jadaud A, Joksimovic A, Pesci P, Piccinetti C, Sion L, et al. 2019. Distribution and spatio-temporal biomass trends of red mullets across the Mediterranean. Sci Mar. 83(S1):43–55. DOI:10.3989/scimar.04888.21A.
Tukey J. 1949. Comparing individual means in the analysis of variance. Biometrics. 5(2):99–114. doi:10.2307/3001913.
Woillez M, Rivoirard J, Petitgas P. 2009. Notes on survey-based spatial indicators for monitoring fish populations. Aquat Living Resour. 22:155–164.

Section 3.7. A benthic hypoxia index (BH-index) for assessing the Good Environmental Status of the Black Sea's north-western shelf waters

Breitburg D, Levin LA, Oschlies A, Grégoire M, Chavez FP, Conley DJ, Garçon V, Gilbert D, Gutiérrez D, Isensee K, et al. 2018. Declining oxygen in the global ocean and coastal waters. Science. 359(6371). DOI:10.1126/science.aam7240.
Capet A, Beckers J-M, Grégoire M. 2013. Drivers, mechanisms and long-term variability of seasonal hypoxia on the Black Sea northwestern shelf – is there any recovery after eutrophication. Biogeosciences. 10 (6):3943–3962.
Capet A, Cook P, Garcia-Robledo E, Hoogakker B, Paulmier A, Rabouille C, Vaquer-Sunyer R. 2020. Editorial: facing marine deoxygenation. Front Mar Sci. 7:46.
Capet A, Meysman FJR, Akoumianaki I, Soetaert K, Grégoire M. 2016. Integrating sediment biogeochemistry into 3D oceanic models: A study of benthic-pelagic coupling in the Black Sea. Ocean Modelling. 101:83–100.
Conley DJ, Paerl HW, Howarth RW, Boesch DF, Seitzinger SP, Havens KE, Lancelot C, Likens GE. 2009. Ecology. Controlling eutrophication: nitrogen and phosphorus. Science. 323(5917):1014–1015.
Fennel K, Testa JM. 2019. Biogeochemical controls on coastal hypoxia. Ann Rev Mar Sci. 11:105–130.
Friedrich J, Balan S, van Beusekom JE, Naderipour C, Secrieru D. 2017. Seasonal seafloor oxygen dynamics on the Romanian Black Sea Shelf. Geophysical Research Abstracts, 2845.
Friedrich J, Janssen F, Aleynik D, Bange HW, Boltacheva N, Çagatay MN, Dale AW, Etiope G, Erdem Z, Geraga M, et al. 2014. Investigating hypoxia in aquatic environments: diverse approaches to addressing a complex phenomenon. Biogeosciences. 11(4):1215–1259.
Friedrich J, van Beusekom JEE, Naderipour C, Balan S, Radulescu V, Secrieru D. 2019. River-born and climate drivers of hypoxia on the NW Black Sea Shelf. Geophysical Research Abstracts, 21. https://meetingorganizer.copernicus.org/EGU2019/EGU2019-16147.pdf.
Grégoire M, Friedrich J. 2004. Nitrogen budget of the northwestern Black Sea shelf inferred from modeling studies and in situ benthic measurements. Mar Ecol Prog Ser. 270:15–39.
Grégoire M, Raick C, Soetaert K. 2008. Numerical modeling of the central Black Sea ecosystem functioning during the eutrophication phase. Prog Oceanogr. 76 (3):286–333.
Hrycik AR, Almeida LZ, Höök TO. 2017. Sub-lethal effects on fish provide insight into a biologically-relevant threshold of hypoxia. Oikos. 126(3):307–317.
Jessen GL, Lichtschlag A, Ramette A, Pantoja S, Rossel PE, Schubert CJ, Struck U, Boetius A. 2017. Hypoxia causes preservation of labile organic matter and changes seafloor microbial community composition (Black Sea). Sci Adv. 3 (2):e1601897.
Kemp WM, Testa JM, Conley DJ, Gilbert D, Hagy JD. 2009. Temporal responses of coastal hypoxia to nutrient loading and physical controls. Biogeosciences. 6(12):2985–3008.
Langmead O, McQuatters-Gollop A, Mee LD, Friedrich J, Gilbert AJ, Gomoiu M-T, Jackson EL, Knudsen S, Minicheva G, Todorova V. 2009. Recovery or decline of the northwestern Black Sea: a societal choice revealed by socio-ecological modelling. Ecol Modell. 220(21):2927–2939.
Lichtschlag A, Donis D, Janssen F, Jessen GL, Holtappels M, Wenzhöfer F, Mazlumyan S, Sergeeva N, Waldmann C, Boetius A. 2015. Effects of fluctuating hypoxia on benthic oxygen consumption in the Black Sea (Crimean Shelf). Biogeosciences. 12:5075–5092.
Low NHN, Micheli F. 2018. Lethal and functional thresholds of hypoxia in two key benthic grazers. Mar Ecol Prog Ser. 594:165–173.
Ludwig W, Dumont E, Meybeck M, Heussner S. 2009. River discharges of water and nutrients to the Mediterranean and Black Sea: major drivers for ecosystem changes during past and future decades? Prog Oceanogr. 80(3):199–217.
Mee L. 2006. Reviving dead zones. Sci Am. 295(5):78–85.
Mikhailov V, Denga Y, Derezyuk N, Kostylyov E, Lisovsky R, Orlova I, Pavlenko M, Popov Y. 2002. State of the Black Sea environment, national report of Ukraine, 1996–2000. Ukrainian Scientific Centre of the Ecology of the Sea, Ministry of Ecology and Natural Resources of Ukraine.
Steckbauer A, Duarte CM, Carstensen J, Vaquer-Sunyer R, Conley DJ. 2011. Ecosystem impacts of hypoxia: thresholds of hypoxia and pathways to recovery. Environ Res Lett. 6 (2):025003.
Stevens T, Mee L, Friedrich J, Aleynik D, Minicheva G. 2019. Partial recovery of macro-epibenthic assemblages on the north-west shelf of the Black Sea. Front Mar Sci. 6:474.
Stow CA, Jolliff J, McGillicuddy DJ, Jr, Doney SC, Allen JI, Friedrichs MAM, Rose KA, Wallhead P. 2009. Skill assessment for coupled biological/physical models of marine systems. J Mar Syst J Eur Assoc Mar Sci Tech. 76 (1–2):4–15.
Vandenbulcke L, Capet A, Beckers JM, Grégoire M, Besiktepe S. 2010. Onboard implementation of the GHER model for the Black Sea, with SST and CTD data assimilation. J Oper Oceanogr. 3(2):47–54.

Vaquer-Sunyer R, Duarte CM. 2008. Thresholds of hypoxia for marine biodiversity. Proc Natl Acad Sci USA. 105 (40):15452–15457.

Vaquer-Sunyer R, Duarte CM. 2011. Temperature effects on oxygen thresholds for hypoxia in marine benthic organisms. Glb Chg Bio. 17(5):1788–1797.

Yunev OA, Carstensen J, Moncheva S, Khaliulin A, Ærtebjerg G, Nixon S. 2007. Nutrient and phytoplankton trends on the western Black Sea shelf in response to cultural eutrophication and climate changes. Estuar Coast Shelf Sci. 74 (1):63–76.

Zaitsev Y, Mamaev V. 1997. Biological diversity in the Black Sea: a study of change and decline. In: Y Zaitsev, V Mamaev, editors Black Sea environmental series, Vol. 3. New York (NY): UN Publications; 208pp. https://digitallibrary.un.org/record/245415?ln=en.

CMEMS OSR5 – Chapter 4

Table of content

Section 4.1. Sea-ice and ocean conditions surprisingly normal in the Svalbard-Barents Sea region after large sea-ice inflows in 2019

Authors: Signe Aaboe, Sigrid Lind, Stefan Hendricks, Emily Down, Thomas Lavergne, Robert Ricker

Statement of main outcome During summer and autumn 2019, the Arctic Ocean experienced an unusual low sea-ice extent, following the long-term negative trend since the late 1970s. Conversely, the Atlantic sector had surprisingly normal sea-ice coverage close to the climatological average (1981–2010), especially Svalbard and parts of the Barents Sea, in contrast to several record lows during the 2010s. We show that older and thicker sea ice was transported across the Arctic Basin towards the Atlantic sector in winter 2018/2019 using satellite observations of sea-ice concentration, thickness, type, and drift. This precondition, combined with persistently northerly winds in 2019 resulted in exceptionally large sea-ice inflows to the Svalbard-Barents region. With in situ ocean temperature and salinity observations, we show that local ocean conditions changed coherently. The ocean was record warm in 2018, with the highest heat content of the upper 100 m observed in the 2000s, and it had record low freshwater content and was weakly stratified. In autumn 2019, the ocean freshwater content had increased, stratification strengthened and heat content declined. This indicates that persistent, large sea-ice inflows have acted to recover the sea-ice cover and ocean stratification through adding sea ice and freshwater to the region. This supports that large sea-ice inflows act to maintain an Arctic-type ocean climate with a cold, stratified, and sea-ice covered water column and is a key player among others in the Arctic climate system. Sea-ice conditions in this region strongly impact ecosystem, weather, and economic activities, such as tourism, fisheries, and shipping.

Products used

Ref. No.	Product name and type	Documentation
4.1.1	SEAICE_GLO_SEAICE_L4_NRT_OBSERVATIONS_011_001 Global Ocean – Arctic and Antarctic – sea ice concentration, edge, type and drift (OSI-SAF)	PUM: http://marine.copernicus.eu/documents/PUM/CMEMS-SI-PUM-011-001.pdf QUID: http://marine.copernicus.eu/documents/QUID/CMEMS-OSI-QUID-011-001to007-009to012.pdf
4.1.2	SEAICE_GLO_SEAICE_L4_REP_OBSERVATIONS_011_009 Global Ocean sea ice concentration time series reprocessed (OSI-SAF)	PUM: http://marine.copernicus.eu/documents/PUM/CMEMS-OSI-PUM-011-009.pdf QUID: http://marine.copernicus.eu/documents/QUID/CMEMS-SI-QUID-011-001to007-009to013.pdf
4.1.3	SEAICE_ARC_SEAICE_L3_REP_OBSERVATIONS_011_013 Arctic Ocean - sea ice thickness reprocessed (C3S)	PUM: http://marine.copernicus.eu/documents/PUM/CMEMS-SI-PUM-011-013.pdf QUID: http://marine.copernicus.eu/documents/QUID/CMEMS-SI-QUID-011-001to007-009to013.pdf
4.1.4	C3S Arctic sea-ice thickness Interim CDR (non CMEMS product)	Data and documentation can be obtained from the Copernicus Climate Date https://cds.climate.copernicus.eu/cdsapp#!/dataset/satellite-sea-ice?tab=overview PUGS: http://datastore.copernicus-climate.eu/documents/satellite-sea-ice/thickness/D3.SIT.1-v1.1_PUGS_of_v1_Sea_Ice_Thickness_Products_v1.3_APPROVED_Ver1.pdf
4.1.5	C3S Arctic sea-ice type CDR and Interim CDR (non CMEMS product)	Data and documentation can be obtained from the Copernicus Climate Date https://cds.climate.copernicus.eu/cdsapp#!/

(*Continued*)

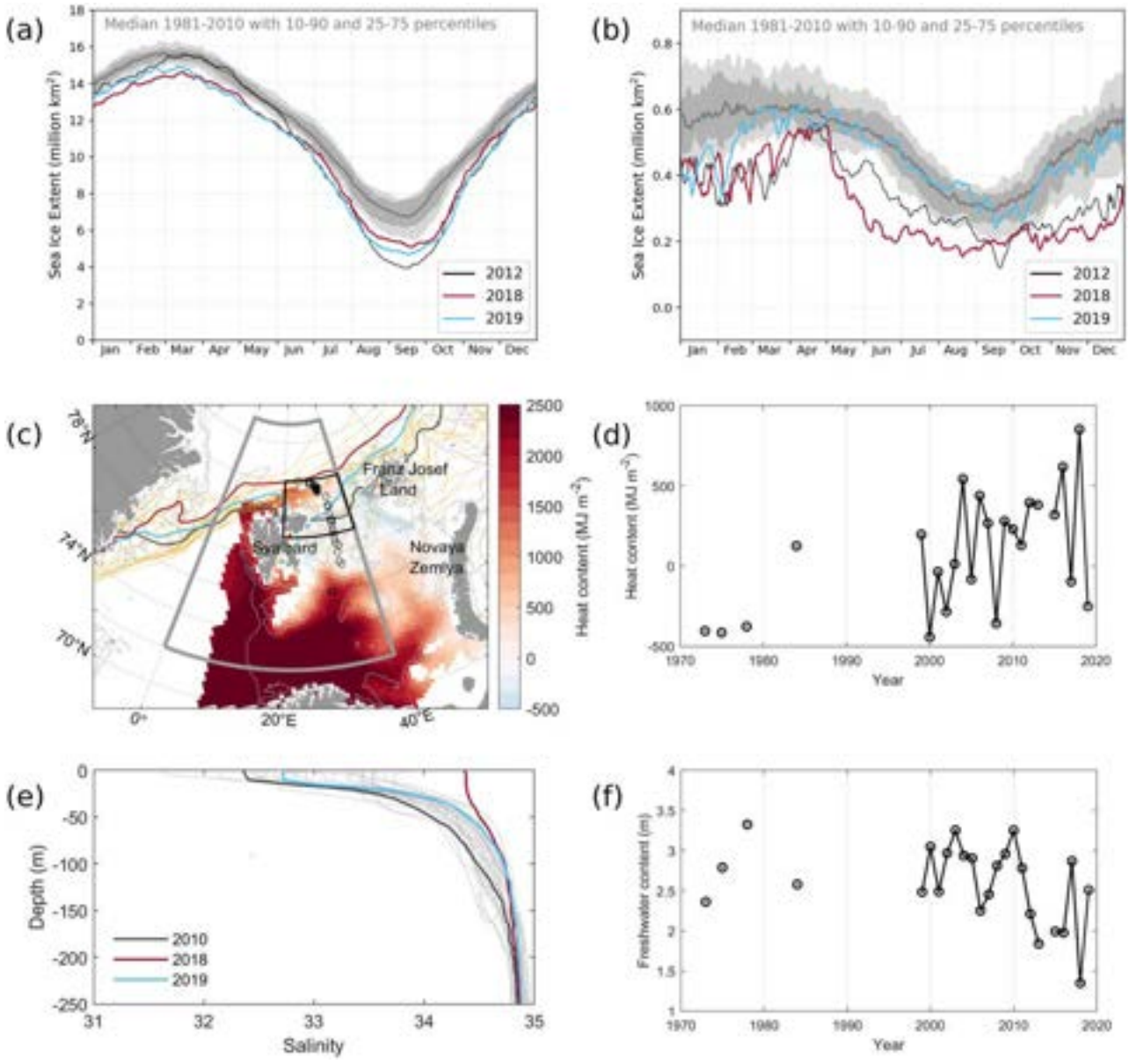

Figure 4.1.1. Sea-ice extent in (a) the entire Arctic and (b) the Svalbard-Barents Sea region, estimated from daily values in 2012, 2018 and 2019 (black, red and blue curves, respectively) and the median extent during the reference period 1981–2010 and corresponding quartiles and 10–90 percentiles in dark and light grey shading. (c) Ocean heat content in the upper 100 m in August–September 1999 with the Svalbard-Barents Sea region (grey outline), the northeast Svalbard region (black outline) and positions of the CTD profiles in 2019 (black circles) and isolines for mean September 15% sea-ice concentration (product 4.1.2) in 1999–2019 (yellow curves), where 2010, 2018 and 2019 isolines are highlighted as thick grey, red and blue curves, respectively. (d) Heat content in the upper 100 m estimated in the northeast Svalbard area. (e) Salinity profiles from individual years in northeast Svalbard region (thin grey curves) with 2010, 2018, and 2019 outlined in thick grey, red and blue curves, respectively. (f) Freshwater content in the upper 100 m estimated in the northeast Svalbard region.

Continued.

Ref. No.	Product name and type	Documentation
4.1.6	Ocean temperature and salinity measurements by the Norwegian Institute of Marine Research and the Nikolai M. Knipovich Polar Research Institute of Marine Fisheries and Oceanography, Russia (non CMEMS product).	Norwegian CTD data available from the World Ocean Data Base https://www.nodc.noaa.gov/OC5/WOD13/ Russian CTD data are not publicly available. Documentation of the interpolation procedure in Lind et al. (2016, 2018).
4.1.7	Ocean temperature and salinity measurements in 2019 by the Nansen Legacy, Norwegian Polar Institute, Norwegian Institute of Marine Research (non CMEMS product)	https://

arvenetternansen.com/data-management-and-synthesis/
Nansen Legacy data are not yet publicly available.

4.1.1. Introduction

Sea ice is a highly variable component of the polar environment with its seasonal cycles of melting and freezing and its mobility forced by winds and ocean circulation. The presence of the sea-ice cover is of crucial importance for the climate and ecosystem. However, the sea-ice conditions are rapidly changing (e.g. Carmack et al. 2015). Over more than four decades of satellite monitoring, the Arctic sea ice has shown a decreasing trend with a loss of 11.3% areal extent per decade in September and 2.6% in March (CMEMS ARCTIC_OMI_SI_extent_obs 2020; cryo.met.no 2020). The negative trend in sea ice mainly occurs in the broad Arctic shelf seas regions. In winter, the largest loss occurs in the seasonally ice-covered seas (listed here by their order of loss contribution: the Barents Sea, Sea of Okhotsk, Greenland Sea, Baffin Bay/Gulf of St. Lawrence), while in summer, the perennial ice-covered seas experience the largest loss (East Siberian Sea, Chukchi Sea, Beaufort Sea, Laptev Sea, Kara Sea) (Onarheim et al. 2018). Moreover, the consolidated ice pack north of Greenland and the Canadian Archipelago, consisting of the oldest and thickest sea ice, has become younger, thinner and consequently more mobile (Comiso 2012; Kwok 2018; Meredith et al. 2019). The more unpredictable behaviour of the thicker multiyear ice brings challenges to the shipping in Arctic regions by blocking sea routes (Kimura et al. 2020).

The Arctic Ocean is generally stratified with an upper layer of colder, fresher Arctic water masses that insulates the sea-ice cover from a layer of warm, saline Atlantic Water below (Nansen 1902; Aagaard et al. 1981). The Atlantic Water is the major oceanic heat carrier entering the Arctic Ocean, in the Fram Strait (Aagaard 1989; Fahrbach et al. 2001) and the Barents Sea (e.g. Loeng 1991; Årthun et al. 2012), but is separated from the surface and sea-ice cover by the less dense Arctic water masses in most of the Arctic Ocean (Aagaard et al. 1981), including in the northern Barents Sea (Mosby 1938; Loeng 1991; Lind and Ingvaldsen, 2012). The sea-ice cover provides freshwater when melting in summer, which acts to maintain this ocean stratification with Arctic water above Atlantic water (Aagaard and Woodgate 2001; Ellingsen et al. 2009; Lind et al. 2018). Sea-ice inflows, therefore, act to increase the freshwater content when melting in summer. After 2005, declines in the sea-ice inflows to the northern Barents Sea have induced a major 40% freshwater loss and weakened the ocean stratification (Lind et al. 2018). This allowed for more vertical mixing with the deep Atlantic layer, bringing up heat and salt and preventing sea-ice formation, and the ocean heat content in the upper 100 m have increased rapidly (Lind et al. 2018).

Arctic amplification of global warming is particularly strong in the northern Barents Sea which has experienced the greatest atmospheric warming and winter sea-ice loss in the entire Arctic Ocean in the 2000s (Screen and Simmonds 2010; Onarheim et al. 2018). The warming and sea-ice loss is enhanced in this region compared with other Arctic regions likely due to several factors, including the declining sea-ice inflows, freshwater loss and associated extreme upper ocean warming (Lind et al. 2018), heat import with Atlantic Water (e.g. Årthun et al. 2012), increasing sea-ice export through Fram Strait (Zamani et al. 2019) and increased cyclone activity (Wickström et al. 2020).

In 2019, the extent of Arctic sea ice was very low with monthly sea-ice extents among the three lowest on record in eight consecutive months, from April to November (Figure 4.1.1(a)). However, while the Arctic as a whole had anomalously little sea ice, the Svalbard-Barents Sea region had a sea-ice extent that was comparable to the climatological median for 1981–2010 from March to December (Figure 4.1.1(b)). It is not known which driver caused the sudden re-establishment of the sea-ice cover in the Svalbard-Barents Sea region in 2019, nor how the oceanic conditions changed concurrently. Our objective is to investigate the role that sea ice inflows played in this special event. Our hypothesis is that large sea-ice inflows from the Arctic Ocean were key for recovering sea-ice and oceanic conditions in the Svalbard-Barents Sea region in 2019, through adding sea ice and freshwater. Using satellite remote sensing data in combination with *in situ* oceanographic observations, we investigated sea-ice drift, thickness, and concentration patterns in the Arctic Ocean in comparison with the reference period 1981–2010 and the accompanied changes in the regional sea-ice cover, ocean stratification and ocean freshwater and heat contents.

4.1.2. Methods

For the sea-ice analysis, we used satellite remote sensing-derived data. Estimates of the sea-ice extent (SIE) were derived from the global Sea-Ice Concentration Climate Data Record (CDR) produced by the EUMETSAT Ocean and Sea Ice Satellite Application Facility (OSISAF, Lavergne et al. 2019) redistributed

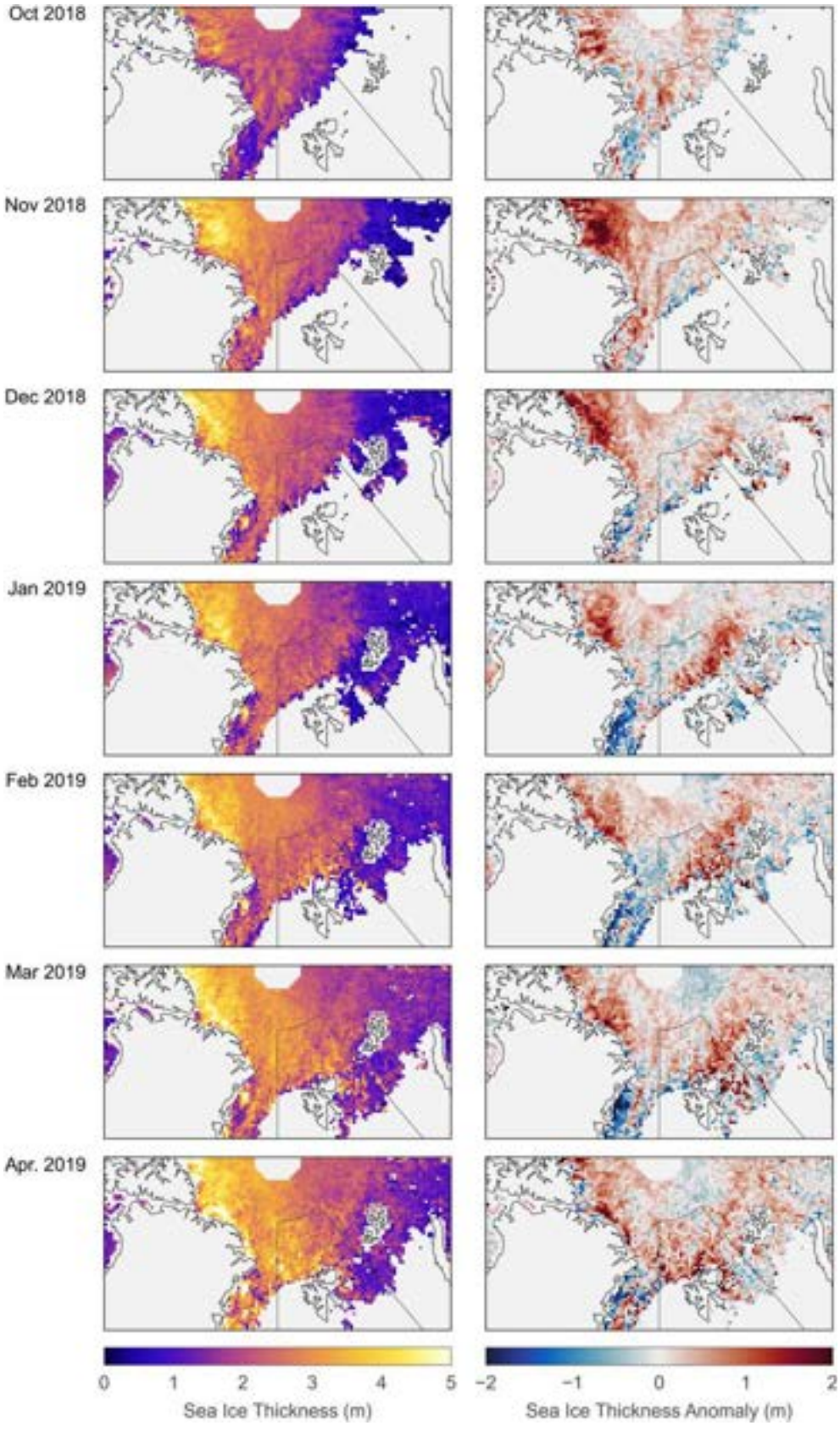

Figure 4.1.2. Left column: Sea ice thickness based on CryoSat-2 radar altimeter data for the Arctic winter month of October 2018 through April 2019 (product 4.1.3 and 4.1.4). Right column: Sea-ice thickness anomaly computed as the difference between monthly grid values (left column) to a mean thickness from the previous months in the CryoSat-2 data record since November 2010. The outlined box indicates the Svalbard-Barents Sea region (0–40°E, 72°N–85°N).

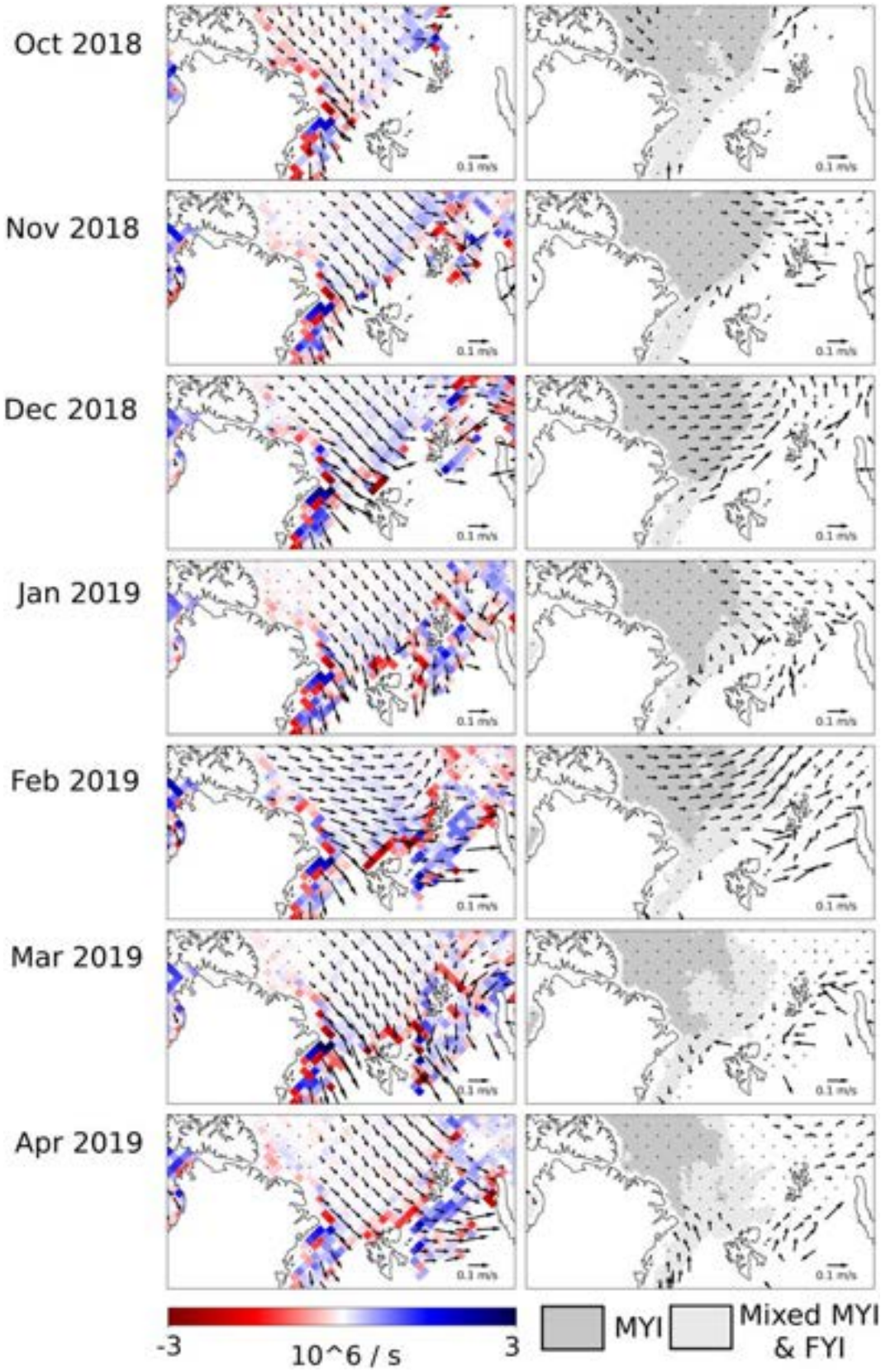

Figure 4.1.3. Left column: Sea-ice drift (arrows, product 4.1.1) and net divergence field (10^6 s^{-1}; coloured background) with positive (negative) values representing divergence (convergence). Each arrow represents average drift over a ten-day period. Right column: Sea-ice drift anomaly (arrows) calculated relative to the monthly average of the eight previous years. Note, that these anomaly vectors represent a change in the drift field and not the drift itself. The background colour is the sea-ice type (product 4.1.5) representing 'pure' multiyear ice as dark grey, mixed classification of both first-year ice and multiyear ice as light grey, and first-year ice/water is colourless.

by CMEMS (product 4.1.2). This OSISAF CDR is based on the passive microwave instruments SMMR, SSM/I and SSMIS and spans the period from 1979 to present. Here, SIE is defined as the cumulative area of grid cells with at least 15% sea-ice concentration. Two time series of daily SIE for the full time period from 1979 to 2019 were computed, one for the entire Arctic and one for a region around the Svalbard archipelago, termed the Svalbard-Barents Sea region, defined as 0–40°E and 72–85°N (grey outline in Figures 4.1.1c and 4.1.2). For each SIE time series, the climatological median and percentiles was estimated for the reference period 1981–2020. In the following, we use the term normal when the sea ice variable (to a large degree) was within the 25/75 percentile of its climatological median.

The monthly sea-ice thickness (SITh) CDR is based on radar altimeter measurements in the winter months of October through April from Envisat between 2002–2010 and CryoSat-2 (Laxon et al. 2013) since November 2010 (provided by Copernicus Climate Change Service (C3S), products 4.1.3 and 4.1.4). In this study, we only used data from the ESA CryoSat-2 mission since the orbit inclination of Envisat allowed only observation up to 81.5°N and does not cover the whole study region. The maximum latitude of CryoSat-2 data is 88°N and thus provides nearly full coverage of the European Arctic within a monthly period. With the CryoSat-2 data, we computed the SITh anomaly from October 2018 through April 2019. The SITh anomaly of one month was defined as the deviation from the mean thickness of all previous corresponding months in the CryoSat-2 data record. The mean fields were based on eight gridded fields from 2010–2017, except October which was based on seven October months, from 2011–2017. The SITh anomaly results (Figure 4.1.2) do not constitute the anomaly from a long-term trend as the SITh data record is comparatively short, but nonetheless indicated the events that led to a significant change in SITh within a few years.

The daily sea-ice drift product (SID, product 4.1.1) is based on passive microwave and scatterometer measurements and is produced operationally by OSI SAF (Lavergne et al. 2010). In this analysis, the monthly averages of SID fields for 2019 are presented (Figure 4.1.3). Similar to SITh, the SID monthly anomalies were calculated as the deviation of the monthly drift vector from the average of the same month in the eight previous years. The monthly divergence fields were computed from the SID in order to see where ice may have accumulated or disappeared due to dynamics. The divergence calculations were carried out on the daily data and averaged by month to prevent unrealistic values along the ice edge which moves a lot during a month. Finally, the daily sea-ice type CDR (product 4.1.5), based on passive microwave data, was averaged by months for comparison with the monthly SITh product. The ice type divides the sea ice into either being classified as multiyear ice (MYI, here defined as sea ice that has survived at least one summer melt) or as first-year ice (FYI).

Ocean heat and freshwater contents were estimated from an extensive set of *in situ* Conductivity-Temperature-Depth (CTD) profiles from ocean monitoring in August and September each year from 1970–2018 (product 4.1.6). Following Lind et al. (2018), temperature and salinity data were interpolated horizontally at every fifth metres depth from the surface to 250 m depth at a 25×25 km horizontal resolution. Ocean heat and freshwater contents were estimated in each grid cell and vertical level and integrated over the upper 100 m. Time series and spatial mean vertical profiles were estimated in a region northeast of Svalbard, termed northeast Svalbard area (black outline in Figure 4.1.1(c)) which is characterised as cold, stratified, sea-ice covered and impacted by sea-ice inflows, to see how the inflows in 2019 impacted the ocean. The data coverage was poor and sporadic prior to 1999 and we therefore used the data field for 1999 as a reference field for the oceanic conditions before the larger warming period started in the 2000s (Figure 4.1.1(c); Lind et al. 2018). In 2019, annual monitoring was restricted by the presence of sea ice. We therefore used CTD profiles from the ice-going vessel FF Kronprins Haakon in August 2019 (product 4.1.7) to estimate the heat and freshwater contents and the mean salinity profile of the region in 2019 (CTD-profiles are shown as black circles in Figure 4.1.1(c)). We

Table 4.1.1. Mean sea-ice thickness and thickness anomaly in the context of the range of thickness variability for the Svalbard-Barents Sea region (domain from 0°E to 40°E and 72° N to 85°N). All values indicate the mean of the ice-covered fraction of the region of interest. The two last columns represent the winters 2010/2011–2017/2018. In bold, is indicated monthly record-high ice thickness within the CryoSat-2 data record period.

Month	SITh 2018/2019 (m)	SITh Anomaly (m)	Previous SITh Minimum Thickness (m)	Previous SITh Maximum Thickness (m)
October	**1.76**	0.21	1.25	1.74
November	1.99	0.05	1.39	2.34
December	1.99	0.05	1.27	2.52
January	1.83	0.15	1.34	2.39
February	2.14	0.20	1.25	2.60
March	2.35	0.24	1.59	2.71
April	**2.47**	0.35	1.68	2.41

focused on how the freshwater content and ocean stratification had changed concurrently with the sea-ice inflows in 2019 and did not attempt a full quantitative analysis of all variables impacting the region, e.g. changes in heat imported with Atlantic Water or surface heat loss.

4.1.3. Results

While the Arctic Ocean SIE was among the lowest three on record from April–November 2019, the Svalbard-Barents Sea region jumped back to normal SIE levels – fluctuating around the 1981–2010-median within the 25/75 percentiles from March to December – which was surprising after several months with record low SIE in the region in the previous year, 2018 (Figure 4.1.1(a,b)). The sea-ice cover here is highly varying and in the northeast Svalbard area, the September minimum condition ranges from the area being fully sea ice-covered to it being completely sea-ice free in some years, including in 2018 (Figure 4.1.1(c), contours). The ocean heat content in the upper 100 m in this region is varying spatially, with a separation between the warmer Atlantic part, where Atlantic Water occupies the whole water column, and the colder Arctic part where fresher and colder Arctic water masses dominate the upper ocean (Figure 4.1.1(c)). The heat content in the northeast Svalbard area, observed at the end of summer in August–September, shows high interannual variability but has been increasing during the 2000s (Figure 4.1.1(d)). It was record high in 2018 but in 2019 it was down at a level comparable with the earlier years in the record (Figure 4.1.1(d)). The ocean stratification has generally been strong but was weakening during the 2000s (cf. Lind et al. 2018) and was record weak in August–September 2018, with surface salinities above 34.3 psu (Figure 4.1.1(e)). In August–September 2019, after the large sea-ice inflows and summer melting, the salinity had declined in the surface and Arctic water layers down to 100 m depth, but the salinity was still higher than that in 2010 down to 200 m depth (Figure 4.1.1(e)). The ocean freshwater content in the upper 100 m has shown declining values since 2010, where 2010 was the latest year with >3 m of freshwater. In autumn 2018, it was reduced to half, <1.5 m, and was record low (Figure 4.1.1(f)). During the following year, the freshwater content increased again to 2.5 m in August–September 2019.

The thickest sea ice is located north of Greenland. During October 2018–April 2019, the area of thicker ice was extending towards east and southeast following the ice-edge expansion (Figure 4.1.2, left column). This resulted in thick ice reaching the Svalbard Archipelago and Franz-Josef Land in March–April 2019. The thickness distribution in winter 2018/2019 was remarkably different from the previous eight winters (Figure 4.1.2, right column). Positive SITh anomalies north of Svalbard and Franz-Josef Land developed already in December–January and persisted through the rest of the winter, and significantly high SITh anomalies encapsulated north and east Svalbard in March–April. On the other side, at the Fram Strait, the sea ice was anomalously thin, especially from January onwards (Figure 4.1.2, right column).

The sea ice drift had all winter 2018/2019 a dominating direction toward southeast (Figure 4.1.3, left column). According to the drift anomalies (Figure 4.1.3, right column) the southeastward drifting this winter was stronger than the previous eight winters, especially in December–February, which coincided with the build-up of a positive thickness anomaly north of Svalbard and a negative thickness anomaly in the Fram Strait (Figure 4.1.2, right column). The prominent southeastward ice drift caused a strong net convergence of sea ice north of Svalbard from December onwards (seen as the red pixels just north of Svalbard in Figure 4.1.3, left column), and from January onwards the net convergence continued across from Svalbard to north of Franz-Josef Land.

The monthly sea-ice type fields are shown in Figure 4.1.3 (right column, grey colour scale), where the dark grey areas are sea ice classified as MYI throughout the month, and the light grey areas are a mixture of both FYI and MYI. Pure FYI (and open water) is here colourless. Comparing thickness in Figure 4.1.2 (left column) with the ice types in Figure 4.1.3 shows that areas with thick sea ice correspond well with areas with older ice. However, the thick sea ice that reached Svalbard in late winter was a mixture of FYI and MYI. In March and April, the thickness differences between the regions with FYI and MYI became less distinct due to faster thermodynamic ice growth of the thinner FYI.

The mean sea-ice thickness, averaged over the Svalbard-Barents Sea region (outlined in Figure 4.1.2), increased from 1.76 m in October 2018 to a maximum of 2.47 m reached in April 2019 (see Table 4.1.1, second-column). Between October and April, the mean thickness showed large variability including a period with apparent decrease of mean sea-ice thickness between November (1.99 m) to January (1.83 m). The decrease may be assigned to diverging sea-ice motion leading both to an expanding ice extent and an increasing fraction of the newer and thinner FYI. The mean thickness anomaly (Table 4.1.1, third-column) within the Svalbard-Barents Sea region is characterised by generally positive values, with values in October 2018 and

April 2019 exceeding the previous maximum thickness in the CryoSat-2 data record (see Table 4.1.1).

4.1.4. Discussion

An unusual circulation pattern brought thick and old sea ice across the Arctic Basin to the Atlantic sector in the winter of 2018/2019 that, together with persistent northerly winds in 2019 led to unusually large sea-ice inflows to the Svalbard-Barents Sea region (Figures 4.1.2 and 4.1.3). This caused a persistent sea-ice cover in large parts of the region throughout 2019, that did not melt completely during the summer but was instead continuously refilled with sea ice. In all, this sudden recovery of the local sea-ice coverage resulted in surprisingly normal sea ice conditions near climatological levels for 1981–2010 after several record lows during the 2010s. This is in contrast to the low sea-ice extent across the Arctic as a whole, reaching the third lowest extent on record in September 2019.

The observations (Figures 4.1.2 and 4.1.3) indicate that the anomalously thick sea-ice cover, stretching from north of Svalbard to north of Franz-Josef Land, was likely a result of unusually strong eastward and southward drift, piling more and thicker sea ice up in this region than usual. This is in accordance with the observed anomalously thin sea ice in the Fram Strait from January onwards, as the strong eastwards drift in December 2018 swept much of the thicker and older sea ice into the Svalbard-Barents Sea region.

In addition, a combination of sea-ice remote sensing products indicates that these advection events were associated with significant sea-ice deformation, leading to a localised dynamic sea-ice growth. Here, this is demonstrated by a colocation of ice convergence (Figure 4.1.3) in the sea-ice drift data and positive sea-ice thickness anomalies observed by CryoSat-2 (Figure 4.1.2). Sea-ice type classification maps indicate increasingly ambiguous sea-ice types in regions with the positive sea-ice thickness anomalies. This is consistent with ice deformation processes leading to generally thicker sea ice but also ice formation in fracturing ice floes. This thicker sea-ice regime resulting from ice dynamics may therefore have been a side effect of the unusual circulation pattern that increased the likelihood of survival in the summer season.

The increase of one metre freshwater content from 2018 to 2019 is the strongest on record during a single year (Figure 4.1.1(f)). With this exceptional freshwater input, the ocean stratification recovered in the upper part of the water column (Figure 4.1.1(e), compare red and blue profiles). This exceptional event concurred with the large inflows of thick sea ice, resulting in the anomalous thick sea-ice cover in winter 2018/2019. The seasonal surface layer with fresher water is typically produced during summer from melt water (Loeng, 1991). It is therefore reasonable to assume that most of the freshwater input likely came from sea ice-melt in summer 2019, after the large sea-ice inflows in winter 2018/2019. This supports that melt water from sea-ice inflows is an important freshwater input that sustains the ocean stratification, in line with Aagaard and Woodgate (2001), Ellingsen et al. (2009) and Lind et al. (2018). It is also in line with the concurrent decrease in heat content (Figure 4.1.1(d)), as heat may have largely gone to melting sea ice instead of warming the upper ocean in summer. However, it is not known if advection of fresher water masses in the upper ocean may also have contributed to the freshwater content increase. The flow of Atlantic Water, eastward along the continental shelf-slope north of Svalbard and the Barents Sea brings in saltier water (e.g. Rudels et al. 2004) and is not a candidate for freshwater input although the heat may contribute to melting sea ice (Renner et al. 2018). This is also in line with Lundesgaard et al. (2021), showing that sea-ice inflows and not Atlantic Water flow is the dominant driver of interannual changes in sea-ice concentration at this location.

A weak stratification implies the water column is more prone to vertical mixing, leading to increased heat fluxes between the different layers in the water column, bringing heat up from the deeper Atlantic layer and preventing sea-ice formation (Lind et al. 2016, 2018). Therefore, the added freshwater from the large sea-ice inflows in 2019 have acted towards making the conditions more favourable for a normal sea-ice coverage with local sea-ice production in winter and less sea-ice melt in summer. This implies that the large sea-ice inflows may have stabilised the local ocean conditions towards a more resilient Arctic type water column, and with the freshwater reservoir now rebuilt, it may take a few years before it gets eroded. However, how the next few years will play out will depend on the sea-ice inflows in the coming years as well as other driving factors, such as surface air temperature and heat fluxes, Atlantic Water inflow, wind directions, storm intrusions, and more (e.g. Smedsrud et al. 2013; Lind et al. 2018; Wickström et al. 2020).

4.1.5. Conclusion

We conclude that the anomalous patterns of sea-ice drift in the Arctic Ocean and the sea-ice inflows toward Svalbard was likely a key factor explaining the recovery of the sea-ice cover and ocean conditions in the Svalbard-Barents Sea region in 2019. The event during

the winter 2018/2019, of persistent, large sea-ice inflows of thick and old ice to the region has contributed to a large freshwater input to the ocean column in summer 2019. This acted towards restoring an Arctic-type ocean climate in the Svalbard-Barents Sea region with a higher ocean freshwater content and a stronger ocean stratification, in line with long-term investigations of the northern Barents Sea during 1970–2016 (Lind et al. 2018). A stronger ocean stratification increases the density differences between the surface, Arctic and Atlantic layers and prevents vertical mixing. This reduces vertical heat fluxes and acts to restore and maintain a cold, stratified and sea-ice covered ocean climate (Lind et al. 2018). Vertical mixing acts to weaken the ocean stratification, bringing salt up to the upper ocean, and freshwater down. Freshwater input is therefore needed to maintain the stratification, and thus maintain conditions suitable for sea ice (Lind et al. 2016). Our findings therefore support that sea-ice inflows play a key role in the Arctic climate system, in keeping outer regions of the Arctic Ocean stratified and sea-ice covered. This driver may become increasingly stochastic, with a higher interannual variability as the Arctic transitions to having a less compact, thinner and more movable sea ice cover. Thus, sea-ice inflows can be expected to cause strong perturbations in parts of the Arctic Ocean in the coming years, despite the general decreasing trends of the Arctic sea-ice cover.

Acknowledgements

The work by SL was partly funded by the Research Council of Norway through the project The Nansen Legacy (RCN # 276730).

Section 4.2: Monitoring storms by merged data sources for the Malta shelf area in 2019

Authors: Aldo Drago, Adam Gauci, Joel Azzopardi, Jorge Sanchez, Andrés Alonso-Martirena

Statement of main outcome: The merging of met-ocean datasets from diverse sources offers the possibility of making more complete assessments by considering more than one aspect of the same process or situation, and hence rendering a more robust and consistent approach. This is especially the case in studies of extreme events where the reliability of observing systems or numerical simulations to measure and replicate harsh atmospheric and sea conditions are pushed to their extreme limits of performance. Such augmented assessments thus rely on data from model ensembles and complementing observing platforms, including from satellite platforms, to measure the same meteo-marine event from different points of view and realisations. This approach is used to anticipate the occurrence of such extreme events, to monitor their evolution in real time, and to post-assess in more detail their dynamics and impact in the Malta shelf area, coastal sea, and nearshore zones. Products from the COPERNICUS Marine Environment and Monitoring Service (CMEMS) provide the core data which are added to data derived from national systems run at the University of Malta by the Physical Oceanography Research Group and published on the dedicated portal www.capemalta.net. This includes the CALYPSO HF radar network and local scale models, providing an exhaustive description of two extreme weather events in February and December 2019 respectively. The use of multiple datasets renders reliable assessments through data redundancy and inter-relation, and further presents the opportunity to provide alerts and a first-hand real

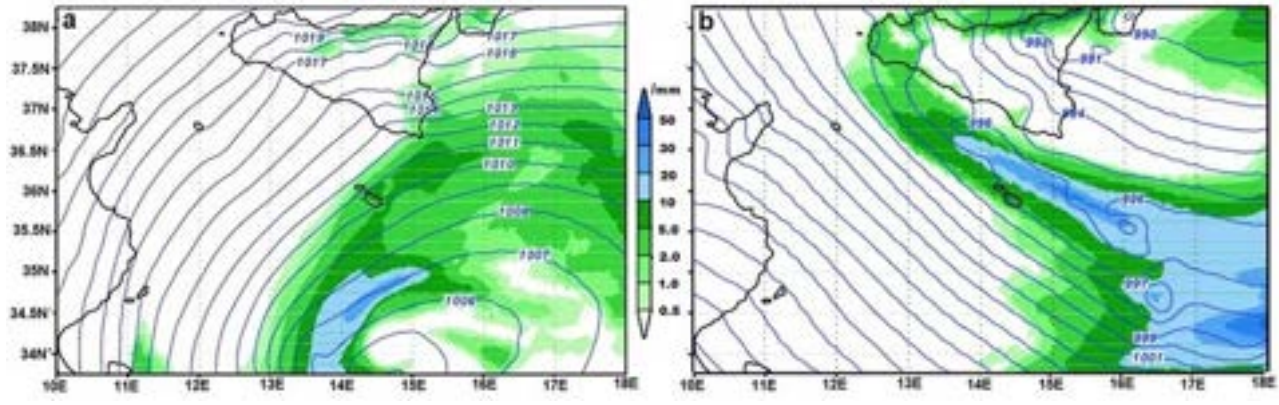

Figure 4.2.1. Synoptic conditions and precipitation (in mm over 3 h) predicted for (a) 4 am on 24 February 2019, and (b) 1 am on 14 December 2019, in the Central Mediterranean. Time in GMT +1. Isolines show curves joining points of equal atmospheric pressure in millibars. Precipitation in mm represents accumulated values over 3 h. Product 4.2.6 with data elaboration from the MARIA/eta model run by the Physical Oceanography Research Group, University of Malta.

time description of evolving meteo-marine harsh conditions to aid security, and to subsequently enable more detailed retrospect analysis successive to the event.

CMEMS products used

Ref. No.	Product name and type	Documentation
4.2.1	WIND_GLO_WIND_L4_NRT_OBSERVATIONS_012_004 Global ocean near-real-time 6-hourly L4 gridded sea surface winds from scatterometer and collocated ECMWF operational model forecast	PUM: http://marine.copernicus.eu/documents/PUM/CMEMS-OSI-PUM-012-004.pdf QUID: http://marine.copernicus.eu/documents/QUID/CMEMS-OSI-QUID-012-004.pdf
4.2.2	MEDSEA_ANALYSIS_FORECAST_PHY_006_013 Hourly sea surface currents from Mediterranean Sea analysis and forecast model	PUM: http://resources.marine.copernicus.eu/documents/PUM/CMEMS-MED-PUM-006-013.pdf QUID: http://resources.marine.copernicus.eu/documents/QUID/CMEMS-MED-QUID-006-013.pdf
4.2.3	GLOBAL Ocean Sea Physical Analysis and Forecasting Products GLOBAL_ANALYSIS_FORECAST_PHY_001_024	PUM: https://resources.marine.copernicus.eu/documents/PUM/CMEMS-GLO-PUM-001-024.pdf QUID: http://marine.copernicus.eu/documents/PUM/CMEMS-GLO-QUID001-024.pdf
4.2.4	Mediterranean Sea Wave Spectra.	This is a product which is not yet available on the CMEMS official portal. It is downloaded via ftp from medmfc.hcmr.gr and contains hourly analysis and 3-hourly forecast wave spectra for the whole Mediterranean Sea model domain in netcdf format. For each grid cell at each time step, it provides spectra for 24 directions over 32 different frequencies.
4.2.5	Sea surface currents and waves from the CALYPSO HF radar network (non-CMEMS product)	https://www.capemalta.net/calypso
4.2.6	MARIA/eta atmospheric forecasting model (non-CMEMS product)	http://oceania.research.um.edu.mt:8080/CalypsoService/atmospheric.html
4.2.7	SWAN coastal wave model for the Maltese Islands (non-CMEMS product)	http://oceania.research.um.edu.mt:8080/CalypsoService/waves.html
4.2.8	MARIA WAM regional wave model for the Sicilian Channel (non-CMEMS product)	http://www.capemalta.net/maria/pages/waveforecast.html
4.2.9	ROSARIO 96 HD forecasting system (non-CMEMS product)	http://www.capemalta.net/MFSTEP/results0.html

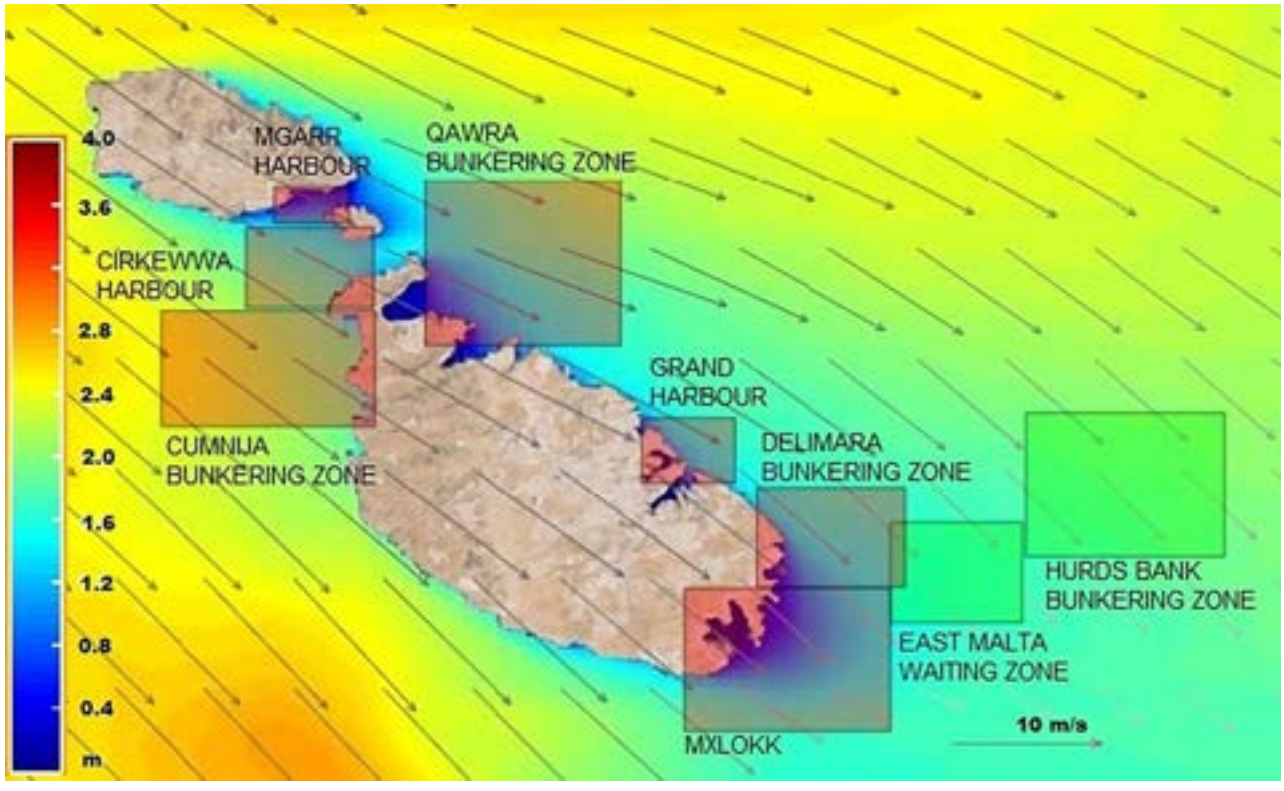

Figure 4.2.2. Marine sub-domains used to provide a multi-area early warning alert system for the Maltese Islands, covering the near-shore, coastal and open sea scales. Vectors show the wind in m s^{-1} from product 4.2.6, verified against product 4.2.1. The background map shows significant wave height in m from product 4.2.7 nested to product 4.2.4.

4.2.1. Introduction

Storm impacts cannot always be avoided by staying away from the highly impacted dangerous areas. Indeed, the anticipation and real time evolution of extreme meteo-marine conditions provided by reliable numerical modelling predictions and multi-platform observations are essential to mitigate risks, increase safety, avoid exposure and provide protection to essential assets. The monitoring of the spatial and temporal evolution of storms is crucial to provide an information service to responsible emergency entities like coastguards and civil protection units which might need to intervene even under harsh weather and sea conditions. In such circumstances, accurate nowcasts and short-term predictions are essential to prepare interventions that are timely, effective and with minimal risk. This kind of service is also essential to provide information and guidance for safer navigation by circumventing the higher impacted sea areas or delaying transits.

This approach was experimented with users during two major storms hitting the Maltese Islands in 2019 as shown by the synoptic maps in Figure 4.2.1. The first in the night between 23rd and 24th February was triggered by a depression over the Ionian Sea, southeast of Malta, and brought gregale winds (a strong cold northeast wind of the central Mediterranean) and high waves hitting the northern coasts of the islands. The second storm was also strong, occurring in the night between 13th and 14th December in relation to a strong depression on the Adriatic Sea leading to steep atmospheric pressure gradients over the Central Mediterranean area and north-westerly gale winds in the open sea areas. These two events presented an opportunity to put in practice the available observational and modelling data resources to predict, monitor, and assess extreme meteo-marine conditions, to verify the evolution of the storms in real time, and to provide improved services to users such as for civil protection, marine safety, and risks to essential assets.

These two experiences also served to distinguish the diverse evolution and impacts triggered on coastal assets and property, hindering operators in their activities. The first storm impacted head-on the northeast low-lying coast with devastating damages on this highly populated stretch of coast especially in Malta; the second storm hit mainly the western and southern coast of the Maltese Islands, with strong waves exhausting their energy against the high standing cliffs and this relatively uninhabited stretch of coast, otherwise the consequences would have been much worse.

In this work the use of *in-situ* and remotely sensed observations are combined with regional and coastal scale numerical model simulations. This includes HF radar data from the CALYPSO network and the operational oceanography services provided by the Physical Oceanography Research Group (ex PO-Unit) of the University of Malta. These services provide a showcase example of merged datasets derived from CMEMS in combination with that generated locally from the national system.

Operational services earmarked to benefit users and stakeholders need to be effective, reliable, and timely. Real time data acquisition, validation, elaboration and delivery is an evolving challenge that is growing with user needs (Tintoré et al. 2019). In the particular example of the monitoring of storms, their incidence and impacts do not reach locations over an extended area at the same time and with the same intensity. A multi-area monitoring and alerting approach (Bartzokas et al. 2010) is therefore needed such as that shown in Figure 4.2.2 where the service is provided not only over the larger domain covering the overall synoptic evolution of the event, but also over dedicated sub-domains in user sensitive areas to resolve the spatial and temporal development of the storm with quantitative assessments on the intensity and impacts of the storm. This permits higher focus on selected sub-areas at key locations where more precise data is required to protect coastal structures and resources, or to better manage operations like bunkering and marine transportation (Villa et al. 2008). This approach therefore provides useful information on the scale required by users at specific locations where reliable forecasted impacts are required ahead of a meteorological extreme event, and flows of real time information are required to better handle operations during the same event.

4.2.2. Data and methods

The two storms hitting the Maltese Islands in 2019 served to showcase how the integration of real time data from earth observations, *in situ* measurements and numerical models can provide augmented assessments on the evolution of extreme events in nowcast, prediction and re-analysis modes. Data ensembles composed of numerical models and observations at regional, coastal scale, and nearshore resolutions, come from various sources, with the merging of core data deriving from CMEMS for the broader scale, and the national observation and forecasting system for the finer scale. The observation data sources include meteorological stations, sea level stations, and high-tech data acquisition systems including

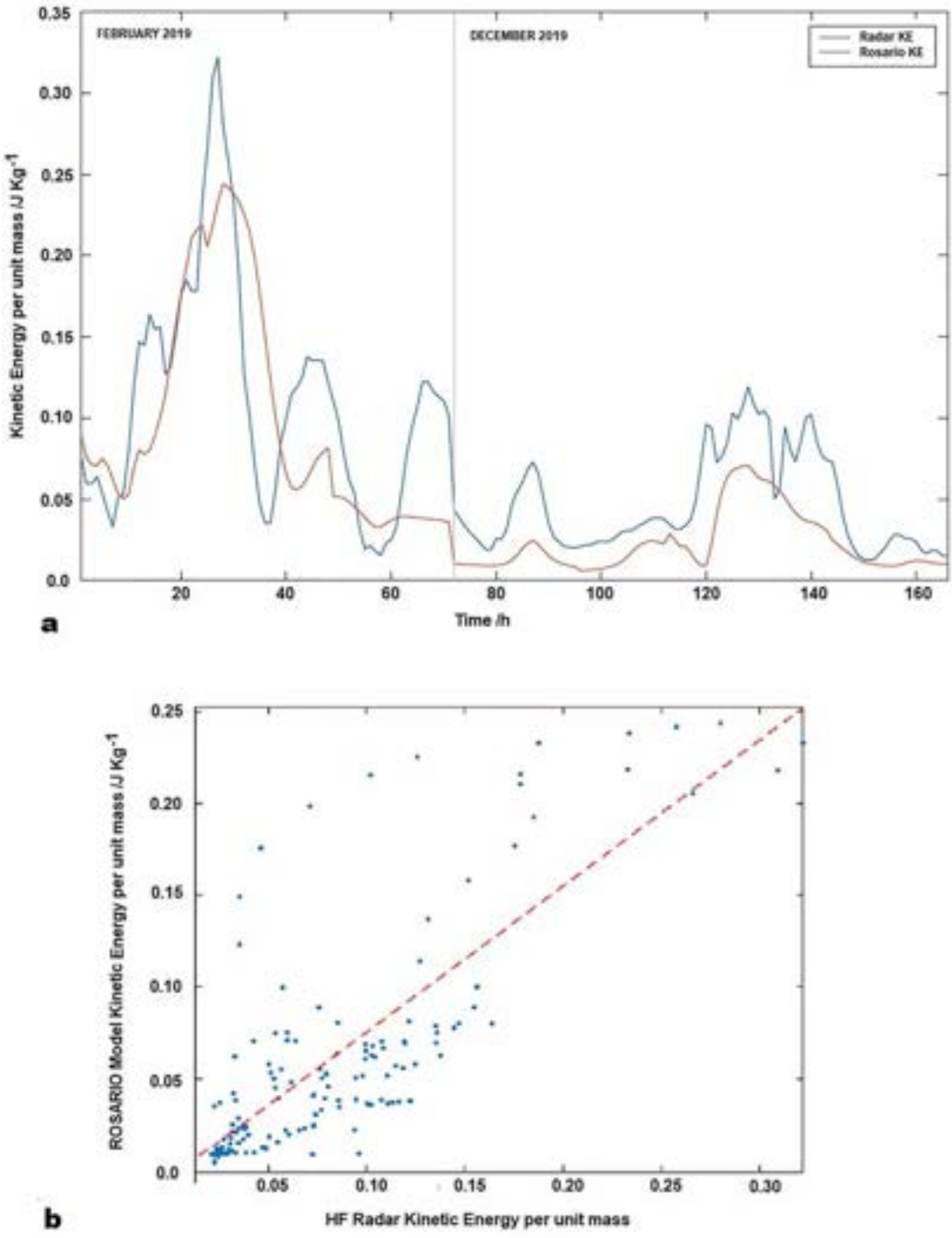

Figure 4.2.3. (a) Joint time series of area averaged surface kinetic energy per unit mass over the HF radar coverage during the two storms. Blue is for hourly HF radar measurements; Red is for 3 h averaged surface currents in the equivalent spatial bins from the ROSARIO hydrodynamic model. Products 4.2.5 and 4.2.9. (b) Scatter plot comparing HFR surface current kinetic energy per unit mass against model data from the ROSARIO Malta shelf forecasting system. Blue dots refer to data points; red dashed line gives the best linear fit. Correlation coefficient = 0.81; RMSD = 0.043. Products 4.2.5 and 4.2.9.

earth observations and the use of remote sensing coastal platforms like the HF radars belonging to the CALYPSO network which provides mostly uninterrupted real time synoptic data on sea surface currents and waves over large sea domains even in extreme conditions. The COPERNICUS data used are the CERSAT Global Blended Mean Wind Fields at $1/4^0$ resolution, the modelled sea surface currents fields from the operational Mercator global ocean forecast system at $1/12^0$, and the Mediterranean Forecasting Physical System (MedFS) at $1/24^0$ resolution. Sources of the local forecasts are the Maria/Eta weather

prediction model, the ROSARIO Malta shelf thermo-hydrodynamic forecasting system, and the local WAM and SWAN models for the Central Mediterranean and Maltese coastal areas respectively.

The CALYPSO HF radar network (Drago et al. 2013, 2015), consisting of four CODAR SeaSonde transmitters, offers a solution to provide real time observations of sea surface currents and waves even in harsh meteo-marine conditions when observations can only be made available by remote sensing techniques. In this case, the HF radars cover 6700 km^2 in the stretch of sea between the Maltese Islands and the southern coast of Sicily, with a spatial resolution of 2.5 km, providing data every hour for currents, and every 10 min for waves. Through the Italia-Malta Interreg VA CALYPSO South project, this HF radar system is being upgraded by an additional radar unit to be installed on the southern coast of Sicily and extending coverage further west, and two other new units on the southern coast of Malta and Gozo to provide data on the southern approaches to the Maltese Islands.

HF radar systems have been demonstrated to be a sound remote sensing tool to retrieve sea surface current fields and wave information (Pascual et al. 2015; Fernandes et al. 2018; Lorente et al. 2018; Orasi et al. 2018; Lopez and Conley 2019). Reyes et al. (2019) merge the CALYPSO HF radar data with satellite observations to further characterise the mesoscale variability in the Malta-Sicily Channel. Overall, these results prove that a synergistic observational and modelling approach can provide a comprehensive characterisation of severe wave conditions in coastal areas, exploiting the benefits from the complementarity of both systems. Ongoing research is devoted to the analysis and enhancement of HF radar-derived wave estimations, and the subsequent application to extreme weather events and maritime safety. Similar research efforts connected to HF radars and wave models are also ongoing along the US East Coast (Roarty et al. 2019).

However, data coming from different sources, observation platforms and models needs to follow some essential protocols before qualifying for merging. Besides the intrinsic QC checks on the individual datasets, such as for the detection and filtering of anomalous values, the data need also to be cross- validated through consistency checks to ensure the compatibility across the available datasets. This check is done across pairs of data with common parameters, and using correlation metrics to quantify the level of agreement before merging the chosen datasets in the integrated analysis. As an example, the surface kinetic energy per unit mass is used to compare the sea current fields derived from the CALYPSO HF radar with those generated by models. Figure 4.2.3(a,b) shows the correlation of the radar observations with the ROSARIO model data by taking into account the data intrinsic to the individual events as well as by considering the events in combination so that the matching can be ascertained to the general expected levels. The matching made in this case is done by taking area averages over grid points with common data values from both the radar and the model domains. In the case of model and HF radar currents the correlations reach the order of 0.8 with RMSD of 0.043 as shown in Figure 4.2.3(b). The performance of HF radars in measuring surface currents has been amply assessed in the literature (Chapman et al. 1997; Emery et al. 2004; Cosoli et al. 2013; Capodici et al. 2019), specifically compare CALYPSO data against surface drifter and near-surface Acoustic Doppler Current Profiler observations, and show that at the HF radar

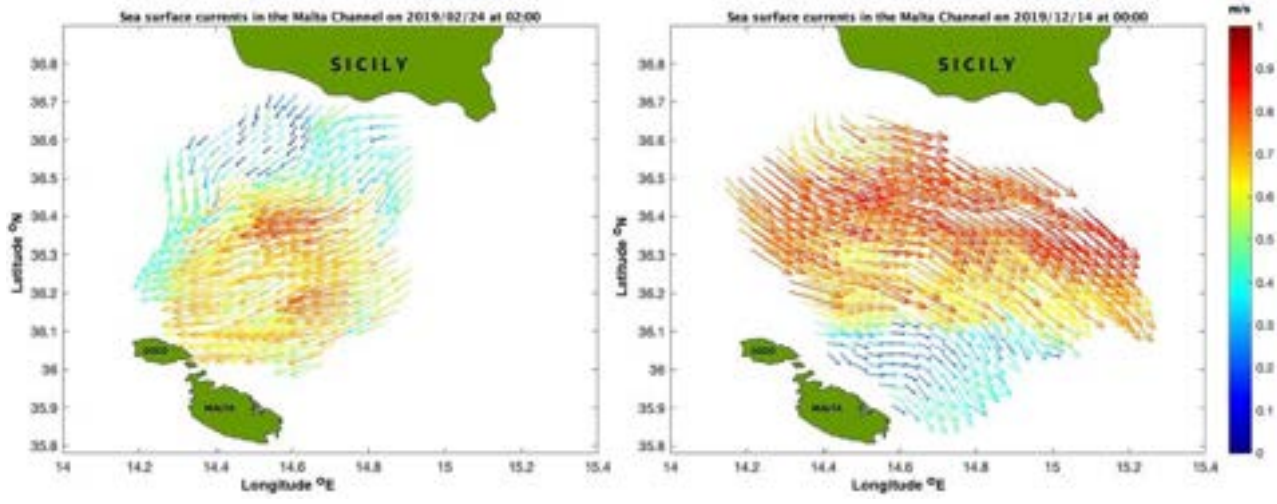

Figure 4.2.4. HF radar Eulerian maps for sea surface currents in the Malta-Sicily Channel during two storms in 2019. Product 4.2.5.

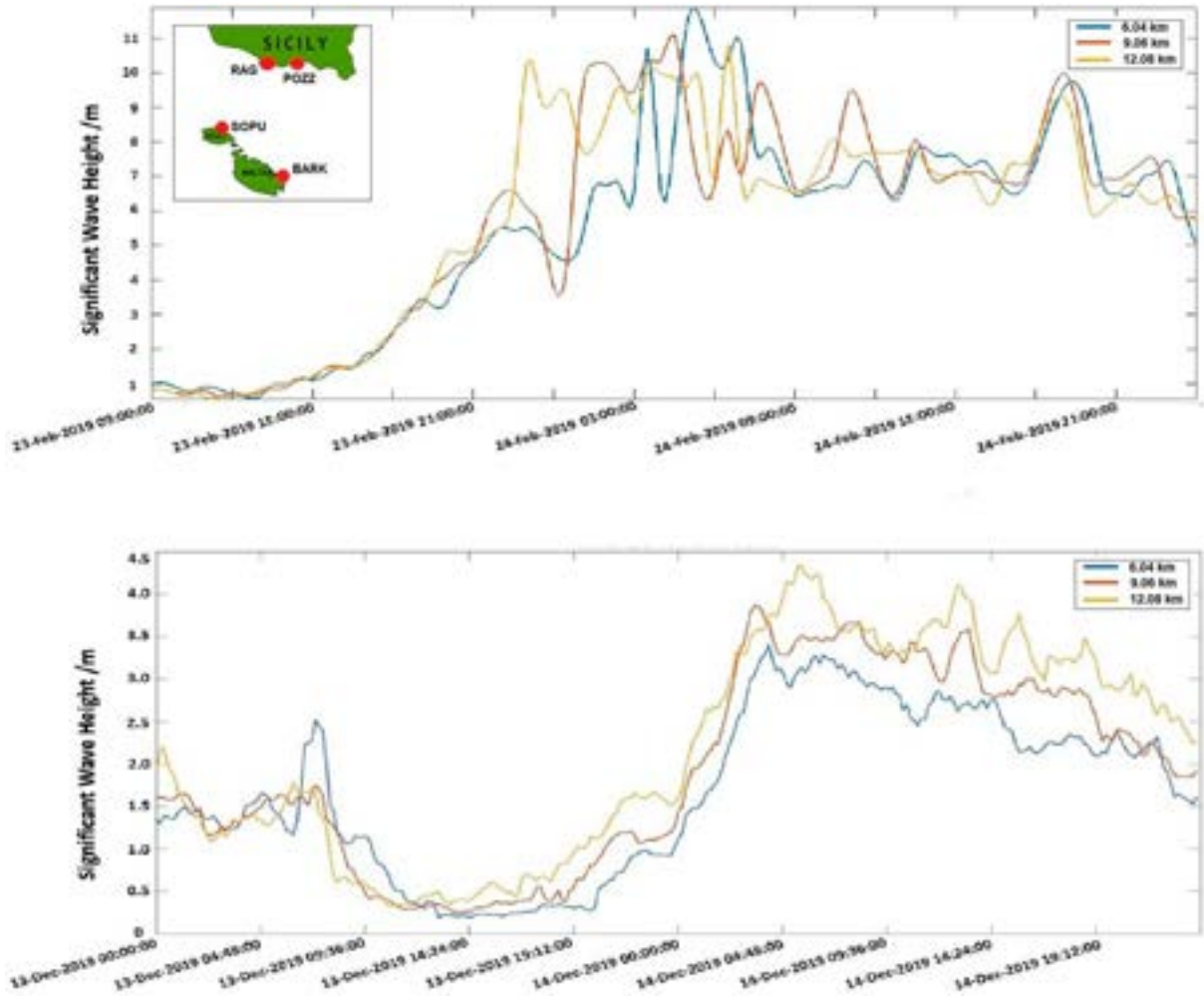

Figure 4.2.5. Time series of significant wave height (averaged in time and space) measured by the BARKAT HF radar station at three annular distances from shore for the February storm (upper panel) and the December storm (lower panel). Product 4.2.5. Insert shows the position of the four CALYPSO HF radars.

frequency used (13.5 MHz) the consistency of the measurements is in some aspects superior to that from systems in other regions. With respect to the ROSARIO model, the radar currents tend to be consistently higher in size, but the matching in the time evolution and scale of variability is adequate. It must be recognised that the model currents are 3-hourly averages whereas the radars provide hourly values; there is furthermore the aspect of how the models handle the air–sea interaction and fluxes, and this may not necessarily perform equally well in extreme meteo-marine conditions. Yet the use of multiple data is still adequate as long as such differences are quantifiable and taken into account.

4.2.3. Results

Data from multiple sources during two major storms hitting the Maltese Islands in 2019 were used operationally, and subsequently in delayed mode, to assess the development, evolution and impact of these extreme events, serving as a prototype exercise to develop a real time system providing essential information to stakeholders in real time on the coast and at sea during such extreme meteo-marine conditions.

The intensification of the first storm started in the evening of 23rd February, gathering its full impact during that same night and persisting at extreme intensities for most of the day on 24th February. The animations of the wind fields and of the atmospheric pressure and precipitation fields show clearly the temporal evolution and severity of the storm which persisted at high intensity for a long spell. The storm was generated by a low pressure system which developed in the southeast of the Maltese Islands, carrying an intense cyclonic circulation that caused gregale (NE) gale winds to impact the northern shores of the Maltese Islands. The trigger was the compulsion of a very warm and humid flow

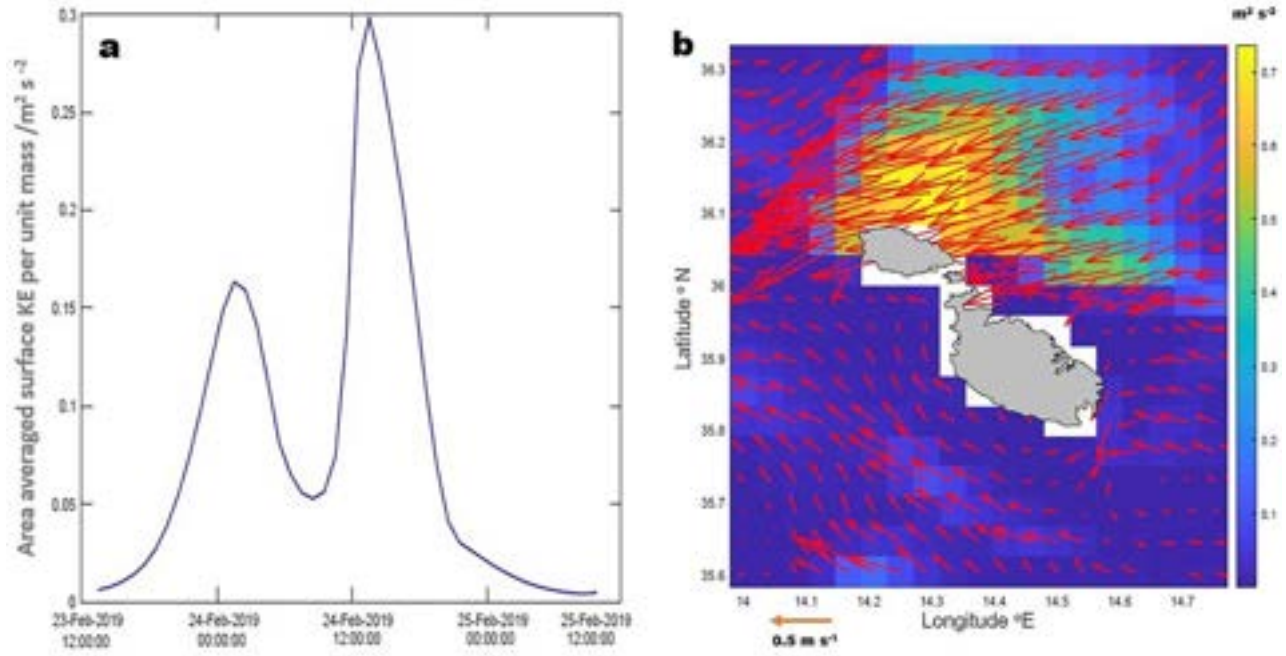

Figure 4.2.6. (a) Time evolution of the total surface kinetic energy per unit mass for the Qawra Bunkering zone area during the February 2019 storm, and (b) Model detail of sea surface currents (red vectors) and total kinetic energy in $m^2\ s^{-2}$ (background map) during the second peak of the storm. Products 4.2.2 and 4.2.9.

of air masses from the south, meeting frigid air from the north which penetrated into the central Mediterranean from over the Balkans. Figure 4.2.1 (left panel) shows a snapshot of the low pressure system as it evolved with strong pressure gradients, associated heavy rain patches including the Maltese Islands, and moved zonally along 34–34.5°N towards west. The associated wind fields reached average speeds of 28 ms^{-1} (~ 100 kph) blowing for long spells and with long fetch from the NE. The filtered sea level observations from an operational real time coastal station on the northern coast of Malta registered a storm surge of the order of 0.25 m on average, swiftly raising the mean sea level by this amount, and persisting with high water levels for about 12 h. Despite the modest size, such a surge has a great impact on raising sea level with respect to land, restraining storm water from draining into the sea and leading to severe flooding in low lying areas.

All the northern stretch of coast spanning from the western tip of Gozo down to the easternmost extremity of Malta were under the impact of very strong waves which quickly gained extreme values with significant wave heights exceeding 4 m inside the embayments. This means that during the storm the maximum wave heights near the shore before breaking were at least in the range of 4.5–6.75 m, and the peak waves theoretically reached up to 9 m. The wave model simulations showed that the total wave field (wind waves and swell) around the Maltese Islands reached significant wave heights of more than 10 m in the open sea areas at just about 1 km east of Malta. The waves with a peak period of 10 s reached their climax later during 24th February as the north-easterly wind persisted with gale force for more than 12 h along a fetch of up to around 300 km. The impact and inundation of the sea waves on land was even more severe as a result of the raised mean sea level during the storm. Direct observations of sea waves were available from the CALYPSO HF radars as shown in Figure 4.2.5 for Barkat station (upper panel). HF radars are able to register spatially averaged wave heights along annular rings at increasing distances offshore, permitting to follow the spatial evolution of the evolving wave field.

The CALYPSO HF radar observing system performed well during the storm and also registered very strong sea currents in excess of 90 cm s^{-1} (refer to Figure 4.2.4 left panel) which are exceptional in size for this marine domain where the circulation intensities are typically of the order of 45 cm s^{-1} or less. This kind of data show the usefulness of HF radars which can operate unattended even in harsh weather conditions, providing essential data when it is most needed, and giving spatial information on sea surface currents and waves over a domain spanning an area of about 6000 km^2. The combination of the numerical models and

the HF radars served to anticipate and provide alerts, and to give quantified information on sea currents and waves intensities as they evolved during the storm. The match between the HF radars and the CMEMS Med-MFC and ROSARIO model data was very effective. The HF radars complemented the models by providing a validation dataset, while the models were able to extend the data closer to the coast and to a wider coverage than that available by the HF radars. This analysis shows that the impact of the storm came in two blows, as evidenced by the sea surface kinetic energy per unit mass averaged over the Qawra Bunkering zone sub-area. The first blow impacted in the first hours of 24th February, followed by a second more intense blow about 12 h later (Figure 4.2.6). The first blow concerned a wider area of sea involving a large section of the Malta-Sicily Channel, the stretch of sea dividing the Maltese Islands from the southern Sicilian coast. The second blow was most intense in the Maltese northern coastal sea areas where the area averaged kinetic energy per unit mass reached up to 0.3 m^2 s^{-2}, this being approximately double that of the first blow. The most intense currents of the order of 0.85 m s^{-1} hit the northern coast of Gozo where the intensification of the currents was strongest.

The same approach and real time monitoring of meteo-marine conditions in the sea domain around the Maltese Islands and the Malta-Sicily Channel was adopted in the storm hitting the area in the night between Friday 13th and Saturday 14th December. A depression on the Adriatic Sea produced a steep atmospheric pressure gradient over the Central Mediterranean, leading to north-westerly gale winds with magnitudes up to 22 m s^{-1} (about 50 mph) in the open sea areas close to Malta and Sicily on Saturday morning. These extreme conditions were predicted and assessed by numerical atmospheric and wave models which verified the evolution of the storm, accompanied by torrential rain especially in the sea north of Malta, and by very high waves reaching a significant wave height of 7 m west of Gozo where the exposure to Mistral wind was conspicuous. Such extreme wind and wave conditions are known to have a return period of the order of 10 years. These very adverse conditions started to attenuate on Saturday afternoon when the depression moved on to the Aegean Sea. The damages reported on land were considerable, but what was witnessed on land cannot be in any way compared to the force and vehemence experienced at sea. Luckily the western coast was hit this time, with waves exhausting their energy against the high standing cliffs and the relatively less populated stretch of coast of Malta and Gozo, otherwise the consequences would have been much worse.

This was the first time that a storm hitting the Maltese Islands could be followed in such detail, providing alerts as well as information during the actual evolution of the storms.

4.2.4. Conclusions and discussion

The two extreme events analysed in this work presented a great opportunity to assess the readiness and effectiveness of combining an ensemble of meteo-marine observations, numerical forecasting models from CMEMS and national models, and alerting tools available in the Malta shelf area to monitor, predict and assess extreme meteo-marine conditions. The results described in this work show the ability of the different sensors and numerical models to provide reliable meteo-marine information, and the very promising potential of the proposed multi-sensor and multi-model approach to assist national authorities with responsibility in civil protection, marine safety and protection of essential infrastructure and assets. Besides the surface current fields, the results confirm that CODAR HF radar wave data are a reliable source of information to also monitor significant wave height, conditions in quasi real-time for the Maltese shelf area.

Further work is needed to raise this work into a full operational service for extreme weather alerts and real time evolution. An important aspect regards the compatibility of the data sources by a cross-data assessment to check the consistency and matching between the available datasets. An ensemble data approach presents several challenges that are intrinsic to these kind of services relying on real time data merging. Ascertaining the individual quality of each data stream in operational mode is a major first step in the process, and performing this in real time requires QC techniques that rely only on previously acquired data values since data in forward time would not yet be available by operational data acquisition systems. In a second stage, it may be necessary to consider more than one option on how to combine the data in the most relevant manner, and this requires an intelligent system to optimise assessments in an automated mode.

Different additional efforts and research at Maltese, European and International levels are currently ongoing to further improve the usefulness of CODAR HF radar technology for the monitoring of extreme meteo-marine events focused among other topics on: (1) improving Quality Control (QC) of HF radar wave data and the

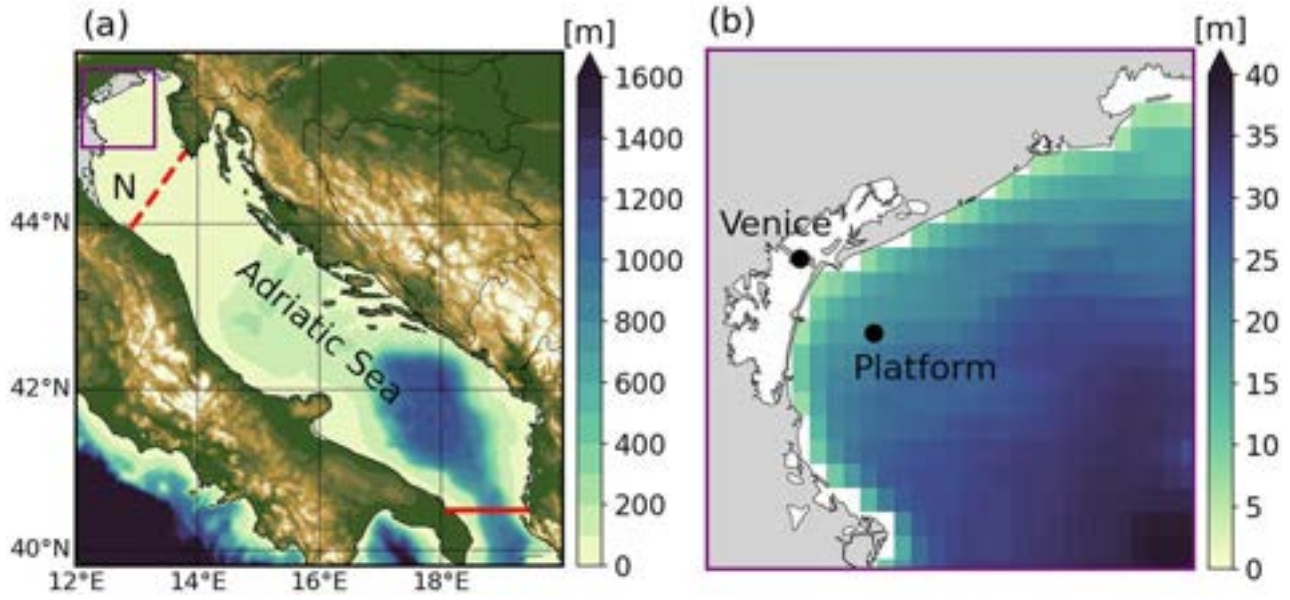

Figure 4.3.1. The MedFS regional ocean model bathymetry for (a) the Adriatic Sea region and (b) the northwestern Adriatic Sea. The solid and dashed red lines in (a) indicate the boundaries used for calculating average values over the Adriatic Sea and northern Adriatic Sea (N), respectively. The mountain ranges of the Apennines and Dinaric Alps are shown in light-brown colours (ETOPO1 1 Arc-Minute Global Relief Model). The location of Venice and the ISMAR Acqua Alta Platform are indicated with black dots in (b), note that the Venice lagoon is not part of the MedFS model domain.

estimation of HF radar wave measurement uncertainty in real-time, (2) improving HF radar wave extraction methods in order to provide differentiated wave data for wind and swell seas components, (3) further assessing and improving the capability of HF radars to provide reliable wave period and wave direction information under different meteo-marine conditions, and (4) using HF radar wave data for automatic and real-time validation and skill assessment of numerical wave models.

The way forward is that of enhancing and merging compatible and complimentary data from observation and modelling systems, aided by the support of artificial intelligence techniques that derive their performance on the basis of previous knowledge from a number of past extreme events which are expected to be repeated under similar forcing conditions in future events.

Section 4.3. The November 2019 record high water levels in Venice, Italy

Authors: Rianne Giesen, Emanuela Clementi, Marco Bajo, Ivan Federico, Ad Stoffelen, Rosalia Santoleri

Statement of main outcome The city of Venice in Italy experienced four exceptionally high tidal peaks in the week from 11 to 18 November 2019, flooding large parts of the city. Venice never suffered from four successive extreme events within one single week before. Our analysis based on a combined use of in situ, satellite and model data revealed that spring tides coincided with a very high mean November sea level during this week. Additionally and concurrent with the tidal maximum, strong Sirocco winds pushed Adriatic Sea water towards Venice during three of the four exceptional water level events. For the most extreme event on 12 November, a storm passed over Venice just at the time of the maximum tide. The official forecast underestimated maximum water levels for this event as the European Centre for Medium-range Weather Forecasts (ECMWF) atmospheric model did not resolve the local storm. Forecasts from a regional marine model included the high tidal peaks from at least two days in advance, although the maximum water level was underestimated. Higher-resolution atmospheric model fields and the use of satellite wind observations for nowcasting may further improve the water level forecasts in extreme conditions.

Products used

Ref. No.	Product name and type	Documentation
4.3.1	WIND_GLO_WIND_L3_NRT_OBSERVATIONS_012_002 Global ocean daily gridded sea surface winds from scatterometer and	PUM: http://marine.copernicus.eu/documents/PUM/CMEMS-WIND-PUM-

(*Continued*)

Continued.

Ref. No.	Product name and type	Documentation
	collocated ECMWF operational model forecast	012-002-005.pdf QUID: http://marine.copernicus.eu/documents/QUID/CMEMS-WIND-QUID-012-002-003-005.pdf
4.3.2	MEDSEA_ANALYSIS_FORECAST_PHY_006_013 Hourly sea surface height from Mediterranean Sea analysis and forecast model	PUM: http://resources.marine.copernicus.eu/documents/PUM/CMEMS-MED-PUM-006-013.pdf QUID: http://resources.marine.copernicus.eu/documents/QUID/CMEMS-MED-QUID-006-013.pdf
4.3.3	Astronomical tidal sea level evaluated using the OTPS tidal model implemented in the Mediterranean Sea (non-CMEMS product)	https://www.tpxo.net/otps
4.3.4	Sea level and meteorological observations at the ISMAR-CNR Acqua Alta Platform (non-CMEMS product)	https://www.comune.venezia.it/it/content/3-piattaforma-ismar-cnr
4.3.5	Wind speed from ECMWF Atmospheric high resolution forecast model at 1/8° horizontal resolution (non-CMEMS product)	https://www.ecmwf.int/en/forecasts/datasets/set-i

4.3.1. Introduction

The monumental city of Venice is situated in northern Italy, at the northern end of the shallow Adriatic Sea (Figure 4.3.1). Water levels in the Venice lagoon vary largely, primarily determined by the astronomical tide and the meteorological conditions. Venice often experiences flooding during so-called Acqua Alta (high water). Acqua Alta events mainly occur between autumn and spring, in conjunction with strong south-easterly winds. These warm Sirocco winds are transient winds that are often connected with depressions moving from west to east over the Mediterranean Sea (Orlić et al. 1994). The winds are channelled by the surrounding orography of the Adriatic basin, pushing the water towards the Venice lagoon (Figure 4.3.1(a); Pasarić et al. 2007). Exceptionally high water events are often caused by a superposition of favourable tidal and meteorological conditions, but sea surges of meteorological origin can also cause extensive flooding at low tides (Pirazzoli and Tomasin 2002). The latter was the case for the most extreme flooding event that occurred in 1966, when water levels rose to 1.94 m above the standard level (De Zolt et al. 2006).

Between 11 and 18 November 2019, Venice was confronted with exceptionally high tidal peaks on four out of the seven days, which was unprecedented. During these Acqua Alta events waters rose to more than 1.40 m above the standard level, flooding over 50% of the city. On the evening of 12 November, the maximum recorded water level in Venice was 1.89 m, the highest since the severe flooding event in 1966. Venetians were not prepared for the exceptional flooding since the water level for the 12 November high tide was underestimated by almost 0.4 m in the official forecast (The ISMAR Team et al. 2020).

In this section, we present in situ and remotely sensed observations, combined with atmospheric and regional ocean model forecasts. We explore the meteorological and tidal conditions in the period 11–18 November 2019, to understand the causes of the four Acqua Alta events, and to assess why the extreme water levels were underestimated in the model forecasts.

4.3.2. Data and methods

In situ observations of the temporal evolution of the water level and relevant meteorological variables near Venice were taken from the Institute of Marine Sciences (ISMAR) Acqua Alta Platform, which is located outside of the lagoon in the open sea (Figure 4.3.1(b), Cavaleri (2000)). Observations are available with a 10-minute temporal resolution, water level values are referred to the local datum.

The spatial and temporal variations in the wind field over the Adriatic Sea were analysed using surface wind vector observations from the Advanced SCATterometer (ASCAT) instrument on board the polar-orbiting satellite series Metop-A, Metop-B and Metop-C. Since the three Metop satellites have the same characteristics (Stoffelen et al. 2017) and local overpass times within 80 min, the three wind fields can be merged into one mosaic wind field at 0.125° horizontal resolution covering most of the study area. The scatterometers passed over the study area during the onset of the four Acqua Alta events. For grid points having observations from multiple scatterometers at an ascending or descending overpass, the observation with the latest timestamp was selected for the mosaic wind field. Although differences between the images are minimal, this ensures the conditions during the Acqua Alta events are approximated as closely as possible.

For each mosaic wind field, the ASCAT wind speed and wind direction were calculated for the northern part of the Adriatic Sea near Venice and the rest of the Adriatic Sea (areas in Figure 4.3.1(a)), each yielding two values per day. In addition, we calculated the directional constancy (d) of the wind field, which is the ratio of the vector-average wind speed to the scalar-average wind speed:

$$d = \frac{\sqrt{\bar{u}^2 + \bar{v}^2}}{\frac{1}{N}\sum_{i=1}^{N} |V_i|}$$

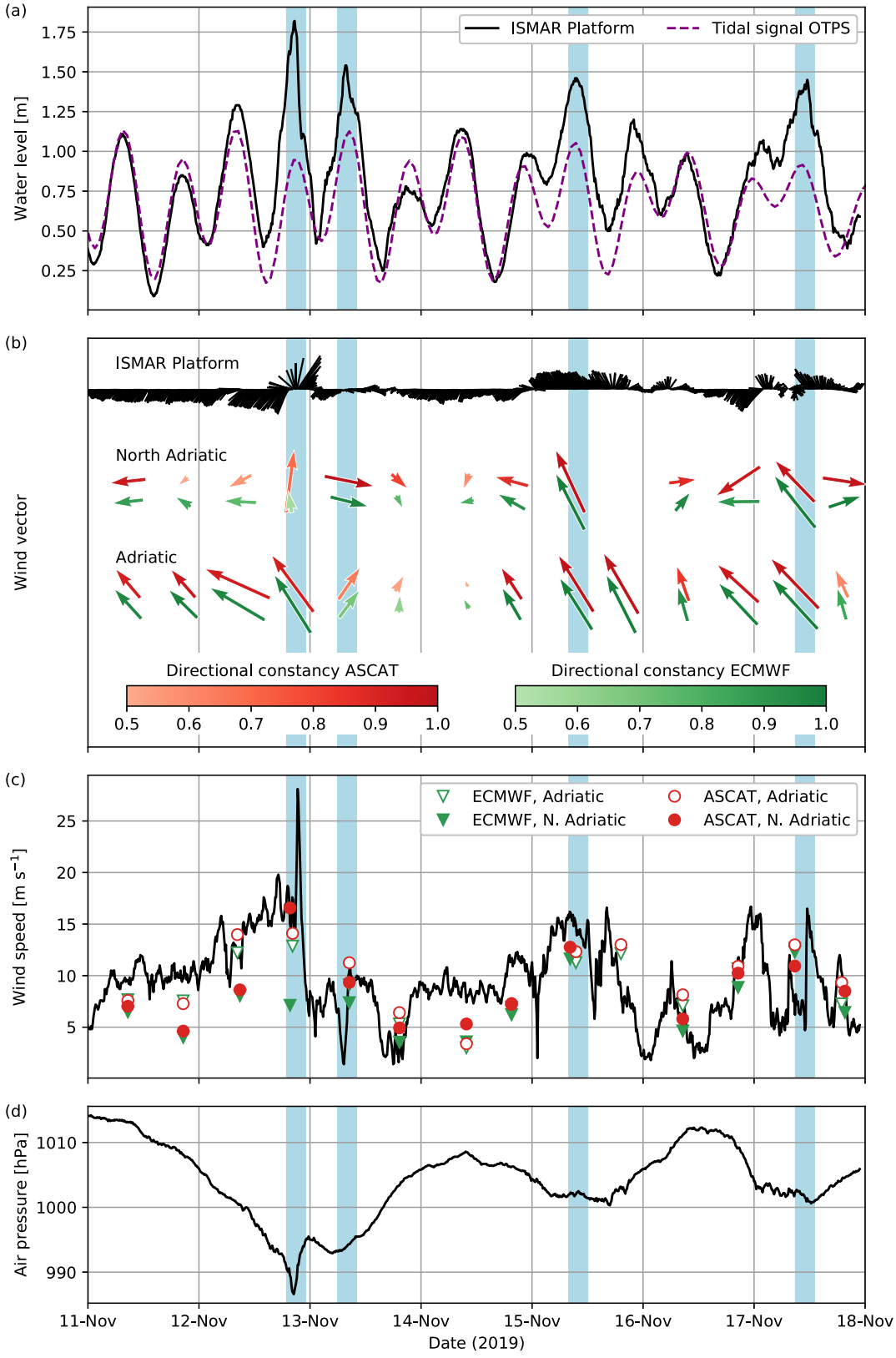

Figure 4.3.2. Time series (in UTC) of (a) water level, (b) wind direction, (c) wind speed and (d) air pressure for the period 11–18 November 2019. In situ point measurements from the ISMAR Acqua Alta Platform near Venice are shown at 10-minute intervals. Scatterometer (ASCAT) and model (ECMWF) spatial averages over the northern and rest of the Adriatic Sea are shown for all ascending and descending Metop satellite overpasses with sufficient data points. The astronomical tidal curve from the OTPS model for the Acqua Alta Platform location is included for reference. The blue vertical bars indicate the four extreme Acqua Alta events in this period.

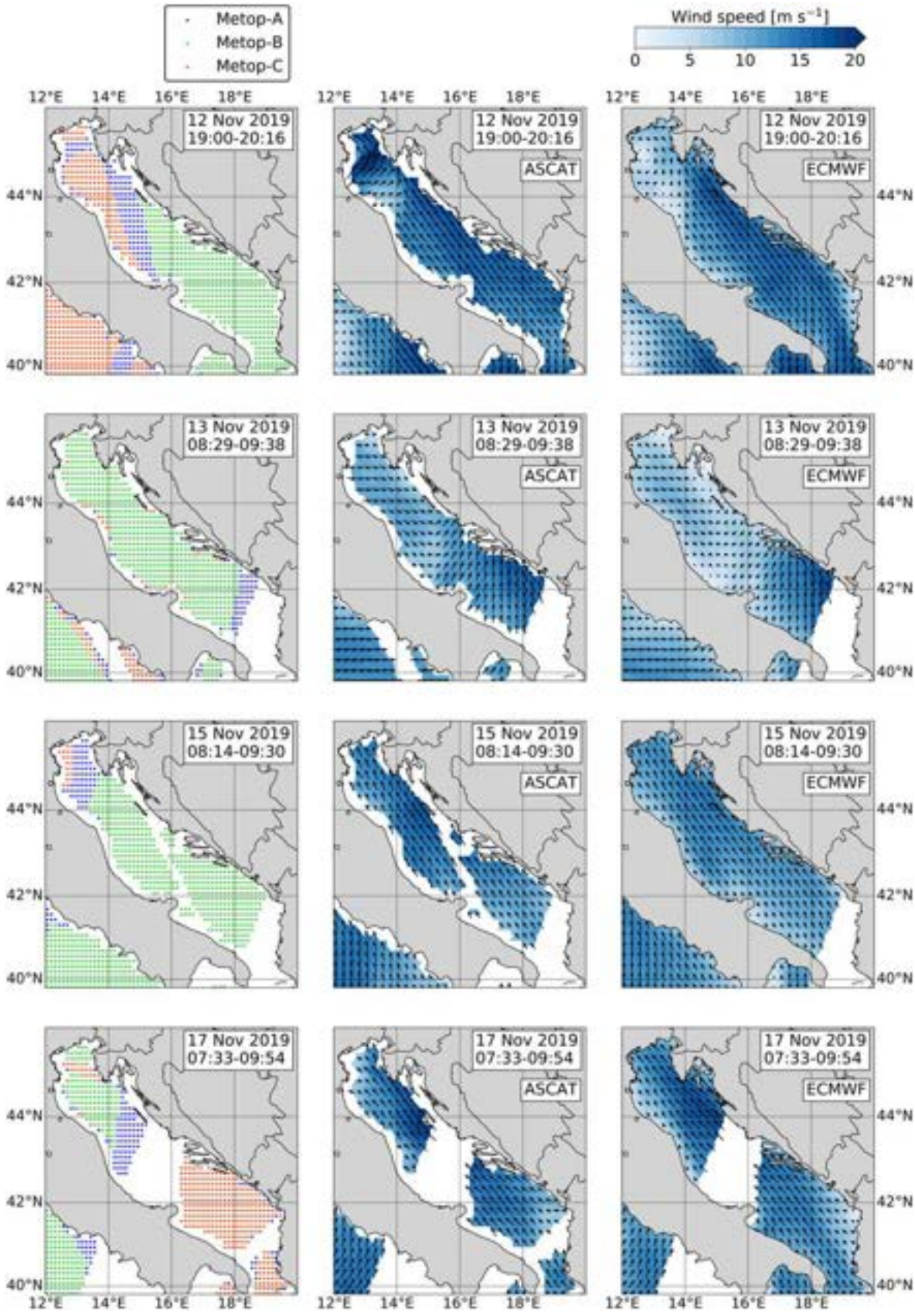

Figure 4.3.3. Surface wind fields over the Adriatic Sea region for the Metop overpass times closest to the four Acqua Alta events in the period 11–18 November 2019. The coloured dots (first column) illustrate the contribution of the three Metop ASCAT instruments to the mosaic images. Surface wind speed (colours) and wind direction (arrows) are shown for the trio of satellite scatterometers (Metop-A, Metop-B and Metop-C ASCAT, second column) and the ECMWF operational model collocated with the ASCAT observations (third column). The time span (in UTC) of the satellite observations over the Adriatic Sea is given in the upper right corner of each image.

Here $\bar{u}$ and $\bar{v}$ are the mean zonal and meridional wind speed, respectively, V is the scalar wind speed and N is the number of observations in the mosaic wind field area of interest. The directional constancy is usually calculated as a temporal average for a particular point and then is a measure of the wind direction variability over time at this point (e.g. Bromwich 1989; Moore and Renfrew 2005). We instead computed the spatial average at each scatterometer overpass time such that d is a measure of the wind direction variability over the area of interest at the particular time.

The L3 wind product includes European Centre for Medium-range Weather Forecasts (ECMWF) 10 meter stress-equivalent winds (de Kloe et al. 2017) collocated with scatterometer observations at Level 2 and interpolated to the L3 regular grid in an identical way. To allow for direct comparison, we applied the same selection and averaging methods to the collocated ECMWF stress-equivalent wind fields.

The observed water levels are compared to modelled sea surface height (SSH) from the operational CMEMS Med-MFC Analysis and Forecasting Physical System (MedFS, Pinardi et al. 2003; Pinardi and Coppini 2010; Tonani et al. 2014; Clementi, Oddo, et al. 2017; Clementi, Pistoia, et al. 2017) with data assimilation component (OceanVar, Dobricic and Pinardi 2008; Storto et al. 2015). MedFS (1/24° horizontal resolution and 141 vertical levels) includes the entire Mediterranean Sea extending to 17.29°W into the Atlantic Ocean and is nested in a global analysis and forecast.[20] The model is forced by momentum, water and heat fluxes interactively computed by bulk formulae using the 6-hourly (for the first 3 days of forecast a 3-hourly temporal resolution is used), 1/8° horizontal-resolution operational analysis and forecast fields from the ECMWF. Every day, MedFS produces a 10-day forecast initialised at 12.00. Along-track satellite sea level anomaly, in situ temperature and salinity profiles are assimilated by the system weekly on Tuesday. Objectively analysed sea surface temperature is used for the correction of surface heat fluxes in analysis mode, when assimilation is performed. For the

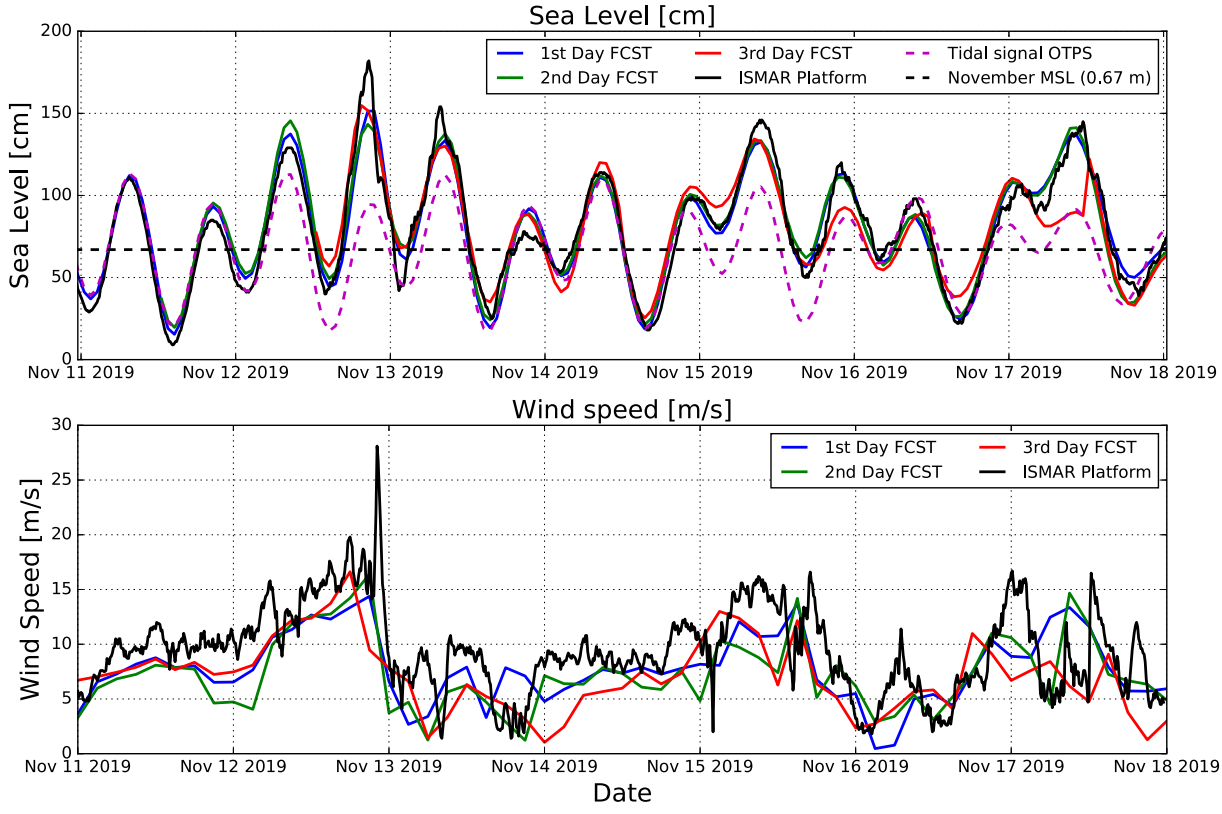

Figure 4.3.4. Top panel: Sea level at the ISMAR Acqua Alta Platform from measurements (black line) and model (MedFS + OTPS) forecasts. The forecast time series represent a concatenation of all the first days of forecasts produced from 10 to 18 November (blue line), all the second days of forecasts (green line) and all the third days of forecasts (red line). The astronomical tidal signal (dashed purple line) and the November 2019 mean sea level (dashed black line) are shown for reference. Bottom panel: Wind Speed at the ISMAR Acqua Alta Platform from measurements (black line) and ECMWF forecasts. The ECMWF time series at different lead times correspond to the MedFS forcing (3-hourly, 10 m wind speed) for the first day (blue line), second day (green line) and third day (red line) of the forecasts.

Table 4.3.1. Sea surface height metrics over the study period for the first three days of the MedFS model forecast and the observations at the Acqua Alta platform. Standard deviations (STD) are provided for the time series of the first, second and third day model forecasts and the observations. The root-mean-square error (RMSE), bias and Pearson correlation coefficient (R) are given for the model forecasts versus the observations.

	STD [m]	RMSE [m]	Bias [m]	*R*
1st day forecast	0.312	0.083	−0.001	0.97
2nd day forecast	0.311	0.092	−0.008	0.96
3rd day forecast	0.279	0.132	0.018	0.91
Observations	0.327			

northern Adriatic Sea, the model sea level anomaly error is of the order of 0.025 m when compared to satellite altimeter data.

Since MedFS is not resolving tidal waves, the Oregon State University Tidal Prediction Software (OTPS) software package (https://www.tpxo.net/otps) based on an efficient inverse model of barotropic ocean tides (Egbert and Erofeeva 2002) has been used to produce the tidal elevation for most significant Mediterranean tidal constituents: M2, S2, N2, K2, K1, O1, P1, Q1. A specific skill assessment of the OTPS tidal amplitudes at the Venice tide gauge gives a mean root-mean-square difference around 0.016 m. The total sea level has been evaluated by adding the tidal elevation from OTPS to the sea surface height provided by the MedFS model. Since the reference levels of MedFS, OTPS and tide gauge observations are different, a constant offset has been added to the model values. This offset corresponds to the mean difference between the forecasted (MedFS + OTPS) and the observed (ISMAR platform) sea level for the considered period.

To illustrate the model forecast improvement when the lead times get shorter, modelled sea surface height is presented as concatenated time series of all first, all second and all third days of each forecast. Discontinuities in the time series may occur at 12.00 when the initial conditions and input fields change between the forecasts.

4.3.3. Results

All four Acqua Alta events in the period 11–18 November 2019 coincided with maxima in the tidal signal (Figure 4.3.2(a)). Because of the spring tide associated with the full moon on 12 November, the tidal conditions were favourable for high water levels during this week. In addition, an anomalous atmospheric depression over the Mediterranean Sea resulted in unusually high mean sea level for November (+0.33 m with respect to the annual mean, The ISMAR Team et al. 2020).

Most persistent Sirocco winds were observed around the times of three of the four Acqua Alta events (Figure 4.3.2(b) and Figure 4.3.3), pushing the water towards the northern part of the basin. Sirocco winds prevailed in the Northern Adriatic during the events on 15 and 17 November, while a strong westerly wind was observed in the morning of 13 November. The extreme event on 12 November was characterised by very strong winds turning from north-easterly to south-westerly in less than one hour.

During all four events, mean wind speeds peaked with values above 10 m s^{-1} (Figure 4.3.2(c)). On the evening of 12 November, local wind speeds exceeded 25 m s^{-1} a few hours after the Metop satellites had passed over. These high wind speeds, the turning of the wind and a sudden drop in air pressure (Figure 4.3.2(d)) were associated with a beta-mesoscale atmospheric system passing over Venice at the lower high tide. The strong south-westerly winds at the peak of the storm created high waves in the Venice lagoon, which combined with the high mean sea level caused huge damage in the southern part of the city (The ISMAR Team et al. 2020).

For the Acqua Alta events on 12, 15 and 17 November, strong Sirocco winds coincided with maxima in the tidal signal. For the event on 13 November, the wind conditions were different with less impact on the high water level. Strong Sirocco winds were also present in the late evening of 15 November and the early morning of 17 November. These did not cause Acqua Alta events, because the tidal maxima were lower and the peak wind speeds did not exactly coincide with the tidal maximum.

On 12 November, just before the exceptional Acqua Alta event, the mean ECMWF wind speed for the Northern Adriatic Sea was almost 10 m s^{-1} lower than the ASCAT wind speed (Figure 4.3.2(b)). The ASCAT scatterometers captured the high wind speeds in the local storm near Venice a few hours before the record water level occurred (Figure 4.3.3). A cyclonic circulation was also present in the ECMWF operational model forecast, but with substantially underestimated wind speeds.

MedFS combined with the OTPS tidal model generally provided accurate sea surface height predictions for the study period from two days in advance (Figure 4.3.4). Comparison of the observed and modelled sea surface height time series revealed a low mean bias and a strong correlation for forecast lead times up to two days (Figure 4.3.4, Table 4.3.1).

Despite the strong correlation for the study period in general, MedFS considerably underestimated the sea

level for the extreme events that occurred on 12, 13 and 15 November. The largest forecast error of 0.30–0.35 m (i.e. a 20% error) occurred during the exceptional sea level peak on 12 November. However, the model was able to predict high sea levels of around 1.50 m since three days in advance of the event. The Acqua Alta events of 13 and 15 November were also present in the forecasted sea surface height from three days in advance. The event on 17 November was accurately represented from the second day forecast onwards. The cause for the underestimated sea level in the third day forecast is uncertain, but is possibly linked to the ECMWF wind forcing that increased considerably from three to two days in advance.

4.3.4. Conclusions and discussion

We analysed the meteorological and tidal conditions for four extreme Acqua Alta events that occurred between 11 and 18 November 2019 to understand the causes of the unprecedented succession of extreme conditions hitting the city of Venice. Furthermore, we assessed the forecast skills of the model systems providing input for the official early warning system, for the study period and the Acqua Alta events.

The month of November 2019 was characterised by unusually high mean sea level near Venice, linked to anomalous persistent low atmospheric pressure conditions over the Mediterranean Sea. Spring tide conditions further increased the high water levels, with maxima on 12 and 13 November.

During the first and most extreme Acqua Alta event on 12 November the water level at the ISMAR Platform reached 1.82 m above the local reference level. The water level recorded in Venice (1.89 m) was the highest value after the 1966 record level of 1.94 m. In addition to the already unusually high water levels, strong Sirocco winds pushed the Adriatic sea water towards Venice. Finally, a local storm with peak wind speeds over 25 m s^{-1} passed over the Venice lagoon just at the lower high tide, creating high waves that damaged the southern part of Venice. The extreme wind speeds were observed by the ASCAT wind scatterometers, but not present in the ECMWF model, contributing to an underestimation of the MedFS sea level forecast by about 0.3 m.

The second Acqua Alta event occurred on 13 November, with a maximum sea level at the ISMAR Platform of 1.54 m. Since Sirocco winds were absent, the general meteorological conditions on top of the high tidal maximum were identified as the main contributors to this event. Strong Sirocco winds did contribute to the Acqua Alta event on 15 November, when sea level at the ISMAR Platform reached a maximum value of 1.46 m above the local reference level.

For the events on 13 and 15 November, the model forecast underestimated local sea levels by about 0.2 and 0.15 m respectively, which may be attributed to several factors. First, errors could have resulted from low spatial and temporal resolution of the ECMWF atmospheric forcing fields. Second, MedFS has a 4.5 km horizontal resolution and cannot properly resolve coastal processes. Third, non-linear interactions between tides and surges are not accounted for since astronomic tides are directly added to the hydrodynamic model solution. This can cause up to 30% sea level underestimation in extreme events (Arns et al. 2020), however non-linear effects are found to be small in the Adriatic Sea (Marcos et al. 2009; Bajo et al. 2019). Last, the impact of seiches in the northern Adriatic Sea could have been underestimated in MedFS.

The last Acqua Alta event in the investigated period happened on 17 November, when the water level at the ISMAR Platform reached 1.45 m. As for the event on 15 November, the extreme sea level was caused by strong Sirocco winds superimposed on the favourable meteorological and tidal conditions for high water levels. The 17 November event was successfully forecasted by MedFS from two days in advance, with about 0.05 m sea level difference between the forecast and the observations.

Our analysis suggests that the forecast accuracy for extreme Acqua Alta events could benefit from using a high-resolution non-hydrostatic regional atmospheric model and from using observations from the growing virtual constellation of scatterometers in data assimilation and nowcasting.

Section 4.4. Extreme waves and low sea level during the storm in the Gulf of Bothnia, Baltic Sea

Authors: Urmas Raudsepp, Aarne Männik, Ilja Maljutenko, Priidik Lagemaa, Sander Rikka, Victor Alari, Rivo Uiboupin

Statement of main outcome: During the storm in January 2019, a record-breaking significant wave height of 8.1 m was recorded in the Bothnian Sea. At the same time, exceptionally low sea levels were recorded in many coastal stations (as low as −1.1 m), both on the Finnish and the Swedish side of the Bothnian Bay. An

interesting situation was documented. High waves coincided with a low coastal sea level. Volumes of water exchange and instantaneous transports between the Northern Baltic Proper and the Gulf of Bothnia ranged to 80 km^3 and 1.5 Sv, respectively, over 4 days during the southward 'diving' cyclone. Taking into account the model errors, actual volume and transport values could be 14–23% larger. Under an anticipated warmer climate, the sea ice extent in the Gulf of Bothnia will likely decrease and the probability of such events will increase.

CMEMS products used

Ref. No.	Product name and type	Documentation
4.4.1	INSITU_BAL_NRT_OBSERVATIONS_013_032 TG – Tide gauge station MO – fixed buoys, mooring time series, fixed observations	PUM: https://resources.marine.copernicus.eu/documents/PUM/CMEMS-INS-PUM-013.pdf QUID: https://resources.marine.copernicus.eu/documents/QUID/CMEMS-INS-QUID-013-030-036.pdf
4.4.2	BALTICSEA_ANALYSIS_FORECAST_PHY_003_006 Model forecast	PUM: http://resources.marine.copernicus.eu/documents/PUM/CMEMS-BAL-PUM-003-006.pdf QUID: http://cmems-resources.cls.fr/documents/QUID/CMEMS-BAL-QUID-003-006.pdf
4.4.3	BALTICSEA_ANALYSIS_FORECAST_WAV_003_010	PUM: http://marine.copernicus.eu/documents/PUM/CMEMS-BAL-PUM-003-010.pdf QUID: http://marine.copernicus.eu/documents/QUID/CMEMS-BAL-QUID-003-010.pdf
4.4.4	SST_BAL_SST_L4_NRT_OBSERVATIONS_010_007_b Satellite observations	PUM: http://marine.copernicus.eu/documents/PUM/CMEMS-SST-PUM-010-007-032.pdf QUID: http://marine.copernicus.eu/documents/QUID/CMEMS-SST-QUID-010-007-032.pdf
4.4.5	SST_BAL_SST_L4_REP_OBSERVATIONS_010_016 Satellite observations	PUM: http://marine.copernicus.eu/documents/PUM/CMEMS-OSI-PUM-010-016.pdf QUID: http://marine.copernicus.eu/documents/QUID/CMEMS-OSI-QUID-010-016.pdf

(*Continued*)

Continued.

Ref. No.	Product name and type	Documentation
4.4.6	C3S ERA5 Model reanalysis	CC3S ERA5 (2017); ECMWF: ERA5 data documentation [accessed 16 February 2019] https://confluence.ecmwf.int/display/CKB/ERA5%3A+data+documentation
4.4.7	Finnish Meteorological Institute Open Data Portal	Honkola et al. (2013); https://en.ilmatieteenlaitos.fi/download-observations#!/

4.4.1. Introduction

The storms asociated with the passage of deep cyclones force high sea level at the coast and a rough sea outside the sheltered areas. Extreme sea levels and high waves may occur in response to the passage of a single storm, as was the case with a very severe storm in Northern Italy on 29 October 2018 (Cavaleri et al. 2019). They may also be caused by a sequence of storms which gradually increase the sea level above the critical value. Post and Kõuts (2014) have argued that this was the case in January 2005 when there was a high sea level at the Estonian coast and flooding in coastal areas. Simultaneous high sea level and waves lead to significant coastal erosion and flooding of low-lying areas. Low sea levels may complicate operations of heavily loaded cargo ships at the ports.

In the long term (1948–2010), an average of about 35 strong cyclones (mean sea level pressure less than 1000-hPa) per year enter the Baltic Sea region (Sepp et al. 2018). The Baltic Sea is located on the edge of the North Atlantic storm tracks where the cyclones are significantly clustered in the cold half-year (Mailier et al. 2006). The seasonally ice-covered Baltic Sea with several semi-enclosed sub-basins has a north–south elongated shape. Sea ice probability is highest (0.7) in the northern Baltic Sea and decreases gradually southward, being as low as 0.05 in the central and southern Baltic Sea (Raudsepp et al. 2020), Sea ice could start to form at the end of October and may last until the end of May. In recent years, mild winters have resulted in a decrease of the sea ice extent in all sub-basins of the Baltic Sea (Raudsepp et al. 2020). During the cold half-year, the seasonal cycle of the sea level variations in the Baltic Sea, with an amplitude of about 0.4 m, is in the higher sea level phase (Raudsepp et al. 1999; Hünicke and Zorita 2008). This adds to the storm surge sea level setup. In general, the

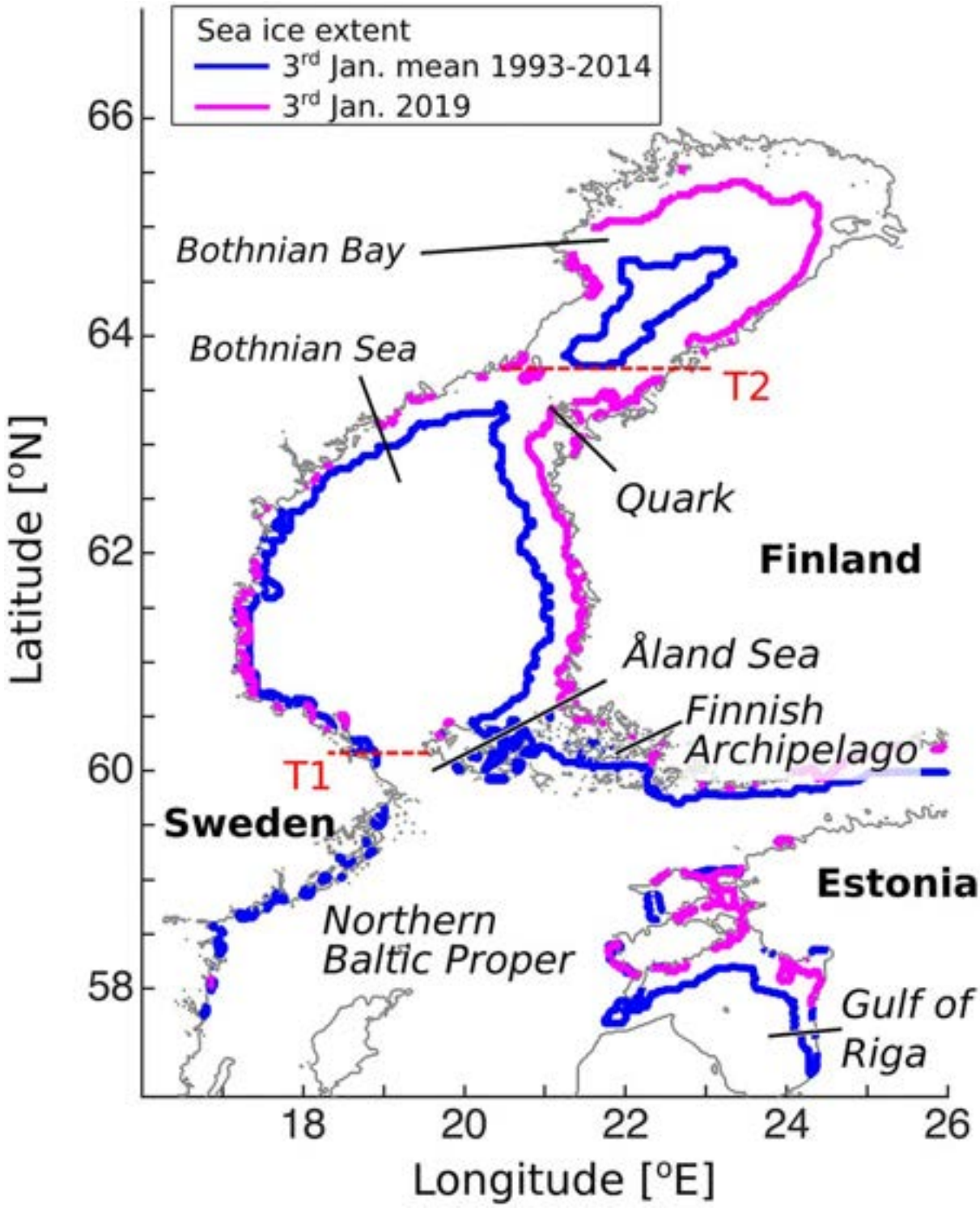

Figure 4.4.1. Map of the northern Baltic Sea (Gulf of Bothnia) and locations mentioned in text. The purple and blue contours show sea ice extent on 03 January 2019 and climatological mean on 3rd January over the period of 1993–2014, respectively (Product reference 4.4.4 and 4.4.5). The storm track is visualised with a dashed purple line. Location of minimum air pressure, complemented with a timestamp and value, is shown with black dots. The grey shade shows the maximum depth of the low-pressure area over the period of 31 December 2018–2 January 2019. The inset in the lower left corner shows the coastline of the Baltic Sea. The minimum at 03:00 UTC 01 January 2019, located off the cyclone track, signifies the development of a secondary low due to the disruptive effect from Norwegian mountains, which later merges with the old low at around 09:00 UTC 01 January 2019 (Product reference 4.4.6).

Baltic Sea level varies on time scales from hours to years. Extreme sea levels range from >−2 m to <3 m, mainly due to storm surges (Wolski and Wiśniewski 2020). Large volume changes of the Baltic Sea (>100 km^3) due to water transport through the Danish Straits associated with a special sequence of atmospheric circulation patterns account for the mean sea level change of more than 0.29 m in the Baltic Sea (Lehmann and Post 2015). Madsen et al. (2019) have estimated the area averaged absolute sea level change for the Baltic Sea of 1.3 ± 0.3 mm/yr for the twentieth century. For a long-term average, the highest significant wave height values have been estimated in the Baltic Proper (Björkqvist et al. 2018). A large number of the wave events with a significant wave height of over 7 m occur in the southern Baltic Proper between November and January. A maximum significant wave height of 8.2 m was measured in the northern Baltic Proper in December 2004 (Björkqvist et al. 2017). In the future, with a warmer climate, when the sea ice extent in the Baltic Sea is expected to decrease (Meier et al. 2004; Granskog et al. 2006), rough sea conditions, in the form of abrupt sea level variations and high waves in winter, might become an increasingly important issue for winter navigation and coastal processes.

The Gulf of Bothnia is the northern sub-basin of the Baltic Sea. It is naturally divided into the Bothnian Bay, which forms the northern part of the gulf, and the Bothnian Sea, which is the southern basin. The Bothnian Bay and the Bothnian Sea are connected through a 50 km wide Quark (mean depth of 25 m; maximum depth of 122 m (Jakobsson et al. 2019)) which limits water exchange between the sub-basins, especially when abrupt changes of water level occur. The Bothnian Sea is cut off from the main Baltic Sea, the Baltic proper, by a shallow Finnish Archipelago area with hundreds of islands. This leaves a narrow, i.e. 40 km wide at the surface, connection through the Åland Sea (mean depth of 37 m; maximum depth of 295 m (Jakobsson et al. 2019)).

Statistical analyses of coastal sea level records over the period of 1960–2010 have categorised the Bothnian Bay as one of the areas with the most intense and long-lasting extreme sea levels in the Baltic Sea (Wolski and Wiśniewski 2020). At the same time, the Bothnian Sea is a sub-basin with a moderate risk of extreme sea level occurrences (Wolski and Wiśniewski 2020), but it has a high joint probability of occurrence of high-water levels and wave heights (Kudryavtseva et al. 2020). In addition, statistically significant negative trends in the duration of the sea ice period have been detected in the Gulf of Bothnia of the Baltic Sea (Figure 4.4.1) over the period of 1982–2019 (Raudsepp et al. 2020). Decrease in both the area and the number of days of sea ice coverage favours the Gulf of Bothnia to become increasingly vulnerable to storm surge sea level variations and rough waves. With the current and anticipated global warming of 1.5°C (IPCC 2018), safety issues in winter navigation that were related to severe sea ice conditions might need to be revised to focus more on high waves and rapid sea level variations in the Gulf of Bothnia.

Due to the meridionally elongated shape of the Gulf of Bothnia, storms with a strong longitudinal wind may cause intensive water exchange between the Gulf of Bothnia and the northern Baltic Proper. Large volume water exchange between the Gulf of Bothnia and the Baltic proper may influence water quality in both basins. In general, the Gulf of Bothnia is, in terms of annual nitrogen fixation rates (Olofsson et al. 2020) or occurrence of hypoxia (Carstensen and Conley 2019), considered to be the least eutrophic sub-basin of the Baltic Sea when compared to, for example, the Baltic proper. Thus, large volume transport from the Gulf of Bothnia may improve water quality in the Baltic proper. In contrast, large volume transport from the Baltic proper to the Gulf of Bothnia might be a significant source of contaminants for the gulf (Maljutenko et al. 2021). So far, the dynamics and quantitative estimates of the water exchange between the Gulf of Bothnia and Baltic proper have not received sufficient attention in the form of scientific research.

Our intention is to analyse extreme variations of the water level and wave fields forced by a single storm in winter. In this study, we focus on the storm surge event during which a very high sea level, but not the highest recorded, changed into an extremely low sea level in the northern Gulf of Bothnia within 36 h. During the decreasing phase of the sea level, extremely high waves were recorded in the Gulf of Bothnia. In addition, we provide quantitative estimates of related water volume exchange between the Gulf of Bothnia and the Baltic proper.

4.4.2. Data and methods

The datasets used in this study consist of in-situ measurements, numerical model analyses of wind and simulation results of sea level and surface waves.

Sea level measurements at 15 coastal stations around the Bothnian Bay and Bothnian Sea (Figure 4.4.2(a)) provide data with hourly intervals (product reference 4.4.1). The locations of stations were selected in such a way that they could represent water level around the whole Gulf of Bothnia. The sea level data of the Swedish and Finnish stations are provided relative to RH2000

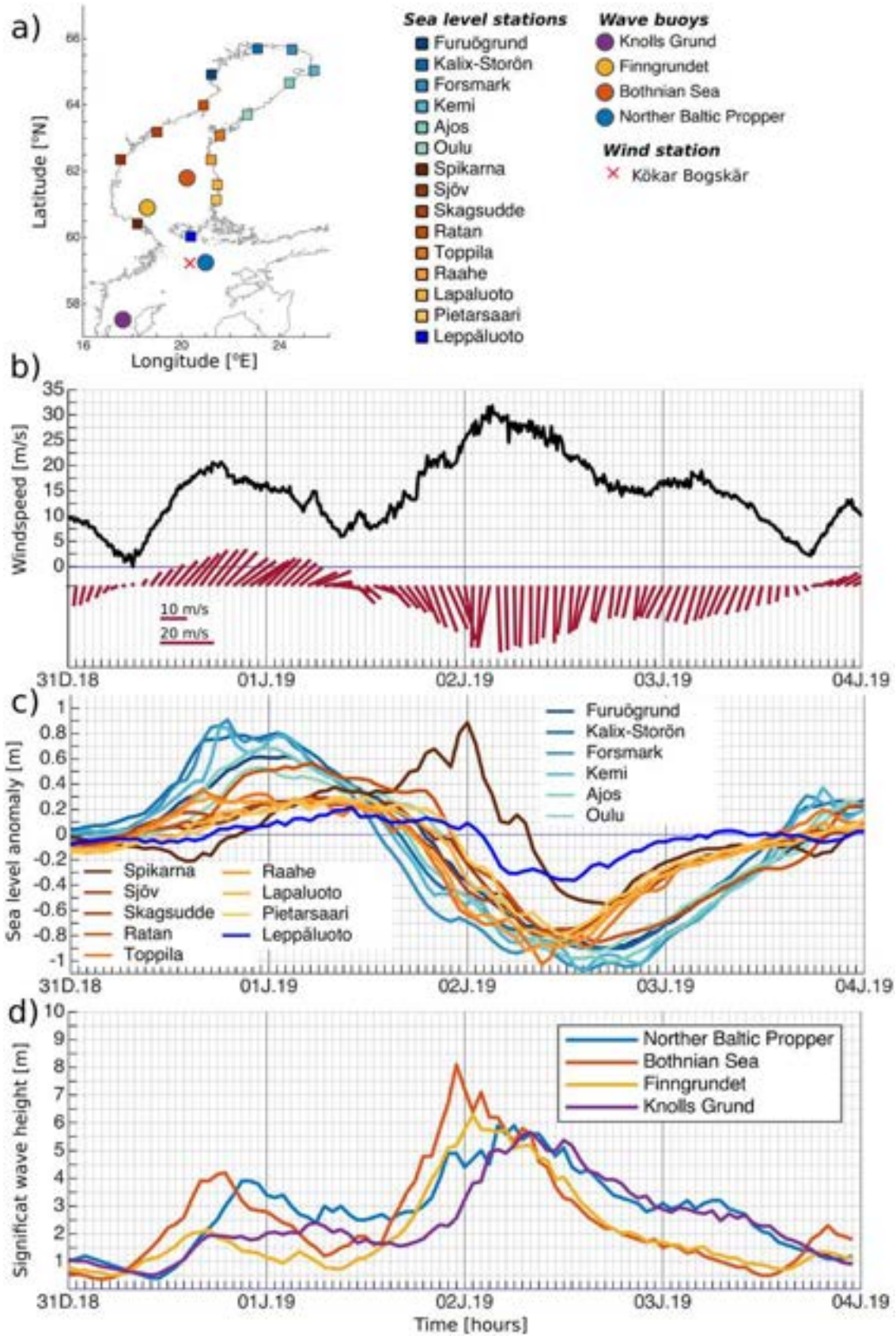

Figure 4.4.2. The map of the northern Baltic Sea with locations of stations (a), time series of measured wind at Kökar Bogskär (Product reference 4.4.7) on (b), sea level anomaly at coastal stations in the Bothnian Bay (blue shades) and the Bothnian Sea (red shades) (Product reference 4.4.1) on (c) and significant wave height measured by FMI and SMHI buoys (Product reference 4.4.1) on (d).

and N2000 height systems, respectively, which are part of the European height system EVRS.

Wave buoy data in the Bothnian Sea for the time of the storm were available from two sites. The Finnish Meteorological Institute has moored a wave buoy in the eastern part of the Bothnian Sea (61° 48' N, 20° 14' E) where the depth is 120 m. The Swedish Meteorological and Hydrological Institute operates a moored buoy at Finngrundet (60° 54' N, 18° 37' E), which is about 10 km south-east of an underwater bank where the depth is around 70 m. Both wave buoys are Datawell Directional Waveriders. For comparison, two additional wave measurements were available for the storm period, one from the Northern Baltic Proper (59° 15' N, 21° 0' E) and one from Knolls Grund (57° 31' N, 17° 37' E) in the western Gotland basin. Wave series were obtained from product reference 4.4.1.

Wind measurements at hourly time intervals from Kökar Bogskär open sea station at a 10 m height, located at 59° 30' N, 20° 21 E and operated by the Finnish Meteorological Institute, were used to show time evolution of wind speed and direction in the Northern Baltic Proper. The data was obtained using the Finnish Meteorological Institute's OpenData framework (product reference 4.4.7).

ERA5 reanalysis (Copernicus Climate Change Service (C3S) 2017) was used to obtain 10 m wind fields with a ca 30 km horizontal resolution and hourly time resolution over the Baltic Sea region for the period of 30th December 2018 to 4th January 2019. The situations with high winds at 15:00 UTC 31st December 2018 and 03:00 UTC 2nd January 2019 were selected as a representative situation of highest winds over the Gulf of Bothnia.

Hourly sea level data is derived from the 1 nautical mile setup of the Hiromb-BOOS Model (Berg and Poulsen 2012) developed and operated by BAL MFC of CMEMS (Tuomi et al. 2017) (product reference 4.4.2). The open boundaries in the North Sea are forced with a 2-dimensional surge model for sea levels and climatological salinity and temperature fields.

The volumetric transports through the Åland Sea and Quark have been calculated from the aforementioned Hiromb-BOOS Model simulation (product reference 4.4.2). The hourly transport of water between the different sub-basins has been calculated as an integral of meridional velocity over zonal transects T1 and T2 (Figure 4.4.1). Integration of the transports over time yields the water volumes which have passed through the passages since 31 December 2018 00:00. The time series of vertical distribution of meridional transports are calculated as integrals of the meridional velocity over each model layer along the transects T1 and T2.

Modelled significant wave height for the duration of the storm is based on the wave model WAM cycle 4.6 (WAve Model, Komen et al. 1994, product reference 4.4.3). Setup of the WAM for the Baltic Sea is described in detail by Tuomi et al. (2019). The significant wave height used in this study is an integrated parameter calculated from the total wave spectrum. Instantaneous values of the significant wave height are provided hourly for the entire Baltic Sea on a 1 nautical mile grid.

The sea ice concentration data for 3 January 2019 was obtained from the near real-time observations (NRT) product reference 4.4.4 on the grid of 1 km horizontal resolution. The sea ice concentration is an estimated fraction of an area which is covered by ice in the grid cell. A grid cell is considered ice covered when the sea ice concentration of the grid cell exceeds 0.15. The satellite remote sensing data of ice coverage from the years 1993–2014 (product reference 4.4.5) is used for the calculation of the mean climatological ice extent for 3 January. We have selected this period as a reference period to be consistent with the climatological reference period used in Copernicus Marine Service in producing Ocean Monitoring Indicators (von Schuckmann et al. 2018). Copernicus product reference 4.4.5 provides daily sea ice concentration data derived from high resolution ice charts at a 5 km horizontal resolution produced in cooperation by the Swedish Meteorological and Hydrological Institute and by the Finnish Meteorological Institute.

4.4.3. Results

4.4.3.1. Measured wind, sea level and waves

At the beginning of January 2019, the sea ice conditions in the Gulf of Bothnia were rather exceptional. In an average winter, Bothnian Bay is to a large extent already covered with ice from the beginning of January (Figure 4.4.1). Sea ice extent on 3 January 2019 was limited to a narrow coastal zone on the northern Bothnian Bay (Figure 4.4.1) due to warm weather in autumn and early winter 2018. The ice coverage might reduce wind fetch in the case of northern winds, which means that wind waves cannot grow as high as they do in the case of an ice-free Gulf of Bothnia. The highest storm surges due to southwesterly winds are damped when the Bothnian Bay is ice covered.

While the Gulf of Bothnia was practically ice free, a cyclone entered the Baltic Sea region during the last days of 2018 (Figure 4.4.1). The cyclone approached the Baltic Sea from the Northern Atlantic in a way that produced two distinct wind speed maxima over the Gulf of Bothnia and Northern Baltic Proper with opposing wind directions during a short period at the

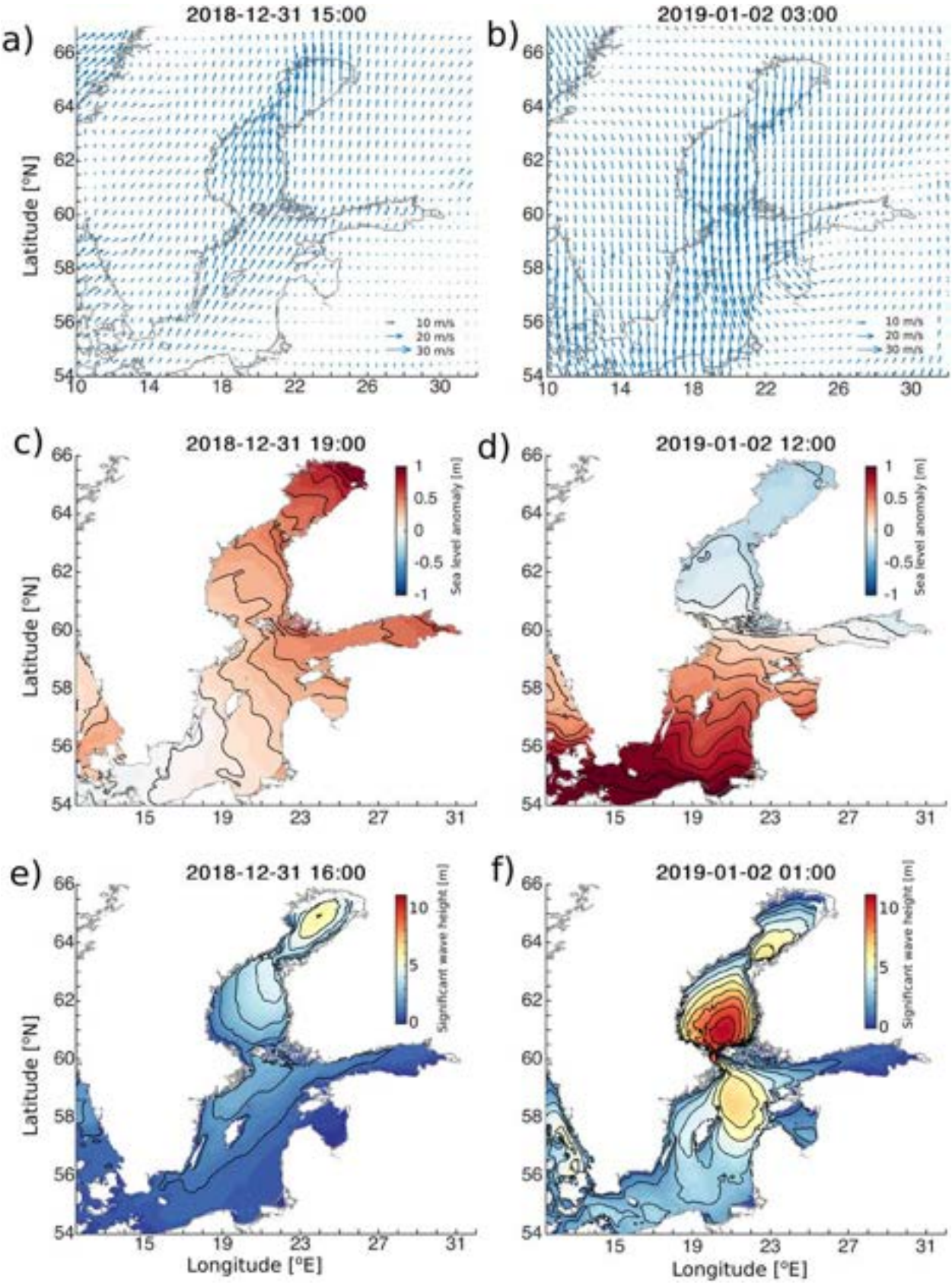

Figure 4.4.3. Horizontal distribution of 10 wind fields (Product reference 4.4.6) on (a–b), sea level (Product reference 4.4.2) on (c–d) and significant wave height (Product reference 4.4.3) on (e–f) at different time instances. Contour interval for sea level is 0.1 m, and for significant wave height it is 1 m.

end of 2018 and beginning of 2019 (see Figure 4.4.2(b)). The first maximum was associated with southwesterly winds with a maximum speed of up to 20 m/s around 18:00 UTC 31 December 2018 when the centre of the cyclone located over the Atlantic. At about 12:00 UTC 01 January 2019 the wind turned northerly, keeping that direction until 18:00 UTC 03 January 2019 (Figure 4.4.2(b)). This happened when the cyclone track shifted eastward from the Gulf of Bothnia and the storm centre took a southward 'dive' over 6 h from 12:00 UTC to 18:00 UTC 01 January 2019 (Figure 4.4.1). During that period, the cyclone caused measured wind speeds of over 30 m/s over the Gulf of Bothnia and the Northern Baltic Proper.

Simultaneously with the peak of the measured southwesterly winds, a high sea level of 0.7–0.9 m was generated at the northern coast of Bothnian Bay (Figure 4.4.2 (c)). The sea level height decreased southward along the coasts of Bothnian Bay, with maximums lagging in time up to 6 h. In the Bothnian Sea, the coastal sea level anomaly remained moderately positive (Figure 4.4.2(c)). Significant wave height increased to a 4 m value in the open Bothnian Sea (Figure 4.4.2(d)) at the peak of southwesterly wind speed (Figure 4.4.2(b)). No wave measurements were available in the Bothnian Bay, and therefore we lack a true representation of the wave conditions there.

A clockwise veering wind from 00:00 UTC 01 January 2019 to 00:00 UTC 02 January 2019 (Figure 4.4.2 (b)) turned northerly and forced sea level to drop (Figure 4.4.2(c)) in the Gulf of Bothnia. In the Bothnian Bay, coastal sea level decreased simultaneously with changing wind direction from southwest to northerly, but in the Bothnian Sea, start of the sea level decrease was delayed by about 20 h. In the Bothnian Sea, the lowest sea level of about −0.8 m was recorded in coastal stations at 12:00 UTC 02 January 2019. In the Bothnian Bay, the lowest sea levels between −1.1 and −0.8 m were recorded 6 h later, at 18:00 UTC 02 January 2019. The time shift in reaching minimum sea levels between Bothnian Bay and Bothnian Sea is carried forward to the relaxation phase of low sea levels (i.e. increase of the sea levels), which shows the hysteresis of temporal evolution of coastal sea levels in these two basins (Figure 4.4.2(c)). Mean sea levels (i.e sea level values around zero) were completely restored in both basins in the afternoon of 3 January 2019.

We would like to note the exceptional short-term response of the sea level to the storm at Föglö Degerby and Forsmark. Measured sea level varied between −0.4–0.2 m at Föglö Degerby, while at the other stations the sea level range was up to −1.1–0.9 m (Figure 4.4.2(c)). The Föglö Degerby sea level station is located inside the Finnish Archipelago where numerous small islands and narrow passages between them could damp short-term sea level changes. At 00.00 UTC 02 January 2019 the Forsmark station reached a maximum sea level of about 0.9 m. At the same time, the other stations in the Bothnian Sea reached low sea levels (−0.2 to −0.6 cm) (Figure 4.4.2(c)). The Forsmark station is located in a small bay which is open to the north, but

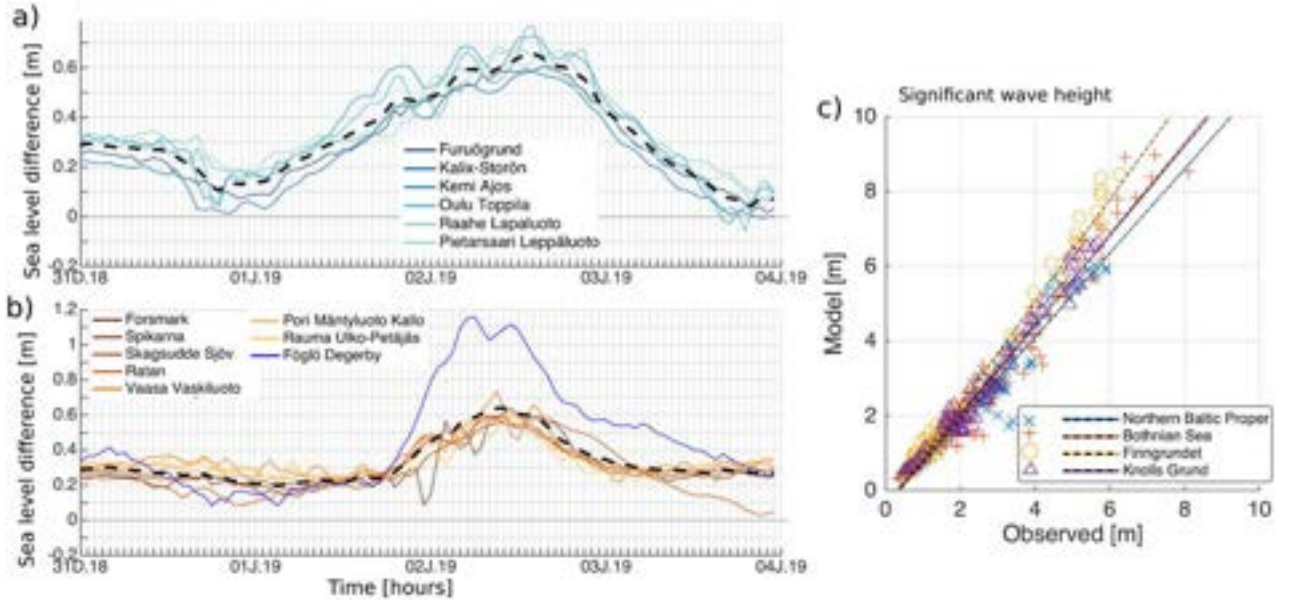

Figure 4.4.4. The time series of sea level difference between model and observed values for the stations of the Bothnian Bay (a) and the Bothnian Sea (b). Black dashed line shows the mean of sea level differences for the Bothnian Bay (a) and the Bothnian Sea (b). Scatter plot of modelled and observed significant wave height values on (c). The lines show the linear relationship between observed and model values.

it has a very narrow passage to the south. The winds from the north could easily pile up water in that bay for a short time period. That was probably the case in the afternoon of 1 January 2019.

The highest measured significant wave height of 8.1 m in the Gulf of Bothnia (Björkqvist et al. 2020) was recorded in the open Bothnian Sea station at 23:00 UTC 01 January 2019 (Figure 4.4.2(d)). This peak value of significant wave height occurred about 5 h earlier than maximum wind speed was measured at about 250 km southward (Figure 4.4.2(b)). Maximum significant wave height is lower (6 m) in the Northern Baltic Proper and the peak value of significant wave height is much more in sync with maximum wind speed. The lower wave height can be explained by the reduced wind fetch due to the presence of the Finnish Archipelago and the narrowness of the Åland Sea (Figure 4.4.1) which hinders the development of extremely high waves in the Northern Baltic Proper in the case of northerly winds. As the measurements of Bothnian Sea station were performed in the open part of the Bothnian Sea, the existence of a significant meridional distance for wave fetch allows us to speculate that even higher waves could be present in southern areas of the Gulf of Bothnia.

4.4.3.2. Model simulated wind, sea level and wave fields

To obtain a broader understanding about cyclone related wind fields and the response of the sea level and the waves to the storm, we complement the measurement with model analyses. We have chosen two time instants from the model that correspond (1) to the highest southwesterly and northerly wind speeds and (2) to the highest and the lowest sea level over the Gulf of Bothnia. For the waves, we have chosen the time instants when significant wave height had maximum value over the Bothnian Bay during the passage of the front edge of the cyclone and in the Bothnian Sea during the southward diving of the storm.

The southeastern edge of the cyclone caused the southwesterly winds over the entire Baltic Sea (Figure 4.4.3(a)). The winds were strongest in the Gulf of Bothnia at 15:00 UTC 31 December 2018. In a later phase, northern winds associated with the western flank of the southward diving cyclone were even more homogeneous over the Baltic Sea area and exceeded the southwesterly winds in strength (Figure 4.4.3(b)). The occurrence times of the highest/lowest sea level (Figure 4.4.3(c,d)) and corresponding high waves (Figure 4.4.3 (e,f)) did not coincide. Extreme values of the sea level lagged the occurrence time of maximum winds, while high waves were closer in time to maximum winds.

To gain confidence in the interpretation of the model sea level data, we have compared simulated sea level values with the measurements at coastal stations (Figure 4.4.4(a,b)). Mean difference between modelled and measured sea levels for the four-day period was 0.32 m in both the Bothnian Bay and the Bothnian Sea, which mainly reflects a mean sea level difference between the model and observations. However, temporal dynamics of the sea level differences should be considered while interpreting the model sea level values. In this process the mean sea level difference will not be considered. The sea level at Föglö Degerby was exceptional. This station is located in the Finnish Archipelago and by no means can the model capture its short-term variability. The other station to drop out of the ensemble is Forsmark. These two stations were excluded in the calculation of sea level statistics. There was no phase difference in the measured and modelled sea level. Observed minimum sea levels and maximum differences between modelled and measured sea occurred simultaneously (Figure 4.4.4(a,b)). Similarly, maximum sea level and minimum difference between modelled and measured sea level coincided in the Bothnian Bay (Figure 4.4.4(a)).

At the northern Bothnian Bay, high sea level lagged maximum southwesterly winds less in time than low sea level lagged maximum northerly winds (Figure 4.4.3(a–d)). High sea level development started from zero sea level, which enabled faster adjustment of the transports through the Quark and Åland Sea to the strong wind. Larger lag of low sea level to the northern winds was caused by two physical processes, the relaxation of high sea level at the northern end of the basin and forced decrease of the sea level in the same area. Limited transport through the Quark and Åland Sea resulted in short term relatively strong sea level gradients between the opposite ends of the connecting passages (not shown). The remaining sea level gradient can be seen in the Åland Sea region (Figure 4.4.3(d)). During southwesterly winds, the water was pumped into the gulf, resulting in a positive sea level everywhere. During northerly winds, water was transported out of the Gulf of Bothnia, which is illustrated by a negative sea level over the entire gulf. In the high sea level phase, Hiromb-BOOS model under-predicts sea level by up to 10 cm in the Bothnian Sea coastal stations and 15 cm in the stations in the Bothnian Bay. This may reflect an under-prediction of the transport through the Quark and Åland Sea by up to 14% with assuming similar relative model errors in the open waters. In the low sea level phase, Hiromb-BOOS model over-predicts sea level by up to 30 cm in the Bothnian Sea coastal stations and 35 cm in the stations

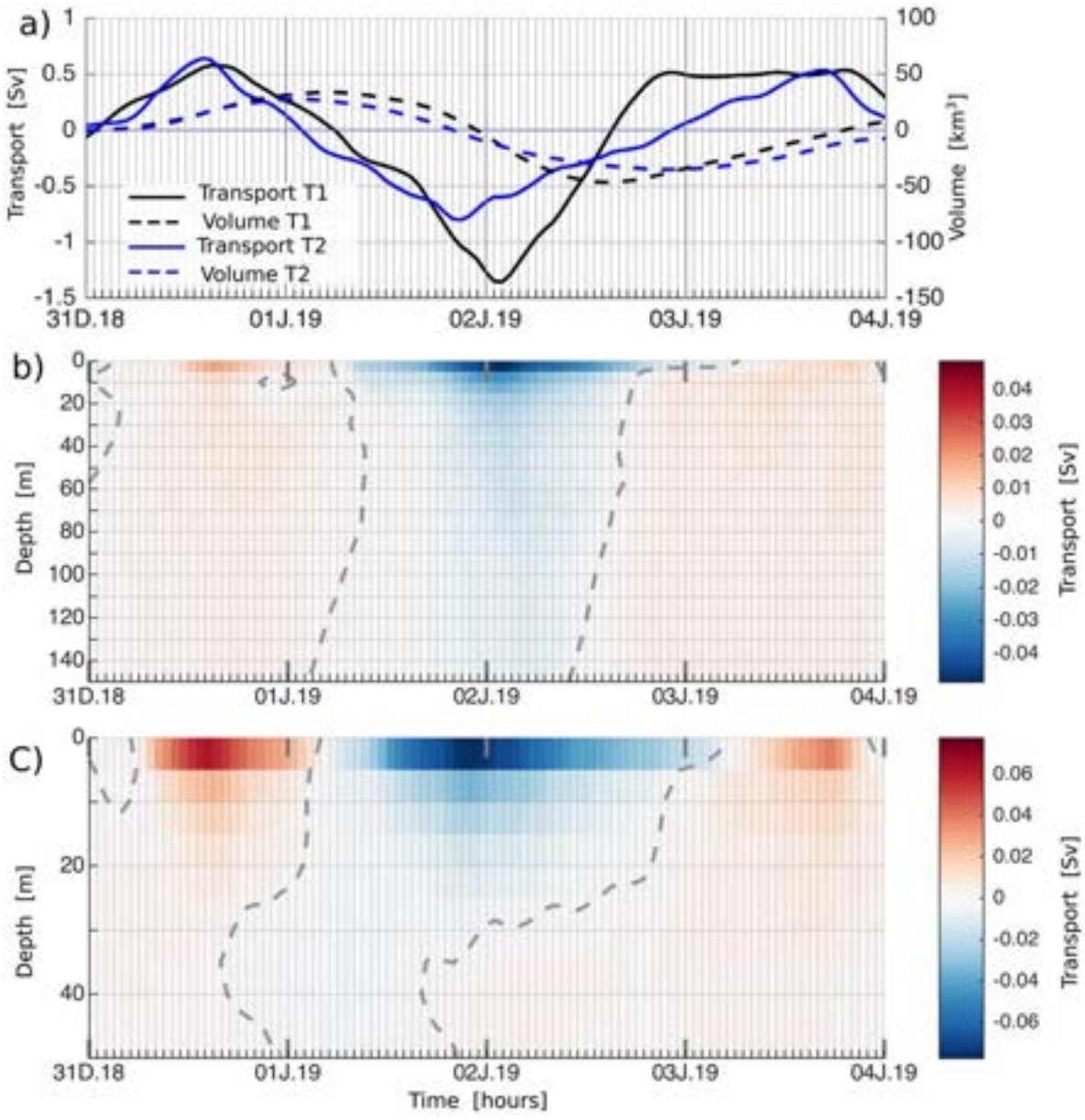

Figure 4.4.5. Transport through the Åland Sea (T1) and Quark (T2) and corresponding volumes (Product reference 4.4.2) as shown in (a). Temporal evolution of vertical distributions of meridional transports at Åland Sea and Quark as shown in (b) and (c), respectively. Transport of 1 Sv = 10^6 m^3/s and positive values indicate northward transport.

in the Bothnian Bay. This suggests an under-prediction of the transport through the Quark and Åland Sea by up to 23% with assuming similar relative model errors in the open waters.

According to numerical model analyses, the first phase of the cyclone generated a significant wave height of 6-7 m in the open Bothnian Bay (Figure 4.4.3(e)). Unfortunately, this is not confirmed by measurements due to a lack of observations. Model and data comparison shows that significant wave height variability is well reproduced for this 4-day period (Figure 4.4.4(c)). Correlation coefficients range from 0.94 at the Northern Baltic Proper to 0.98 at Finngrundet. The model has a clear tendency to overestimate high waves, the worst of which being Finngrundet. At the Bothnian Sea, linear regression equation for the prediction of modelled significant wave height had a slope of 1.22 and intercept of −0.46 m. The situation on 31 December, 2018 describes a classical situation with high sea level and waves at the downwind side of the elongated semi-enclosed sea area similar to the Adriatic Sea and Venice lagoon (Cavaleri et al. 2019). The environmental impact of high waves and high sea level to the coast is weakened by the presence of ice which damps high waves close to the coast (Figures 4.4.1 and 4.4.3(c, e)). During the second phase of the storm, significant wave height over the southern Bothnian Sea, and

especially at the Finnish Archipelago, had a model value of up to 10 m (Figure 4.4.3(f)). This is extreme, even if we correct it with the model error.

4.4.3.3. Water transport

The last objective of this study is to analyse water transport through the Quark and Åland Sea during the storm using the circulation model results (Figure 4.4.5). Vertically, water transport through the Åland Sea was mainly unidirectional (Figure 4.4.5(b)). During the build-up of high sea level in the Bothnian Bay, the transport through the Quark was also unidirectional (Figure 4.4.5(c)). The volume transports were in the direction of wind and much higher in the upper 20 m layer than below that depth (Figure 4.4.5(b,c)). While southwesterly winds continued to drive water into the Bothnian Bay in the upper 25 m layer in the Quark, the increased sea level induced the opposing force in the water column through a barotropic pressure gradient. When sea level at the northern end of the bay reached its maximum of 0.9 m (Figure 4.4.2(c)) the flow turned southward at the near bottom layer of the Quark (Figure 4.4.5(c)). The southward flow in the bottom layer continued to develop, which led to a decrease of the net volume transport to Bothnian Bay. Cumulative volume transported to the Bothnian Bay continued to increase (Figure 4.4.5(a)). When flow through the Quark was bidirectional, the flow through Åland Sea was unidirectional. Also, during the reformation of the currents, the flow through the Aland Sea became bidirectional with the turning of the transport in the bottom layer. This was caused by the sea level gradient between the northern Baltic proper and the Bothnian Sea (Figure 4.4.3(c)). The strongest instantaneous and cumulative volume transports through the Quark and Åland Sea were similar, being slightly in excess of 0.5 Sv and 30 km^3, respectively.

The transports reversed and volume started to decrease before the wind turned southward (Figures 4.4.2(b) and 4.4.5(a)). This was caused by barotropic forcing of southward flow in the Bothnian Bay and Bothnian Sea that became larger than wind forcing. Still, we would like to note that there was a 4-hour time period when there was transport to the Botnian Sea both from the Bothnian Bay and from the Baltic Proper. Initially, negative transport was vertically unidirectional, but it became bidirectional through the Quark at about 18:00 UTC 01 January 2019 (Figure 4.4.5(c)). Bidirectional transport through the Quark prevailed during the storm until about 20:00 UTC 02 January 2019. The transport also turned bidirectional through the Åland Sea, but much later, at about 12:00 UTC 02 January 2019 (Figure 4.4.5(b)).

During the reformation of the water transport between the Bothnian Bay, the Bothnian Sea and the northern Baltic proper, instantaneous transports decreased from 0.6 to −0.8 Sv through the Quark and Åland Sea almost simultaneously (Figure 4.4.5(a)). Thereafter, the transport continued to decrease and reached a value of −1.4 Sv through the Åland Sea at 00:00 UTC 02 January 2019. Total volume of water that was transported from the Bothnian Sea to the Baltic proper was estimated to be at 80 km^3 within 1.3 days (Figure 4.4.5(a)). About 60 km^3 of it was compensated by the outflow from the Bothnian Bay to the Bothnian Sea.

Recovery of the volume of the Bothnian Sea started at 13:00 UTC 02 January 2019 (Figure 4.4.5(a)). The transport became larger through T1 than through T2, which resulted in the accumulation of water in the Bothnian Sea and in increasing sea levels (Figure 4.4.2(c)). Transport through T2 turned positive around 22:00 UTC 02 January 2019, and thereafter, sea levels in the Bothnian Bay started to increase as well. The period of positive transports is characterised by ceasing wind and vertically unidirectional flow through T1 and T2. The pre-storm level of water volume in the Bothnian Sea and Bothnian Bay was reached by 00:00 UTC 04 January 2019. Thus, the recovery of water volume in Bothnian Bay was faster than in the Bothnian Sea, which is explained by the smaller water volume of the Bothnian Bay (around 1453 km^3) compared to the Bothnian Sea (around 4147 km^3). The larger volume transport through T1 than T2 from 13:00 UTC 02 January 2019 to 14:00 UTC 03 January 2019 (Figure 4.4.5(a)) explains hysteresis in the increase of coastal sea levels in the Bothnian Bay and the Bothnian Sea (Figure 4.4.2(c)).

4.4.4. Discussion and summary

An interesting case of a southward diving cyclone over the Baltic Sea and its dynamical implications were documented and analysed. In its initial phase, while approaching Scandinavia from the west, the southwesterly winds forced a high sea level (up to 0.9 m) in the Bothnian Bay. Within the next 36 h, low sea levels (as low as −1.1 m) were recorded in many coastal stations, both on the Finnish and the Swedish side of the Bothnian Bay. In the southern Bothnian Sea, a record-breaking significant wave height of 8.1 m was recorded (Björkqvist et al. 2020). At that time, 23:00 UTC 01.01.2019, coastal sea level was as low as −0.8 m in the northern and −0.3 m in the southern Gulf of Bothnia. Such a simultaneous occurrence of low sea level and exceptionally high waves has not been analysed earlier. However, the minimum coastal sea levels of this event were recorded about 12–18 h later. Low sea level events

on their own are not unique in the Bothnian Bay (Wolski et al. 2014), but their frequency has increased in the 2000s (She and Viktorsson 2018). It is still debatable whether low sea levels and high waves are interlinked with the decrease of the sea ice extent in the Gulf of Bothnia or not (She and Viktorsson 2018; Björkqvist et al. 2020).

In a complex system, like the Gulf of Bothnia, sea level variations in the case of rapidly changing storms are dependent on the water transport through the Quark and the Åland Sea (Figure 4.4.1). When strong winds from southwest change into strong winds from the north over a short time period, the volume transport through the connections and the corresponding sea level changes do not respond to the forcing linearly. When the system is being forced from an equilibrium state (about zero sea level in the whole Gulf of Bothnia, Figure 4.4.2(c)), the volume transports through both of the connections respond to the forcing in a similar manner (Figure 4.4.5(a)). But in the case of a forced relaxation from the highly disturbed state (high sea level in the Bothnian Bay), the response of transports through the connections (wind forcing in the direction of the barotropic pressure gradient forcing) differs and is much more complicated due to limited permeability of the connections. In total, 30 km^3 of water was transported to the Gulf of Bothnia during southwesterly winds. Based on inter-comparison of simulated and observed sea level, it is estimated that the transport through the Quark and Åland Sea is underestimated by up to 14%. During the 'diving' storm, 80 km^3 was transported out of the gulf. Similarly it is estimated that this amount is underestimated by about 23%. After the storm, 50 km^3 flowed back in. Estimating how much Gulf of Bothnia water remained in the Baltic proper or vice versa is out of the scope of the current study, although it is significant with regards to water quality in both basins.

Significant wave heights were relatively well reproduced by the WAM model (product reference 4.4.3). Overestimation of significant wave heights by the model increases with the increase of wave height (Figure 4.4.4(c)). The model-simulated maximum significant wave height during the storm was 10 m (Figure 4.4.3 (f)), which was corrected to 8.5 m.

The events of simultaneous extreme sea levels and waves may have a devastating impact on coastal erosion and ship navigation. High sea level along with simultaneous extremely high waves are physically more consistent and have been the subject for many more studies (e.g. Cavaleri et al. 2019; Kudryavtseva et al. 2020) than simultaneous low sea level and extremely high waves. The latter case may still lead to the significant erosion of coastal slope and sediment transport of usually submerged and undisturbed water areas.

Section 4.5. Establishment of *Pterois miles* (Bennett, 1828) in the Ionian Sea

Authors: Laura Bray, Dimitris Kassis

Statement of the main outcome: The presence of invasive species in the Mediterranean Sea is much higher than in other European seas, and understanding the reasons behind the range expansion of this invasive species is important for minimising any possible impacts to the already highly pressurised Mediterranean marine ecosystem. In this work, a brief description of sightings of the invasive lionfish *Pterois miles* (Bennett, 1828) in the Ionian Sea is provided, and a broad analysis of temperature patterns throughout the region is given to strengthen the understanding of lionfish range expansion in the Ionian Sea. As of 2018, lionfish expansion into the Ionian Sea was relatively abated, however a substantial increase in the temperature of the upper layers of the Eastern Mediterranean occurred during the late spring of 2018 and likely contributed towards the northward spread of this thermophilic species in the Ionian during 2019. Combining *in-situ* observations, CMEMS products, and citizen science data could assist in the monitoring of the range of this invasive species; a legal requirement for European countries under the Marine Strategy Framework Directive (Commission Decision (EU) 2017/848).

Products used:

Ref. No.	Product name and type	Documentation
4.5.1	MEDITERRANEAN SEA PHYSICS ANALYSIS AND FORECAST. MEDSEA_ANALYSIS_ FORECAST_PHY_006_013	PRODUCT USER MANUAL (CMEMS-MED-PUM-006-013) http://marine.copernicus.eu/documents/PUM/CMEMS-MED-PUM-006-013.pdf QUALITY INFORMATION DOCUMENT (CMEMS-MED-QUID-006-013) http://marine.copernicus.eu/documents/QUID/CMEMS-MED-QUID-006-013.pdf https://doi.org/10.25423/CMCC/MEDSEA_ANALYSIS_FORECAST_PHY_006_013_EAS5
4.5.2	MEDITERRANEAN SEA PHYSICS REANALYSIS. MEDSEA_REANALYSIS_ PHYS_006_004	PRODUCT USER MANUAL (CMEMS-MED-PUM-006-004) http://marine.copernicus.

(*Continued*)

Continued.

Ref. No.	Product name and type	Documentation
		eu/documents/PUM/CMEMS-MED-PUM-006-004.pdf QUALITY INFORMATION DOCUMENT (CMEMS-MED-QUID-006-004) http://marine.copernicus.eu/documents/QUID/CMEMS-MED-QUID-006-004.pdf https://doi.org/10.25423/MEDSEA_REANALYSIS_PHYS_006_004
4.5.3	Data of Pterois miles sightings in the Ionian	Data source: A literature review regarding the observations of *P. miles* throughout the Mediterranean Sea, with a particular focus on the Ionian Sea was conducted. All published geo-referenced reports were considered, alongside available data points presented by several citizen science projects (e.g. online Database MedMIS (IUCN Center for Mediterranean Cooperation, http://www.iucn-medmis.org); "Is it Alien to you … Share it!!!" Environmental Organisation iSea, https://isea.com.gr)
4.5.4	MEDITERRANEAN SEA HIGH RESOLUTION AND ULTRA HIGH RESOLUTION SEA SURFACE TEMPERATURE ANALYSIS SST_MED_SST_L4_NRT_OBSERVATIONS_010_004	PRODUCT USER MANUAL (CMEMS-SST-PUM-010-004-006-012-013) http://marine.copernicus.eu/documents/PUM/CMEMS-SST-PUM-010-004-006-012-013.pdf QUALITY INFORMATION DOCUMENT (CMEMS-SST-QUID-010-004-006-012-013) http://marine.copernicus.eu/documents/QUID/CMEMS-SST-QUID-010-004-006-012-013.pdf

4.5.1. Introduction

Nationally and internationally, the Ionian Sea is an important socio-economic region for both the fishing and tourism sectors (Politou et al. 2003; Tzanatos et al. 2006; Diamantopoulou and Voudouris 2008). However, due to an intensive over-exploitation of marine resources and changes in ocean productivity, the Ionian marine ecosystem is at risk of ecological deterioration and species loss, especially at deeper depths (Capezzuto et al. 2010; Piroddi et al. 2010). A decrease in ecological status and number of native species is directly related to the number of observed alien species at several rocky circalittoral and infralittoral Ionian Sea habitats (Corriero et al. 2016). With the opening and gradual expansion of the Suez Canal, the spread of thermophilic Lessepsian fish species throughout the Eastern Basin of the Mediterranean has proliferated (Katsanevakis et al. 2014), and the South-east Ionian Sea is a hot spot for Lessepsian species spreading on their way towards the Western Mediterranean (Bardamaskos et al. 2009).

Since 2012, the invasive lionfish *Pterois miles* (Bennett, 1828) has been regularly sighted along the warmer southern coasts of the Mediterranean in the vicinity of the Suez Canal (Kletou et al. 2016), with aggregations of up to 70 lionfish being observed on rocky grounds in one sighting off the Island of Cyprus in 2018 (Savva et al. 2020). The ecological role *P. miles* plays in the Mediterranean was until recently unknown (however see Poursanidis et al. 2020; Savva et al. 2020), and many ecologists fear that the generalist predator will reap the same ecological impacts as observed in other regional seas (Lesser and Slattery 2011; Green et al. 2012; Benkwitt 2015). Recent observations of increased predation by lionfish on native species, as opposed to other introduced species (Poursanidis et al. 2020), could have wide-ranging impacts on an already vulnerable marine ecosystem. Despite suggestions that *P. miles* are 'here to stay', at least on the Island of Cyprus (due to rapid growth rates, generalist diet, and adult/juvenile year-round presence) (Savva et al. 2020), many regional marine managers are considering initiatives aimed at the reduction of *P. miles* range expansion (Kletou et al. 2016). Halting or slowing range expansion of successful invasive species, especially those which easily adapt to available prey, is a steep challenge, and successful implementation strongly relies on citizen scientists, stakeholder participation, and the ability to predict where resources are likely to be needed most (e.g. range expansion modelling).

Discerning the drivers of invasive species range expansion is important for not only understanding the ecology of an effective Lessepsian species but also for discerning potential spread to other sea units. Temperature increases are often cited as a driver for range expansion for this thermophilic Lessepsian fish (Dimitriadis et al. 2020; Poursanidis et al. 2020), and until 2016 this seemed applicable for lionfish in the Eastern Mediterranean, as no individuals were observed in the colder Northern Aegean and Ionian Seas. The first presence of a *P. miles* specimen in the Ionian Sea was recorded in 2016 using a citizen science platform, outside of Koroni Harbour, SW Peloponnese (Dimitriadis et al. 2020), albeit without any further sightings in the Ionian for

Table 4.5.1. Recorded sightings (2016–2019) of Pterois miles in the Ionian Sea.

Latitude	Longitude	Location	No. of ind.	Observation year	Source
36.797665	21.961816	Laconia Peninsula	1	2016	Dimitriadis et al. (2020)
36.257694	22.914722	Kythera Island	1	2018	Mitsou and Maximiadi (2018)
38.27	20.6828	Kefalonia Island	1	2019	Vavasis et al. (2019)
38.487569	20.802001	Atakos Island	1	2019	Dimitriadis et al. (2020)
39.741207	19.938717	Corfu Island	1	2019	Dimitriadis et al. (2020)
36.454956	22.97832	Elafonisos Island	1	2019	Dimitriadis et al. (2020)
38.589213	20.887964	Kalamos Island	1	2019	Dimitriadis et al. (2020)
38.06995	20.803222	Kefalonia Island	1	2019	Dimitriadis et al. (2020)
38.073062	20.801371	Kefalonia Island	1	2019	Dimitriadis et al. (2020)
38.0731	20.8014	Kefalonia Island	1	2019	Dimitriadis et al. (2020)
36.132838	22.990012	Kythera Island	1	2019	Dimitriadis et al. (2020)
36.517128	22.986805	Laconia Peninsula	1	2019	Dimitriadis et al. (2020)
36.655178	22.81716	Laconia Peninsula	1	2019	Dimitriadis et al. (2020)
36.681357	22.844878	Laconia Peninsula	1	2019	Dimitriadis et al. (2020)
36.687078	22.837481	Laconia Peninsula	1	2019	Dimitriadis et al. (2020)
37.0431	21.5465	Proti Island	1	2019	Dimitriadis et al. (2020)
37.050883	21.556289	Proti Island	1	2019	Dimitriadis et al. (2020)
37.653304	20.807333	Zakynthos Island	1	2019	Dimitriadis et al. (2020)
37.653595	20.85902	Zakynthos Island	1	2019	Dimitriadis et al. (2020)
37.658634	20.804318	Zakynthos Island	1	2019	Dimitriadis et al. (2020)
37.720047	20.953352	Zakynthos Island	1	2019	Dimitriadis et al. (2020)
37.88405	20.723433	Zakynthos Island	1	2019	Dimitriadis et al. (2020)
37.8860463	20.7241151	Zakynthos Island	1	2019	Dimitriadis et al. (2020)
37.908555	20.712123	Zakynthos Island	1	2019	Dimitriadis et al. (2020)
36.428568	22.485772	Mani Peninsula	1	2019	Dimitriadis et al. (2020)
36.462491	22.43427	Mani Peninsula	1	2019	Dimitriadis et al. (2020)
36.463354	22.424111	Mani Peninsula	1	2019	Dimitriadis et al. (2020)
36.486163	22.511302	Mani Peninsula	1	2019	Dimitriadis et al. (2020)
36.4862	22.5113	Mani Peninsula	1	2019	Dimitriadis et al. (2020)
36.540627	22.390963	Laconia Peninsula	1	2019	Dimitriadis et al. (2020)
36.862111	22.249439	Laconia Peninsula	1	2019	Dimitriadis et al. (2020)
36.879868	22.233608	Laconia Peninsula	1	2019	Dimitriadis et al. (2020)
36.3991	22.4883	Mani Peninsula	3	2019	Present study
36.4006	22.4879	Mani Peninsula	1 (Juvenile)	2019	Present study
36.4751	22.3953	Mani Peninsula	4 (1 Adult pair, 2 juveniles)	2019	Present study

several years (Mitsou and Maximiadi 2018; Vavasis et al. 2019). Despite a general presence in the South Aegean and Levantine Sea from 2014, it appears that the systematic spread of *P. miles* into the Ionian was relatively abated until several years later. As of 2019 however, lionfish are regularly spotted throughout the Southern Ionian basin (Dimitriadis et al. 2020).

To investigate whether changes in regional sea temperatures regimes around the period lionfish expanded their range into the Ionian Sea (circa 2018) may have been a contributing factor for expansion, a description of recent lionfish sightings in the Eastern Mediterranean is presented alongside a broad analysis of Eastern Mediterranean temperature patterns for a five-year period (2014–2019).

4.5.2. Methods

4.5.2.1. Ionian lionfish sightings

A literature review regarding the observations of *P. miles* throughout the Mediterranean Sea was conducted. All published geo-referenced reports were considered, alongside available data points presented by several citizen science projects (e.g. online Database MedMIS (IUCN Center for Mediterranean Cooperation, http://www.iucn-medmis.org); 'Is it Alien to you … Share it!!!' Environmental Organisation iSea, https://isea.com.gr) (Product Ref. No 4.5.3). Reported sightings were grouped by observation year from 2015 onwards. In addition, due to the possibility of spatial or temporal citizen science sightings bias (Tiago et al. 2017), and to verify the presence of *P. miles* in the area, in-situ transects of 1.5 km were conducted by two divers at two locations along the Mani Peninsula, the southernmost tip of the Greek Ionian coastline (Transect 1: 36.401N, 22.487E – 36.398N, 22.492E; Transect 2: 36.481N, 22.399E – 36.471N, 22.394E), during August 2019. Transects covered the whole 0–10 m coastal contour, and all crevices were carefully checked. Each diver recorded the location and number of all *P. miles* individuals, and where differences in observations occurred by observers, average values were calculated.

4.5.2.2. Temperature field variability

To assess whether sea temperatures could assist in *P. miles* range expansion into the Ionian, modelled temperature output for upper surface layers (8 m depth) and satellite data for sea surface temperature were analysed on a monthly basis for the Eastern Mediterranean region within the domain of 16° E – 36° E &

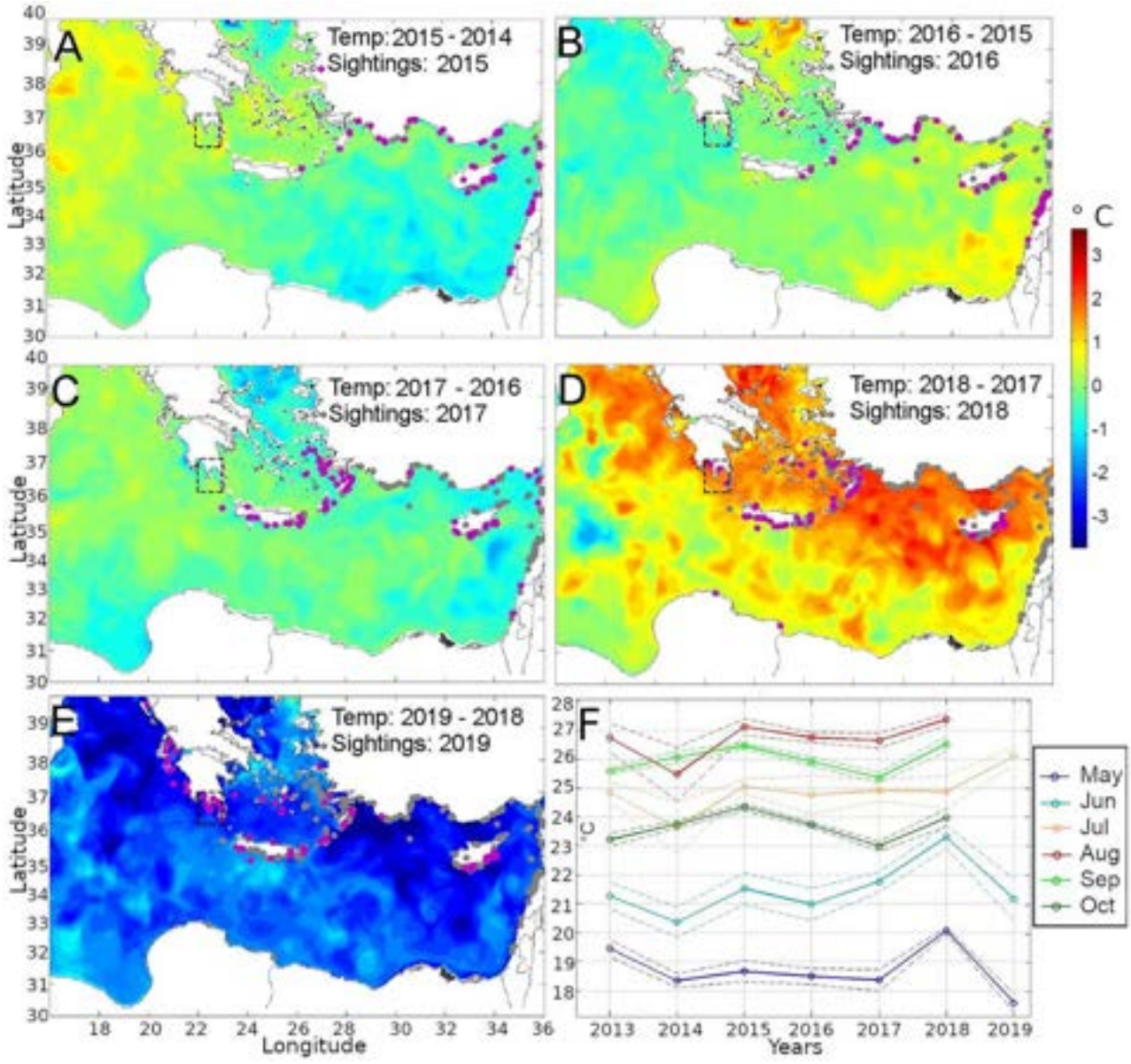

Figure 4.5.1. Yearly differences in 8 m depth water potential temperature for the month of May for the years 2014–2019 (A–E), compared to the average summer temperatures (May–October) (F) for the region highlighted by the black box (Mani Peninsula–Southern Ionian Sea). Locations of recorded sightings obtained from the literature review are plotted (grey circles) based on observation year; sightings within the Ionian are highlighted in red.

30° N – 40° N. The raw datasets for the modelled surface layers were acquired by the Copernicus Marine Environment Monitoring Service (CMEMS). The study period spans from 01/2013 to 07/2019 and consisted of two CMEMS products: (a) the Product Ref. No 4.5.1 for the 01/2017 to 07/2019 period, and (b) the Product Ref. No 4.5.2 for the 01/2013 to 12/2017 period. Both datasets are produced by the Mediterranean Forecasting System, physical analysis and reanalysis components supplied by the Nucleous for European Modelling of the Ocean (NEMO), with a horizontal grid resolution of 1/24° (ca. 4 km) and 1/16° (ca. 6–7 km) accordingly. The former is corrected by a variational data assimilation scheme (3DVAR) of temperature and salinity vertical profiles and along-track satellite Sea Level Anomaly observations and the latter with a variational-data assimilation scheme (OceanVAR) for temperature and salinity vertical profiles and satellite Sea Level Anomaly along-track data (Clementi et al., 2019; Simoncelli et al., 2014). For the analysis of the satellite sea surface temperature field (2016–2019) the CMEMS Product Ref. No 4.5.4 was used. The dataset provides daily anomalies of the remotely sensed L4 sea surface temperature based on a pentad climatology (Buongiorno Nardelli et al. 2013). For both model and satellite data, monthly mean values were calculated for

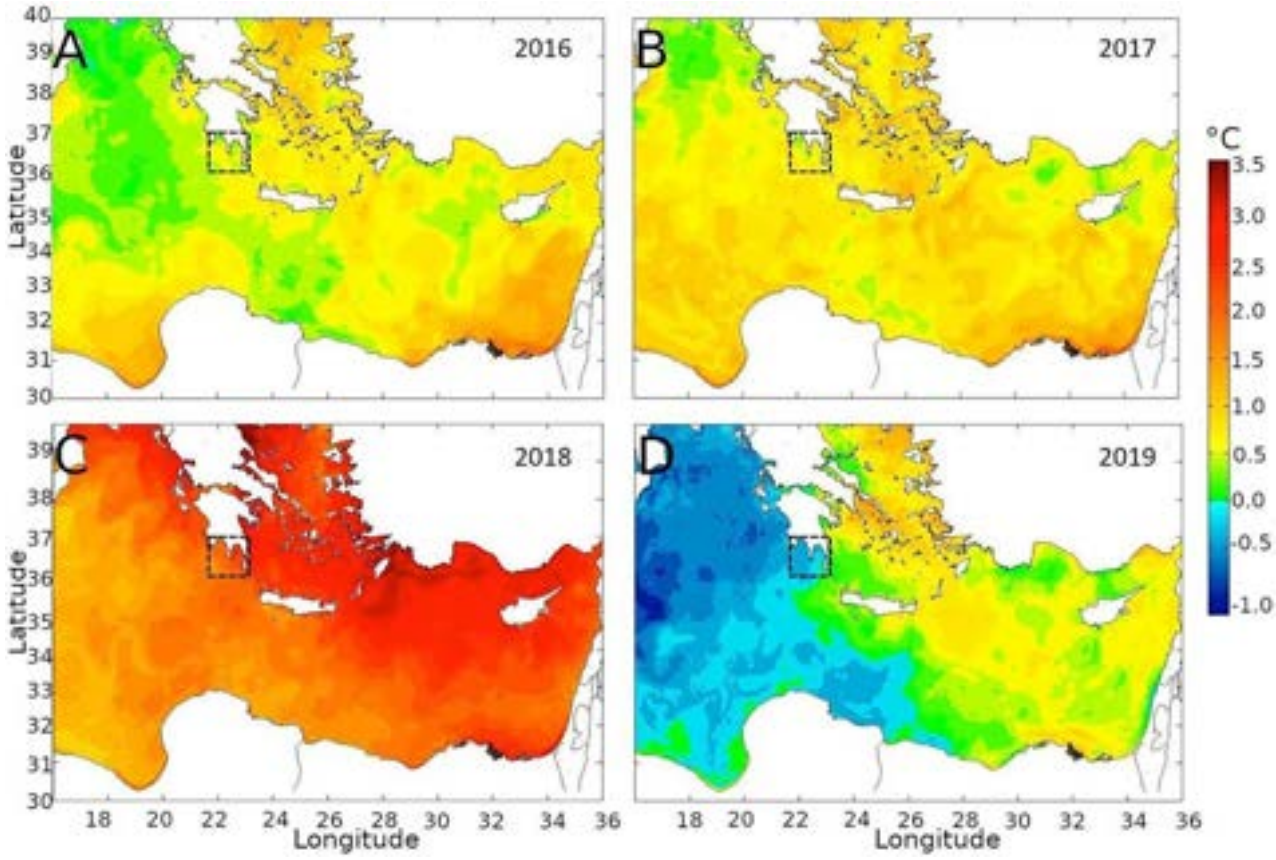

Figure 4.5.2. Sea surface temperature anomaly (°C) based on a pentad climatology for May 2016 (a), May 2017 (b), May 2018 (c), and May 2019 (d). The dotted square indicates the Mani Peninsula target area.

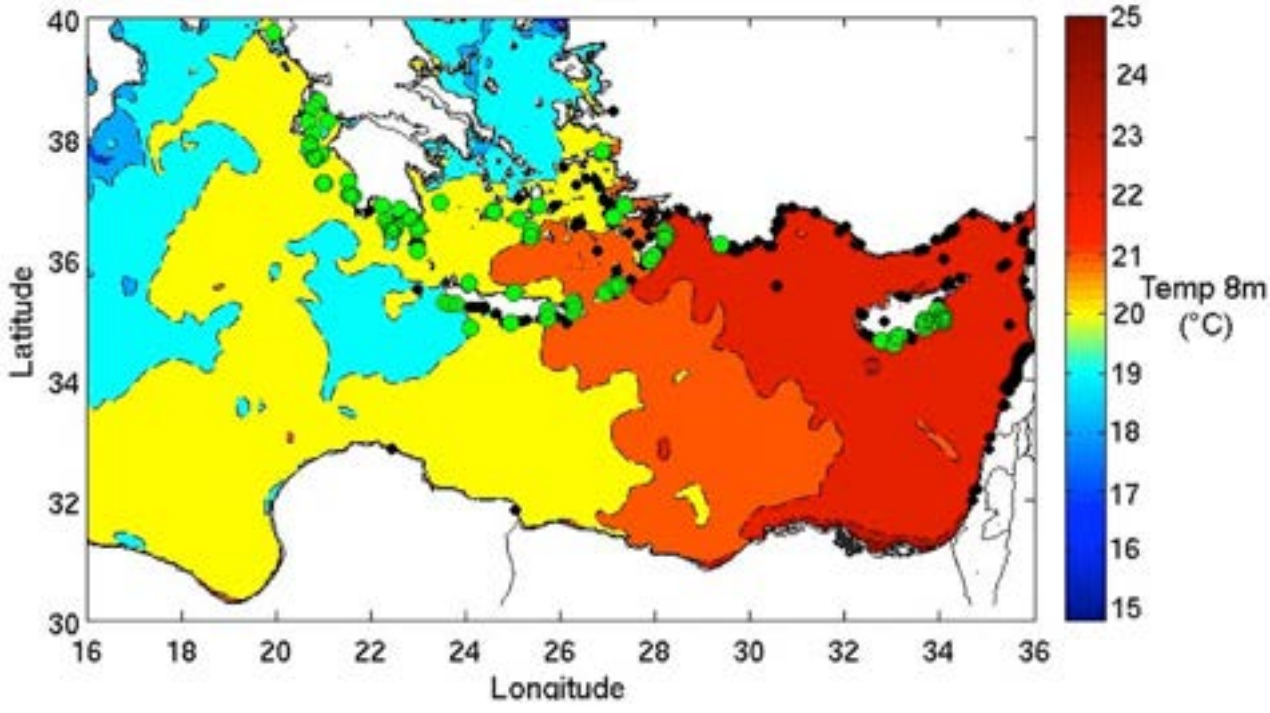

Figure 4.5.3. Eastern Mediterranean monthly sea surface temperature (8 m depth) for the month of May, year 2018, with isobars showing 1°C increments. Lionfish sightings for 1991–2018 plotted with black circles, and lionfish sightings of the following year (2019) highlighted in green.

the wider eastern Mediterranean area, whilst monthly time series were produced for the Mani Peninsula (Southernmost point of Ionian coastline) (22° E–23° E & 36° N–37° N), as lionfish sightings dramatically increased along the peninsula after 2018.

4.5.3. Results

4.5.3.1. Ionian sightings

From a total of over 650 distinct sightings identified by the literature review throughout the Mediterranean, at least 40 *Pmiles* individuals were observed in the Ionian, including the eight individuals (consisting of juveniles, adults, and pairs of adults) recorded *in-situ* for the present study (Table 4.5.1). The majority of sightings were obtained from citizen science initiatives (Dimitriadis et al. 2020). Only one sighting was recorded in 2016 (Lakonia Peninsula), one in 2018 (Kythera Island), and 33 separate locations were observed as having at least one *P. miles* individual present in 2019. Sightings after 2018 were well distributed with 20 individuals sighted on the mainland (Laconia Peninsula $n = 4$, Mani peninsula $n = 16$) and 20 individuals spread across eight islands. Considering the characteristic colouring and silhouette of the fish, and the large presence of fisherman and water-going tourists in the area it is unlikely that *P. miles* was widespread on the Greek Mainland before 2019, a notion corroborated by local fishermen. Due to the thermophilic nature of the invasive lionfish (Barker

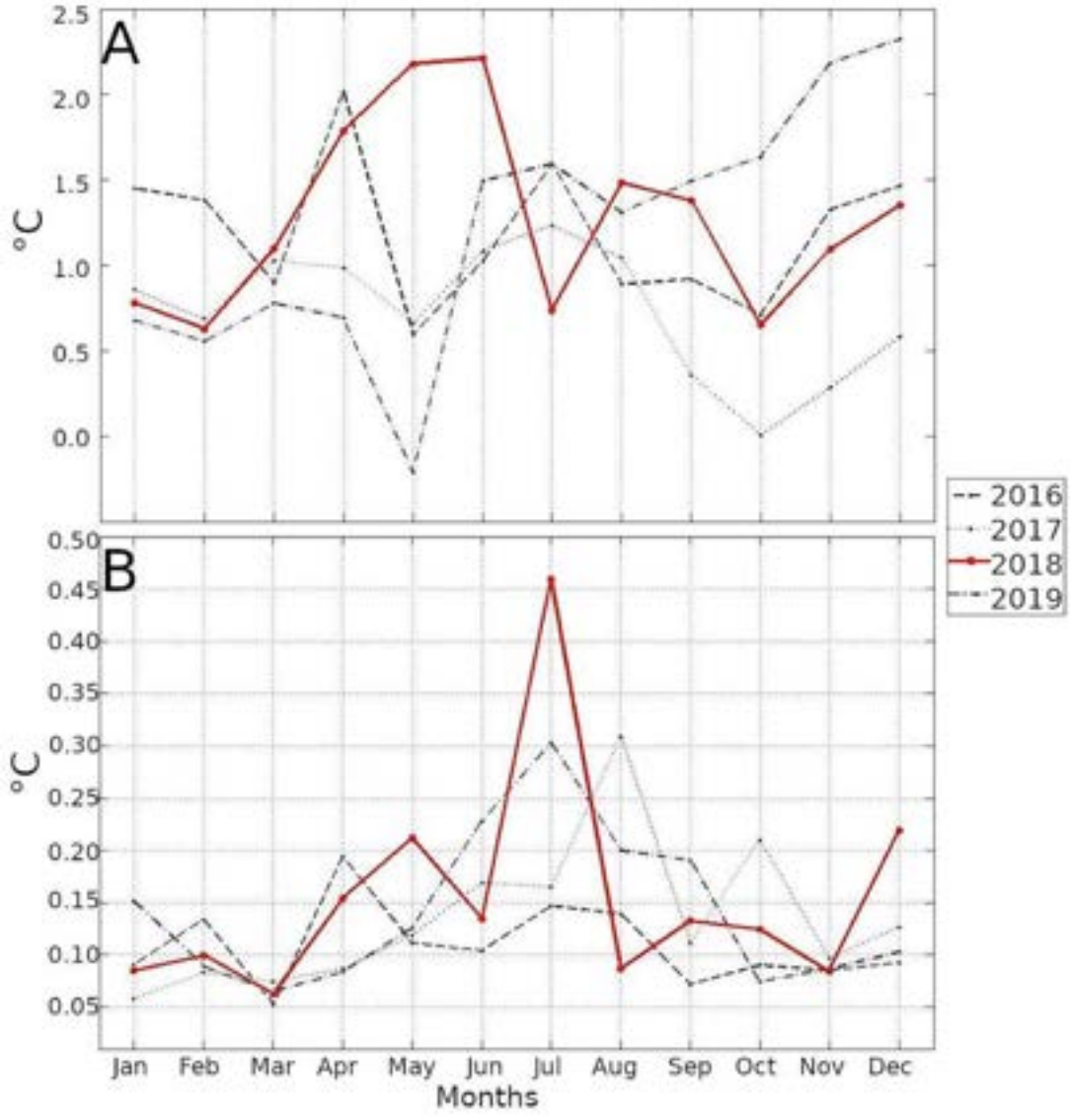

Figure 4.5.4. Time series of the monthly mean sea surface temperature anomaly (°C) for the Mani Peninsula area (Figure 4.5.1) for the period 2016–2019. The year 2018 is highlighted in red.

et al. 2018), these empirical observations suggest an excessive warming event in the upper layers of the wider area occurred during 2018 (possibly during spawning events), which may have encouraged the observation of large lionfish individuals in the Ionian during 2019, however further studies are required to identify temperature increases as the sole driver of lionfish range expansion in the Mediterranean.

4.5.3.2. Temperature field variability

The temperature field variability of the Eastern Mediterranean indicates a generally positive inter-annual temperature trend from 2014 both from the modelled data outputs and the remote sensing observations. The thermohaline variability in the upper layers of the Eastern Mediterranean can be partly assigned to air–sea heat exchanges, reduced upwelling events, alternations of the mesoscale circulation in the area and anomalies in large-scale atmospheric systems such as the North Atlantic Oscillation (Chronis et al. 2011; Kalimeris and Kolios 2019), and the positive inter-annual temperature trend is in agreement with previous studies on the sea surface temperature, and the upper layers of the Eastern Mediterranean, derived from satellite data (i.e. Pastor et al. 2019) and in-situ measurements (Kassis and Korres 2020) accordingly.

The analysis of the model output data indicated that from 2014, and up until 2017, the sea surface temperature increase is largely depicted in the surface layers (8 m) of the western part, especially in the South Aegean and Libyan Seas (Figure 4.5.1). This coincides with increased observations of *P. miles* in these areas for the same period (Figure 4.5.1). However, the most important finding is the positive temperature anomaly depicted during May 2018 when significant warming of the surfacer layers is presented across the wider area of the Eastern Mediterranean, followed by an intense cooling during the same month of 2019 (Figure 4.5.1). During the 2018 warming event, the water masses around the Mani Peninsula are approximately 2°C warmer than in 2017 at the 8 m depth level (Figure 4.5.1). This warm signal is also evident during the following months until the late autumn of 2018, with the exception of July.

The investigation into the remote sensed sea surface temperature fields depicted in general, as expected, similar warming trends with the model outputs since the former are utilised for the correction of the model's estimation for surface heat fluxes. Thus, we utilised the L4 satellite product as being a high-resolution reanalysis product used for the evaluation of the model outputs. Our analysis on the sea surface temperature anomaly based on pedant climatology presented intense warming over the eastern Mediterranean area, especially during 2016 and 2018 whilst an increasing trend, is also recorded towards the last months of 2019. More specifically, in 2016 positive anomalies were recorded during the whole year reaching particularly high values (1–3° C) in April 2016 across the wider eastern Mediterranean area. A similar trend, albeit with reduced values, is observed during 2017 when the higher values are mainly depicted in the Levantine Sea.

During 2018, an additional peak of sea surface warming was also depicted during the April–June period, with May 2018 as the epicentre when the positive anomaly exceeded 3.5°C in certain areas (Figure 4.5.2). During the first months of 2019, the positive trends remain mainly in the eastern Levantine and Aegean Sea whilst, in the southern and western areas of the eastern Mediterranean, negative anomalies that reach −1.5°C are also recorded. However, warming is re-established over the wider area during the second half of the year.

An examination of the monthly sea surface temperatures for the May 2018 warming peak indicates a strong positive correlation between the 20°C isobar extension into the Southern Ionian Sea and the lionfish observed during the following year (2019) (Figure 4.5.3). Interestingly, this figure highlights the difference in temperature between the cooler Northern Aegean (where no lionfish were observed in 2019) and the warmer Southern Ionian (which does experience a lionfish range expansion in 2019), however, it should be noted that correlation does not imply causation and other factors (e.g. prey availability, dispersal potential, predator-prey interactions) are also likely to contribute to lionfish spread throughout the Mediterranean (Diaz-Ferguson and Hunter 2019).

With regards to the Mani peninsula, positive monthly averaged surface temperature anomalies prevail during the examined 4-year period (Figure 4.5.4). Particularly during May–June of 2018, the performed analysis depicts a warming anomaly that exceeds 2.1° C, which especially for the case of May 2018 it is 1.5° C higher than the two previous years and more than 2°C compared to May 2019 (Figure 4.5.4). During the first half of 2019, the warming has decreased in the area however; it significantly rises in the second half reaching the highest values recorded in December 2019 (2.35°C) (Figure 4.5.4). In general, the statistical distribution of the daily values for this selected area presents homogeneity, which is reflected in the monthly STD variability that spans between 0.05 and slightly above 0.2°C apart from a few exceptions (Figure 4.5.4(B)). Such an example is July 2018, when a longitudinal temperature gradient is presented (not

shown here) and expressed by negative anomalies westward of Mani Peninsula and positive at the eastern side that results in increased standard deviation (Figure 4.5.4(B)).

A recent paper assessed the spread of lionfish sightings with the assumption that the 15.3°C winter sea surface temperature as the sole limiting factor of the range expansion (Dimitriadis et al. 2020). However, Poursanidis et al. (2020) indicated that of all the abiotic climatic parameters measured for their study, mean annual sea surface temperature (SST) contributed most to explaining model outputs of lionfish spread throughout the Mediterranean, with the SST of the coldest month contributing very little. These findings are echoed here, in that the colder the winter months of 2018 show lower variabilities with the previous years, and it is during the late spring period (May–June) that substantial changes in Southern Ionian surface temperatures were observed in relation to previous years. As spawning of *P. miles* in the Mediterranean is assumed to occur year-round with an increase of intensity during the summer months (Gardner et al. 2015), it is plausible that the 2018 late-spring excessive warming event coincided with an increase in the level of regional lionfish spawning in the Southern Ionian and facilitated the range expansion observed in 2019. However, further abiotic and biotic measurements are required before this hypothesis can be sustained, and the empirical results reported here should be considered in light of several limitations.

The two major limitations associated with the results presented above are: (1) whether a complete picture of lionfish distribution in the Eastern Mediterranean exists due to temporal and spatial biases of citizen science reporting data (possible false negative skew), and (2) whether other parameters which are not measured here (e.g. prey availability, larval dispersal potential, predator-prey interactions), could be (at least partially) responsible for lionfish expansion into the Ionian. The establishment of fixed monitoring station networks and common transect protocols would greatly assist in the assimilation of long-term, standardised datasets, thus enabling for future studies, enhanced trend analyses for lionfish distribution changes in the Eastern Mediterranean.

4.5.4. Conclusions

During 2019, the invasive lionfish established itself throughout the Ionian Sea, with a northward spread along the coast of the Mani Peninsula and the Greek mainland. The strong positive sea surface temperature anomaly that started in the spring of 2018 across a wider area of the southern Peloponnese, and especially along the Mani Peninsula, may have favoured the spawning and spread of *Pterois miles* into the Ionian Sea. It is plausible that these results could assist ecological modellers interested in defining the drivers of *P. miles* expansion in the Mediterranean, and regional stakeholders involved in the initiatives aimed at reducing the spread of this generalist predator in their waters.

Note

20. CMEMS product GLOBAL_ANALYSIS_FORECAST_PHY_001_024 (1/12° horizontal resolution).

References

Section 4.1. Sea-ice and ocean conditions surprisingly normal in the Svalbard-Barents Sea region after large sea-ice inflows in 2019

Aagaard K. 1989. A synthesis of the Arctic Ocean circulation. Rapports et proceès verbaux des réunions – Conseil international pour l'exploration de la mer. 188(1):11–22.

Aagaard K, Coachman LK, Carmack E. 1981. On the halocline of the Arctic Ocean. Deep Sea Res A Oceanogr Res Pap. 28 (6):529–545. DOI:10.1016/0198-0149(81)90115-1.

Aagaard K, Woodgate RA. 2001. Some thoughts on the freezing and melting of sea ice and their effects on the ocean. Ocean Model. 3(1–2):127–135. DOI:10.1016/S1463-5003(01)00005-1.

Årthun M, Eldevik T, Smedsrud LH, Skagseth Ø, Ingvaldsen RB. 2012. Quantifying the influence of Atlantic heat on Barents Sea ice variability and retreat. J Clim. 25 (13):4736–4743. DOI:10.1002/2016GL068421.

Carmack E, Polyakov I, Padman L, Fer I, Hunke E, Hutchings J, Jackson J, Kelly D, Kwok R, Layton C, et al. 2015. Toward quantifying the increasing role of oceanic heat in sea ice loss in the new Arctic. Bull Am Meteorol Soc. 96 (12):2079–2105. DOI:10.1175/BAMS-D-13-00177.1.

CMEMS ARCTIC_OMI_SI_extent_obs. 2020. Arctic monthly mean sea ice extent from satellite observations. https://marine.copernicus.eu/science-learning/ocean-monitoring-indicators/catalogue/.

Comiso JC. 2012. Large decadal decline of the Arctic multiyear ice cover. J Clim. 25:1176–1193. DOI:10.1175/JCLI-D-11-00113.1.

cryo.met.no. 2020. 'Arctic sea ice extent monthly time series' figure (daily updated). https://cryo.met.no/en/sea-ice-climate-indicator.

Ellingsen I, Slagstad D, Sundfjord A. 2009. Modification of water masses in the Barents Sea and its coupling to ice dynamics: a model study. Ocean Dyn. 59(6):1095–1108. DOI:10.1007/s10236-009-0230-5.

Fahrbach E, Meincke J, Østerhus S, Rohardt G, Schauer U, Tverberg V, Verduin J. 2001. Direct measurements of volume transports through Fram Strait. Polar Res. 20:217–224. DOI:10.1111/j.1751-8369.2001.tb00059.x.

Hattermann T, Isachsen PE, von Appen WJ, Albretsen J, Sundfjord A. 2016. Eddy-driven recirculation of Atlantic water in Fram Strait. Geophys Res Lett. 43(7):3406–3414.
Kimura N, Tateyama K, Sato K, Krishfield RA, Yamaguchi H. 2020. Unusual drift behaviour of multi-year sea ice in the Beaufort Sea during summer 2018. Polar Res. 39. DOI:10.33265/polar.v39.3617.
Kwok R. 2018. Arctic sea ice thickness, volume, and multiyear ice coverage: losses and coupled variability (1958–2018). Environ Res Lett 13:105005. DOI:10.1088/1748-9326/aae3ec.
Lavergne T, Eastwood S, Teffah Z, Schyberg H, Breivik L-A. 2010. Sea ice motion from low-resolution satellite sensors: an alternative method and its validation in the Arctic. J Geophys Res. 115:C10032. DOI:10.1029/2009JC005958.
Lavergne T, Sørensen AM, Kern S, Tonboe R, Notz D, Aaboe S, Bell L, Dybkjær G, Eastwood S, Gabarro C, et al. 2019. Version 2 of the EUMETSAT OSI SAF and ESA CCI sea-ice concentration climate data records. Cryosphere. 13:49–78. DOI:10.5194/tc-13-49-2019.
Laxon SW, Giles KA, Ridout AL, Wingham DJ, Willatt R, Cullen R, Kwok R, Schweiger A, Zhang J, Haas C, et al. 2013. Cryosat-2 estimates of Arctic sea ice thickness and volume. Geophys Res Lett. 40:732–737. DOI:10.1002/grl.50193.
Lind S, Ingvaldsen RB, Furevik T. 2016. Arctic layer salinity controls heat loss from deep Atlantic layer in seasonally ice-covered areas of the Barents Sea. Geophys Res Lett. 43(10):5233–5242. DOI:10.1002/2016GL068421.
Lind S, Ingvaldsen RB, Furevik T. 2018. Arctic warming hotspot in the northern Barents Sea linked to declining sea-ice import. Nat Clim Change. 8(7):634–639. DOI:10.1038/s41558-018-0205-y.
Lundesgaard Ø, Sundfjord A, Renner AH. 2021. Drivers of interannual sea ice concentration variability in the Atlantic water inflow region north of Svalbard. J Geophys Res Oceans. 126(4):e2020JC016522. DOI:10.1029/2020JC016522.
Marnela M, Rudels B, Houssais MN, Beszczynska-Möller A, Eriksson PB. 2013. Recirculation in the Fram Strait and transports of water in and north of the Fram Strait derived from CTD data. Ocean Sci. 9(3):499–519.
Meredith M, Sommerkorn M, Cassotta S, Derksen C, Ekaykin A, Hollowed A, Kofinas G, Mackintosh A, Melbourne-Thomas J, Muelbert MMC, et al. 2019. Polar regions. In: Pörtner H-O, Roberts DC, Masson-Delmotte V, Zhai P, Tignor M, Poloczanska E, Mintenbeck K, Alegría A, Nicolai M, Okem A, Petzold J, Rama B, Weyer NM, editors, IPCC special report on the ocean and cryosphere in a changing climate. In press.
Mosby H. 1938. Svalbard waters. Geofys Publ. 12:1–86.
Nansen F. 1902. Oceanography of the North Polar basin: The Norwegian North Polar expedition 1893–1896. Sci Results. 3(9):427.
Onarheim IH, Eldevik T, Smedsrud LH, Stroeve JC. 2018. Seasonal and regional manifestation of Arctic Sea ice loss. J Clim. 31:4917–4932. DOI:10.1175/JCLI-D-17-0427.1.
Renner AHH, Sundfjord A, Janout MA, Ingvaldsen RB, Beszczynska-Möller A, Pickart RS, Pérez-Hernández MD. 2018. Variability and redistribution of heat in the Atlantic water boundary current north of Svalbard. J Geophys Res Oceans. 123(9):6373–6391. DOI:10.1029/2018JC013814.
Rudels B, Jones EP, Schauer U, Eriksson P. 2004. Atlantic sources of the Arctic Ocean surface and halocline waters. Polar Res. 23(2):181–208.
Screen JA, Simmonds I. 2010. Increasing fall-winter energy loss from the Arctic Ocean and its role in Arctic temperature amplification. Geophys Res Lett. 37(16). DOI:10.1029/2010GL044136.
Smedsrud LH, Esau I, Ingvaldsen RB, Eldevik T, Haugan PM, Li C, Lien VS, Olsen A, Omar AM, Otterå OH, Risebrobakken B. 2013. The role of the Barents Sea in the Arctic climate system. Rev Geophys. 51(3):415–449. DOI:10.1002/rog.20017.
Wickström S, Jonassen MO, Vihma T, Uotila P. 2020. Trends in cyclones in the high-latitude North Atlantic during 1979–2016. Q J R Metereol Soc. 146(727):762–779.
Zamani B, Krumpen T, Smedsrud LH, Gerdes R. 2019. Fram Strait sea ice export affected by thinning: comparing high-resolution simulations and observations. Clim Dyn. 53(5–6):3257–3270.

Section 4.2. Monitoring storms by merged data sources for the Malta shelf area in 2019

Bartzokas A, Azzopardi J, Bertotti L, Buzzi A, Cavaleri L, Conte D, Davolio S, Dietrich S, Drago A, Drofa O, et al. 2010. The RISKMED project: philosophy, methods and results. Nat Hazards Earth Syst Sci. 10:1391–1401.
Capodici F, Cosoli S, Ciraolo G, Naselli C, Maltese A, Poulaine P-M, Drago A, Azzopardi J, Gauci A. 2019. Validation of HF radar sea surface currents in the Malta-Sicily channel. Remote Sens Environ. 225:65–76.
Chapman RD, Shay LK, Graber HC, Edson JB, Karachintsev A, Trump CL, Ross DB. 1997. On the accuracy of HF radar surface current measurements: intercomparisons with ship-based sensors. J Geophys Res Oceans. 102:18737–18748. DOI:10.1029/97JC00049.
Cosoli S, Ličer M, Vodopivec M, Malačič V. 2013. Surface circulation in the Gulf of Trieste (northern Adriatic Sea) from radar, model, and ADCP comparisons. J Geophys Res Oceans. 118:6183–6200. DOI:10.1002/2013JC009261.
Drago A, Azzopardi J, Gauci A, Tarasova R, Ciraolo G, Capodici F, Cosoli S, Gacic M. 2013. Sea surface currents by HF radar in the Malta channel. Rapp Comm Int Mer Medit. 40:144.
Drago A, Ciraolo G, Capodici F, Cosoli S, Gacic M, Poulain P-M, Tarasova R, Azzopardi J, Gauci A, Maltese A, et al. 2015. CALYPSO – an operational network of HF radars for the Malta-Sicily Channel. In: Dahlin H, Fleming NC, Petersson SE, editors, Proceedings of the Seventh International Conference on EuroGOOS; Oct 28–30, 2014, Lisbon. First published 2015. Eurogoos Publication No. 30. p. 167–176. ISBN 978-91-974828-9-9.
Emery BM, Washburn L, Harlan JA. 2004. Evaluating radial current measurements from CODAR high-frequency radars with moored current meters. J Atmos Ocean Technol. 21:1259–1271. DOI:10.1175/1520-0426(2004)021<1259:ERCMFC>2.0.CO;2.
Fernandes M, Fernandes C, Barroqueiro T, Agostinho P, Martins N, Alonso-Martirena A. 2018. Extreme wave

height events in Algarve (Portugal): comparison between HF radar systems and wave buoys. 5as Jornadas de Engenharia Hidrográfica, Lisboa. p. 222–225.
Lopez G, Conley DC. 2019. Comparison of HF radar fields of directional wave spectra against in situ measurements at multiple locations. J Mar Sci Eng. 7(8):271–271.
Lorente P, Sotillo MG, Aouf L, Amo-Baladrón A, Barrera E, Dalphinet A, et al. 2018. Extreme wave height events in NW Spain: a combined multi-sensor and model approach. Remote Sens. 10:1. DOI:10.3390/rs10010001.
Orasi A, Picone M, Drago A, Capodici F, Gauci A, Nardone G, Inghilesi R, Azzopardi J, Galea A, Ciraolo G. 2018. HF radar for wind waves measurements in the Malta-Sicily channel. Measurement. 128:446–454. DOI:10.1016/j.measurement.2018.06.060. ISSN 0263-2241. http://www.sciencedirect.com/science/article/pii/S0263224118305864.
Pascual A, Lana A, Troupin C, Ruiz S, Faugère Y, Escudier R, Tintoré J. 2015. Assessing SARAL/AltiKa delayed-time data in the coastal zone: comparisons with HF radar observations. Mar Geod. 8(sup1):260–276. DOI:10.1080/01490419.2015.1019656.
Reyes S, Cook NC, Gačić MS, Paduan M, Drago A, Cardin V. 2019. Sea surface circulation structures in the Malta-Sicily channel from remote sensing data. Water. 11:1589.
Roarty H, Cook T, Hazard L, George D, Harlan J, Cosoli S, Wyatt L, Alvarez Fanjul E, Terrill E, Otero M, Largier J. 2019. The global high frequency radar network. Front Mar Sci. DOI:10.3389/fmars.2019.00164. ISSN 2296-7745.
Tintoré J, Pinardi N, Álvarez-Fanjul E, Aguiar E, Álvarez-Berastegui D, Bajo M, Balbin R, Bozzano R, Nardelli BB, Cardin V, Casas B. 2019. Challenges for sustained observing and forecasting systems in the Mediterranean Sea. Front Mar Sci. DOI:10.3389/fmars.2019.00568.
Villa L, Nieddu C, Marsiaj P, Corsini S, Orasi A, Mariani S, Trovatore E, Pedemonte L, Gallino S, Sacchetti D, et al. 2008. Chapter 4: numerical modelling for weathrrouting. In: Delitala A, Speranza A, editors, WERMED Weatherrouting dans la Méditerranée – results of the project. p. 53–68.

Section 4.3. The November 2019 record high water levels in Venice, Italy

Arns A, Wahl T, Wolff C, Vafeidis AT, Haigh ID, Woodworth P, Niehüser S, Jensen J. 2020. Non-linear interaction modulates global extreme sea levels, coastal flood exposure, and impacts. Nat Commun. 11:1918. DOI:10.1038/s41467-020-15752-5.
Bajo M, Međugorac I, Umgiesser G, Orlić M. 2019. Storm surge and seiche modelling in the Adriatic Sea and the impact of data assimilation. Q J R Meteorol Soc. 145:2070–2084. DOI:10.1002/qj.3544.
Bromwich DH. 1989. An extraordinary katabatic wind regime at Terra-Nova Bay, Antarctica. Mon Wea Rev. 117:688–695.
Cavaleri L. 2000. The oceanographic tower Acqua Alta – activity and prediction of sea states at Venice. Coastal Eng. 39:29–70. DOI:10.1016/S0378-3839(99)00053-8.
Clementi E, Oddo P, Drudi M, Pinardi N, Korres G, Grandi A. 2017. Coupling hydrodynamic and wave models: first step and sensitivity experiments in the Mediterranean Sea. Ocean Dyn. DOI:10.1007/s10236-017-1087-7.
Clementi E, Pistoia J, Delrosso D, Mattia G, Fratianni C, Storto A, Ciliberti S, Lemieux B, Fenu E, Simoncelli S, et al. 2017. A 1/24 degree resolution Mediterranean analysis and forecast modeling system for the Copernicus Marine Environment Monitoring Service. Extended abstract to the 8th EuroGOOS Conference, Bergen.
de Kloe J, Stoffelen A, Verhoef A. 2017. Improved use of scatterometer measurements by using stress-equivalent reference winds. J Sel Top Appl Earth Obs Remote Sens. 10(5):2340–2347. DOI:10.1109/JSTARS.2017.2685242.
De Zolt S, Lionello P, Nuhu A, Tomasin A. 2006. The disastrous storm of 4 November 1966 on Italy. Nat Hazards Earth Syst Sci. 6:861–879. DOI:10.5194/nhess-6-861-2006.
Dobricic S, Pinardi N. 2008. An oceanographic three-dimensional variational data assimilation scheme. Ocean Model. 22(3–4):89–105.
Egbert G, Erofeeva S. 2002. Efficient inverse modeling of barotropic ocean tides. J Atmos Ocean Tech. 19:183–204.
The ISMAR Team, Cavaleri L, Bajo M, Barbariol F, Bastianini M, Benetazzo A, Bertotti L, Chiggiato J, Ferrarin C, Trincardi F, Umgiesser G. 2020. The 2019 flooding of Venice and its implications for future predictions. Oceanography. 33(1):42–49. DOI:10.5670/oceanog.2020.105.
Marcos M, Tsimplis MN, Shaw AGP. 2009. Sea level extremes in Southern Europe. J Geophys Res. 114:C01007. DOI:10.1029/2008JC004912.
Moore GW, Renfrew IA. 2005. Tip jets and barrier winds: a QuikSCAT climatology of high wind speed events around Greenland. J Clim. 18:3713–3725. DOI: 10.1175/JCLI3455.1.
Orlić M, Kuzmić M, Pasarić Z. 1994. Response of the Adriatic Sea to the bora and sirocco forcing. Cont Shelf Res. 14:91–116. DOI:10.1016/0278-4343(94)90007-8.
Pasarić Z, Belušić D, Klaić ZB. 2007. Orographic influences on the Adriatic sirocco wind. Ann Geophys. 25:1263–1267. DOI:10.5194/angeo-25-1263-2007.
Pinardi N, Allen I, Demirov E, De Mey P, Korres G, Lascaratos A, Le Traon P-Y, Maillard C, Manzella G, Tziavos C. 2003. The Mediterranean ocean forecasting system: first phase of implementation (1998–2001). Ann Geophys. 21:3–20. DOI:10.5194/angeo-21-3-2003.
Pinardi N, Coppini G. 2010. Operational oceanography in the Mediterranean Sea: the second stage of development. Ocean Sci. 6:263–267.
Pirazzoli PA, Tomasin A. 2002. Recent evolution of surge-related events in the northern Adriatic area. J Coastal Res. 18:537–554.
Stoffelen A, Verspeek J, Vogelzang J, Verhoef A. 2017. The CMOD7 geophysical model function for ASCAT and ERS wind retrievals. J Sel Top Applied Earth Obs Remote Sens. 10(5):2123–2134. DOI:10.1109/JSTARS.2017.2681806.
Storto A, Masina S, Navarra A. 2015. Evaluation of the CMCC Eddy-permitting global ocean physical reanalysis system (C-GLORS, 1982–2012) and its assimilation components. QJR Meteorol Soc. 142(695):738–758.

Tonani M, Teruzzi A, Korres G, Pinardi N, Crise A, Adani M, Oddo P, Dobricic S, Fratianni C, Drudi M, et al. 2014. The Mediterranean Monitoring and Forecasting Centre, a component of the MyOcean system. In: Dahlin H, Fleming NC and Petersson SE, editors, Proceedings of the Sixth International Conference on EuroGOOS Oct 4–6, 2011, Sopot. First published 2014. Eurogoos Publication no. 30. ISBN 978-91-974828-9-9.F.

Section 4.4. Extreme waves and low sea level during the storm in the Gulf of Bothnia, Baltic Sea

Berg P, Poulsen JW. 2012. Implementation details for HBM. DMI Technical Report No. 12-11. http://beta.dmi.dk/fileadmin/Rapporter/TR/tr12-11.pdf.

Björkqvist JV, Lukas I, Alari V, van Vledder GP, Hulst S, Pettersson H, Behrens A, Männik A. 2018. Comparing a 41-year model hindcast with decades of wave measurements from the Baltic Sea. Ocean Eng. 152:57–71. DOI:10.1016/j.oceaneng.2018.01.048.

Björkqvist JV, Rikka S, Alari V, Männik A, Tuomi L, Pettersson H. 2020. Wave height return periods from combined measurement-model data: a Baltic Sea case study. Nat Hazards Earth Syst Sci. 20(12):3593–3609.

Björkqvist J-V, Tuomi L, Tollman N, Kangas A, Pettersson H, Marjamaa R, Jokinen H, Fortelius C. 2017. Brief communication: characteristic properties of extreme wave events observed in the northern Baltic Proper, Baltic Sea. Nat Hazards Earth Syst Sci. 17:1653–1658. DOI:10.5194/nhess-17-1653-2017.

Carstensen J, Conley DJ. 2019. Baltic Sea hypoxia takes many shapes and sizes. Limnol Oceanogr Bull. 28:125–129. DOI:10.1002/lob.10350.

Cavaleri L, Bajo M, Barbariol F, Bastianini M, Benetazzo A, Bertotti L, Chiggiato J, Davolio S, Ferrarin C, Magnusson L, et al. 2019. The October 29, 2018 storm in Northern Italy – an exceptional event and its modeling. Prog Oceanogr. 178:102178. DOI:10.1016/j.pocean.2019.102178.

CC3S ERA5. 2017. Copernicus Climate Change Service (C3S), 2017. ERA5: fifth generation of ECMWF atmospheric reanalyses of the global climate. Copernicus Climate Change Service Climate Data Store (CDS) [accessed 2020 May 20]. https://cds.climate.copernicus.eu/cdsapp#!/home.

Ekman M, Mäkinen J. 1996. Mean sea surface topography in the Baltic Sea and its transition area to the North Sea: a geodetic solution and comparisons with oceanographic models. J Geophys Res Oceans. 101(C5):11993–11999. DOI:10.1029/96jc00318.

Granskog M, Kaartokallio H, Kuosa H, Thomas DN, Vainio J. 2006. Sea ice in the Baltic Sea – a review. Estuarine Coastal Shelf Sci. 70:145–160. DOI:10.1016/j.ecss.2006.06.001.

Honkola ML, Kukkurainen N, Saukkonen L, Petäjä A, Karasjärvi J, Riihisaari T, Tervo R, Visa M, Hyrkkänen J, Ruuhela R. 2013. The finnish meteorological institute: final report for the open data project. Finnish Meteorological Institute, Helsinki, Finland.

Hünicke B, Zorita E. 2008. Trends in the amplitude of Baltic Sea level annual cycle. Tellus. 60A:154–164. DOI:10.1111/j.1600-0870.2007.00277.x.

IPCC. 2018. Global warming of 1.5°C. An IPCC special report on the impacts of global warming of 1.5°C above pre-industrial levels and related global greenhouse gas emission pathways, in the context of strengthening the global response to the threat of climate change, sustainable development, and efforts to eradicate poverty, Masson-Delmotte V, Zhai P, Pörtner H-O, Roberts D, Skea J, Shukla PR, Pirani A, Moufouma-Okia W, Péan C, Pidcock R, Connors S, Matthews JBR, Chen Y, Zhou X, Gomis MI, Lonnoy E, Maycock T, Tignor M, Waterfield T, editors. In Press.

Jakobsson M, Stranne C, O'Regan M, Greenwood SL, Gustafsson B, Humborg C, Weidner E. 2019. Bathymetric properties of the Baltic Sea. Ocean Sci. 15:905–924. DOI:10.5194/os-15-905-2019.

Komen GJ, Cavaleri L, Donelan M, Hasselmann K, Hasselmann S, Janssen PAEM. 1994. Dynamics and modelling of ocean waves. Cambridge: Cambridge University Press; p. 554.

Kudryavtseva N, Räämet A, Soomere T. 2020. Coastal flooding: joint probability of extreme water levels and waves along the Baltic Sea coast. In: Malvárez G, Navas, F, editors, Proceedings from the International Coastal Symposium (ICS) 2020 (Seville, Spain). Journal of Coastal Research, Special Issue No. 95. p. 1–5. Coconut Creek (FL), ISSN 0749-0208.

Lehmann A, Post P. 2015. Variability of atmospheric circulation patterns associated with large volume changes of the Baltic Sea. Adv Sci Res. 12:219–225. DOI:10.5194/asr-12-219-2015.

Madsen KS, Høyer JL, Suursaar Ü, She J, Knudsen P. 2019. Sea level trends and variability of the Baltic Sea from 2D statistical reconstruction and altimetry. Front Earth Sci. 7:243. DOI:10.3389/feart.2019.00243.

Mailier PJ, Stephenson DB, Ferro CAT, Hodges KI. 2006. Serial clustering of extratropical cyclones. Mon Weather Rev. 134:2224–2240. DOI:10.1175/MWR3160.1.

Maljutenko I, Hassellöv I-M, Eriksson KM, Ytreberg E, Yngsell D, Johansson L, Jalkanen J-P, Kõuts M, Kasemets M, Moldanova J, et al. 2021. Modelling spatial dispersion of contaminants from shipping lanes in the Baltic Sea. Environ Pollut. [under review].

Meier HEM, Döscher R, Halkka A. 2004. Simulated distributions of Baltic sea-ice in warming climate and consequences for the winter habitat of the Baltic ringed seal. Ambio. 33:249–256. DOI:10.1579/0044-7447-33.4.249.

Olofsson M, Klawonn I, Karlson B. 2020. Nitrogen fixation estimates for the Baltic Sea indicate high rates for the previously overlooked Bothnian Sea. Ambio. DOI:10.1007/s13280-020-01331-x.

Post P, Kõuts T. 2014. Characteristics of cyclones causing extreme sea levels in the northern Baltic Sea. Oceanlogia. 56:241–258. DOI:10.5697/oc.56-2.241.

Raudsepp U, Toompuu A, Kõuts T. 1999. A stochastic model for the sea level in the Estonian coastal area. J Marine Syst. 22:69–87. doi:10.1016/S0924-7963(99)00031-7.

Raudsepp U, Uiboupin R, Laanemäe K, Maljutenko I. 2020. Geographical and seasonal coverage of sea ice in the Baltic Sea. In: Copernicus Marine Service Ocean State report, issue 4. J Oper Oceanogr. 13(sup1):s111–s115. DOI:10.1080/1755876X.2020.1785097.

Sepp M, Post P, Mändla K, Aunap R. 2018. On cyclones entering the Baltic Sea region. Boreal Env Res. 23:1–14.
She J, Viktorsson L. 2018. Extremes of low sea level in the Northern Baltic Sea. In: Copernicus Marine Service Ocean State report, issue 2. J Oper Oceanogr. 11(sup1): s131–s135. DOI:10.1080/1755876X.2018.1489208.
Tuomi L, Kanarik H, Björkqvist J-V, Marjamaa R, Vainio J, Hordoir R, Höglund A, Kahma KK. 2019. Impact of ice data quality and treatment on wave hindcast statistics in seasonally ice-covered seas. Front Earth Sci. 7:1–16. DOI:10.3389/feart.2019.00166.
Tuomi L, She J, Lorkowski I, Axell L, Lagemaa P, Schwichtenberg F, Huess V. 2017. Overview of CMEMS BAL MFC service and developments. Proceedings of the Eight EuroGOOS International Conference. p. 261–267. ISBN 978-2-640 9601883-3-2.
Wolski T, Winiewski B, Giza A, Kowalewska-Kalkowska H, Boman H, Grabbi-Kaiv S, Hammarklint T, Holfort J, Lydeikait Ž. 2014. Extreme sea levels at selected stations on the Baltic Sea coast. Oceanologia. 56(2):259–290.
Wolski T, Wiśniewski B. 2020. Geographical diversity in the occurrence of extreme sea levels on the coasts of the Baltic Sea. J Sea Res. 159:101890. DOI:10.1016/j.seares.2020.101890.
von Schuckmann K, Le Traon P-Y, Smith N, Pascual A, Brasseur P, Fennel K, Djavidnia S. 2018. Copernicus Marine Service Ocean State report, issue 2. J Oper Oceanogr. 11(sup1):s1–s142. DOI:10.1080/1755876X.2018.1489208.

Section 4.5. Establishment of Pterois miles (Bennett, 1828) in the Ionian Sea

Bardamaskos G, Tsiamis K, Panayotidis P, Megalofonou P. 2009. New records and range expansion of alien fish and macroalgae in Greek waters (south-east Ionian Sea). Mar Biodivers Rec. 2. DOI:10.1017/s1755267209001055.
Bariche M, Kleitou P, Kalogirou S, Bernardi G. 2017. Genetics reveal the identity and origin of the lionfish invasion in the Mediterranean Sea. Sci Rep. 7(1):6782.
Barker BD, Horodysky AZ, Kerstetter DW. 2018. Hot or not? Comparative behavioral thermoregulation, critical temperature regimes, and thermal tolerances of the invasive lionfish Pterois sp. versus native western North Atlantic reef fishes. Biol Invasions. 20(1):45–58.
Benkwitt CE. 2015. Non-linear effects of invasive lionfish density on native coral-reef fish communities. Biol Invasions. 17(5):1383–1395. DOI:10.1007/s10530-014-0801-3.
Buongiorno Nardelli B, Tronconi C, Pisano A, Santoleri R. 2013. High and ultra-high resolution processing of satellite Sea surface temperature data over Southern European seas in the framework of MyOcean project. Remote Sens Environ. DOI:10.1016/j.rse.2012.10.012. ISSN 0034-4257.
Capezzuto F, Carlucci R, Maiorano P, Sion L, Battista D, Giove A, Indennidate A, Tursi A, D'Onghia G. 2010. The bathyal benthopelagic fauna in the north-western Ionian Sea: structure, patterns and interactions. Chem Ecol. 26 (sup1):199–217. DOI:10.1080/02757541003639188.
Chronis T, Raitsos DE, Kassis D, Sarantopoulos A. 2011. The summer North Atlantic Oscillation influence on the eastern Mediterranean. J Clim. 24(21):5584–5596.
Corriero G, Pierri C, Accoroni S, Alabiso G, Bavestrello G, Barbone E, Bastianini M, Bazzoni AM, Bernardi Aubry F, Boero F, et al. 2016. Ecosystem vulnerability to alien and invasive species: a case study on marine habitats along the Italian coast. Aquat Conserv Mar Freshw Ecosyst. 26 (2):392–409. DOI:10.1002/aqc.2550.
Diamantopoulou P, Voudouris K. 2008. Optimization of water resources management using SWOT analysis: the case of Zakynthos Island, Ionian Sea, Greece. Environ Geol. 54(1):197–211. DOI:10.1007/s00254-007-0808-5.
Diaz-Ferguson EE, Hunter ME. 2019. Life history, genetics, range expansion and new frontiers of the lionfish (Pterois volitans, Perciformes: Pteroidae) in Latin America. Reg Stud Mar Sci. 31:100793.
Dimitriadis C, Galanidi M, Zenetos A, Corsini-Foka M, Giovos I, Karachle PK, Fournari-Konstantinidoy I, Kytinou E, Issaris Y, Azzurro E, et al. 2020. Updating the occurrences of Pterois miles in the Mediterranean Sea, with considerations on thermal boundaries and future range expansion. Mediterr Mar Sci. 21(1):62. DOI:10.12681/mms.21845.
Gardner PG, Frazer TK, Jacoby CA, Yanong RPE. 2015. Reproductive biology of invasive lionfish (Pterois spp.). Front Mar Sci. 2:7. DOI:10.3389/fmars.2015.00007.
Green SJ, Akins JL, Maljkovic A, Cô té IM, Jane Goldstien S. 2012. Invasive Lionfish drive Atlantic coral reef fish declines. PLoS ONE. 7(3):32596. DOI:10.1371/journal.pone.0032596.
Kalimeris A, Kolios S. 2019. TRMM-based rainfall variability over the central Mediterranean and its relationships with atmospheric and oceanic climatic modes. Atmos Res. 230:104649.
Kassis D, Korres G. 2020. Hydrography of the Eastern Mediterranean basin derived from argo floats profile data. Deep Sea Res Part II. 171:104712.
Katsanevakis S, Coll M, Piroddi C, Steenbeek J, Ben Rais Lasram F, Zenetos A, Cardoso AC. 2014. Invading the Mediterranean Sea: biodiversity patterns shaped by human activities. Front Mar Sci. 1:32.
Kletou D, Hall-Spencer JM, Kleitou P. 2016. A lionfish (*Pterois miles*) invasion has begun in the Mediterranean Sea. Mar Biodivers Rec. 9(1):46. DOI:10.1186/s41200-016-0065-y.
Lesser MP, Slattery M. 2011. Phase shift to algal dominated communities at mesophotic depths associated with lionfish (Pterois volitans) invasion on a Bahamian coral reef. Biol Invasions. 13(8):1855–1868. DOI:10.1007/s10530-011-0005-z.
Mitsou E, Maximiadi M. 2018. New records of *Lagocephalus sceleratus* (Gmelin, 1789), *Cassiopeia andromeda* (Forsskål, 1775) and *Pterois miles* (Bennett, 1828) in Greek MSFD areas. In: new Mediterranean biodiversity records (Yokes et al.). Mediterr Mar Sci. 19 (3):673–689.
Pastor F, Valiente JA, Palau JL. 2019. Sea surface temperature in the Mediterranean: trends and spatial patterns (1982–2016). In: Meteorology and climatology of the Mediterranean and Black Seas. Cham: Birkhäuser; p. 297–309.
Piroddi C, Giovanni B, Villy C. 2010. Effects of local fisheries and ocean productivity on the northeastern Ionian Sea

ecosystem. Ecol Modell. 221(11):1526–1544. DOI:10.1016/j.ecolmodel.2010.03.002.

Politou CY, Kavadas S, Mytilineou C, Tursi A, Carlucci R, Lembo G. 2003. Fisheries resources in the deep waters of the eastern Mediterranean (Greek Ionian Sea). J Northwest Atl Fish Sci. 31:35–46. DOI:10.2960/J.v31.a3.

Poursanidis D, Kalogirou S, Azzurro E, Parravicini V, Bariche M, zu Dohna H. 2020. Habitat suitability, niche unfilling and the potential spread of Pterois miles in the Mediterranean Sea. Mar Pollut Bull. 154:111054. DOI:10.1016/j.marpolbul.2020.111054.

Savva I, Chartosia N, Antoniou C, Kleitou P, Georgiou A, Stern N, Hadjioannou L, Jimenez C, Andreou V, Hall-Spencer JM, Kletou D. 2020. They are here to stay: the biology and ecology of lionfish (*Pterois miles*) in the Mediterranean Sea. J Fish Biol. 97(1):148–162. DOI:10.1111/jfb.14340.

Tiago P, Pereira HM, Capinha C. 2017. Using citizen science data to estimate climatic niches and species distributions. Basic Appl Ecol. 20:75–85. DOI:10.1016/j.baae.2017.04.001.

Tzanatos E, Dimitriou E, Papaharisis L, Roussi A, Somarakis S, Koutsikopoulos C. 2006. Principal socio-economic characteristics of the Greek small-scale coastal fishermen. Ocean Coast Manag. 49(7–8):511–527. DOI:10.1016/j.ocecoaman.2006.04.002.

Vavasis C, Simotas G, Spinos E, Konstantinidis E, Minoudi S, Triantafyllidis A, Perdikaris C. 2019. Occurrence of Pterois miles in the Island of Kefalonia (Greece): the northernmost dispersal record in the Mediterranean Sea. Thalass Int J Mar Sci. 1–5.